CALIFORNIA INSTITUTE OF TECHNOLOGY

EARTHQUAKE ENGINEERING RESEARCH LABORATORY

THREE-DIMENSIONAL NONLINEAR INELASTIC ANALYSIS OF STEEL MOMENT-FRAME BUILDINGS DAMAGED BY EARTHQUAKE EXCITATIONS

BY

ANDERS E. CARLSON

REPORT NO. EERL 99-02

A REPORT ON RESEARCH SUPPORTED BY GRANTS FROM CUREE AND THE PEER/PGE RESEARCH PROGRAM

PASADENA, CALIFORNIA
1999

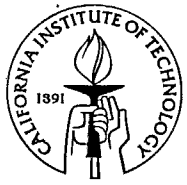

THIS INVESTIGATION WAS SUPPORTED IN PART BY GRANTS FROM CUREE AND THE PEER-PGE RESEARCH PROGRAM UNDER THE SUPERVISION OF JOHN F. HALL. ANY OPINIONS, FINDINGS, CONCLUSIONS OR RECOMMENDATIONS EXPRESSED IN THIS PUBLICATION ARE THOSE OF THE AUTHORS AND DO NOT NECESSARILY REFLECT THE VIEWS OF THE SPONSORING ORGANIZATIONS.

Three-Dimensional Nonlinear Inelastic Analysis of Steel Moment-Frame Buildings Damaged by Earthquake Excitations

Thesis by
Anders E. Carlson

In Partial Fulfillment of the Requirements
for the Degree of
Doctor of Philosophy

California Institute of Technology
Pasadena, California

1999

(Defended April 2, 1999)

Acknowledgements

It has been a great privelege to have John Hall as my advisor. He encouraged me to work on what I wanted to work on. He always had a well-thought response to each of my questions, and usually was available more hours to answer questions than I was around to ask them. His insights and recommendations have greatly affected the quality of this work, and his editing was crucial to the structure and completion of this thesis. He's not a bad landlord, either.

I am grateful to have been a recipient of the Harold Hellwig Graduate Fellowship in Structural Engineering.

I would like to thank my committee for taking the time to read this voluminous work and suggest changes: Drs. J. Beck, T. Heaton, W. D. Iwan, and G. Ravichandran. I am indebted to Cecelia Lin for the wonderful figures she produced for this thesis. These are figures 2.1, 2.2, 2.4, 2.5, 2.6, 2.7, 2.9, 2.12, 2.13, 4.3, and 4.11. All other figures were created by the author using MATLAB or AutoSketch.

I am grateful to the gods of room assignments who gave me my officemates for my first three years: Scott May, David Polidori, and Michael Vanik. Their help the first two years made passing candidacy possible and their continuing friendship and support are greatly appreciated. I would also like to thank the friendship of the basement dwellers of SOPS. They have made Caltech a fun place to work hard. Two non-basement students who have shared many hours at the Red Door and ECF with me helped make Caltech downright silly: Russell Todres and Nancy Winfree.

Above all, I acknowledge the incredible support of my wife Lyn Yasumura. She made many tremendous sacrifices over the years to make this work possible. While writing my thesis, we looked for a house, bought a house, and moved. I looked for a job, accepted two, and started both jobs. Lyn was pregnant, gave birth to our wonderful son Maxwell, and took care of him while maintaining her crazy schedule as an obstetrician. If "life is what happens to you when you're busy making other plans (John Lennon)," then I guess we were living the highlife through all this. Thank you for keeping us sane, and thank you for your unlimited patience and love. It is appreciated more than I can express.

Abstract

The Northridge earthquake of January 17, 1994, highlighted the two previously known problems of premature fracturing of connections and the damaging capabilities of near-source ground motion pulses. Large ground motions had not been experienced in a city with tall steel moment-frame buildings before. Some steel buildings exhibited fracture of welded connections or other types of structural degradation.

A sophisticated three-dimensional nonlinear inelastic program is developed that can accurately model many nonlinear properties commonly ignored or approximated in other programs. The program can assess and predict severely inelastic response of steel buildings due to strong ground motions, including collapse.

Three-dimensional fiber and segment discretization of elements is presented in this work. This element and its two-dimensional counterpart are capable of modeling various geometric and material nonlinearities such as moment amplification, spread of plasticity and connection fracture. In addition to introducing a three-dimensional element discretization, this work presents three-dimensional constraints that limit the number of equations required to solve various three-dimensional problems consisting of intersecting planar frames.

Two buildings damaged in the Northridge earthquake are investigated to verify the ability of the program to match the level of response and the extent and location of damage measured. The program is used to predict response of larger near-source ground motions using the properties determined from the matched response.

A third building is studied to assess three-dimensional effects on a realistic irregular building in the inelastic range of response considering earthquake directivity. Damage levels are observed to be significantly affected by directivity and torsional response.

Several strong recorded ground motions clearly exceed code-based levels. Properly designed buildings can have drifts exceeding code specified levels due to these ground motions. The strongest ground motions caused collapse if fracture was included in the model. Near-source ground displacement pulses can cause columns to yield prior to weaker-designed beams. Damage in tall buildings correlates better

with peak-to-peak displacements than with peak-to-peak accelerations.

Dynamic response of tall buildings shows that higher mode response can cause more damage than first mode response. Leaking of energy between modes in conjunction with damage can cause torsional behavior that is not anticipated.

Various response parameters are used for all three buildings to determine what correlations can be made for inelastic building response. Damage levels can be dramatically different based on the inelastic model used. Damage does not correlate well with several common response parameters.

Realistic modeling of material properties and structural behavior is of great value for understanding the performance of tall buildings due to earthquake excitations.

Contents

List of Figures

List of Tables

Chapter 1

Introduction

The Northridge earthquake of January 17, 1994, produced some of the strongest ground motions ever recorded in California even though the magnitude (M_L = 6.7) was only moderate. The strongest shaking was recorded in areas with little building development. Smaller ground motions did affect areas with a high density of development and some types of modern buildings exhibited unexpected degradation mechanisms, such as the fracture of welded connections in steel frames (Bertero, Anderson, and Krawinkler 1994).

Steel moment frame buildings have been considered to be the most ductile type of construction, so codes allowed engineers to design for elastic displacements due to one-twelfth of the expected energy demand on a building. This design level corresponds to earthquakes having a 10% probability of exceedance in 50 years. The large reduction in demand is based on the assumption that a building possesses enough ductility to dissipate the expected energy demand through inelastic deformations (SEAOC 1990). The unexpected brittle behavior of beam-to-column connections in these frames caused great concern in the engineering community. Many researchers and practitioners have investigated new connections and ways of repairing existing connections. Other researchers and practitioners have developed new analytical tools to predict or assess damage to steel moment frame buildings.

The philosophy of the building code in the U.S. has historically been to protect lives by avoiding structural collapse during strong earthquakes. However, much

evidence now exists that ground shaking from earthquakes can be more severe than what is represented in the building code (Hall, Heaton, Halling, and Wald 1995). Large, rapid ground displacements produced in the region toward which the fault is rupturing (near-source effects) can be particularly damaging for flexible structures, and thus their potential for causing collapse is a concern. Amplitudes of near-source ground displacements, both fault-parallel and fault-normal components, can be on the order of ten meters for magnitude 7 and larger earthquakes. Occurrence of a large earthquake close to a major city is inevitable (Heaton 1997).

There is still a debate over the level of strong ground motions to be used in building design. Other investigators claim that the simulated ground motions used in Hall, Heaton, Halling, and Wald (1995) exceed measured ground motions and that we should rely on existing records only. The simulations used in that study were scaled *down* from the Landers earthquake of 1992. One investigator told the author that he discarded results that suggested collapse because he thought the engineering community would not believe such results.

While there is great dissent among researchers as to how strong design ground motions should be and as to the extent of possible damage (collapse), they are all in agreement as to the need for more sophisticated analysis techniques. The reviewer of research on seismic response of structures at the 1997 NEHRP Northridge earthquake research conference concluded, "Some investigators question the rationality of current code design procedures based solely on implicit life safety considerations and suggest application of more sophisticated analysis techniques for design of major buildings in near source regions" (Naeim 1997). The reviewer of research on steel buildings concurred, stating it is "clear that the ability to analyze structural behavior may not be as good as many engineers have expected. It is clear that models often need to consider a wide range of factors such as composite action, P-Δ effects, nonstructural walls, and offsets in geometry if models are to accurately predict structural behavior. Engineers need to examine the validity of their models carefully if the analyses are to provide useful results" (Roeder 1997).

There is a need for increasingly sophisticated analysis techniques to evaluate the

safety of buildings that could be subjected in the future to ground motions more severe than anticipated by design codes. Such assessment techniques should have the capability of predicting the likelihood of collapse and so must include all features of a structure that contribute to its performance.

1.1 Objectives

The objectives of this work are to develop a sophisticated three-dimensional analytical program capable of modeling structural behavior in severely inelastic response and to use the program to assess and predict response of several buildings. The goal is to show that realistic modeling of material properties and structural behavior is of great value for understanding the performance of tall buildings due to earthquake excitations. Realistic modeling includes slab and non-structural stiffness contributions and panel zone and foundation flexibility among other commonly ignored effects.

In order to analyze common frame layouts of three-dimensional structures, a three-dimensional element needs to be developed that is discretized along its length into segments and through its cross section into fibers. This element should be capable of modeling various geometric and material nonlinearities such as moment amplification, spread of plasticity and connection fracture.

Objectives of the analysis in this work include:

- Investigate two buildings damaged by the Northridge earthquake that have recorded roof displacements and reported connection fractures. Verify the accuracy of this program to predict the level of response and extent and location of damage observed.

- Upon verification, use the program to assess effects of larger near-source earthquake records on these buildings.

- Use the program to determine what correlations can be made between various response parameters from different building models. This includes the difference in response between ductile and brittle connection behavior.

- Use the program to assess three-dimensional effects on irregular buildings in the inelastic range of response considering earthquake directivity.

Analysis of building response to strong motions considering connection fracture and other nonlinear behaviors requires new tools. The development of a tool capable of performing such analysis and its use are described in this work.

1.2 Background

1.2.1 Fractured Connections

Fracture of beam-flange to column-flange moment connections is *not* a new "discovery" (SAC 1998) of the Northridge earthquake. Few full-scale tests have been performed on these connections, and premature fracturing in the weld or immediately adjacent have occurred in a significant number of these tests. In Popov and Stephen (1970), good levels of inelastic behavior were achieved in each of eight specimens, but five of the eight specimens had connection fractures. The investigators concluded emphatically that "the quality of workmanship and inspection is exceedingly important for the achievement of best results" (Popov and Stephen 1970). A later investigation (Popov, Amin, Louie, and Stephen 1985) claimed to be testing the largest specimens to date for this type of application — beams and columns 40 cm (18 in) deep each. Each of the eight specimens fractured with very little inelastic beam rotation. Adequate levels of inelastic behavior were achieved, mostly due to plastic deformations of the panel zone. A month before the Northridge earthquake, Engelhardt and Husain (1993) investigated welded flange-bolted web connections and found that "Plastic rotations developed by the beams prior to connection failure were judged to be poor to marginal for severe seismic applications. All connections failed by fracture at or near the beam-flange groove welds." Collecting earlier studies and their own work, Engelhardt and Husain (1993) concluded, "A careful review of design and detailing practices, as well as welding and quality control issues appears to be warranted for this connection detail."

An additional problem that was not documented is that engineers extrapolated

the minimal results available on small section sizes without considering size dependence of fracture. Changes in architecture introduced the need for larger column spacing and this demand was filled by advancements in milling capabilities. Larger sizes became available and were used without testing. Larger flange thicknesses inherently have more flaws than thinner sections and require more passes of larger beads of weld material. The tests that suggested steel moment frame connections had substantial ductility were based on member sizes with flange thicknesses less than 1.8 cm (0.71 in). Two buildings damaged in the Northridge earthquake and investigated in this work have flange thicknesses exceeding 3.2 cm (1.26 in).

1.2.2 Ground Motions

Some of the strongest ground motions ever recorded were recorded during the Northridge earthquake. A general conclusion of investigators was that strong pulses in the records created by near-source effects were responsible for a lot of damage and that building codes do not account for these motions in any way (Naeim 1997). The 1997 Uniform Building Code (ICBO 1997) now addresses stronger ground motions due to near-source effects to some extent. Like the connection fractures, the knowledge of damaging strong pulses is not new, either. Bertero, Mahin, and Herrara (1978) pointed out, "Near-fault records of the 1971 San Fernando earthquake contain severe, long duration acceleration pulses that result in unusually large ground velocity increments. A review of these records along with the results of available theoretical studies of near-fault ground motions indicates that such acceleration pulses may be characteristic of near-fault sites in general." They performed an analytical study of a severely damaged building and concluded that the main features of the damage were due to these pulses.

A later study, Anderson and Bertero (1987), made several conclusions about strong ground motions. Impulse ground motions require more ductility from buildings with fundamental periods close to the pulse duration. Directivity of fault propagation is important. Code static lateral loads cannot be used to evaluate the behavior of structures that experience significant inelastic behavior. Peak ground

accelerations are not a good measure of the impact of the ground motions on a building. While these conclusion are sound, no changes were made to the code.

The Northridge earthquake highlighted the two previously known problems of premature fracturing of connections and the damaging capabilities of near-source ground motion pulses. Large ground motions had not been experienced in a city with tall steel moment-frame buildings before. These buildings had been designed with codes that do not account for such strong near-source motions and the member sizes exceeded tested sizes. The combination of questionable connections with extrapolated sizes experiencing ground motions not accounted for in design certainly would explain the damage that was uncovered as a result of the earthquake. Still, no steel moment frame building with the connection type discussed has ever collapsed in the United States (SAC 1998). On the other hand, several steel buildings collapsed in Kobe after the 1995 Kobe earthquake and earlier in Mexico City after the 1985 Mexico City earthquake.

Now that a known problem and more strong-motion records exist, analytical sophistication must be developed to assess or predict the behavior of steel moment frame buildings subject to these strong motions. Recent studies ((Hall 1995), (Hall 1997) and (Maison and Kasai 1997)) have suggested that some recorded strong motions and other hypothetical motions can cause collapse in these structures. These investigations have all been two-dimensional, so the impacts of torsional mode excitation and mass and stiffness irregularities have not been explored.

1.2.3 Analysis

This thesis presents a three-dimensional time history analysis approach that combines many inelastic and nonlinear effects to produce a very realistic model to capture severely inelastic structural behaviors. This approach can model connection fracture and predict response due to strong ground motions of arbitrary orientation.

Many investigators have developed nonlinear analysis software for building structures, but they are mostly simplified and limited in the scope of nonlinear behavior

they can model. A small number of programs are available for use in a typical design office that include nonlinear effects, such as SAP90 and ETABS. These programs perform nonlinear time history analysis by integrating nonlinear modal equations with Ritz modal vectors included for each nonlinear element (Wilson 1997). This technique is fast when there are only a few nonlinear elements, but when every beam and column end can behave inelastically, this technique will no longer be efficient or accurate. Some engineers have used more advanced programs like DYNA3D (Hallquist 1988) intended for other fields at great financial and computational cost. Other firms have developed in-house programs originally developed in academia like ISTAR-ST (Lobo (1994) and Lobo, Skokan, Huang, and Hart (1998)). In academics, there are several nonlinear time history programs such as DRAIN-2DX (Allahabadi and Powell 1988) and (Prakash, Powell, and Filippou 1992), DRAIN-3DX (Prakash, Powell, and Campbell 1994), CU-DYNAMIX (El-Tawil and Deierlein 1996) and FEAP-STRUC (Taucer, Spacone, and Filippou 1991).

Most of the programs above are limited to allowing plastic hinges to form at the ends of members. There has been a lot of research on modeling the full inelastic behavior of a member through zero-length hinges at member ends. Various models of axial-bending interaction surfaces that will initiate plasticity have been proposed. Recently, Attalla, Deierlein, and McGuire (1994) have proposed a concentrated hinge model that accurately captures the spread of plasticity with the computational ease of an elastic-plastic hinge model and without the need to discretize across the section or length of a member. They use nonlinear force-strain relations to calibrate data from inelastic analysis that does consider actual spreading of plasticity.

Other hinge models include using nonlinear rotational springs that can model beam plastic hinging or column panel-zone yielding. These models have been modified since the Northridge earthquake to account for connection fracture by specifying a strain at which the hinge capacity will drop (Maison and Kasai 1997). The program CU-DYNAMIX models fracture using a stiffness and strength degradation model that is based on the amount of inelastic energy absorption in a member. A bounding surface models the inelastic member cross section response without

explicit discretization (Chi, El-Tawil, Deierlein, and Abel 1996).

The programs DRAIN-2DX and DRAIN-3DX developed at Berkeley have element libraries that continue to evolve. For many of the SAC analytical investigations (SAC 1995), investigators used DRAIN-2DX with members modeled as Element 2 and panel zones modeled as Element 4. Element 2 allows yielding to take place only in concentrated plastic hinges at the element ends. Strain hardening is approximated by assuming the element consists of elastic and inelastic components in parallel. Inelastic axial deformation is assumed not to occur, so only approximate interaction effects are considered. One investigator found that it was difficult for DRAIN-2DX to maintain numerical stability during rapid decrease in strength after weld fracture (Krawinkler, Alali, Thiel, and Dunlea 1995), so fractured connections were modeled as pre-fractured, i.e., a simple connection instead of a rigid connection was used.

The programs discussed so far are limited to modeling plastic hinges without any explicit modeling of the spread of plasticity. Models that approximate fracture with stiffness degradation do not capture the realistic behavior of regaining contact and load capacity upon displacement reversals. With advancements in computational speed and storage space, a few programs are starting to include these effects explicitly.

The program ISTAR-ST is a three-dimensional nonlinear program developed at John A. Martin & Associates. Beams are modeled as elasto-plastic elements with concentrated plastic hinges at element ends that can account for the strength loss of fracturing when a specified plastic rotation is reached (Lobo, Skokan, Huang, and Hart 1998). For columns only, fiber elements discretize the cross section of an element to capture nonlinear interaction between axial force and biaxial moments using a unique stress-strain relationship. The ends of the columns are modeled with fibers and an elastic segment is used in between with constant axial force and moments that are linear functions of the end moments. This model will not capture the overall inelastic behavior of a severely loaded or displaced column. The beam is adapted from DRAIN-2DX Element 2, and the column is adapted from DRAIN-3DX

fiber elements.

Another program developed at Berkeley is FEAP-STRUC, which uses flexibility-based distributed inelastic elements (Filippou 1995). Frame elements are divided into control sections along the element length. The element section is divided into layers (two-dimensional) or fibers (three-dimensional). Each fiber can be modeled by a number of nonlinear stress-strain relationships. Fracture can be modeled by specifying negative stiffness for a tri-linear tension envelope while maintaining an independent tri-linear compression envelope. At the time of this writing, the author is unaware of any three-dimensional results using this software. Anderson and Filippou (1995) used a two-dimensional version of FEAP-STRUC in their SAC investigation. This software is the most similar to the work presented in this thesis. Fiber divisions of steel members to capture the spread of plasticity and other nonlinear effects have been very limited to this date.

The three-dimensional fiber and segment discretization of elements presented in this work is an extension of the two-dimensional elements described in Hall and Challa (1995) and used in the analytical works Heaton, Hall, Wald, and Halling (1995), Hall, Heaton, Halling, and Wald (1995), Hall (1997), Hall (1995), Carlson and Hall (1997), Hall and Carlson (1998) and Hall (1998). In addition to introducing a three-dimensional element discretization, this work presents three-dimensional constraints that limit the number of equations required to solve various three-dimensional problems consisting of intersecting planar frames. The combination of this three-dimensional fiber-discretized element and other rarely used advancements produces an analytical model that captures more material and geometric nonlinearities than any other known program for three-dimensional analysis of steel buildings.

1.3 Organization of the Thesis

This thesis is arranged in theory chapters (2–6) followed by results chapters (7–11).

Chapter 2 presents an overview of the elements that comprise a planar frame.

Emphasis is placed on presenting the nonlinear capabilities of each element. While these elements have been used in previous works, they have never been fully documented. Chapter 3 provides the mathematical formulation of these building components, deriving their stiffness and force contributions to the equations of motion.

Chapter 4 introduces the three-dimensional constraints used to produce quasi-three-dimensional analysis for buildings with non-intersecting frames. The limitations and effects produced by these constraints are discussed. The three-dimensional fiber-discretized column element is explained in chapter 5. Modeling considerations, three-dimensional issues and the mathematical formulation are provided.

Chapter 6 explains the solution techniques used in this work to perform nonlinear time history analysis and static pushover analysis that includes unloading. The linearization of the equations and the time stepping formulation are derived.

The program described by the previous chapters is used to analyze three steel moment-resisting frame buildings. Modeling assumptions common to all three buildings are given and compared in chapter 7. Chapter 8 presents the results of analyses performed on a 17-story building damaged by the Northridge earthquake. This building has stiffness eccentricities that require three-dimensional analysis to understand the measured behavior. Chapter 9 presents the results of analyses performed on a 13-story building damaged by the Northridge earthquake. This building suffered damage of a random nature that could not have been predicted even with today's analytical tools. Chapter 10 presents the results of analyses performed on a 10-story building designed by the author to meet the requirements of the 1994 Uniform Building Code (ICBO 1994), which has more stringent requirements than the codes the other two buildings were designed to meet. The building represents a realistic irregular building with only one plane of symmetry that is not parallel to framing planes. Three-dimensional effects are investigated, including earthquake directional effects. Chapter 11 compares the results from the three building investigations to determine if certain parameters can predict the level of response and damage measured. Conclusions are summarized in chapter 12.

Appendix A provides information on the ground motions used in this work.

1.4 Notation

Several notational conventions are used in this work. Vectors are denoted by bold lower-case letters, e.g., $\mathbf{a}$. Matrices are denoted by bold upper-case letters, e.g., $\mathbf{A}$. Changes in quantities are represented by preceding the quantity with the symbol Δ. The change of a scalar quantity is expressed as Δa, and the change of a vector quantity is expressed as $\mathbf{\Delta a}$. For clarity, brackets are sometimes used to denote vectors, e.g., $\{\mathbf{a}\}$, and braces are sometimes used to denote matrices, e.g., $[\mathbf{A}]$.

The buildings investigated in this work used standard American Institute of Steel Construction member size designations (AISC 1989). For example, a W14X730 member is a wide-flange section that is nominally 14 inches deep and weighs 730 pounds per linear foot.

The units in this work (with the exception of the previous paragraph) are SI units. The unit of length is the centimeter (cm), the unit of weight is the Newton (N), the unit of mass is the kilogram (kg) and the unit of time is the second (sec). The Imperial system equivalents are given in parentheses for some results. The units of length are inches (in) or feet (ft) and the unit of weight is pounds (lbs) or kilo-pounds (k).

Chapter 2

Overview of the Planar Frame Module

2.1 Introduction

The three-dimensional formulation discussed later is based on a simpler planar frame analysis that utilizes the fiber method. This analysis applies specifically to steel moment frame buildings or concentrically braced frame buildings and is described in this chapter and in the following one. Only a single planar frame is treated in these two chapters and it can be considered as the basic module of the three-dimensional formulation. The three-dimensional formulation will be treated in chapters 4 and 5.

2.2 Planar Frame Model

A frame consists of a planar arrangement of beams, columns, braces and panel zones (figure 2.1), all of which can exhibit nonlinear behavior. Panel zones occupy the joint regions, and the beams (at the sides) and the columns (top and bottom) are connected to them (Hall 1997). Braces can also connect to panel zones diagonally. Each panel zone is a rectangular element that deforms in shear, and its actual dimensions are represented. A beam, column or brace member spans between two panel zones and is subdivided along its length into segments (figure 2.1). The segments allow the member geometry to be updated and any inelastic behavior along the length of the member to be captured. Each segment is further subdivided into fibers so that residual stresses and inelastic behavior can vary through the

member cross section. Beam members can have additional fibers to include the effect of concrete on metal deck acting compositely with the steel girder. A frame can also have wall elements used to model basement walls and foundation springs to model the soil-structure interaction in horizontal and vertical components.

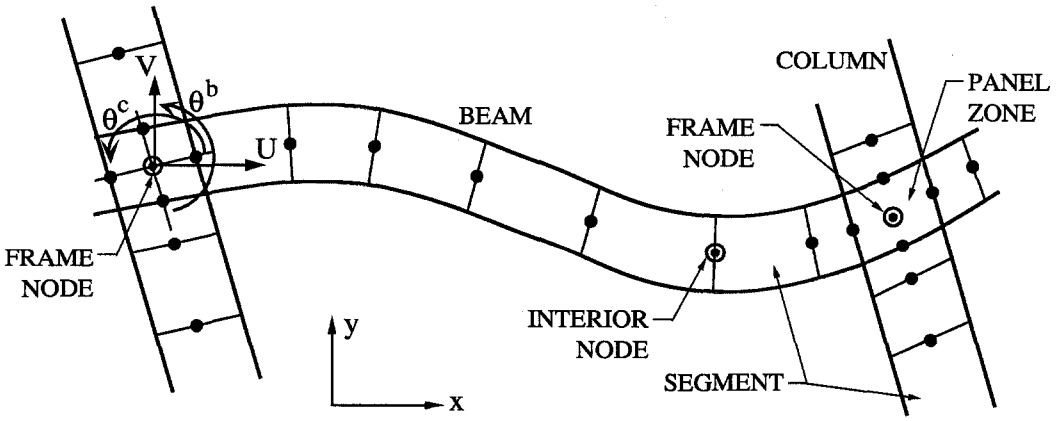

Figure 2.1 Details of planar frame model.

Masses and static loads may be applied to the frame joints. Damping in general and out-of-plane static and dynamic loading will be discussed in a later chapter. The solution technique is iterative to capture the nonlinear effects. Nodal updating allows the P-Δ effects to be implicitly included.

Interior nodes of the members do not have external loads or masses so the solution of the global frame can be accomplished with the interior degrees of freedom (dofs) condensed out. In this way, the frame can be solved globally for only the dofs at the joints. The member end displacements and forces resulting from the global joint solution can then be used to solve for each member's interior dofs and the updated member end forces can be used in the global frame problem for the next iteration. The global frame problem will have the same number of dofs as a simple model that does not have segmented members, greatly reducing the solution time required considering the total number of dofs. As an example, a node with a panel zone and two beams and two columns framing into it will have four degrees of freedom associated with it — horizontal and vertical translation and beam and

column end rotations. If the four members each have eight segments, consider half of the interior nodes are associated with this node and half are associated with the nodes at the members' other ends. This means 14 interior nodes are lumped at this one node. Each interior node has three dofs — two translations and a rotation — giving a total of 46 dofs including the end node. The number of frame dofs is an order of magnitude smaller in this example, pointing out the importance of separating the frame solution from the member solutions.

2.3 Beam-Columns

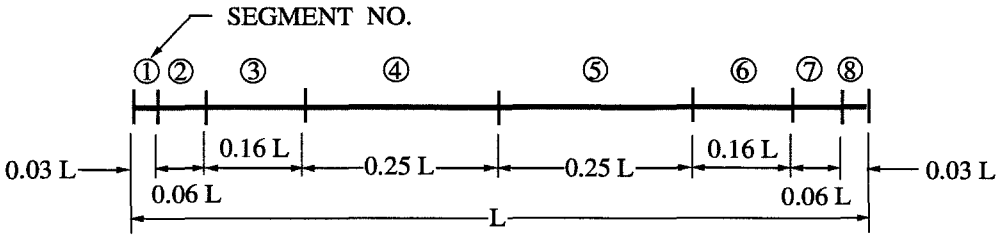

(a)

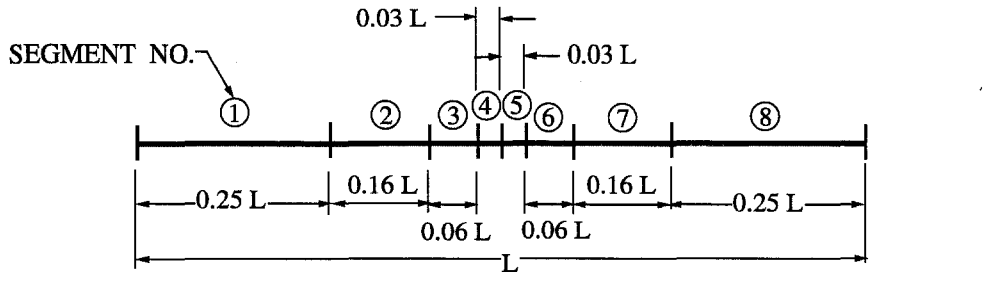

(b)

Figure 2.2 Possible segment layouts. (a) Beam or column. (b) Brace.

Frame members can be columns, beams, or braces. Any member that exhibits both axial force and bending can in general be called a beam-column. Each member

is subdivided along its length into segments (figure 2.2). One set of segment lengths is defined for beams and columns, and another set for braces. Inelastic effects of beams and columns are typically more important at the member ends, so the segment sizes are smaller there. For braces, buckling is a concern so segments are smaller at the midspan. With ends assumed pinned, the segments of a brace do not need to be small at the ends.

Segmentation of the members allows several nonlinear behaviors to be captured in the model without the use of empirically based end conditions. Material nonlinearities affect finite portions of the member length instead of concentrating the effect to zero-length end regions. A portion of a beam can be yielding while other portions are undergoing strain hardening or simple elastic behavior. If a member is loaded in compression with end moments, the interaction of axial force and bending will be accurately modeled.

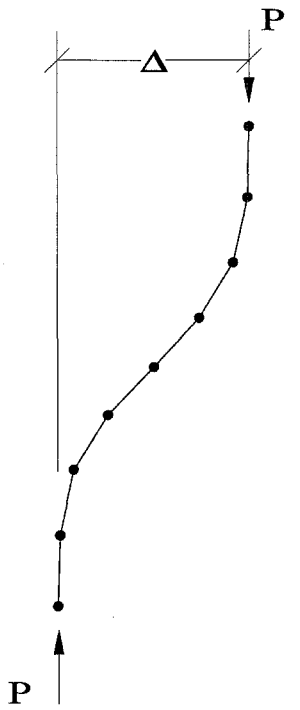

Figure 2.3 P-Δ effects: geometric updating of interior nodes.

Axial force in a member with member ends displaced with respect to each other gives rise to the P-Δ effect (figure 2.3). The geometric updating of the interior nodes will capture the resulting moment amplification and possible buckling. With the segment approach, the structure can undergo large displacements during a dynamic analysis or a pushover static analysis, and properly account for this type of geometric nonlinearity in an iterative solution.

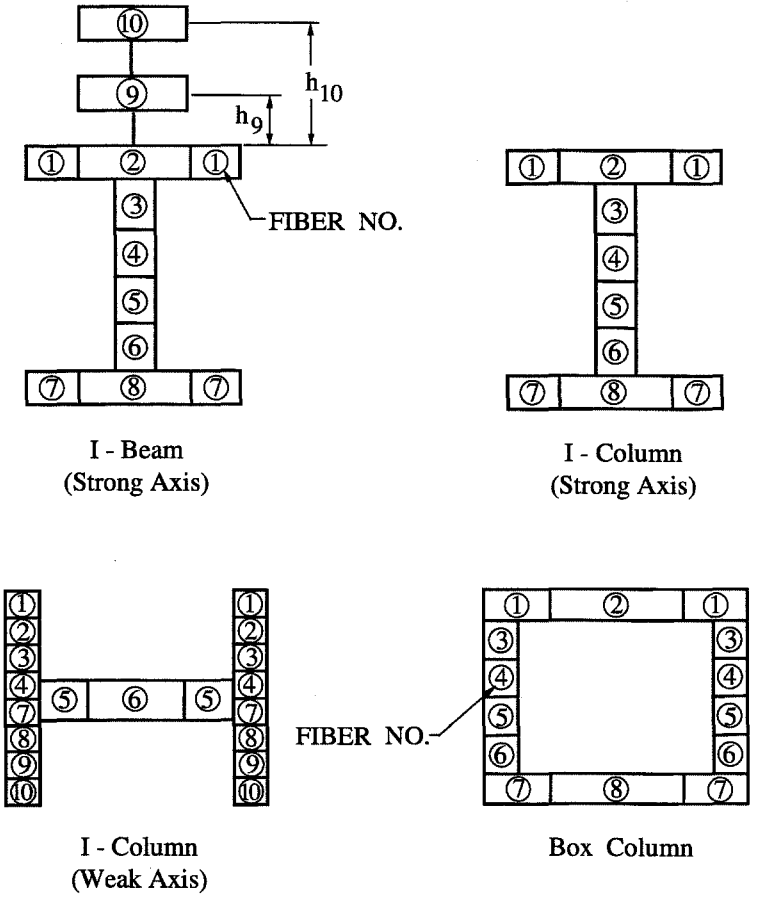

Figure 2.4 Possible fiber layouts.

Each segment of a member is further subdivided into fibers that comprise the member cross section. Several layouts can be used to model wide flanges, weak-axis wide flanges, box members, and composite members (figure 2.4). The fiber model also allows a great deal of flexibility in modeling various member end conditions and

nonlinearities. A beam can be rigidly attached to a column face or connected in simple shear by using the full area of the flange fibers in the end segment or zeroing out these areas in the end segments, respectively. A beam can be modeled compositely by using fibers 9 and 10 (figure 2.4) to represent the metal deck and concrete, respectively. Residual stresses can be applied, varying over the cross section of the member. For inelastic behavior, the spread of plasticity can be achieved through portions of the member cross section in addition to the ability to model zones of plasticity along the member's length utilizing the member segments. Because the fiber model allows modeling of strain hardening, axial-flexural interaction, residual stresses and gradual spread of yielding within the cross section, it is a more realistic model than the more common plastic hinge beam-column model (Allahabadi and Powell 1988).

2.4 Fiber Model

Several models exist for the inelastic behavior of steel. The model used here (Hall and Challa 1995) is physically motivated from actual uniaxial test data of structural steel bars. Explicit expressions for stress in terms of strain also give the instantaneous stiffness, making the model ideal for iterative nonlinear analysis. Other models have loading regime dependent rules that are computationally expensive. This model is simple and efficient, yet adequately represents real hysteretic behavior (Challa 1992).

Each fiber carries an axial stress that is ruled by a hysteretic stress-strain relationship. The monotonic stress-strain relationship is shown in figure 2.5, and its hysteretic behavior is discussed in great detail in (Challa and Hall 1994). Verification with experimental data and modeling capabilities are described in (Challa 1992).

Characteristics of this model include a realistic monotonic loading curve, elliptical unloading and reloading curves and explicit computation of stress and tangent modulus given strain. The virgin curve (0-1-2-3'-4' in figure 2.6) is the original

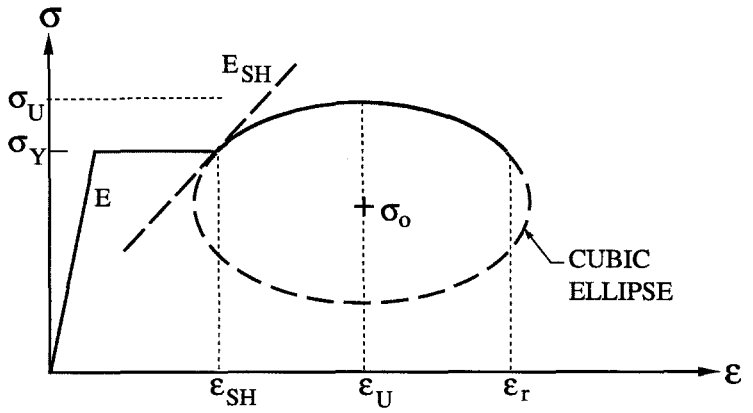

Figure 2.5 Fiber backbone stress-strain relationship.

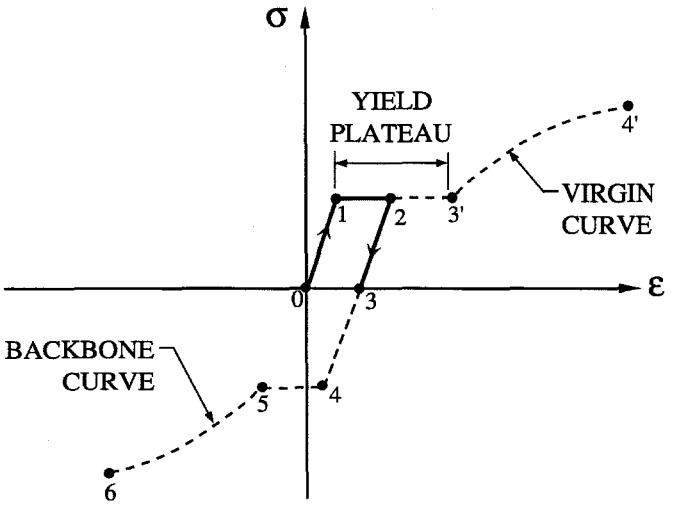

Figure 2.6 Fiber stress-strain curve definitions.

monotonic loading curve of the steel stress strain relation and is fully determined by the following quantities (Hall 1997):

- E, initial elastic Young's Modulus
- E_{SH}, initial modulus at strain hardening
- σ_y, yield stress

- σ_u, ultimate stress
- ϵ_{SH}, strain at strain hardening
- ϵ_u, strain at ultimate strength
- ϵ_r, strain at rupture

A cubic ellipse (figure 2.5) determined from ϵ_{SH}, ϵ_u, E_{SH}, σ_u and σ_y has half width, a, half height, b, and center, σ_o. The ellipse explicitly defines the virgin curve beyond the strain-hardening strain and is described by the equation (Challa and Hall 1994):

$$\left(\frac{\epsilon - \epsilon_u}{a}\right)^3 + \left(\frac{\sigma - \sigma_o}{b}\right)^3 = 1. \tag{2.1}$$

Once the fiber has reached the yield plateau (1-3' in figure 2.6), future reversals will be off the virgin curve. The backbone curves (3-4-5-6 in figure 2.6) that determine the post-yielding history are the virgin curves for compression and tension shifted along the strain axis depending on the maximum tensile and compressive strains in the loading history, respectively. Complex loading histories can efficiently and accurately be followed with this model (figure 2.7).

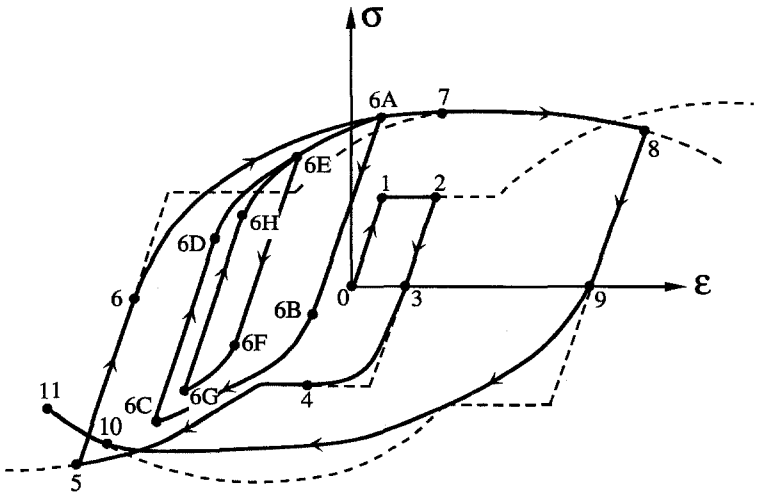

Figure 2.7 Axial stress-strain hysteretic relation for steel fiber.

The stress-strain relation is the same for compression and tension. Residual stresses shift the curve along the strain axis until the residual stress level is located at zero strain. Thus, adjacent fibers can have different levels of residual stress as is typical of both wide flange and box members. Rolled steel sections always have some level of residual stresses and built-up members also incur stresses from differential cooling (McGuire 1968, pp. 233-234). The stress pattern is defined in such a way that equilibrium is maintained, but the maximum residual stress can be chosen by the user (figure 2.8).

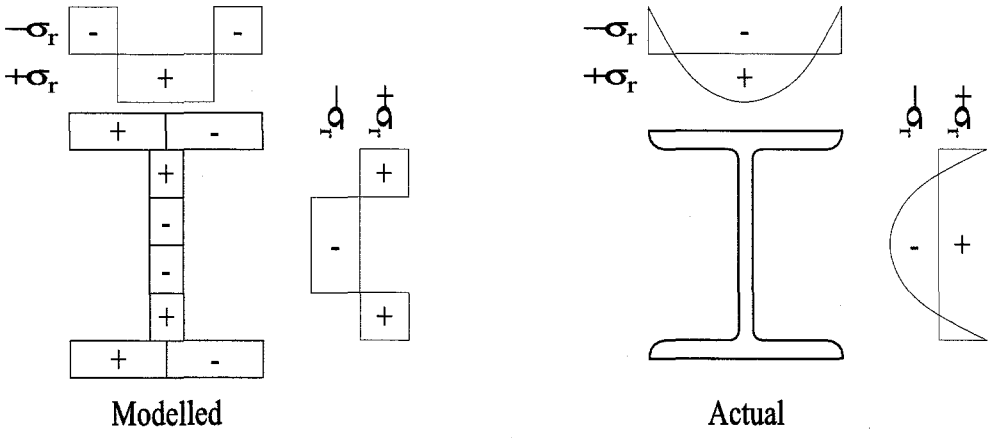

Figure 2.8 Wide flange section residual stress pattern.

A nonlinear stress-strain relation is used to model the concrete fiber representing the fill on the deck of a beam acting compositely (figure 2.9). The stress-strain behavior is linearly elastic-perfectly plastic in compression (yield stress σ_{YC}) and linear to fracture in tension (cracking strength σ_{FC}). Cracking releases the tensile stress and no tension can be subsequently carried (Hall 1997). A crack can later close and carry compression. A composite beam can also have a fiber to model the steel deck and the concrete reinforcing. The same properties are used as for the steel beam fiber. User input can vary the amount of concrete and steel acting compositely, and their heights above the top flange of the beam. Exterior vs. interior bays can be distinguished and deck parallel and perpendicular to beam direction can also be modeled.

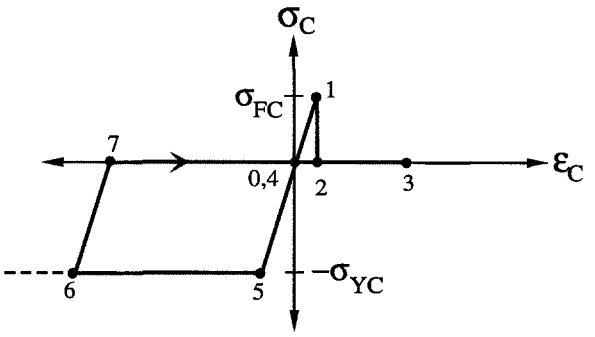

Figure 2.9 Axial stress-strain hysteretic relation for concrete fiber.

The user may reduce the area of a fiber for various realistic conditions. If beam flanges taper at the ends to connect to a narrow column, the flange fiber areas can be reduced by different amounts for the segments approaching the beam's ends. If a frame contains beams with simple connections, the area of the flange fibers for segments 1,2,7 and 8 are zeroed out and the areas of web fibers 3 to 6 are reduced by an amount appropriate to represent the flexibility of a bolted web to shear tab. The fiber areas can also be reduced to appropriately model a semi-rigid connection.

2.5 Connection Fracture

The Northridge earthquake uncovered the fact that steel moment resisting frames may not always be as ductile as engineers expected. Several steel-framed buildings had numerous fractures at beam-to-column moment connections. Most of these cracks stemmed from the welds between the beam and column, and cracking spread into the beam or column flanges and beyond (SAC 1994).

Instead of trying to capture every type of observed damage, the formulation models fracture of individual fibers that are deemed susceptible. Potential fracture areas include those shown in figure 2.10. For example, a beam is likely to fail at its connections to columns, so if the beam has eight segments, segments 1 and 8 can be identified as potential fracture zones. Similarly, the base of the lowest level column (segment 1) can be modeled to predict base plate failure. Since most

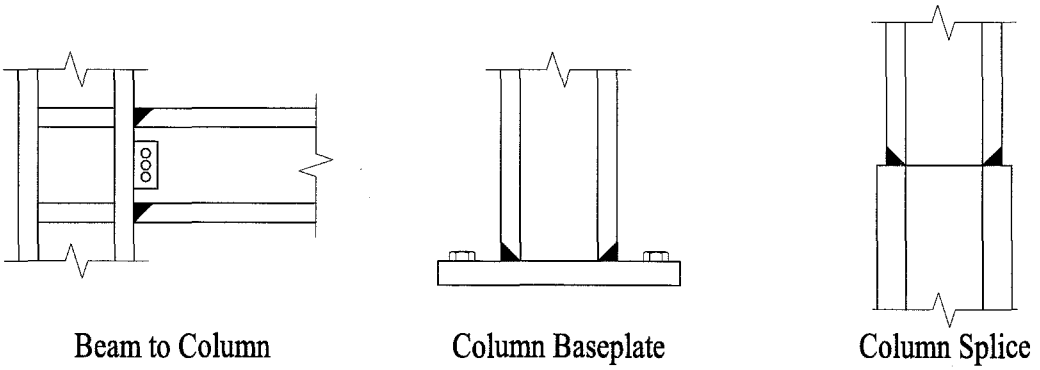

Figure 2.10 Welds that may pose a problem.

column splices occur several feet above floor level (to avoid maximum moment and to make on-site welding easier), the fourth segment out of eight can be modified to model splice connection fracture. Other fracture areas could be modeled, including brace to gusset plate welds. Fibers not representing weld fracture will all follow their individual hysteretic stress-strain relations with rupture as the only failure mechanism.

The actual level of cracking for a group of connections can be chosen in several ways. There have been several large-scale tests of beam-column connections performed in recent years. Static studies have been performed at the Earthquake Engineering Research Center, University of California, San Diego, University of California Berkeley, and University of Texas at Austin (SAC 1997a). Dynamic testing has been performed at Lehigh University (Xue, Kaufmann, Lu, and Fisher 1997). Unfortunately, there have not been enough tests on various member sizes to adequately predict a probabilistic distribution of tensile strains or plastic rotations at failure. The formulation used in this work assigns a fracture strain ϵ_f to a fiber using a randomized process (Hall 1998). Sets of fracture strains are established with associated probabilities of occurrence in units of 10%. An example of a set is: $\epsilon_f = 0.7\epsilon_y$ at 20%; $\epsilon_f = 1.0\epsilon_y$ at 50%; $\epsilon_f = 2.0\epsilon_y$ at 30%, where ϵ_y is the yield strain. The ten strain values in a set can be chosen to approximate a normal distribution, or all ten values can be the same making it deterministic, or some other distribution

can be chosen. A continuous model instead of this discretization is not warranted due to the lack of data available.

Fibers to be assigned fracture strains are placed into groups of which there are four types that model the potential fracture areas mentioned above. These types are column splice, column base plate, top beam flange, and bottom beam flange. A group of column-splice fibers consists of all eight fibers of segment 4 in a column containing a slice. A group of column-base-plate fibers consists of all eight fibers of segment 1 in a column attached to a base plate. A group of top beam-flange fibers consists of fibers 1 to 4 in segment 1 or 8 where a moment connection exists, and similarly for a bottom beam flange group except that the fibers are 5 to 8. Each group type is associated with one of the sets of fracture strains. Once the sets of fracture strains and the groups of fibers are established, the fracture strains are assigned randomly to the groups within each type using the specified occurrence probabilities of the associated set. All fibers in a group receive the same fracture strain, but the fracture strain would vary from group to group within each type throughout the building (Hall 1998).

As an example, assume the same probability distribution is desired for the fracture strains at the top and bottom of both ends of all the beams in a building. The top left beam-flange fibers (segment 1, fibers 1 to 4) are one group. The bottom-left beam-flange fibers (segment 1, fibers 1 to 4) are a second group. The right beam-flange fibers form two more groups, (segment 8, fibers 1 to 4) and (segment 8, fibers 5 to 8). Even though each group uses the same fracture set, the fracture strains are assigned randomly so that one beam could have four different fracture strains (top left, bottom left, top right and bottom right). The strain will be the same for all fibers in a group, but the same group of fibers in another beam could have a different fracture strain.

When an identified fiber reaches its specified tensile fracture strain value, it releases its tensile stress and loses its ability to carry tension in the future, but it can carry compression if contact is regained. If all fibers of a column splice fracture, the column is assumed not to carry any load thereafter (tension or compression).

The assumption here is that the lateral offset of the story would be sufficient to bring the column-section plates out of alignment, and so the load carrying capacity would be reduced dramatically. For a base plate, tensile capacity will be lost, but compression can be achieved if contact is regained. If all beam fibers of a beam-to-column connection fracture, the shear transfer capacity is assumed to remain intact.

2.6 Panel Zones

The load on a panel zone is a double couple derived from the end moments and shears of the connected beams and columns, one couple coming from the beam end moments and column shears and the other coming from the column end moments and beam shears (figure 2.11). This double couple is self-equilibrating since the

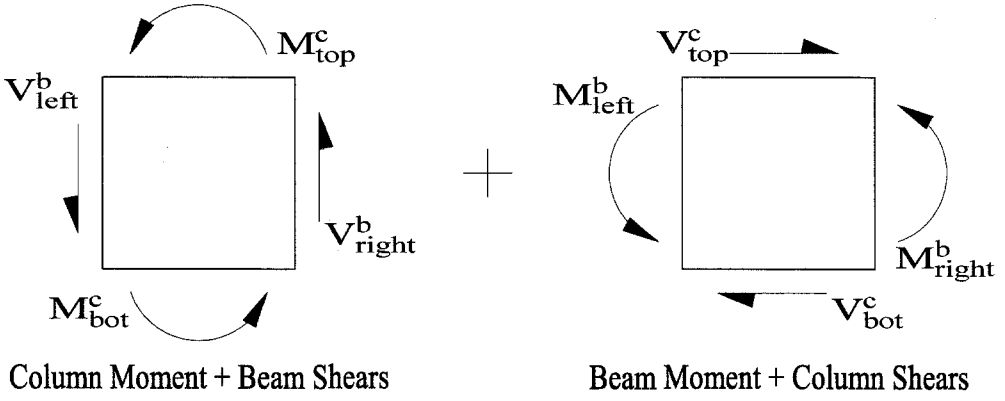

Figure 2.11 Panel zone double couple.

moments of each couple are equal and opposite. Behavior of a panel zone is defined by a nonlinear hysteretic relation between this moment and the resulting shear strain (Hall 1997). The thickness of the panel zone can be increased to account for the addition of doubler plates.

The panel zone hysteretic relation is for moment M^{PZ} and shear strain γ^{PZ} (figure 2.12). The monotonic loading curve begins with a linear segment to $0.8M_y^{PZ}$,

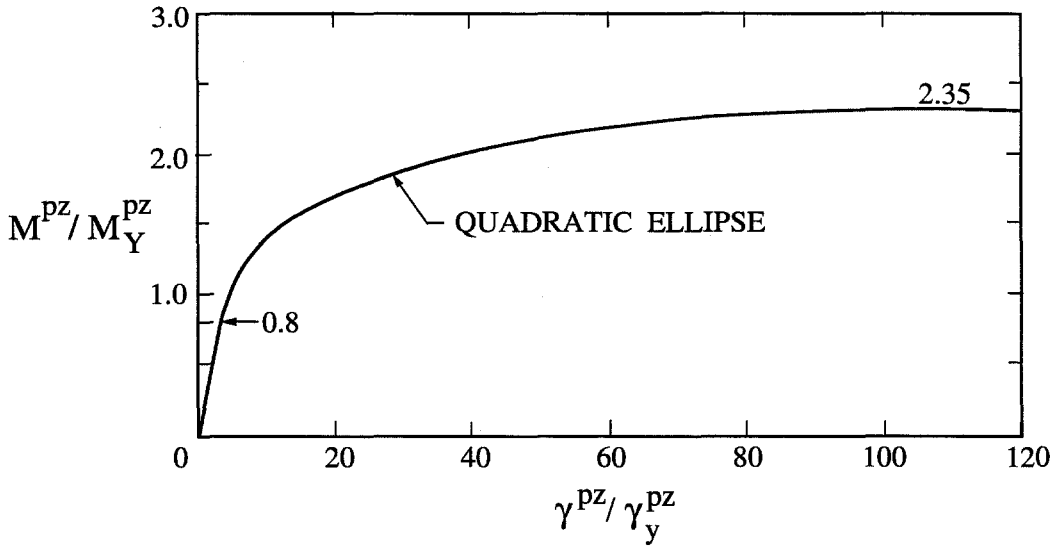

Figure 2.12 Backbone curve for panel zone.

where the yield moment is described by (Tsai and Popov 1988)

$$M_y^{PZ} = \tau_y d^c d^b t. \tag{2.2}$$

The shear yield stress is $\tau_y = \sigma_y/\sqrt{3}$ and d^c, d^b and t are the panel zone dimensions depth of column, depth of beam, and thickness of panel zone, respectively. Following the linear segment is a quadratic ellipse that is tangent to the preceding linear segment and reaches a zero slope at $\gamma_u = 100\gamma_y$, $M_u^{PZ} = 2.35M_y^{PZ}$, where γ_y is the shear yield strain, τ_y/G. This form of the monotonic loading curve is chosen to match a set of experimental data summarized in (Kato 1982). The curve is flat beyond γ_u due to lack of information. Similar rules govern the history as for the steel fiber hysteresis, and good agreement between the model and experimental data has been shown (Challa and Hall 1994; Challa 1992).

The panel zone has its own dimensions, so beams and columns are considered to be of the length spanning between edges of the panel zones. While this is realistic in terms of panel zone deformations and end forces that must be transmitted from the beam to the column, the axial deformations will be slightly low for a building with

relatively deep girders since the panel zone will only deform in shear, neglecting the axial deformation through the depth of the panel zone. This will be discussed more in chapter 10. Several other options can be chosen concerning beam-to-column joints. The node can be modeled without a panel zone using clear span dimensions of beams and columns or the panel zone can be used, but considered rigid.

2.7 Foundation Springs

Foundation interaction is included through a horizontal and vertical spring attached to the bottom of each column line. Each spring is bilinear, and the hardening behavior is kinematic (figure 2.13). Parameters of the springs are as follows (Hall

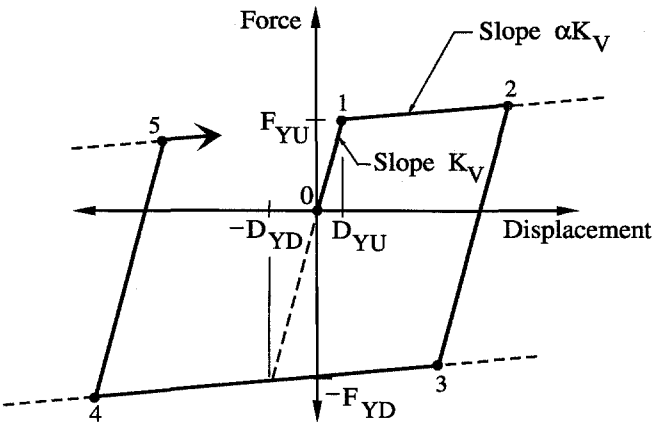

Figure 2.13 Load-deflection hysteretic relation for vertical foundation spring.

1997):

- K_H, initial stiffness of horizontal spring
- K_V, initial stiffness of vertical spring
- α, ratio of secondary stiffness to initial stiffness
- F_{yH}, D_{yH}, yield strength, displacement of horizontal spring
- F_{yU}, D_{yU}, yield strength, displacement of vertical spring in upward direction

- F_{yD}, D_{yD}, yield strength, displacement of vertical spring in downward direction.

Chapter 3

Mathematical Details of the Planar Frame Module

3.1 Introduction

The solution to the nonlinear problem requires that the stiffnesses be determined for the current deformation state of the members and frame. For this reason, tangent stiffnesses are derived in this chapter which describe the stiffness in a given deformation state and are used to solve for an increment of displacement. The forces on the structure which give rise to the displacement increments are also formulated. The assumptions used for each element type and the global assumptions affecting the solution of a single planar frame are described. Three-dimensional capabilities and assumptions as well as the contributions from mass and damping will be discussed in later chapters.

3.2 Degrees of Freedom

The various degrees of freedom (dofs) attributed to different structural elements are summarized here. Each node in a frame can have three or four degrees of freedom associated with it (figure 3.1), specifically horizontal and vertical translation and one rotation (two if there is a panel zone). Individual dofs can be fixed, as at the base of a column if the foundation is rigid.

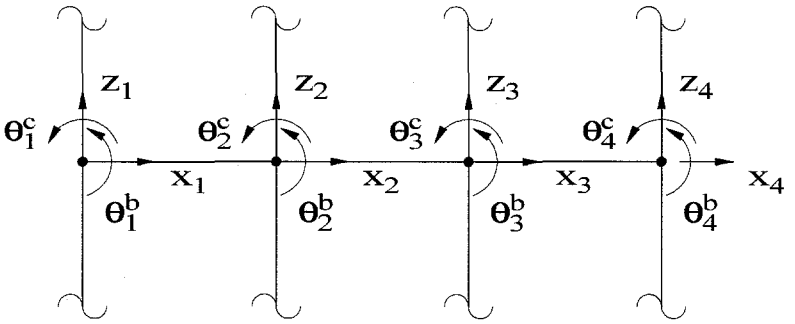

Figure 3.1 Frame and master node degrees of freedom.

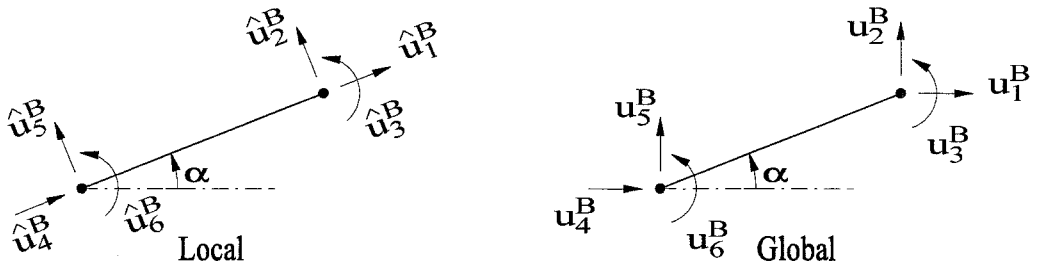

Figure 3.2 Beam degrees of freedom.

Beam-columns have six exterior (end) dofs corresponding to the in-plane axial, shear and moment forces at each end of the member. Braces have four exterior dofs corresponding to the in-plane axial and shear forces at each end of the member. The local and global degrees of freedom for beams, columns and braces can be seen in figures 3.2 and 3.3. These members are comprised of segments, and each interior node between segment ends has three dofs — two translations and a rotation (figure 3.4). The interior dofs are condensed from the global solution since no damping or mass is associated with these dofs. Member solutions are performed individually using the end displacements resulting from a frame solution. The fiber elements which comprise a segment each have two translational dofs at each end (figure 3.4). These dofs are not independent; they are defined by the end conditions of the segment.

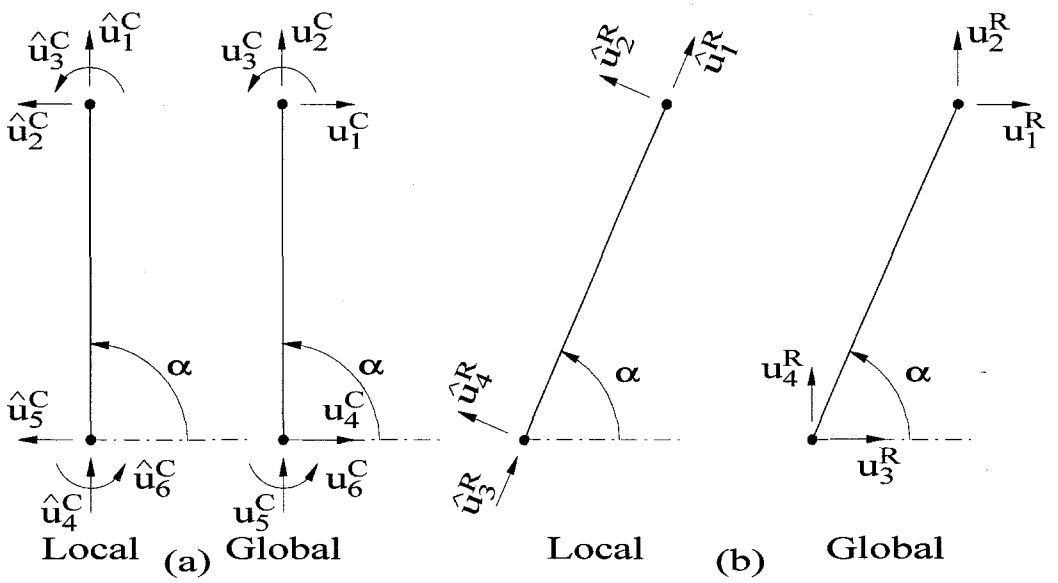

Figure 3.3 (a) Column degrees of freedom. (b) Brace degrees of freedom.

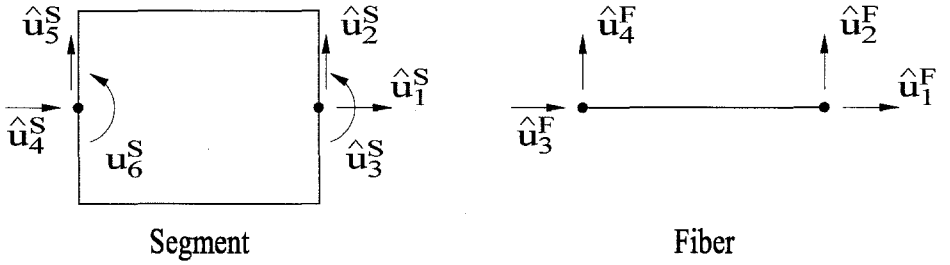

Figure 3.4 Segment and fiber degrees of freedom.

A panel zone has two rotational degrees of freedom which are determined from the end rotations of beams and columns framing into it (figure 3.5).

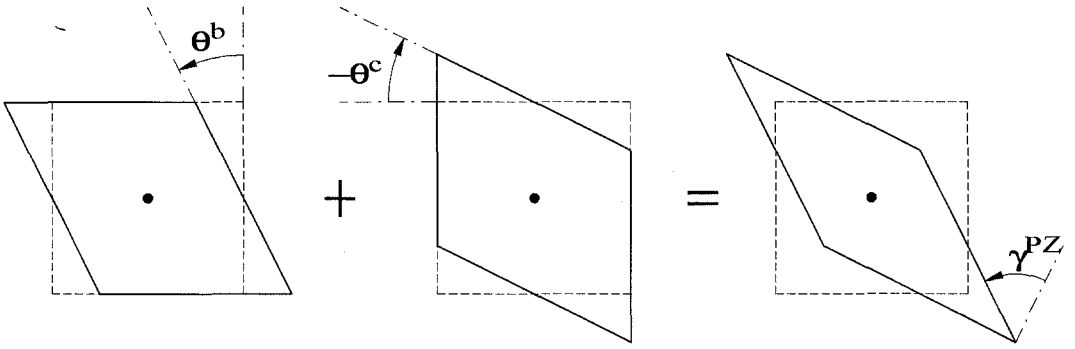

Figure 3.5 Panel zone degrees of freedom.

3.3 Stiffness Formulation

The stiffness properties used in the various elements are explained including some derivations in the following sections. Standard stiffness contributions that are well known in the literature will not be re-derived here.

For a static nonlinear problem, the stiffness forces $\mathbf{p}^{k+1}$ equal the applied forces $\mathbf{f}^{k+1}$ at any iteration $k+1$ of the solution for the unknown displacements:

$$\mathbf{p}^{k+1} = \mathbf{f}^{k+1} \tag{3.1}$$

As will be shown in chapter 6, the problem can be linearized for a linear tangent stiffness matrix $\mathbf{K}_T$ that represents the instantaneous stiffness of the frame at the latest deformed state. The linearization allows the stiffness forces for iteration $k+1$ to be written in terms of the tangent stiffness and known forces from iteration k and the unknown displacement increments $\mathbf{\Delta u}$ for iteration $k+1$:

$$\mathbf{p}^{k+1} = \mathbf{K}_T^k \mathbf{\Delta u}^{k+1} + \mathbf{p}^k. \tag{3.2}$$

This can be substituted for the unknown stiffness forces in equation (3.1) resulting

in:

$$\mathbf{K}_T^k \Delta \mathbf{u}^{k+1} = \mathbf{f}^{k+1} - \mathbf{p}^k. \tag{3.3}$$

In this chapter, this equation will be written as

$$\mathbf{K}_T \Delta \mathbf{u} = \Delta \mathbf{p}. \tag{3.4}$$

The loading $\mathbf{f}$ has not yet been defined, but member and frame forces $\mathbf{p}$ will be developed, so the incremental form of the force vector has been chosen to reflect this for the following derivations.

3.3.1 Fiber Stiffness

The fiber element is an uniaxial member which can only sustain an axial force. A fiber may undergo transverse displacement resulting in a geometric component of the segment stiffness. The fiber stiffness gives the following relationship between end forces and displacement in local coordinates:

$$\mathbf{K}_l^A \Delta \hat{\mathbf{u}}^F = \Delta \hat{\mathbf{p}}^F. \tag{3.5}$$

The forces and displacement can be seen in figure 3.6. The fiber local stiffness

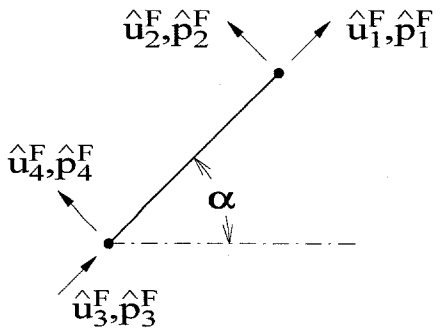

Figure 3.6 Fiber local displacements and forces.

matrix is:

$$\mathbf{K}_l^A = \frac{E_T A_f}{l} \begin{bmatrix} 1 & 0 & -1 & 0 \\ 0 & 0 & 0 & 0 \\ -1 & 0 & 1 & 0 \\ 0 & 0 & 0 & 0 \end{bmatrix} \tag{3.6}$$

where E_T is the tangent modulus of the particular fiber determined from the hysteretic model described in section 2.4. The area of the fiber is A_f, which depends on whether it was initially reduced. If the fiber cracks or ruptures, the tangent modulus can be zeroed out. Recall that a fiber that cracks in tension can regain contact and carry compression.

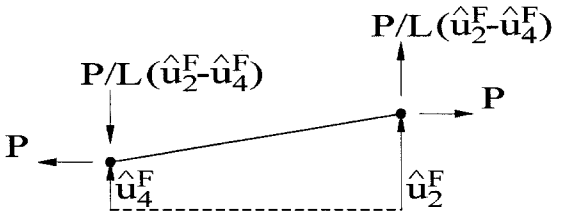

Figure 3.7 Geometric stiffness of fiber.

The geometric contribution to the local stiffness matrix can be determined by displacing the fiber transversely (figure 3.7) as

$$\mathbf{K}_l^G = \frac{P}{L} \begin{bmatrix} 0 & 0 & 0 & 0 \\ 0 & 1 & 0 & -1 \\ 0 & 0 & 0 & 0 \\ 0 & -1 & 0 & 1 \end{bmatrix} \tag{3.7}$$

For each fiber, the total stiffness matrix is $\mathbf{K}_{l,i}^F = \mathbf{K}_{l,i}^A + \mathbf{K}_{l,i}^G$, summing the axial and geometric contributions. For a single fiber i, the total fiber force displacement

relation becomes

$$\mathbf{K}^F_{l,i}\Delta\hat{\mathbf{u}}^F_i = \Delta\hat{\mathbf{p}}^F_i. \tag{3.8}$$

The individual fiber stiffness matrices are assembled for each segment as described below.

3.3.2 Segment Stiffness

The segment stiffness is assembled from the fiber stiffness contributions plus a separate shear stiffness contribution. The formulation uses separate interpolation of displacements and rotations. Since the fiber does not include shear deformations, shearing will not involve interaction with axial force or bending. Shearing is assumed to remain elastic. Plane sections normal to the neutral axis before bending remain plane after bending though not normal to it.

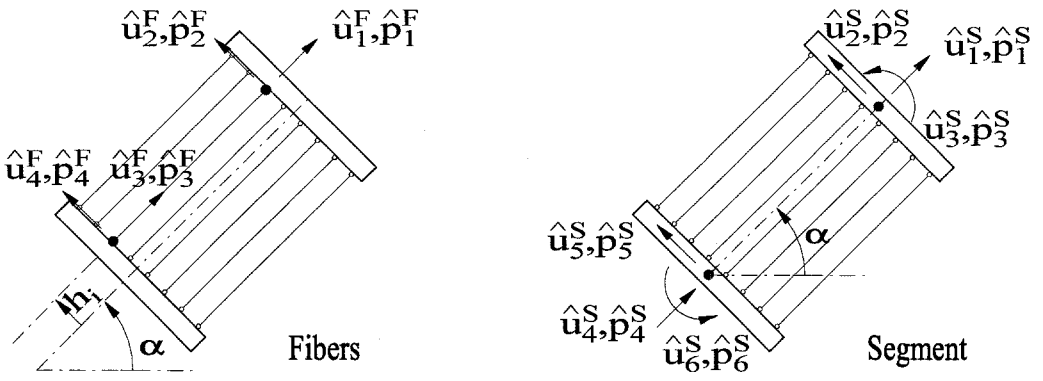

Figure 3.8 Relation between fiber and segment degrees of freedom.

The relation between fibers and segments is shown in figure 3.8. Each fiber has its centroid located a distance h_i from the neutral axis. The transformation from segment displacements to fiber displacements is easily determined by individually displacing the segment degrees of freedom. Axial, shearing, and rotational displacements at the right end of the segment are shown with the corresponding fiber displacements in figure 3.9. The resulting relation between segment displacements

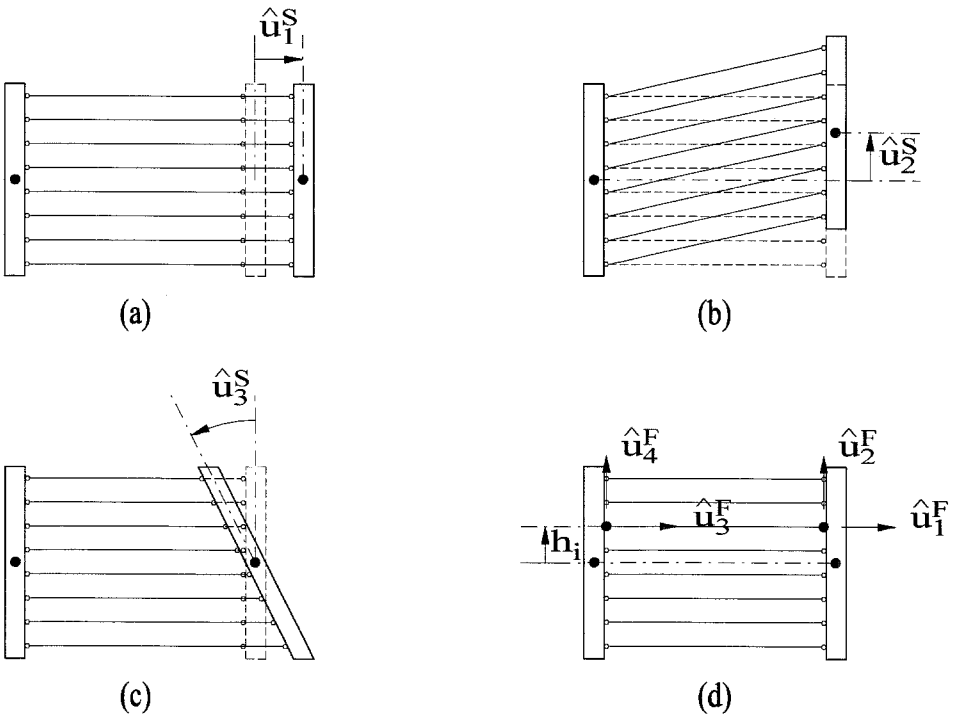

Figure 3.9 Relation between fiber and segment displacements.

$\hat{\mathbf{u}}^S$ and individual fiber displacements $\hat{\mathbf{u}}_i^F$ is

$$\hat{\mathbf{u}}_i^F = \mathbf{R}_i^{SF}\hat{\mathbf{u}}^S \tag{3.9}$$

where the transformation from segment to fiber displacements is given by

$$\mathbf{R}_i^{SF} = \begin{bmatrix} 1 & 0 & -h_i & 0 & 0 & 0 \\ 0 & 1 & 0 & 0 & 0 & 0 \\ 0 & 0 & 0 & 1 & 0 & -h_i \\ 0 & 0 & 0 & 0 & 1 & 0 \end{bmatrix}. \tag{3.10}$$

The contribution of a fiber's forces $\hat{\mathbf{p}}_i^F$ to the segment forces is denoted by $\hat{\mathbf{p}}_i^S$

and their relation is

$$\hat{\mathbf{p}}_i^S = [\mathbf{R}_i^{SF}]^T \hat{\mathbf{p}}_i^F \tag{3.11}$$

Using the fiber equation (3.8), and substituting the displacement transformation (3.9) and the force transformation (3.11) in incremental form gives

$$[\mathbf{R}_i^{SF}]^T \mathbf{K}_{l,i}^F \mathbf{R}_i^{SF} \boldsymbol{\Delta}\hat{\mathbf{u}}^S = \boldsymbol{\Delta}\hat{\mathbf{p}}_i^S. \tag{3.12}$$

Summing the contributions from each fiber gives

$$\mathbf{K}_l^{S,F} \boldsymbol{\Delta}\hat{\mathbf{u}}^S = \boldsymbol{\Delta}\hat{\mathbf{p}}^S \tag{3.13}$$

where the tangent segment stiffness due to fibers is summed for the number of fibers in the segment, n_F, as

$$\mathbf{K}_l^{S,F} = \sum_{i=1}^{n_F} ([\mathbf{R}_i^{SF}]^T \mathbf{K}_{l,i}^F [\mathbf{R}_i^{SF}]). \tag{3.14}$$

The shear stiffness is determined using mid-span sampling. This ensures that shear locking will not occur, resulting in the segment shear stiffness (Hall and Challa 1995)

$$\mathbf{K}_l^{S,SH} = GA_S \begin{bmatrix} 0 & 0 & 0 & 0 & 0 & 0 \\ & \frac{1}{l} & -\frac{1}{2} & 0 & -\frac{1}{l} & -\frac{1}{2} \\ & & \frac{l}{4} & 0 & \frac{1}{2} & \frac{l}{4} \\ & & & 0 & 0 & 0 \\ & sym & & & \frac{1}{l} & \frac{l}{2} \\ & & & & & \frac{l}{4} \end{bmatrix}. \tag{3.15}$$

The shear area A_S is dt_w for the strong axis of a wide flange section and $5/6(2bt_f)$ for the minor axis.

Local segment forces can be determined from fiber stresses σ_i, geometric properties and end rotations. The axial force P, the shear Q and the end moments M_1 and M_2 are

$$P = \sum_{i=1}^{n_F} \sigma_i A_i \tag{3.16}$$

$$Q = \frac{1}{2} G A_S (\theta_1 + \theta_2 - 2\alpha) \tag{3.17}$$

$$M_1 = -\sum_{i=1}^{n_F} \sigma_i A_i h_i + \frac{1}{2} Q l \tag{3.18}$$

$$M_2 = \sum_{i=1}^{n_F} \sigma_i A_i h_i + \frac{1}{2} Q l \tag{3.19}$$

Notice that the midspan sampling averages the end values of shear:

$$Q = G A_S \frac{(\theta_1 - \alpha) + (\theta_2 - \alpha)}{2}. \tag{3.20}$$

The strains developed in the fibers are determined from the segment end displacements

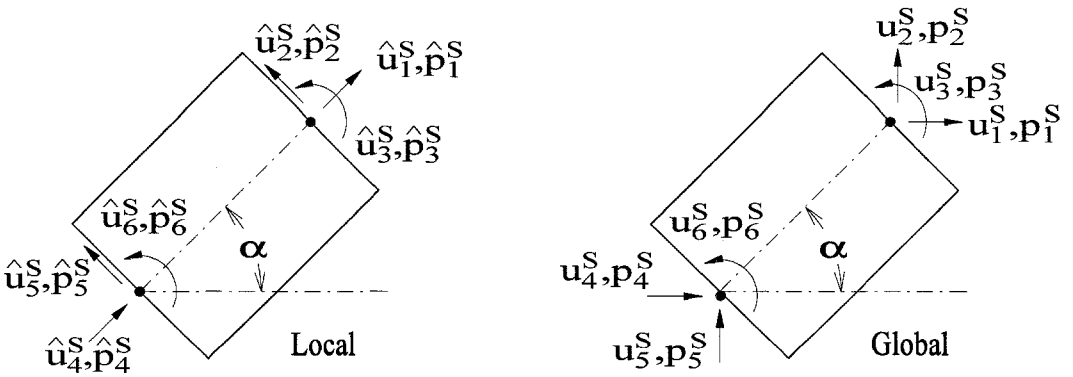

Figure 3.10 Segment local and global properties.

$$\epsilon_i = \frac{\hat{u}_1^F}{l} - \frac{h_i}{l}(\theta_1 - \theta_2). \tag{3.21}$$

Refer to figure 3.11(a) to see the contribution from rotation.

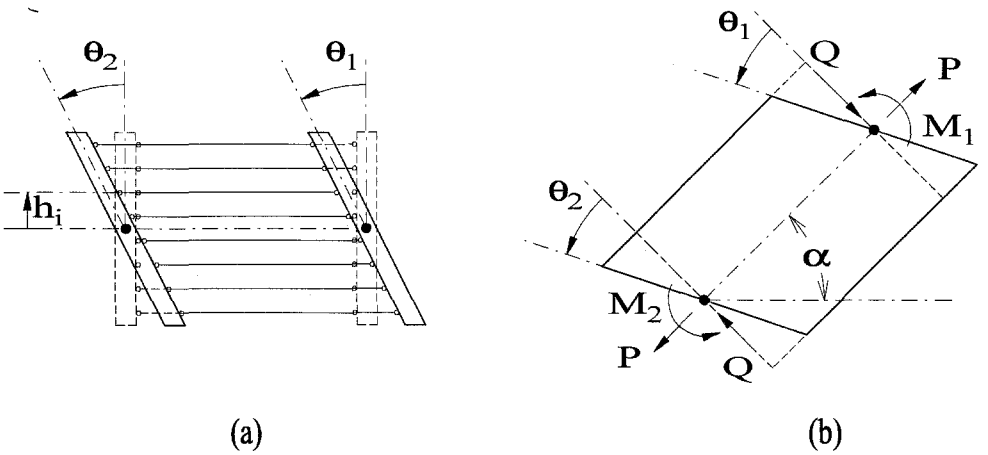

Figure 3.11 Positive directions of various segment parameters.

The global end forces of the segment are determined from the transformation

$$\mathbf{p}^S = \mathbf{T}^T \begin{Bmatrix} P \\ -Q \\ M_1 \\ -P \\ Q \\ M_2 \end{Bmatrix} = \mathbf{T}^T \begin{Bmatrix} \hat{p}_1 \\ \vdots \\ \hat{p}_6 \end{Bmatrix} = \mathbf{T}^T \hat{\mathbf{p}}^S \tag{3.22}$$

where

$$\mathbf{T} = \begin{bmatrix} \cos\alpha & \sin\alpha & 0 & 0 & 0 & 0 \\ -\sin\alpha & \cos\alpha & 0 & 0 & 0 & 0 \\ 0 & 0 & 1 & 0 & 0 & 0 \\ 0 & 0 & 0 & \cos\alpha & \sin\alpha & 0 \\ 0 & 0 & 0 & -\sin\alpha & \cos\alpha & 0 \\ 0 & 0 & 0 & 0 & 0 & 1 \end{bmatrix}. \tag{3.23}$$

The displacement transformation is $\hat{\mathbf{u}}^S = \mathbf{T}\mathbf{u}^S$. Refer to figure 3.11(b) for the positive sense of the segment end forces and to figure 3.10 for local and global parameters. The global segment stiffness matrix can be determined from the segment transformation

$$\mathbf{K}_g^S = \mathbf{T}^T(\mathbf{K}_l^{S,F} + \mathbf{K}_l^{S,SH})\mathbf{T} \tag{3.24}$$

giving the relation

$$\mathbf{K}_g^S \Delta\mathbf{u}^S = \Delta\mathbf{p}^S. \tag{3.25}$$

3.3.3 Beam-Column Stiffness

Now that the global segment relations have been determined, the segment stiffnesses are assembled to formulate the member stiffness. For now, the superscripts denoting that the displacements, forces and stiffness are for beam-column elements will be dropped. The member stiffness matrix is assembled from the segment stiffness matrices using the assembly operator $\mathcal{A}$, and denoting the number of segments per member as n_S:

$$\mathbf{K} = \mathop{\mathcal{A}}_{i=1}^{n_S}(\mathbf{K}_g^S) \tag{3.26}$$

The member equation becomes

$$\mathbf{K}\Delta\mathbf{u} = \Delta\mathbf{p}. \tag{3.27}$$

Earlier derivations in this chapter considered only the member stiffness forces resulting from deformations. At this level of the development, applied forces must also be considered. This expression can be written for all interior and exterior dofs as

$$\mathbf{K}\Delta\mathbf{u} = \mathbf{f} - \mathbf{p}, \tag{3.28}$$

where $\mathbf{f}$ are the applied forces and $\mathbf{p}$ are the member stiffness forces. The out-of-balance between these values is solved for iteratively. The member incremental displacements are solved with individual member iterations using the exterior dof displacement increments recovered from the frame as input. The resulting end forces are returned to the frame level for iterative solution at that level. In order to perform the iterations on just the interior dofs, the member stiffness needs to be partitioned. Let subscripts I and E denote interior and exterior dofs, respectively. The member equation can be rewritten

$$\begin{bmatrix} \mathbf{K}_{II} & \mathbf{K}_{IE} \\ \mathbf{K}_{EI} & \mathbf{K}_{EE} \end{bmatrix} \begin{Bmatrix} \Delta\mathbf{u}_I \\ \Delta\mathbf{u}_E \end{Bmatrix} = \begin{Bmatrix} \mathbf{f}_I \\ \mathbf{f}_E \end{Bmatrix} - \begin{Bmatrix} \mathbf{p}_I \\ \mathbf{p}_E \end{Bmatrix} \tag{3.29}$$

where the top equations are for the interior dofs and the bottom equations are for the exterior dofs. For the formulation used, $\mathbf{f}_I$ are zero since interior loading is not applied. The first set of equations is

$$\mathbf{K}_{II}\Delta\mathbf{u}_I = -\mathbf{K}_{IE}\Delta\mathbf{u}_E - \mathbf{p}_I. \tag{3.30}$$

This is the equation for member iterative analysis. The exterior nodal increments are applied in the first step and iterations are performed updating the stiffness forces $\mathbf{p}_I$ until convergence is achieved ($-\mathbf{K}_{IE}\Delta\mathbf{u}_E - \mathbf{p}_I \approx \mathbf{0}$) or the maximum number of

member iterations is reached.

For the solution at the frame level, the member dofs need to be condensed to the exterior dofs only. Multiplying the interior equations of (3.29) by $\mathbf{K}_{II}^{-1}$ gives:

$$\begin{bmatrix} \mathbf{I} & \mathbf{K}_{II}^{-1}\mathbf{K}_{IE} \\ \mathbf{K}_{EI} & \mathbf{K}_{EE} \end{bmatrix} \begin{Bmatrix} \boldsymbol{\Delta}\mathbf{u}_I \\ \boldsymbol{\Delta}\mathbf{u}_E \end{Bmatrix} = \begin{Bmatrix} \mathbf{0} \\ \mathbf{f}_E \end{Bmatrix} - \begin{Bmatrix} \mathbf{K}_{II}^{-1}\mathbf{p}_I \\ \mathbf{p}_E \end{Bmatrix}. \tag{3.31}$$

Subtract $\mathbf{K}_{EI}$ times the interior equations from the exterior equations:

$$\begin{bmatrix} \mathbf{0} & \mathbf{K}_{EE} - \mathbf{K}_{EI}\mathbf{K}_{II}^{-1}\mathbf{K}_{IE} \end{bmatrix} \begin{Bmatrix} \boldsymbol{\Delta}\mathbf{u}_I \\ \boldsymbol{\Delta}\mathbf{u}_E \end{Bmatrix} = \{\mathbf{f}_E - \mathbf{p}_E + \mathbf{K}_{EI}\mathbf{K}_{II}^{-1}\mathbf{p}_I\}. \tag{3.32}$$

This is the condensed equations for a member in terms of its end (exterior) degrees of freedom:

$$\mathbf{K}^{BC}\boldsymbol{\Delta}\mathbf{u}^{BC} = \boldsymbol{\Delta}\mathbf{p}^{BC}, \quad \text{where} \tag{3.33}$$

$$\boldsymbol{\Delta}\mathbf{p}^{BC} = \mathbf{f}^{BC} - \mathbf{p}^{BC} \tag{3.34}$$

$$\mathbf{f}^{BC} = \mathbf{f}_E \tag{3.35}$$

$$\mathbf{p}^{BC} = \{\mathbf{p}_E - \mathbf{K}_{EI}\mathbf{K}_{II}^{-1}\mathbf{p}_I\} \tag{3.36}$$

$$\mathbf{u}^{BC} = \mathbf{u}_E \quad \text{and} \tag{3.37}$$

$$\mathbf{K}^{BC} = \left[\mathbf{K}_{EE} - \mathbf{K}_{EI}\mathbf{K}_{II}^{-1}\mathbf{K}_{IE}\right]. \tag{3.38}$$

The end forces $\mathbf{p}^{BC}$ are applied to the edges of the panel zones and assembled to the frame nodal forces which have applied forces $\mathbf{f}$ already assembled. The forces $\mathbf{f}^{BC}$ never actually have to be determined since the members are not solved individually for the condensed exterior-only system. The tangent stiffness matrix $\mathbf{K}^{BC}$ is assembled to the frame stiffness matrix. Equation (3.33) gives the member end displacements and forces in member global coordinates.

The member forces (figure 3.12) in local coordinates are calculated for output purposes only using the updated geometry as follows:

$$P = \frac{1}{n_S} \sum_{i=1}^{n_S} P_i^S \tag{3.39}$$

$$M_1 = M_1^S, \text{ segment } 1 \tag{3.40}$$

$$M_2 = M_2^S, \text{ segment } n_S \tag{3.41}$$

$$Q = -\frac{1}{L}(M_1 + M_2). \tag{3.42}$$

The calculation for P takes into account varying axial force for a member with large displacements.

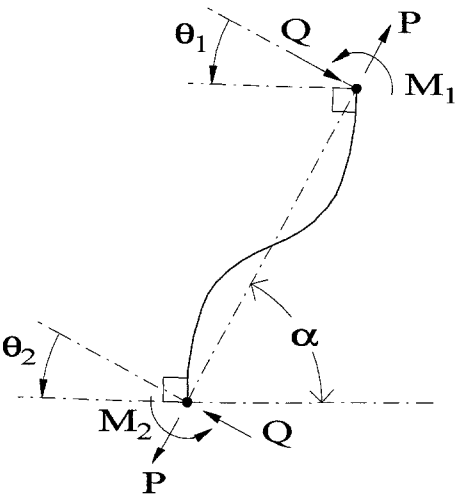

Figure 3.12 Positive beam-column calculated end forces.

The member forces act at the end of the member that is located at the face of a panel zone. These forces must be transformed to frame nodal forces that are applied at the center of the panel zone. This transformation will be different for beams, columns and braces. The panel zone depth d_i^b, width d_i^c, and the beam and column rotations θ_i^b and θ_i^c at each end of the members (ends i and j) are used to determine the frame nodal loading from the members. Referring to figure 3.13 the

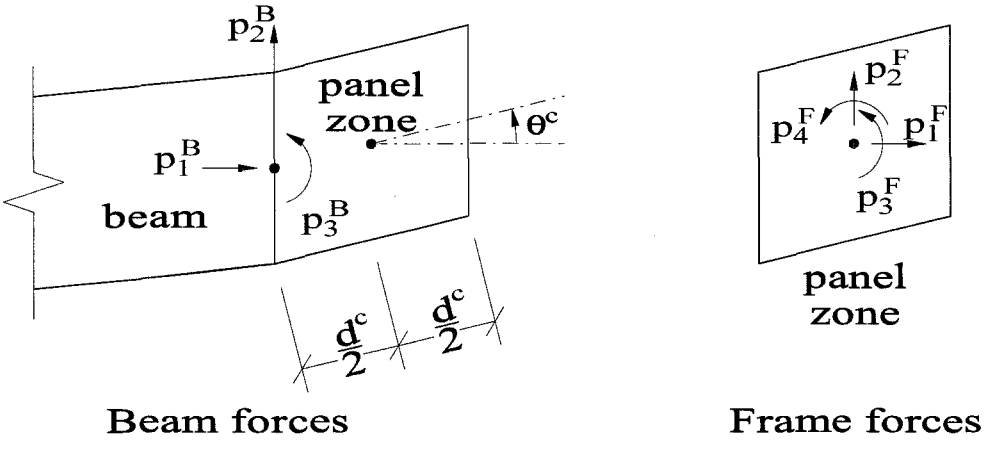

Figure 3.13 Converting beam end forces to frame nodal forces.

beam transformation $[\mathbf{S}^B]^T$ from beam global forces $\mathbf{p}^B$ to frame global forces $\mathbf{p}^{F-B}$ is

$$[\mathbf{S}^B]^T\mathbf{p}^B = \mathbf{p}^{F-B} \tag{3.43}$$

where

$$\mathbf{S}^B = \begin{bmatrix} 1 & 0 & 0 & \frac{d_i^c}{2}\sin\theta_i^c & 0 & 0 & 0 & 0 \\ 0 & 1 & 0 & -\frac{d_i^c}{2}\cos\theta_i^c & 0 & 0 & 0 & 0 \\ 0 & 0 & 1 & 0 & 0 & 0 & 0 & 0 \\ 0 & 0 & 0 & 0 & 1 & 0 & 0 & -\frac{d_j^c}{2}\sin\theta_j^c \\ 0 & 0 & 0 & 0 & 0 & 1 & 0 & \frac{d_j^c}{2}\cos\theta_j^c \\ 0 & 0 & 0 & 0 & 0 & 0 & 1 & 0 \end{bmatrix}. \tag{3.44}$$

The frame forces affected by beams is denoted by the superscript $F-B$, but note

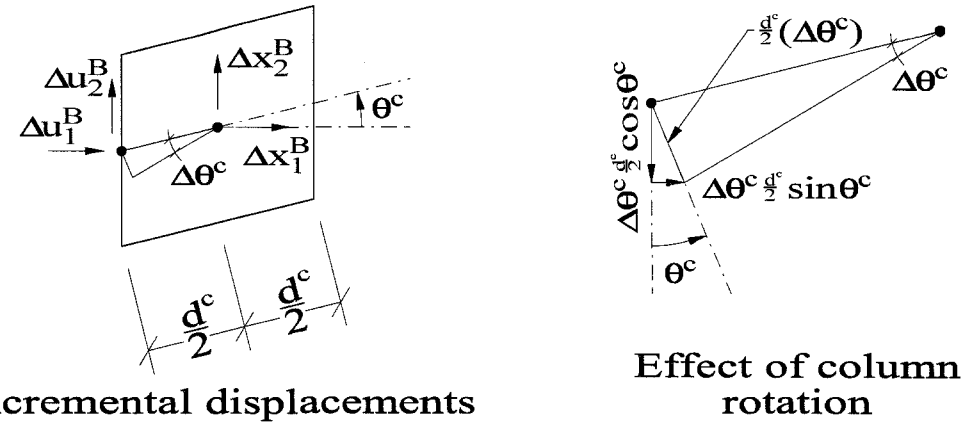

Figure 3.14 Converting beam end displacements to frame nodal displacements.

that in the following figures the frame forces will be denoted with a superscript F regardless of the contributing member for clarity of the figures. The incremental displacements can be found by imposing small displacements of each of the frame nodal degrees of freedom (figure 3.14). The frame node dofs will be denoted by $\mathbf{x}$

and the dofs affected by a beam will be denoted by $\mathbf{x}^B$. The resulting transformation from nodal increment $\mathbf{\Delta x}^B$ to beam end increment $\mathbf{\Delta u}^B$ is

$$\mathbf{S}^B \mathbf{\Delta x}^B = \mathbf{\Delta u}^B \tag{3.45}$$

where $\mathbf{S}^B$ is defined by (3.44). Note that this relationship only holds for displacement increments, not totals. Substituting (3.45) into (3.33) and pre-multiplying by $[\mathbf{S}^B]^T$ gives

$$[\mathbf{S}^B]^T \mathbf{K}^{BC} \mathbf{S}^B \mathbf{\Delta x}^B = [\mathbf{S}^B]^T \mathbf{\Delta p}^B. \tag{3.46}$$

Substituting the incremental form of (3.43), the frame nodal equation of the beam contribution becomes

$$\mathbf{K}_T^B \mathbf{\Delta x}^B = \mathbf{\Delta p}^{F-B} \tag{3.47}$$

where

$$\mathbf{K}_T^B = [\mathbf{S}^B]^T \mathbf{K}^{BC} \mathbf{S}^B. \tag{3.48}$$

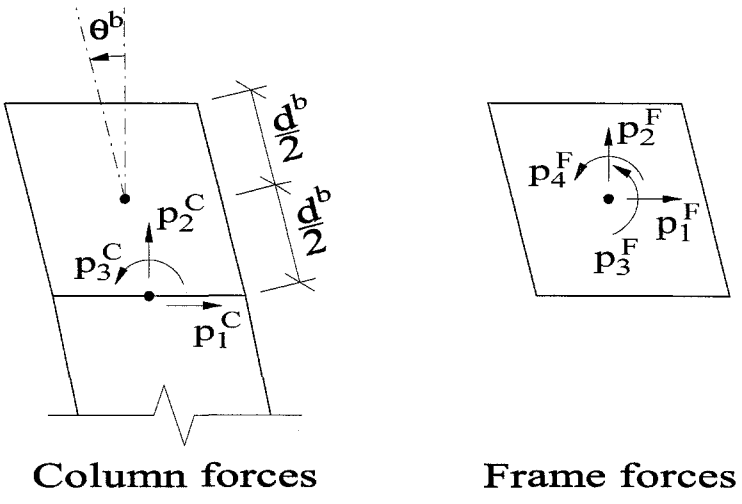

Figure 3.15 Converting column end forces to frame nodal forces.

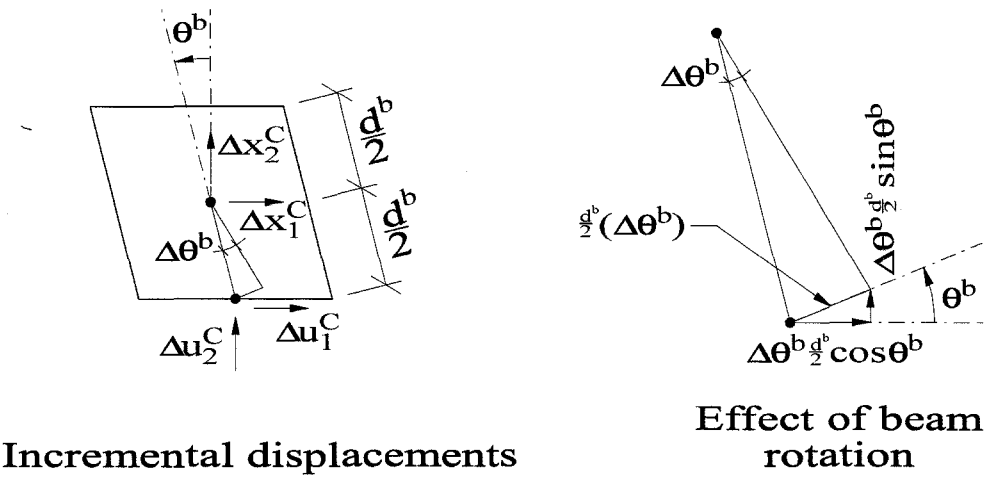

Figure 3.16 Converting column end displacements to frame nodal displacements.

A column element has a similar derivation. Referring to figures 3.15 and 3.16, the column transformation is

$$\mathbf{S}^C = \begin{bmatrix} 1 & 0 & \frac{d_i^b}{2}\cos\theta_i^b & 0 & 0 & 0 & 0 & 0 \\ 0 & 1 & \frac{d_i^b}{2}\sin\theta_i^b & 0 & 0 & 0 & 0 & 0 \\ 0 & 0 & 0 & 1 & 0 & 0 & 0 & 0 \\ 0 & 0 & 0 & 0 & 1 & 0 & -\frac{d_j^b}{2}\cos\theta_j^b & 0 \\ 0 & 0 & 0 & 0 & 0 & 1 & -\frac{d_j^b}{2}\sin\theta_j^b & 0 \\ 0 & 0 & 0 & 0 & 0 & 0 & 0 & 1 \end{bmatrix} \tag{3.49}$$

and the column contribution to the frame nodal equations is

$$\mathbf{K}_T^C \Delta\mathbf{x}^C = \Delta\mathbf{p}^{F-C} \tag{3.50}$$

where

$$\mathbf{K}_T^C = [\mathbf{S}^C]^T \mathbf{K}^{BC} \mathbf{S}^C \quad \text{and} \quad \mathbf{p}^{F-C} = [\mathbf{S}^C]^T \mathbf{p}^C. \tag{3.51}$$

Note that the forces $\mathbf{p}^{F-C}$ are denoted by $\mathbf{p}^F$ in figure 3.15.

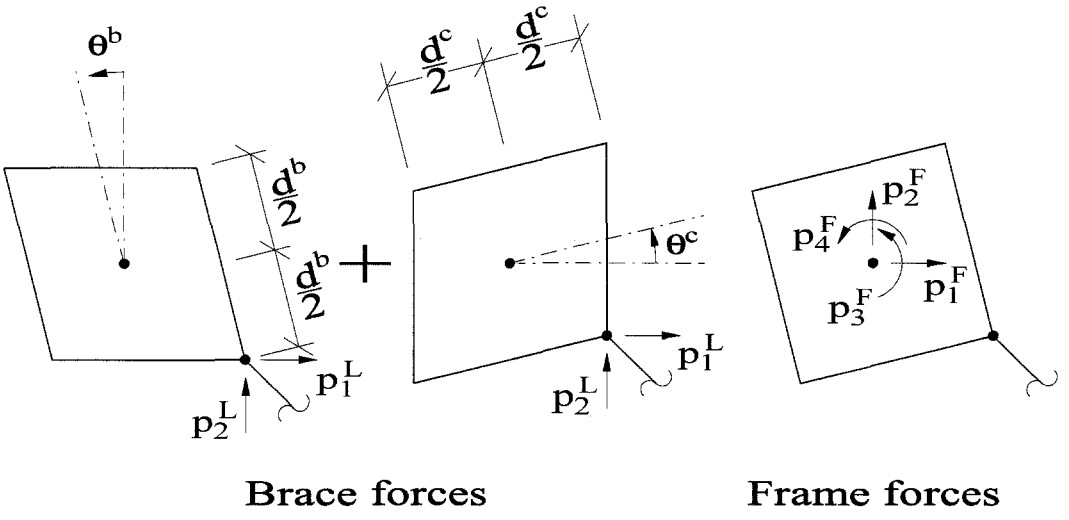

Figure 3.17 Converting left brace end forces to frame nodal forces.

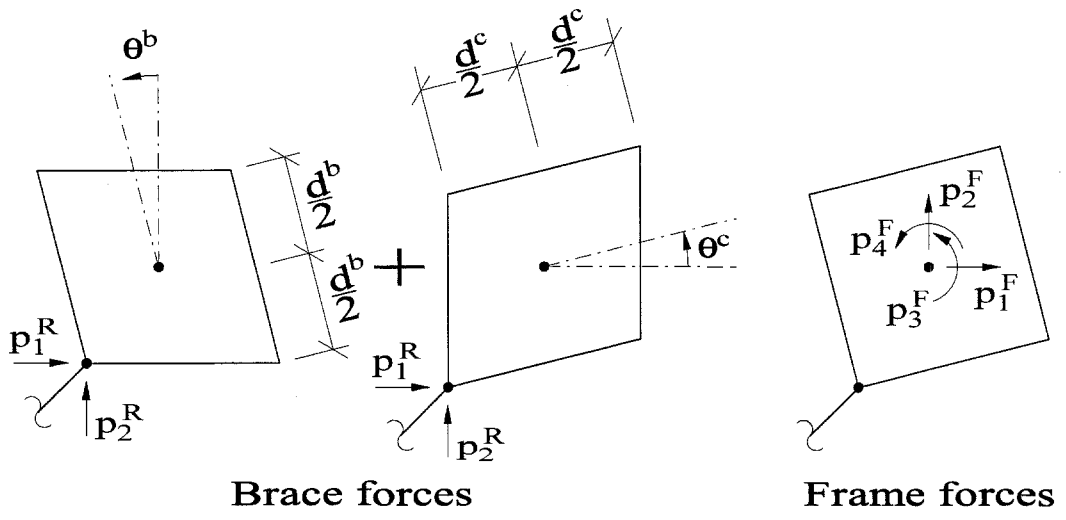

Figure 3.18 Converting right brace end forces to frame nodal forces.

Brace elements also have a similar derivation. Referring to figure 3.17 the brace transformation for left braces is

$$\mathbf{S}^L = \begin{bmatrix} 1 & 0 & \frac{d_i^b}{2}\cos\theta_i^b & \frac{d_i^c}{2}\sin\theta_i^c & 0 & 0 & 0 & 0 \\ 0 & 1 & -\frac{d_i^b}{2}\sin\theta_i^b & \frac{d_i^c}{2}\cos\theta_i^c & 0 & 0 & 0 & 0 \\ 0 & 0 & 0 & 0 & 1 & 0 & -\frac{d_j^b}{2}\sin\theta_j^b & -\frac{d_j^c}{2}\sin\theta_j^c \\ 0 & 0 & 0 & 0 & 0 & 1 & \frac{d_j^b}{2}\cos\theta_j^b & -\frac{d_j^c}{2}\cos\theta_j^c \end{bmatrix} \tag{3.52}$$

and referring to figure 3.18 for right braces is

$$\mathbf{S}^R = \begin{bmatrix} 1 & 0 & \frac{d_i^b}{2}\cos\theta_i^b & \frac{d_i^c}{2}\sin\theta_i^c & 0 & 0 & 0 & 0 \\ 0 & 1 & \frac{d_i^b}{2}\sin\theta_i^b & -\frac{d_i^c}{2}\cos\theta_i^c & 0 & 0 & 0 & 0 \\ 0 & 0 & 0 & 0 & 1 & 0 & -\frac{d_j^b}{2}\cos\theta_j^b & -\frac{d_j^c}{2}\sin\theta_j^c \\ 0 & 0 & 0 & 0 & 0 & 1 & -\frac{d_j^b}{2}\sin\theta_j^b & \frac{d_j^c}{2}\cos\theta_j^c \end{bmatrix} \tag{3.53}$$

resulting in the brace contribution to the frame nodal equations

$$\mathbf{K}_T^{L(orR)} \Delta \mathbf{x}^{L(orR)} = \Delta \mathbf{p}^{F-L(orR)} \tag{3.54}$$

where

$$\mathbf{K}_T^{L(orR)} = [\mathbf{S}^{L(orR)}]^T \mathbf{K}^{BC} \mathbf{S}^{L(orR)} \quad \text{and} \quad \mathbf{p}^{F-L(orR)} = [\mathbf{S}^{L(orR)}]^T \mathbf{p}^{L(orR)}. \tag{3.55}$$

Braces are assumed pinned at their ends, so the rotational degrees of freedom at the ends are considered to be interior dofs. A frame joint will thus pass only translational displacements to the member for local iterations. The rotations at the ends will be solved in these member local iterations, and the zero moment does not need to be passed back to the frame joints. Brace ends are also assumed to be aligned with the panel zone corners. This assumption will produce a moment at the joints if the panel zone dimensions are not proportional to the bay dimensions.

3.3.4 Panel Zone Stiffness

The panel zone stiffness relates the shearing strain γ^{PZ} of the steel volume considered to be acting in the plane of the panel zone and the moment M^{PZ} that resists this strain. The shear modulus is determined from a nonlinear stress-strain relationship, and its instantaneous value is denoted G_T. The volume being sheared is $d^c d^b t$, where d^c is the depth of the column, d^b is the depth of the deeper beam framing into the column and t is the contributing thickness. Doubler plate may be included in the thickness of the panel zone. The shearing strain is related to the beam and column rotations in incremental form by

$$\Delta \gamma^{PZ} = \Delta \theta^b - \Delta \theta^c. \tag{3.56}$$

The resulting stiffness equation is

$$\mathbf{K}_T^{PZ} \Delta \mathbf{x}^{PZ} = \Delta \mathbf{p}^{F-PZ} \tag{3.57}$$

where $\mathbf{\Delta p}^{F-PZ}$ and $\mathbf{\Delta x}^{PZ}$ are the panel zone incremental moments and rotations associated with the frame dofs and

(3.58)
$$\mathbf{K}_T^{PZ} = G_T d^c d^b t \begin{bmatrix} 1 & -1 \\ -1 & 1 \end{bmatrix} \quad , \quad \mathbf{\Delta x}^{PZ} = \begin{Bmatrix} \Delta\theta^b \\ \Delta\theta^c \end{Bmatrix} \quad , \quad \mathbf{p}^{F-PZ} = \begin{Bmatrix} M^b \\ M^c \end{Bmatrix}.$$

3.3.5 Foundation Stiffness

A simple bilinear spring is used to model the soil-structure interaction at the foundation. Different limits can be set for horizontal, upward (tension) and downward (compression) loading. Each base of each column can have two springs acting on it. There is no coupling so the equations for a base node are

(3.59)
$$\mathbf{K}_T^{FN}\mathbf{\Delta x}^{FN} = \mathbf{\Delta p}^{F-FN} \quad \text{where} \quad \mathbf{\Delta x}^{FN} = \begin{Bmatrix} \Delta x^H \\ \Delta x^V \end{Bmatrix} \quad \text{and} \quad \mathbf{p}^{F-FN} = \begin{Bmatrix} p^H \\ p^V \end{Bmatrix}.$$

The tangent stiffnesses depend on the current displacement and force level for the horizontal (H) and vertical (V) base node degrees of freedom.

3.3.6 Frame Stiffness

All of the above stiffnesses which contribute to the frame have been written in the frame coordinate system. The beam, column and brace stiffnesses (3.47, 3.50, 3.54), the panel zone stiffness (3.57) and the foundation stiffness (3.59) can be assembled to appropriate degrees of freedom to formulate the overall frame stiffness

(3.60)
$$\mathbf{K}_T^F = \mathcal{A}\left(\mathbf{K}_T^B + \mathbf{K}_T^C + \mathbf{K}_T^L + \mathbf{K}_T^R + \mathbf{K}_T^{PZ} + \mathbf{K}_T^{FN}\right).$$

All of the stiffness contributions are tangent stiffnesses, so the governing total frame stiffness is also. The forces at all the degrees of freedom of the frame can also be

assembled from the various components:

$$\mathbf{p}^F = a\left(\mathbf{p}^{F-B} + \mathbf{p}^{F-C} + \mathbf{p}^{F-L} + \mathbf{p}^{F-R} + \mathbf{p}^{F-PZ} + \mathbf{p}^{F-FN}\right). \tag{3.61}$$

Chapter 4

Three-Dimensional Modeling

The behavior of real structures is necessarily three dimensional. Many nonlinear programs exist which can evaluate the response of a structure assumed to behave in-plane only and the planar frames developed in the previous chapters can be used to represent this two-dimensional response. Three-dimensional response is commonly modeled with the assumption that each floor acts as a rigid body in plane. Each floor of such a three-dimensional model will have three dofs associated with it: horizontal translation in orthogonal directions and rotation about a vertical axis (figure 4.1(a)).

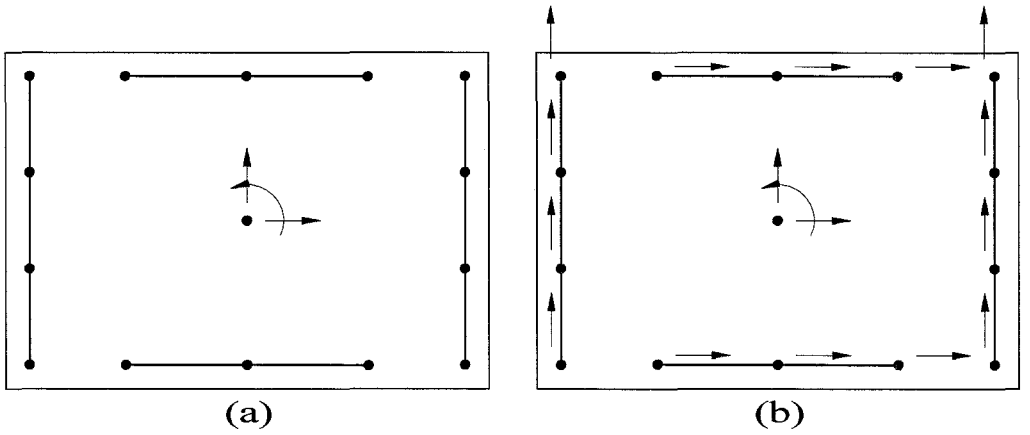

Figure 4.1 Rigid body constraints: (a) Common approach. (b) This work.

The planar frames of the previous chapters can also be constrained with the

rigid floor assumption to achieve quasi-three-dimensional behavior. This is the approach followed here except that it is the average of the horizontal dofs that are constrained to move as a rigid body in the plane of each floor. This particular constraint requires the individual frame column in-plane horizontal dofs to remain active at floor levels (figure 4.1(b)). Additional degrees of freedom are necessary at *master nodes*: two horizontal translational and one rotational in-plane degrees of freedom. The constraints link the frame horizontal dofs to the master node dofs. The master node dofs are in the global coordinates and the frame dofs remain in their individual frame coordinates (figure 4.1(b)).

This is not a fully three-dimensional model because it neglects the out-of-plane stiffness of the frames, but such stiffness is small for typical steel framed structures. The constraint and planar frame assumptions can model the class of structures that have noncontiguous planar frames. Structures with corner columns or curved frames cannot be appropriately modeled under these assumptions. Corner columns will be developed in the next chapter to allow a larger class of problems to be solved.

In addition to introducing the three-dimensional constraints, this chapter will explain other three-dimensional effects which need to be considered separately from the planar frame module described in the previous chapters. Additional strength and stiffness contributions to the building that come from sources other than the frames can be included in the model. P-Δ effects from gravity loads not carried by the frames as well as out-of-plane P-Δ effects of the frames are included in the formulation. The assembly of the global load vector and global stiffness, mass and damping matrices for the general three-dimensional problem are also explained in this chapter.

4.1 Constraint Methods

The individual frames need to be connected to the master nodes in some manner. The average displacement of each frame's horizontal translations at each story is constrained to move as a rigid body consistent with the master node motions. This

allows beams to have some axial deformation that is more realistic than a truly rigid diaphragm assumption. The axial deformation of beams is especially important for the nonlinear inelastic analyses performed in this work. Even if there is only one frame in the model, it needs to be constrained to act with the master node which has additional geometric and stiffness effects included.

Consider the simplest form of this constraint in which a two dimensional analysis is being performed with one frame plus a master node at each floor. The average of the frame nodal horizontal displacements is constrained to be equal to the master node displacement at each floor. This can be written for floor j with n frame horizontal dofs as

$$\frac{1}{n}(x_1 + \cdots + x_n) = x_j^{MN} \tag{4.1}$$

where x_i is the global horizontal frame displacement at frame joint i and x_j^{MN} is the global horizontal master node displacement. This can be rewritten for the augmented vector $\mathbf{x}_j$ of story displacements which includes the frame horizontal displacements and the master node displacement at floor j as

$$\begin{bmatrix} -\frac{1}{n} & \cdots & -\frac{1}{n} & 1 \end{bmatrix} \mathbf{x}_j = 0, \tag{4.2}$$

which is of the form $\mathbf{C}_j\mathbf{x}_j = 0$ where $\mathbf{C}_j$ is a constraint matrix.

Several methods exist for including constraints. The method that seems best suited to the iterative method used in this program is the penalty method. Lagrange multipliers, for example, add unknowns and result in a stiffness matrix with some zeroes on the diagonals. The penalty method adds large stiffness penalties to degrees of freedom that are constrained, and they can be chosen so that sufficient accuracy is obtained.

Assume that all of the story constraints for each frame are assembled into a global constraint matrix $\mathbf{C}$ operating on all of the degrees of freedom $\mathbf{x}$ so that the

desired constraints can be expressed as

$$\mathbf{Cx} = \mathbf{0}. \tag{4.3}$$

If the constraint equations are not exactly satisfied there will be some non-zero entries on the right side of the equation, so the actual expression will be

$$\mathbf{Cx} = \mathbf{t}. \tag{4.4}$$

By choosing a set of penalty numbers α_i which form a diagonal matrix $[\boldsymbol{\alpha}]$, the penalty function $\frac{1}{2}\mathbf{t}^T[\boldsymbol{\alpha}]\mathbf{t}$ can be defined.[1] This penalty function can be added to the potential of the structural system Π_p giving the augmented potential

$$\Pi_p = \frac{1}{2}\mathbf{x}^T\mathbf{K}\mathbf{x} - \mathbf{x}^T\mathbf{f} + \frac{1}{2}\mathbf{t}^T[\boldsymbol{\alpha}]\mathbf{t}. \tag{4.5}$$

Note that if the residuals $\mathbf{t} = \mathbf{0}$, the potential is unchanged. If $\mathbf{t} \neq \mathbf{0}$, there is a large penalty for violating the constraints as the α_i increase. By substituting (4.4) and minimizing the potential $\{\partial\Pi_p/\partial\mathbf{x}\} = \mathbf{0}$ the result is

$$[\mathbf{K} + \mathbf{C}^T[\boldsymbol{\alpha}]\mathbf{C}]\mathbf{x} = \mathbf{f}. \tag{4.6}$$

Since all the degrees of freedom being constrained are horizontal displacements, it is reasonable to choose one penalty number α so that $\boldsymbol{\alpha} = \alpha\mathbf{I}$. The previous equation can now be rewritten in incremental form as

$$[\mathbf{K}_T + \mathbf{K}^C]\boldsymbol{\Delta}\mathbf{x} = \boldsymbol{\Delta}\mathbf{f} \quad \text{where} \quad \mathbf{K}^C = \alpha\mathbf{C}^T\mathbf{C}. \tag{4.7}$$

In the above derivation, the stiffness matrix $\mathbf{K}_T$ was assumed not to be a function of the displacements $\mathbf{x}$. While this is not true for nonlinear behavior in general, the constraint methodology still holds for each instantaneous tangent stiffness matrix. It also works for dynamic problems. The constraint matrix for the three-dimensional

[1] The following derivation is adapted from (Cook, Malkus, and Plesha 1989).

formulation is considered in the next section.

A large value of α is desired to accomplish the constraint to a high degree, but too large a value will cause ill conditioning and subsequent loss of accuracy when the equations are solved. However, experience with structural problems has shown that, except in unusual cases, the use of double precision allows α to be selected to accomplish the constraint sufficiently while avoiding excessive loss of digits due to ill conditioning.

The penalty method was selected over other common methods of constraint for its ease of implementation in the iterative nonlinear solution technique. The constraints being imposed are prescribed interactions of certain degrees of freedom, and there are three common methods for including this type of constraint — the penalty method, the transformation method, and Lagrange multipliers.

The transformation method (McGuire and Gallagher 1979; Cook, Malkus, and Plesha 1989) uses the constraint equations to eliminate degrees of freedom from the global stiffness matrix. If there are r equations of constraint, then the method reduces the total number of dofs by r. This method is not suitable for this analysis for several reasons. The number of constraint equations equals the number of eliminated dofs that could require peculiar non-intuitive choices for constraints. The method also requires a substantial amount of effort for, "reordering, partitioning and matrix multiplications.[2]" The condensed system uses constraint equations that replace some equilibrium equations instead of retaining all of the equilibrium equations. This can cause certain equilibrium equations of the original system to not be met even though the condensed system satisfies its equilibrium equations. (Cook, Malkus, and Plesha 1989).

The method of Lagrange multipliers forms the scalar product of the homogeneous constraint equations with an equal number of unknown multipliers, λ_i. This zero sum is added to the system's potential in the same way as the penalty method

[2](Cook, Malkus, and Plesha 1989, p. 273)

(equation 4.5):

$$\Pi_p = \frac{1}{2}\mathbf{x}^T\mathbf{K}_T\mathbf{x} - \mathbf{x}^T\mathbf{f} + \boldsymbol{\lambda}^T\{\mathbf{C}\mathbf{x} - \mathbf{t}\}. \tag{4.8}$$

Minimizing the potential results in the equation

$$\begin{bmatrix} \mathbf{K} & \mathbf{C}^T \\ \mathbf{C} & \mathbf{0} \end{bmatrix} \begin{Bmatrix} \mathbf{x} \\ \boldsymbol{\lambda} \end{Bmatrix} = \begin{Bmatrix} \mathbf{f} \\ \mathbf{t} \end{Bmatrix} \tag{4.9}$$

where the homogeneous constraint equations are the latter equations above. Note that there are zeros on the diagonal. If the equations are arranged as shown, Gaussian elimination can still be used since the zeros will be filled in before they are reached, although the bandedness of the stiffness matrix is affected. If the constraint equations are interspersed in such a way that whenever one is reached, all the dofs that it couples appear before it, then the system can maintain its smaller bandwidth and the zeros on the diagonal will not halt the solution process (Cook, Malkus, and Plesha 1989). The Lagrange multiplier method and the penalty method are closely related and Bathe presents an augmented Lagrange multiplier method that adds both a Lagrange multiplier zero-value term and a penalty zero-value term to the system's potential. The method is used for iterative procedures and gives reasonable results for all values of penalty factor α (Bathe 1996). The augmented potential is

$$\Pi_p = \frac{1}{2}\mathbf{x}^T\mathbf{K}_T\mathbf{x} - \mathbf{x}^T\mathbf{f} + \frac{\alpha}{2}\{\mathbf{C}\mathbf{x} - \mathbf{t}\}^T\{\mathbf{C}\mathbf{x} - \mathbf{t}\} + \boldsymbol{\lambda}^T\{\mathbf{C}\mathbf{x} - \mathbf{t}\}. \tag{4.10}$$

The Lagrange multiplier method can be used if a reordering scheme were developed to avoid zero diagonals during Gaussian elimination. Additional dofs corresponding to the number of constraint equations would be required.

The penalty method is simpler because no reordering or additional dofs are required. The penalty "stiffness" is assembled just like any other stiffness contribution. If desired, the penalty stiffness could approximate the in-plane stiffness of

a structure's floor diaphragm providing an intuitive physical interpretation of the method. The only potential drawback of the penalty method is ill conditioning. As discussed earlier, the penalty factor can usually be chosen in a range to avoid ill conditioning if double precision is employed.

4.2 Constraint Equations

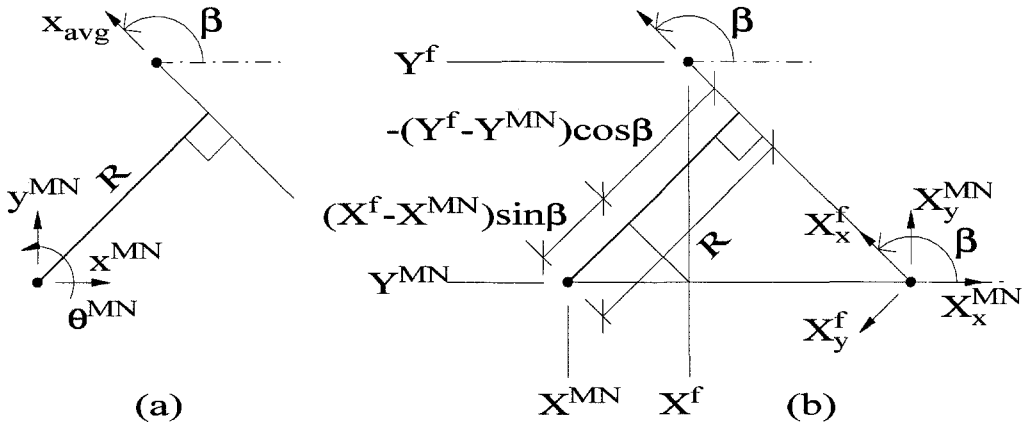

Figure 4.2 (a) Average displacement of frame. (b) Calculation of R.

The constraint method described above needs to be developed for three-dimensional analysis. Each frame will have a constraint equation for each floor. The average in-plane global horizontal displacement of a frame's individual nodes, Δx_{avg}, is constrained to act as a rigid body with the master node global horizontal displacements, Δx^{MN} and Δy^{MN}, and rotation, $\Delta\theta^{MN}$. In general, the global coordinate system for a frame is oriented an angle β from the global coordinate system for the master nodes. If the frame orientation is β, and the perpendicular distance from the plane of the frame to the master node is R, then the average displacement assuming rigid body motion will be (see figure 4.2(a)):

$$\Delta x_{avg} = \Delta x^{MN}\cos\beta + \Delta y^{MN}\sin\beta + \Delta\theta^{MN}R. \tag{4.11}$$

This can be written as a constraint equation for the frame nodal horizontal displace-

ments $\Delta x_1 \cdots \Delta x_n$ as

$$\left[\frac{1}{n} \quad \cdots \quad \frac{1}{n} \quad -\cos\beta \quad -\sin\beta \quad -R\right] \begin{Bmatrix} \Delta x_1 \\ \vdots \\ \Delta x_n \\ \Delta x^{MN} \\ \Delta y^{MN} \\ \Delta \theta^{MN} \end{Bmatrix} = 0. \tag{4.12}$$

The frame distance R is determined from the coordinates of the master node, X^{MN} and Y^{MN}, and the frame origin, X^f and Y^f, all given in master node global coordinates, by (see figure 4.2(b)):

$$R = (X^f - X^{MN})\sin\beta - (Y^f - Y^{MN})\cos\beta. \tag{4.13}$$

The distance R can be positive or negative depending on the orientation of the frame. If positive in-plane horizontal displacements of a frame are consistent with a counter-clockwise rotation of the master node, then R is positive. Frames can have any orientation desired and their average motions will remain consistent in a rigid body sense with the master node motions.

The constraint equation (4.12) must be transformed to a constraint stiffness as per equation (4.7). The resulting constraint stiffness for one frame at floor j

considering only the horizontal dofs being constrained will be

(4.14)

$$\alpha\mathbf{C}^T\mathbf{C} = \alpha \begin{bmatrix} \frac{1}{n^2} & \cdots & \frac{1}{n^2} & \frac{-\cos\beta}{n} & \frac{-\sin\beta}{n} & \frac{-R}{n} \\ & \ddots & \vdots & \vdots & \vdots & \vdots \\ & & \frac{1}{n^2} & \frac{-\cos\beta}{n} & \frac{-\sin\beta}{n} & \frac{-R}{n} \\ & & & \cos^2\beta & \sin\beta\cos\beta & R\cos\beta \\ & \text{SYM} & & & \sin^2\beta & R\sin\beta \\ & & & & & R^2 \end{bmatrix} \begin{matrix} \Longleftarrow \text{ dof } x_1 \\ \\ \Longleftarrow \text{ dof } x_n \\ \Longleftarrow \text{ dof } x^{MN} \\ \Longleftarrow \text{ dof } y^{MN} \\ \Longleftarrow \text{ dof } \theta^{MN}, \end{matrix}$$

which can be written as a story constraint stiffness matrix

$$\mathbf{K}_j^C = \alpha\mathbf{C}^T\mathbf{C}. \tag{4.15}$$

The constraint stiffness matrix for the entire structure can be assembled from the story constraints as

$$\mathbf{K}_T^C = \overset{n_s}{\underset{j=1}{\mathcal{A}}} \left[\mathbf{K}_j^C\right] \tag{4.16}$$

where n_s is the number of stories. The constraint equation is linear, so the forces that result from its stiffness are simply

$$\mathbf{p}^C = \mathbf{K}_T^C\mathbf{x}. \tag{4.17}$$

Another issue raised by the constraints is the conditioning of the stiffness matrix. Note that the master node rotational degree of freedom has a term on the order of αR^2 (equation 4.14), which can be relatively large for large α and R. The concern is that the main diagonal values of the stiffness will vary by many orders of magnitude. This alone is not necessarily a problem, but the stiffness matrix is actually an assembly of singular matrices, so one extremely large singular matrix could potentially cause numerical problems. In this formulation, an estimate of the accuracy of

the solution is obtained by comparing the size of the diagonals encountered during forward reduction to an average of the original diagonal values. A better estimate would compare the size of a newly computed diagonal to its previous value. In this way, a change in magnitude will reflect possible ill conditioning.

In the Gaussian elimination scheme, when the row corresponding to the master node rotational dof is reached, elimination of the terms below the main diagonal will require operations like:

$$k_{\theta\theta} = k_{\theta\theta} - k_{j\theta}\frac{k_{\theta j}}{k_{jj}}$$

Exaggeration of any existing ill conditioning due to the αR^2 term of a rotational degree of freedom will not occur from these operations. Compare the elimination required for a two-dimensional problem with stiffness ϵ and a three-dimensional problem with rotational stiffness ϵR^2:

$$\begin{matrix} \begin{bmatrix} \alpha & -\alpha \\ -\alpha & \alpha+\epsilon \end{bmatrix} & \begin{bmatrix} \alpha & -\alpha R \\ -\alpha R & \alpha R^2 + \epsilon R^2 \end{bmatrix} \\ \text{2D case} & \text{3D case} \end{matrix} \tag{4.18}$$

Each of the matrices above will have a ratio of post-elimination (new) to pre-elimination (old) for the lower diagonal of

$$\frac{k_{22}^{new}}{k_{22}^{old}} = \frac{k_{22} - k_{12}\frac{k_{21}}{k_{11}}}{k_{22}} = \frac{\epsilon}{\alpha+\epsilon}.$$

This would imply the same level of ill conditioning, so the master node rotational dofs are skipped when determining the conditioning of the stiffness matrix based on the range of main diagonal values. The program will stop when the average of the main diagonal values (excluding $k_{\theta\theta}$'s) is larger than 10^{10} times the smallest diagonal. This tolerance is used to flag a potential problem, not necessarily eliminate ill conditioning. No ill conditioning has been observed for the buildings studied in this or previous works so more rigorous conditioning checks are not deemed

necessary.

4.3 Shear Spring Elements

Many sources contribute to the lateral analysis of a building besides the bare-steel moment and braced frames. Even though the formulation includes composite slab behavior, panel zone deformations, and foundation springs, there are still other sources of stiffness and strength.

Several non-structural components of a structure may provide a certain amount of lateral stiffness and strength to the overall structure that is not accounted for in a typical structural design. Curtain walls, partitions, CMU in-fill around openings, and stair framing may all contribute to the lateral resistance of the structure. Additionally, structural gravity framing not intended to be part of the lateral system can have stiffness and strength contributions due to bending resistance of the columns and to partial restraint of presumed simple connections. In general, it is too computationally expensive to include the gravity framing in a three-dimensional analysis, although it could be included with the use of simple beam-to-column connections.

To simplify the model, an element called a *shear spring* is used to model stiffness and strength. The shear springs can be located anywhere in a building, not necessarily at nodal locations. They span between floors just like a column of the frame, but they do not have any degrees of freedom associated with them. Their contributions are lumped to the master node degrees of freedom at each floor. As an example of their use, a vertical arrangement of shear springs could model a shear building.

A shear spring resists relative horizontal displacements (top to bottom) in the global x or y directions. A bilinear model defines the shear spring force-displacement relationship by providing the initial stiffness k_x or k_y and a yield force F_C^{SH} (figure 4.3). Engineering judgment and attempts to match measured building response can be used to determine an appropriate amount of shear building stiffness and strength.

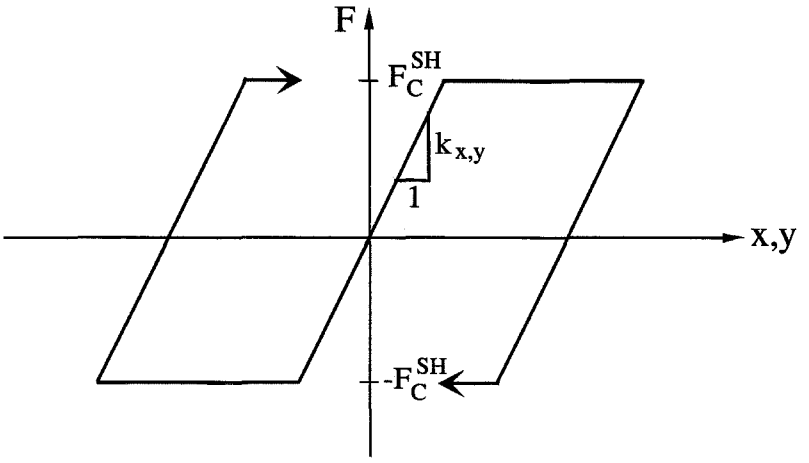

Figure 4.3 Load-deflection relation for shear springs.

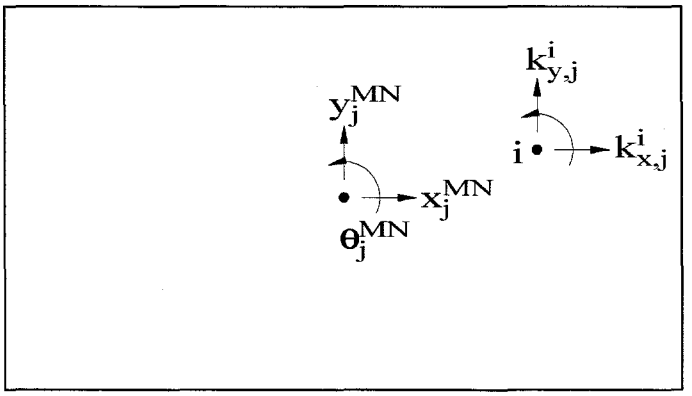

Figure 4.4 Shear spring stiffnesses.

The stiffness formulation of the shear springs is now derived. Each shear spring i of each story j can have orthogonal tangent nonlinear story stiffnesses $k^i_{x,j}$ and $k^i_{y,j}$ (figure 4.4). The displacements at the shear spring location first need to be written in terms of the master node displacements using the three-dimensional small rotation transformation. For a general location c on a particular floor, this geometric

transformation is

$$(4.19) \qquad \begin{Bmatrix} \Delta x^c \\ \Delta y^c \\ \Delta \theta^c \end{Bmatrix} = \begin{bmatrix} 1 & 0 & -Y^{cMN} \\ 0 & 1 & X^{cMN} \\ 0 & 0 & 1 \end{bmatrix} \begin{Bmatrix} \Delta x^{MN} \\ \Delta y^{MN} \\ \Delta \theta^{MN} \end{Bmatrix} \quad \text{or} \quad \mathbf{\Delta x}^c = \mathbf{T}\mathbf{\Delta x}^{MN}$$

where $X^{cMN} = X^c - X^{MN}$ and $Y^{cMN} = Y^c - Y^{MN}$ (figure 4.5). Note that the

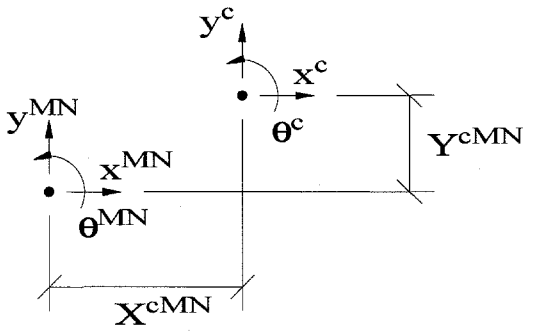

Figure 4.5 Transformation of displacements from master node to location c.

rotation of location c is also included in the transformation. This is an unnecessary variable to keep track of, but the forces in a shear spring at location c will contribute to the torsion at the master node, so the master node rotation θ^{MN} must remain in the formulation. This transformation written for shear spring i connecting floors j and $j+1$ becomes

$$(4.20) \qquad \mathbf{\Delta x}_j^i = \mathbf{T}_j^i \mathbf{\Delta x}_j^{MN}.$$

Considering only story j bounded by floor j below and floor $j+1$ above, the force

displacement relationship for a shear spring is

$$\begin{bmatrix} k^i_{x,j} & 0 & 0 & -k^i_{x,j} & 0 & 0 \\ 0 & k^i_{y,j} & 0 & 0 & -k^i_{y,j} & 0 \\ 0 & 0 & 0 & 0 & 0 & 0 \\ -k^i_{x,j} & 0 & 0 & k^i_{x,j} & 0 & 0 \\ 0 & -k^i_{y,j} & 0 & 0 & k^i_{y,j} & 0 \\ 0 & 0 & 0 & 0 & 0 & 0 \end{bmatrix} \begin{Bmatrix} \Delta x^i_{j+1} \\ \Delta y^i_{j+1} \\ \Delta \theta^i_{j+1} \\ \Delta x^i_j \\ \Delta y^i_j \\ \Delta \theta^i_j \end{Bmatrix} = \begin{Bmatrix} \Delta p^i_{x,j+1} \\ \Delta p^i_{y,j+1} \\ \Delta p^i_{\theta,j+1} \\ \Delta p^i_{x,j} \\ \Delta p^i_{y,j} \\ \Delta p^i_{\theta,j} \end{Bmatrix}. \tag{4.21}$$

A notation for the 3×3 sub-matrices is introduced as

$$\mathbf{k}^{i,SS}_j = \begin{bmatrix} k^i_{x,j} & 0 & 0 \\ 0 & k^i_{y,j} & 0 \\ 0 & 0 & 0 \end{bmatrix}, \tag{4.22}$$

allowing equation 4.22 to be written as

$$\begin{bmatrix} \mathbf{k}^{i,SS}_j & -\mathbf{k}^{i,SS}_j \\ -\mathbf{k}^{i,SS}_j & \mathbf{k}^{i,SS}_j \end{bmatrix} \begin{Bmatrix} \mathbf{\Delta x}^i_{j+1} \\ \mathbf{\Delta x}^i_j \end{Bmatrix} = \begin{Bmatrix} \mathbf{\Delta p}^i_{j+1} \\ \mathbf{\Delta p}^i_j \end{Bmatrix}. \tag{4.23}$$

The transformation $\mathbf{T}^i_j$ from eqs. 4.19 and 4.20 gives the exact relationship between the forces of a shear spring and their contribution to the master node at level j:

$$\mathbf{p}^{MN}_j = [\mathbf{T}^i_j]^T \mathbf{p}^i_j, \tag{4.24}$$

which can also be expressed in incremental form. Substituting (4.20) and (4.24) into (4.23), the contribution of a single shear spring i to the master node dofs becomes

$$\begin{bmatrix} [\mathbf{T}^i_{j+1}]^T \mathbf{k}^{i,SS}_j \mathbf{T}_{j+1} & -[\mathbf{T}^i_{j+1}]^T \mathbf{k}^{i,SS}_j \mathbf{T}_j \\ -[\mathbf{T}^i_j]^T \mathbf{k}^{i,SS}_j \mathbf{T}_{j+1} & [\mathbf{T}^i_j]^T \mathbf{k}^{i,SS}_j \mathbf{T}_j \end{bmatrix} \begin{Bmatrix} \mathbf{\Delta x}^{MN}_{j+1} \\ \mathbf{\Delta x}^{MN}_j \end{Bmatrix} = \begin{Bmatrix} \mathbf{\Delta p}^{MN}_{j+1} \\ \mathbf{\Delta p}^{MN}_j \end{Bmatrix}, \tag{4.25}$$

which can be written as

$$\mathbf{K}_j^{i,SS}\Delta\mathbf{x}_j^{MN} = \Delta\mathbf{p}_j^{MN} \tag{4.26}$$

for story j. Note that a shear spring on story j contributes to the master node dofs on floor $j+1$ above and floor j below the story. The overall story stiffness is the sum of all the shear spring stiffnesses associated with that story (a total of n_j^{SS} shear springs in story j):

$$\mathbf{K}_j^{SH}\Delta\mathbf{x}_j^{MN} = \Delta\mathbf{p}_j^{MN} \quad \text{where} \quad \mathbf{K}_j^{SH} = \overset{n_j^{SS}}{\underset{i=1}{\mathcal{A}}}\left[\mathbf{K}_j^{i,SS}\right]. \tag{4.27}$$

The shear building stiffnesses $\mathbf{K}_j^{SH}$ are tangent stiffnesses, and the total shear building tangent stiffness involves all of the master node dofs by the set of equations

$$\mathbf{K}_T^{SH}\Delta\mathbf{x}^{MN} = \Delta\mathbf{p}^{MN} \quad \text{where} \quad \mathbf{K}_T^{SH} = \overset{n_s}{\underset{j=1}{\mathcal{A}}}\left[\mathbf{K}_j^{SH}\right]. \tag{4.28}$$

In the assembly above, n_s is the number of stories. This stiffness only contributes to the master node degrees of freedom. The forces at the master nodes can be assembled similarly. Using equation 4.24, the forces can be summed for all shear springs i associated with floor j, and these master node forces can be assembled into the $\mathbf{p}^{SH}$ vector of all building forces. This summation and assembly can be expressed as

$$\mathbf{p}^{SH} = \overset{n_s}{\underset{j=1}{\mathcal{A}}}\left[\sum_{i=1}^{n_j^{SS}}\left([\mathbf{T}_j^i]^T\mathbf{p}_j^i\right)\right]. \tag{4.29}$$

As mentioned above, the shear springs can be placed at arbitrary locations within each story of the building. In the absence of specific information, one strategy is to place a shear spring at each column location, including columns that are present in the model (frame columns) and those that are not (gravity columns). The x and y stiffness and strength of each shear spring would be made the same, equal to the desired lateral stiffness and strength in a story divided by the number of shear

springs in that story. This method will automatically establish specific values for the torsional stiffness and strength in the story due to the shear springs. In the deformed state, the alignment of frame columns and shear springs positioned in the same location will not be perfect since the shear springs are moving as a rigid body connected to the master nodes, whereas the *average* of a frame's column movements is constrained to rigid body motion with the master nodes.

4.4 P-Δ Effects

Planar frames can act as a three-dimensional structure using the constraint equations, but additional P-Δ effects must be accounted for and assembled to the master node degrees of freedom. Vertical loading carried by gravity columns not included in the model will create a P-Δ effect discussed in the next subsection. The P-Δ effects on frame columns in the plane of the frames is automatically accounted for through geometric updating, but the P-Δ effect in the out-of-plane direction must also be included, and is discussed in the following subsection.

4.4.1 Gravity Columns

Vertical loading not carried by the frame columns will create a P-Δ effect. Since the frames and shear springs provide all of the lateral resistance, when the top of a gravity column moves relative to the bottom, the resulting P-Δ horizontal couple will be carried by the frames and shear springs, not the relatively flexible gravity column. Gravity columns are typically not included in the model, and if they are, they are represented as single column frames. To include this P-Δ effect, cumulative gravity loads are placed in plan at gravity column locations. In this way, the P-Δ effect can be determined in each direction for gravity columns and tied to the frames through the master node constraints.

Many programs account for P-Δ effects by assigning a force couple at floor levels to induce the incurred moment and by reducing the stiffness of the story between the floors based on the force and displacement levels. These programs can give accurate

results, but there are drawbacks to these techniques. For example, ETABS assumes the input mass at each floor can be used as a constant load on the columns of the structure on a floor-by-floor basis. This allows the geometric stiffness reduction that is dependent on axial load to be assembled to the building stiffness prior to analysis. In this way, ETABS can approximate the P-Δ effect without any iteration (Wilson 1997). The drawback is that if a column has uplift from overturning, it will still receive a P-Δ stiffness reduction as if a constant downward load were being applied. This approach assumes small lateral displacements relative to story heights and ignores nonlinear beam-column stiffness effects altogether in its global approach (Wilson and Habibullah 1987). While this method is simplistic, it will be used for the gravity column P-Δ effects.

The cumulative gravity load P_j^i associated with gravity column i of story j produces a negative geometric stiffness written in the same form as the 3×3 shear spring stiffness (eq. 4.22):

$$\mathbf{k}_j^{i,P-\Delta} = \begin{bmatrix} -\frac{P_j^i}{L_j} & 0 & 0 \\ 0 & -\frac{P_j^i}{L_j} & 0 \\ 0 & 0 & 0 \end{bmatrix}. \tag{4.30}$$

This can be assembled the same way the shear spring stiffness was by replacing $\mathbf{k}_j^{i,SS}$ with $\mathbf{k}_j^{i,P-\Delta}$ in equation (4.25) and summed for all gravity loads for story j as

$$\mathbf{K}_j^{P-\Delta} \mathbf{\Delta x}_j^{MN} = \mathbf{\Delta p}_j^{MN}. \tag{4.31}$$

The resulting geometric stiffness equation is the same as developed in Wilson and Habibullah (1987). The geometric stiffness associated with the gravity column loads for the entire structure is

$$\mathbf{K}_T^{P-\Delta} = \overset{n_s}{\underset{j=1}{\mathbf{A}}} \left[\mathbf{K}_j^{P-\Delta} \right] \tag{4.32}$$

where n_s is the number of stories.

As in the case of shear springs, the transformation $\mathbf{T}_j^i$ from equation 4.19 provides the exact relation between the forces at gravity column location i and the master node at level j:

$$\mathbf{p}_j^{MN} = [\mathbf{T}_j^i]^T \mathbf{p}_j^i. \tag{4.33}$$

The forces can be summed for the $n_j^{P-\Delta}$ locations at each floor j where gravity loads have been placed and assembled into the total force vector as

$$\mathbf{p}^{P-\Delta} = \mathop{\mathbf{A}}_{j=1}^{n_s} \left[\sum_{i=1}^{n_j^{P-\Delta}} \left([\mathbf{T}_j^i]^T \mathbf{p}_j^i \right) \right]. \tag{4.34}$$

4.4.2 Frame Columns Out-of-Plane

Out-of-plane frame displacement will create a geometric effect that must be carried by frames and shear springs providing transverse resistance. The out-of-plane displacements and column forces are tracked, and their contribution as force couples is summed at the master nodes. The original orientation of a frame (β) is used to determine the out-of-plane direction ($\beta + \pi/2$) in which to apply the couples. The out-of-plane geometric stiffness reduction is not considered in the updating of the global tangent stiffness matrix. While the tangent stiffness is a function of the current deformation state, no other stiffness contribution is directly a function of the current forces. Neglecting the contribution prevented the load vector from being passed to the stiffness assembly routine. Convergence did not appear to be greatly affected.

The out-of-plane geometric stiffness effects are included when updating the residual force vector, summing the effects at the master nodes. For the gravity loads of the previous subsection, the force couples are applied to the master nodes based on relative displacements of gravity columns at adjacent floors. These displacements are determined by transforming the master node displacements to the gravity column locations based on rigid body motion (equation 4.19). For frames, the force couples are determined from components of displacement perpendicular to the *orig-*

inal orientation of the frame (figure 4.6). This is consistent with other assumptions, including the constraint stiffness that also uses the original frame orientation. A

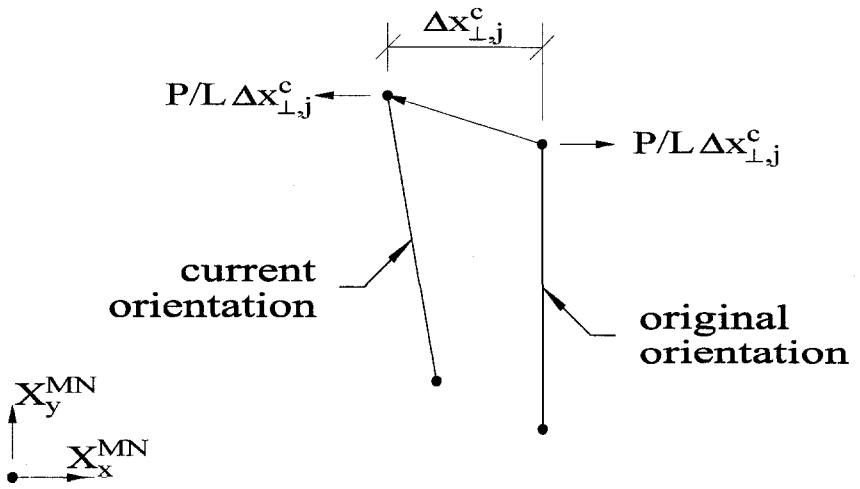

Figure 4.6 Out-of-plane P-Δ effects for frame columns.

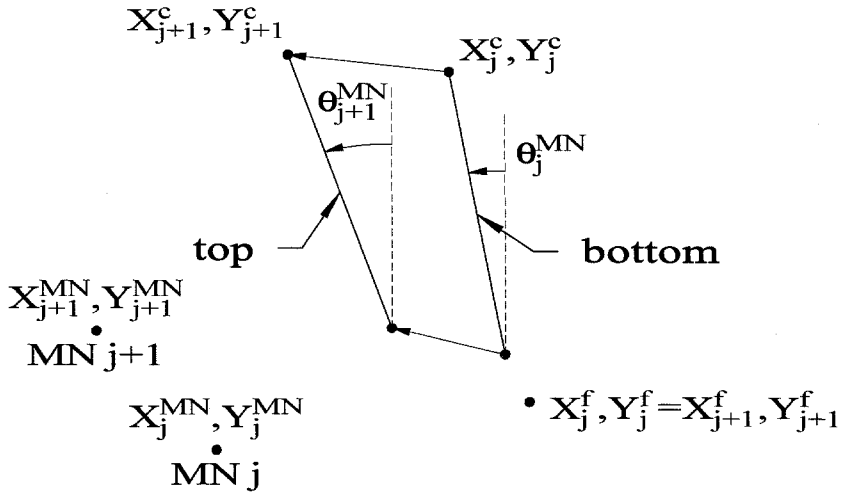

Figure 4.7 Column current location at floors j and $j+1$.

frame has local in-plane displacement $x_{\parallel}$ and out-of-plane displacement $x_{\perp}$. The in-plane displacement comes directly from the frame degrees of freedom, whereas

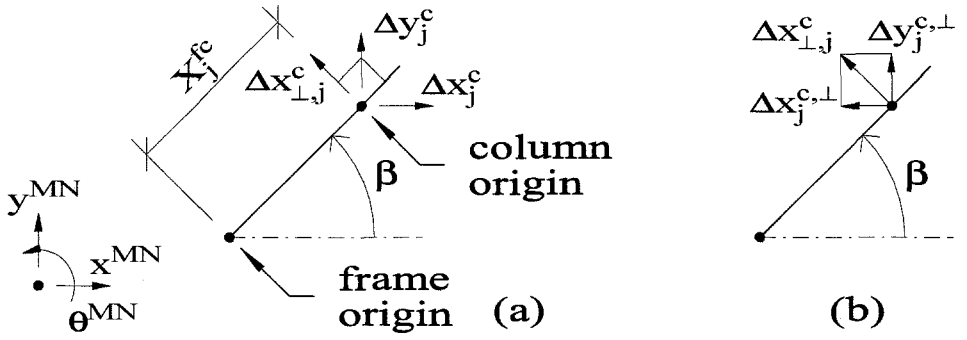

Figure 4.8 (a) Component of column displacement perpendicular to original frame orientation. (b) Global components of out-of-plane displacement.

the out-of-plane displacement must be approximated from the master node displacements assuming rigid body motion. The relative out-of-plane displacement between floors at a column location c will be determined from the updated coordinates at each floor (figure 4.7). The column is located a distance X_j^{cf} from the frame origin measured along the axis of the frame (figure 4.8). The coordinates of column c at floor j are X_j^c and Y_j^c in the global coordinate system. They are updated based on the current location and orientation of the frame they come from. The frame origin is located a fixed distance (X_j^{fMN}, Y_j^{fMN}) from the master node in the original orientation, where $X_j^{fMN} = X_j^f - X_j^{MN}$ and $Y_j^{fMN} = Y_j^f - Y_j^{MN}$. The frame location is adjusted for the master node motions, and the column is then located along the current orientation of the frame:

$$X_j^c = X_j^{MN} + X_j^{fMN}\cos\theta_j^{MN} - Y_j^{fMN}\sin\theta_j^{MN} + X_j^{cf}\cos(\beta + \theta_j^{MN}) \tag{4.35}$$

$$Y_j^c = Y_j^{MN} + X_j^{fMN}\sin\theta_j^{MN} + Y_j^{fMN}\cos\theta_j^{MN} + X_j^{cf}\sin(\beta + \theta_j^{MN}). \tag{4.36}$$

The master node rotation, θ_j^{MN}, locates the frame origin. Once located, the column is located a distance X_j^{cf} along the *current* frame orientation, $\beta + \theta_j^{MN}$. The locations of the top and bottom of the column are determined in this manner, and

the difference in their locations is represented as $\Delta x_j^c, \Delta y_j^c$ in global coordinates:

$$\Delta x_j^c = X_{j+1}^c - X_j^c \tag{4.37}$$

$$\Delta y_j^c = Y_{j+1}^c - Y_j^c. \tag{4.38}$$

Now, only the portion of this story displacement which is perpendicular to the *original* orientation of the frame (β) is desired for the out-of-plane P-Δ force application. The out-of-plane displacement, $\Delta x_{\perp,j}^c$, of a column (figure 4.8(a)) can be expressed in frame coordinates based on the column story displacements

$$\Delta x_{\perp,j}^c = \begin{bmatrix} -\sin\beta & \cos\beta \end{bmatrix} \begin{Bmatrix} \Delta x_j^c \\ \Delta y_j^c \end{Bmatrix}. \tag{4.39}$$

The global components of this perpendicular distance, $\Delta x_j^{c,\perp}$ and $\Delta y_j^{c,\perp}$, (figure 4.8(b)) are

$$\Delta x_j^{c,\perp} = -(\Delta x_{\perp,j}^c)\sin\beta \tag{4.40}$$

$$\Delta y_j^{c,\perp} = (\Delta x_{\perp,j}^c)\cos\beta. \tag{4.41}$$

The master node dofs are updated for the P-Δ forces using the distances between the column top and bottom and the master nodes at floors $j+1$ and j, namely X_{j+1}^{cMN} and X_{j+1}^{cMN} at floor $j+1$ and X_j^{cMN} and X_j^{cMN} at floor j. See figure 4.5 for the definition of these distances. The update uses the global components of

perpendicular displacements determined from equations 4.40 and 4.41:

$$(4.42)\qquad \begin{Bmatrix} p^{MN}_{x,j+1} \\ p^{MN}_{y,j+1} \\ p^{MN}_{\theta,j+1} \\ p^{MN}_{x,j} \\ p^{MN}_{y,j} \\ p^{MN}_{\theta,j} \end{Bmatrix} = \begin{Bmatrix} p^{MN}_{x,j+1} \\ p^{MN}_{y,j+1} \\ p^{MN}_{\theta,j+1} \\ p^{MN}_{x,j} \\ p^{MN}_{y,j} \\ p^{MN}_{\theta,j} \end{Bmatrix} + \frac{P^c_j}{L_j} \begin{bmatrix} 1 & 0 \\ 0 & 1 \\ -Y^{cMN}_{j+1} & X^{cMN}_{j+1} \\ -1 & 0 \\ 0 & -1 \\ Y^{cMN}_j & -X^{cMN}_j \end{bmatrix} \begin{Bmatrix} \Delta x^{c,\perp}_j \\ \Delta y^{c,\perp}_j \end{Bmatrix}$$

These forces at the master nodes can be assembled into the global force vector:

$$(4.43)\qquad \mathbf{p}^{OUT} = \overset{n_s}{\underset{j=1}{\mathbf{A}}} \left[\begin{Bmatrix} \mathbf{p}^{MN}_{j+1} \\ \mathbf{p}^{MN}_j \end{Bmatrix} \right]$$

where n_s is the number of stories and $\mathbf{p}^{MN}_j = \langle p^{MN}_{x,j} p^{MN}_{y,j} p^{MN}_{\theta,j} \rangle^T$.

4.5 Geometric Nonlinearity

Two assumptions concerning the size of angles are made in the three-dimensional stiffness formulations. First, the total angle of twist of a building in the plane of a floor is assumed to be small. This will be called the *small angle assumption.* It affects the constraint equations and the P-Δ effect of out-of-plane displacement of frame columns. Second, the incremental rotation of a master node is assumed to be small. This will be called the *small rotation assumption.* It affects the shear spring stiffness, the P-Δ effect of gravity loads not carried by frames and the story-damping formulation.

4.5.1 Small Angle Assumption

The frame module is a two-dimensional entity which provides resistance only in the original plane of the frame. Nodal updating in this plane accounts for moment

amplification (member buckling) and in-plane P-Δ. For three-dimensional analysis, the constraints connecting frames together use the original orientation of the frame, β, and the fixed perpendicular distance to the master node, R. A frame will assemble in its local in-plane direction regardless of whether one story has rotated relative to another. Since these geometric quantities are not updated, the constraint equations are linear. Implicit here is the assumption that the total rotation of the building is small. This assumption is not detrimental to the solution since rotations will not exceed a few degrees for the variety of buildings investigated in this work.

The P-Δ contribution of frame columns in their out-of-plane direction uses the same small angle assumption of the constraint equations: the out-of-plane direction is assumed to be $\beta + \pi/2$, without updating the current angle. The current orientation is used to determine locations of frame columns, but the assembly assumes the original orientation to determine the direction of the load, so there will be some error due to cumulative rotations. However, the out-of-plane P-Δ effect is secondary in nature. There will be a small error in the orientation of force couples that are due to the out-of-plane displacement of frame columns only. In most cases, this will be a small error (in angle) of a small fraction (out-of-plane frame columns vs. in-plane frame columns plus gravity columns) of a secondary effect (P-Δ forces). Further attention is not warranted based on the level of accuracy of other assumptions being used in the program.

4.5.2 Small Rotation Assumption

The stiffness formulations in this work are for nonlinear analysis with a time-stepping solution. Small increments in displacements occur in each step, so displacement transformations take this into account. Specifically, the displacement transformation used for the shear springs (eq. 4.19) assumes the rotational increment is small. The same transformation provides exact results for forces (eq. 4.24). The P-Δ contribution of loads carried by gravity columns is assembled to the master nodes and uses the same small rotational increment assumption used for the shear spring contributions. The damping formulation to be developed later in the chapter also

uses the small rotation assumption.

The small rotation assumption has been used commonly to linearize the equations of motion (Weaver and Nelson 1966; Wilson and Allahabadi 1975; Wakabayashi 1986; Chopra 1995) by removing trigonometric functions of the rotations from transformation equation. This assumption is valid for the nonlinear inelastic problems solved here. The program solves iteratively for small time steps, so the incremental displacements are small and the approximation will not lose any accuracy. Some buildings are eccentric and exhibit torsional response from the lateral excitations, but even in the inelastic range for severe records the cumulative rotations are not large enough to affect accuracy with the small rotation assumption being used for the increments.

If small rotations are not assumed, the transformation of displacements from the master node to any location c will be of the form

$$\begin{aligned} \Delta x^c &= \Delta x^{MN} + X^{cMN}\cos(\Delta\theta^{MN}) - Y^{cMN}\sin(\Delta\theta^{MN}) - X^{cMN} \\ \Delta y^c &= \Delta y^{MN} + X^{cMN}\sin(\Delta\theta^{MN}) + Y^{cMN}\cos(\Delta\theta^{MN}) - Y^{cMN} \\ \Delta\theta^c &= \Delta\theta^{MN} \end{aligned} \tag{4.44}$$

where $X^{cMN} = X^c - X^{MN}$ and $Y^{cMN} = Y^c - Y^{MN}$ (figure 4.5). If the small rotation assumption is used, the transformation is equation (4.19), repeated here in equation form for comparison.

$$\begin{aligned} \Delta x^c &= \Delta x^{MN} - Y^{cMN}\sin(\Delta\theta^{MN}) \\ \Delta y^c &= \Delta y^{MN} + X^{cMN}\sin(\Delta\theta^{MN}) \\ \Delta\theta^c &= \Delta\theta^{MN} \end{aligned}$$

A pure torsion example can quantify the error associated with the linearized equations for small rotations. Assume a point is being rotated about the master node with the starting point at $(X_O, Y_O) = (1, 0)$ and the master node located at $(X^{MN}, Y^{MN}) = (0, 0)$ (figure 4.9). If equal incremental twists occur each step until a total rotation of $\Pi/4$ radians is achieved, then there will be a cumulative error

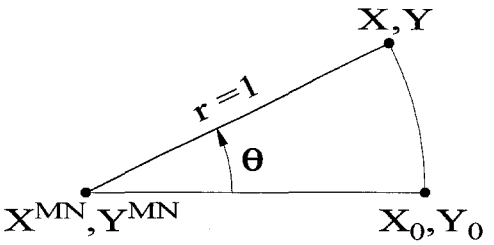

Figure 4.9 Pure torsion example.

$\Delta\theta$ ($\times\Pi$)	Cumulative Error in X	Cumulative Error in Y	Average Error in X	Average Error in Y
0.050	7.0%	5.6%	1.4%	1.1%
0.025	3.3%	3.0%	0.33%	0.30%
0.005	0.63%	0.61%	0.013%	0.012%

Table 4.1 Small rotation error for large twist.

based on the increment size. The results for several increment sizes are shown in table 4.1.

The total twist is 45°, which is much larger than most buildings will achieve before collapse. The incremental rotations 0.05Π, 0.025Π and 0.005Π radians correspond to 9°, 4.5° and 0.9°, respectively. Considering the small time steps used for time history analysis in this work, 1° would still exceed the maximum rotation observed in a time step. If the incremental rotations were this size and occurred monotonically as in the above example to always add to the cumulative error, a total twist of 45° will still have less than 1% total error.

The small rotation assumption is concerned with increments, not with total rotations. If the increments were small enough, this assumption would be valid for large total rotations of building floors. The small angle assumption is concerned with the total angle, so even if the small rotation assumption does not introduce large cumulative errors, the constraint equations and out-of-plane P-Δ forces can have large errors for large total rotations.

4.6 Stiffness Assembly

Now that all of the individual stiffness contributions have been described, the full building stiffness matrix can be assembled. The assembled frame stiffness (3.60) for each frame, the shear building stiffness (4.28), the constraint stiffness (4.16) and the gravity column geometric stiffness (4.32) can be assembled into the building stiffness

$$\mathbf{K}_T = \overset{n_f}{\underset{1}{\mathcal{A}}} \left[\mathbf{K}_T^F\right] + \mathcal{A}\left[\mathbf{K}_T^{SH}\right] + \mathcal{A}\left[\mathbf{K}_T^C\right] + \mathcal{A}\left[\mathbf{K}_T^{P-\Delta}\right] \tag{4.45}$$

where n_f is the number of frames.

The force vector is assembled in a similar manner from the frames (3.61), the shear building (4.29), the constraints (4.17), the gravity column P-Δ (4.34) and the out-of-plane frame column P-Δ (4.43):

$$\mathbf{p} = \overset{n_f}{\underset{1}{\mathcal{A}}} \left[\mathbf{p}^F\right] + \mathcal{A}\left[\mathbf{p}^{SH}\right] + \mathcal{A}\left[\mathbf{p}^C\right] + \mathcal{A}\left[\mathbf{p}^{P-\Delta}\right] + \mathcal{A}\left[\mathbf{p}^{OUT}\right]. \tag{4.46}$$

The stiffness equations for all of the building degrees of freedom for a static problem is

$$\mathbf{K}_T \Delta\mathbf{x} = \mathbf{f} - \mathbf{p} = \Delta\mathbf{p} \tag{4.47}$$

where $\mathbf{f}$ are applied static loads. The dynamic problem formulation and the solution of equations will be discussed in chapter 6.

The assembly of the global building stiffness matrix raises a concern about the effect on the bandwidth of the constraint stiffness matrix. Proper numbering of the nodes and their dofs will lead to no affect on the bandwidth. If the numbering is done by floor across frames, a minimum bandwidth will be achieved. Consider a two-dimensional structure with two moment frames and four columns per frame and master nodes with only one dof per floor (figure 4.10). Each column joint has four dofs/node so each frame will have 16 dofs/floor, which are connected to the 16 dofs above and below. This means that by numbering the dofs by floor, there will be 33 dofs/floor (16 dofs/frame plus 1 dof/master node) and a semi-

bandwidth of 37, since a column horizontal displacement (dof 1) at the bottom of a column will be coupled to the rotations (dofs 36,37) at the top. The shear building stiffness described in section 4.3 ties adjacent floor master nodes together. With the master node, there are 33 dofs/floor, so the semi-bandwidth is 34 based on the shear stiffness contribution or 37 based on the stiffness of any column. If there were no master nodes, the semi-bandwidth would be 36, so only a minimal increase is observed. Denoting the number of degrees of freedom per frame i per floor j by n_i^j and the number of frames by n_f, an upper bound to the semi-bandwidth N_{SB} can be expressed in general as

$$N_{SB} = \max_j \left(\sum_{i=1}^{n_f} n_i^j + 4 + 1 \right). \tag{4.48}$$

For a problem with diagonal braces, the semi-bandwidth would increase by four.

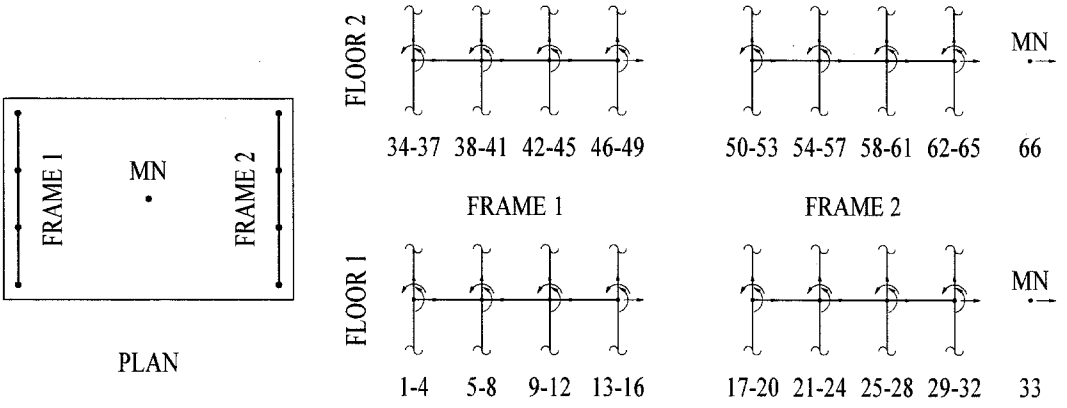

Figure 4.10 Numbering of dofs for a 2D example. MN = master node.

The formulation calculates the semi-bandwidth by looking for the maximum difference in dof number for each element type. It searches through each beam, column, brace, and master node looking for all connecting elements and storing the largest difference in dof number. This largest number is the semi-bandwidth. The building stiffness matrix $\mathbf{K}_T$ is stored in banded form to reduce storage requirements.

The effect of the constraints on the sparsity of the global stiffness matrix can

be observed by denoting rectangular non-zero regions of a matrix by [A]. Let the contributions of frame elements, shear springs and constraints be represented by [x], [s] and [○], respectively. For example, if there were four frames in a three-story structure, the combined stiffness matrix will have the form:

[Ⓧ]				[○]	[x]							FRAME 1, FL 1
	[Ⓧ]			[○]		[x]						FRAME 2, FL 1
		[Ⓧ]		[○]			[x]					FRAME 3, FL 1
			[Ⓧ]	[○]				[x]				FRAME 4, FL 1
[○]	[○]	[○]	[○]	[Ⓢ]					[Ⓢ]			MSTR ND, FL 1
[x]					[Ⓧ]				[○]	[x]		FRAME 1, FL 2
	[x]					[Ⓧ]			[○]		[x]	FRAME 2, FL 2
		[x]					[Ⓧ]		[○]			FRAME 3, FL 2
			[x]					[Ⓧ]	[○]			FRAME 4, FL 2
				[Ⓢ]	[○]	[○]	[○]	[○]	[Ⓢ]			MSTR ND, FL 2
					[x]					[Ⓧ]		FRAME 1, FL 3
						[x]					[Ⓧ]	FRAME 2, FL 3
							[x]				[Ⓧ]	FRAME 3, FL 3
								[x]			[Ⓧ]	FRAME 4, FL 3
									[Ⓢ]	[○]	[○]	MSTR ND, FL 3

[X]: frame member stiffnesses

[S]: shear spring stiffnesses

[○]: constraint stiffnesses

As can be seen from the above qualitative matrix representation, the constraint stiffness does not adversely affect the bandwidth of the global stiffness matrix. Denoting the number of degrees of freedom per frame i per story j by n_i^j and the number of frames by n_f, an upper bound to the semi-bandwidth N_{SB} can be expressed in general as

$$N_{SB} = \max_j \left(\sum_{i=1}^{n_f} n_i^j + 4 + 3 \right). \tag{4.49}$$

Note the similarity to equation (4.48) for the two-dimensional case. As with the 2D case, the semi-bandwidth will increase by four if there are braces in the structure. The only difference is that there are now three dofs at the master node instead of one.

4.7 Mass Formulation

Masses can be located at frame nodes and master nodes. The frame nodes can have both in-plane horizontal and vertical masses assigned to their respective degrees of freedom. The two masses at a frame node c, m_x^c and m_z^c, can be different if so desired. Typically, an engineer will include a portion of a building's live load in the calculation of the reactive horizontal mass. Because of the potential for live loads to slide relative to the floor, a smaller portion of the live load can be considered for the horizontal mass than for the vertical mass. No contribution to joint rotational dofs is made.

Master nodes will have masses associated with them to account for additional horizontal mass that the frames must support. All of the horizontal inertia of the mass must be carried by the lateral system (frames and shear springs), whereas gravity columns which do not provide lateral resistance will only carry their tributary vertical inertia. These vertical inertia forces are assumed to be carried straight down the gravity columns to the ground. If the vertical dynamic response of these masses is important for a specific structure, gravity columns could be modeled as single column frames so that the total vertical mass is included. The input required

for a master node is M_x^{MN}, M_y^{MN} and I^{MN}. These are the masses tributary to the gravity (non-frame) columns for the two orthogonal horizontal dofs of the master nodes and the corresponding mass moment of inertia, respectively.

If a frame is in motion out of plane, the transverse response of the in-plane mass will cause inertia forces on the frames providing resistance in that direction. The out-of-plane inertia effects need to be summed at the master node, but the mass being lumped at the master node only contributes to the response in one direction. Frame out-of-plane contributions will therefore produce unequal horizontal master-node masses.

Consider the out-of-plane motion at a frame column. The displacement of a node c determined from a rigid body motion of the master node is

$$\begin{Bmatrix} \Delta x^c \\ \Delta y^c \end{Bmatrix} = \begin{bmatrix} 1 & 0 & -Y^{cMN} \\ 0 & 1 & X^{cMN} \end{bmatrix} \begin{Bmatrix} \Delta x^{MN} \\ \Delta y^{MN} \\ \Delta \theta^{MN} \end{Bmatrix} \tag{4.50}$$

where $X^{cMN} = X^c - X^{MN}$ and $Y^{cMN} = Y^c - Y^{MN}$ (figure 4.5). The portion of this displacement which is out-of-plane, $\Delta x_\perp^c$, (figure 4.8(a)) is determined from

$$\Delta x_\perp^c = \begin{bmatrix} -\sin\beta & \cos\beta \end{bmatrix} \begin{Bmatrix} \Delta x^c \\ \Delta y^c \end{Bmatrix}. \tag{4.51}$$

This allows the column motion and master node motion to be expressed as

$$\begin{Bmatrix} \Delta x_\parallel^c \\ \Delta x_\perp^c \\ \Delta x^{MN} \\ \Delta y^{MN} \\ \Delta \theta^{MN} \end{Bmatrix} = \begin{bmatrix} 1 & 0 & 0 & 0 \\ 0 & -\sin\beta & \cos\beta & Y^{cMN}\sin\beta + X^{cMN}\cos\beta \\ 0 & 1 & 0 & 0 \\ 0 & 0 & 1 & 0 \\ 0 & 0 & 0 & 1 \end{bmatrix} \begin{Bmatrix} \Delta x_\parallel^c \\ \Delta x^{MN} \\ \Delta y^{MN} \\ \Delta \theta^{MN} \end{Bmatrix} \tag{4.52}$$

where $\Delta x_{\|}^{c}$ is the in-plane horizontal motion of the column node. This can be written as $\mathbf{x}^{*} = \mathbf{T}_{M}\mathbf{x}$, where $\mathbf{x}^{*}$ are the augmented displacements including the dependent out-of-plane motion of the column. The forces can be derived from the augmented forces similarly as $\mathbf{f} = \mathbf{T}_{M}^{T}\mathbf{f}^{*}$. Using the relation $\mathbf{M}^{*}\ddot{\mathbf{x}}^{*} = \mathbf{f}^{*}$ and the transformations just mentioned, the mass matrix for the independent dofs instead of the augmented dofs will be

$$\mathbf{M} = \mathbf{T}_{M}^{T}\mathbf{M}^{*}\mathbf{T}_{M}. \tag{4.53}$$

Considering only one column and one master node, the augmented mass matrix would be

$$\mathbf{M}^{*} = \begin{bmatrix} m_x^c & 0 & 0 & 0 & 0 \\ 0 & m_x^c & 0 & 0 & 0 \\ 0 & 0 & M_x^{MN} & 0 & 0 \\ 0 & 0 & 0 & M_y^{MN} & 0 \\ 0 & 0 & 0 & 0 & I^{MN} \end{bmatrix}. \tag{4.54}$$

Note that the frame node horizontal mass m_x^c is assembled to both the in-plane and out-of-plane dofs. The mass matrix for the actual set of degrees of freedom (equation 4.53) becomes

(4.55)

$$\mathbf{M} = \begin{bmatrix} m_x^c & 0 & 0 & 0 \\ & M_x^{MN} + m_x^c \sin^2\beta & -m_x^c \sin\beta\cos\beta & -m_x^c \sin\beta \begin{pmatrix} Y^{cMN}\sin\beta \\ + \\ X^{cMN}\cos\beta \end{pmatrix} \\ & & M_y^{MN} + m_x^c \cos^2\beta & m_x^c \cos\beta \begin{pmatrix} Y^{cMN}\sin\beta \\ + \\ X^{cMN}\cos\beta \end{pmatrix} \\ SYM & & & I^{MN} \end{bmatrix}.$$

Note that the mass matrix is no longer diagonal. The mass matrix is never inverted in the solution technique and modal separation is not required, so this does not

pose any problem. The off diagonal terms all occur at master node dofs. The resulting mass matrix has a semi-bandwidth of three, so storage and multiplications are adapted accordingly.

The in-plane and out-of-plane motions of frame masses have now been addressed. The rotational inertia of the frame masses must also be considered, though. The mass moment of inertia that results from the frame in-plane masses is automatically summed. Out-of-plane mass contributions are added to the input mass moment of inertia at the master nodes:

$$I^{MN} = I^{MN} + \sum_i m_i^c \left((X_P^{MN} - X_i^c)^2 + (Y_P^{MN} - Y_i^c)^2 \right), \tag{4.56}$$

where X_P^{MN} and Y_P^{MN} are the coordinates of the intersection of the plane of the frame and a line drawn from the master node perpendicular to the frame.

The mass matrix remains constant, independent of the configuration and state of the structure.

4.8 Damping Formulation

Rayleigh damping is a common model used in practice. Modal damping is also frequently used for modal analysis, but is not practical for nonlinear time history analysis. Classical or Caughey damping is sometimes used to get a better fit over several modes than Rayleigh damping can provide. In nonlinear time history analyses, excessively large and unrealistic damping forces can be observed with linear damping since the resulting damping forces can easily exceed the physical means by which damping would actually occur. The damping forces have been observed to be large relative to the forces carried by a yielding frame. Damping remains a poorly understood or measurable quantity in building structures, so another type of damping is used in this program which is more physically intuitive. Nonlinear damping called *story damping* has been chosen to limit the viscous forces to specified values so that unrealistically large damping forces are not generated when structural yielding causes high relative velocities. These nonlinear inter-story dashpots resist

relative horizontal motions between floors. Forces in the dashpots will be capped at a specified inter-story velocity. The dashpots can be placed at the same location as shear springs and assembled in the same way. Dashpot "stiffness" can be chosen to provide a desired percentage of critical damping.

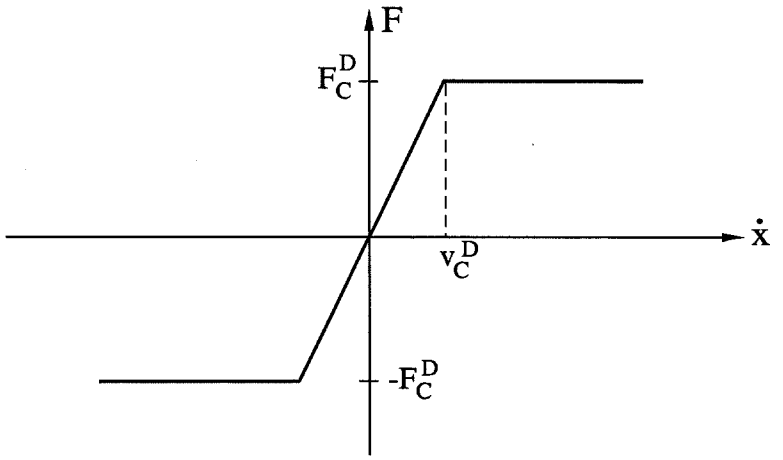

Figure 4.11 Nonlinear inter-story damping force.

Nonlinear, inter-story damping is appealing because it makes sense physically. Initially, when a structure has only been mildly shaken by an earthquake, many non-structural components can absorb energy and dampen the response. For large amplitude excitation, these elements will most likely be damaged and no longer able to dissipate more energy. When this source of damping is limited, the inelastic behavior of the structural frame will provide the remaining damping. A bilinear model (figure 4.11) defines the force-velocity relationship by providing a cutoff velocity v_C^D that corresponds to a yield force F_C^D. The yield force is chosen to maintain reasonable damping force levels. The cutoff velocity is chosen for the given yield damping force to provide acceptable elastic damping in the lowest mode of the building (1% to 5%). The velocity required to achieve a desired level of damping in the first mode can be determined experimentally, and this will be discussed in chapter 7. As the structure undergoes nonlinear response, the damping will level off when inter-story velocities exceed the cutoff velocity.

Additional mass and stiffness proportional damping can be used in the formulation, but they are set by the original mass and stiffness matrices and do not vary as the stiffness changes in nonlinear response of the structure. A small amount of this Rayleigh damping is used for numerical purposes. The overall damping is nonclassical, so even in modal form the equations of motion are coupled by off diagonal damping terms. The effective modal damping resulting from the story damping will be discussed in chapter 7.

Three types of damping can be provided: mass proportional, stiffness proportional, and story damping resulting in the following equation for damping:

$$\mathbf{C} = a_0\mathbf{M} + a_1\mathbf{K} + \mathbf{C}^{ST}(\dot{\mathbf{x}}(t)) \tag{4.57}$$

where $\mathbf{C}^{ST}$ is the nonlinear story damping. Higher order terms of a Caughey Series for classical damping are not used, but Rayleigh damping can be achieved by choosing coefficients a_0 and a_1 so that

$$\begin{Bmatrix} \zeta_m \\ \zeta_n \end{Bmatrix} = \frac{1}{2}\begin{bmatrix} 1/\omega_m & \omega_m \\ 1/\omega_n & \omega_n \end{bmatrix}\begin{Bmatrix} a_0 \\ a_1 \end{Bmatrix} \tag{4.58}$$

is satisfied (Clough and Penzien 1993, p. 236). For equal damping in two modes, this simplifies to

$$\begin{Bmatrix} a_0 \\ a_1 \end{Bmatrix} = \frac{2\zeta}{\omega_m + \omega_n}\begin{Bmatrix} \omega_m\omega_n \\ 1 \end{Bmatrix}. \tag{4.59}$$

The story damping can be assembled the same way the shear spring stiffness was by replacing $\mathbf{k}_j^{i,SS}$ with $\mathbf{c}_j^{i,ST}$, $\mathbf{\Delta x}$ with $\dot{\mathbf{x}}_j^{MN}$, and $\mathbf{\Delta p}_j^{MN}$ with $\mathbf{q}_j^{MN}$ in equation

(4.25). Here, the 3×3 sub-matrix is

$$\mathbf{c}_j^{i,ST} = \begin{bmatrix} \frac{F_{C,x}^D}{v_C^D} & 0 & 0 \\ 0 & \frac{F_{C,y}^D}{v_C^D} & 0 \\ 0 & 0 & 0 \end{bmatrix}, \tag{4.60}$$

where the damping force yield level can be different in the two orthogonal horizontal directions. The effect of one story dashpot i becomes

$$\begin{bmatrix} [\mathbf{T}_{j+1}^i]^T \mathbf{c}_j^{i,ST} \mathbf{T}_{j+1} & -[\mathbf{T}_{j+1}^i]^T \mathbf{c}_j^{i,ST} \mathbf{T}_j \\ -[\mathbf{T}_j^i]^T \mathbf{c}_j^{i,ST} \mathbf{T}_{j+1} & [\mathbf{T}_j^i]^T \mathbf{c}_j^{i,ST} \mathbf{T}_j \end{bmatrix} \begin{Bmatrix} \dot{\mathbf{x}}_{j+1}^{MN} \\ \dot{\mathbf{x}}_j^{MN} \end{Bmatrix} = \begin{Bmatrix} \mathbf{q}_{j+1}^{MN} \\ \mathbf{q}_j^{MN} \end{Bmatrix}, \tag{4.61}$$

which can be written as

$$\mathbf{C}_j^{i,ST} \dot{\mathbf{x}}_j^{MN} = \mathbf{q}_j^{MN} \tag{4.62}$$

for story j. Note that this relationship is not linearized as in the case of shear building stiffness. Linearization for velocity nonlinearities is not as straightforward as for displacement nonlinearities. Because the story damping is calculated based on initial elastic properties, the total damping matrix can be expressed as $\mathbf{C}$ from equation 4.57 *assuming* the damping is linear. This is why the damping force equation can be written above for total motion, not incremental motion. The nonlinearities are accounted for by corrections to the residual force vector. This will be discussed in chapter 6.

The story damping is summed for the n_j^d dashpots on story j as

$$\mathbf{C}_j^{ST} \dot{\mathbf{x}}_j^{MN} = \mathbf{q}_j^{MN} \quad \text{where} \quad \mathbf{C}_j^{ST} = \overset{n_j^d}{\underset{i=1}{\mathcal{A}}} \left[\mathbf{C}_j^{i,ST} \right]. \tag{4.63}$$

The story damping for the entire structure is assembled over the total number of

stories n_s as

$$\mathbf{C}^{ST} = \mathop{A}_{j=1}^{n_s} \left[\mathbf{C}_j^{ST}\right] \tag{4.64}$$

where n_s is the number of stories.

The total damping forces using the complete damping matrix (4.57) are

$$\mathbf{q}^L = \mathbf{C}\dot{\mathbf{x}}, \tag{4.65}$$

and the resulting forces are linear. The portion of the forces *assumed* to be linear is

$$\mathbf{q}^{ST,L} = \mathbf{C}^{ST}\dot{\mathbf{x}}. \tag{4.66}$$

As in the case of shear springs, the transformation $\mathbf{T}_j^i$ from equation 4.19 provides the exact relation between the nonlinear forces at dashpot location i and the master node at level j:

$$\mathbf{q}_j^{ST,NL} = [\mathbf{T}_j^i]^T \mathbf{q}_j^{i,NL}. \tag{4.67}$$

The forces can be summed for the n_j^d dashpot locations at each floor j and assembled into the total story damping force vector as

$$\mathbf{q}^{ST,NL} = \mathop{A}_{j=1}^{n_s} \left[\sum_{i=1}^{n_j^d} \left([\mathbf{T}_j^i]^T \mathbf{q}_j^{i,ST} \right) \right]. \tag{4.68}$$

This allows the nonlinear damping forces to be written as a linear portion and a nonlinear correction:

$$\overbrace{\mathbf{q}(\dot{\mathbf{x}})}^{total} = \overbrace{\mathbf{q}^L}^{linear} + \overbrace{(\mathbf{q}^{ST,NL} - \mathbf{q}^{ST,L})}^{correction}. \tag{4.69}$$

The effect of nonlinear damping on the equations of motion will be discussed in chapter 6 and quantification of the damping level will be discussed in chapter 7.

Chapter 5

Three-Dimensional Columns

The developments thus far allow a structure with unconnected, arbitrarily oriented planar frames to be analyzed. A broader class of problems could be solved with the addition of a special column element that ties orthogonal frames together. Many modern steel buildings fall into this classification, so the planar frame model developed in chapter 3 using the constraints developed in chapter 4 can accurately model three-dimensional behavior of these structures with the addition of a three-dimensional column element.

5.1 Modeling Considerations

The sophistication of the three-dimensional segmented fiber element model should match the level of approximations and types of assumptions already used in the program development. The following assumptions have been made for the three-dimensional columns:

- Only orthogonal orientations of the plane frames are permitted.
- Torsional stiffness is neglected, giving five dofs at each end of a segment.
- Shear deformations are assumed elastic (same as planar case).
- Plane sections remain plane (same as planar case).
- Uses the same fiber elements as in the planar case.

Torsion has been neglected for several reasons. The global analysis is capable of large displacements, but assumes small rotations. Even a torsionally irregular building subjected to a large near-source pulse excitation may exhibit only small rotations even if its columns experience 20% drift. In the next chapter, some example structures are analyzed for different assumptions to quantify the amount of rotation that the program should be able to accurately model. The resulting twists are small, and the corresponding torsional stresses will also be small. Englekirk writes

> ... torsional stresses, however induced, are seldom calculated, for they have little or no impact on the strength limit state of a member. [1]

The three-dimensional rigid body constraints imposed on the frames will cause corner columns to twist a small amount for unsymmetrical loading or an irregular structure. The small rotations will cause low stresses that can be ignored. The program does not address the lateral-torsional stability of the column in this twisted state. Additionally, for most buildings relying on corner columns, the section is typically a tubular section or a stocky wide flange. These members provide a great deal of torsional resistance and generally do not experience lateral-torsional buckling. Torsional dofs have not been included, but a member's torsional resistance could be assembled to the rotational dofs of the master joints. This contribution tends to be small for a realistic building and is ignored. It is not believed that this will be a non-conservative assumption because of the aforementioned small rotations.

Orthogonal framing allows the beam and panel zone forces to be accounted for easily, especially considering that torsion has been neglected. Further developments of the three-dimensional column could allow arbitrarily oriented framing, but this has not been developed in this work.

There are several methods for determining the orientation of the members resulting from the geometric updating of segment internal nodes. Chen and Atsuta present a method for determining the orientation of a segmented plastic beam-column (Chen and Atsuta 1977, Ch. 11). They keep track of segment orientation for arbitrary displacements and rotations at each end. Their method requires many

[1] (Englekirk 1994, p. 281)

transformations and is based on a formulation that considers torsion. A method that determines orientation based solely on the location of segment ends is desired since rotational transformations do not commute and the problem is nonlinear. Because the assumed displacements do not have large rotations, there is no concern that the member could accidentally be oriented 90 degrees out of alignment.

A projection method has been developed to maintain the forces and displacements associated with the five dofs at each end of a segment. The method conveniently eliminates torsion consistent with the torsion assumptions. In this manner, the five end forces of an arbitrarily oriented segment are projected onto five in-plane forces associated with the major and minor axes of the segment. Other standard methods would convert the five end forces to six orthogonal forces, introducing a torsion that would then be eliminated.

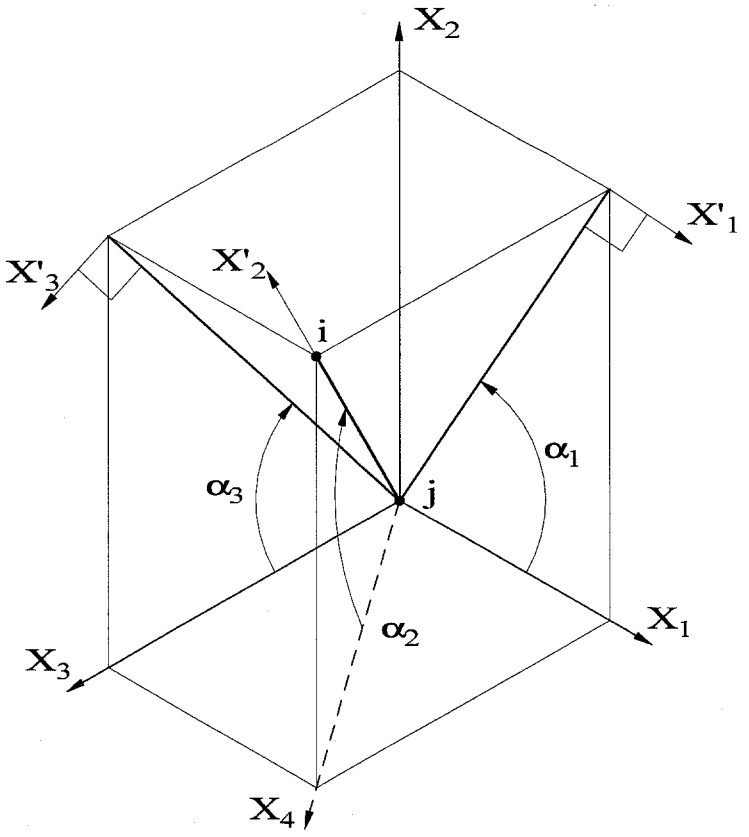

Figure 5.1 Segment local (primed) and global (unprimed) axes.

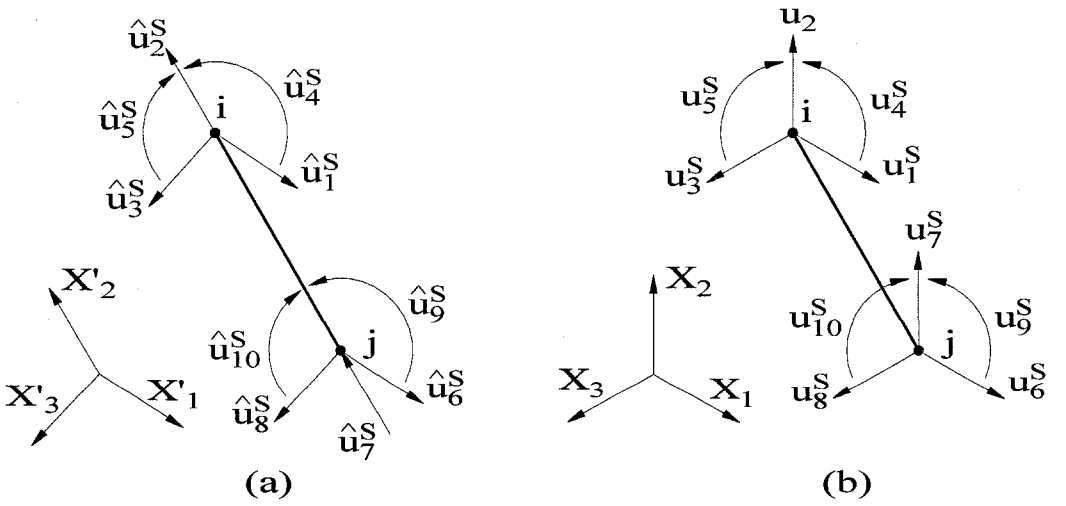

Figure 5.2 (a) Segment local degrees of freedom. (b) Segment global degrees of freedom.

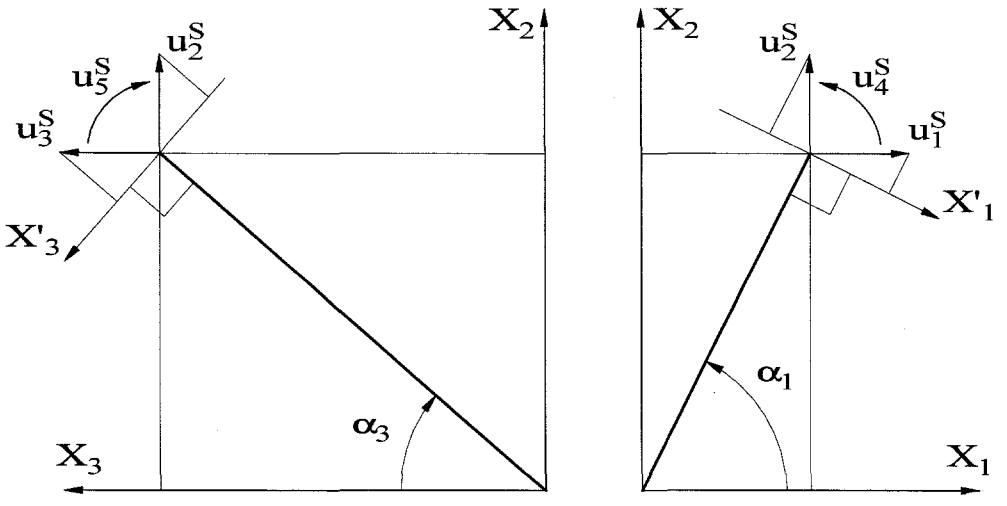

Figure 5.3 Projection of global displacements on local X_3' and X_1' axes.

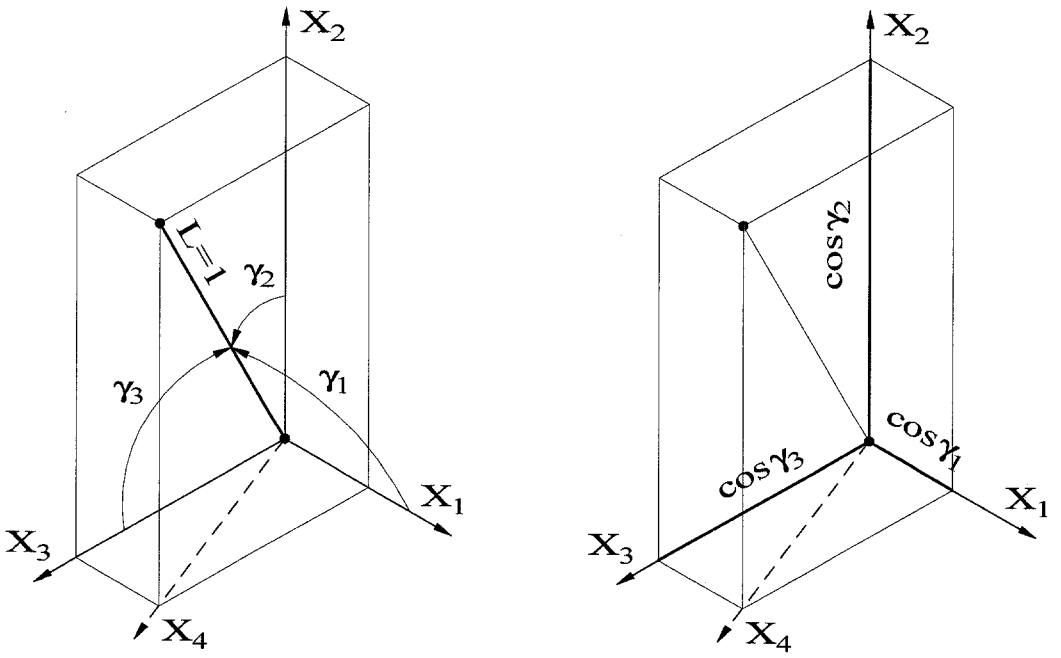

Figure 5.4 Global directional cosines for X_2' axis.

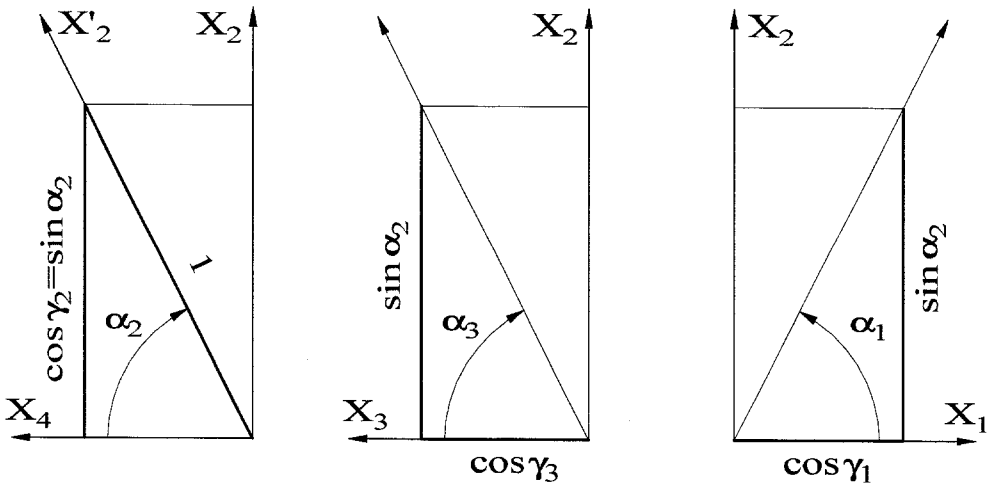

Figure 5.5 Projection of global displacements on local X_2' axis.

The projection method considers the location of both ends of a segment in global frame coordinates, X_1, X_2 and X_3. Using the current and previous lengths of the member, the axial deformation is determined. Projecting the current configuration onto the X_1-X_2 and X_2-X_3 planes defines the local member axes, X_1' and X_3', respectively. The X_2' axis is aligned with the current segment axis (fig. 5.1). The displacements in the local dofs can be determined from displacements in the five dofs in the global coordinates. The local and global degrees of freedom are shown in figure 5.2. The contributions of u_1 through u_3 are shown in figures 5.3 and 5.5. In figure 5.3, the global displacements u_2 and u_3 are projected onto the local X_3' axis and u_2 and u_1 are projected onto the local X_1' axis. Global displacements u_1, u_2 and u_3 can be projected onto the local X_2' axis using the global directional cosines γ_i (figure 5.4). These projections are instead made using the local angles α_i from figure 5.1. The relation between the directional cosines and local angles is shown in figure 5.5. Note in figure 5.2 that rotational dofs u_4 and u_5 are unchanged from global to local axes since the local axes are in the planes perpendicular to the rotational axes. The resulting transformation for all dofs is:

$$(5.1) \qquad \begin{Bmatrix} \hat{u}_1 \\ \hat{u}_2 \\ \hat{u}_3 \\ \hat{u}_4 \\ \hat{u}_5 \end{Bmatrix} = \begin{bmatrix} \sin\alpha_1 & -\cos\alpha_1 & 0 & 0 & 0 \\ \frac{\sin\alpha_2}{\tan\alpha_1} & \sin\alpha_2 & \frac{\sin\alpha_2}{\tan\alpha_3} & 0 & 0 \\ 0 & -\cos\alpha_3 & \sin\alpha_3 & 0 & 0 \\ 0 & 0 & 0 & 1 & 0 \\ 0 & 0 & 0 & 0 & 1 \end{bmatrix} \begin{Bmatrix} u_1 \\ u_2 \\ u_3 \\ u_4 \\ u_5 \end{Bmatrix} \quad \text{or} \quad \hat{\mathbf{u}} = \mathbf{T}\mathbf{u}.$$

The global displacements that result from solving the equations of motion produce the new configuration, which determines the angles used in the transformation above. The transformation is used to obtain the local displacements that in turn are used to determine fiber strains. The fiber strains are used to determine the axial force. Shear forces are obtained from the configuration and end rotations of the segment. Moments are calculated from the shear forces plus the bending due to fiber axial stresses. These end forces are then transferred to global coordinates

using the transpose of the previous transformation (figure 5.6):

$$\mathbf{p} = \mathbf{T}^T \hat{\mathbf{p}}. \tag{5.2}$$

A closer look at just the local translational forces shows that the transformation

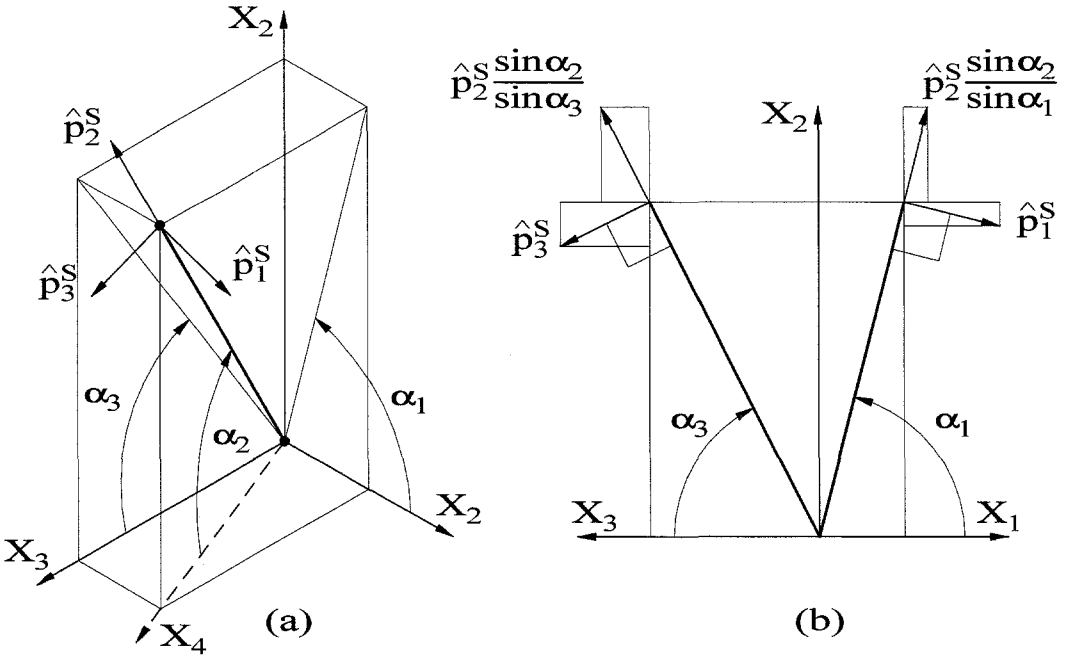

Figure 5.6 Projection of local segment forces on global axes.

does not preserve orthogonality:

$$\hat{\mathbf{p}}^T \hat{\mathbf{p}} = p_1^2 + p_2^2 + p_3^2 \quad \text{whereas} \tag{5.3}$$

$$\mathbf{p}^T \mathbf{p} = \hat{\mathbf{p}}^T [\mathbf{T}][\mathbf{T}^T] \hat{\mathbf{p}} \tag{5.4}$$

$$= \hat{p}_1^2 + \hat{p}_2^2 \sin^2 \alpha_2 (1 + \frac{1}{\tan^2 \alpha_1} + \frac{1}{\tan^2 \alpha_3}) + \hat{p}_3^2 + 2\hat{p}_1 \hat{p}_3 \cos \alpha_1 \cos \alpha_3 \tag{5.5}$$

$$= \hat{p}_1^2 + \hat{p}_2^2 + \hat{p}_3^2 + 2\hat{p}_1 \hat{p}_3 \cos \alpha_1 \cos \alpha_3 \tag{5.6}$$

$$\text{since} \quad \sin^2 \alpha_2 (1 + \frac{1}{\tan^2 \alpha_1} + \frac{1}{\tan^2 \alpha_3}) \equiv 1. \tag{5.7}$$

The error in the magnitude of the resultant will be small, even for large deformations. Assume equal forces and displacements in the X_1' and X_3' directions and no force in the X_2' direction. This configuration is possible for a building with predominantly torsional response. The assumptions can be represented by

$$\hat{p} = \hat{p}_1 = \hat{p}_3 \quad \text{equal forces} \tag{5.8}$$

$$\hat{p}_2 = 0 \quad \text{no axial load} \tag{5.9}$$

$$\alpha = \alpha_1 = \alpha_3 \quad \text{equal displacement.} \tag{5.10}$$

The error can then be expressed as

$$\text{Error} = \frac{\sqrt{\mathbf{p}^T\mathbf{p}} - \sqrt{\hat{\mathbf{p}}^T\hat{\mathbf{p}}}}{\sqrt{\hat{\mathbf{p}}^T\hat{\mathbf{p}}}} \tag{5.11}$$

$$= \sqrt{1 + \cos^2\alpha} - 1. \tag{5.12}$$

One common criterion chosen for ending an analysis is when story drift reaches 20%. If a column manages to reach 20% drift in each direction, $\cos\alpha_1 \cong 0.2$ and the error will be less than 2%. Any axial force (2-direction force) will reduce this error since the projection method does not corrupt this component in the transformation from local to global forces.

5.2 Three-Dimensional Issues

Keeping track of three-dimensional properties can sometimes be confusing. The orientation of a member in particular can be misinterpreted. For clarification, the two orthogonal axes, X_1 and X_3, do not necessarily correspond to the major and minor axes of a column section. Major and minor axes will refer to the strong and weak axes of the member section, respectively. The user can define the major axis to coincide with one of the orthogonal axes and the minor axis will automatically coincide with the other axis or its negative component.

A frame node for planar frames has four dofs: horizontal and vertical transla-

tion and beam and column rotations. With a corner column present, the frame node requires an additional horizontal translation and additional column and beam rotations for the orthogonal axis. A frame node thus requires seven dofs if a corner column is framing into it (figures 5.7 and 5.8).

Each segment of a 3D column requires five dofs instead of the three required for a 2D column. It has an additional horizontal translation and corresponding rotation.

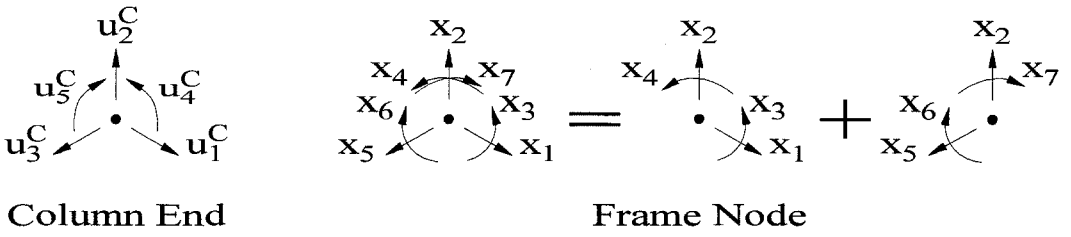

Figure 5.7 Orthogonal view of column and frame node degrees of freedom.

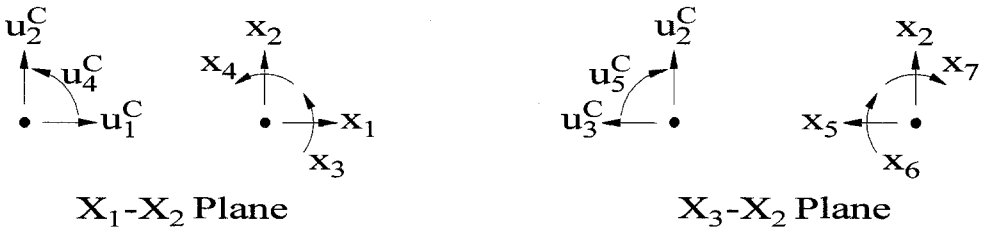

Figure 5.8 Planar views of column and frame node degrees of freedom.

The elemental fiber is unchanged, but it can now have geometric stiffness effects in two orthogonal directions. In two-dimensional analysis, a column has eight fibers. For three-dimensional effects, the breakdown of the member cross section is of more concern, so a total of 20 fibers is used for 3D columns (figures 5.9 and 5.10). Gradual yielding across the section can be accurately modeled for biaxial loading. A wide flange and two types of box columns have been developed to cover the cases of the structures analyzed.

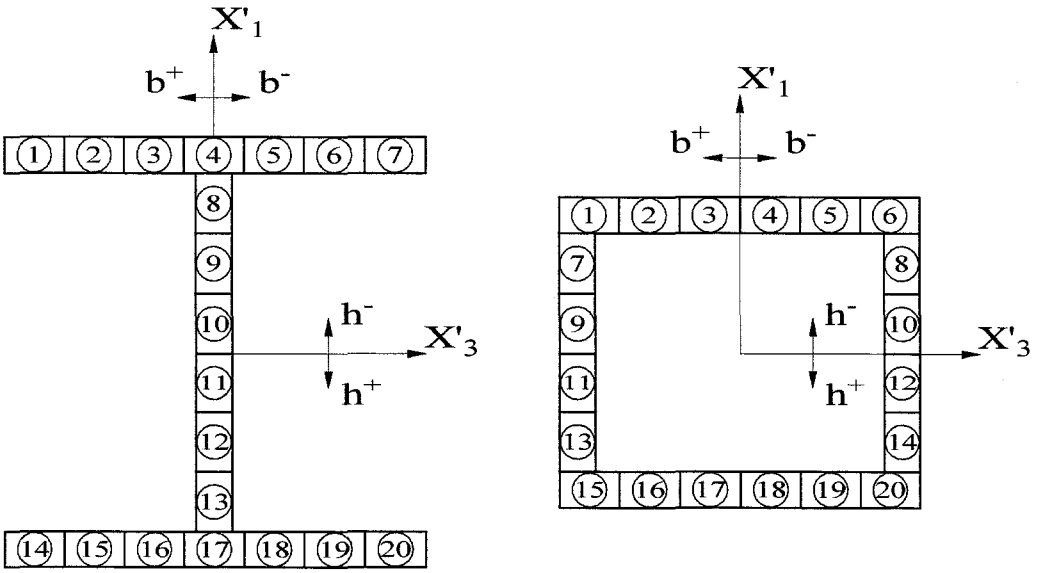

Figure 5.9 Fibers for wide flange and box three-dimensional columns.

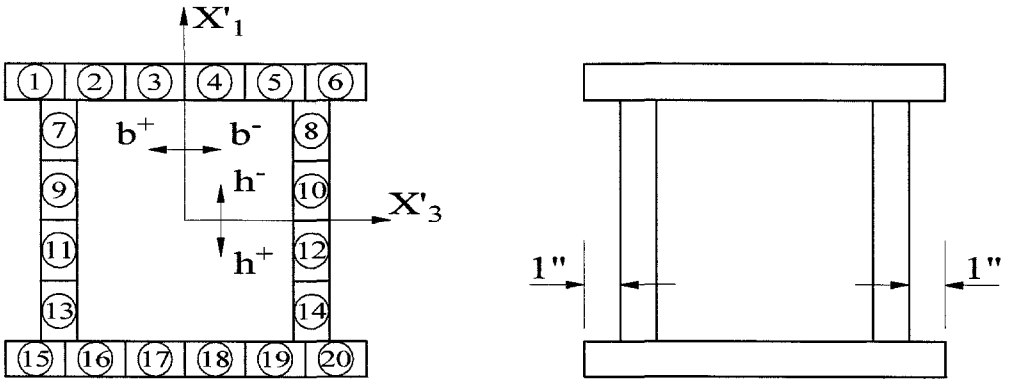

Figure 5.10 Fibers and dimensions for flanged box columns.

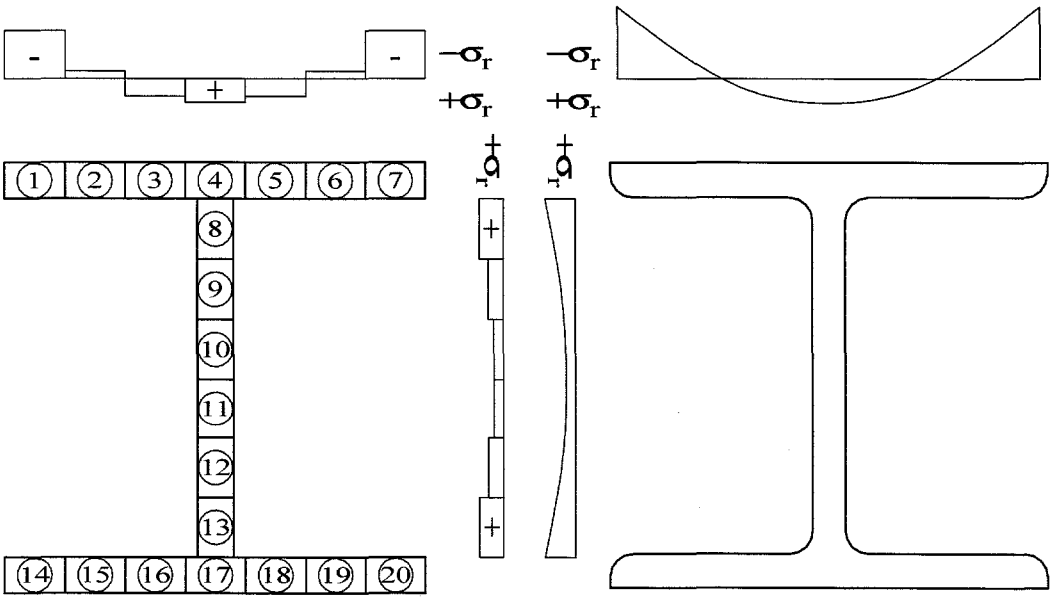

Figure 5.11 Residual stress distribution for wide flange section.

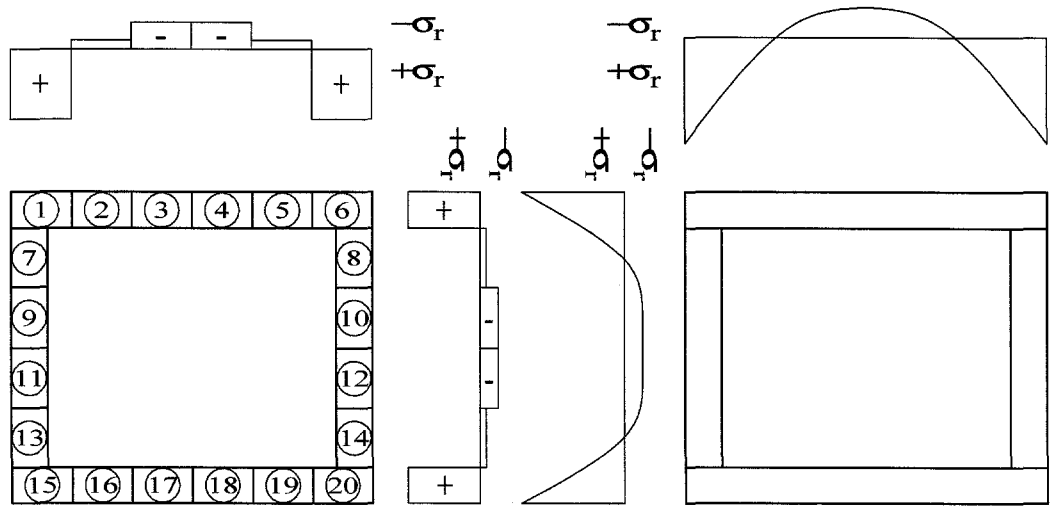

Figure 5.12 Residual stress distribution for built-up box section.

Fiber No.	Wide Flange (times σ_R)	Fiber No.	Box Section (times σ_R)
1,7,14,20	-1.0	1,6,15,20	1
2,6,15,19	-0.15	2,5,16,19	-1/8
3,5,16,18	0.375	3,4,17,18	-3/8
4,17	0.5	—	—
8,13	$0.525A_f/A_w$	7,8,13,14	$-1/8(A_f/A_w)$
9,12	$0.315A_f/A_w$	9,10,11,12	$-3/8(A_f/A_w)$
10,11	$0.210A_f/A_w$	—	—

Table 5.1 Residual stresses for fibers of three-dimensional column.

With a finer mesh of fiber elements, the residual forces can be modeled more precisely than for the 2D case. Specifically, a distribution which is more appropriate for stocky members has been chosen for the wide flange members (McGuire 1968, pp. 233-234). Since these members are intended to be used as corner columns, the typical member size will be stocky. A parabolic distribution is assumed, and the values for each fiber are chosen to maintain equilibrium. There is no net axial force resulting from the residual stresses in an unloaded member. A heavy wide flange section has maximum compression at the flange tips and tension where the flanges meet the web (figure 5.11) whereas built-up box sections have residual tension at the corners and compression at the midspan (figure 5.12). The flanged box section is assumed to have the same stresses as the regular box section. The residual stresses for the fibers defined in figure 5.9 are shown in table 5.1. The values have been chosen to ensure zero net axial force, so large discrepancies in flange to web areas may cause an unrealistic distribution, but it will be in equilibrium. A_f and A_w represent the areas of flange and web fibers, respectively.

The panel zone of a corner column has been chosen to have the same depth in both orthogonal directions. Recall that there is no axial deformation within the panel zone, so all of the axial deformation in a column line occurs in the column clear spans. The clear span needs to be uniquely defined for corner columns, so the panel zone is the depth of the deepest beam framing into it. Recall that columns

frame into the mid-point of the panel zone top and bottom edges. For the 2D case, the panel zone moment-couples cause the panel zone to shear. For a corner column, the shearing will occur independently in each direction, but the interaction of the resulting deformations must be considered. For the 2D case, the displacements of the mid-point of the panel zone edges are determined from the beam and column frame rotations $\theta^b = \theta_1^b$ and $\theta^c = \theta_1^c$ (figure 5.13(b)):

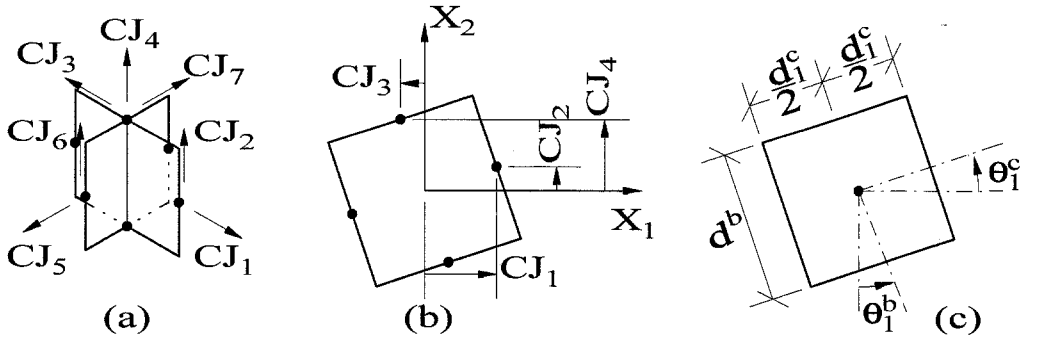

Figure 5.13 (a) 3D panel zone displacements. (b) X_1'-X_2' plane displacements, also 2D displacements. (c) Dimensions.

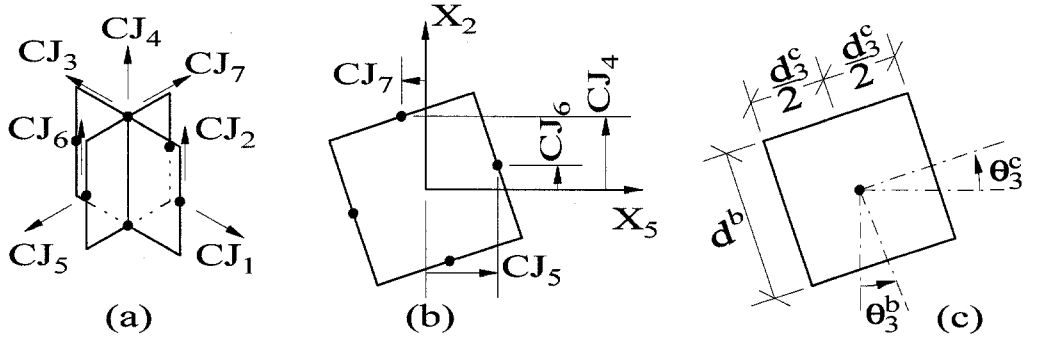

Figure 5.14 (a) 3D panel zone displacements. (b) X_5'-X_2' plane displacements, also 2D displacements. (c) Dimensions.

$$CJ_1 = \frac{d^c}{2} \cos\theta^c \tag{5.13}$$

$$CJ_2 = \frac{d^c}{2} \sin\theta^c \tag{5.14}$$

$$CJ_3 = \frac{d^b}{2} \sin\theta^b \tag{5.15}$$

$$CJ_4 = \frac{d^b}{2} \cos\theta^b. \tag{5.16}$$

For the 3D case, when the four rotations have been calculated for the panel zone, namely θ_1^b, θ_1^c, θ_3^b and θ_3^c, the displacements are as follows (figures 5.13 and 5.14):

$$CJ_1 = \frac{d_1^c}{2} \cos\theta_1^c \tag{5.17}$$

$$CJ_2 = \frac{d_1^c}{2} \sin\theta_1^c \tag{5.18}$$

$$CJ_3 = \frac{d^b}{2} \sin\theta_1^b \cos\theta_3^b \tag{5.19}$$

$$CJ_4 = \frac{d^b}{2} \cos\theta_1^b \cos\theta_3^b \tag{5.20}$$

$$CJ_5 = \frac{d_3^c}{2} \cos\theta_3^c \tag{5.21}$$

$$CJ_6 = \frac{d_3^c}{2} \sin\theta_3^c \tag{5.22}$$

$$CJ_7 = \frac{d^b}{2} \sin\theta_3^b \cos\theta_1^b, \tag{5.23}$$

where the interaction can be clearly seen.

The major axis properties of a panel zone are determined in the same way as for 2D analysis except for the beam depth, which is now based on the deepest beam framing into the column. The minor axis properties are based on the following assumptions, whether the column is a wide flange or a box section:

- The area of the column flanges times the panel zone depth is used for the panel zone volume.
- The column width is used to determine the clear span for the minor axis beam.

5.3 Stiffness Formulation

5.3.1 Fiber Stiffness

The 2D fiber element was described in section 3.3.1. A 3D fiber may undergo two orthogonal transverse displacements resulting in geometric stiffness contributions to the segment stiffness. The fiber stiffness gives the following relationship between axial force and displacement:

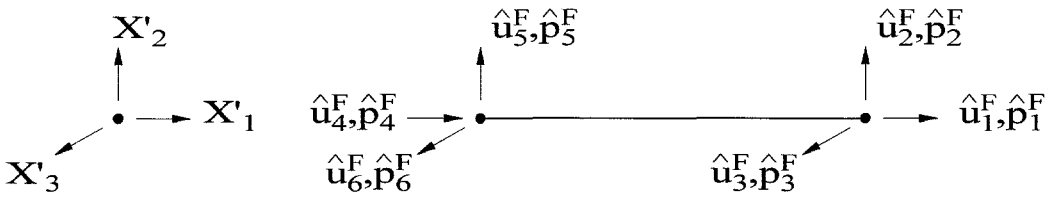

Figure 5.15 Fiber local properties.

$$\mathbf{K}_l^A \Delta\hat{\mathbf{u}}^F = \Delta\hat{\mathbf{p}}^F. \tag{5.24}$$

The forces and displacement can be seen in figure 5.15. The fiber local stiffness (denoted with subscript l for local) is:

$$\mathbf{K}_l^A = \frac{E_T A_f}{l}\begin{bmatrix} 1 & 0 & 0 & -1 & 0 & 0 \\ 0 & 0 & 0 & 0 & 0 & 0 \\ 0 & 0 & 0 & 0 & 0 & 0 \\ -1 & 0 & 0 & 1 & 0 & 0 \\ 0 & 0 & 0 & 0 & 0 & 0 \\ 0 & 0 & 0 & 0 & 0 & 0 \end{bmatrix}. \tag{5.25}$$

The geometric contribution to the stiffness for transverse displacements in the

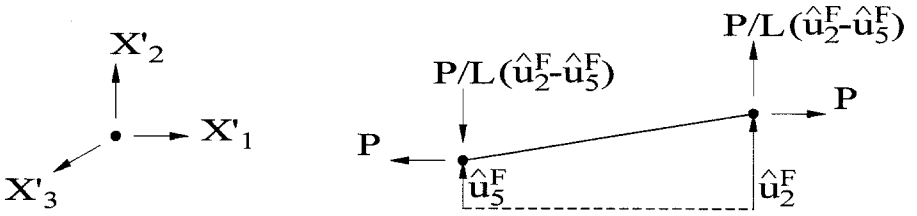

Figure 5.16 Geometric stiffness of fiber in X_1'-X_2' plane.

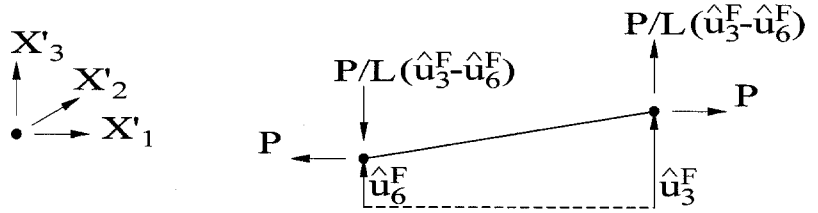

Figure 5.17 Geometric stiffness of fiber in X_3'-X_2' plane.

X_2' direction (figure 5.16) is computed as

$$\mathbf{K}_l^{G1} = \frac{P}{L}\begin{bmatrix} 0 & 0 & 0 & 0 & 0 & 0 \\ 0 & 1 & 0 & 0 & -1 & 0 \\ 0 & 0 & 0 & 0 & 0 & 0 \\ 0 & 0 & 0 & 0 & 0 & 0 \\ 0 & -1 & 0 & 0 & 1 & 0 \\ 0 & 0 & 0 & 0 & 0 & 0 \end{bmatrix}. \tag{5.26}$$

Similarly, the geometric stiffness in the X_3' direction (figure 5.17) is computed as

$$\mathbf{K}_l^{G3} = \frac{P}{L}\begin{bmatrix} 0 & 0 & 0 & 0 & 0 & 0 \\ 0 & 0 & 0 & 0 & 0 & 0 \\ 0 & 0 & 1 & 0 & 0 & -1 \\ 0 & 0 & 0 & 0 & 0 & 0 \\ 0 & 0 & 0 & 0 & 0 & 0 \\ 0 & 0 & -1 & 0 & 0 & 1 \end{bmatrix}. \tag{5.27}$$

For each fiber, the total stiffness is $\mathbf{K}_{l,i}^F = \mathbf{K}_{l,i}^A + \mathbf{K}_{l,i}^{G1} + \mathbf{K}_{l,i}^{G3}$, summing the axial and geometric contributions. The total fiber force displacement relation for fiber i becomes

$$\mathbf{K}_{l,i}^F \boldsymbol{\Delta}\hat{\mathbf{u}}_i^F = \boldsymbol{\Delta}\hat{\mathbf{p}}_i^F. \tag{5.28}$$

The individual fiber stiffness matrices are assembled for each segment as described below.

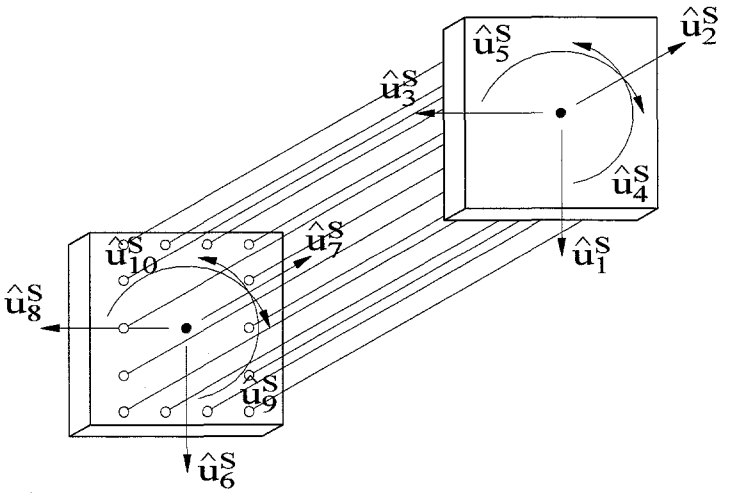

Figure 5.18 Segment local degrees of freedom.

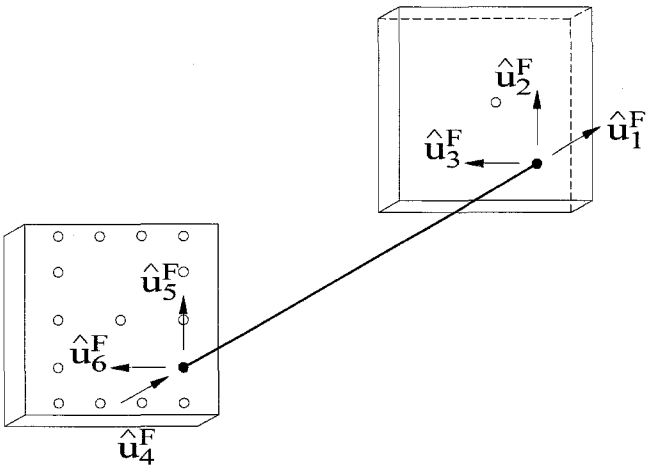

Figure 5.19 Fiber local degrees of freedom.

5.3.2 Segment Stiffness

The segment stiffness for 2D elements was formulated in section 3.3.2. The 3D formulation is similar, using separate interpolation of displacements and rotations. As with the 2D segment, shearing is elastic and considered separately.

The relation between fibers and segments is shown in figures 5.18 and 5.19. Each fiber i has its centroid located a distance h_i from the neutral axis in the X_1' direction and b_i in the X_3' direction. The transformation from segment displacements to fiber displacements is easily determined by individually displacing the segment degrees of freedom. Axial, shearing, and rotational displacements at the right end of the segment are shown for both X_1'-X_2' plane and X_3'-X_2' plane displacements in figure 5.20. The resulting relation between segment displacements $\boldsymbol{\Delta}\hat{\mathbf{u}}^S$ and individual fiber displacements $\boldsymbol{\Delta}\hat{\mathbf{u}}_i^F$ is

$$\hat{\mathbf{u}}_i^F = \mathbf{R}_i^{SF}\hat{\mathbf{u}}^S \tag{5.29}$$

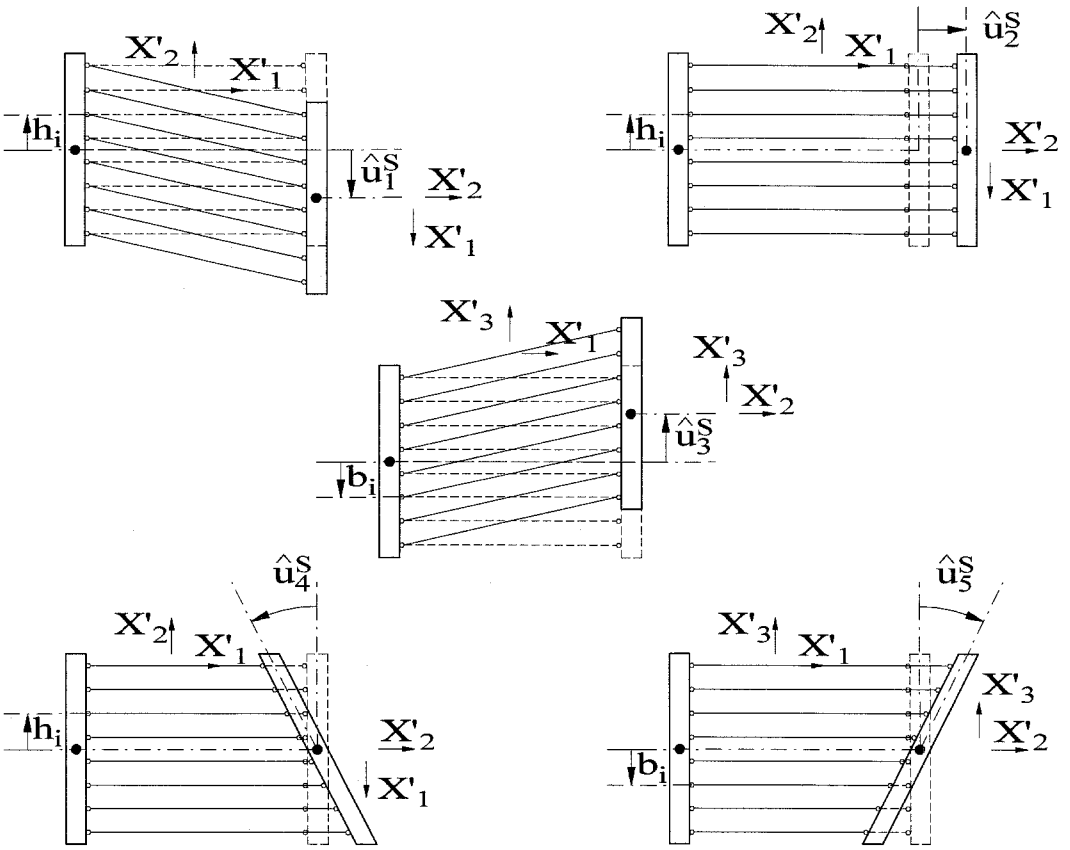

Figure 5.20 Relation between fiber and segment displacements.

where the transformation from segment to fiber displacements is given by

$$\mathbf{R}_i^{SF} = \begin{bmatrix} 0 & 1 & 0 & -h_i & -b_i & 0 & 0 & 0 & 0 & 0 \\ -1 & 0 & 0 & 0 & 0 & 0 & 0 & 0 & 0 & 0 \\ 0 & 0 & 1 & 0 & 0 & 0 & 0 & 0 & 0 & 0 \\ 0 & 0 & 0 & 0 & 0 & 0 & 1 & 0 & -h_i & -b_i \\ 0 & 0 & 0 & 0 & 0 & -1 & 0 & 0 & 0 & 0 \\ 0 & 0 & 0 & 0 & 0 & 0 & 0 & 1 & 0 & 0 \end{bmatrix}. \tag{5.30}$$

The contribution of a fiber's forces $\hat{\mathbf{p}}_i^F$ to the segment forces is denoted by $\hat{\mathbf{p}}_i^S$

and their relation is

$$\hat{\mathbf{p}}_i^S = [\mathbf{R}_i^{SF}]^T \hat{\mathbf{p}}_i^F. \tag{5.31}$$

Using the fiber equation (5.28), and substituting the displacement transformation (5.29) and the force transformation (5.31) in incremental form, gives

$$[\mathbf{R}_i^{SF}]^T [\mathbf{K}_{l,i}^F][\mathbf{R}_i^{SF}] \boldsymbol{\Delta}\hat{\mathbf{u}}^S = \boldsymbol{\Delta}\hat{\mathbf{p}}_i^S. \tag{5.32}$$

Summing the contributions from each fiber gives

$$\mathbf{K}_l^{S,F} \boldsymbol{\Delta}\hat{\mathbf{u}}^S = \boldsymbol{\Delta}\hat{\mathbf{p}}^S \tag{5.33}$$

where the tangent segment stiffness due to fibers is summed for the total number of fibers, n_F:

$$\mathbf{K}_l^{S,F} = \sum_{i=1}^{n_F} ([\mathbf{R}_i^{SF}]^T [\mathbf{K}_{l,i}^F][\mathbf{R}_i^{SF}]). \tag{5.34}$$

The shear stiffness is determined using mid-span sampling as in the 2D case:

$$\mathbf{K}_l^{S,SH} = G \begin{bmatrix} \frac{A_1}{l_1} & 0 & 0 & \frac{A_1}{2} & 0 & -\frac{A_1}{l_1} & 0 & 0 & \frac{A_1}{2} & 0 \\ & 0 & 0 & 0 & 0 & 0 & 0 & 0 & 0 & 0 \\ & & \frac{A_3}{l_3} & 0 & \frac{A_3}{2} & 0 & 0 & -\frac{A_3}{l_3} & 0 & \frac{A_3}{2} \\ & & & \frac{A_1 l_1}{4} & 0 & -\frac{A_1}{2} & 0 & 0 & \frac{A_1 l_1}{4} & 0 \\ & & & & \frac{A_3 l_3}{4} & 0 & 0 & -\frac{A_3}{2} & 0 & \frac{A_3 l_3}{4} \\ & & & & & \frac{A_1}{l_1} & 0 & 0 & -\frac{A_1}{2} & 0 \\ & & & & & & 0 & 0 & 0 & 0 \\ & & sym & & & & & \frac{A_3}{l_3} & 0 & -\frac{A_3}{2} \\ & & & & & & & & \frac{A_1 l_1}{4} & 0 \\ & & & & & & & & & \frac{A_3 l_3}{4} \end{bmatrix}. \tag{5.35}$$

The projected lengths are used in the formulation since the local axes are in the projected planes (figure 5.1). Theses projected lengths are:

$$l_1 = l\left(\frac{\sin\alpha_2}{\sin\alpha_1}\right) \tag{5.36}$$

$$l_3 = l\left(\frac{\sin\alpha_2}{\sin\alpha_3}\right). \tag{5.37}$$

The shear area A_1 is dt_w for the strong axis of a wide flange section or $5/6(2bt_f)$ for the minor axis. For a box column, A_1 is $2dt_w$ for the strong axis or $2bt_f$ for the weak axis. The shear area A_3 corresponds to the direction not being used for the X_1 axis. For example, if the weak axis is aligned with the X_1 axis, then strong axis properties should be used for the X_3 axis.

Local segment forces can be determined from fiber stresses σ_i, geometric prop-

erties and end rotations:

$$P = \sum_{i=1}^{N_F} \sigma_i A_i \tag{5.38}$$

$$Q_1 = \frac{1}{2} G A_1 (\theta_{11} + \theta_{12} - 2\alpha_1) \tag{5.39}$$

$$Q_3 = \frac{1}{2} G A_3 (\theta_{31} + \theta_{32} - 2\alpha_3) \tag{5.40}$$

$$M_{11} = -\sum_{i=1}^{N_F} \sigma_i A_i h_i + \frac{1}{2} Q_1 l_1 \tag{5.41}$$

$$M_{12} = \sum_{i=1}^{N_F} \sigma_i A_i h_i + \frac{1}{2} Q_1 l_1 \tag{5.42}$$

$$M_{31} = -\sum_{i=1}^{N_F} \sigma_i A_i b_i + \frac{1}{2} Q_3 l_3 \tag{5.43}$$

$$M_{32} = \sum_{i=1}^{N_F} \sigma_i A_i b_i + \frac{1}{2} Q_3 l_3. \tag{5.44}$$

The strains developed in the fibers are determined from the segment end displacements in each plane

$$\epsilon_i = \frac{1}{l}(\hat{u}_2^S - \hat{u}_7^S) - \frac{h_i}{l}(\theta_{11} - \theta_{12}) - \frac{b_i}{l}(\theta_{31} - \theta_{32}). \tag{5.45}$$

Refer to figures 5.21 and 5.22 to see the positive sense of all segment local properties in the X_1'-X_2' and X_3'-X_2' planes, respectively. Additionally, these figures define the end angles, θ_{11}, θ_{12}, θ_{11} and θ_{12}, in terms of the segment rotations, $\hat{u}_4$, $\hat{u}_9$, $\hat{u}_5$ and $\hat{u}_{10}$, respectively.

The global end forces of the segment are determined from the transformation

$$\begin{aligned} \mathbf{p}^S &= \mathbf{T}_S^T < -Q_1 \quad P \quad -Q_3 \quad M_{11} \quad M_{31} \quad Q_1 \quad -P \quad Q_3 \quad M_{11} \quad M_{31} >^T \\ &= \mathbf{T}_S^T < \hat{p}_1 \quad \cdots \quad \hat{p}_{10} >^T \\ &= \mathbf{T}_S^T \hat{\mathbf{p}}^S \end{aligned} \tag{5.46}$$

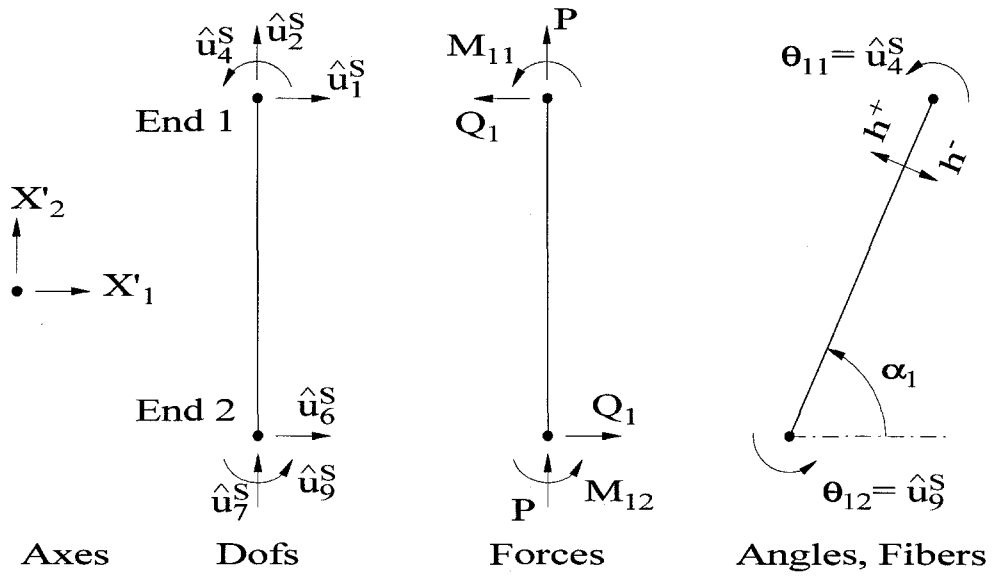

Figure 5.21 Positive directions of various segment parameters, X_1'-X_2' plane.

where

$$\mathbf{T}_S = \begin{bmatrix} \mathbf{T} & \mathbf{0} \\ \mathbf{0} & \mathbf{T} \end{bmatrix} \tag{5.47}$$

and $\mathbf{T}$ is the transformation from equation (5.1). The displacement transformation is $\hat{\mathbf{u}}^S = \mathbf{T}_S \mathbf{u}^S$. Refer to figures 5.21 and 5.22 for the positive sense of the segment end forces and to figures 5.1 and 5.2 for local and global parameters. The global segment stiffness matrix can be determined from the segment transformation

$$\mathbf{K}_g^S = \mathbf{T}_S^T (\mathbf{K}_l^{S,F} + \mathbf{K}_l^{S,SH}) \mathbf{T}_S \tag{5.48}$$

resulting in

$$\mathbf{K}_g^S \Delta \mathbf{u}^S = \Delta \mathbf{p}^S. \tag{5.49}$$

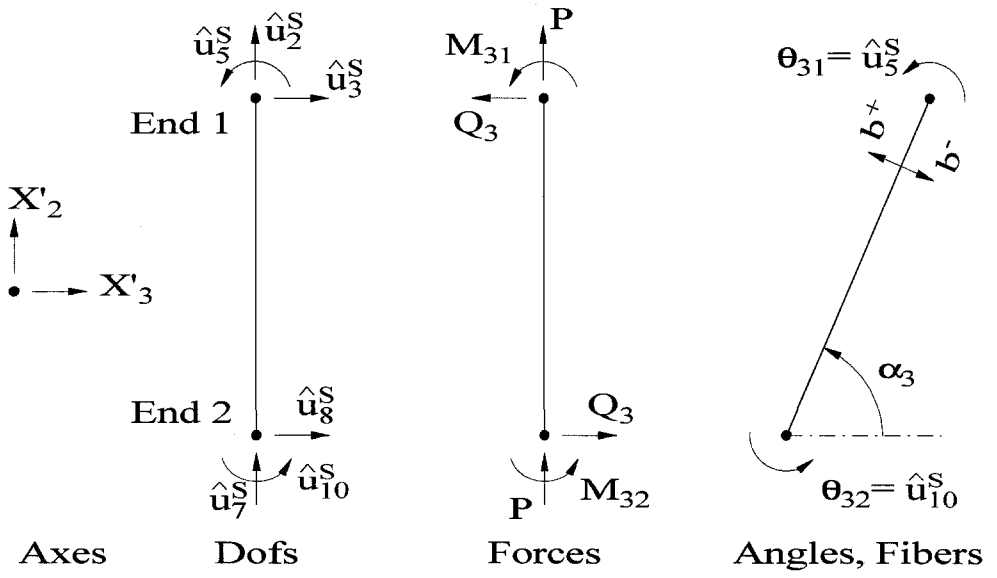

Figure 5.22 Positive directions of various segment parameters, X_3'-X_2' plane.

5.3.3 Column Stiffness

Now that the global segment relations have been determined, the segment stiffnesses are summed to formulate the member stiffness. Dropping superscripts denoting 3D columns, the member stiffness is

$$\mathbf{K} = \overset{N_S}{\underset{i=1}{A}}[\mathbf{K}_g^S] \tag{5.50}$$

and the member equation for all interior and exterior dofs is

$$\mathbf{K}\Delta\mathbf{u} = \mathbf{f} - \mathbf{p} = \Delta\mathbf{p}, \tag{5.51}$$

where $\mathbf{f}$ are the applied forces and $\mathbf{p}$ are the member stiffness forces. The stiffness matrix can be partitioned as in the case of beam-columns from section 3.3.3:

$$\mathbf{K} = \begin{bmatrix} \mathbf{K}_{II} & \mathbf{K}_{IE} \\ \mathbf{K}_{EI} & \mathbf{K}_{EE} \end{bmatrix}. \tag{5.52}$$

The member incremental displacements are solved with individual member iterations using the exterior dof displacement increments recovered from the frame as input, as discussed for the 2D members. The same derivation (section 3.3.3) provides the equation for a 3D column (denoted CC) in terms of its end (exterior) degrees of freedom

$$\mathbf{K}^{CC}\Delta\mathbf{u}^{CC} = \Delta\mathbf{p}^{CC}, \quad \text{where} \tag{5.53}$$

$$\Delta\mathbf{p}^{CC} = \mathbf{f}^{CC} - \mathbf{p}^{CC} \tag{5.54}$$

$$\mathbf{f}^{CC} = \mathbf{f}_E \tag{5.55}$$

$$\mathbf{p}^{CC} = \{\mathbf{p}_E - \mathbf{K}_{EI}\mathbf{K}_{II}^{-1}\mathbf{p}_I\} \tag{5.56}$$

$$\mathbf{u}^{CC} = \mathbf{u}_E \quad \text{and} \tag{5.57}$$

$$\mathbf{K}^{CC} = \left[\mathbf{K}_{EE} - \mathbf{K}_{EI}\mathbf{K}_{II}^{-1}\mathbf{K}_{IE}\right]. \tag{5.58}$$

The column end forces $\mathbf{p}^{CC}$ are applied to the edges of the panel zones and assembled to the frame nodal forces that have applied forces $\mathbf{f}$ already assembled. The forces $\mathbf{f}^{CC}$ never actually have to be determined since the columns are not solved individually for the condensed exterior-only system. The tangent stiffness matrix $\mathbf{K}^{CC}$ is assembled to the frame stiffness matrix. Equation (5.53) gives the column end displacements and forces in column global coordinates.

The column output forces (see figures 5.21 and 5.22 for segments, which are

analogous) in local coordinates are calculated using the updated geometry as follows:

$$P = \frac{1}{N_S}\sum_{i=1}^{N_S} P_i^S \tag{5.59}$$

$$M_{11} = M_{11}^S, \text{ segment 1} \tag{5.60}$$

$$M_{12} = M_{12}^S, \text{ segment } N_S \tag{5.61}$$

$$Q_1 = -\frac{1}{L\frac{\sin\alpha_2}{\sin\alpha_1}}(M_{11} + M_{12}) \tag{5.62}$$

$$M_{31} = M_{31}^S, \text{ segment 1} \tag{5.63}$$

$$M_{32} = M_{32}^S, \text{ segment } N_S \tag{5.64}$$

$$Q_3 = -\frac{1}{L\frac{\sin\alpha_2}{\sin\alpha_3}}(M_{31} + M_{32}). \tag{5.65}$$

These forces are for output purposes only.

The column end forces (equation 5.56) act at the end of the column which is located at the edge of a panel zone. These forces must be transformed to frame nodal forces that are applied at the center of the panel zone. The panel zone depth d_i^b and widths d_{1i}^c and d_{3i}^c, and the beam and column rotations θ_{1i}^b, θ_{3i}^b, θ_{1i}^c and θ_{3i}^c at each end (i or j) of the columns are used to determine the frame nodal loading from the columns.

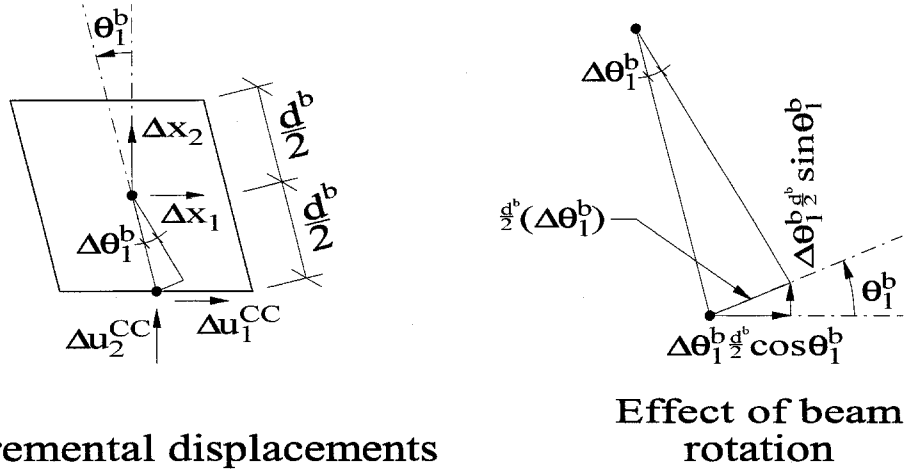

Figure 5.23 Converting column end displacements to frame nodal displacements, X_1'-X_2' plane.

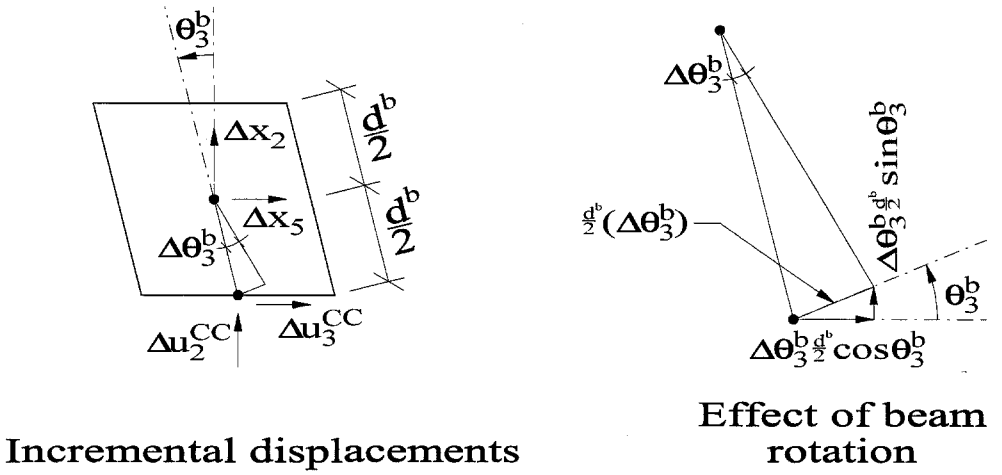

Figure 5.24 Converting column end displacements to frame nodal displacements, X_3'-X_2' plane.

The incremental displacements can be found by imposing small displacements of each of the frame nodal degrees of freedom (figures 5.23 and 5.24). Note that the subscripts for the column ends (i or j) are not used in these figures which represent the top end of a column. The resulting transformation from nodal increment $\mathbf{\Delta x}$ to column end increment $\mathbf{\Delta u}^{CC}$ is

$$\mathbf{S}^{CC}\mathbf{\Delta x} = \mathbf{\Delta u}^{CC} \tag{5.66}$$

where

(5.67) $\mathbf{S}^{CC} =$

$$\begin{bmatrix}
1 & 0 & \frac{d_i^b}{2}\cos\theta_{1i}^b & 0 & 0 & 0 & 0 & 0 & 0 & 0 & 0 & 0 & 0 & 0 \\
0 & 1 & \frac{d_i^b}{2}\sin\theta_{1i}^b & 0 & 0 & \frac{d_i^b}{2}\sin\theta_{3i}^b & 0 & 0 & 0 & 0 & 0 & 0 & 0 & 0 \\
0 & 0 & 0 & 0 & 1 & \frac{d_i^b}{2}\cos\theta_{3i}^b & 0 & 0 & 0 & 0 & 0 & 0 & 0 & 0 \\
0 & 0 & 0 & 1 & 0 & 0 & 0 & 0 & 0 & 0 & 0 & 0 & 0 & 0 \\
0 & 0 & 0 & 0 & 0 & 0 & 1 & 0 & 0 & 0 & 0 & 0 & 0 & 0 \\
0 & 0 & 0 & 0 & 0 & 0 & 0 & 1 & 0 & -\frac{d_j^b}{2}\cos\theta_{1j}^b & 0 & 0 & 0 & 0 \\
0 & 0 & 0 & 0 & 0 & 0 & 0 & 0 & 1 & -\frac{d_j^b}{2}\sin\theta_{1j}^b & 0 & 0 & -\frac{d_j^b}{2}\sin\theta_{3j}^b & 0 \\
0 & 0 & 0 & 0 & 0 & 0 & 0 & 0 & 0 & 0 & 0 & 1 & -\frac{d_j^b}{2}\cos\theta_{3j}^b & 0 \\
0 & 0 & 0 & 0 & 0 & 0 & 0 & 0 & 0 & 0 & 1 & 0 & 0 & 0 \\
0 & 0 & 0 & 0 & 0 & 0 & 0 & 0 & 0 & 0 & 0 & 0 & 0 & 1
\end{bmatrix}$$

The forces can be transformed from the column end forces ($\mathbf{\Delta p}^{CC}$ from equation (5.53)) to frame global coordinates $\mathbf{\Delta p}^{F-CC}$ (figures 5.25 and 5.26) by the transpose of the same transformation

$$\mathbf{\Delta p}^{F-CC} = [\mathbf{S}^{CC}]^T \mathbf{\Delta p}^{CC}. \tag{5.68}$$

Note that the superscript in the figures is F, not $F-CC$ for clarity of the figures. The column contribution to the frame nodal equations is

$$\mathbf{K}_T^{CC} \mathbf{\Delta x} = \mathbf{\Delta p}^{F-CC} \tag{5.69}$$

where

$$\mathbf{K}_T^{CC} = [\mathbf{S}^{CC}]^T [\mathbf{K}^{CC}][\mathbf{S}^{CC}]. \tag{5.70}$$

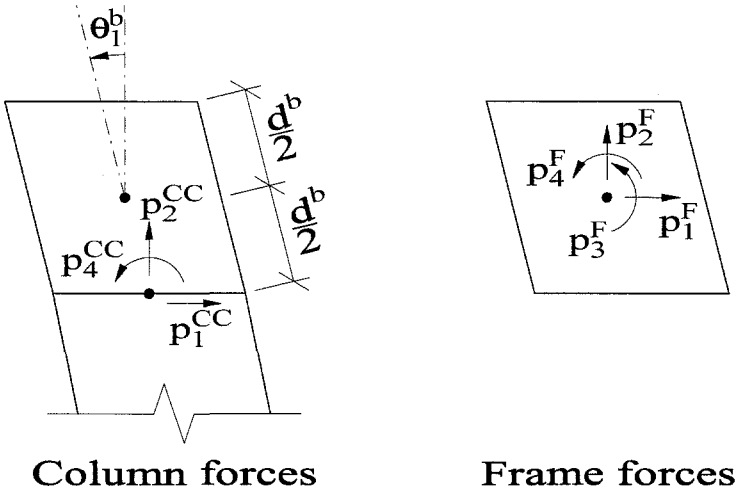

Figure 5.25 Converting column end forces to frame nodal forces, X_1'-X_2' plane.

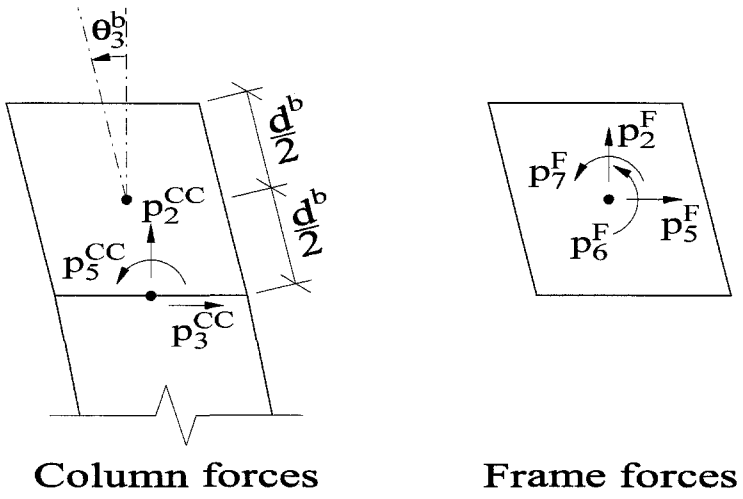

Figure 5.26 Converting column end forces to frame nodal forces, X_3'-X_2' plane.

5.3.4 Panel Zone Stiffness

For 3D columns, there are two panel zones per column acting in the planes of the beams framing into the column. Both directions ($i = 1, 3$) have a panel zone stiffness which relates the shearing strain γ_i^{PZ} of the steel volume acting in the plane of the panel zone and the moment M_i^{PZ} that resists this strain. As for the 2D case, the shear modulus is determined from a nonlinear stress-strain relationship, and its instantaneous value is denoted G_{iT}. The volume being sheared is

$$ddt_i = \begin{cases} d^c d^b t_w & \text{if strong axis of wide flange,} \\ d^c d^b (t_w + t_{dp}) & \text{same as above with doubler plate,} \\ 2d^c d^b t_w & \text{if strong axis of box,} \\ 2b^c d^b t_f & \text{if weak axis of wide flange or box} \end{cases} \tag{5.71}$$

where d^c is the depth of the column, d^b is the depth of the deepest beam framing into the column, b^c is the width of the column, t_{dp} is the thickness of the doubler plate, and t_f and t_w are the thicknesses of the flange and web, respectively. The shearing strain is related to the beam and column rotations in incremental form by

$$\Delta\gamma_i^{PZ} = \Delta\theta_i^b - \Delta\theta_i^c. \tag{5.72}$$

The resulting stiffness equation is

$$\mathbf{K}_{iT}^{PZ} \boldsymbol{\Delta}\mathbf{x}_i^{PZ} = \boldsymbol{\Delta}\mathbf{p}_i^{F-PZ} \tag{5.73}$$

where $\boldsymbol{\Delta}\mathbf{p}_i^{F-PZ}$ and $\boldsymbol{\Delta}\mathbf{x}_i^{PZ}$ are the panel zone incremental moments and rotations associated with the frame dofs in planes $i = 1, 3$ and

$$\mathbf{K}_{iT}^{PZ} = G_{iT} ddt_i \begin{bmatrix} 1 & -1 \\ -1 & 1 \end{bmatrix}, \quad \boldsymbol{\Delta}\mathbf{x}_i^{PZ} = \begin{Bmatrix} \Delta\theta_i^b \\ \Delta\theta_i^c \end{Bmatrix}, \quad \mathbf{p}_i^{F-PZ} = \begin{Bmatrix} M_i^b \\ M_i^c \end{Bmatrix}. \tag{5.74}$$

5.3.5 Assembly to Frame Stiffness

5.3.6 Frame Stiffness

The stiffnesses which contribute to the frame have been written in the frame coordinate system. The three-dimensional column stiffness, 5.69, and the panel zone stiffness, (5.73), can be assembled to appropriate degrees of freedom and added to the frame stiffness (3.60):

$$\mathbf{K}_T^F = \mathbf{K}_T^F + \mathcal{A}\left(\mathbf{K}_T^{CC} + \mathbf{K}_{1T}^{PZ} + \mathbf{K}_{3T}^{PZ}\right). \tag{5.75}$$

All of the stiffness contributions are tangent stiffnesses, so the governing total frame stiffness is also. The stiffness forces at all the degrees of freedom of the frame can also be assembled from the columns, (5.68), and the panel zones, (5.74), as

$$\mathbf{p}^F = \mathbf{p}^F + \mathcal{A}\left(\mathbf{p}^{F-CC} + \mathbf{p}_1^{F-PZ} + \mathbf{p}_3^{F-PZ}\right). \tag{5.76}$$

These contributions to the frame stiffness matrix and stiffness force vector are assembled into the global building stiffness matrix (4.45) and stiffness force vector (4.46), respectively.

5.4 Influence on Three-Dimensional Solution

The addition of the 3D column has several impacts on the solution of the system of equations including extra storage and frame interaction considerations.

The 3D column requires additional storage for fiber properties, member dofs, and frame dofs. Since the program is written in FORTRAN 77 , dynamic allocation is explicitly performed within the program. Because of this, storage is provided for seven dof/node instead of the four dof/node for three-dimensional analysis without 3D columns. Separate variables are used for most of the other 3D column properties to limit excessive storage that is never used.

For most analyses, all of the column horizontal dofs are constrained to the master

joints. For a 3D column, one axis acts in one frame and another axis acts in another frame. Since constraints are applied by frame (see section 4.2), different dofs of a 3D column can be constrained to act with different frames. This is an additional reason for requiring only orthogonal framing to the 3D columns since the current constraint method would not be appropriate for skewed framing.

The foundation elements are modified to be capable of tracking nonlinear response in two orthogonal directions corresponding to the column.

The stiffness in terms of the column itself and its effects on panel zones, constraints and foundations have been enumerated. The contribution of mass must be considered separately, though. Recall that the mass associated with a frame node has an out-of-plane contribution to the master joint which results in a non-diagonal mass matrix (section 4.7). Considering the 3D column, out-of-plane motion for one plane will be in-plane motion for the orthogonal plane. Thus, the in-plane mass for the two orthogonal frames to which the column is constrained will fully account for the horizontal translational motion of the mass, which in turn accounts for the rotational motion. No mass or mass cross terms are assembled to the master node for 3D columns.

Chapter 6

Equations of Motion

The equations of motion are assembled from the individual element contributions excluding the interior dofs of the beam-columns. The gravity loading is applied to the structure first followed by the earthquake loading. The equations of motion are integrated implicitly with iterations in each time step until convergence is achieved. The tangent stiffness matrix is used, which produces increments in the displacements at the nodal dofs in each iteration. Incremental member end displacements are calculated from the nodal increments and applied to the individual members. The member behavior is also nonlinear, so iterations are performed in the analysis of these members. Each beam, column and brace is solved individually for its end forces that are assembled into the right side residual force vector of the frame equations. The frame tangent stiffness is also updated from changes in the member tangent stiffnesses. Panel zones, foundations and the shear building contribute to the residual force vector and the tangent stiffness used in the frame equations. The residual force vector is also updated when using the nonlinear story damping.

The basic multiple degree of freedom dynamic problem for a linear system is

$$\mathbf{M}\ddot{\mathbf{x}}(t) + \mathbf{C}\dot{\mathbf{x}}(t) + \mathbf{K}\mathbf{x}(t) = \mathbf{f} = \mathbf{f}_S - \mathbf{M}\ddot{\mathbf{x}}_g(t), \tag{6.1}$$

where $\mathbf{f}_S$ is static loading and $\mathbf{M}\ddot{\mathbf{x}}_g(t)$ are the inertial forces created by the ground motion acceleration inputs, $\ddot{x}_g(t)$, $\ddot{y}_g(t)$, $\ddot{z}_g(t)$. The three orthogonal acceleration inputs are repeated at all degrees of freedom corresponding to the respective directions

of excitation.

The actual problem is complicated by the nonlinearities of stiffness and damping, with $\mathbf{K}$ depending on the current state and history of $\mathbf{x}(t)$ and $\mathbf{C}$ depending on the current state and history of $\dot{\mathbf{x}}(t)$. This nonlinear problem can be expressed as

$$\mathbf{M}\ddot{\mathbf{x}}(t) + \mathbf{q}(t) + \mathbf{p}(t) = \mathbf{f}, \tag{6.2}$$

where $\mathbf{q}(t)$ represents the damping forces and $\mathbf{p}(t)$ represents the restoring forces. To solve a nonlinear structure subjected to a loading time history, the formulation uses a time-stepping scheme that performs iterations within each time step. The Newmark method is used for the dynamic time integration and an improved modified Newton-Raphson (IMNR) scheme is used for iterative convergence of the nonlinearities in stiffness. The damping nonlinearities are corrected by modifying the residual forces in each iteration instead of linearizing the problem as for the stiffness nonlinearities.

6.1 The Newmark Method of Time Integration

The Newmark method is a class of implicit methods for time integration. Different choices of two parameters lead to different assumptions about the acceleration between time steps and to different levels of stability. The method assumes that displacement and velocity can be written as

$$\mathbf{x}(t+\Delta t) = \mathbf{x}(t) + \dot{\mathbf{x}}(t)\Delta t + \{(\frac{1}{2} - \beta)\ddot{\mathbf{x}}(t) + \beta\ddot{\mathbf{x}}(t+\Delta t)\}\Delta t^2 \tag{6.3}$$

$$\dot{\mathbf{x}}(t+\Delta t) = \dot{\mathbf{x}}(t) + \{(1-\gamma)\ddot{\mathbf{x}}(t) + \gamma\ddot{\mathbf{x}}(t+\Delta t)\}\Delta t \tag{6.4}$$

where γ and β are the two parameters which determine the resulting scheme. The choices used in the analyses presented here are $\gamma = \frac{1}{2}$ and $\beta = \frac{1}{4}$, which correspond to a constant average acceleration from time t to time $t+\Delta t$. This choice of parameters results in an implicit method that is unconditionally stable for linear problems and has no artificial damping. Stability is not guaranteed for nonlinear problems, but the use of small time steps and the level of nonlinear response observed in this work

have provided stable solutions. Such time integration schemes do induce period elongation, but this is roughly 1% for $\Delta t = 0.05T_i$. Considering that most recorded time histories are given in 0.02 sec increments, this effect should be minimal and could be reduced further by interpolating the time history. Equation (6.3) can be solved for $\ddot{\mathbf{x}}(t+\Delta t)$ giving

$$\ddot{\mathbf{x}}(t+\Delta t) = \frac{1}{\beta \Delta t^2}\{\mathbf{x}(t+\Delta t) - \mathbf{x}(t)\} - \frac{1}{\beta \Delta t}\dot{\mathbf{x}}(t) - (\frac{1}{2\beta} - 1)\ddot{\mathbf{x}}(t). \tag{6.5}$$

Equations (6.4) and (6.5) represent velocity and acceleration at time $t+\Delta t$ as functions of $\mathbf{x}(t), \dot{\mathbf{x}}(t), \ddot{\mathbf{x}}(t)$ and $\mathbf{x}(t+\Delta t)$. If equations (6.4) and (6.5) were substituted into the linear equations of motion evaluated at time $t+\Delta t$, the resulting equations could be rearranged to solve for $\mathbf{x}(t+\Delta t)$ as a function of displacement, velocity and acceleration at time t. This is an implicit scheme since it requires estimates of velocity and acceleration at time $t+\Delta t$ to solve for displacements at time $t+\Delta t$. Once the displacements are determined, equations (6.4) and (6.5) can be used to obtain the velocity and acceleration, respectively, at time $t+\Delta t$.

For a linear system, the implicit scheme above can accurately determine the structural response to an earthquake time history. There will be minimal error since the scheme is unconditionally stable and has no artificial damping. For small enough time increments, the period elongation will be irrelevant. Unfortunately, the response to large ground motions is neither linear nor elastic so the above scheme cannot be used unless linearization is performed.

6.2 Stiffness Linearization

The stiffness forces $\mathbf{p}(t)$ require linearization. The solution technique of the program uses an improved scheme that provides the strength of the modified Newton-Raphson method, but with faster convergence. The Newton-Raphson scheme derives from a truncated Taylor series approximation for the nonlinear forces. The

nonlinear relationship for one variable is

$$p(x) = f \tag{6.6}$$

and the Taylor series expansion about x^k is

$$p(x^k) + \frac{dp}{dx}\Big|_{x=x^k}(x - x^k) + \overbrace{\frac{1}{2}\frac{d^2p}{dx^2}\Big|_{x=x^k}(x - x^k)^2 + \cdots}^{Remainder} = f. \tag{6.7}$$

After truncating the series, the equation is linear, but is not exactly satisfied for x^k and $p(x^k)$ which approximate x and $p(x)$, respectively. This leads to an iterative solution, so the next approximation to $p(x)$ will be $p(x^{k+1})$ obtained in the k^{th} iteration where

$$p(x^{k+1}) = p(x^k) + \frac{dp}{dx}\Big|_{x=x^k}(x^{k+1} - x^k). \tag{6.8}$$

Substituting this into equation (6.6) gives

$$p(x^k) + \frac{dp}{dx}\Big|_{x=x^k}(x^{k+1} - x^k) = f, \tag{6.9}$$

which is solved for $\Delta x^{k+1} = x^{k+1} - x^k$. Note that Δx^{k+1} will satisfy equation (6.9) exactly, whereas equation (6.8) is only approximately satisfied.

In our problem, the stiffness forces $\mathbf{p}$ are nonlinear, but are a vector, so the linearization is a generalization of equation (6.8):

$$\mathbf{p}(\mathbf{x}^{k+1}) = \mathbf{p}(\mathbf{x}^k) + \frac{\partial \mathbf{p}(\mathbf{x})}{\partial \mathbf{x}}\Big|_{\mathbf{x}=\mathbf{x}^k}\Delta\mathbf{x}^{k+1}. \tag{6.10}$$

Our problem is actually a history of potentially nonlinear steps, so a step can be denoted by Δt, a counting variable which is time for a dynamic problem. In a load or time step, the variable changes from t to $t + \Delta t$. The stiffness forces are thus $\mathbf{p}(\mathbf{x}^{k+1}(t + \Delta t))$, or $\mathbf{p}^{k+1}(t + \Delta t)$ to be concise. The tangent stiffness matrix, $\mathbf{K}_T^k$, represents the instantaneous stiffness of the structure at the latest deformed state.

It is analogous to the derivative expression from equation (6.10), $\frac{\partial \mathbf{p}(\mathbf{x})}{\partial \mathbf{x}}\big|_{\mathbf{x}=\mathbf{x}^k}$.

These substitutions produce the linearization for nonlinear stiffness forces in a time or load-stepping solution scheme:

$$\mathbf{p}^{k+1}(t+\Delta t) = \mathbf{K}_T^k \boldsymbol{\Delta}\mathbf{x}^{k+1} + \mathbf{p}^k(t+\Delta t). \tag{6.11}$$

6.3 Nonlinear Time-Stepping Formulation

Now that an integration scheme and a linearization of the stiffness matrix have been developed, the nonlinear equations of motion can be solved by substituting these formulations. The equations of motion (equation (6.2)) evaluated at time $t+\Delta t$ and iteration $k+1$ become

$$\mathbf{M}\ddot{\mathbf{x}}^{k+1}(t+\Delta t) + \mathbf{q}^{k+1}(t+\Delta t) + \mathbf{p}^{k+1}(t+\Delta t) = \mathbf{f}(t+\Delta t). \tag{6.12}$$

The nonlinear damping can be divided into a linearly proportional component and a nonlinear correction term (see equation 4.69):

$$\overbrace{\mathbf{q}^{k+1}(t+\Delta t)}^{nonlinear} = \overbrace{\mathbf{C}\dot{\mathbf{x}}^{k+1}(t+\Delta t)}^{linear} + \overbrace{\mathbf{d}^{k+1}(t+\Delta t)}^{correction}. \tag{6.13}$$

The estimate of $\mathbf{q}^{k+1}(t+\Delta t)$ uses information known at iteration k and also the Newmark approximation of velocity at iteration $k+1$ (equation (6.4)).

The linearized restoring forces (equation (6.11)) and damping forces (equation (6.13)) are substituted into equation (6.12), and the nonlinear portion of damping, $\mathbf{d}^{k+1}$, is moved to the right-hand side of the equation giving:

$$\mathbf{M}\ddot{\mathbf{x}}^{k+1}(t+\Delta t) + \mathbf{C}\dot{\mathbf{x}}^{k+1}(t+\Delta t) + \mathbf{K}_T^k \boldsymbol{\Delta}\mathbf{x}^{k+1} = \mathbf{f}(t+\Delta t) - \mathbf{d}^{k+1}(t+\Delta t) - \mathbf{p}^k(t+\Delta t). \tag{6.14}$$

The nonlinear portion of the damping and the restoring force from the previous step are treated as applied forces. The equations of motion are now solved for the

incremental deformation, $\Delta\mathbf{x}^{k+1}$. To obtain this solution, the Newmark equations for velocity and acceleration (6.4 and 6.5) are rewritten for the incremental form of the deformations $\mathbf{x}^{k+1}(t+\Delta t) = \mathbf{x}^{k}(t) + \Delta\mathbf{x}^{k+1}$ and the parameter values $\gamma = \frac{1}{2}$ and $\beta = \frac{1}{4}$ are used throughout this work. The new form of the equations is:

$$\dot{\mathbf{x}}^{k+1}(t+\Delta t) = \dot{\mathbf{x}}(t) + \frac{\Delta t}{2}\{\ddot{\mathbf{x}}(t) + \ddot{\mathbf{x}}^{k+1}(t+\Delta t)\} \quad \text{and} \tag{6.15}$$

$$\ddot{\mathbf{x}}^{k+1}(t+\Delta t) = \frac{4}{\Delta t^2}\{\mathbf{x}^{k}(t+\Delta t) + \Delta\mathbf{x}^{k+1} - \mathbf{x}(t)\} - \frac{4}{\Delta t}\dot{\mathbf{x}}(t) - \ddot{\mathbf{x}}(t). \tag{6.16}$$

Substitution of these values into equation (6.14) results in

$$\overbrace{\left[\frac{4}{\Delta t^2}\mathbf{M} + \frac{2}{\Delta t}\mathbf{C} + \mathbf{K}_T^k\right]}^{\hat{\mathbf{K}}_T^k}\Delta\mathbf{x}^{k+1} = \mathbf{f}(t+\Delta t) - \mathbf{d}^{k+1}(t+\Delta t) \tag{6.17}$$
$$\overbrace{-\mathbf{p}^{k+1}(t+\Delta t) - \left[\frac{4}{\Delta t^2}\mathbf{M} + \frac{2}{\Delta t}\mathbf{C}\right]\mathbf{x}^{k}(t+\Delta t)}^{\mathbf{p}^{k}(t+\Delta t)}$$
$$\overbrace{+\left[\frac{4}{\Delta t^2}\mathbf{M} + \frac{2}{\Delta t}\mathbf{C}\right]\mathbf{x}(t) + \left[\frac{4}{\Delta t}\mathbf{M} + \mathbf{C}\right]\dot{\mathbf{x}}(t) + [\mathbf{M}]\ddot{\mathbf{x}}(t).}^{\mathbf{g}(t)}$$

This can be written in the simpler form

$$\hat{\mathbf{K}}_T^k\Delta\mathbf{x}^{k+1} = \mathbf{f}(t+\Delta t) - \mathbf{d}^{k+1}(t+\Delta t) - \mathbf{p}^{k}(t+\Delta t) + \mathbf{g}(t) \tag{6.18}$$

using the definitions from equation (6.17). Note that $\mathbf{p}^k(t+\Delta t)$ now includes all effects due to the displacement $\mathbf{x}^k(t+\Delta t)$, not just stiffness forces. The transformed stiffness $\hat{\mathbf{K}}_T^k$ includes mass and damping terms which only have to be formulated once at the beginning of the time history. The tangent stiffness matrix is calculated for each iteration of each step using elastic or tangent material properties, depending on what the IMNR method requires for a particular iteration. Equation (6.18) is solved for the increment of displacement in each iteration. The first increment in each time step is the solution for the external load application associated with that time step. If any nonlinearities have occurred in this increment, the answer will

be wrong and additional iterations will be performed solving for the displacement increments due to the residual force application. The residual forces are represented by the right side of equation (6.18).

Iterations within a time step can cause artificial unloading if the load increments are summed for each iteration of displacement increments. Instead, updating the step displacement increment from the previous step will keep track of the load increment properly. If a beam fiber has yielded, then displacement increments imposed by the frame will cause the fiber to continue along the yield plateau with increasing displacement (figure 6.1(a)). If the next iteration of the frame equations imposes a negative displacement on the fiber, the load will follow an elastic unloading path. If the updated version of the displacement increment is used, i.e., the cumulative increment, the load will remain on the yield plateau, merely further to the left (figure 6.1(b)). Thus, the program updates the stiffnesses and forces of members and frames using the cumulative displacement increment and the updated total displacement, avoiding artificial unloading. The total displacement is used to determine P-Δ effects, among other things.

Tolerances are set for forces and moments at member ends, frame nodes and master nodes to confirm convergence. Once the residual forces at all of the degrees of freedom satisfy the individual tolerances, the time step has converged and the program moves on to the next step. A maximum number of iterations within a time step is set in case the load application is causing divergence. This happens under severe deformations incipient to structural collapse. If the tolerances are set too low, a precise solution requiring many iterations can be achieved. This will take a longer time to execute, and the precision achieved may be outweighed by the accuracy limitations imposed by the numerical integration scheme.

The solution technique is robust and very efficient. Failure to achieve convergence in a time step rarely occurs except under very large lateral displacements of the frames involving severe member deformations.

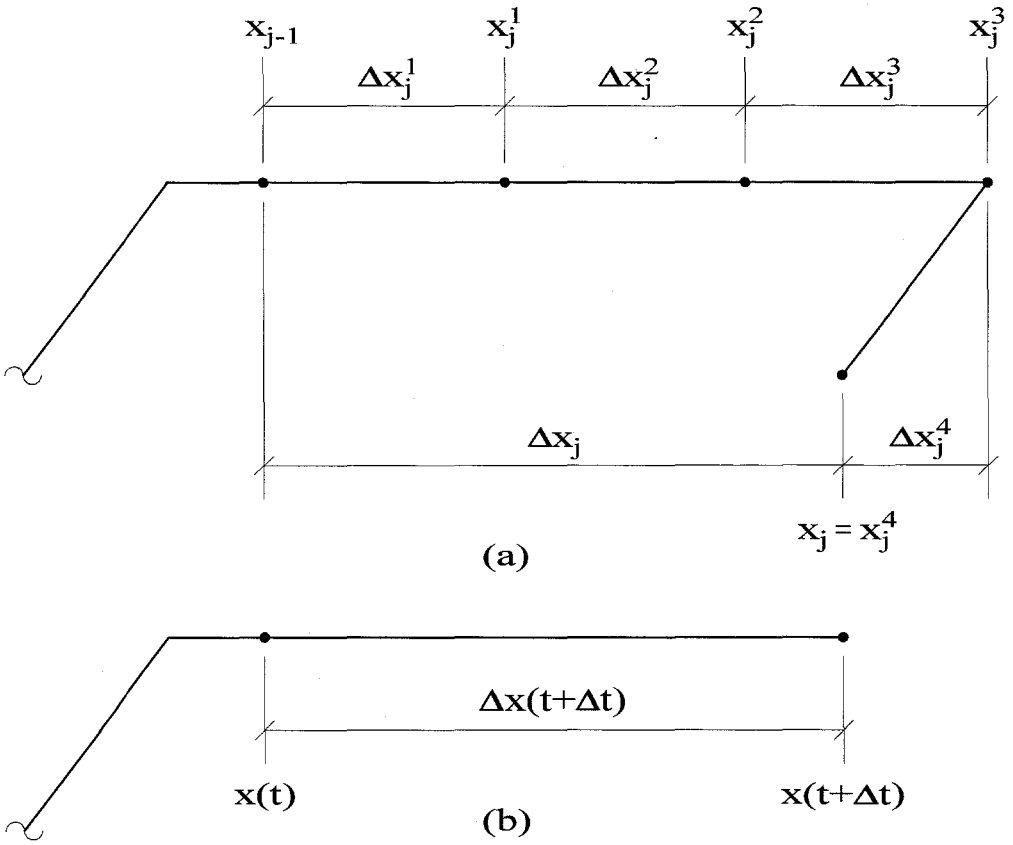

Figure 6.1 (a) Iterations during a time step. (b) Updating at the last iteration.

6.4 Static Solution

The solution technique just described will now be examined in detail. In section 4.6, the tangent stiffness matrix, $\mathbf{K}_T$, is fully assembled in equation (4.45). The stiffness force vector, $\mathbf{p}$, is also assembled in equation (4.46). The time-stepping equation of the previous section can be trimmed down for static analysis. Removing any inertial or damping terms, equation (6.17) becomes

$$\mathbf{K}_T^k \Delta \mathbf{x}^{k+1} = \mathbf{f}(t + \Delta t) - \mathbf{p}^k(t + \Delta t), \tag{6.19}$$

where the stiffness and stiffness forces are as described above.

This equation can be used to solve for the static loading where mass and damping

have no effect. The loads that can be applied include horizontal loading at the master nodes and both horizontal and vertical loading at the individual frame nodes. If large forces are being applied which might result in nonlinearities more severe than P-Δ effects, the static load may be broken up into increments. The load vector can be represented as

$$\mathbf{f}(t+\Delta t) = s(t+\Delta t)\mathbf{f}_S, \tag{6.20}$$

where $\mathbf{f}_S$ is the static load vector, $s(t+\Delta t)$ are the load factors, and the variable t represents load steps where a step is denoted by Δt. Typically, the load factors are ramped from zero to one.

The stiffnesses used in static analysis are

$$\mathbf{K}_T^k = \begin{cases} \mathbf{K}_E & \text{for} \quad k = 0 \\ \mathbf{K}_T & \text{for} \quad k > 0. \end{cases} \tag{6.21}$$

This means the tangent stiffness is assembled assuming elastic material properties in the first iteration of each load step.

Once the increment of displacement $\mathbf{\Delta x}^{k+1}(t+\Delta t)$ has been solved,[1] the total displacement is updated. Assuming the displacement from the previous step has converged, the estimate of the total displacement for iteration $k+1$ is

$$\mathbf{x}^{k+1}(t+\Delta t) = \mathbf{x}^k(t+\Delta t) + \mathbf{\Delta x}^{k+1}(t+\Delta t). \tag{6.22}$$

The updated incremental displacement for this load step is

$$\mathbf{\Delta x}(t+\Delta t) = \mathbf{x}^{k+1}(t+\Delta t) - \mathbf{x}(t), \tag{6.23}$$

where $\mathbf{x}(t)$ is the converged solution from the previous step after n iterations, $\mathbf{x}^n(t)$.

The updated incremental displacements of the building analysis are then used

[1]The first iterative displacement increment of static analysis can be on the order of the total displacement if the total load is being applied.

to update the interior nodes of the members for each iteration of each global load step. Following similar iterative procedures for the global building unknowns, the member interior dofs are solved by equation (3.30) for the loading produced by the end displacements imposed by the frame. The solution of the interior displacements will produce a set of forces at the frame dofs, $\mathbf{p}^{k+1}(t+\Delta t)$, which are updated for all beams, columns, braces, panel zones, foundations and shear building contributions. Each stiffness matrix used is updated for any nonlinearities involving displacement. Once the frame forces have been updated for all the elements of the building, the right hand side of equation (6.19) is updated for these new forces by

$$\mathbf{r}^{k+1}(t+\Delta t) = s(t+\Delta t)\mathbf{f}_S - \mathbf{p}^{k+1}(t+\Delta t). \tag{6.24}$$

These updated forces are the residual forces, $\mathbf{r}^{k+1}(t+\Delta t)$, which are the static loads applied at this load step, $s(t+\Delta t)\mathbf{f}_S$, minus the forces calculated in the displaced geometry, $\mathbf{p}^{k+1}(t+\Delta t)$. If the problem is completely linearly elastic, the forces calculated will be identical to the forces applied, other than differences from numerical error. Since the problem is not linearly elastic, iterations must be performed until the residual forces are all reduced to an acceptable tolerance. The necessary condition can be expressed as

$$\max_{force} \mathbf{r}^{k+1}(t+\Delta t) < tol_{force} \quad \text{and} \quad \max_{moment} \mathbf{r}^{k+1}(t+\Delta t) < tol_{moment} \tag{6.25}$$

Assuming the solution has not converged, the stiffness matrix for the building is updated for changes to all the elemental stiffness matrices. Another displacement increment is calculated from the application of the residual forces. The solution steps (6.19–6.25) can be repeated until convergence is achieved. This can be summarized

for iteration k of load step $(t + \Delta t)$ by the following steps:

(6.26)	Solve	$\mathbf{K}_T^k \Delta \mathbf{x}^{k+1}(t + \Delta t) = \mathbf{r}^k(t + \Delta t)$
(6.26a)	Update total disp.	$\mathbf{x}^{k+1}(t + \Delta t) = \mathbf{x}^k(t + \Delta t) + \Delta \mathbf{x}^{k+1}(t + \Delta t)$
(6.26b)	Update incr. disp.	$\Delta \mathbf{x}(t + \Delta t) = \mathbf{x}^{k+1}(t + \Delta t) - \mathbf{x}(t)$
(6.27)	Update forces,	$\mathbf{p}^{k+1}(t + \Delta t)$
(6.26c)	Update loads	$\mathbf{r}^{k+1}(t + \Delta t) = s(t + \Delta t)\mathbf{f}_S - \mathbf{p}^{k+1}(t + \Delta t)$
(6.26d)	Check force tolerances	$\max_{force} \mathbf{r}^{k+1}(t + \Delta t) < tol_{force}$
(6.26e)	Check moment tolerances	$\max_{moment} \mathbf{r}^{k+1}(t + \Delta t) < tol_{moment}$

If the tolerances are not met, update the building stiffness $\mathbf{K}_T^{k+1}$ and repeat steps (6.26–6.26e). Once convergence is achieved in a load step, repeat the procedure for the following load step, $\mathbf{f}(t + 2\Delta t)$. The first iteration of each load step is the application of a load and subsequent iterations are solved for the residual forces due to the nonlinear nature of the problem.

The steps in equations (6.26–6.26e) can be seen in figure 6.2. Subscripts $(j - 1)$ and j are used to represent times t and $(t + \Delta t)$, respectively. The notation in the figure can be explained by the following analogies:

$$\mathbf{p}^k(t + \Delta t) \Longrightarrow \mathbf{p}_j^k$$
$$\Delta \mathbf{x}^k(t + \Delta t) \Longrightarrow \Delta \mathbf{x}_j^k$$
$$\mathbf{x}(t + \Delta t) \Longrightarrow \mathbf{x}_j$$
$$s(t + \Delta t)\mathbf{f}_S \Longrightarrow \mathbf{f}_j$$
$$\mathbf{r}^k(t + \Delta t) \Longrightarrow \mathbf{f}_j - \mathbf{p}_j^k$$

6.5 Dynamic Solution

Once the static analysis is complete, dynamic analysis can be performed. The program accepts one vertical and two orthogonal horizontal time histories of accel-

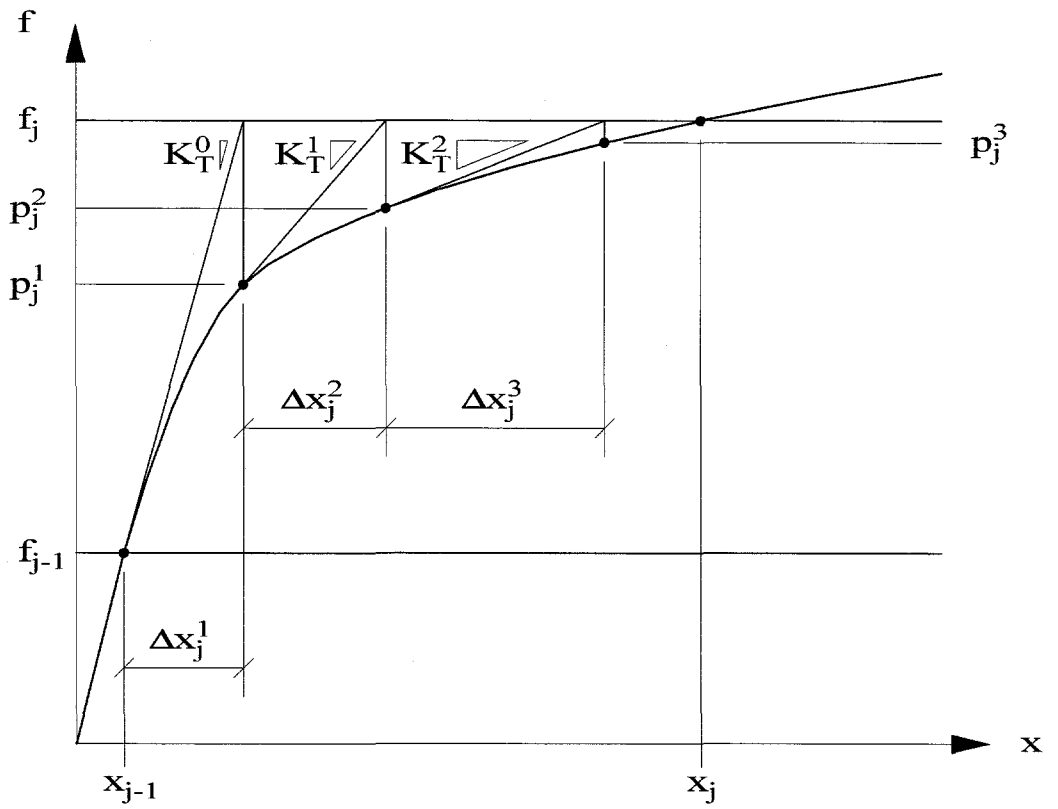

Figure 6.2 Detailed steps of the Newton-Raphson method.

eration. The time step must be constant, but may be input by the user. The units can be converted by an input factor if they do not match the other data provided.

At the start of the dynamic analysis, the mass and damping are assembled as per sections 4.7 and 4.8. The mass remains constant throughout the analysis. The damping matrix is also a linear operator, so the nonlinear story damping is taken into account by updating the residual force vector. In this way, the mass and damping matrices only have to be assembled once.

The initial stiffness matrix is evaluated using elastic material properties, but it also considers the geometric effects of the final static displacements. The initial load vector includes the full static loading plus the inertial forces due to the first acceleration in the time history.

The equations developed in section 6.3 are used to perform the dynamic iterative analysis. Only the major steps involved are summarized below since the method can easily be ascertained from the static solution already presented.

- Determine $\mathbf{f}(t+\Delta t)$, which includes static loads plus dynamic loads applied at time step $(t+\Delta t)$.
- Determine $\mathbf{g}(t)$, which consists of forces calculated from the converged solution of time step t.
- Assemble right side of equation (6.18) using $\mathbf{f}(t+\Delta t)$ and $\mathbf{g}(t)$. If $k > 0$, assemble $\mathbf{d}^{k+1}(t+\Delta t)$ and $\mathbf{p}^{k}(t+\Delta t)$.
- If $k > 0$, check tolerances (right-hand side residual force levels). If met, apply the following load step. If not met, continue with current iteration.
- Determine $\hat{\mathbf{K}}_T^k$, which is updated each iteration for the tangent stiffness contribution $\mathbf{K}_T^k$.
- Solve equation (6.18) for the displacement increment $\boldsymbol{\Delta}\mathbf{x}^{k+1}$.
- Update the total displacement, $\mathbf{x}^{k+1}(t+\Delta t) = \mathbf{x}^{k}(t+\Delta t) + \boldsymbol{\Delta}\mathbf{x}^{k+1}$.
- Update the total increment for time step $(t+\Delta t)$, $\boldsymbol{\Delta}\mathbf{x}(t+\Delta t) = \mathbf{x}^{k+1}(t+\Delta t) - \mathbf{x}(t)$.
- Apply new displacements to member ends and iteratively solve for internal displacements and member end forces.
- Determine the frame forces $\mathbf{p}^{k+1}(t+\Delta t)$ based on the member forces, the displacements from iteration k, $\mathbf{x}^{k+1}(t+\Delta t)$, and the updated incremental displacements, $\boldsymbol{\Delta}\mathbf{x}(t+\Delta t)$.

6.6 Other Newton-Raphson Iterative Schemes

Typically, the Newton-Raphson iterative equation for nonlinear problems is solved using Gaussian elimination on the banded tangent stiffness matrix. It has quadratic

convergence under certain conditions, but requires factoring the stiffness matrix in each iteration. The Modified Newton-Raphson (MNR) method was developed to achieve a faster solution. Instead of reevaluating the stiffness matrix each iteration, the elastic stiffness matrix is used throughout the analysis or the tangent stiffness is evaluated only at the beginning of each time step. Factoring of the matrix is performed at the beginning of a time step. All iterations within the time step use this same stiffness, so the computational effort is greatly reduced from the Newton-Raphson method. Convergence will take more steps for a softening system (figure 6.3), but the savings in computational effort per iteration is sufficient to warrant the additional iterations in most cases. However, sometimes the MNR method may exhibit slow convergence, require small time steps for convergence, or not converge at all. The NR method has better convergence properties and apparently would be able to use larger time steps. The latter is not really a benefit since a small time step is usually selected to limit discretization errors associated with path-dependent problems and time integration. Additionally, the time step of recorded ground motions is typically 0.005–0.02 sec.

The MNR method has more trouble converging for stiffening systems (figure 6.4), but can be advantageous over the NR method for the stiffening associated with unloading after yielding (figure 6.5). The numbering in this figure follows the iterations in the following order 0-1'-1-2'-2-1'-1-2'-2, etc., without convergence for the NR method.

The improved modified Newton-Raphson (IMNR) method is used in this program. In the first iteration of each step the tangent stiffness matrix is computed using elastic material properties. Additional steps use tangent material properties. If the residual forces grow in an iteration, the following two iterations again use the elastic properties to recover convergence. Thus, the IMNR method will converge like the NR method for well-behaved problems. For extreme nonlinearities that the NR method has trouble with, the IMNR method will converge like the MNR method. Thus, the IMNR will converge for a broader range of problems than either the NR or the MNR methods will. See figure 6.6 for convergence of the IMNR method in

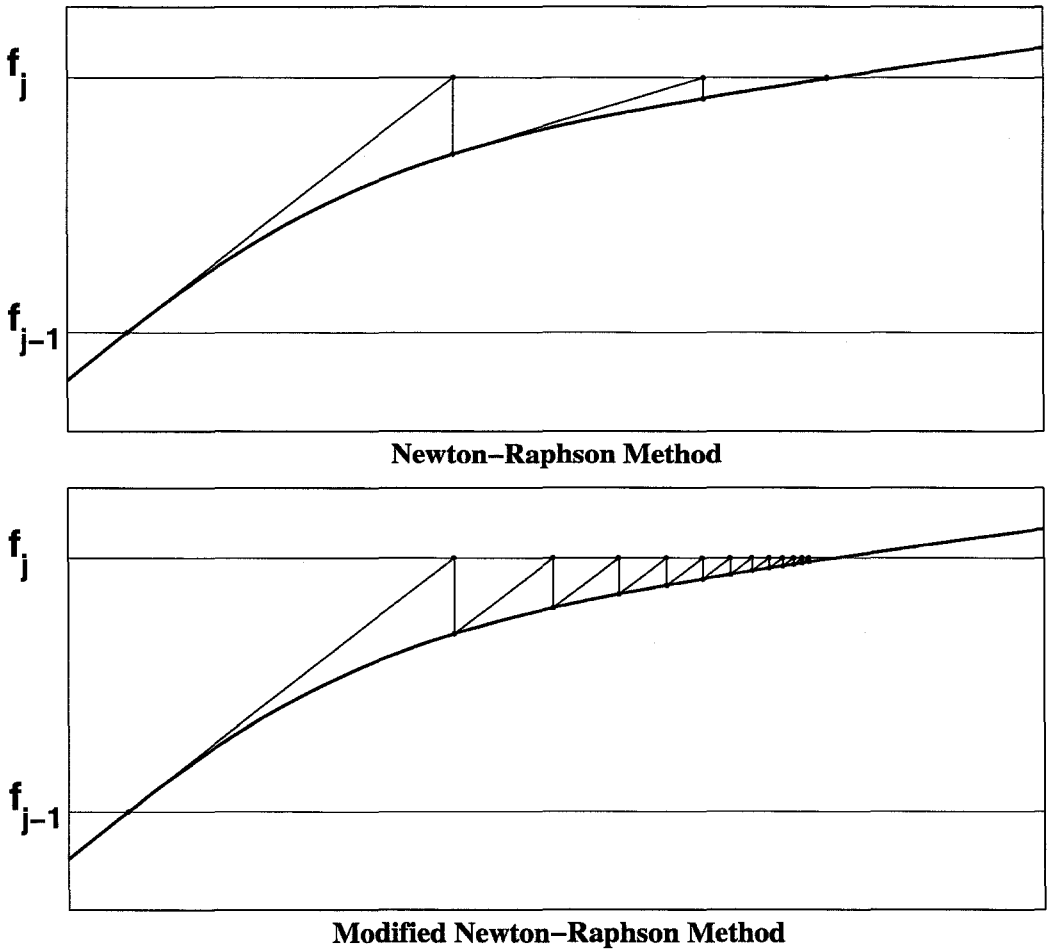

Figure 6.3 Convergence for a softening system.

all cases described. The numbering is shown for the stiffening system for clarity.

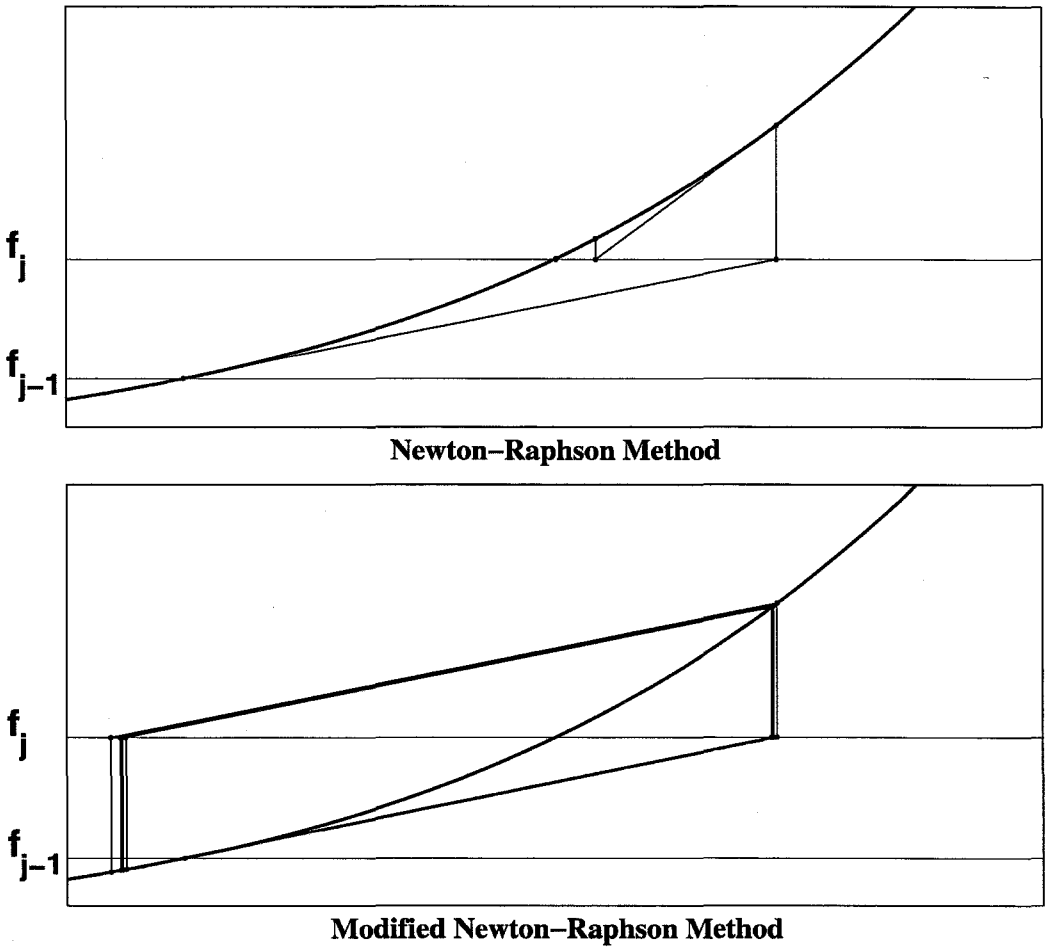

Figure 6.4 Convergence or nonconvergence for a stiffening system.

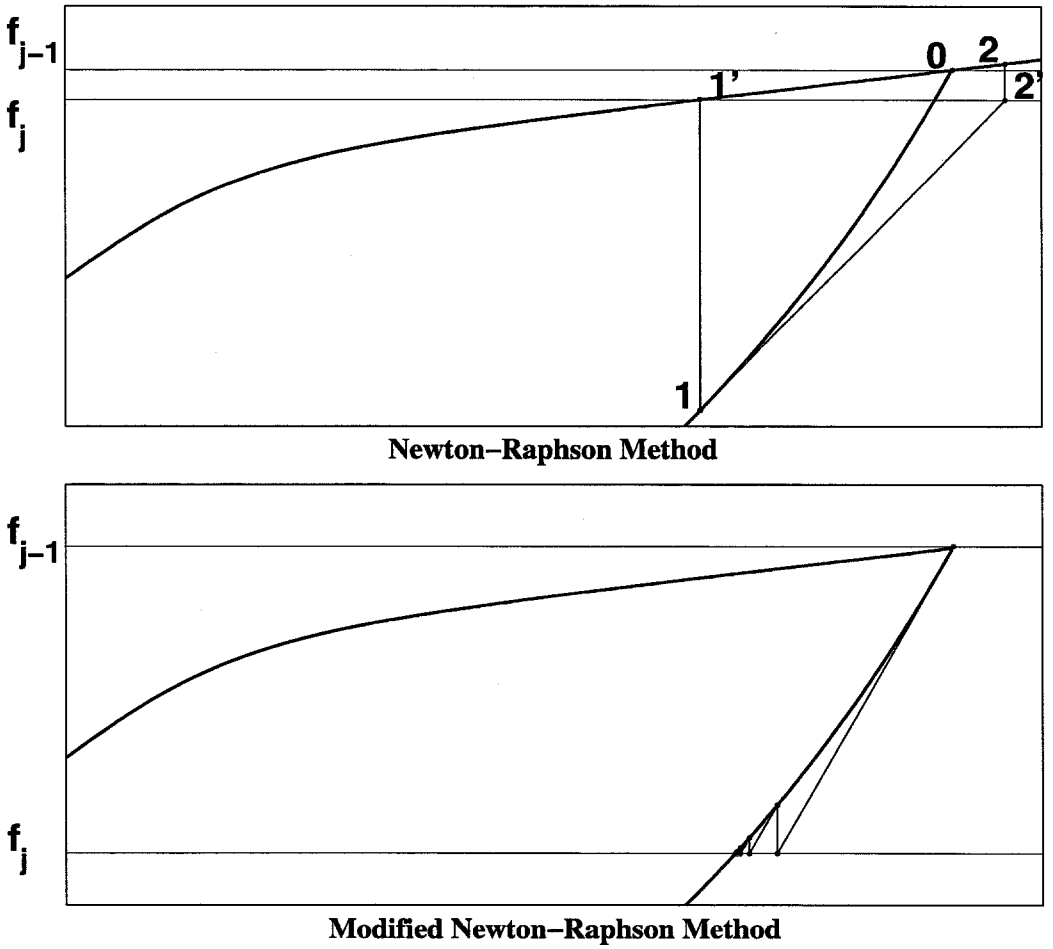

Figure 6.5 Convergence or nonconvergence for unloading.

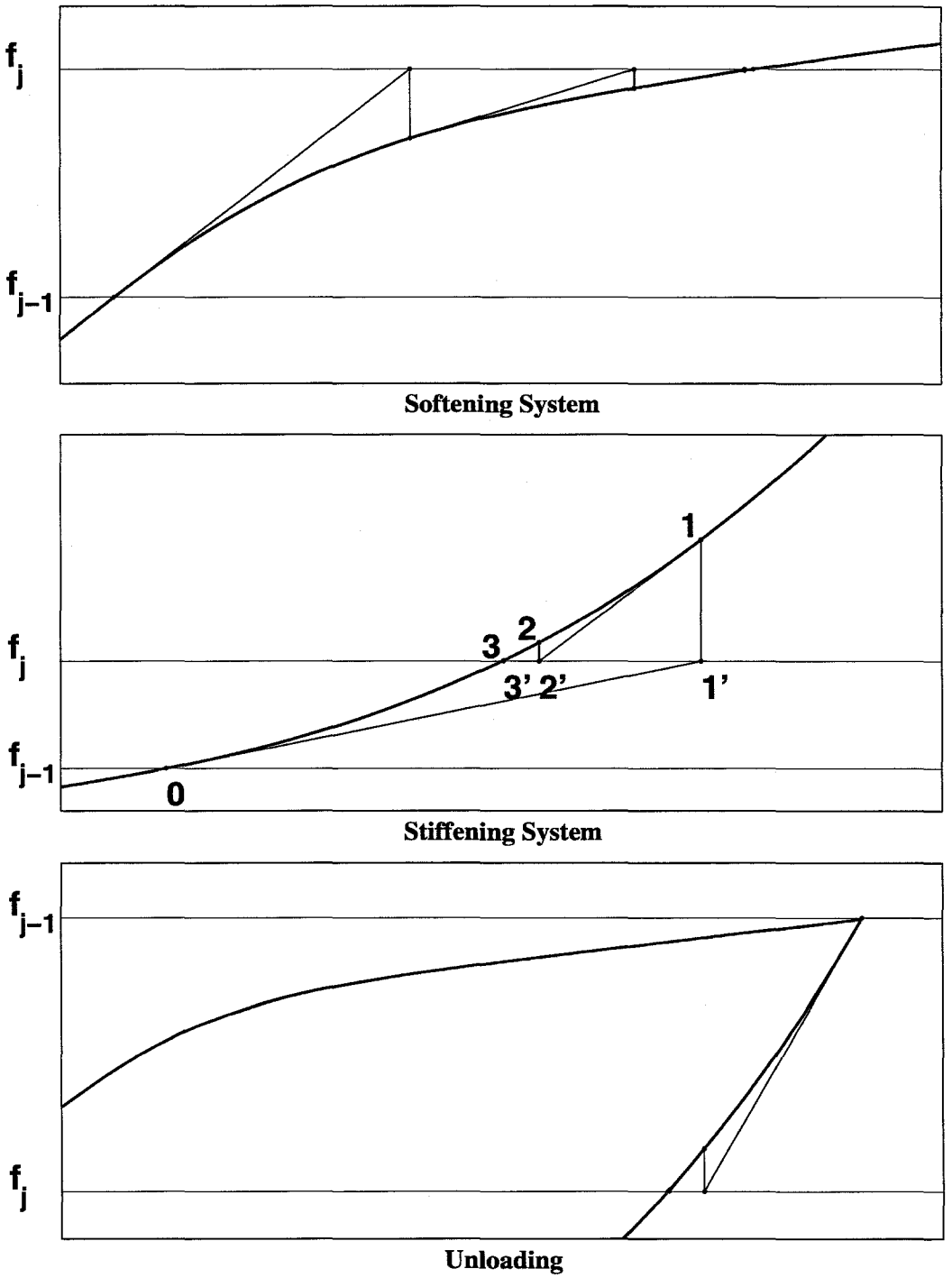

Figure 6.6 Convergence for the improved modified Newton-Raphson method.

6.7 Displacement Control Solution

In addition to time history analysis, a pushover analysis is often called for. Static lateral loads are applied to a structure in proportional increments until failure is achieved. If this type of analysis were performed using the static analysis solution of section 6.4, the loading would be monotonically increasing. For a ductile structure, there will typically be an ultimate load, followed by load relaxation. Once the ultimate load is reached, the following step will not converge since the structure is incapable of carrying that large a load. Hence, no information about the behavior of the structure on the descending branch of the load-deflection curve will be obtained.

Instead of a load based input, static pushover analysis can be run using a displacement control (DC) method of solution which allows unloading to occur. Basically, a load increment is applied to the structure and the displacements are calculated. If they do not match the control displacements, a scaled fraction of the load increment is applied iteratively to obtain the desired displacements. The method is complicated by trying to control (and hence, constrain) too many displacements, but works well for pushover analysis where only a single displacement needs to be controlled. The horizontal displacement at the roof of a structure is the standard parameter used for reporting the results of a pushover analysis, so it is an obvious choice for the sole control displacement.

The displacement control method is described in detail in Yang and Kuo (1994). The method finds the fraction of a predetermined lateral load, $\mathbf{f}_L$, corresponding to a specified displacement history of a particular degree of freedom. While this is a static analysis, the displacement history steps will be denoted by Δt to facilitate comparisons to other techniques. The history is displacement increments for each step, so the history for dof q will be denoted by

$$\Delta x_q(\Delta t), \Delta x_q(2\Delta t), \cdots, \Delta x_q(t), \Delta x_q(t+\Delta t). \tag{6.28}$$

Consider the solution for step $t+\Delta t$ with a converged solution for step t. At $t+\Delta t$,

the relationship between nonlinear restoring forces $\mathbf{p}(t+\Delta t)$ and applied load is

$$\mathbf{p}(t+\Delta t) = \mathbf{f}_S + \lambda(t+\Delta t)\mathbf{f}_L \tag{6.29}$$

where $\mathbf{f}_S$ is the static gravity loading applied before the displacement history and $\lambda(t+\Delta t)$ is the unknown factor of the predetermined lateral forces, $\mathbf{f}_L$, to be applied at this step. Since this is a nonlinear problem, the restoring forces and load factor need to be linearized as follows:

$$\mathbf{p}(t+\Delta t) = \mathbf{K}_T\boldsymbol{\Delta}\mathbf{x} + \mathbf{p}(t) \tag{6.30}$$

$$\lambda(t+\Delta t) = \lambda(t) + \Delta\lambda. \tag{6.31}$$

Rewriting equation (6.29) for an iterative solution, the first iteration in step $t+\Delta t$ is

$$\mathbf{K}_T^0\boldsymbol{\Delta}\mathbf{x}^1 = (\lambda^0(t+\Delta t) + \Delta\lambda^1)\mathbf{f}_L + \mathbf{f}_S - \mathbf{p}^0(t+\Delta t) \tag{6.32}$$

$$\text{where} \quad \mathbf{K}_T^0 = [\mathbf{K}_T(\mathbf{x}(t))] \tag{6.33}$$

$$\lambda^0(t+\Delta t) = \lambda(t) \tag{6.34}$$

$$\text{and} \quad \mathbf{p}^0(t+\Delta t) = \mathbf{p}(t). \tag{6.35}$$

Solve equation (6.32) for $\boldsymbol{\Delta}\mathbf{x}^1$ and $\Delta\lambda^1$ such that the control displacement is satisfied:

$$x_q^1(t+\Delta t) - x_q(t) = \Delta x_q(t+\Delta t). \tag{6.36}$$

The displacements and load factor are updated as follows:

$$\mathbf{x}^1(t+\Delta t) = \mathbf{x}(t) + \boldsymbol{\Delta}\mathbf{x}^1 \tag{6.37}$$

$$\lambda^1(t+\Delta t) = \lambda(t) + \Delta\lambda^1. \tag{6.38}$$

The stiffness matrix $\mathbf{K}_T^1$ and restoring forces $\mathbf{p}^1(t+\Delta t)$ are updated using these

updated displacements.

For the second iteration, solve

$$\mathbf{K}_T^1 \Delta \mathbf{x}^2 = (\lambda^1(t+\Delta t) + \Delta\lambda^2)\mathbf{f}_L + \mathbf{f}_S - \mathbf{p}^1(t+\Delta t) \tag{6.39}$$

for $\Delta\mathbf{x}^2$ and $\Delta\lambda^2$ such that the control displacement is satisfied:

$$x_q^2(t+\Delta t) - x_q^1(t+\Delta t) = 0. \tag{6.40}$$

Note that the right-hand side of equation (6.40) is zero. In the first iteration, the control displacement increment at dof q is satisfied by equation (6.36) and the corresponding factor $\Delta\lambda^1$ so that in future iterations the current displacement at the control dof should not change. This can be thought of as imposing the control displacement in the first iteration and iterating to reduce the residual forces until they are smaller than a specified tolerance as shown in figure 6.7. The solution keeps returning to the control displacement similar to the way in which the Newton-Raphson (NR) method (section 6.2) keeps returning to the applied load. The DC method can thus work past an ultimate load by reducing the applied load, allowing investigation of behavior in this region that the NR method cannot achieve.

The procedure for determining the load factor will now be discussed. Let the control displacement be represented as a function of iteration step k as follows:

$$\Delta x_q^k(t+\Delta t) = \begin{cases} \Delta x_q(t+\Delta t) & \text{if } k = 1, \\ 0, & \text{if } k \geq 2. \end{cases} \tag{6.41}$$

The equilibrium equations (6.32) for a general iteration step k are

$$\mathbf{K}_T^{k-1} \Delta \mathbf{x}^k = (\lambda^{k-1}(t+\Delta t) + \Delta\lambda^k)\mathbf{f}_L + \mathbf{f}_S - \mathbf{p}^{k-1}(t+\Delta t). \tag{6.42}$$

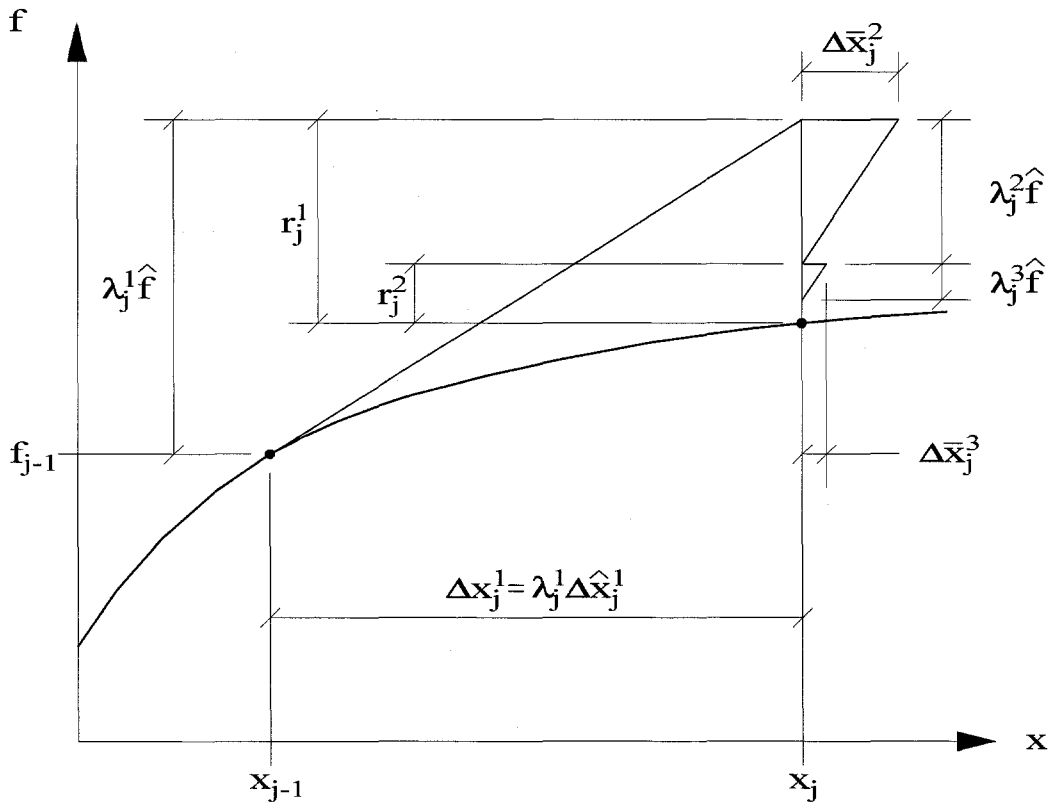

Figure 6.7 Displacement control iterative method.

Separating these equations to solve for two separate loadings gives

$$\mathbf{K}_T^{k-1}\Delta\hat{\mathbf{x}}^k = \mathbf{f}_L \tag{6.43}$$

$$\mathbf{K}_T^{k-1}\Delta\bar{\mathbf{x}}^k = (\lambda^{k-1}(t+\Delta t))\mathbf{f}_L + \mathbf{f}_S - \mathbf{p}^{k-1}(t+\Delta t). \tag{6.44}$$

The right-hand side of equation (6.44) consists of all loads applied through all prior steps and iterations within the current step minus the restoring forces calculated at the previous iteration. This is simply the residual stresses from the previous step, $\mathbf{r}^{k-1}(t+\Delta t)$, so the equation is rewritten as

$$\mathbf{K}_T^{k-1}\Delta\bar{\mathbf{x}}^k = \mathbf{r}^{k-1}(t+\Delta t). \tag{6.45}$$

Note that the solution to the original equation (6.42) can be obtained from the solutions of equations (6.43) and (6.45) by the following relationship:

$$\mathbf{\Delta x}^k = \Delta\lambda^k \mathbf{\Delta \hat{x}}^k + \mathbf{\Delta \bar{x}}^k. \tag{6.46}$$

Specifically, the displacement increments at the control dof q can be written

$$\Delta x_q^k = \Delta\lambda^k \Delta \hat{x}_q^k + \Delta \bar{x}_q^k. \tag{6.47}$$

This defines the factor $\Delta\lambda^k$

$$\Delta\lambda^k = \frac{\Delta x_q^k - \Delta \bar{x}_q^k}{\Delta \hat{x}_q^k}. \tag{6.48}$$

Now, equations (6.43) and (6.45) for the first iteration become

$$\mathbf{K}_T^0 \mathbf{\Delta \hat{x}}^1 = \mathbf{f}_L \tag{6.49}$$

$$\mathbf{K}_T^0 \mathbf{\Delta \bar{x}}^1 = \mathbf{r}^0(t + \Delta t). \tag{6.50}$$

For simpler implementation of the DC method, it will be assumed that the residual force $\mathbf{r}^0(t + \Delta t) \equiv \mathbf{0}$, which means that the previous step converged exactly. This is a fair assumption for small tolerances. Under this assumption, the displacement increment $\mathbf{\Delta \bar{x}}^1 = \mathbf{0}$ and thus at dof q the displacement increment $\Delta \bar{x}_q^1$ is also zero. The solution of equation (6.49) provides a displacement $\Delta \hat{x}_q^1$ which is scaled to the control displacement Δx_q^1 by equation (6.48) for iteration $k = 1$ as

$$\Delta\lambda^1 = \frac{\Delta x_q^1}{\Delta \hat{x}_q^1}. \tag{6.51}$$

For iterations $k \geq 2$, the control displacement Δx_q^k is zero, so equation (6.48) becomes

$$\Delta\lambda^k = -\frac{\Delta \bar{x}_q^k}{\Delta \hat{x}_q^k}. \tag{6.52}$$

The displacement control method can be summarized in the following steps. In the first iteration of a control step:

- Apply specified load $\mathbf{f}_L$ and solve for $\boldsymbol{\Delta}\hat{\mathbf{x}}^1$.
- Calculate $\Delta\lambda^1$ and adjust incremental and total displacements.

In the following iterations:

- Determine nodal forces and assemble in $\mathbf{p}^{k-1}(t+\Delta t)$. Determine $\mathbf{r}^{k-1}(t+\Delta t)$.
- Solve equation (6.43) for specified load $\mathbf{f}_L$.
- Solve equation (6.45) for residual forces $\mathbf{r}^{k-1}(t+\Delta t)$.
- Calculate $\Delta\lambda^k$ and adjust incremental and total displacements, $\boldsymbol{\Delta}\mathbf{x}^k$ and $\mathbf{x}^k(t+\Delta t)$.
- Repeat until residual forces are less than tolerances.

Note that the incremental displacement for iterations $k \geq 2$ will be equal to zero at the control degree of freedom q. Even though it is zero at this dof, the other dofs may experience an increment. Similarly, the total displacement at the control dof will remain the same throughout a step, but total displacements must be updated at all the other dofs for the non-zero incremental changes.

To implement this approach for pushover analysis, the vertical gravity loading is applied first. This is the load $\mathbf{f}_S$ from equation (6.29). Once the solution is obtained for the gravity loading, the displacement control increments may be imposed. The load used for the first iteration of the first step is chosen to be proportional to the UBC static lateral force load distribution. Any fraction of the load can be used for $\mathbf{f}_L$ since the factors $\Delta\lambda$ will adjust the load level to match the control displacement at the control degree of freedom.

The solution technique requires two solutions each iteration, but uses the same stiffness matrix for both (equations 6.43 and 6.45). For the first solution, Gaussian elimination with forward reduction and backward substitution is performed. For the second solution, only backward substitution is required, reducing the processing

time. In the IMNR method used in the program, elastic material properties are used in the tangent stiffness matrix for the first iteration and subsequent iterations use the tangent material properties to provide faster convergence. In the IMNR method, the objective is to minimize the number of iterations required to reach the displacement associated with a fixed load level. In the DC method, the objective is to minimize the number of iterations required to reach the load level associated with a fixed displacement. Because of the fixed displacements, the fraction of the predetermined lateral load (e.g., $\mathbf{f}_L = \mathbf{f}_{UBC}$ or $\mathbf{f}_L = 0.01\mathbf{f}_{UBC}$) will be immaterial since scaling will make the control steps the same independent of this value. The tangent stiffness will require fewer iterations, but using the elastic stiffness will help the solution converge when the displacements become large and localized instabilities have occurred.

Chapter 7

Analysis Preliminaries

Analysis of three buildings is performed in this work. Two of the buildings are actual buildings that were damaged in the Northridge earthquake. The SAC Joint Venture report included three investigations of a 17-story building (Paret and Sasaki (1995), Filippou (1995), and Anderson and Filippou (1995)), and one investigation of a 13-story building (Uang, Yu, Sadre, Bonowitz, and Youssef 1995). Further investigation of the 17-story building was performed at Cornell University (Chi (1996) and Chi, El-Tawil, Deierlein, and Abel (1996)). Two other articles have been written on the 13-story building in EERI Earthquake Spectra (Uang, Yu, Sadre, Bonowitz, Youssef, and Vinkler (1997) and Maison and Kasai (1997)). A third 10-story building was designed for the 1994 UBC to investigate three-dimensional effects of a realistic irregular building.

All three buildings investigated provide lateral resistance with steel moment resisting frames. The 13-story and 17-story buildings both suffered damage due to the Northridge Earthquake. They exhibited cracking at the girder-to-column connections while the members themselves remained essentially elastic. The inelastic behavior of these connections has been investigated with two-dimensional analysis packages in the works mentioned above, but there has been little investigation of the three-dimensional inelastic behavior of these structures. The formulation described in the previous chapters is used to determine if this type of damage can be accurately modeled. The importance of this for existing buildings is tremendous. The effect

of various retrofitting schemes could be accurately measured. If damage can be modeled closely, then scenarios for larger earthquake excitations can be predicted with more confidence. Since larger ground motions will cause greater nonlinearities, the results of such simulations should not be relied on with too much confidence.

The 17-story building had an accelerometer record the motions experienced at the penthouse floor level during the Northridge Earthquake. No record was made at the basement level. The 13-story building had accelerometers record motions at the basement, sixth and twelfth floors. Most of the connections in both buildings were inspected to determine the extent of damage.

The connection damage reports and time histories of floor motions provide information that is used to match the response with a computer model. Additional assumptions are required to produce models that can reasonably approximate the measured responses. The assumptions for shear building stiffness and foundation-soil springs were the same for each building. Cracking properties were adjusted to match damage levels and nonlinear story damping was adjusted to match roof displacement records.

7.1 Modeling Assumptions

Several assumptions used in modeling the three buildings are the same for all the buildings. Other assumptions unique to each building will be discussed in the individual building results chapters.

7.1.1 Material Properties

The buildings in this study used two types of steel, ASTM A36 carbon steel and ASTM A572 Grade 50 high-strength low-alloy steel. These materials have changed over the years, and mill reports show that actual strengths frequently exceed the nominal values. For the 17-story and 13-story buildings, the values suggested by Anderson and Filippou (1995) are used. These strengths are quite similar to those used by Chi (1996). The ultimate strength was set to 1.2 times these yield strengths.

	ASTM A36	ASTM A572 Gr 50
Nominal yield F_y (ksi)	36	50
Nominal tensile F_u (ksi)	58	65
Anderson and Filippou, F_y (ksi)	47	57
Anderson and Filippou, F_u (ksi)	56.4	68.4
SAC 1997b, Group 2, F_y (ksi)	58	—
SAC 1997b, Group 2, F_u (ksi)	65	—
SAC 1997b, Group 4, F_y (ksi)	—	57
SAC 1997b, Group 4, F_u (ksi)	—	65

Table 7.1 Steel material properties.

For the 10-story building, the nominal values are used as a check on the design. The 10-story building was designed to meet the 1994 UBC strong-column weak-beam criterion. By using the nominal design values for strength, the results of time history analyses will show whether this criterion holds up to stronger ground motions. If average strength values from the SAC Interim Guidelines (SAC 1997b) were used for the member size groups represented in the building, the columns would definitely yield before the beams. See table 7.1 for a summary of strength values. See the individual building chapters for the strength values used. The SAC (1997b) values are not used.

The concrete strength f'_c is known for the existing buildings, and those nominal values are used ($f'_c = 4000$ ksi for every building). The concrete is assumed to fail in tension at a rupture strength $f_r = 0.05f'_c$. The 13-story building does not have concrete included because it is assumed that it does not behave compositely with the steel beams.

7.1.2 Mass and Gravity Loading

Other investigators provided enough data to produce massing and gravity loading for the two existing buildings. Assumed values of massing were used to model the 10-story building. A small portion of live load was included in the mass for the 17-story building since other investigations included it. No live load was included

Building	17-Story		13-Story		10-Story	
	psf	Floor	psf	Floor	psf	Floor
Dead Load 1	87	1-4,PH,RF	82.5	PL-12	85	1-10
Dead Load 2	82	5-17	62.5	RF	65	RF
Self Weight	—	—	—	—	9.7	ALL
Live Load	8	ALL	—	—	10	1-10
LL as mass	8	ALL	—	—	10	1-10
Curtain Wall	15	ALL	20	ALL	20	ALL

Table 7.2 Gravity loading for the three buildings investigated.

as mass for the 13-story building to compare with other investigations. Live load was included as mass for the 10-story building. The same mass was used for the horizontal and vertical degrees of freedom. Assumed loading properties are shown in table 7.2.

7.1.3 Fiber Cracking Models

Several models for connection fracture are used in this work. As mentioned in section 2.5, ten discrete levels of fracture strain form a set from which a fiber group can have a value randomly selected. The fracture strain values are designated as multiples of the yield strain, ϵ_y. The models are as follows:

- Randomly sampled distribution based on Hall (1998).
- Randomly sampled normal distribution discretization based on Maison and Kasai (1997).
- Uniform (all ten strains the same in a set), representative of poor performance.
- Uniform, representative of better performance.

Note that all of these models are deterministic even though two of them are based on random sampling of probabilistic distributions.

The Hall random values of strain are used for the 17-story building. They were used previously in Hall and Carlson (1998) and are intended to represent conditions

in U.S. buildings built before the post-Northridge era of improved connections. Some correlation of the assumed fracture criteria to the Northridge earthquake experience is presented in Hall (1998). This distribution also includes fracture strains that are used at column bases and splices. The normal distribution random values are used for the 13-story building. The distribution is based on the Maison and Kasai (1997) investigation of the same building. The uniform values of poor performance were chosen to match levels of failure observed in the damaged buildings. These values are a best fit of the data achieved through iterative analyses of trial fracture strains.

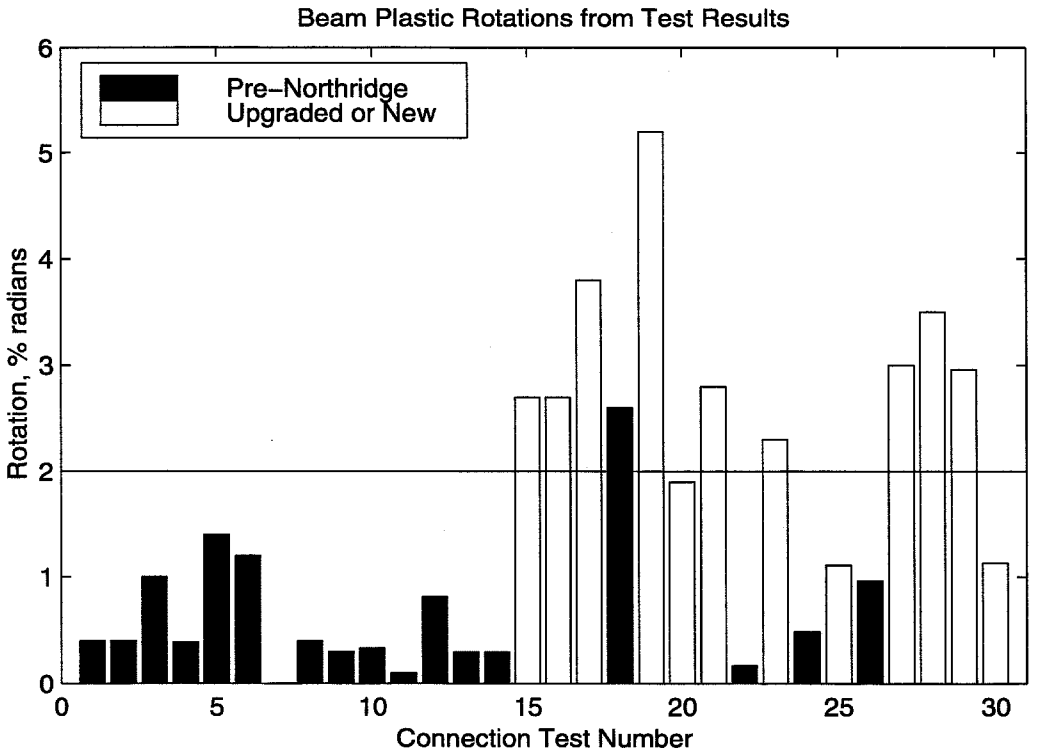

Figure 7.1 Connection test plastic rotations achieved.

The uniform values of better performance are based on an assumed plastic rotation of the girders of 0.02 radians. Designers and academics have both assumed that the members should be able to sustain a plastic rotation of 0.03 radians without fracture. This corresponds to overall high building ductility and performance. This level of ductility was the basis for code provisions allowing the greatest reduction

in design forces for steel moment frame buildings (forces divided by $R_w = 12$ in the 1994 UBC). Recent tests have shown that this level of ductility is not achieved with current typical specifications. In light of the low strain levels at failure of existing buildings and many experiments performed after the Northridge Earthquake (SAC 1997a), choosing 0.02 radians as an ultimate rotation before fracture would overestimate the fracture strength of typical "better" pre-Northridge connections. The results of 30 tests on steel moment frame connections are presented in figure 7.1. These tests are from SAC (1997a). All but one pre-Northridge connection failed well below the 0.02 radian level. The one that achieves greater than 0.02 radians of plastic rotation is a repaired connection. Some of the connections that do not reach the 0.02 radian level are also repaired connections.

The strain level of the flange fibers at a plastic rotation of 0.02 radians was determined by displacement-control time-history analyses of girder and column assemblies. A vertical load is placed at the free end of a girder with a length half of the moment-frame bay length. Each column and girder size combination was investigated for each building, but results were grouped for convenience. Girders were grouped by nominal depth to set one strain level for each group. Loading was performed both upward and downward to determine the difference in strain for the bottom and top flanges, respectively. Composite slab action is assumed for the 17-story building, but both top and bottom flanges use the higher strain levels corresponding to the bottom flange in tension. This direction of load engages the composite concrete in compression, so higher strain levels are achieved for the same rotation. It was desired to have at least the same fracture limit for the top flanges as for the bottom flanges. The strains were chosen so that all the members in each group met or exceeded the 0.02 radian plastic rotation limit. The plastic rotation was assumed to occur over the first two segments of the member. This corresponds to $0.18L$ (or 9.0% of a moment frame bay), where L is the length of the girder from the face of the column to the vertical load. The strain level in the fibers of these segments was recorded when the limiting plastic rotation was reached.

10% each	ϵ_f	ϵ_f	ϵ_f	ϵ_f	ϵ_f	ϵ_f	ϵ_f	ϵ_f	ϵ_f	ϵ_f
Uniform distribution, poor performance										
Top	10.	10.	10.	10.	10.	10.	10.	10.	10.	10.
Bottom	0.9	0.9	0.9	0.9	0.9	0.9	0.9	0.9	0.9	0.9
Hall distribution										
Column	10.	10.	10.	20.	20.	20.	40.	40.	80.	80.
Top	10.	10.	10.	20.	20.	20.	40.	40.	80.	80.
Bottom	0.9	0.9	2.0	2.0	5.0	5.0	15.	15.	40.	40.
13-Story, Maison distribution										
Top A	0.7	3.9	6.4	8.4	10.1	11.9	13.6	15.6	18.1	22.3
Bottom A	0.7	0.7	0.7	0.7	0.7	0.7	2.0	3.4	5.3	8.3
Top B	4.6	8.3	10.5	12.3	13.8	15.4	16.9	18.7	20.9	24.6
Bottom B	0.7	0.7	1.6	3.1	4.4	5.6	6.9	8.4	10.2	13.2
Top C	4.6	8.3	10.5	12.3	13.8	15.4	16.9	18.7	20.9	24.6
Bottom C	0.7	1.7	3.4	4.7	5.9	7.1	8.3	9.6	11.3	14.1
17-Story, 0.02 plastic rotation										
Top	30.	30.	30.	30.	30.	30.	30.	30.	30.	30.
Bottom	30.	30.	30.	30.	30.	30.	30.	30.	30.	30.
13-Story, 0.02 plastic rotation										
A	22.2	22.2	22.2	22.2	22.2	22.2	22.2	22.2	22.2	22.2
B	21.6	21.6	21.6	21.6	21.6	21.6	21.6	21.6	21.6	21.6

Table 7.3 Fracture strain probabilistic sets. Data for beams unless noted. Top and bottom refer to flange.

The same procedure outlined above was used to determine strain levels corresponding to the plastic rotation capacities from Maison and Kasai (1997).

Table 7.3 shows all the fracture strain distributions used in this work. The groups A, B, and C are explained in chapter 9.

7.1.4 Panel Zone Properties

Panel zone thickness is determined empirically from code values. The criterion used in this work to determine the panel zone thickness requires the panel zone strength (i.e., the yield moment) to be at least 0.8 times the plastic capacity of the connecting beams. The thickness is either the web thickness of the column t_w^c or the web thickness plus an additional doubler plate thickness calculated to satisfy

$$M_y^{PZ} = \tau_y d^c d^b t \geq 0.8 \sum M_p^b \tag{7.1}$$

where the sum of the plastic moments of the beams framing into the column is used.

7.1.5 Foundation Properties

The foundation stiffness and yield force are determined from an arbitrary empirical formulation. The stiffness for vertical deformation is based on the largest column gravity load in a building producing 2.54 cm (1 inch) of displacement. The yield force at which the stiffness reduces to 15% of the original stiffness is the larger of twice the largest column gravity load or half of the column load capacity. For upward displacements, the yield force and displacement are half the downward values. Horizontal properties are identical to downward properties.

7.1.6 Shear Building Stiffness

Real buildings have contributions to the lateral resistance from many sources that are not typically modeled in the design of the lateral force resisting system. Partition walls, masonry walls, rigid façade panels, stairwells and the stairs themselves can provide resistance to lateral motion of a building. Where simple framing is present

in the gravity system, incidental restraint in the connections may cause these elements to provide lateral restraint. These contributions are called the incidental contributions and they are modeled as story shear springs located throughout the plan of a building. The shear springs are lumped together as the shear building stiffness.

The stiffness determined from code-specified static earthquake analysis can be used to approximate the actual story stiffnesses, and a small percentage of this can be used for the shear building stiffness to be distributed to the shear springs of the model. The yield force can also be estimated from a static analysis. For example, one could choose values of story shears resulting from an analysis using a base shear equal to 1% of the building weight. This value is lower than required strengths of typical steel buildings. It is reasonable in that it assumes that the incidental contributions of stiffness will be apparent for smaller displacements, but will no longer provide resistance for larger displacements. Large displacements cause bolts on curtain walls and simple framing to loosen, lessening the stiffness of these incidental components, but still allowing some load to be carried. This combination of lost stiffness and sustained strength is idealized as an elastic-perfectly plastic shear spring.

For the buildings in this work, the shear building stiffness is determined from the loading distribution resulting from the 1994 UBC static lateral analysis. For example, assume the design base shear is $V = 0.030W$, where W is the total weight of the structure. The base shear is applied in a code-specified distribution through the height of the building. The minimum stiffness in any story will require that the given loading not cause that story to exceed $0.0025H_j$ drift, where H_j is the height of story j. The minimum UBC story stiffness is thus

$$K_{UBC,j} = \frac{F_j}{0.0025H_j} \tag{7.2}$$

where F_j is the cumulative load applied above the story level. The amount of additional stiffness due to incidental contributions can thus be applied as a fraction

of the UBC minimum story stiffnesses. In this work, a shear building stiffness of $0.10K_{UBC}$ is used. This seems like a reasonable level, and it also makes the models match measured building periods better. The shear building strength F_C^{SH} is limited to 1.0% of the story shears resulting from a code-specified distribution of load applied with a total base shear equal to the building weight, or $V/W = 1$.

7.1.7 Damping

In section 4.8 the use of non-classical nonlinear damping was mentioned. Nonlinear inter-story damping is assembled through the use of story dampers. The damping strength, F_C^D, and the cutoff velocity, v_C^D, are chosen to give a reasonable elastic damping in the lowest mode of the building. Figure 4.11 is repeated here to show these values. In each story, the damping strength is chosen to be equivalent to

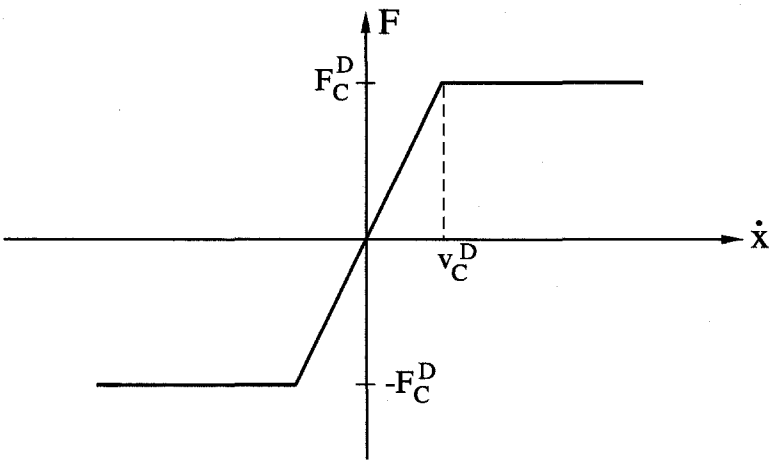

Figure 7.2 Nonlinear inter-story damping force.

the shear spring strength F_C^{SH} defined above. This model makes sense physically, since the damping force provided by non-structural elements will level off as those elements get damaged. To make the inter-story damping proportional to the shear

building stiffness, two coefficients a_2 and a_3 are chosen so that

$$a_2 = \mathrm{v}_C^D \tag{7.3}$$

$$\text{and} \quad a_3 = \frac{F_C^D}{F_C^{SH}}. \tag{7.4}$$

Since $F_C^D = F_C^{SH}$, $a_3 = 1.0$ for each story. The velocity required to achieve a desired level of damping in the first mode can be determined experimentally by applying a small impulse to the building and determining the damping from the observed decay in roof response. This will be the damping for low levels of excitation. For higher levels of excitation, the damping forces will level off when inter-story velocities exceed the cutoff velocity. The impulse loading is thus used to determine the factor $a_2 = \mathrm{v}_C^D$ in an iterative manner.

A half-period step impulse of low excitation is applied to the models. The decay in response at the roof is determined. The excitation is low enough to ensure elastic response. For stiffness-proportional damping, the damping in the first mode can be expressed as

$$\zeta = \frac{a_1 \omega}{2} \tag{7.5}$$

where a_1 is the coefficient defined in section 4.8 for which $\mathbf{C} = a_1\mathbf{K}$.

For shear building stiffness-proportional damping, $\mathbf{C} = (a_3/a_2)\mathbf{F}^{SH}$ must be satisfied for the unknown a_2 and $a_3 = 1$. Recalling the values of these parameters, this becomes $\mathbf{C}\mathbf{v}_C^D = \mathbf{F}_C^D$, which is true by definition. While the damping is actually proportional to the *strength* of the shear building, the yield shear and damping strengths are equivalent, so the damping "stiffness" is proportional to the shear building stiffness.

The rate of decay of the impulse loading determines the level of damping. For a

single degree of freedom system, the equation of motion without forcing is

$$m\ddot{x} + c\dot{x} + kx = 0 \tag{7.6}$$

$$\text{or} \quad \ddot{x} + 2\zeta\omega_n\dot{x} + \omega_n^2 x = 0 \tag{7.7}$$

where $2\zeta\omega_n = c/m$ and $\omega_n^2 = k/m$. The response can be determined from

$$x(t) = Ae^{-\zeta\omega_n t}\sin(\omega_d t + \phi) \tag{7.8}$$

where $\omega_d = \omega_n\sqrt{1-\zeta^2}$. The response at peak n occurs at time t. The response at the next peak $n+1$ occurs one damped period later, or at time $t+2\pi/\omega_d$. The ratio of displacements at these steps can be expressed as

$$\frac{x_n}{x_{n+1}} = \frac{e^{-\zeta\omega_n t}}{e^{-\zeta\omega_n t}e^{-\zeta\omega_n(2\pi/\omega_d)}} = e^{2\pi\frac{\zeta}{\sqrt{1-\zeta^2}}}. \tag{7.9}$$

This can be rewritten as

$$\ln\frac{x_n}{x_{n+1}} = 2\pi\frac{\zeta}{\sqrt{1-\zeta^2}}. \tag{7.10}$$

For small ζ, this can be solved for ζ as

$$\zeta \approx \frac{1}{2\pi}\ln\frac{x_n}{x_{n+1}}. \tag{7.11}$$

When the response to an impulse is recorded, the first five or six peaks are determined, and an average damping value is determined using equation (7.11).

If the approximated value of a_2 is not correct, the next approximation can be determined from the following relationship

$$\frac{\zeta_{desired}}{\zeta_{current}} \approx \frac{(a_3/a_2)_{desired}}{(a_3/a_2)_{current}} \tag{7.12}$$

$$\text{or} \quad (a_2)_{desired} \approx (a_2)_{current}\frac{\zeta_{current}}{\zeta_{desired}}. \tag{7.13}$$

Equation (7.13) is used to approximate the value of a_2 that should be used to achieve

the desired level of damping and another impulse loading is performed to confirm the resulting damping.

The damping for elastic response in the first mode is easily determined from the preceding approximations and trial impulses. Special consideration was made for the 10-story building that has two almost equivalent first modal frequencies. If the impulse is applied in a direction other than one of the principal directions, both modes are excited and the observed decay in one mode is actually accelerated by the other mode picking up energy from that mode. This can be seen in figure 7.3, which shows an impulse applied in the E-W direction of the 10-story building, and a second impulse applied along the axis of symmetry. The impulse in the E-W direction shows energy increasing at first in the N-S direction. Energy is transferred into both of the two lowest modes and decays in both modes. The impulse along the axis of symmetry decays without energy transferring to another mode. The damping for this building was calculated using the axis of symmetry impulse (figure 7.4).

Once the damping matrix is determined, the damping for higher modes or non-linear levels of response can be assessed. In classical damping, the damping matrix can be diagonalized by the same modal matrix transformation used to diagonalize the mass and stiffness matrices. Classical damping allows the equations of motion to be separated into modal equations. If the damping matrix is not constructed from a Caughey series, or nonlinear response is being modeled, then the damping should be considered non-classical (Chopra 1995). The damping used in this work is considered non-classical because it is not proportional to stiffness and mass as in a Caughey series and also because it is nonlinear. While the damping is proportional to the shear building stiffness, this stiffness in turn is not proportional to the global stiffness. Additionally, the stiffness will change for nonlinear response, so the damping will change. There will be off-diagonal terms that cause interaction between modes during damped response, similar to the coupling mentioned above for multiple equal modes in elastic response. This effect exists even for the first mode, but the impulses used produce energy predominantly in the first mode. Since

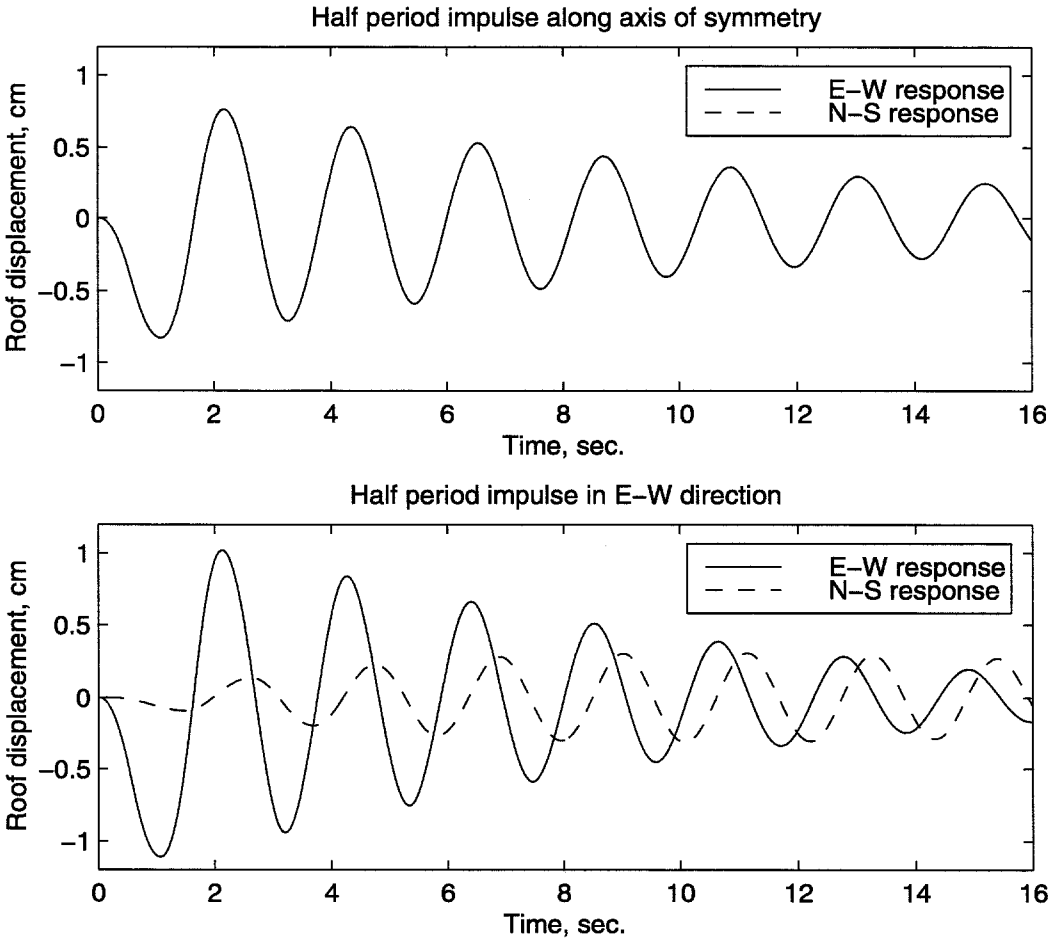

Figure 7.3 Effect of impulse direction.

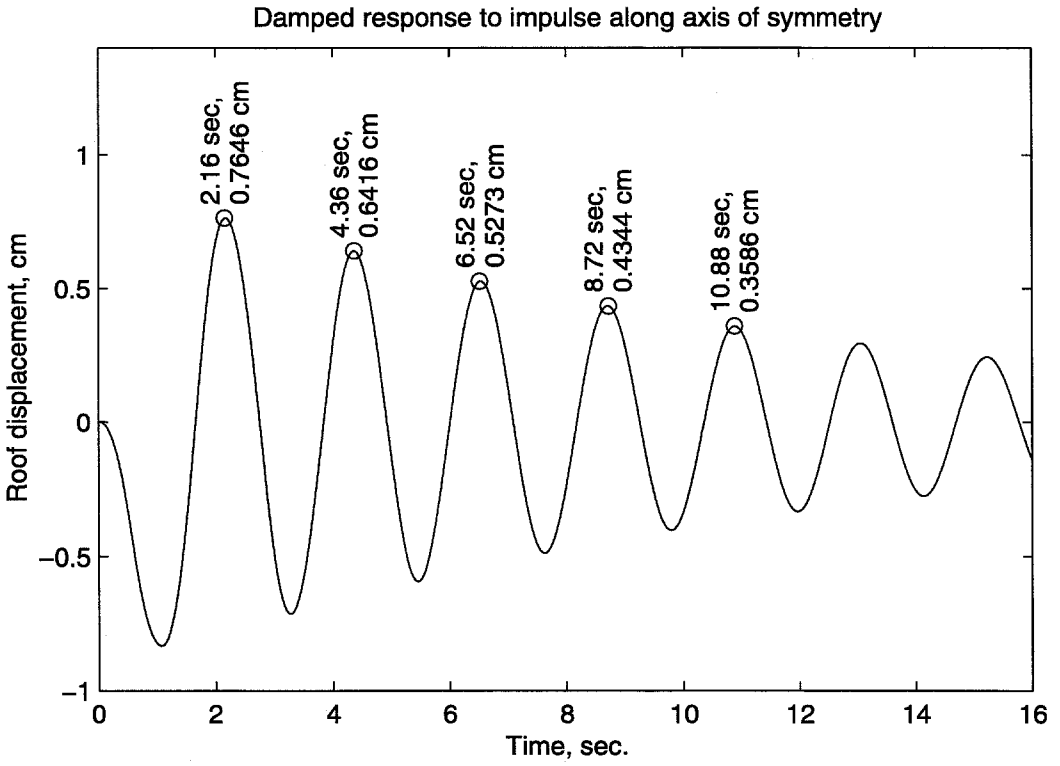

Figure 7.4 10-story impulse damped response.

stiffness proportional damping increases with frequency, any energy that leaks to higher modes from the first mode is quickly damped out.

The coupling of modes in a damped non-classical system makes it difficult to quantify the level of damping in each mode as a function of excitation level. Free vibrations initiated in one mode may end up in a lower mode even as the vibrations of the original mode are damped out. If instead the system is forced with a forcing function set to a specific modal frequency and shape, the level of damping for that mode can be estimated by determining the amplitude of the steady state response. Consider a single degree of freedom system as an analogy:

$$m\ddot{x} + c\dot{x} + kx = p_o \sin \omega t. \tag{7.14}$$

The steady state response is

$$x_P = \frac{p_o}{k} \frac{(1 - (\omega/\omega_n)^2) \sin \omega t - 2\zeta\omega/\omega_n \cos \omega t}{(1 - (\omega/\omega_n)^2)^2 + (2\zeta\omega/\omega_n)^2} \tag{7.15}$$

which can be simplified for the case desired where $\omega = \omega_n$ as

$$x_P = -\frac{p_o}{k} \frac{1}{2\zeta} \cos \omega_n t = -a_P \cos \omega_n t. \tag{7.16}$$

The value p_o/k is just the static displacement, a_S. Looking at the amplitude of response at steady state, a_P, and making the static displacement substitution, the damping ratio can be determined from

$$\zeta = \frac{a_S}{2a_P}. \tag{7.17}$$

While this is only true for the single degree of freedom system, the damping estimated for multiple dof systems using this approach is accurate because the energy is forced into the desired mode. With free response from a displaced shape equal to one mode, the energy can leak to other modes as it is damped out of the desired mode. While energy can leak from the forced mode, steady state response in that mode was observed for the analyses performed, so the amount of energy leaked to

other modes is small relative to the input energy in the desired mode.

A quantitative example of the nonlinear damping used in this work follows for the 13-story building. Note that this is just an example to show the behavior of the nonlinear damping. The shear building damping is estimated by approximating the 13-story building as a thirteen-degree of freedom spring and nonlinear damping system with 3% damping in the first mode for low levels of excitation. For this system, the tangent damping matrix is approximated as

$$\mathbf{C} = a_1\mathbf{K} + \frac{a_3}{a_2}\mathbf{K}^{SH}. \tag{7.18}$$

The overall target damping for the first mode is 3.0%, and the coefficient a_1 was chosen so that there would be 0.5% damping due to classical, stiffness proportional damping. Even for the most extreme nonlinear response, there will still be 0.5% damping in the first mode due to this elastic damping contribution.

The nonlinear equation of motion for the 13 dofs were solved using the same iterative scheme as formulated in the previous chapters. The forcing function is accelerations applied to the masses at the frequencies *and* shapes of each of the first five modes. The mode shapes are normalized so that the largest amplitude at any story is 1.0. The largest magnitude of the input accelerations range from 0.02g to 0.50g. In this way, the damping as a function of both frequency and amplitude can be approximated. The results are compared to Rayleigh damping, where coefficients were chosen to achieve 3.0% damping in both the first and second modes. The results are shown in figure 7.5 for acceleration amplitudes of 0.02g, 0.05g, 0.10g, 0.15g, 0.25g, and 0.50g, where g is gravitational acceleration. The lines are drawn solely to keep track of the damping across modes for constant levels of excitation. The minimum nonlinear damping (Min NL Damping) will be the 0.05% linear stiffness-proportional damping that was included in the total damping.

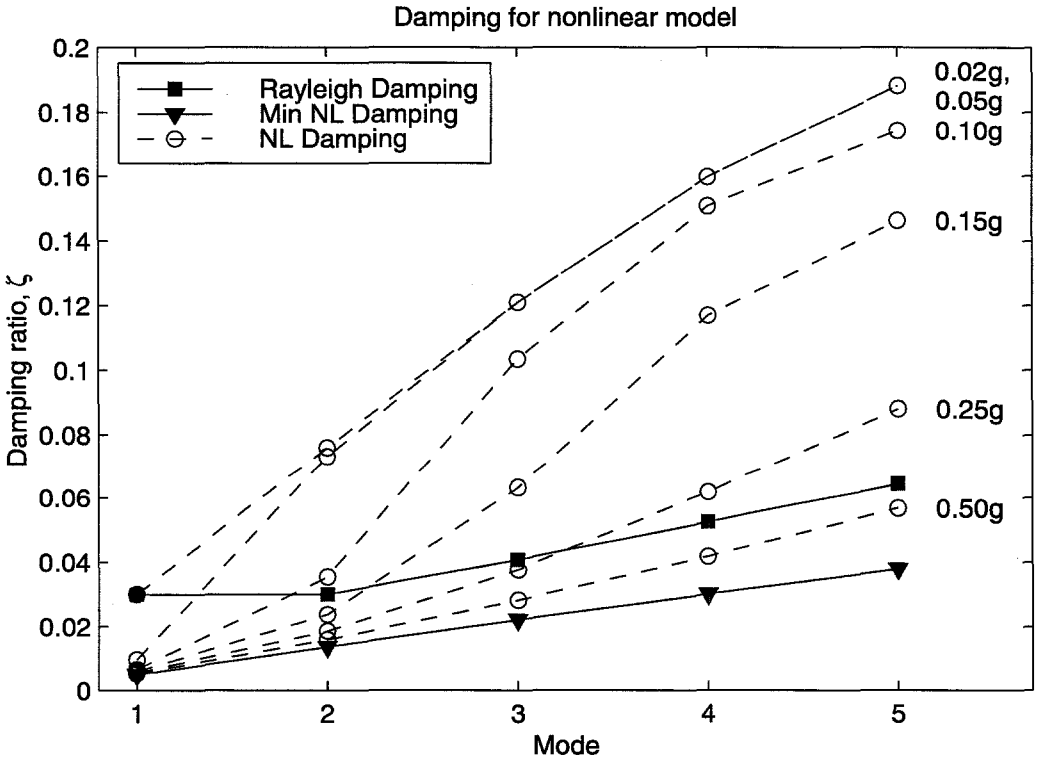

Figure 7.5 Nonlinear damping for several modes and excitation levels.

7.2 Comparison of Buildings

While all three buildings are steel moment resisting frames, various attributes differ so that together they produce a range of steel buildings that are a representative sample of a West-Coast city building stock. Several features of the buildings and the computer models that represent them are presented in table 7.4. See the individual building chapters for determination of code values for building periods.

One discrepancy between code values and analytical and measured response is the period of the building. In Goel and Chopra (1997), the authors determined appropriate bounds for building period as a function of height by analyzing the vibration properties of 42 existing steel moment resisting frame buildings. The bounds they came up with are plotted in figure 7.6. For comparison, the 1994 UBC upper and lower bounds are plotted. The periods of the three buildings analyzed

Building	17-Story	13-Story	10-Story
Design Properties			
Height	260.3'	188.5'	154'
Plan Dimensions	155'x117'	160'x160'	180'x180'
Design Code	1982 UBC	1973 UBC	1994 UBC
T_{UBC} Code Approx	1.7 sec	1.30 sec	1.53 sec
T_{UBC} Code Analysis	4.6 sec (EW) 4.1 sec (NS)	—	1.99 sec (1.3Ta)
V/W (UBC static)	0.0268W, 0.0304W	0.0307W	0.0316W
V/W (ultimate)	0.097W, 0.090W	0.1325W	0.1997W
Drift Limit	0.0033	no limit	0.0025
Δ_{roof} (static)	11.4", 11.4"	4.8"	3.0"
Average Drift	0.0036, 0.0036	0.0021	0.0016
Column Range	W14x311– W14x730	W14x176– W14x500	W14x193– W14x550
Column Nominal F_y	50 ksi	36 ksi	50 ksi
Girder Range	W30x90– W36x300	W27x84– W36x230	W24x76– W36x280
Girder Nominal F_y	36 ksi	36 ksi	36 ksi
Weight of Frames	7.9 psf (2468^k)	7.0 psf (2497^k)	9.7 psf (2500^k)
Model Properties			
Column Assumed F_y	57 ksi	47 ksi	50 ksi
Girder Assumed F_y	47 ksi	47 ksi	36 ksi
NDOF	995	1330	1485
NHB	63	102	142
T_1 (Lateral)	4.88 sec	2.90 sec	2.16 sec
T_2 (Lateral)	4.52 sec	2.90 sec	2.06 sec
T_3 (Torsion)	2.90 sec	2.03 sec	1.52 sec
Damping (Mode 1)	3.0%	5.0%	3.0%
K^{SH}/K_{UBC}	10%	10%	10%

Table 7.4 Comparison of the three buildings investigated.

are also plotted. Note that the 17-story building exceeds the newer limits by a substantial margin. This building was built at a time when code specified base shears were low and drift limits were high which could explain its lower stiffness and higher period.

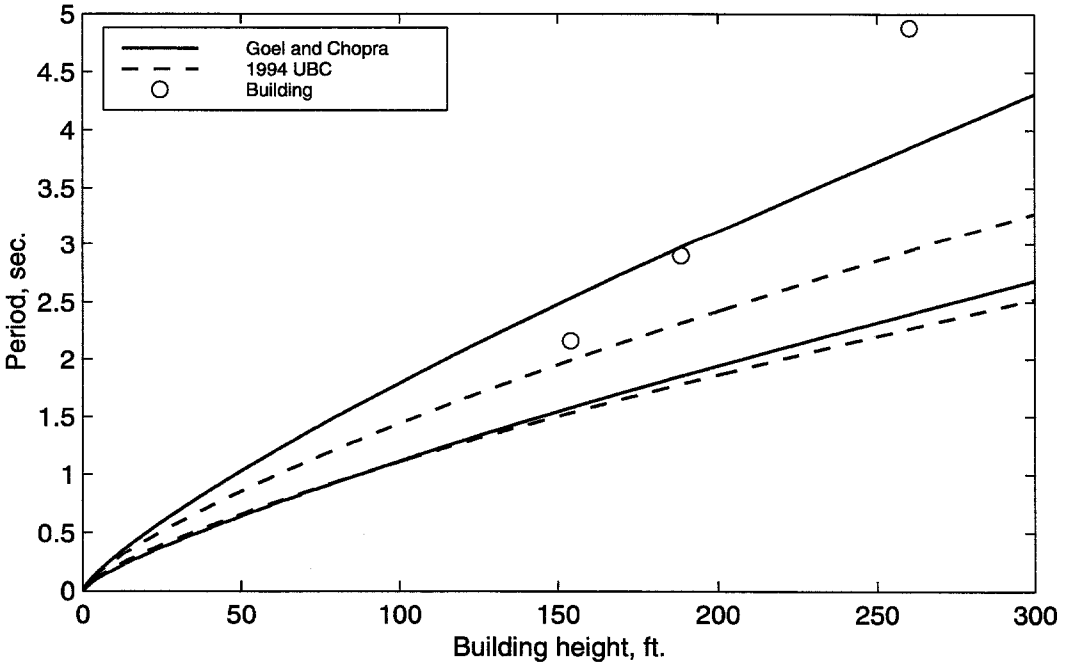

Figure 7.6 Period calculations.

7.3 Earthquake Records

Ground motions from the Northridge earthquake representative of the two building sites are used. Other ground motions are used to determine building performance under more severe ground shaking. The ground motions used in this work are described in detail in Appendix A.

Chapter 8

17-Story Building

Many steel moment frame buildings exhibited brittle fracture in their beam-to-column connections during the Northridge earthquake, including a 17-story building in Woodland Hills. The lateral system of this building consists of two double-bay moment frames in each direction, none of which are connected to each other. See figure 8.1, and note that because of the voluminous nature of the output in the following chapters, most of the tables and all of the figures are at the ends of each chapter. The north frame is not on the perimeter of the building, creating an unsymmetrical lateral system. This structure can be analyzed using the techniques and finite elements developed in this work. Corner columns are not needed for this building.

The investigated building was instrumented at its penthouse floor to record three orthogonal motions. Unfortunately, instrumentation did not exist at the basement. The building was fully inspected, providing data on all the beam-to-column connections that exhibited fracture.

This building has been investigated extensively with 2D and 3D elastic analysis and 2D inelastic analysis (Paret and Sasaki 1995), (Filippou 1995), (Anderson and Filippou 1995), (Chi 1996) and (Chi, El-Tawil, Deierlein, and Abel 1996). None of these investigations included fracture and only the Chi investigations used limited three-dimensional inelastic analysis.

The 17-story building is a good candidate for investigation because of the pre-

ceding reasons. The following issues are examined:

- Ability of bare steel frame model to predict damage location through standard code static analyses.
- Torsional response of unsymmetrical structure.
- Difference between 2D and 3D response.
- Ability of 3D nonlinear model to reproduce fracture pattern observed.
- Ability of 3D nonlinear model to reproduce measured roof response.
- Comparison of different models.
- Effect of larger ground motions.

8.1 Building Description

Geometry and Materials

The building has 17 stories plus a penthouse and one basement level. The plan dimensions of the building are 47.24 m by 35.66 m (155 ft by 117 ft), and a typical story height is 396 cm (156 in). The first story height is 620 cm (244 in). Frame columns range in size from W14x311 to W14x730, and girders from W30x90 to W36x300 (figures 8.2–8.3). The columns are A572 Grade 50 and the girders are A36 steel. The columns have a yield strength of 393 kN/mm^2 (57 ksi) and an ultimate strength of 472 kN/mm^2 (68.4 ksi) and the beams have yield 324 kN/mm^2 (47 ksi) and ultimate 389 kN/mm^2 (56.4 ksi). Smaller members are used for the gravity system. The beams are all composite with metal deck and lightweight concrete on top. See Paret and Sasaki (1995) or Chi (1996) for a complete description of the building.

Mass

The seismic mass and center of gravity are calculated for each floor based on the framing plans and assumed properties from Chi (1996). The weight of the building

was estimated to be 133 MN (29960 k). The weight of the steel moment frames is 11.0 MN (2468 k).

Basement Stiffness

Concrete basement walls are assumed to exist in each direction, and the steel columns extend to the base of the walls. The stiffness of the walls is modeled by shear springs assuming the walls at the perimeter of the building are 30.48 cm (12 in) thick. The lateral framing for the penthouse story is unknown in the north-south direction, so story stiffness approximately 20% of the east-west direction frame stiffness is used. The roof mass is lumped at the penthouse level to avoid problems associated with this lack of framing information.

Story Stiffness

The gravity framing, partitions, and nonstructural walls are assumed to be capable of some lateral resistance provided by shear springs. The total lateral force capacity in each direction provided by the shear springs is set to 1% of the story shear forces produced by the seismic design loads computed for $V/W = 1$. The sum of shear spring stiffnesses in a story is set to 10% of the minimum UBC story stiffness (see section 7.1.6). This corresponds to spring yielding at a story drift of H/120.

Foundation

The foundation has an elastic stiffness of 2.626 MN/cm (1500 k/in) horizontally and vertically and a secondary stiffness of 0.394 MN/cm (225 k/in). Yield strengths are 26.9 MN (6000 k) horizontally and downward and 13.34 MN (3000 k) upward. See section 7.1.5 for formulation of these values.

Damping

Inter-story damping is capped at a force level corresponding to 0.01W, reached at an inter-story velocity of 20.32 cm/sec (8.0 in/sec). This corresponds to 2.5% of critical damping in the linear range of the fundamental mode. The total damping is 3.0%, with an additional 0.5% of critical damping provided by linear stiffness proportional damping.

Fracture Models

End segments of girders representing the welds to the columns are allowed to fracture. The post-earthquake inspection of the building found fractures only at the bottom-flange welds of the girders. Since the girders did not exhibit any local buckling or other signs of plastification, a strain level below yield is reasonable for the bottom flange. The top flange is most likely a better weld since continuous passes can be made, and so a higher fracture strain there is justified. Three different fracture models are used for this building. In the poor performance model, the bottom fibers have a uniform fracture strain of $0.9\epsilon_y$ and the top fibers $10.0\epsilon_y$. In the random fracture level model (Hall), the fracture strain levels are randomly chosen from the distribution shown in table 7.3. The lowest strain levels in this distribution are $0.9\epsilon_y$ and $10.0\epsilon_y$ for the bottom and top fibers, respectively. This model also allows fractures at column bases and splices. A third model for fracture levels assumes that the individual girders can achieve 0.02 radians of plastic rotation before failure. See section 7.1.3 and table 7.3 for more on these distributions.

Modal properties

The model possesses natural periods of vibration of 4.88 seconds in the east-west direction, 4.52 north-south, and 2.90 seconds in torsion. See figures 8.4–8.9 for depictions of the first six natural modes.

8.2 Building Design

The lateral system was designed using the 1982 Uniform Building Code (ICBO 1982). Without any site-specific data, the design would be as follows. The parameters used for design are:

- Ductile Moment-Resisting Space Frame (MRF)
- $W = DL$ (dead load only)
- $I = 1.0$

- $Z = 1$
- $T = 0.1N$, N = number of stories, T not substantiated and system is 100% MRF
- $T = 2\pi\sqrt{\frac{\sum w_i \delta_i^2}{g \sum f_i \delta_i}}$, to substantiate T. This version is used here.
- $K = 0.67$
- $C = \frac{1}{15\sqrt{T}} \leq 0.12$
- $T_S = 2.5$ (If T properly established and greater than 2.5 sec)
- $S = 1.2 + 0.6(\frac{T}{T_S}) - 0.3(\frac{T}{T_S})^2 \geq 1.0$ for $T/T_S > 1.0$
- $CS \leq 0.14$
- $V = ZIKCSW$, base shear
- $F_t = 0.07TV \leq 0.25V$ for $T > 0.7$ sec
- $F_x = \frac{(V - F_t) w_x h_x}{\sum w_i h_i}$, force at floor x
- Drift limit = 0.005 based on $1/K$ times the required loading (or drift limit = 0.0033 using required loading)

The resulting values are:

- $T = 4.6$ sec, E-W direction
- $T = 4.1$ sec, N-S direction
- $S = 1.288$, E-W direction
- $S = 1.377$, N-S direction
- $C = 0.0311$, E-W direction
- $C = 0.0329$, N-S direction
- $V = 0.0268W$, E-W direction

- $V = 0.0304W$, N-S direction

Note that the equivalent static force V in the E-W direction is less than the lower limit of $V = 0.03W$ for the 1994 UBC (ICBO 1994).

A model with rigid foundations and solely the lateral system steel columns and girders providing resistance is used here for the design check. This is consistent with standard practice. A static analysis using the UBC forces above produces penthouse displacements of 29.0 cm (11.4 in) E-W and 29.0 cm (11.4 in) N-S. Considering that the N-S stiffness is approximately 25% more than the E-W stiffness ($(4.6/4.1)^2$), it is apparent that the design used the different code minimum forces in each direction to produce equal drifts.

The resulting demand capacity ratios (DCR's) for the structure from the static analysis can be seen in figures 8.10 and 8.11 for the E-W and N-S directions, respectively. The definition of DCR used here is member moment divided by the product of member nominal design strength and section modulus (DCR = M/FySx). Thus, it is the ratio of moment observed to yield moment. In these figures, the circle diameter is proportional to the DCR and the circle is drawn offset from the member end to distinguish multiple members framing into a joint. As a comparison, the DCR ratios for the Oxnard time history are given using the actual values of member material strengths and the inelastic model without fracture (figure 8.12). See section 8.4 for an explanation of the inelastic model.

8.3 Pushover Analysis

Five different models were subjected to a pushover analysis using the 1982 UBC static force distribution. A displacement control analysis (section 6.7) was performed to establish the behavior beyond yielding. All analyses include P-Δ effects and nonlinear material properties. Since all of the observed damage was in the N-S direction, the pushover results for this direction only are shown in figure 8.13. A base model that seems closest to a standard analysis model is included. The effect of various changes to this model can be seen, including the final fully nonlinear inelastic

model. The base model includes the bare frame (BF) and foundation (FN). The next model includes the inter-story stiffness (SB). The next model includes composite action of the girders (CM), and the final model includes the poor performance fracture strains (FR). The base model has an ultimate strength of 0.090W at a penthouse displacement of 147 cm (58 in) and the inelastic model without fracture (BF+FN+SB+CM) has an ultimate strength of 0.100W at 145 cm (57 in). The fully inelastic model including fracture has an ultimate strength of 0.058W at 63.5 cm (25 in). Notice that the composite action has little effect on the total stiffness or strength of the building.

8.4 Simulations

Several time-history analyses of various types are performed to seek answers to the issues mentioned at the beginning of the chapter. In each instance, a time step of 0.02 seconds and a total duration of 40 seconds for each record are used. Two ground motions which were recorded close to the building, Oxnard Blvd. #4 (Darragh, Cao, Graizer, Shakal, and Huang 1994) and Canoga (USC 1994), are used to represent the ground motion at the site. A third record, Sylmar County Hospital Parking Lot (Darragh, Cao, Cramer, Huang, and Shakal 1994), is used to represent the stronger ground motions of the Northridge earthquake. Additional records from larger earthquakes are also used. Table 8.1 shows the analyses performed for each ground motion, where the symbol • represents one analysis. More information on the ground motions appears in Appendix A.

The analysis types include two-dimensional analysis, elastic analysis, inelastic analysis witout fracture, and inelastic analysis with connection fracture. The two-dimensional analysis includes the entire structure, but motion is constrained to the north-south (N-S) direction, which is the direction with all of the observed damage. For the elastic analysis, yield strengths for steel, concrete and damping were set to large values not reached in the analyses. All of the analyses include the foundation elements, composite action, P-Δ effects, and the shear building.

Ground Motion	Poor Performance Fracture	2D Poor Performance Fracture	Random Fracture	$0.02\theta_{plastic}$ Fracture	Inelastic	Elastic
Oxnard	• •	•	•	•	•	•
Sylmar	•	•	•	•	•	
E.P. G05	•	•	•	•	•	
Tabas	•	•	•	•	•	
Takatori	•	•	•	•	•	
Canoga	•					
Rinaldi	•					
E.P. D05	•					
E.P. J06	•					
Kobe JMA	•					
Kobe NGT	•					

Table 8.1 Time history analyses performed for 17-story building model.

8.4.1 Figure Descriptions

Time Histories

The relative-to-ground penthouse displacement response is tracked for the duration of the analyses, 40 seconds. The response at the center of mass (master node location) and at two corner locations is calculated so that torsional effects can be observed (figure 8.14). Note that the same scale is used wherever possible to compare the response levels for the different ground motions.

- See figures 8.15–8.25 for the relative penthouse histories of the poor performance fracture model for all 11 ground motions.
- See figures 8.26–8.30 for the penthouse histories of the inelastic model.

To get a better understanding of the global building behavior, relative histories of every other floor are shown together for the N-S component of motion only. The N-S direction is the stronger ground motion in every case, so the N-S response alone will suffice to present this behavior.

- See figures 8.31–8.35 for the building histories of the poor performance fracture model.

- See figures 8.36–8.40 for the building histories of the inelastic model.

The Oxnard and Canoga ground motions were both recorded close to the 17-story building. The measured penthouse response is compared to the calculated response for the poor performance fracture model, which most closely represents the actual behavior of the building. The Oxnard record was run a second time with the E-W motion reversed since the E-W response seemed reversed. Compare the initial pulse directions for velocity and displacement for the E-W component of the Canoga and Oxnard records in Appendix A figures A.1 and A.2. The Oxnard motion seems reversed.

- See figure 8.41 for the comparison of absolute penthouse displacements resulting from the Oxnard motion and the measured response.

- See figure 8.42 for the comparison of absolute penthouse displacements resulting from the Oxnard record with reversed E-W motion and the measured response.

- See figure 8.43 for the comparison of absolute penthouse displacements resulting from the Canoga motion and the measured response.

The Oxnard motion is used for all three buildings studied in this work to investigate the differences in models used for each building. The difference in penthouse response for the various fracture models is minimal, so only the poor performance fracture model is presented.

- See figure 8.44 for the comparison of relative penthouse displacements resulting from the Oxnard motion due to various models.

Inter-Story Drifts

The maximum drifts in the N-S direction for each story are used as a damage indicator. Note that the same scale is used for all plots. Values that exceed these

limits are plotted on the right-hand side of the figure. The analysis will stop if a drift of 20% is reached, and the maximum drift prior to halting the analysis will be reported. Drifts above this arbitrary limit are not reported.

- See figures 8.45–8.49 for the maximum story drifts for each record. Each figure represents the response to a different model: poor performance fracture, 2D poor performance fracture, random fracture, $\theta_{plastic} = 0.02$ fracture, and inelastic.

- See figure 8.50 for the maximum story drifts for each model resulting from the Oxnard record.

Fractures

The member end fractures are plotted for each simulation that uses a fracture model. Top and bottom girder-flange to column-flange connection fractures are distinguished separately. For comparison, the actual fractures discovered after the Northridge earthquake are also plotted.

- See figures 8.51–8.62 for the fractures resulting from the poor performance fracture model for all 11 ground motions and the reversed Oxnard motion.

- See figures 8.63–8.67 for the fractures resulting from the 2D poor performance fracture model.

- See figures 8.68–8.72 for the fractures resulting from the Hall random fracture model.

- See figures 8.73–8.77 for the fractures resulting from the $\theta_{plastic} = 0.02$ fracture model.

Plastic Rotations

The member end plastic rotations are plotted for each simulation using an inelastic model with no fracture. In these figures, the circle diameter is proportional to the plastic rotation and the circle is drawn offset from the member end to distinguish multiple members framing into a joint.

- See figures 8.78–8.82 for the plastic rotations resulting from the inelastic model.

8.4.2 Table Descriptions

Damage Indicators for Model Type

Several indicators of damage include the maximum drift, the penthouse relative displacement Δ_P, the base shear and the number of fractures. These have been summarized for each model comparing across ground motions. The ratio of base shear V to building weight W is used in these tables. For the inelastic model, the number of member end plastic rotations greater than 0.01 radians is used in place of the number of fractures.

- See tables 8.2–8.6 for the damage indicators for each model.

Damage Indicators for Ground Motion

The same data is presented for each ground motion comparing across model type. The Elysian Park G05 and Tabas records are not presented in this form since collapse occurred for all fracture models.

- See tables 8.7–8.9 for the damage indicators for each ground motion.

8.5 Discussion

Static Analysis

The demand capacity ratios (DCRs) reported in figure 8.10 for E-W loading show that the lower six stories have beams with ratios exceeding 0.50. The largest ratio is 0.61, and the code permits the ratio to be as large as 1.0. The upper stories and columns have lower DCR values. The interior bay frame, Frame 4, has higher demand than the exterior frame, Frame 3, partly because the interior frame has smaller member sizes to account for mechanical services passing underneath.

The DCRs for the N-S loading (figure 8.11) are relatively uniform above the third floor. The extra bay in the lowest levels reduces the load resisted by the other

two bays. The uniform nature of the DCRs for both static lateral force applications provides no indication of concentrated yielding or fracture.

The DCRs for the Oxnard record (figure 8.12) are all below 1.0. This indicates that the building remains elastic for this time history. Higher mode effects can be seen in the N-S direction from the increased ratios in some of the upper levels.

Pushover Analysis

The pushover analysis (figure 8.13) indicates that the building can achieve a base shear to building weight (V/W) ratio of 0.100, or roughly three times larger than the UBC code value used for design with allowable stresses. Even with fracture included in the model, the building can achieve a V/W ratio twice the code value.

Relative Penthouse Displacements, Poor Performance Fracture Model

These time history plots (figures 8.15–8.19) show the response level of the penthouse in lateral directions, and by plotting three locations on the penthouse level, they indicate torsional response by differences in the histories. Eleven ground motions are used as input on the 17-story building model with poor performance fracture strains.

The Oxnard ground motion shows little torsional response. Note that the same displacement scale is used for all the ground motions, shifted where necessary. The Sylmar record indicates torsional response induced after a large N-S pulse. The Elysian Park G05 and Tabas records show that the building is unable to recover from pulses much larger than the Sylmar pulse. Torsion is observed after a smaller pulse at 5 sec in the Tabas record. The Kobe Takatori record indicates torsional response. The response is highly damped toward the end of the record due to severe cracking (see figure 8.56). Each crack formation releases stored strain energy, reducing the response.

Other ground motions used just for this building have similar response amplitudes (figures 8.20–8.25) to the five ground motions just described. The Canoga response is similar to the Oxnard response. The Rinaldi response is similar to the Sylmar response. The Elysian Park D05 response is similar to the G05 response.

The J06 ground motion is smaller than the D05 and G05 ground motions, so the building survives the pulse with a huge permanent offset. The Kobe JMA and NGT responses are similar to the Northridge Oxnard and Canoga responses. Due to these similarities, the first five ground motions are chosen to be representative of the 11 total ground motions considered.

Relative Penthouse Displacements, Inelastic Model

The five representative ground motions are used to determine the response of the inelastic model (figures 8.26–8.30). The inelastic model responses to the Oxnard and Sylmar records are similar to the responses for the fracture model. The inelastic response differs from the fracture response for the G05, Tabas and Takatori records, however. For the G05 record, the building narrowly avoids collapse, but there is a large permanent offset at the penthouse of about 170 cm (or 2% drift over the building height). The Tabas response is similar to the G05 response for the fracture model, but the inelastic model exhibits more torsional response. The Takatori inelastic response exhibits less damping than the fracture response.

Relative Floor Displacements, Poor Performance Fracture Model

In these figures (8.31–8.35), every other floor response is shown using the fracture model. The Oxnard response appears to be mostly elastic as there is no permanent offset observed in any level, even though some fractures occur (figure 8.51). The Sylmar record shows four histories producing the bulk of the permanent offset. This corresponds to the eight lowest stories since every other floor is depicted. Relatively little permanent offset is seen in the remaining stories. Keeping the scale the same for all histories limits the information provided by the G05 response. What can be seen is that the lower stories exhibit severe deformation resulting in collapse. The Tabas record shows higher frequency energy reaching all levels of the building. Other responses are smoothed toward the upper levels due to inherent stiffness proportional damping that tends to reduce higher mode effects. The extent to which this high frequency energy travels through the building indicates that there must be a lot more energy in this frequency range for the Tabas ground motion relative to the

other ground motions. A similar higher-frequency response can also be seen for the Takatori record. Examining the response spectra for these two records, they are seen to have a lot more energy in the high frequency range relative to other records. See Appendix A for these records. Collapse is apparent from the Tabas response, and six stories produce most of the offset in the Takatori response.

Relative Floor Displacements, Inelastic Model

In these figures (8.36–8.40), building response for the inelastic model is shown. As for the fracture model, the Oxnard response appears to be mostly elastic since no permanent offsets are observed. The Sylmar response shows permanent offset more uniformly distributed over all the stories than for the fracture model. In the middle stories, the histories are very close together in the figure, but they spread out again for upper stories. This indicates localized inelastic behavior at the lower and upper stories with more elastic response in the middle stories. The G05 response indicates that roughly ten stories share the inelastic deformation. The Tabas response shows that four stories produce most of the permanent offset. This is interesting because even the pure-pulse ground motion G05 produces more spreading of inelastic behavior than this record does. The Takatori response is similar to the Sylmar response in that localized inelastic offsets can be seen in lower and upper stories without offset in middle stories. This compares well with observed cracking in the fracture model (see figure 8.56).

Time History Comparisons

The response of the poor performance fracture model to the Oxnard ground motion is compared to the measured roof response in figure 8.41. Absolute displacements are used since there is a measured roof record, but no basement record. The N-S response is a very good match. This is the direction with all of the observed damage. Even the period elongation with increasing damage is observed. The extent of period elongation in the measured record has been investigated by Anderson and Filippou (1995).

The E-W response does not match very well. This response is essentially elastic

since there were no observed fractures or plastification of members in this direction. The Oxnard record is ground motion from a site close to the building site, so it cannot exactly represent the ground motions experienced by the building. Note in particular how the E-W response is 180° out of phase with the measured response at the beginning of the record. Because of this mirrored response, the Oxnard record was used a second time, but with the E-W motion reversed. Figure 8.42 shows the response to this modified record. There is a close match in both directions for 8 seconds. Beyond that, the N-S is a good match to 30 seconds, but damping and energy transfer to the E-W dominated modes reduce the response dramatically thereafter.

The response of the fracture model to the Canoga ground motion is compared to the measured roof response in figure 8.43. The Canoga ground motion was also recorded close to the building site. The calculated penthouse response does not match the measured response very well. The level of response is off, and period elongation is not observed in the N-S direction even though a similar level of fracture damage was observed.

Three different model responses to the Oxnard record are compared in figure 8.44. Comparing the elastic and inelastic responses shows little difference. This indicates that the Oxnard ground motion produces very little inelastic response. Comparing the inelastic and poor performance fracture model responses, a much larger level of damping is observed in the damaged N-S direction. The damping of strain energy release of opening and closing the cracks outweighs the hysteretic damping provided by inelastic strain excursions. Note that both the inelastic and fracture models produce period elongation due to stiffness degradation. It is more pronounced in the fracture model.

Drift Ratios

Different drift ratio comparisons are shown in figures 8.45–8.50. The five representative ground motions are used, and drifts for the poor performance fracture, 2D poor performance fracture, random fracture, $\theta_P = 0.02$ and inelastic models are

given. For the Oxnard record, drifts for the various models are compared in figure 8.50.

For the poor performance and random fracture models, there is an observed increase in drift for stories 12–15 for the Sylmar and Takatori records, and to a lesser extent for the Oxnard record. This is consistent with some of the observations made about the time histories. For the Tabas and G05 records, the drift is concentrated in stories 3–9. Similar results were obtained for the 2D poor performance fracture model. When fractures occur in the lower stories, energy is released and input energy has a harder time reaching the upper levels.

The $\theta_P = 0.02$ and inelastic models show a more uniform distribution of drift relative to the other fracture models. The Sylmar and Takatori records still show increased drift in the upper stories. The Tabas and G05 records still have concentrated drifts in stories 3–7 for the inelastic model, but the G05 shows a greater spread of drift that cannot be achieved with the fracture models, all of which cause collapse.

The Oxnard comparison shows very little difference between the models demonstrating that the response to this record is mostly elastic. The exception to this is the increased drift in stories 12–14 for the poor performance fracture model. This can be explained by the fractures in floors 12–14 (figure 8.51).

Fracture Distributions

The calculated fractures for the various fracture models are depicted in figures 8.51–8.73. All 11 ground motions are used for the poor performance fracture model and the 5 representative ground motions are used for all other models.

For the poor performance fracture model, member connections will fail at the same strain level, regardless of where the member is located. Because the static analysis DCR values indicate uniform member strength, the resulting fracture patterns should be proportional to the distribution of energy in the building for a given ground motion.

The Oxnard fractures show the effect of higher modes. The concentration of

damage in the upper levels indicates that strong levels of input energy at higher mode frequencies occurred. Due to the uniform strength of the building, this local damage must be attributed to higher mode response, not locally weaker members. This record also exhibits 3D effects — more damage is calculated in Frame 2 (east frame) than in Frame 1 (west frame), contrary to the observed damage. This distribution would not result from a 2D analysis, calling attention to the importance of 3D analysis. Additionally, the calculated fracture results match the amount and vertical distribution of the observed damage fairly well. While not being able to predict which connections will fracture, the simulation indicates the general nature of the observed damage.

The Oxnard record was used a second time with the E-W ground motion reversed. The resulting fracture distribution shows a reversal of the damage level in the two N-S frames. Frame 1 now has more damage than Frame 2 just like the observed damage. The eccentricity of the north frame causes torsional response that can account for this reversal. By negating the E-W ground motion, the torsional and N-S lateral responses are compounded in the western Frame 1 and reduced in the eastern Frame 2 instead of the other way around. In addition to matching the observed fracture pattern better, the calculated time histories match the recorded motions better, too. Other investigators recognized the importance of a 3D model, and even modeled the stairs and CMU walls surrounding the stairs which sustained significant damage (Chi, El-Tawil, Deierlein, and Abel 1996). This damage implied they were carrying part of the lateral load. Chi, El-Tawil, Deierlein, and Abel (1996) conclude "the plan eccentricity caused by the inset north frame is not of much consequence" and "that torsion caused by the stair/wall assembly probably had a significant amplifying effect on the deformations." Without modeling the stairwell, the simulations of this work show that the torsional response can be fully attributed to the eccentric frame. Regardless of the cause of the torsional behavior, the importance of the effect of ground motion direction on the three-dimensional response is clearly affirmed by the Oxnard simulations.

The Sylmar response shows the effect of higher modes, also. In Frame 2, there

are two distinct zones of fracturing even though the member strengths are uniform throughout. For N-S motion, note that most of the fractures are on the bottom of the west end of beams. This is consistent with northward displacement. Looking at the Sylmar ground motion (figure A.3) and the Sylmar relative penthouse response (figure 8.16), a southward ground motion pulse causes the bottom of the building to move south before the top of the building can react. This increases the relative *northern* motion of the penthouse. Note that even though there is a significant number of bottom-connection fractures, there are no top-connection fractures.

The G05 response shows local damage in the lower stories. Frames 1 and 2 show that upper level connection fractures occurred during southward motion. The fractures observed in equal distribution at both ends of beams in the lower stories indicate a load reversal. The lower levels were damaged as the base of the building moved south, corresponding to relative northward motion. After the ground pulse switches to northward motion, the penthouse starts moving south. The ground motions are so severe in this record that the penthouse still moves south after the pulse is over and the building is unable to recover due to overstraining of its already compromised members. Local inelastic behavior in the lower stories is consistent with such ground motion pulses.

The Tabas response shows apparent load reversals and some higher mode damage.

The Takatori response has energy in both directions as indicated by the damage to all four frames. There is pronounced localized behavior, including the most severe E-W damage of all 11 records used. Looking at the response spectrum for this record (figure A.10), the E-W pseudo acceleration (PSA) is greater than 2g at the second lateral mode periods (T= 1.39 sec and 1.33 sec from figures 8.7 and 8.8). The second lateral modes are unfortunately close to peaks in the Takatori E-W response spectrum.

The Canoga response is a very good match to the observed level and distribution of damage. As with the Oxnard record, this ground motion is from a site close to the building site. The Canoga record and Oxnard record with reversed E-W motion

produce extremely similar fracture patterns even though the penthouse displacement response for these motions is dissimilar (figures 8.42 and 8.43).

The remaining records produce fracture patterns similar to those of the five representative records.

The fracture patterns resulting from the 2D poor performance fracture model capture behaviors such as higher mode effects, reversals and pulse-induced directional damage. Torsional behavior is lost, though. The Oxnard record has equal levels of damage in Frames 1 and 2 instead of being localized in one frame. The Tabas record appears to have lost higher mode effects (compare figures 8.55 and 8.66). This may mean that these effects are due to high energy levels at the fundamental torsional mode period as opposed to the second lateral mode periods. Higher mode effects are observed in the Oxnard, Sylmar and Takatori responses.

The random fracture model has more strong connections than the poor performance fracture model, so less damage is produced. It is uncertain from the limited runs as to whether a random model can introduce torsional response that would not be there otherwise. The importance of such a model is that it can closely match the observed random field conditions and help predict the level of response expected from such a realistic distribution. A suite of random runs, as performed in Hall (1997), would be required to understand the extent to which global behavior could be modified by various random distributions of low fracture limits.

The $\theta_P = 0.02$ fracture model is the strongest of the fracture models. The Oxnard and Sylmar responses show that no members reach 0.02 radians of plastic rotation. The G05 record does have some members fracture, without a reversal of damaging motion observed. The directivity of the fractures indicates that they occur during southward motion. This means they occur as the ground moves northward relative to the top of the building, which is still recovering from the southward half of the displacement pulse. The Tabas record has similar localized lower level fractures, but they occur during northward motion. The Takatori response has little damage, but it is from higher mode energy.

Plastic-Rotation Distributions

The plastic rotations at member ends for the inelastic model are presented in figures 8.78–8.82.

The Oxnard response is essentially elastic, so no sizable plastic rotations are observed in member ends. The Sylmar response is almost elastic with some higher mode damage indicated by the plastic rotations. The G05 response shows that code writers clearly did not envision this ground motion. Many plastic rotations greater than 0.03 radians occur. Note that this model is stronger than the fracture models, which allows inelastic behavior to spread over more stories than fracture models allow. Fractures act as fuses, limiting energy that can pass to higher stories. The Tabas response has very local damage with higher rotations than the spread G05 response. The response spectrum for the Tabas ground motion (figure A.11) indicates the highest PSA for the first several modes is in the first mode N-S which corroborates the local damage. The Takatori record indicates response in several modes.

Damage Indicator Summary Tables

The eleven ground motion responses for the poor performance fracture model are summarized in table 8.2. Drift, penthouse displacement, base shear, and number of fractures are the damage indicators tabulated. Three of the ground motions cause collapse (D05, G05 and Tabas), so damage indicators for those records are unreliable for quantitative comparisons.

The data in this table shows that several basic indicators are not good predictors of damage. The base shear to building weight ratio, V/W, is used to determine the force level of static analysis in many codes. Comparing the Sylmar and Takatori records, Sylmar has $V/W = 0.104$ and Takatori has $V/W = 0.108$, but the building ended up with 108 fractures due to Sylmar and 241 fractures due to Takatori. Local damage can limit the base shear and create large drifts imminent to collapse. Higher mode effects are not associated with the largest base shear in general. The base shear will be higher when all masses in the building are accelerating in the same direction (first mode) rather than when masses move in opposite directions (higher modes).

The maximum penthouse displacement is also an unreliable predictor of damage levels. The Oxnard, JMA and NGT records have maximum penthouse displacements of 53, 54 and 52 cm, respectively. These records produced 22, 102 and 53 connection fractures, respectively. Higher-mode loading reversals can cause a great deal of damage while limiting the largest penthouse displacement.

The maximum story drift can be a better indicator of damage. It indicates damage by looking at data from one story instead of the whole building. Most damage resulting from the simulations is localized, whether in an upper or lower story. While the maximum story drift cannot indicate the spread of inelastic behavior, it is a good indicator of the level of inelastic behavior incurred. This indicator can be unreliable, however. The Canoga record has a maximum drift of 0.0124 and 26 fractures and the JMA record has 0.0123 drift and 102 fractures. This type of difference could arise from a small pulse causing local behavior and producing a small number of fractures versus a sustained periodic record increasing drift and damage throughout a building.

The number of fractures *is* the damage, so it should not really be called an indicator. However, just counting the fractures cannot describe the entire inelastic behavior. A small number of fractures could result from a moderate earthquake, or from a strong earthquake pulse that localizes the damage in a few lower stories. This type of damage could be incipient to collapse, whereas the former could be retrofitted and survive future earthquakes unscathed. Having a large number of fractures does not fully describe the underlying behavior, either. They could result from an earthquake having energy at several modes of a building, spreading damage throughout the structure. This type of inelastic redistribution may sometimes be easily retrofitted, posing no danger, as opposed to a building hit with a pulse having fewer fractures but larger permanent lateral offsets.

The other models also have damage indicators summarized in tables 8.3 to 8.6. The G05 and Tabas records cause collapse for every model type that includes some level of fracture. The only model that does not collapse due to these ground motions is the inelastic model. While the building does not collapse in this instance, an

unsettling drift level and penthouse displacement can be observed.

The inadequacy of the base shear ratio to indicate damage can also be seen for the inelastic runs. The Sylmar record has $V/W = 0.141$ and G05 has $V/W = 0.142$, whereas the corresponding maximum drifts are 0.0213 and 0.0613. The corresponding number of member ends exceeding 0.01 radians of plastic rotations are 4 and 103, respectively.

The pushover results can be compared to the poor performance fracture and inelastic model tables. The pushover analysis with fracture resulted in an ultimate base shear ratio of $V/W = 0.058$ at 63.5 cm. Note that all eleven records produce V/W ratios that exceed this value. Since input energy occurs over a range of frequencies, a higher base shear can be achieved than for the pushover analysis that assumes a uniformly distributed loading. Some of the maximum penthouse displacements are less than 63.5 cm with associated high V/W ratios. This can be attributed to higher modes attracting load without all stories moving in the same direction, allowing the building to appear stiffer than the pushover predicts.

The pushover analysis for the inelastic model resulted in an ultimate base shear ratio of $V/W = 0.100$ at 145 cm. Except for the Oxnard record, this was exceeded for every ground motion. The same reasons can be stated as for the fracture model case. The lower Oxnard base shear corroborates its apparent elastic behavior.

The same information in the tables mentioned above is tabulated for each ground motion to compare the responses of different models (tables 8.7–8.9). A couple of interesting trends are worth noting. The Oxnard record has essentially constant maximum penthouse response and base shear ratios across all models (the 2D penthouse displacement is lower because this is a three-dimensional quantity and the east-west component is lost in this model). The maximum story drift increases monotonically with increasing damage. The Sylmar record, on the other hand, exhibits reduced drift with increasing damage. The main reason for this difference is that the Oxnard response is primarily elastic, whereas the Sylmar response is inelastic. For the Oxnard response, small amounts of damage tend to increase the observed drift. Once a building has reached a certain level of inelastic response,

a large amount of energy can be damped out by hysteretic behavior and energy release. The fracturing of connections in the Sylmar model provides a large amount of damping through the release of stored strain energy. This damping cannot be matched by the inelastic model which thus attracts more load and results in higher drifts. The poor performance fracture model has a maximum drift of 0.0190 and a base shear ratio of 0.104 while the inelastic model has a maximum drift of 0.0213 and a base shear ratio of 0.141.

8.6 Figures

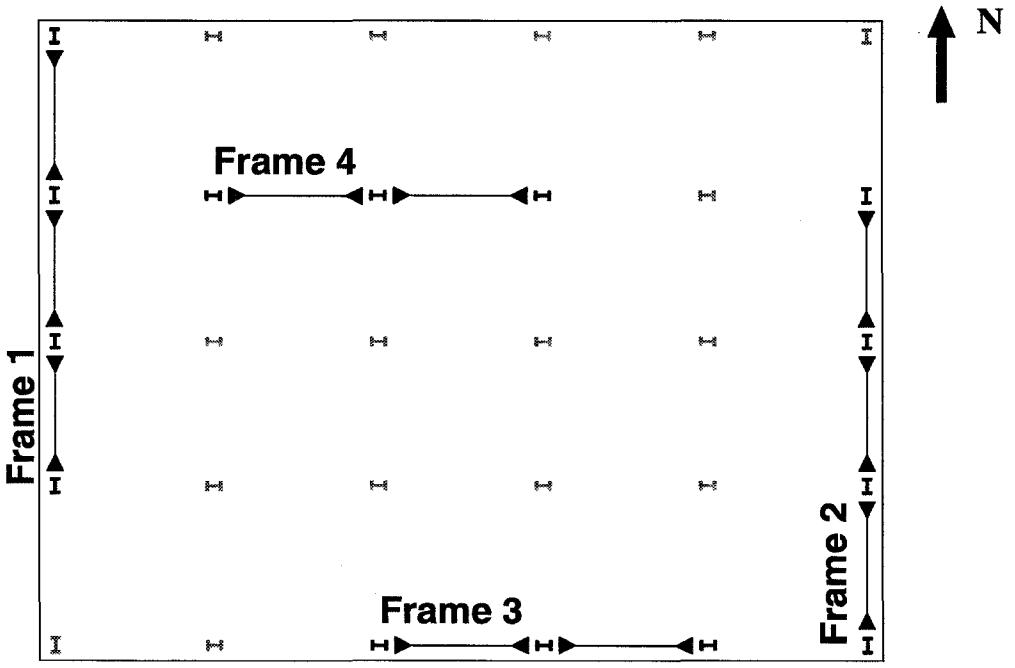

Figure 8.1 Plan of building with frame labels.

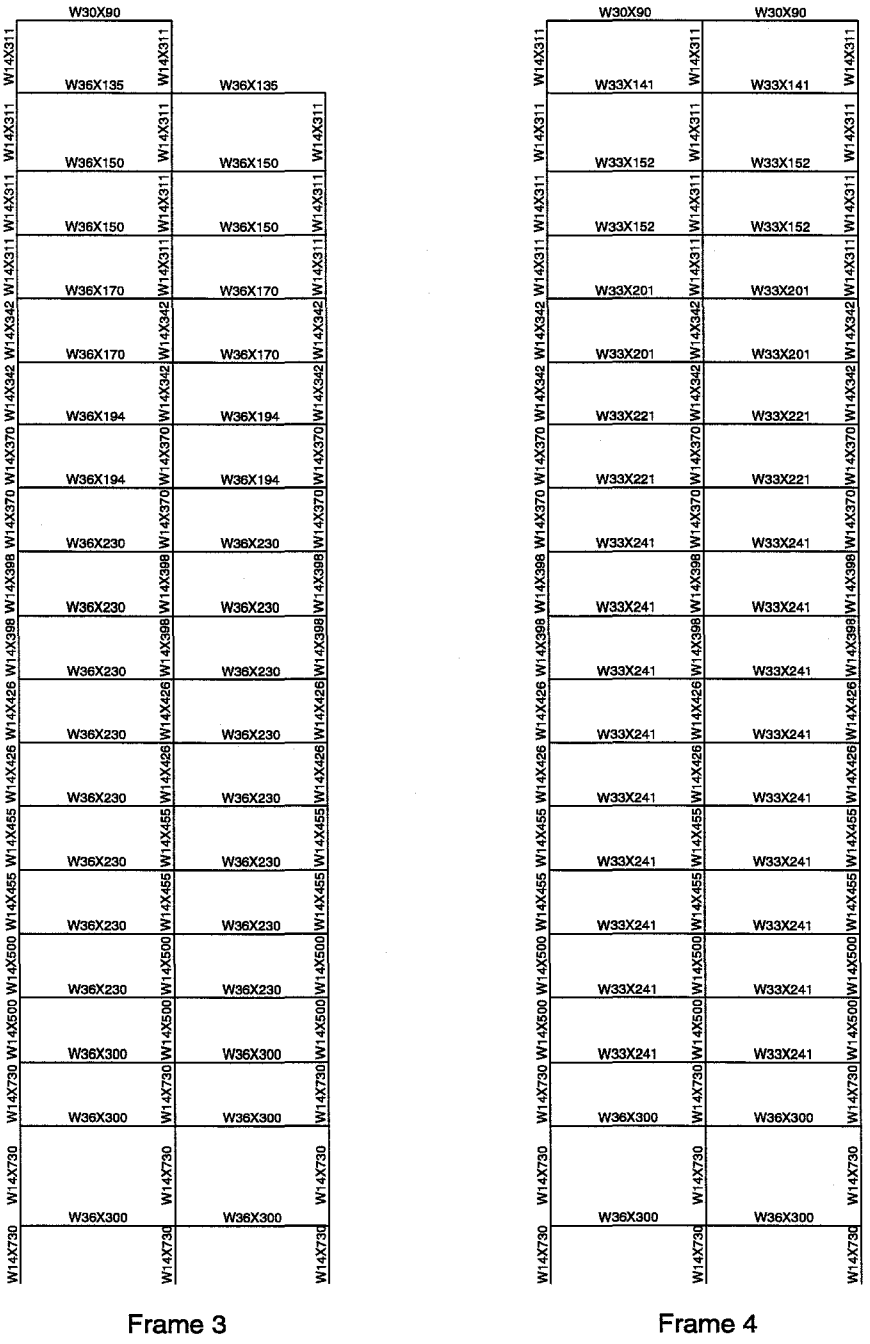

Figure 8.2 South and North frame section properties.

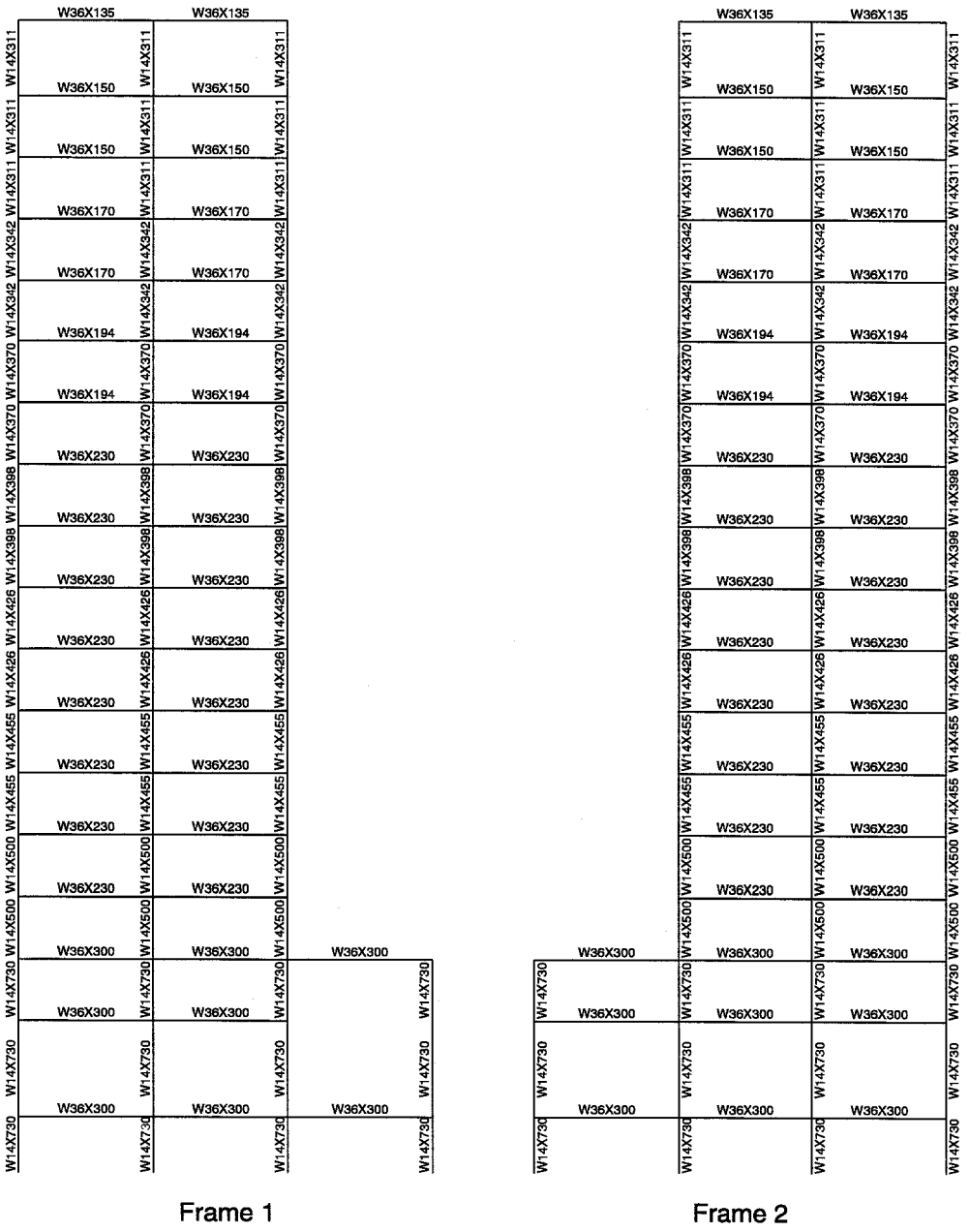

Figure 8.3 West and East frame section properties.

MODE SHAPES OF 17–STORY BUILDING

Mode 1, Period = 4.882 sec.

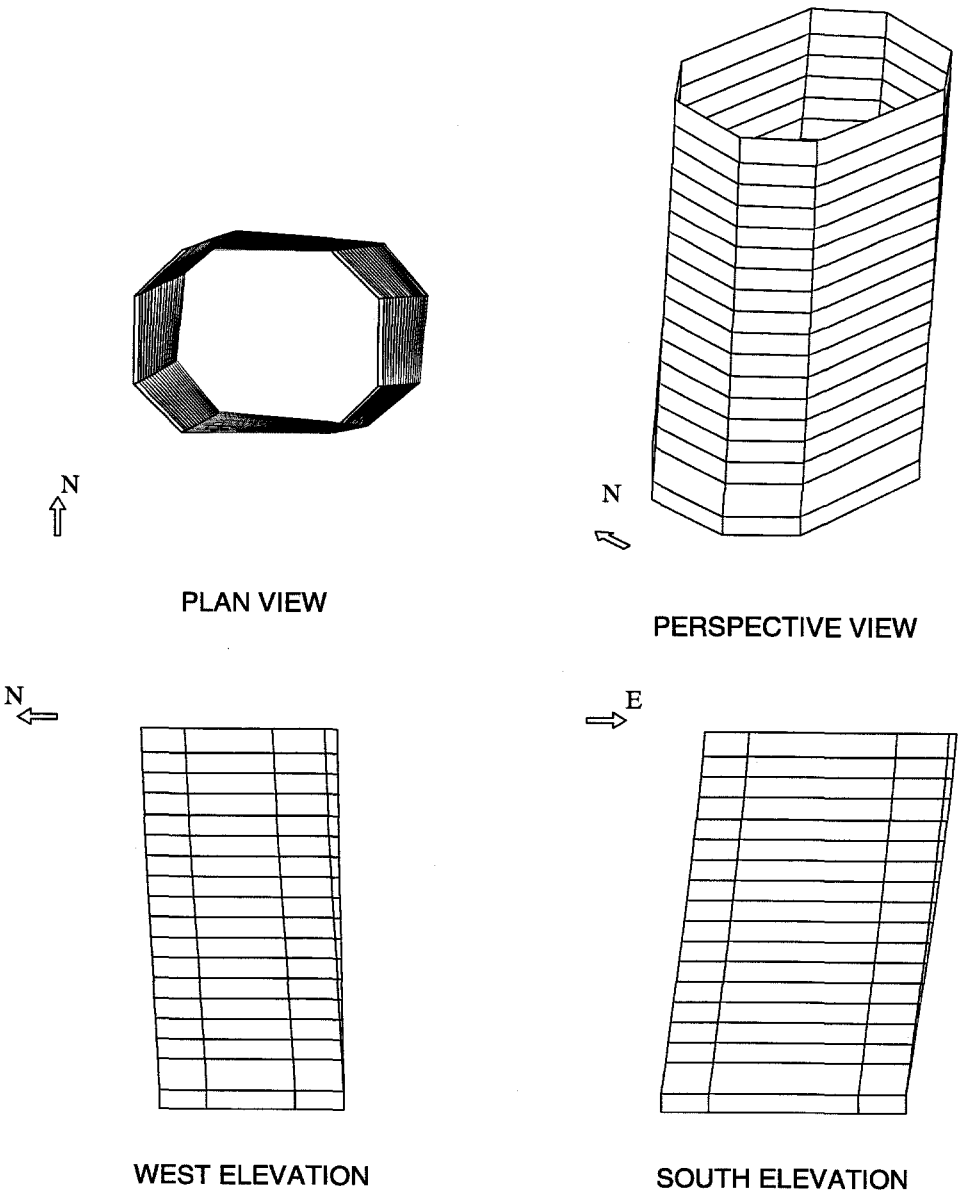

Figure 8.4 17-story building mode 1.

MODE SHAPES OF 17–STORY BUILDING

Mode 2, Period = 4.518 sec.

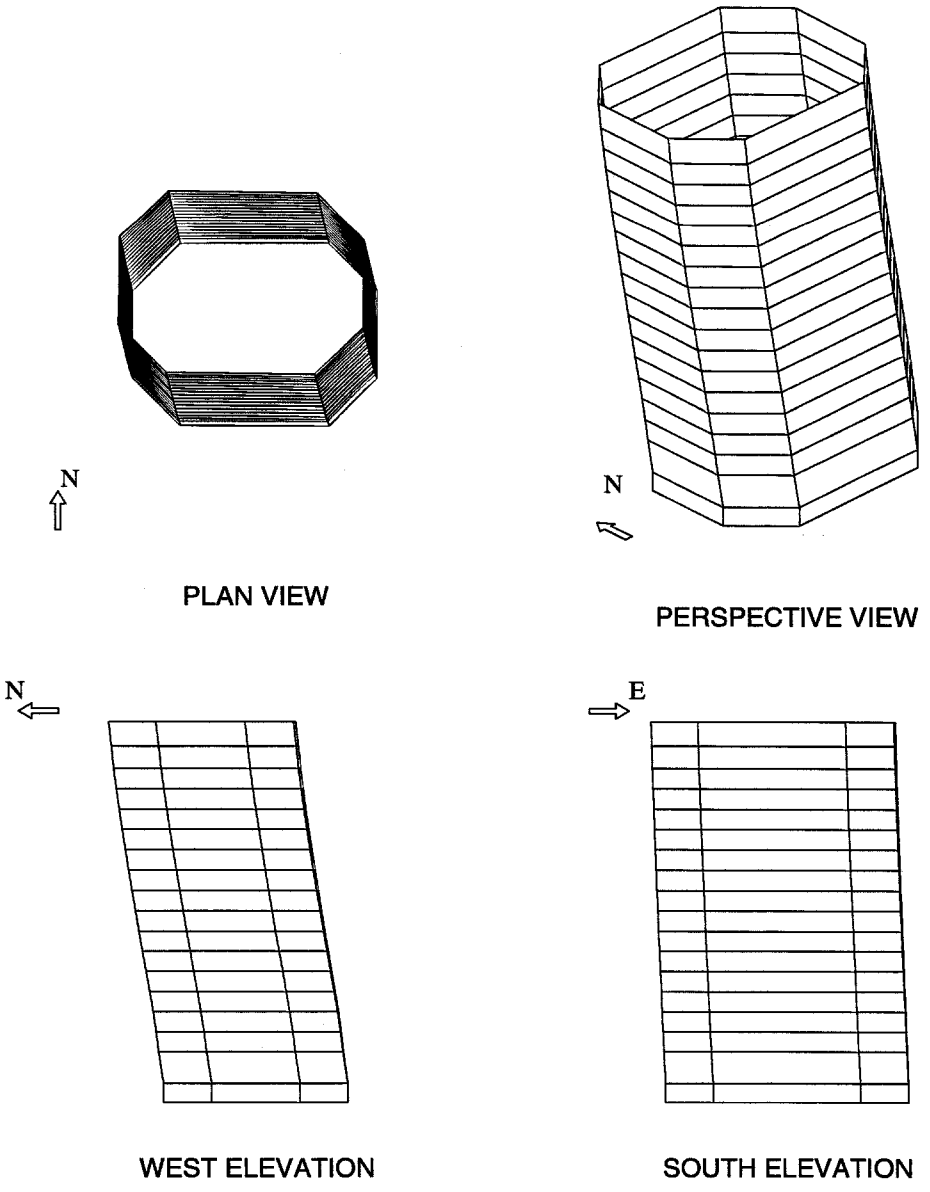

Figure 8.5 17-story building mode 2.

MODE SHAPES OF 17–STORY BUILDING

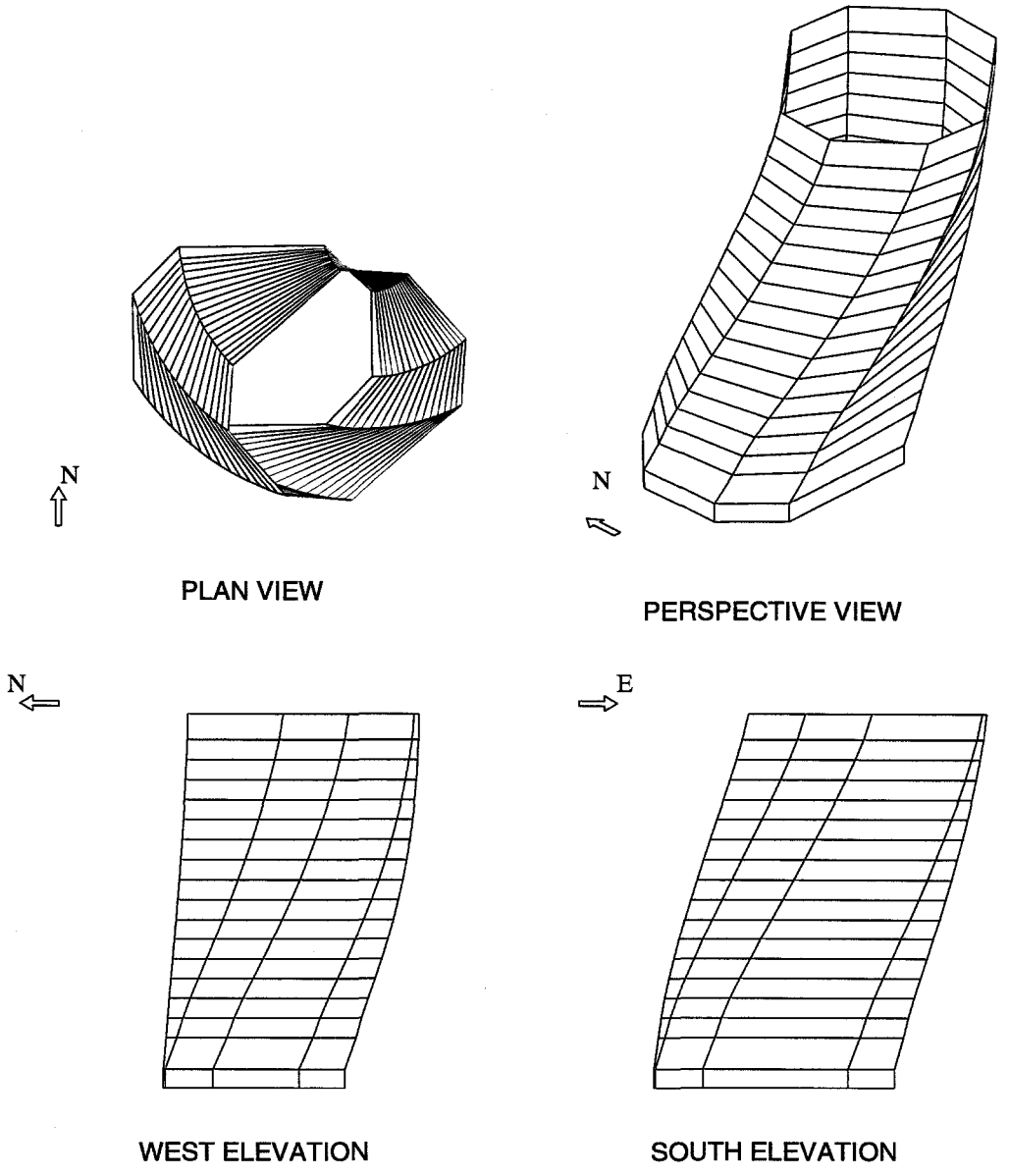

Figure 8.6 17-story building mode 3.

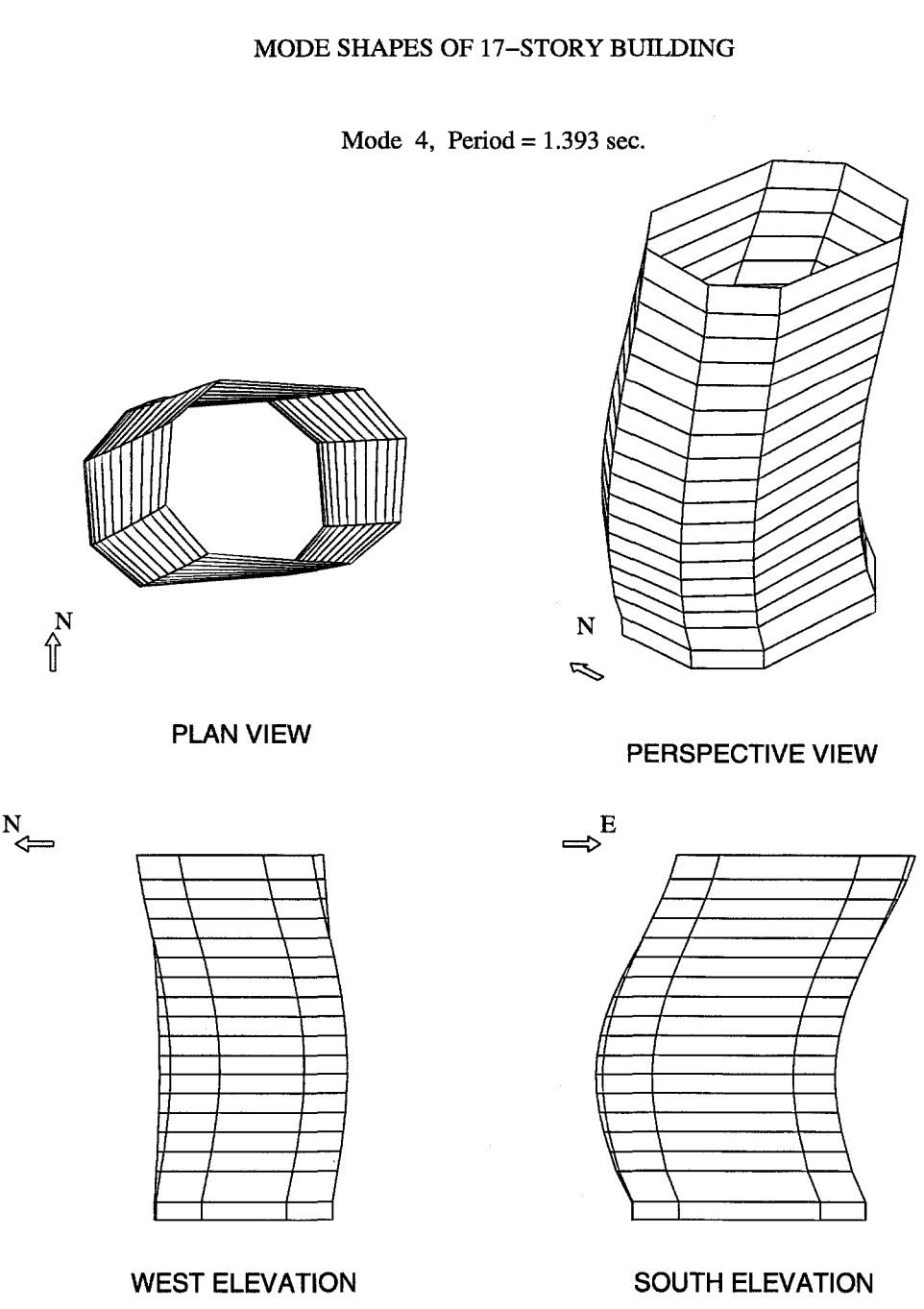

Figure 8.7 17-story building mode 4.

MODE SHAPES OF 17–STORY BUILDING

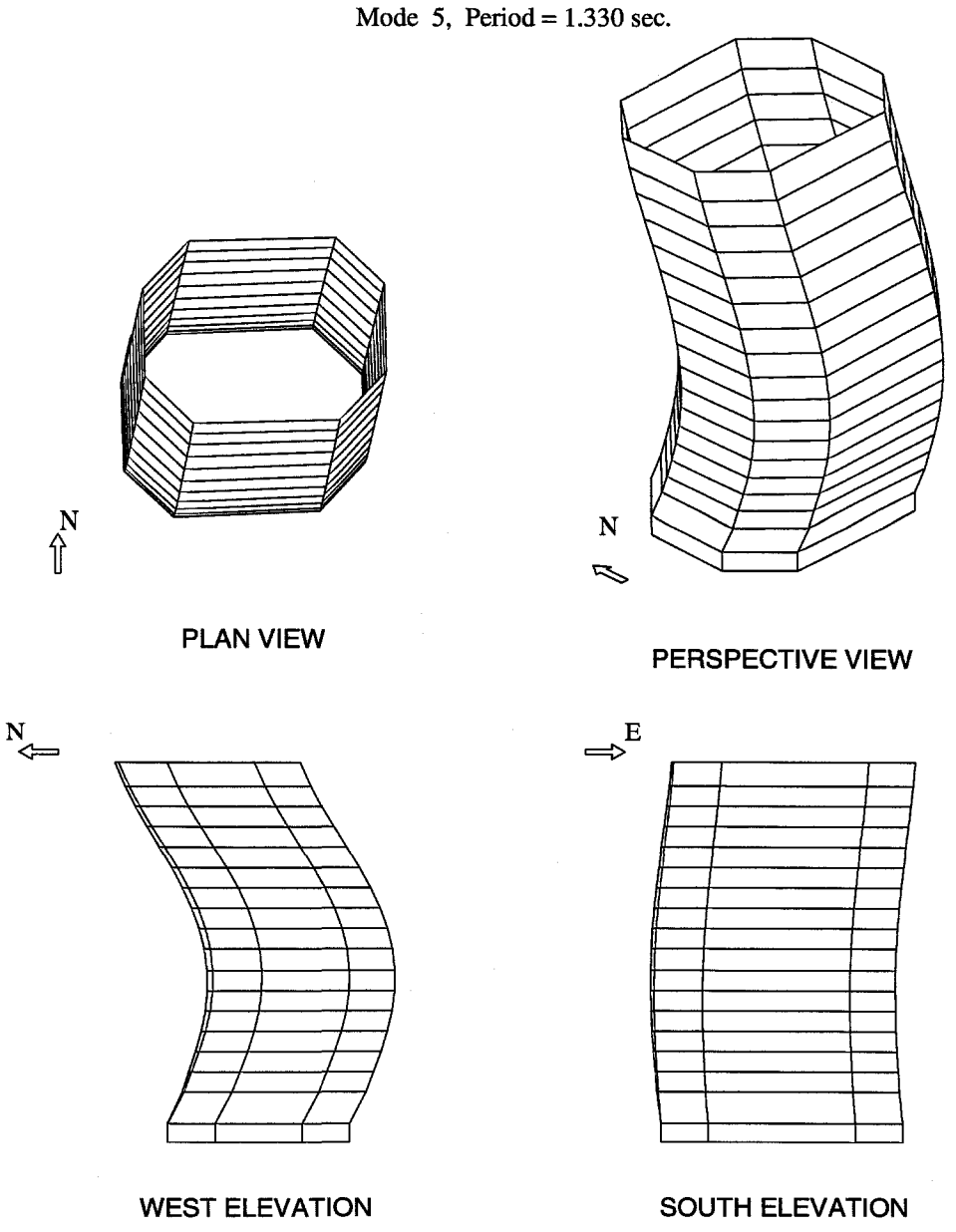

Figure 8.8 17-story building mode 5.

MODE SHAPES OF 17–STORY BUILDING

Mode 6, Period = 0.845 sec.

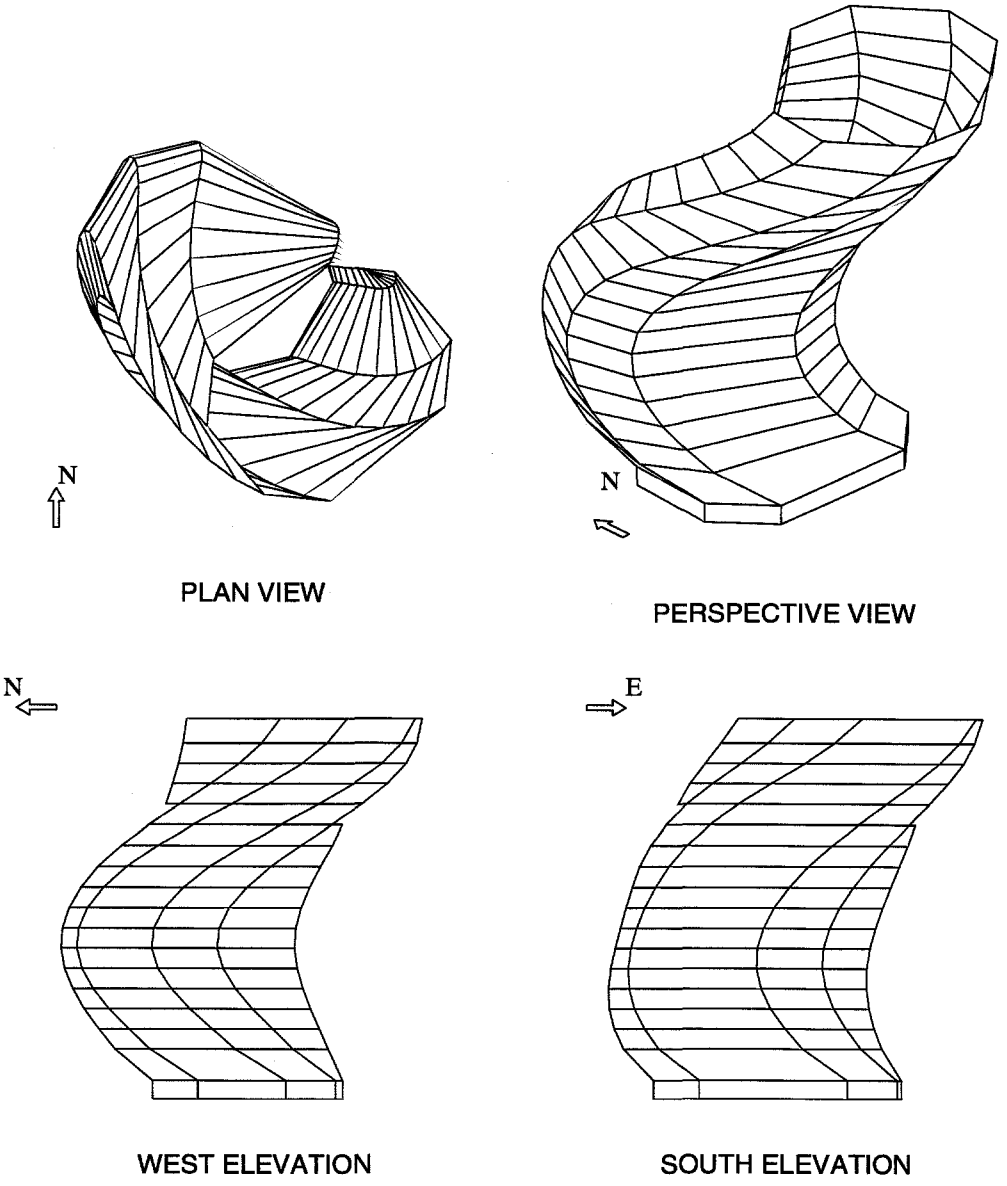

Figure 8.9 17-story building mode 6.

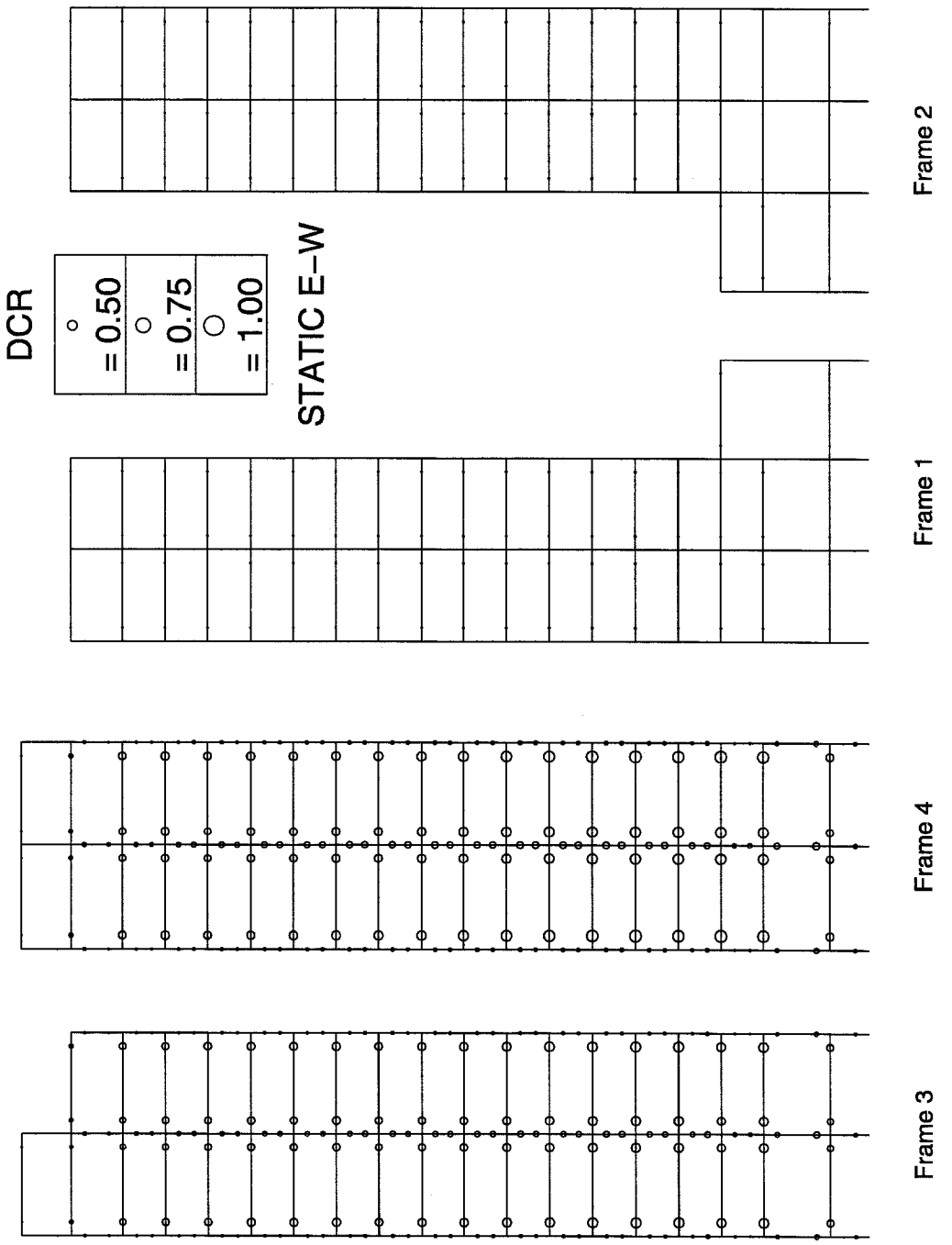

Figure 8.10 17-story building demand capacity ratios, E-W direction.

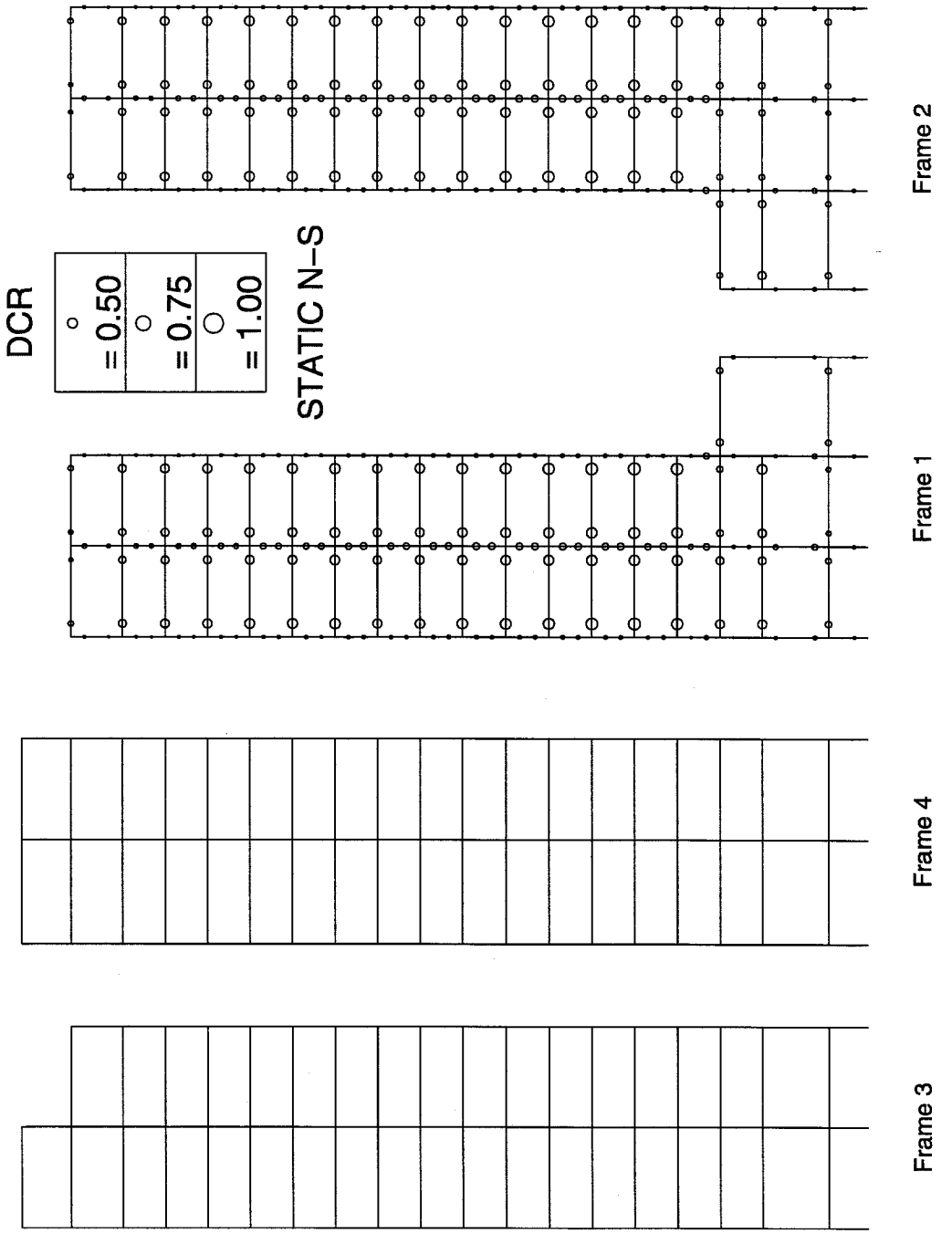

Figure 8.11 17-story building demand capacity ratios, N-S direction.

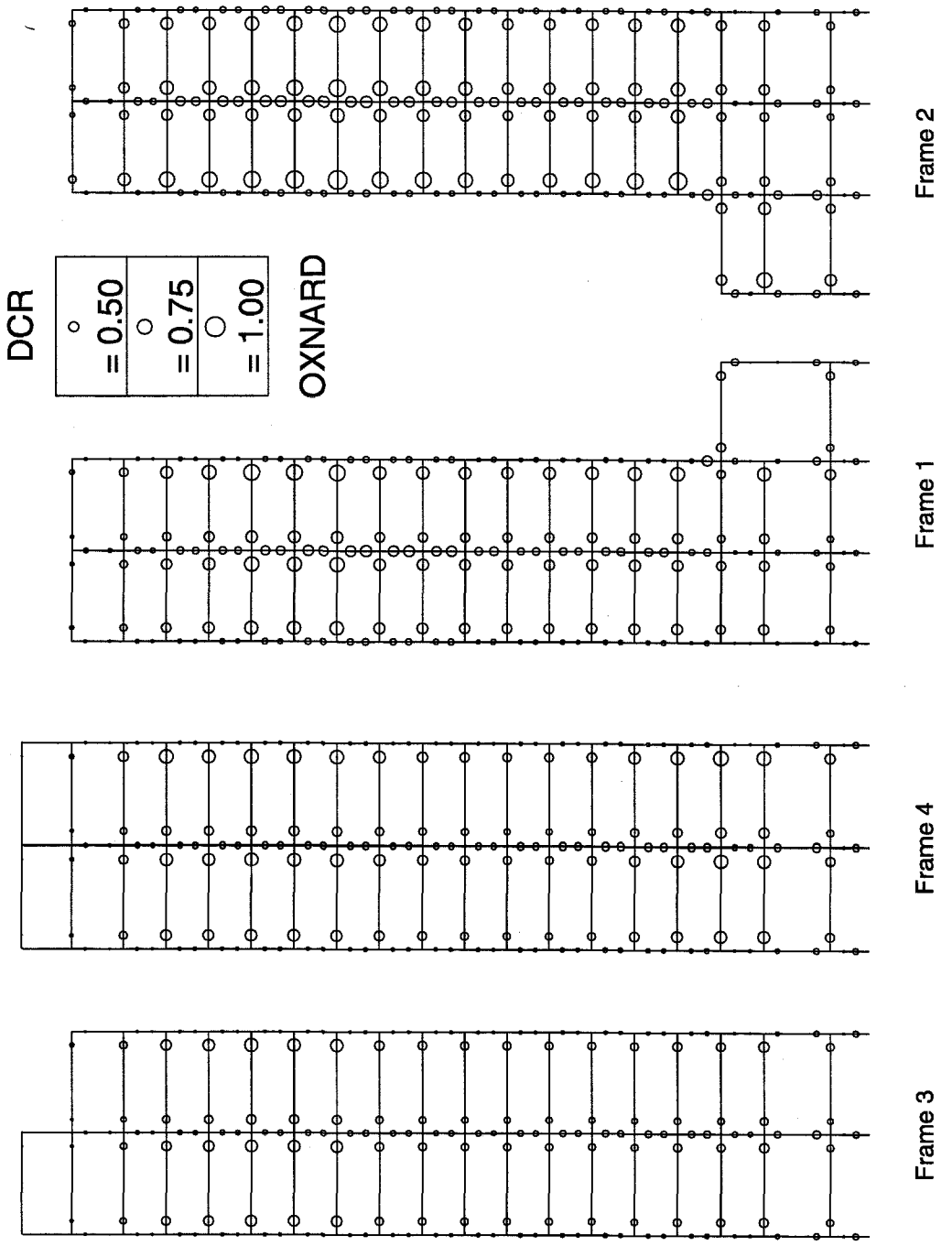

Figure 8.12 17-story building demand capacity ratios, Oxnard record.

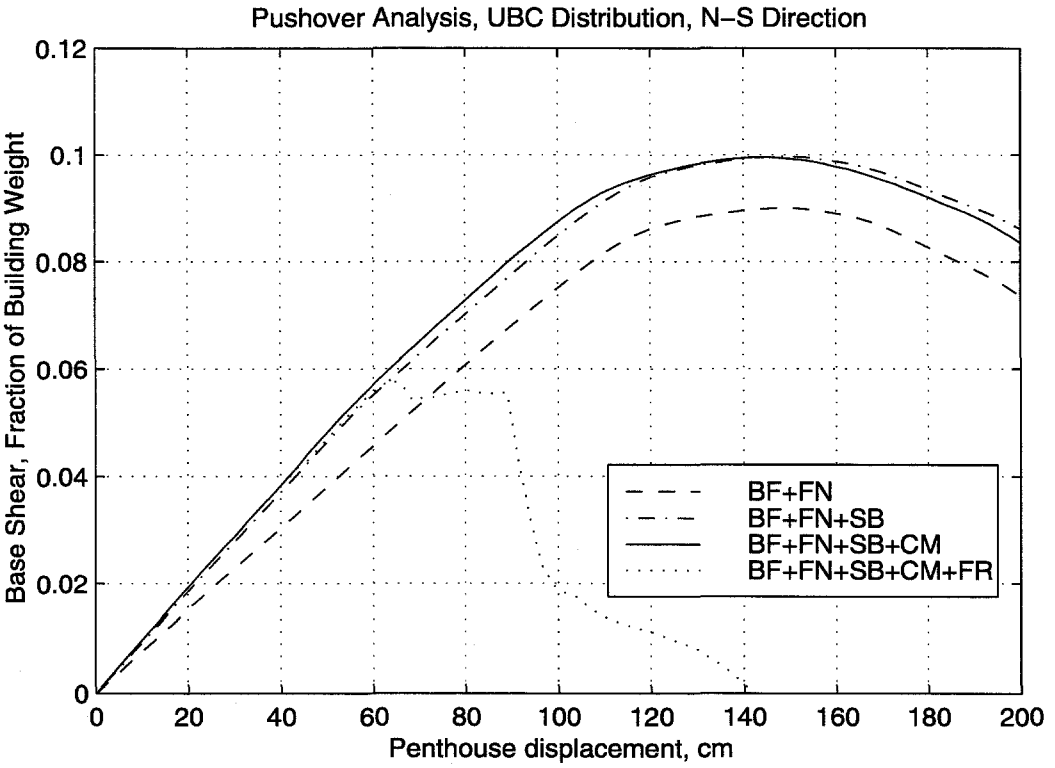

Figure 8.13 17-story pushover analysis.

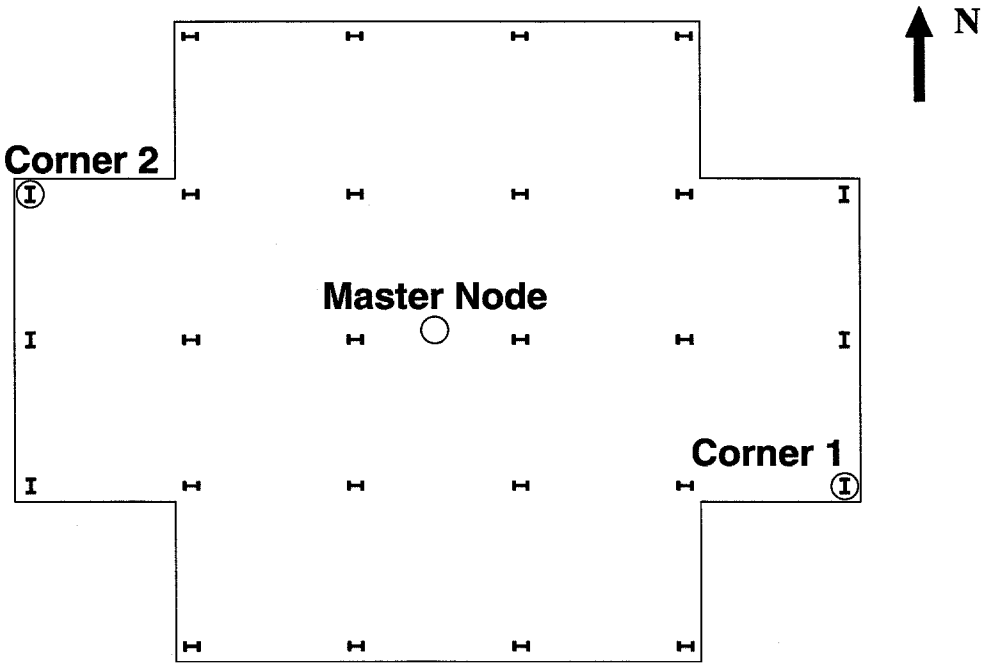

Figure 8.14 Locations at penthouse for time histories.

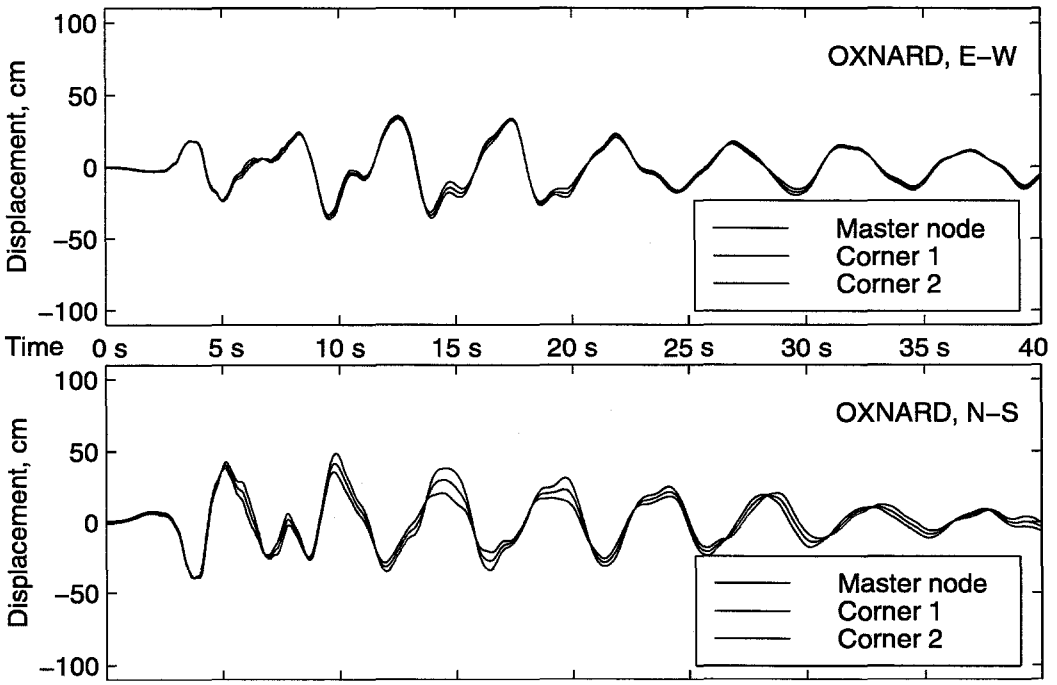

Figure 8.15 Relative penthouse displacements, poor fracture model and Oxnard record.

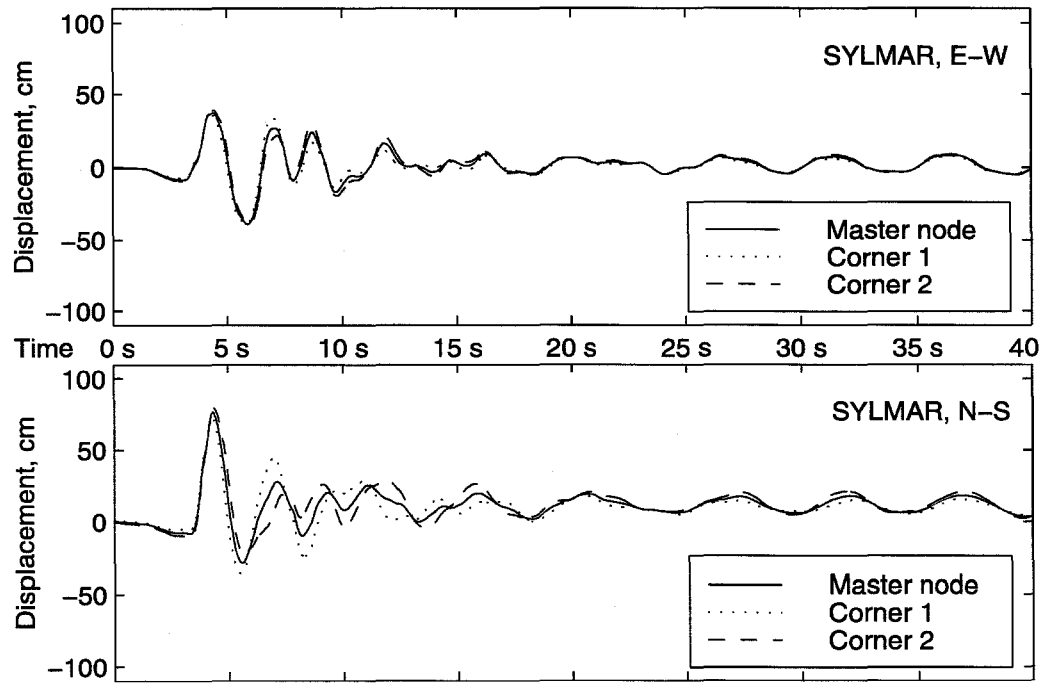

Figure 8.16 Relative penthouse displacements, poor fracture model and Sylmar record.

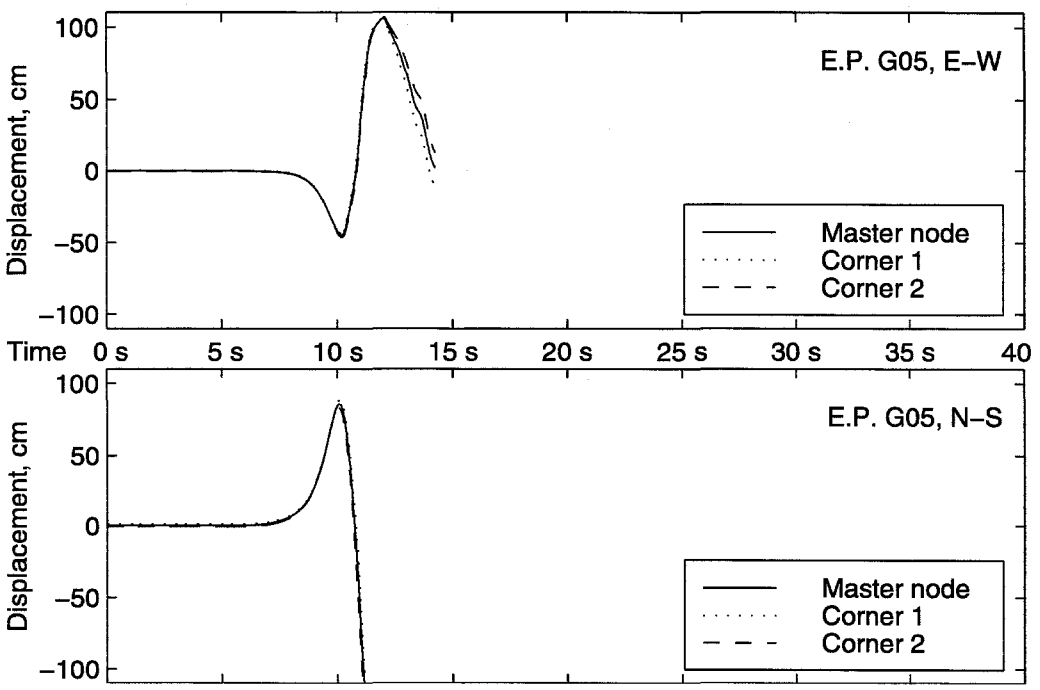

Figure 8.17 Relative penthouse displacements, poor fracture model and E. P. G05 record.

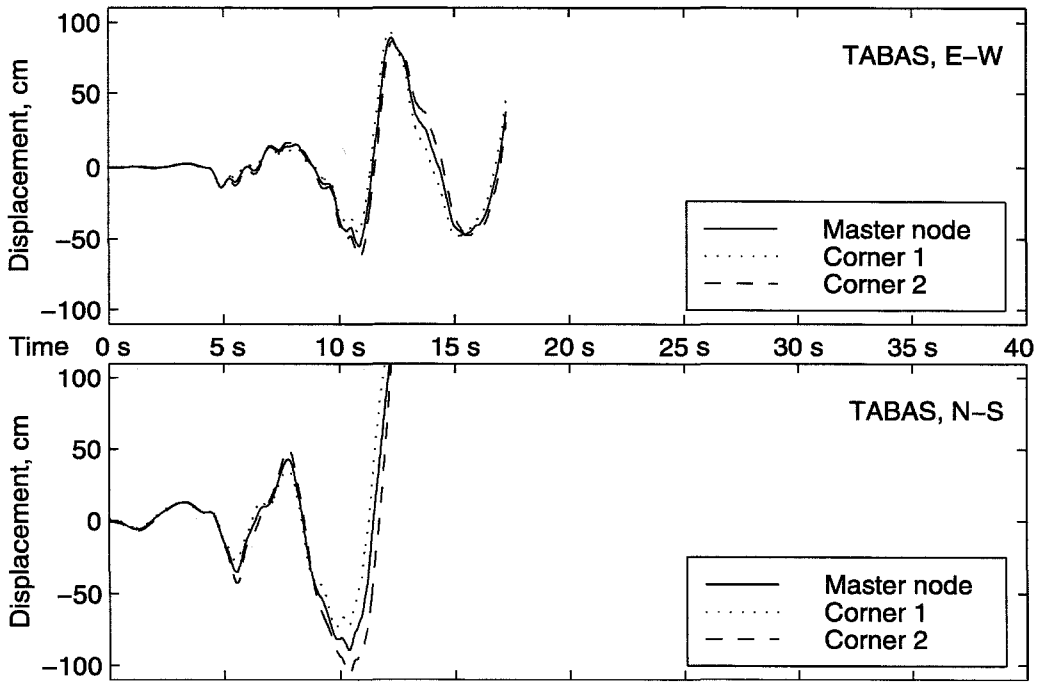

Figure 8.18 Relative penthouse displacements, poor fracture model and Tabas record.

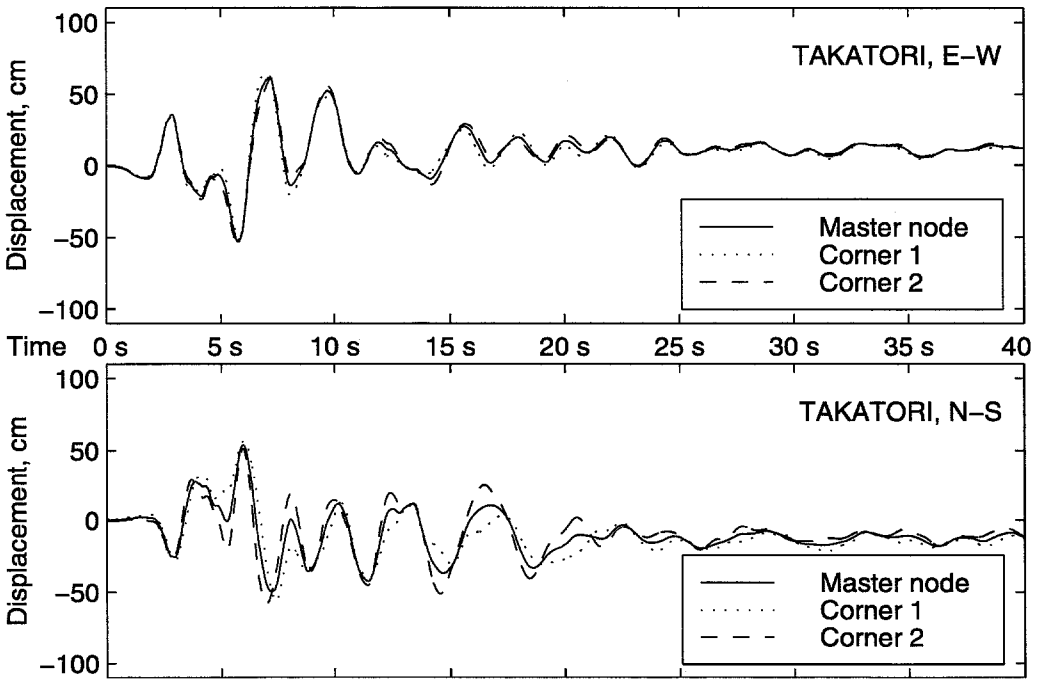

Figure 8.19 Relative penthouse displacements, poor fracture model and Takatori record.

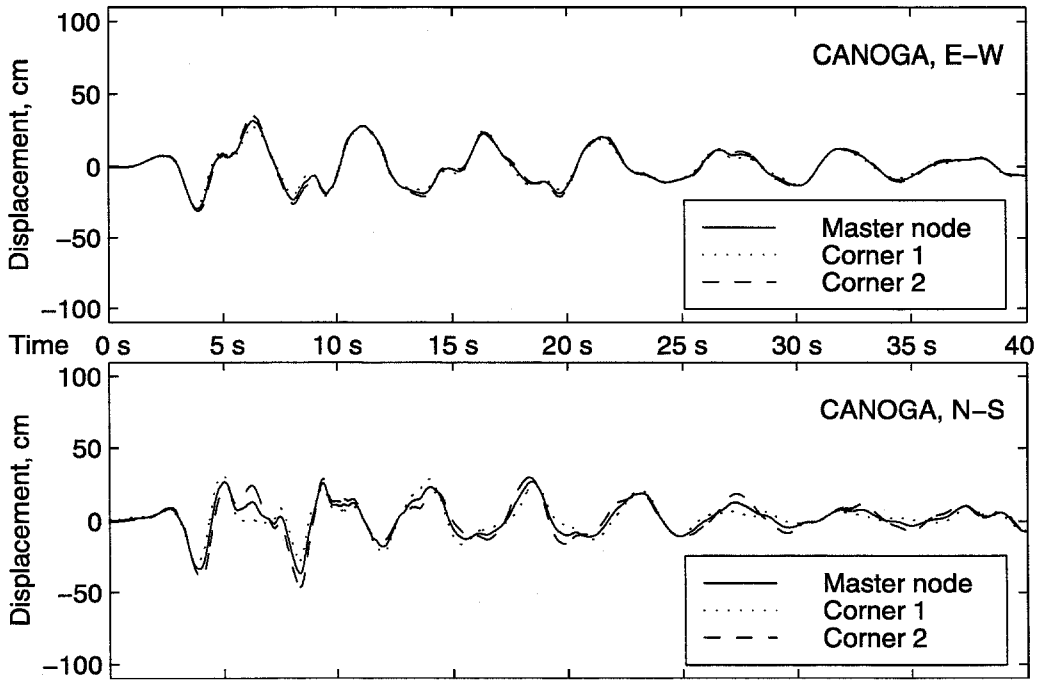

Figure 8.20 Relative penthouse displacements, poor fracture model and Canoga record.

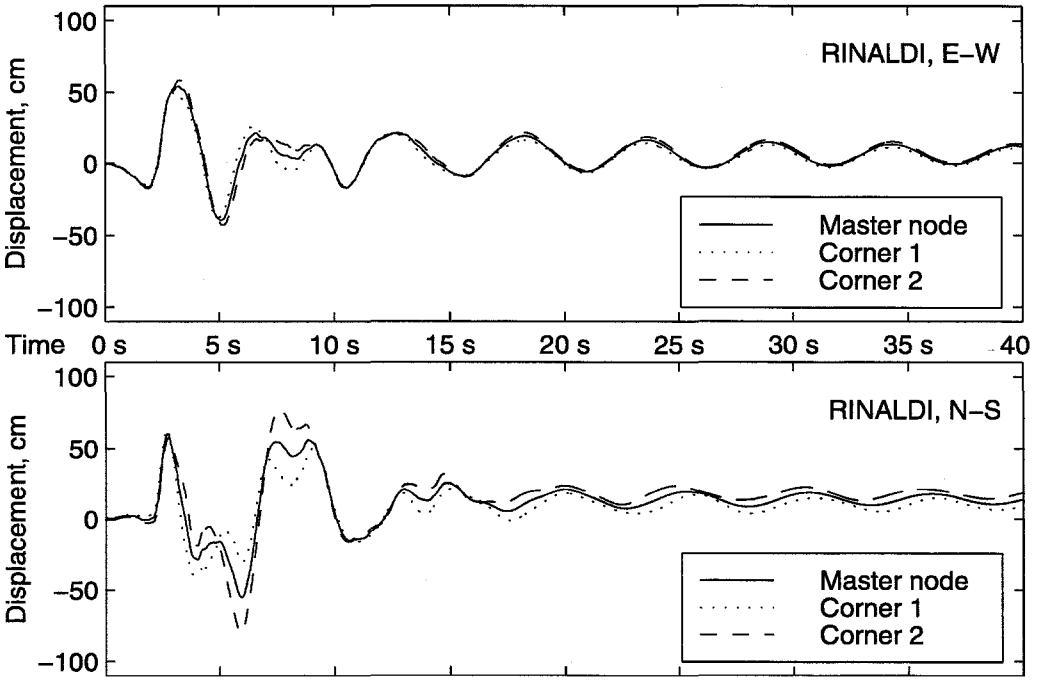

Figure 8.21 Relative penthouse displacements, poor fracture model and Rinaldi record.

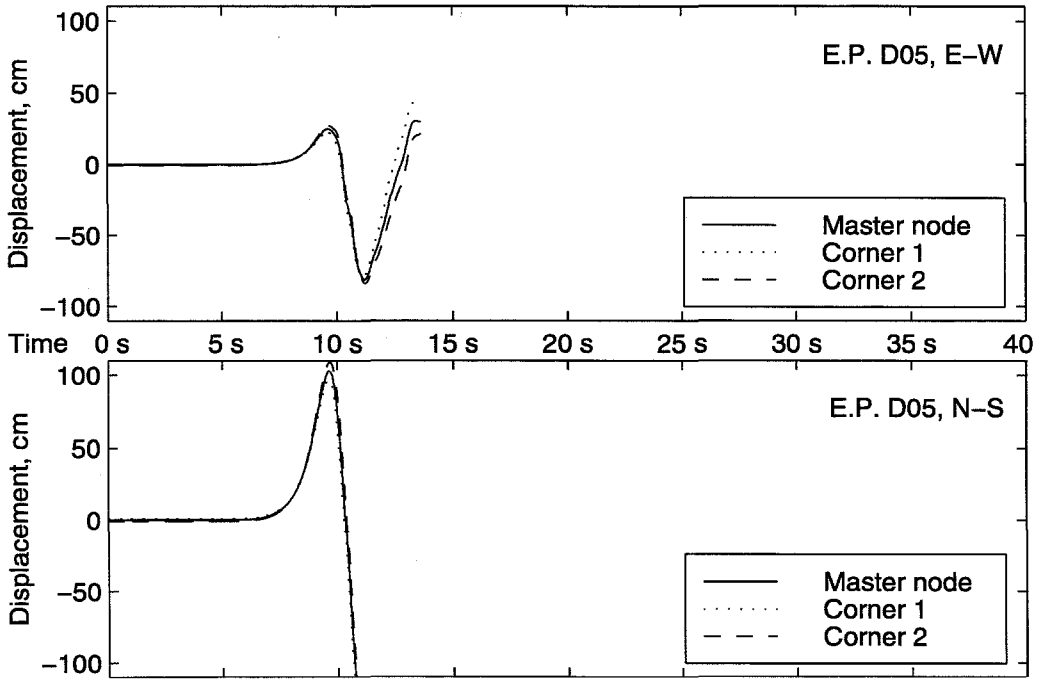

Figure 8.22 Relative penthouse displacements, poor fracture model and E. P. D05 record.

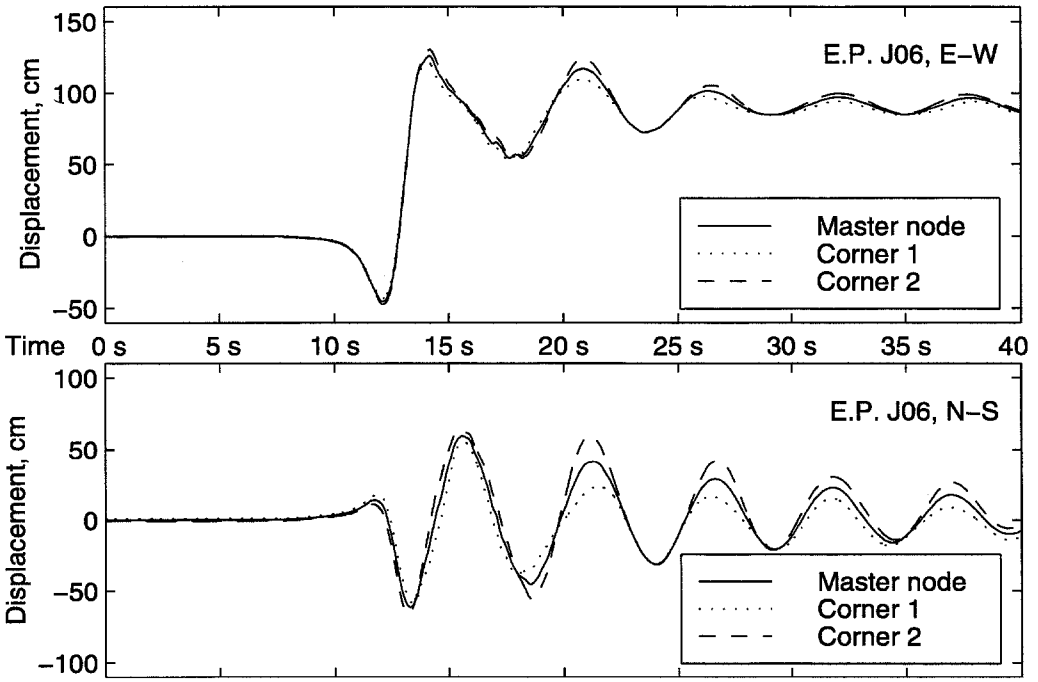

Figure 8.23 Relative penthouse displacements, poor fracture model and E. P. J06 record.

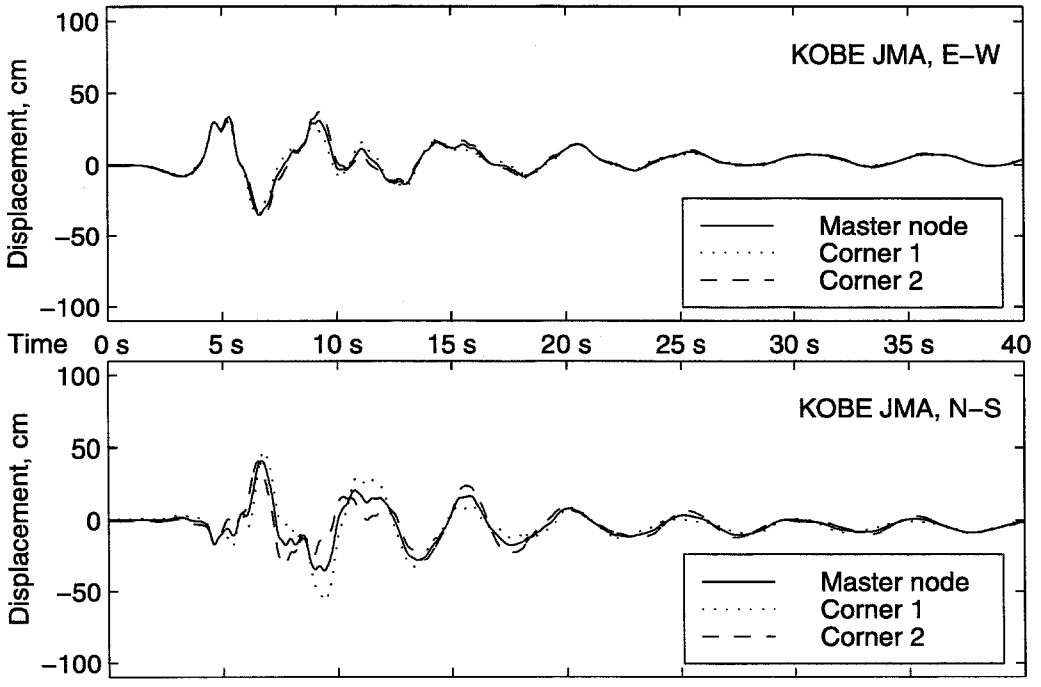

Figure 8.24 Relative penthouse displacements, poor fracture model and Kobe JMA record.

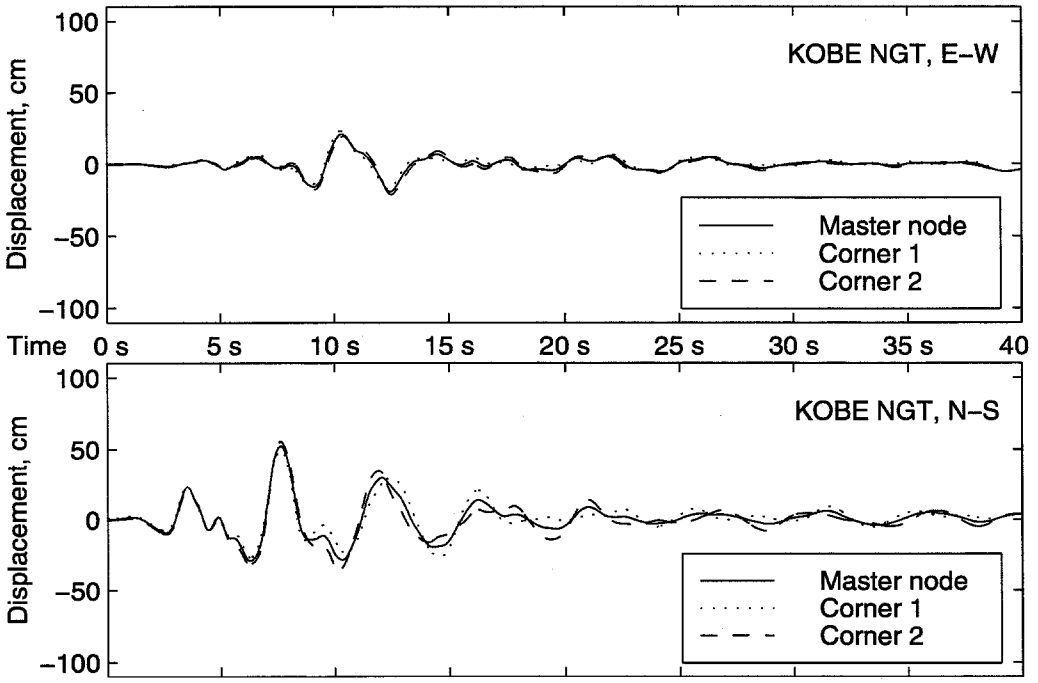

Figure 8.25 Relative penthouse displacements, poor fracture model and Kobe NGT record.

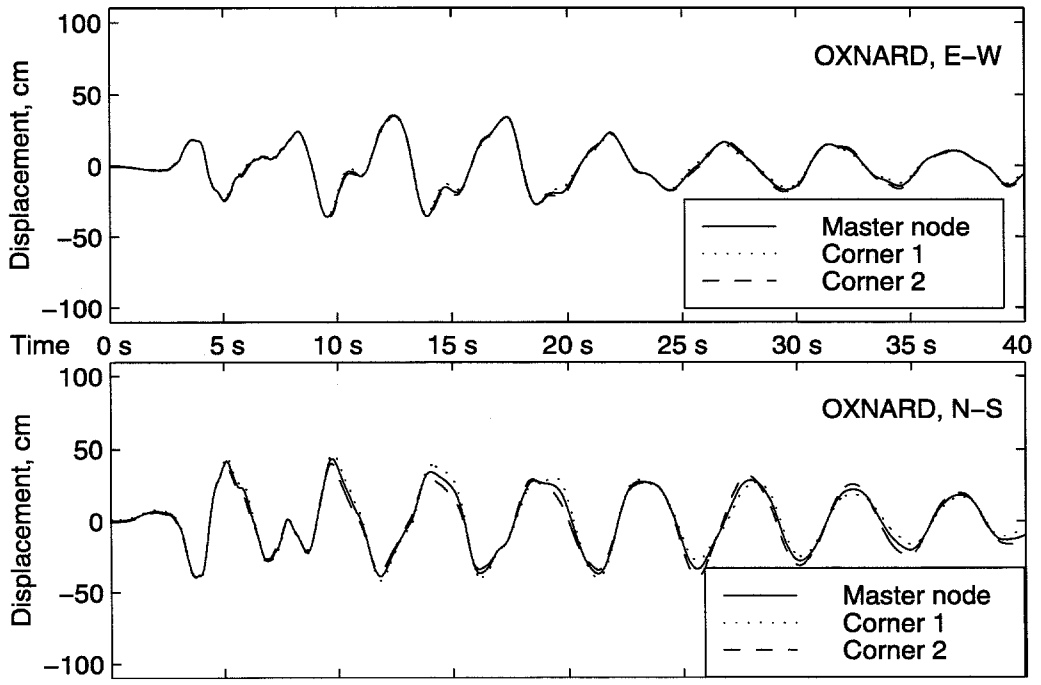

Figure 8.26 Relative penthouse displacements, inelastic model and Oxnard record.

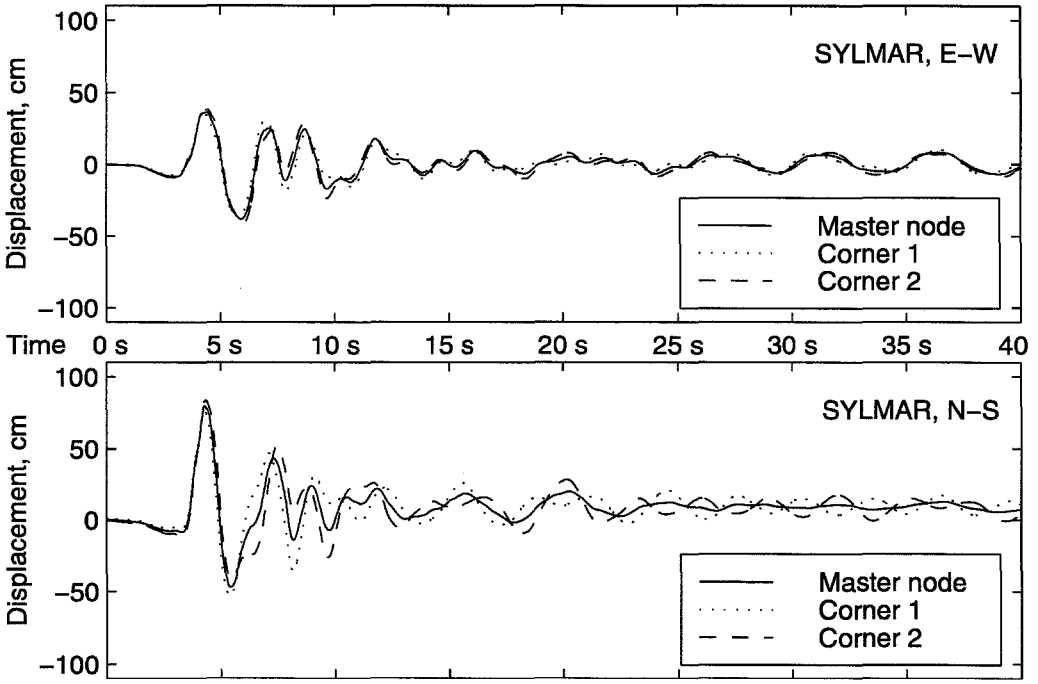

Figure 8.27 Relative penthouse displacements, inelastic model and Sylmar record.

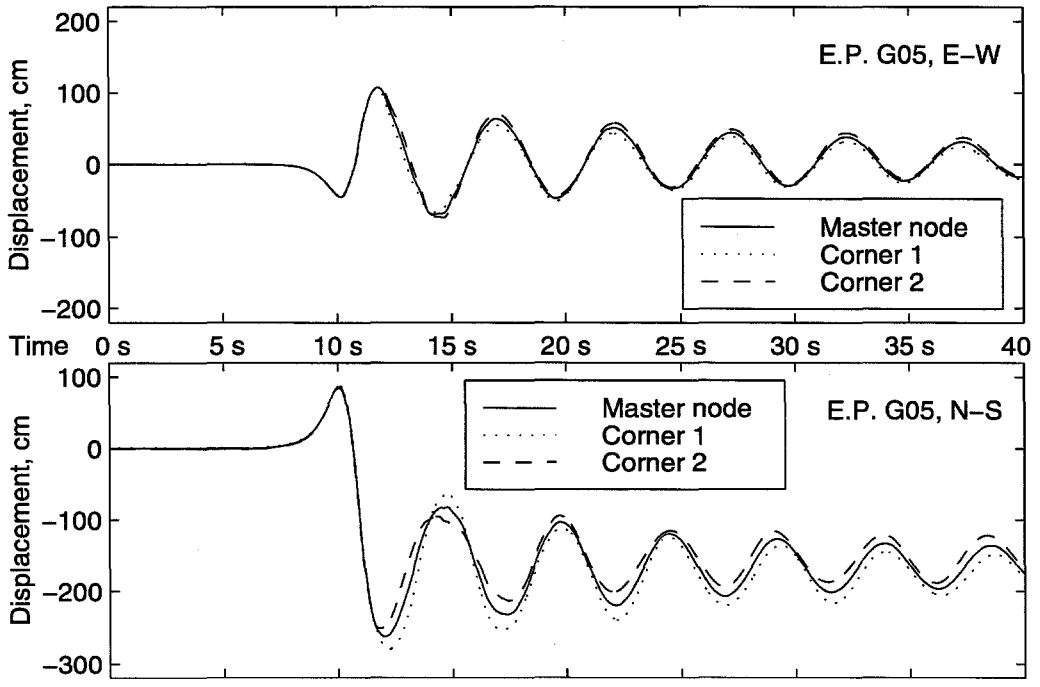

Figure 8.28 Relative penthouse displacements, inelastic model and E. P. G05 record.

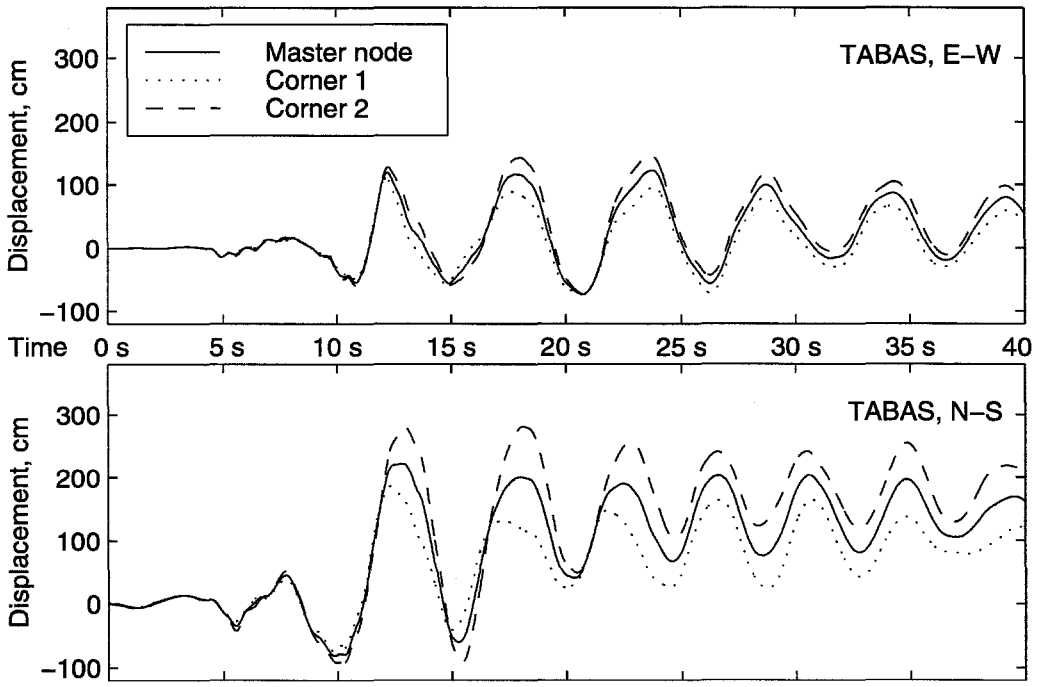

Figure 8.29 Relative penthouse displacements, inelastic model and Tabas record.

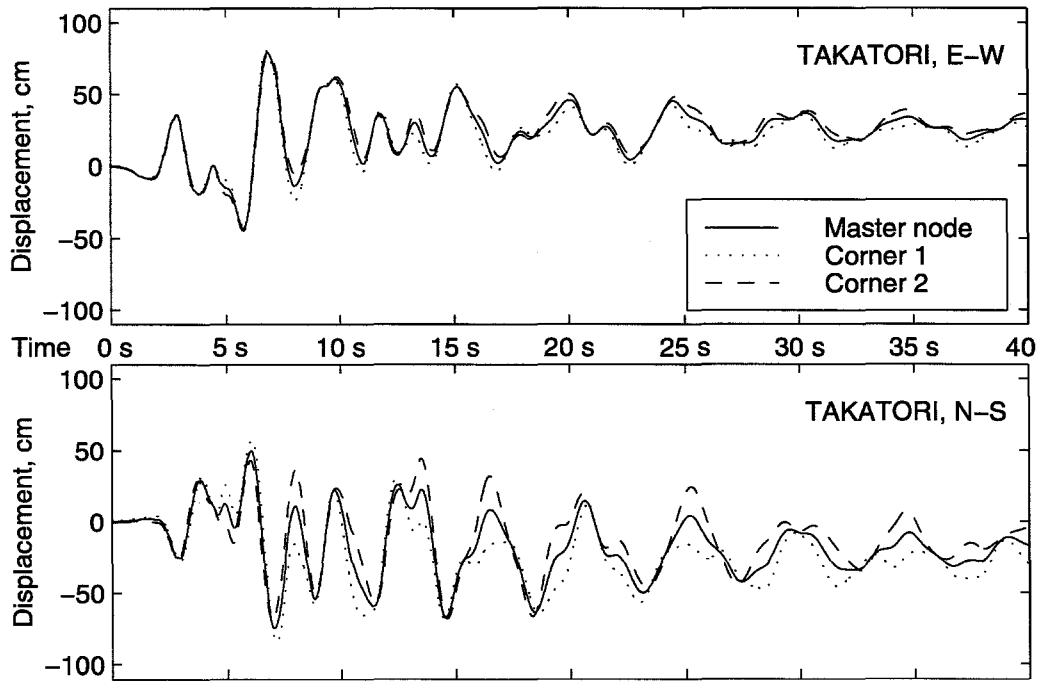

Figure 8.30 Relative penthouse displacements, inelastic model and Takatori record.

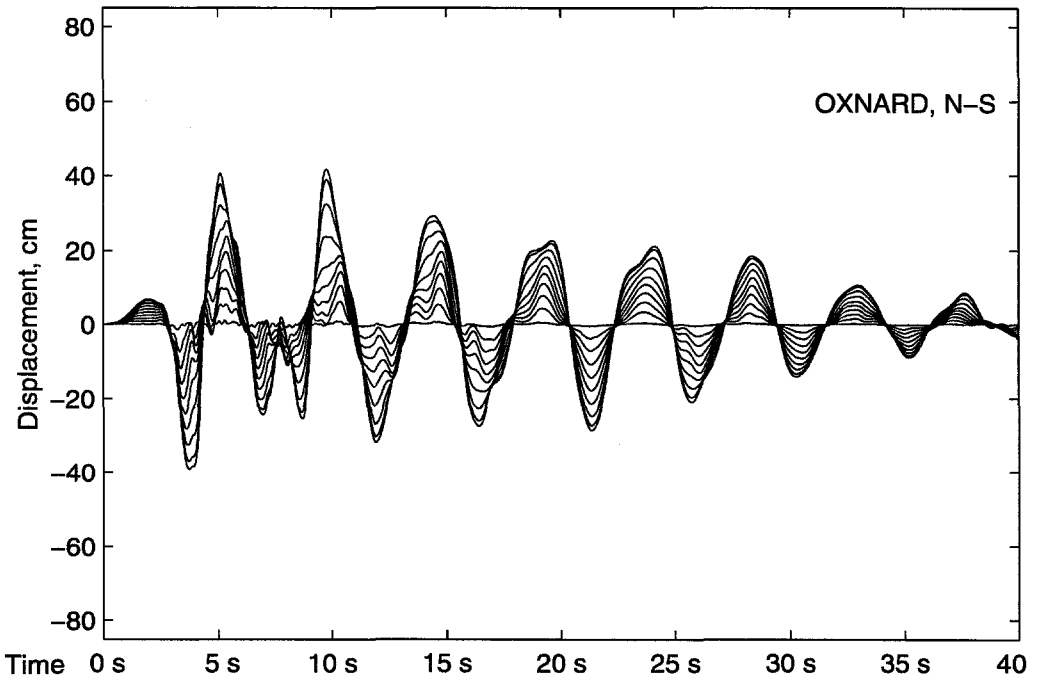

Figure 8.31 Relative floor displacements, poor fracture model and Oxnard record.

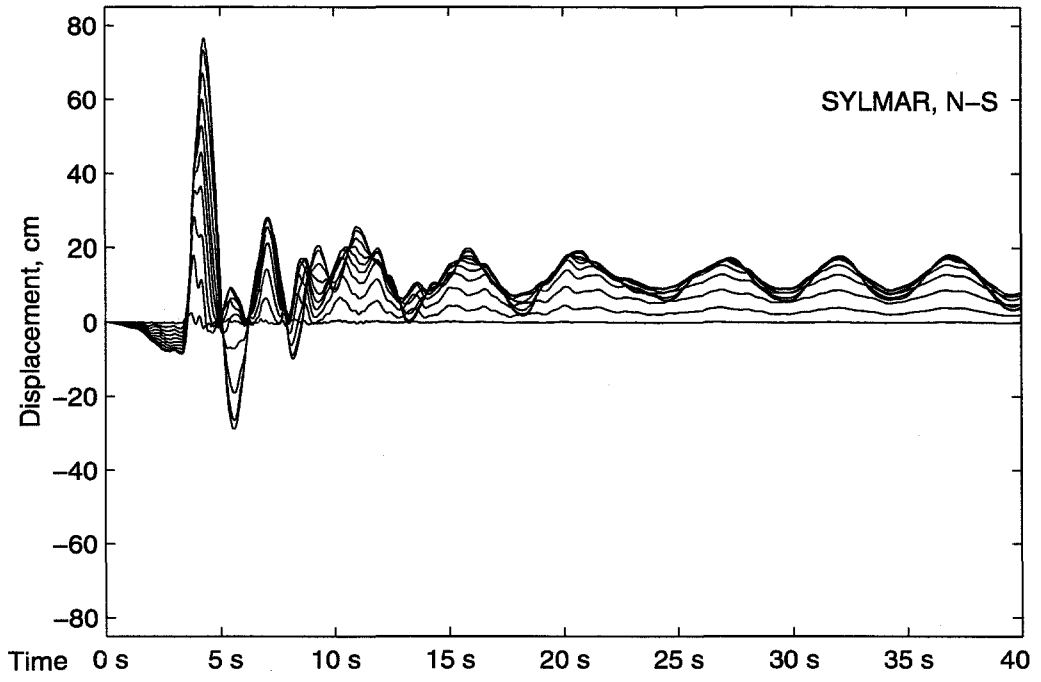

Figure 8.32 Relative floor displacements, poor fracture model and Sylmar record.

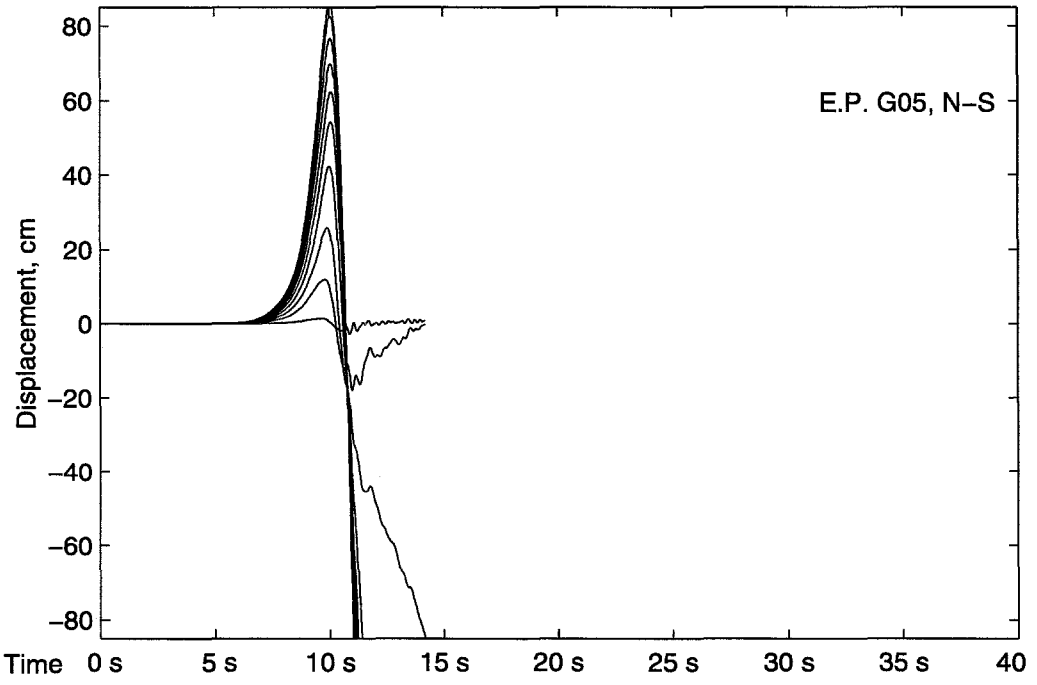

Figure 8.33 Relative floor displacements, poor fracture model and E.P. G05 record.

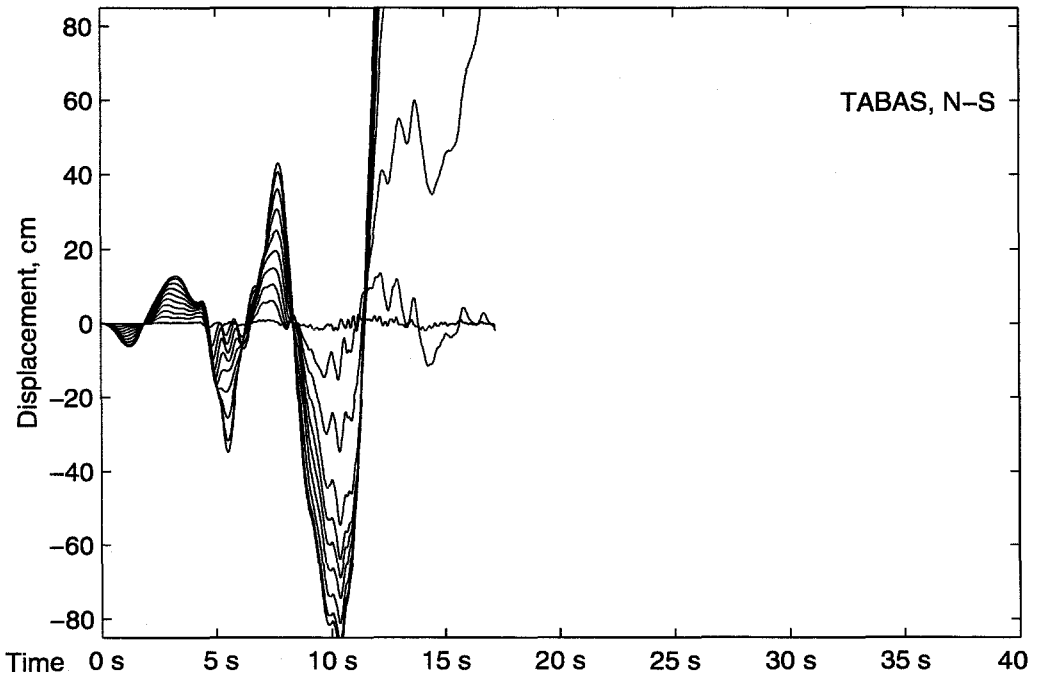

Figure 8.34 Relative floor displacements, poor fracture model and Tabas record.

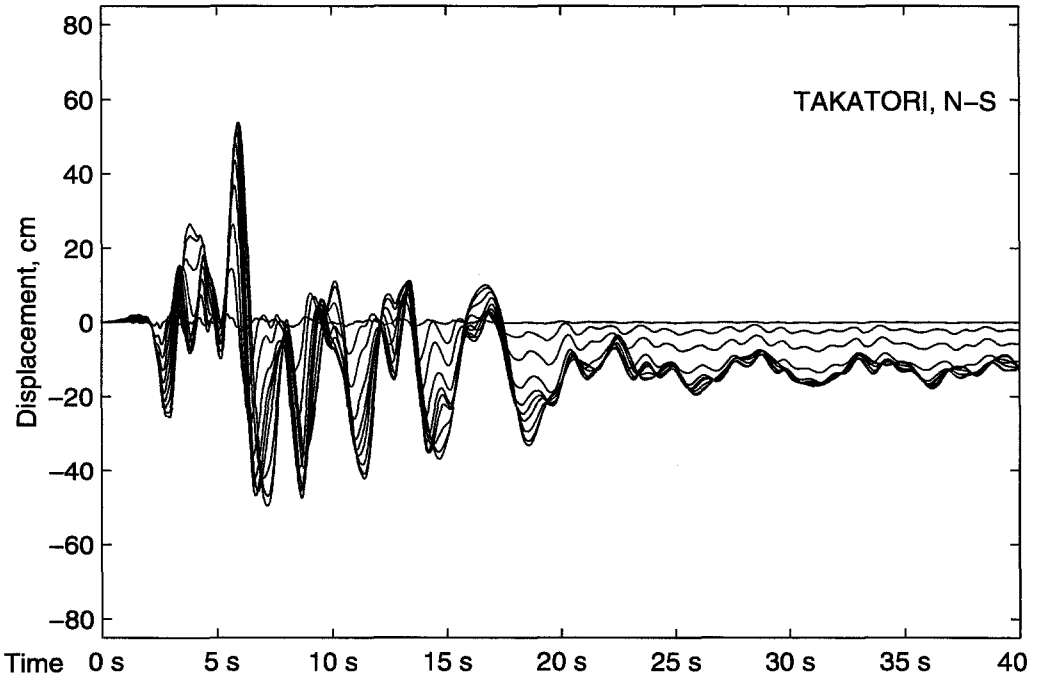

Figure 8.35 Relative floor displacements, poor fracture model and Takatori record.

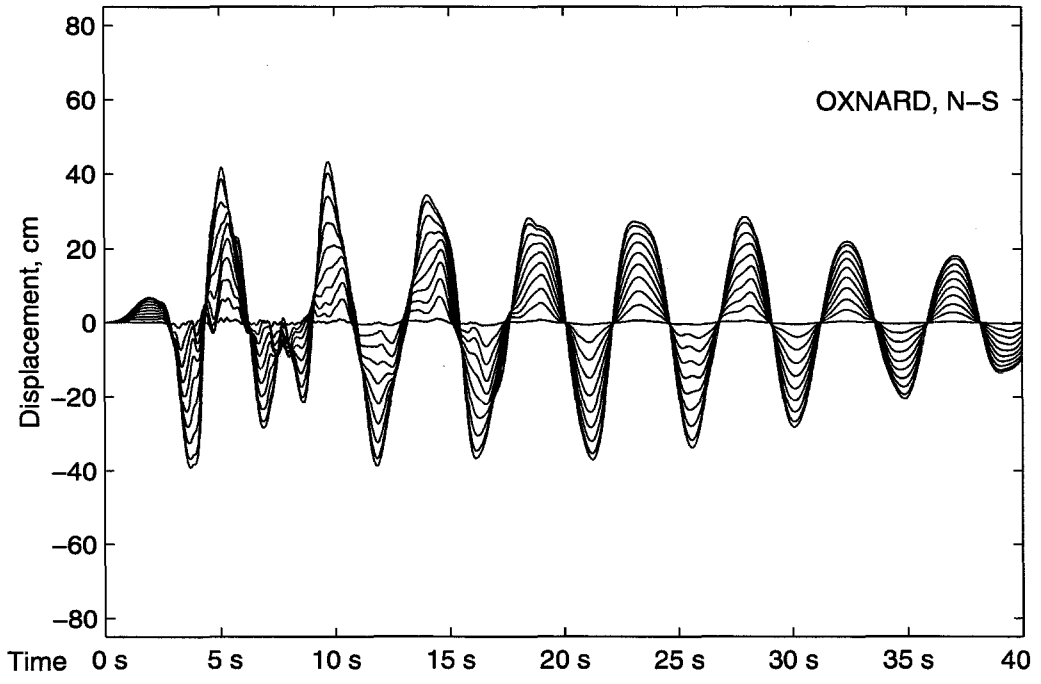

Figure 8.36 Relative floor displacements, inelastic model and Oxnard record.

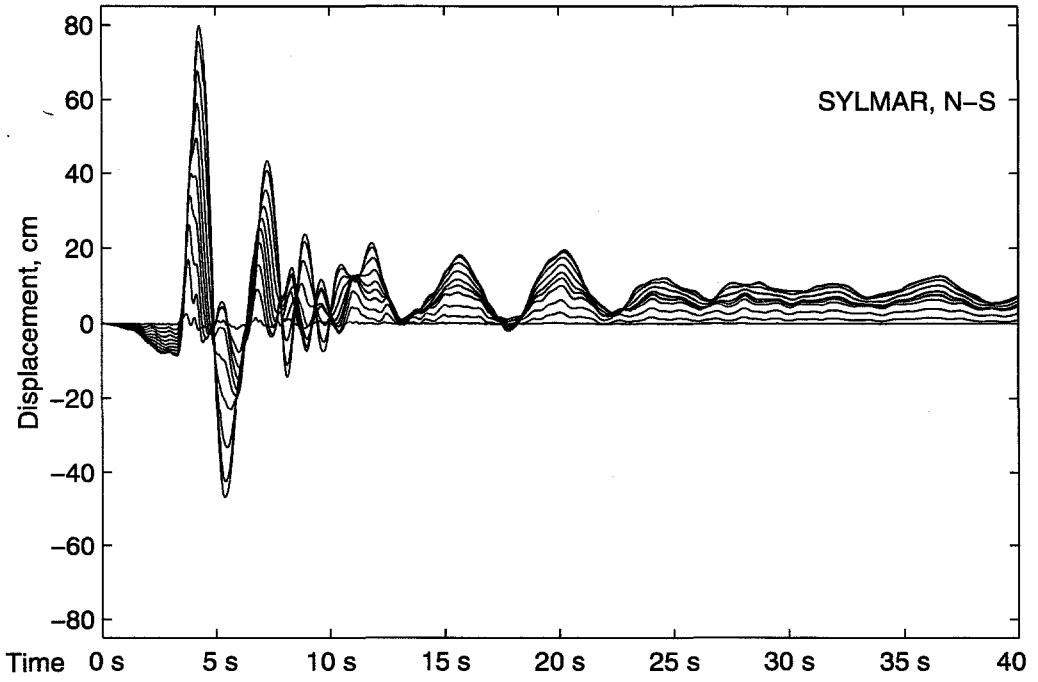

Figure 8.37 Relative floor displacements, inelastic model and Sylmar record.

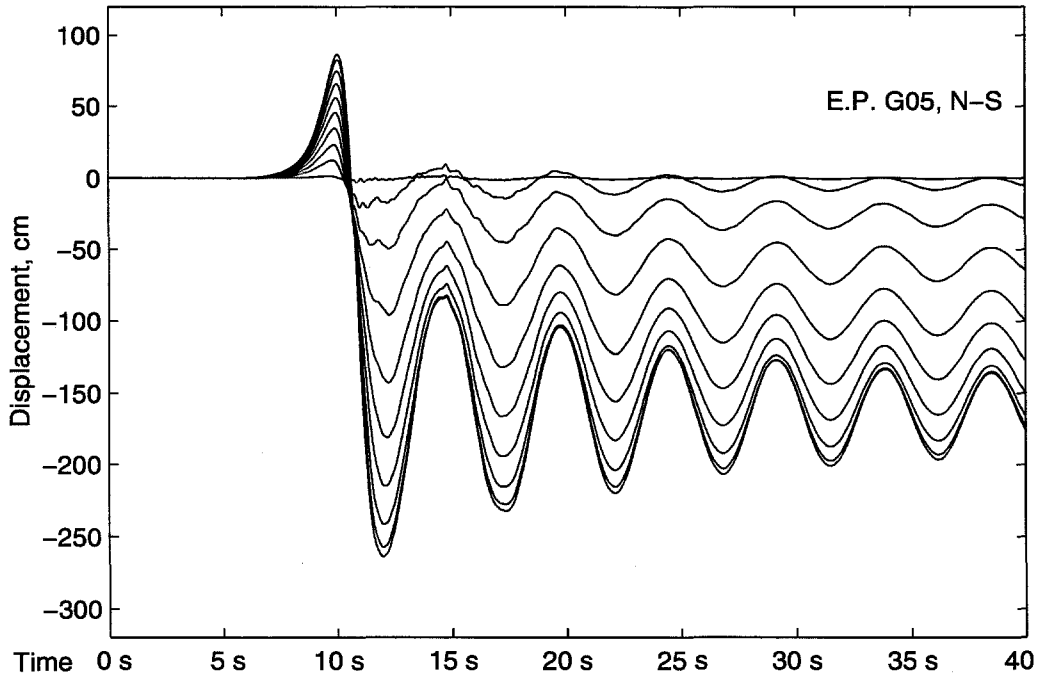

Figure 8.38 Relative floor displacements, inelastic model and E. P. G05 record.

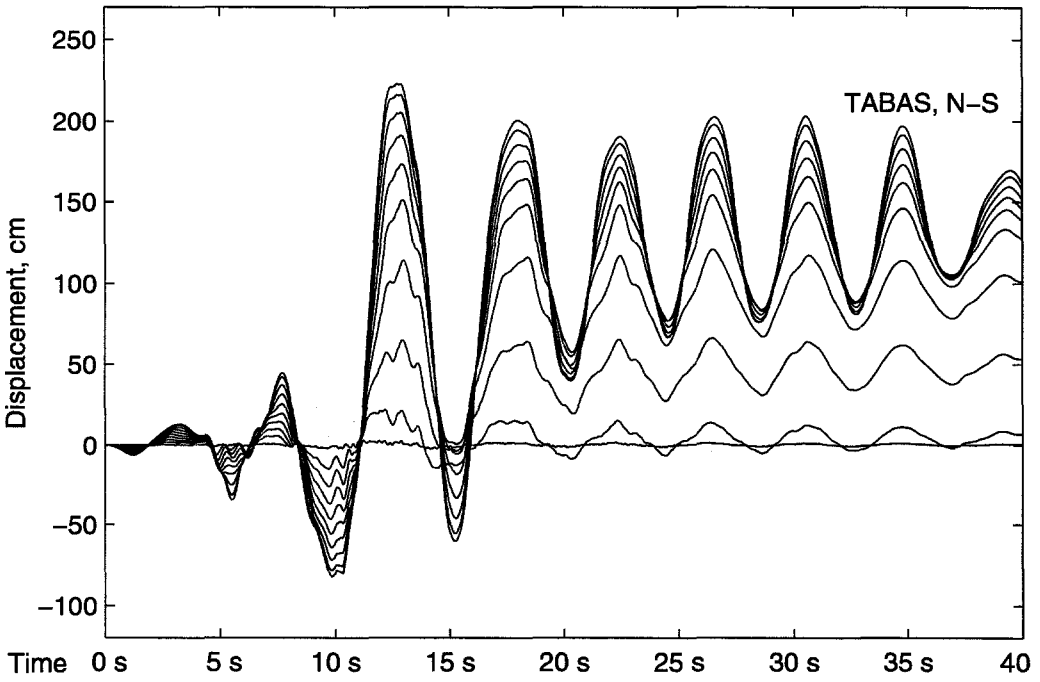

Figure 8.39 Relative floor displacements, inelastic model and Tabas record.

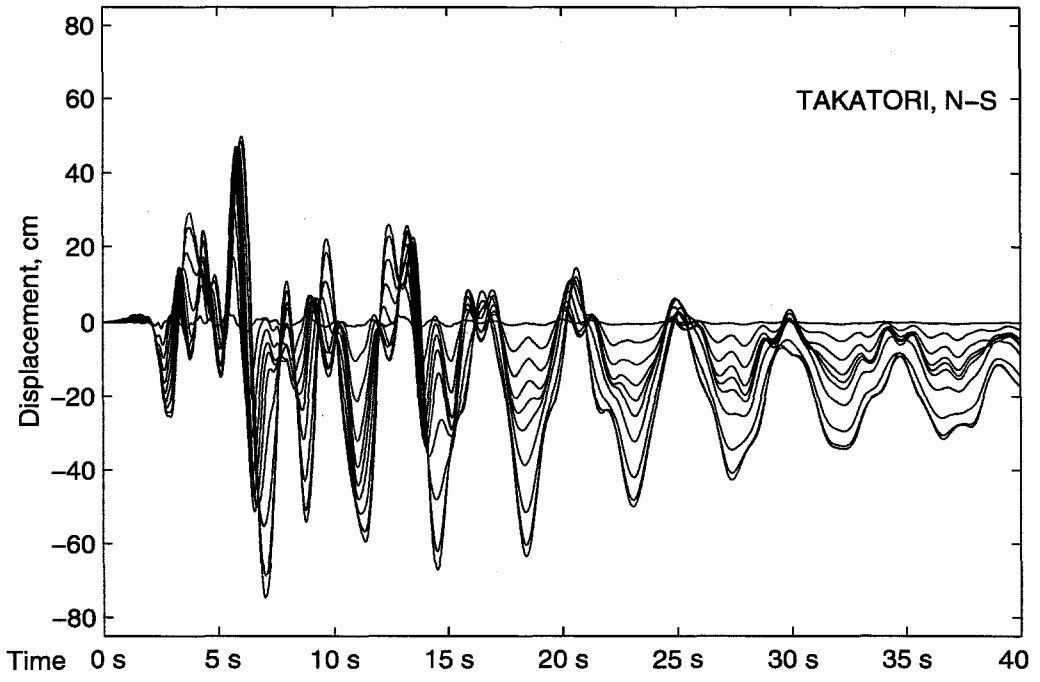

Figure 8.40 Relative floor displacements, inelastic model and Takatori record.

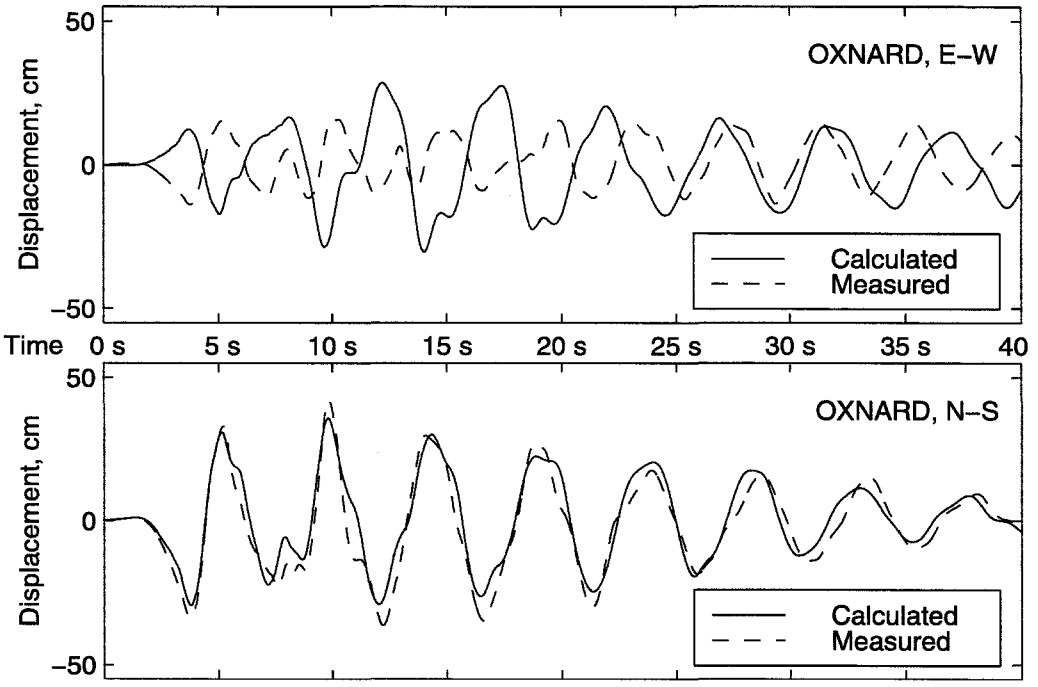

Figure 8.41 Measured vs. calculated for Oxnard record & poor fracture model.

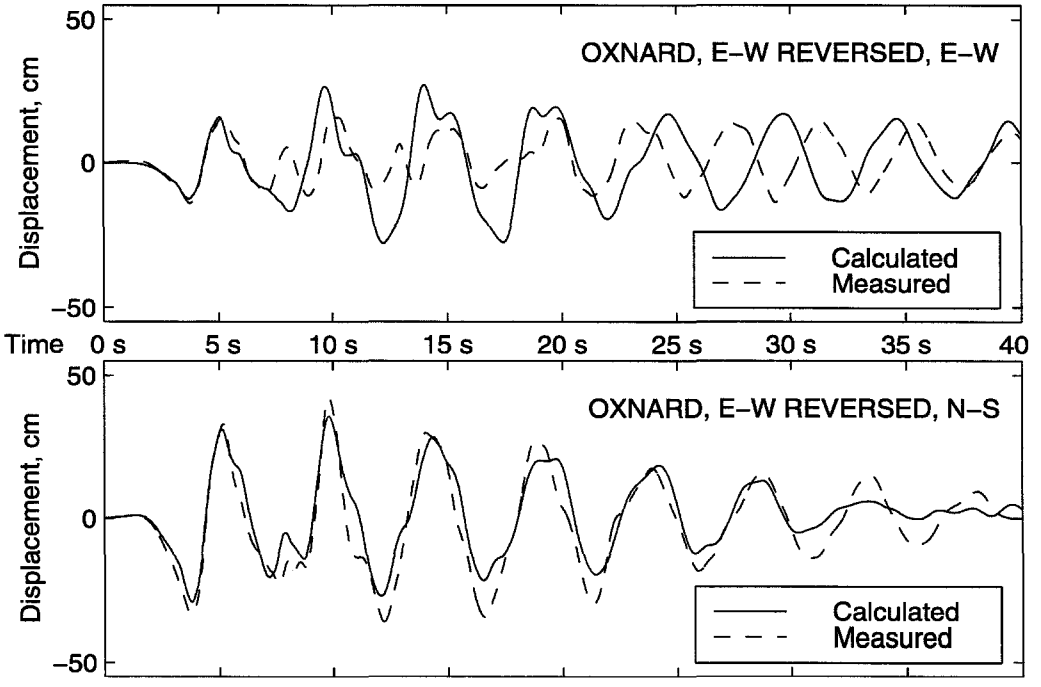

Figure 8.42 Measured vs. calculated for Oxnard record with E-W reversed & poor fracture model.

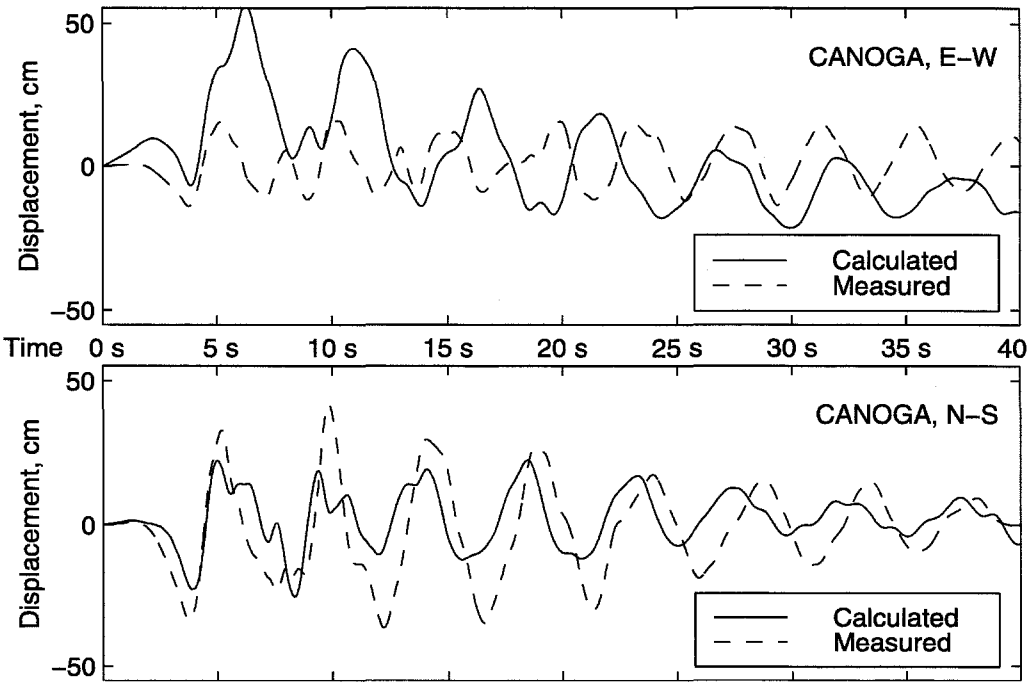

Figure 8.43 Measured vs. calculated for Canoga record & poor fracture model.

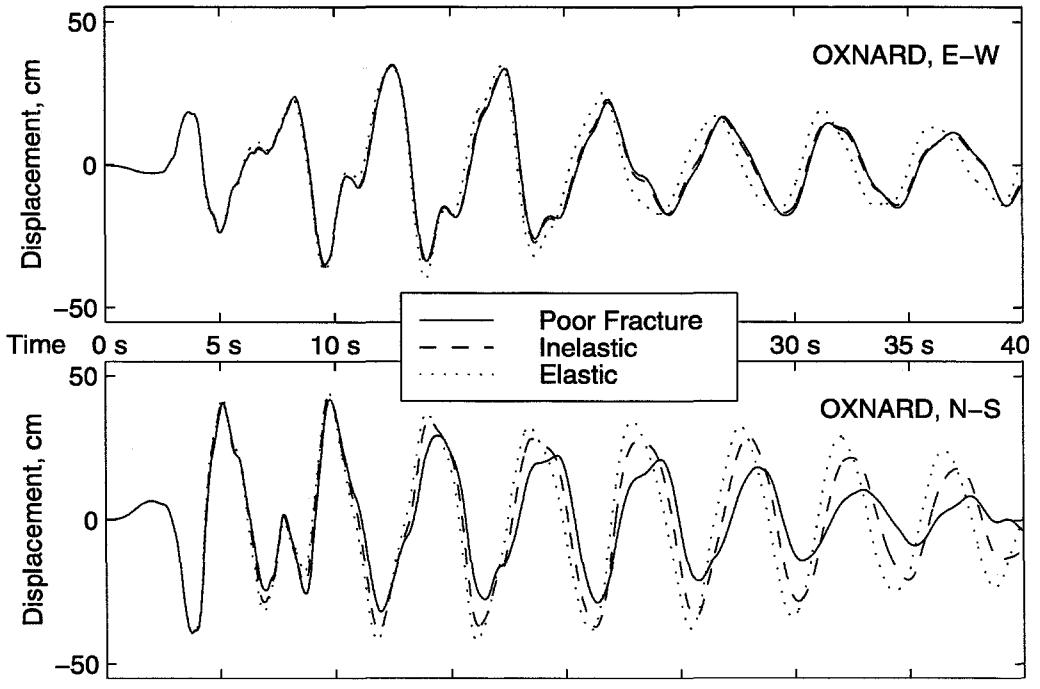

Figure 8.44 Model comparison for Oxnard record.

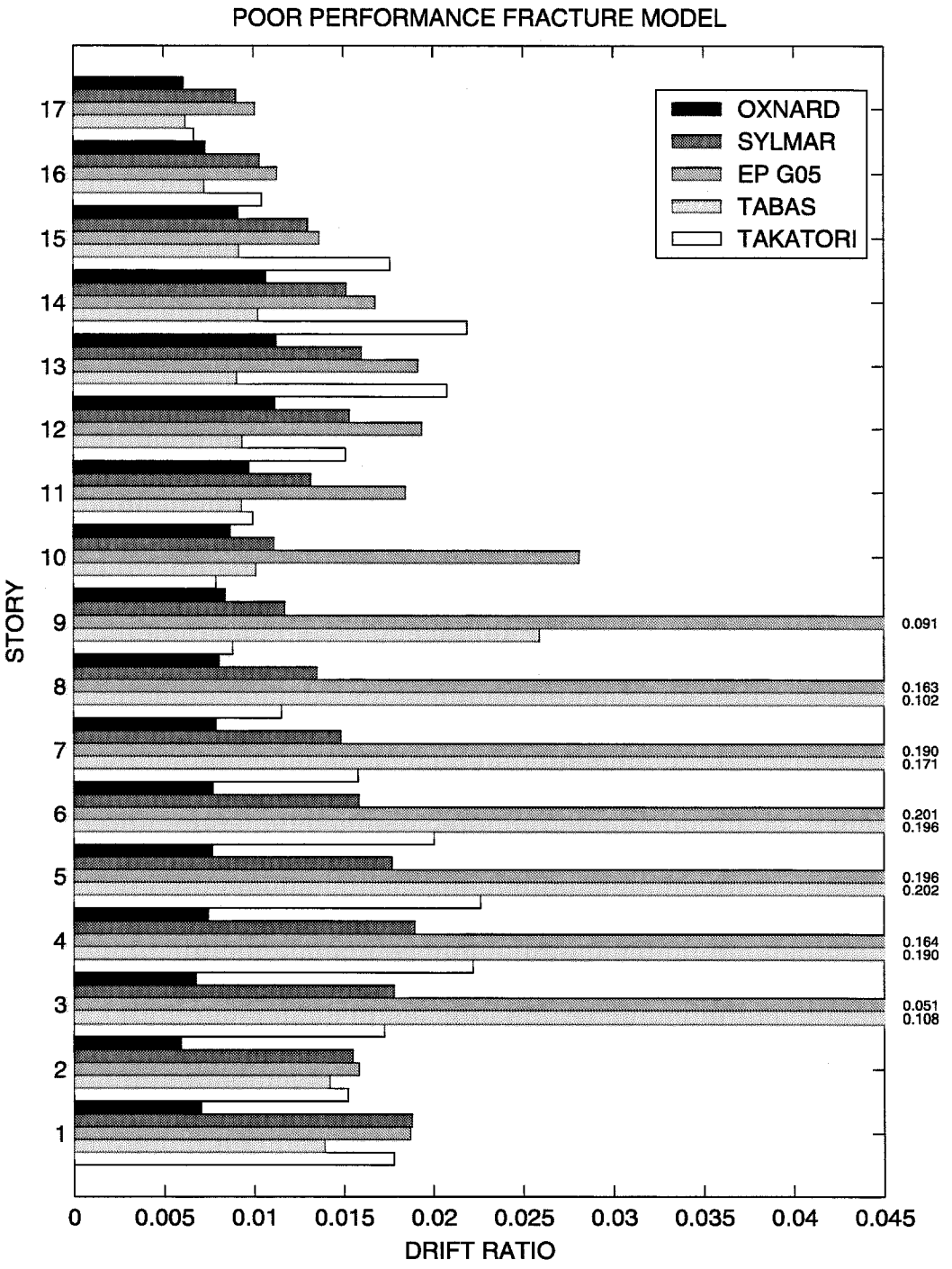

Figure 8.45 17-story building peak drift ratios for poor performance fracture model.

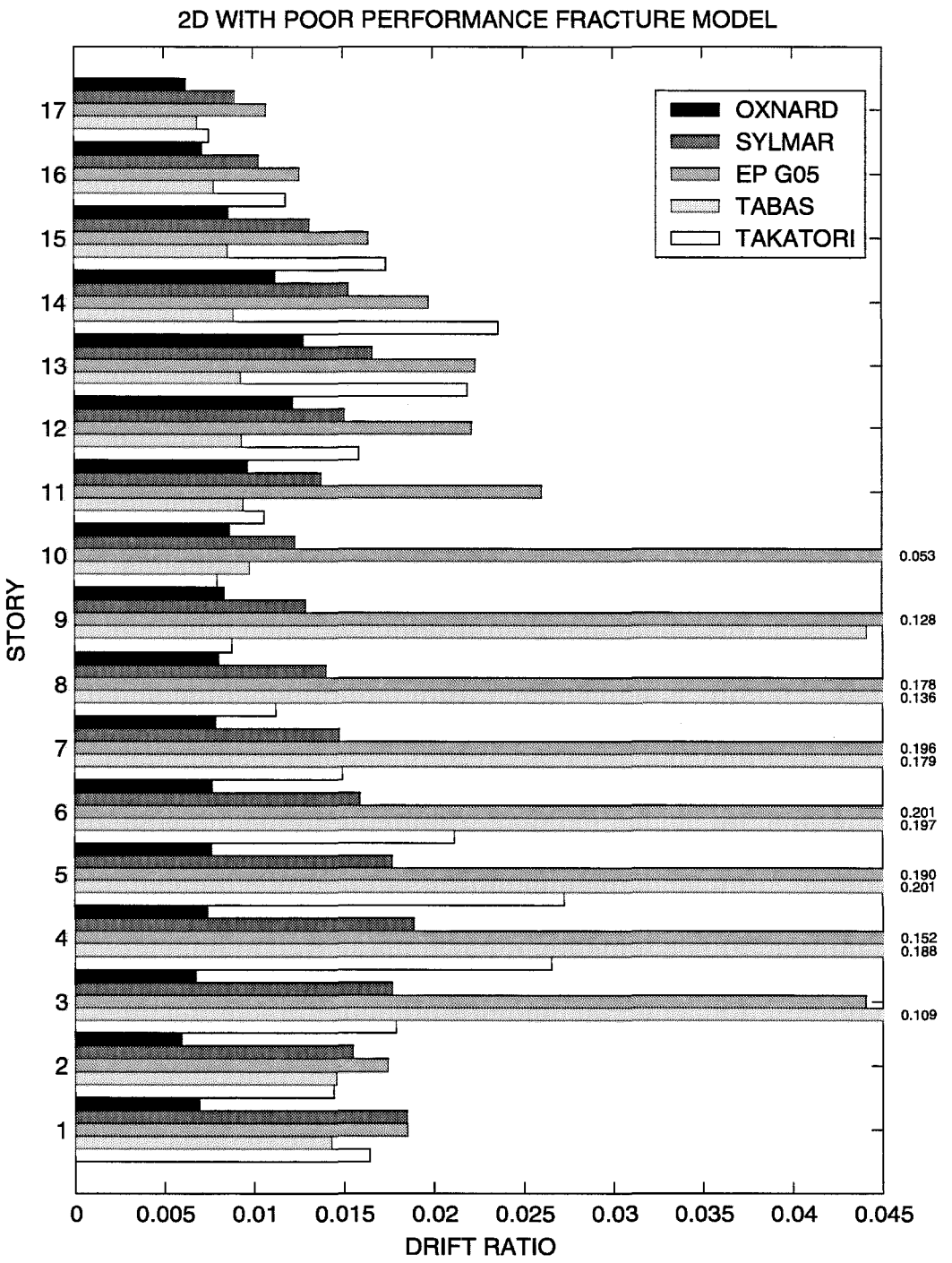

Figure 8.46 17-story building peak drift ratios for 2D poor performance fracture model.

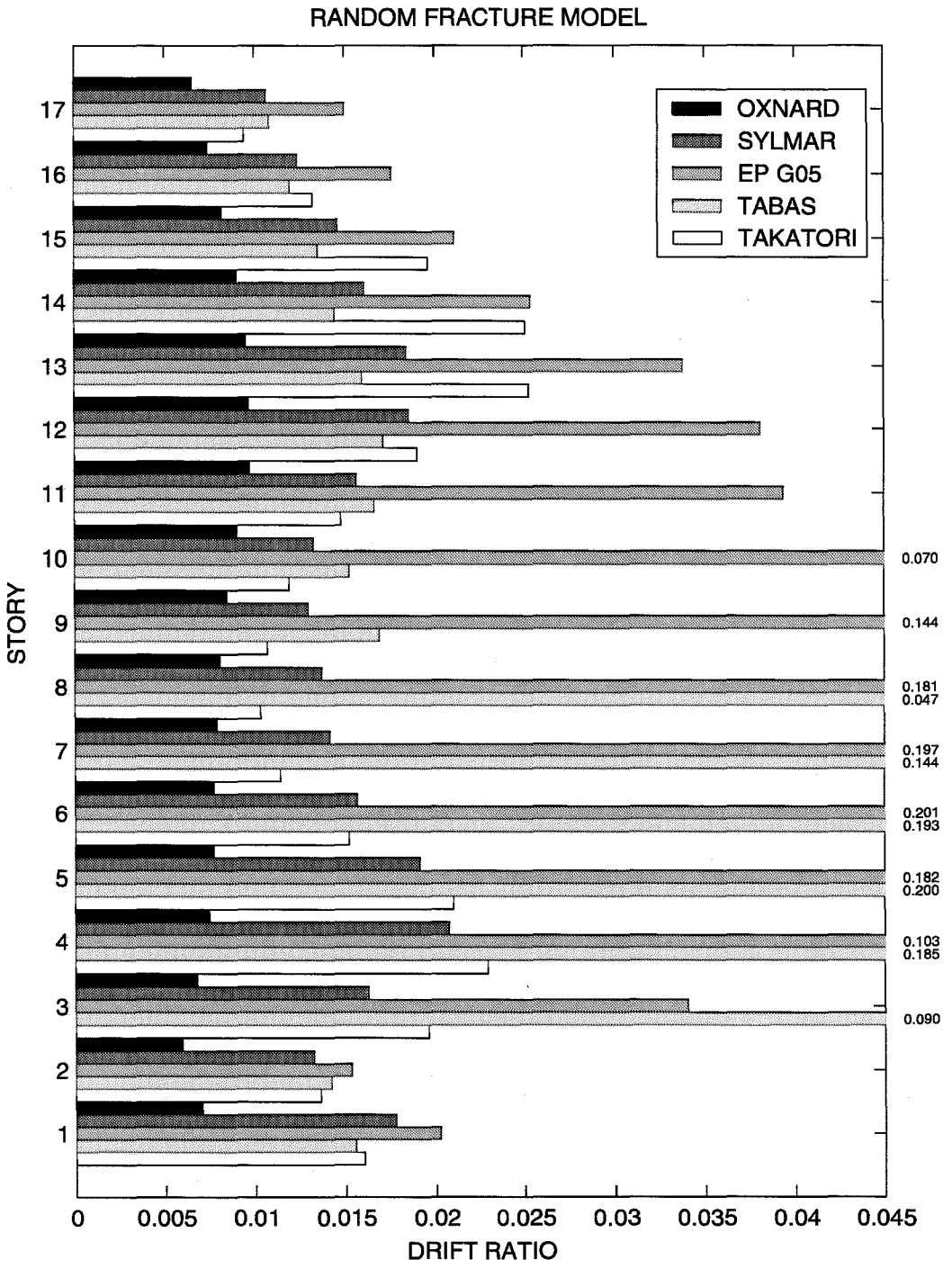

Figure 8.47 17-story building peak drift ratios for random fracture model.

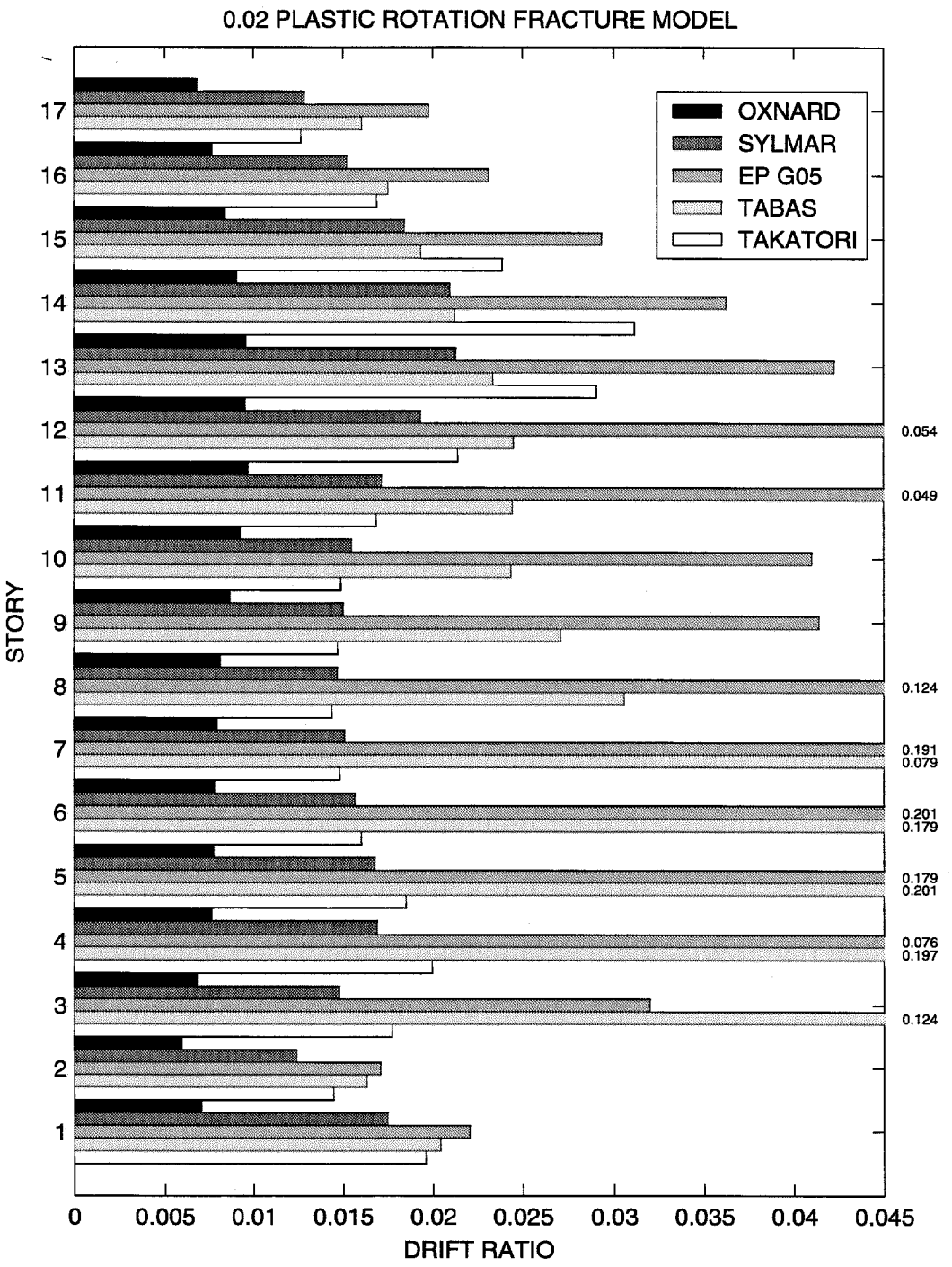

Figure 8.48 17-story building peak drift ratios for 0.02 plastic-rotation fracture model.

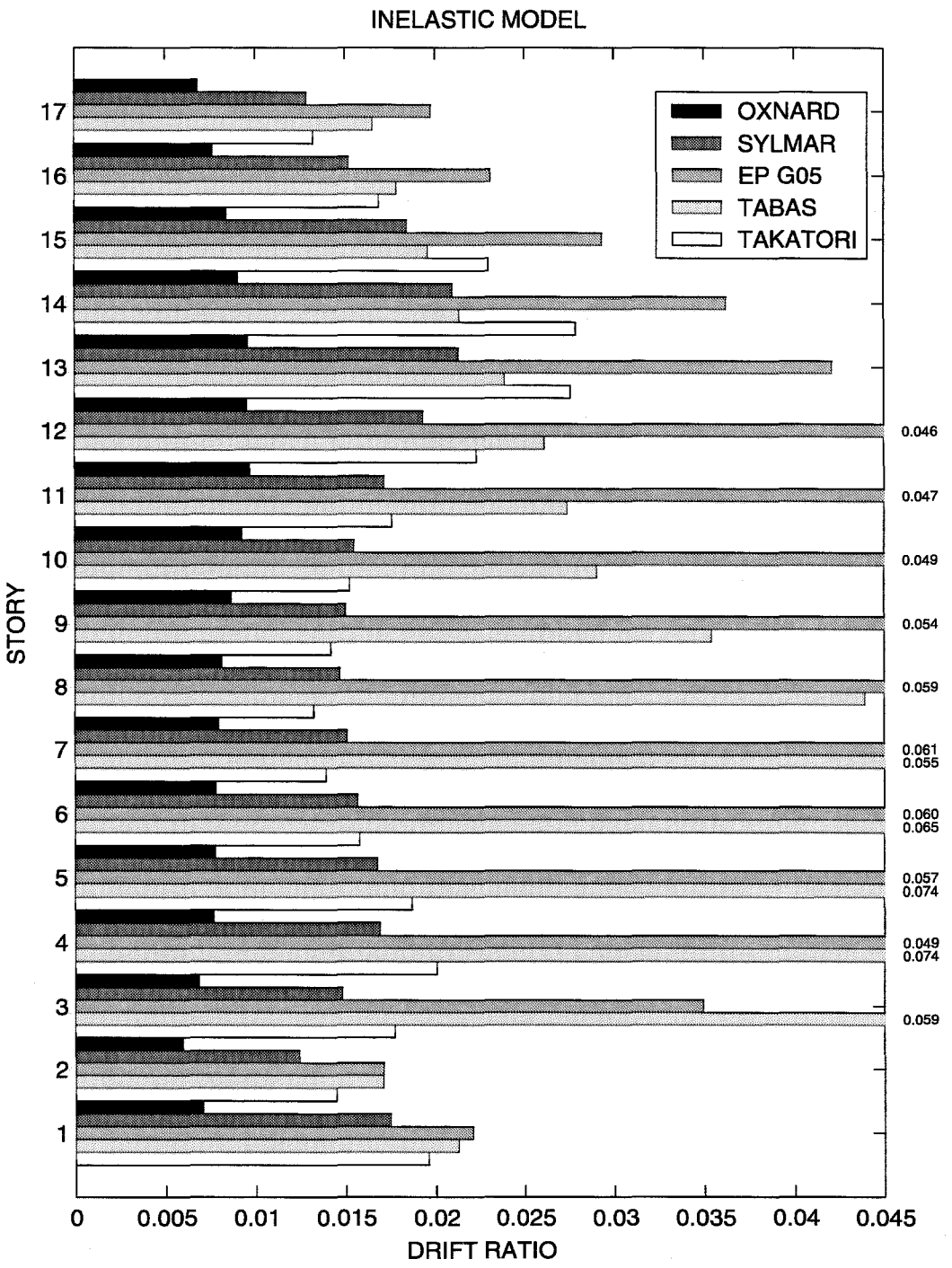

Figure 8.49 17-story building peak drift ratios for inelastic model.

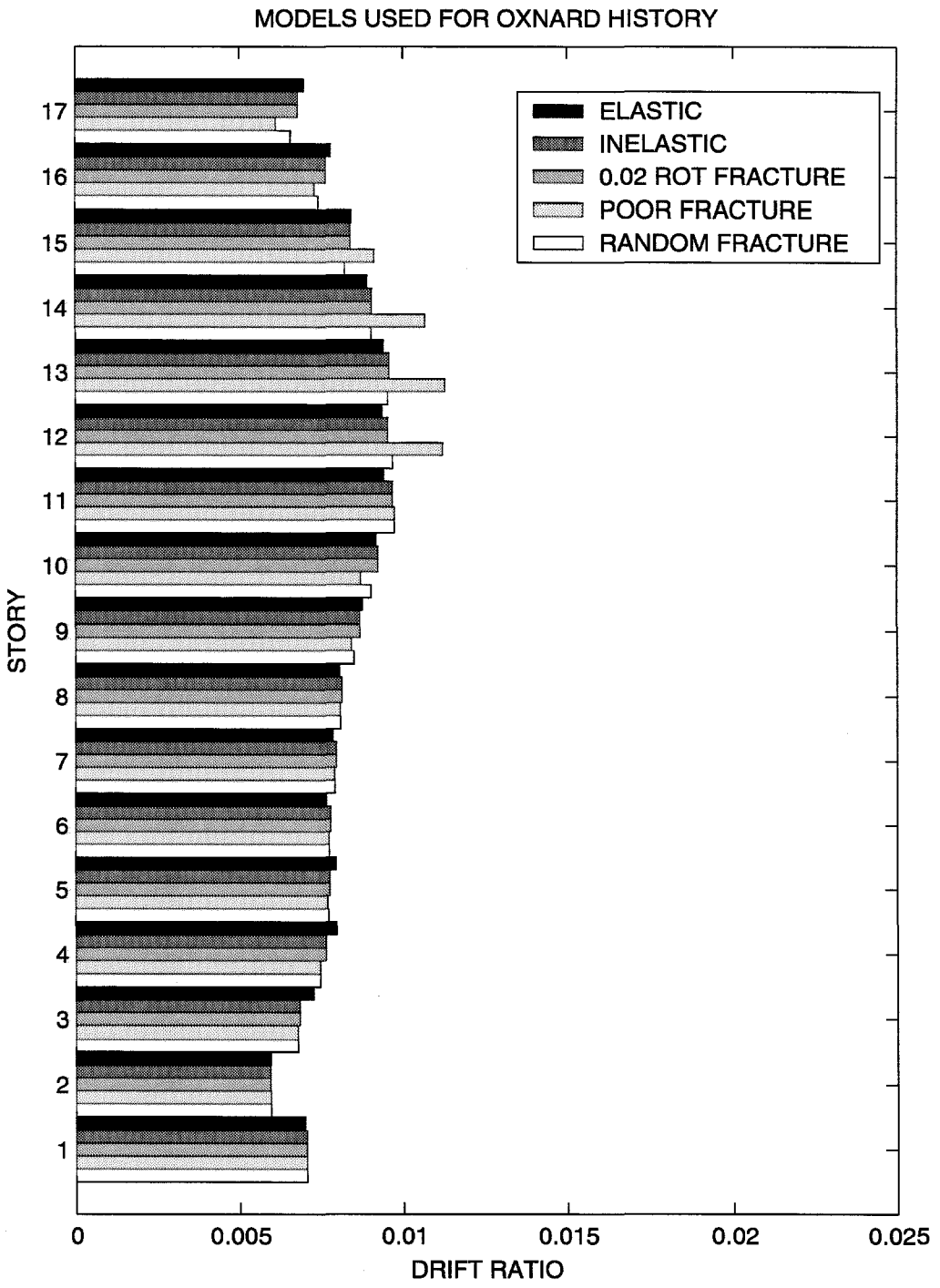

Figure 8.50 17-story building peak drift ratios for Oxnard history.

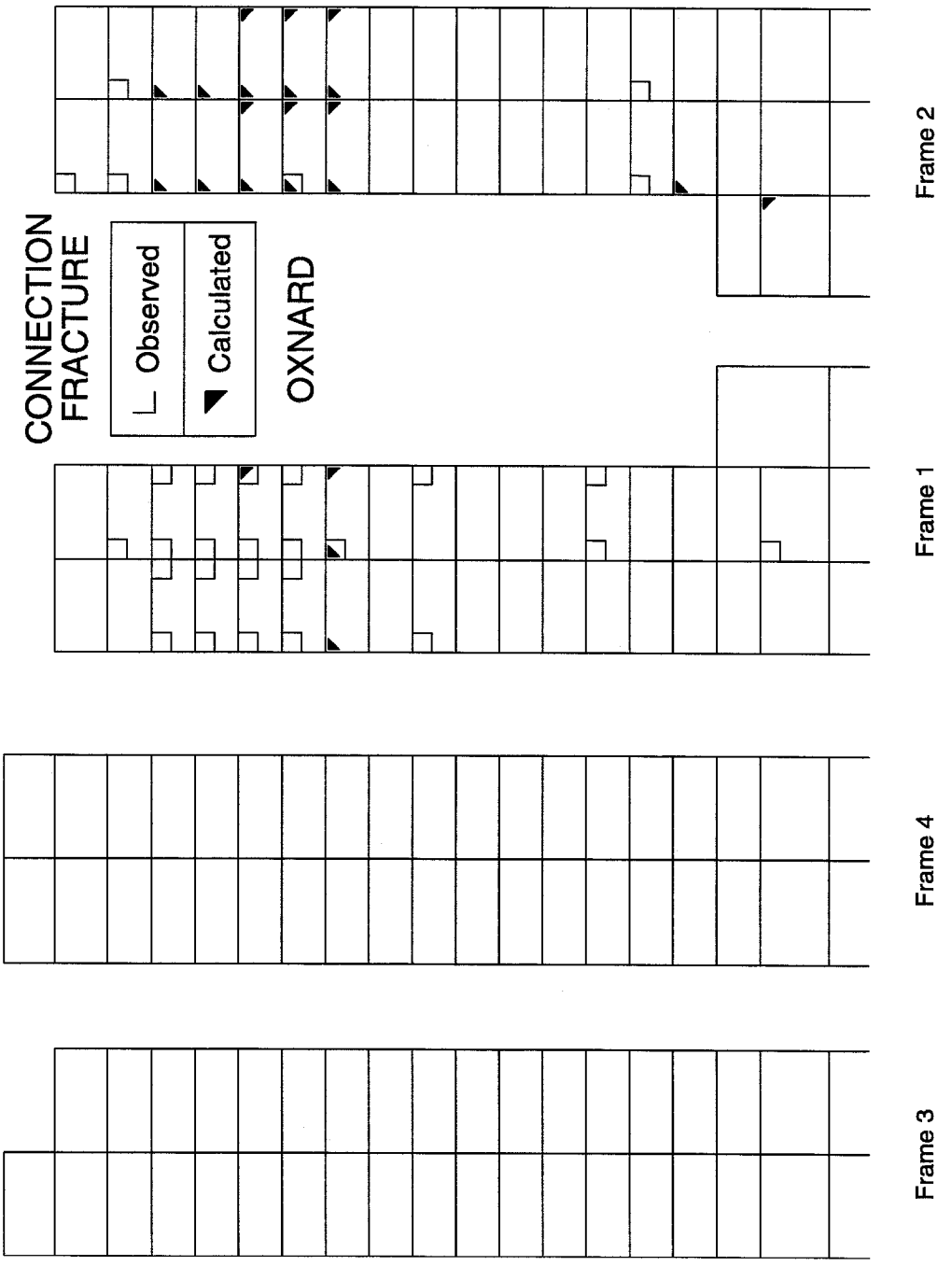

Figure 8.51 Fracture of member ends, poor performance model and Oxnard record.

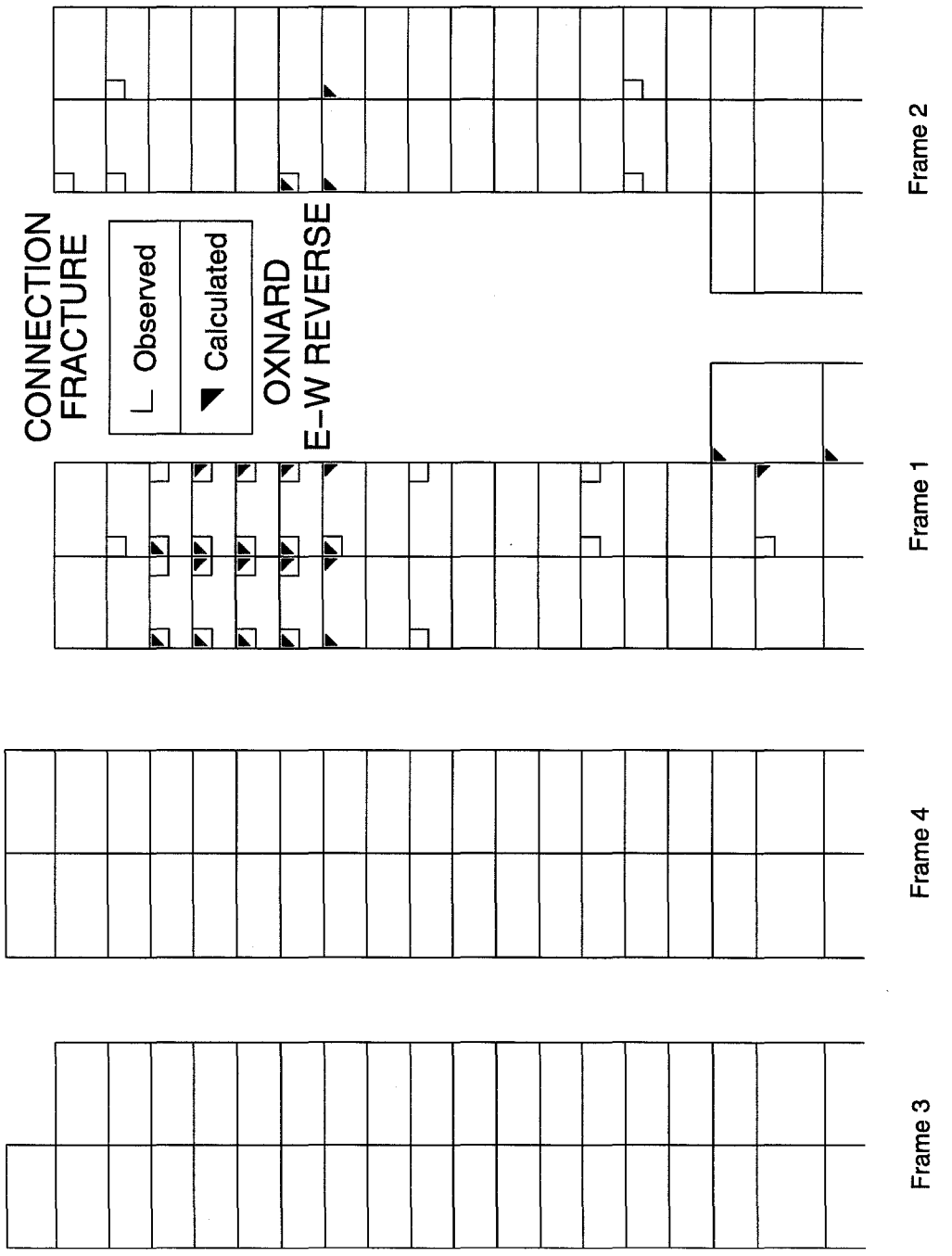

Figure 8.52 Fracture of member ends, poor performance model and Oxnard record with E-W reversed.

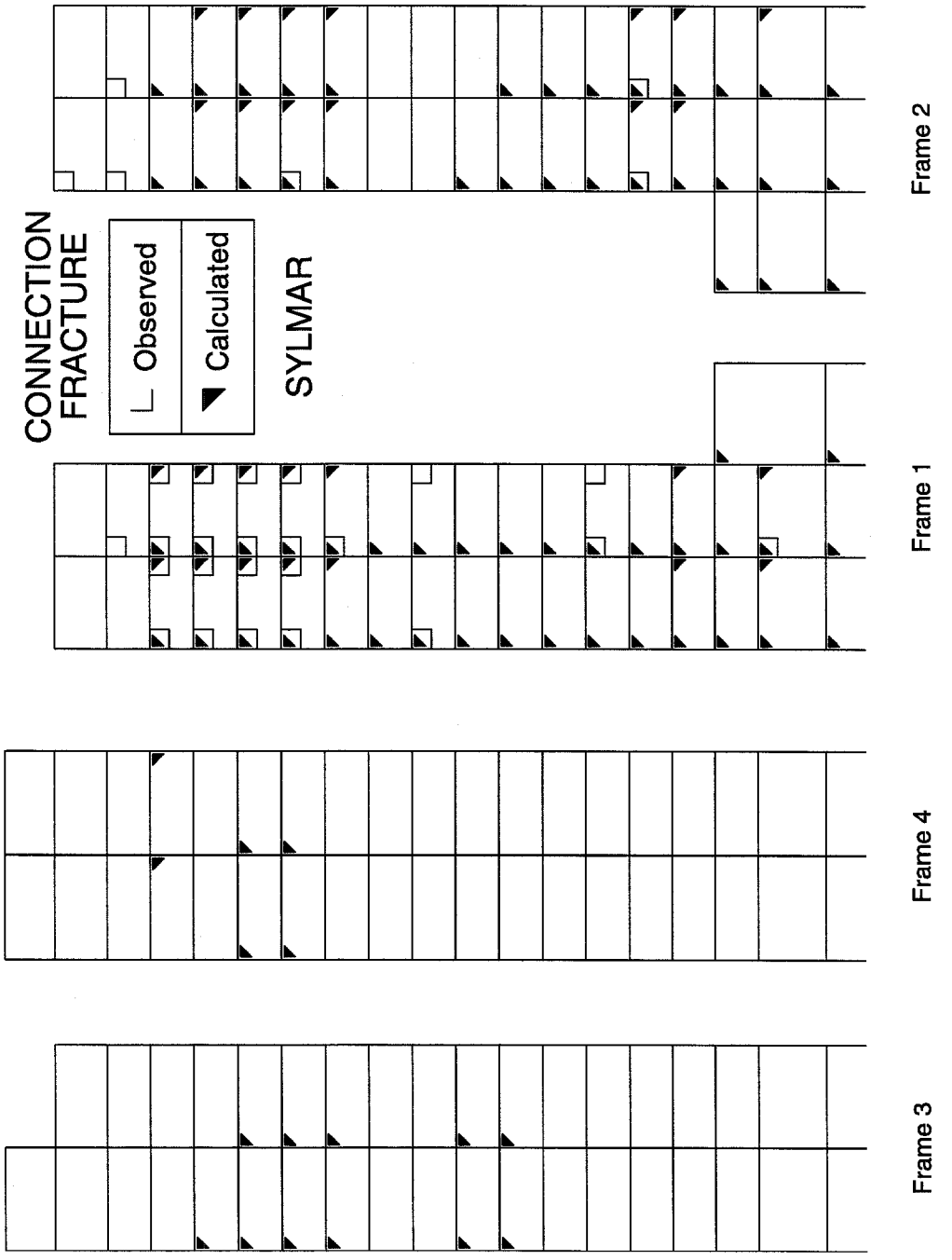

Figure 8.53 Fracture of member ends, poor performance model and Sylmar record.

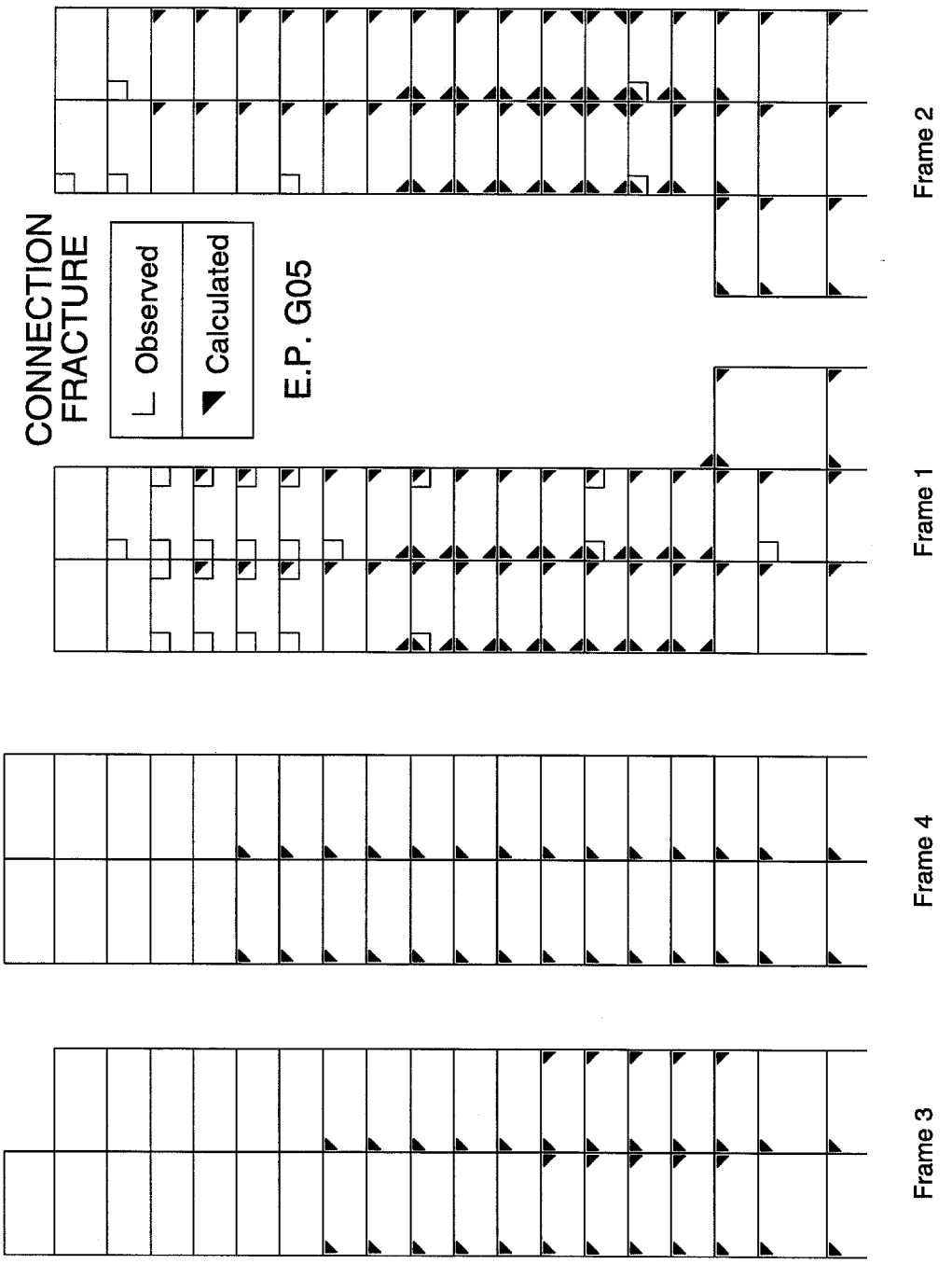

Figure 8.54 Fracture of member ends, poor performance model and E. P. G05 record.

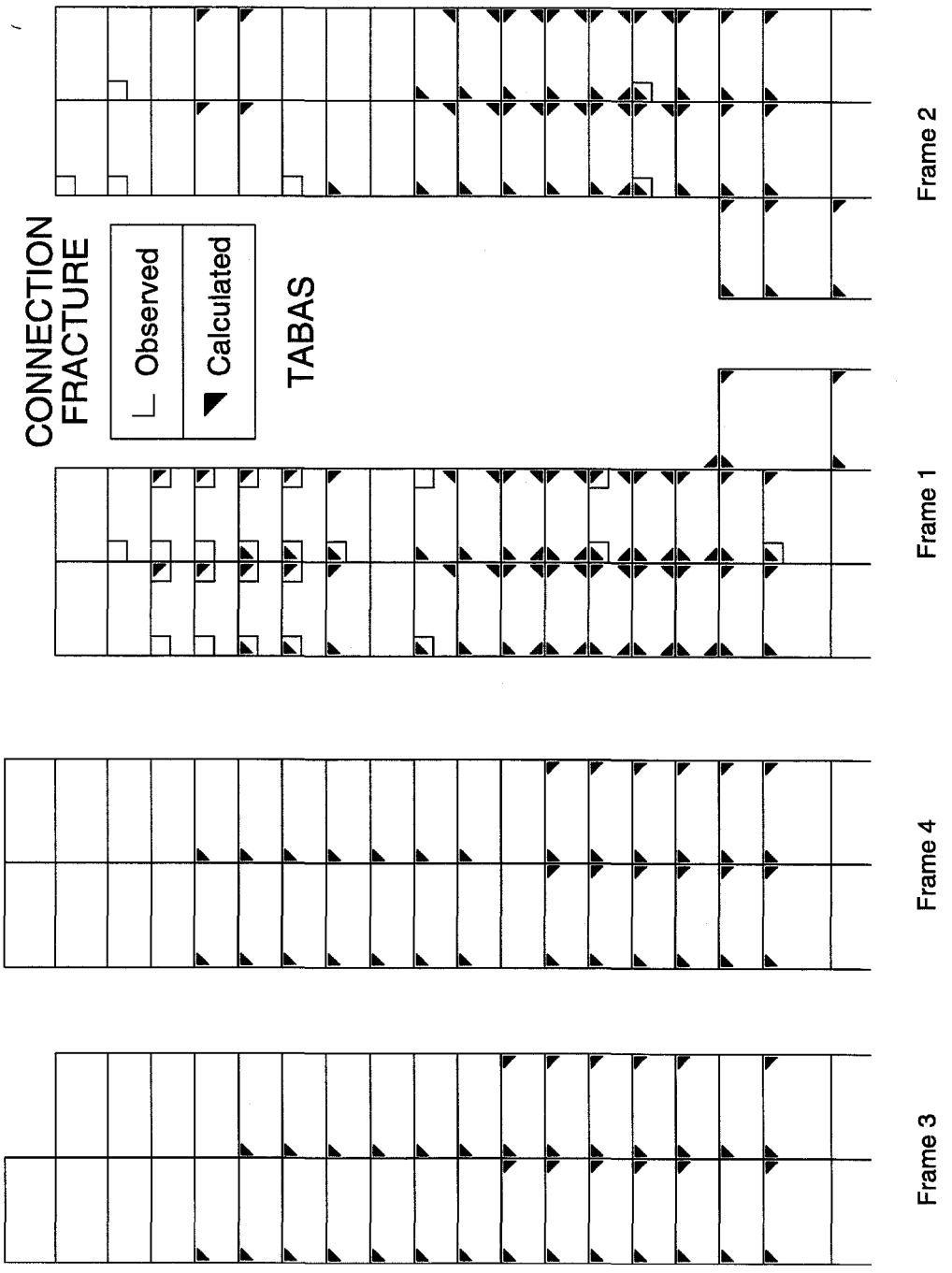

Figure 8.55 Fracture of member ends, poor performance model and Tabas record.

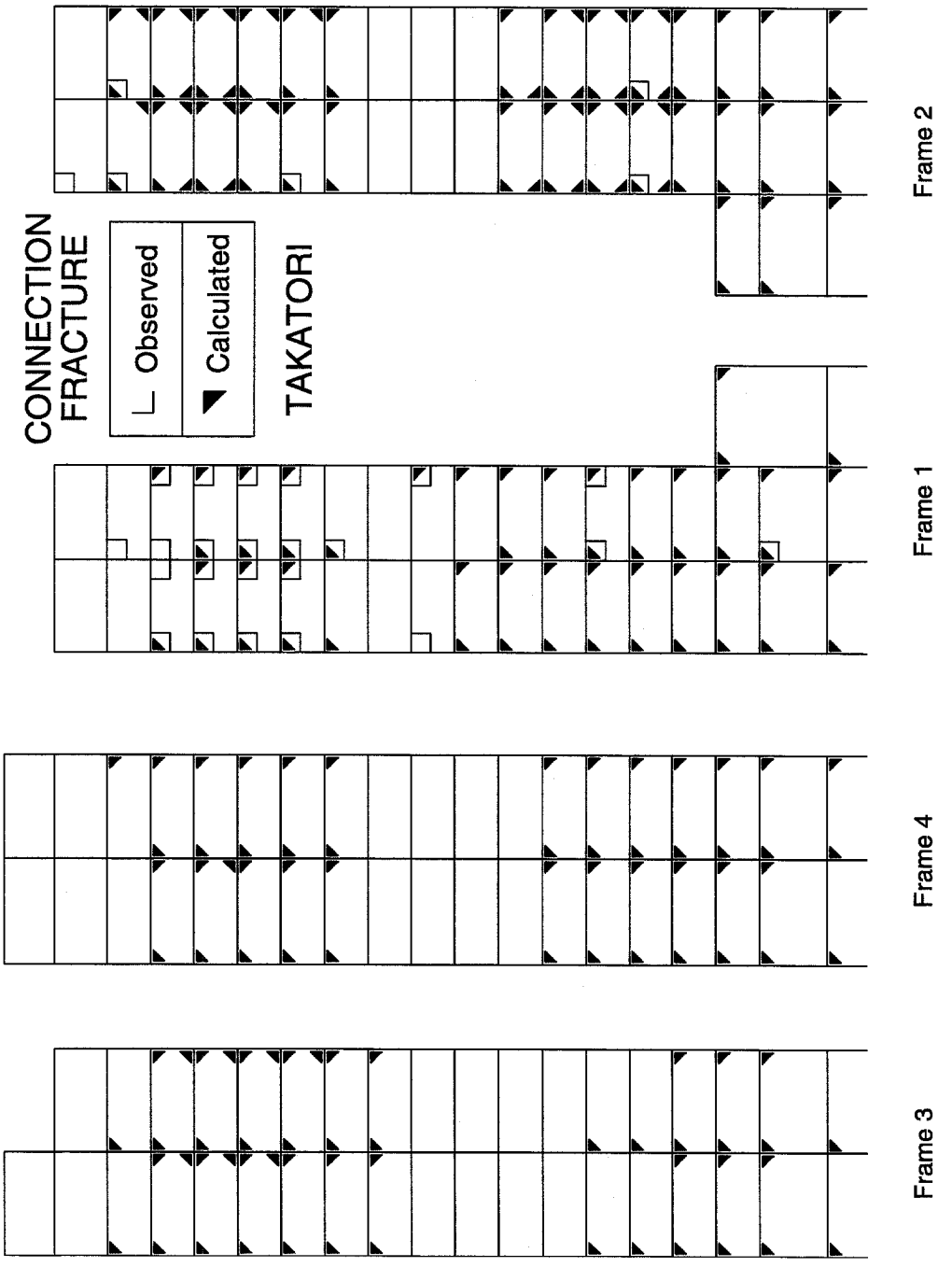

Figure 8.56 Fracture of member ends, poor performance model and Takatori record.

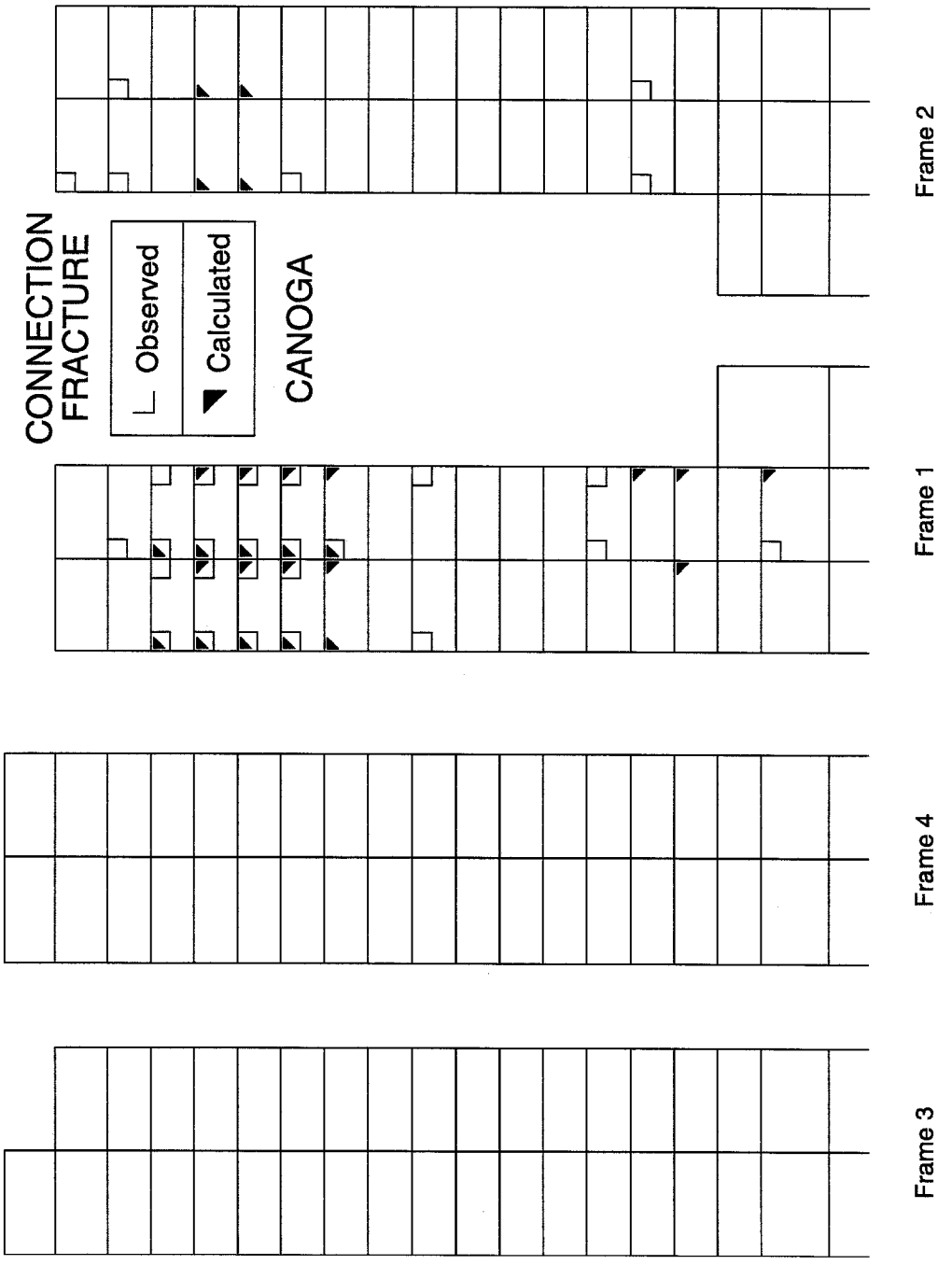

Figure 8.57 Fracture of member ends, poor performance model and Canoga record.

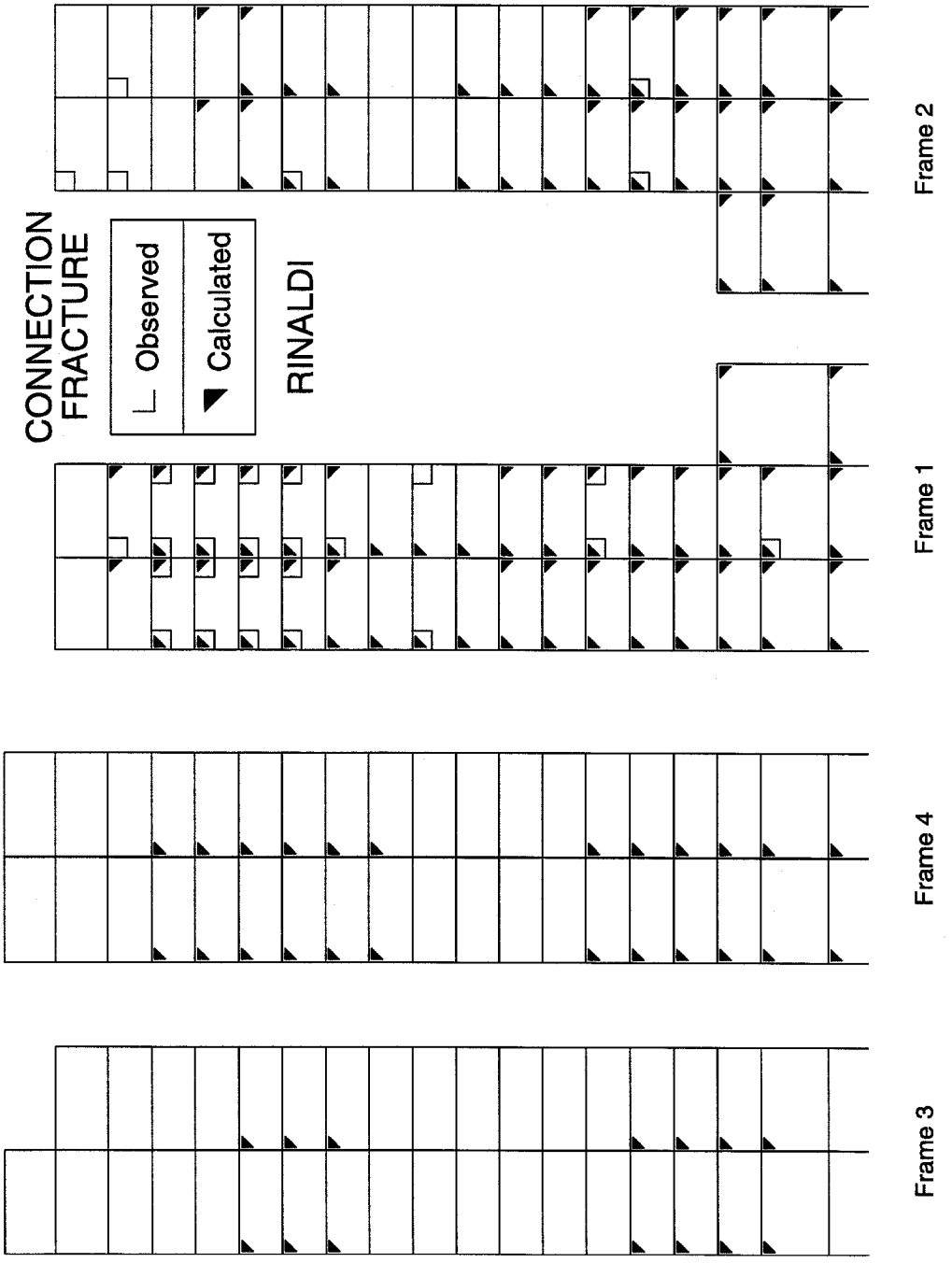

Figure 8.58 Fracture of member ends, poor performance model and Rinaldi record.

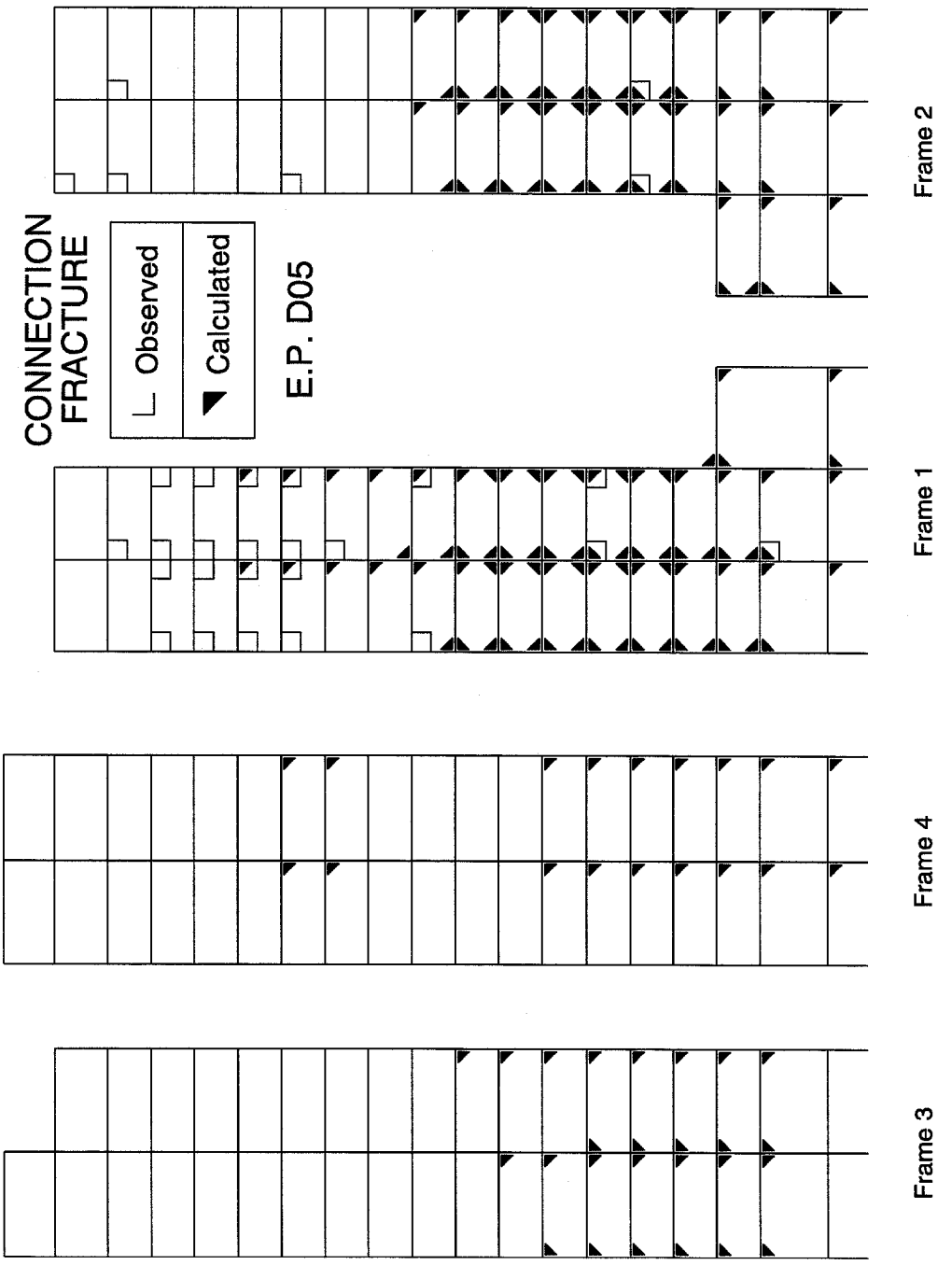

Figure 8.59 Fracture of member ends, poor performance model and E. P. D05 record.

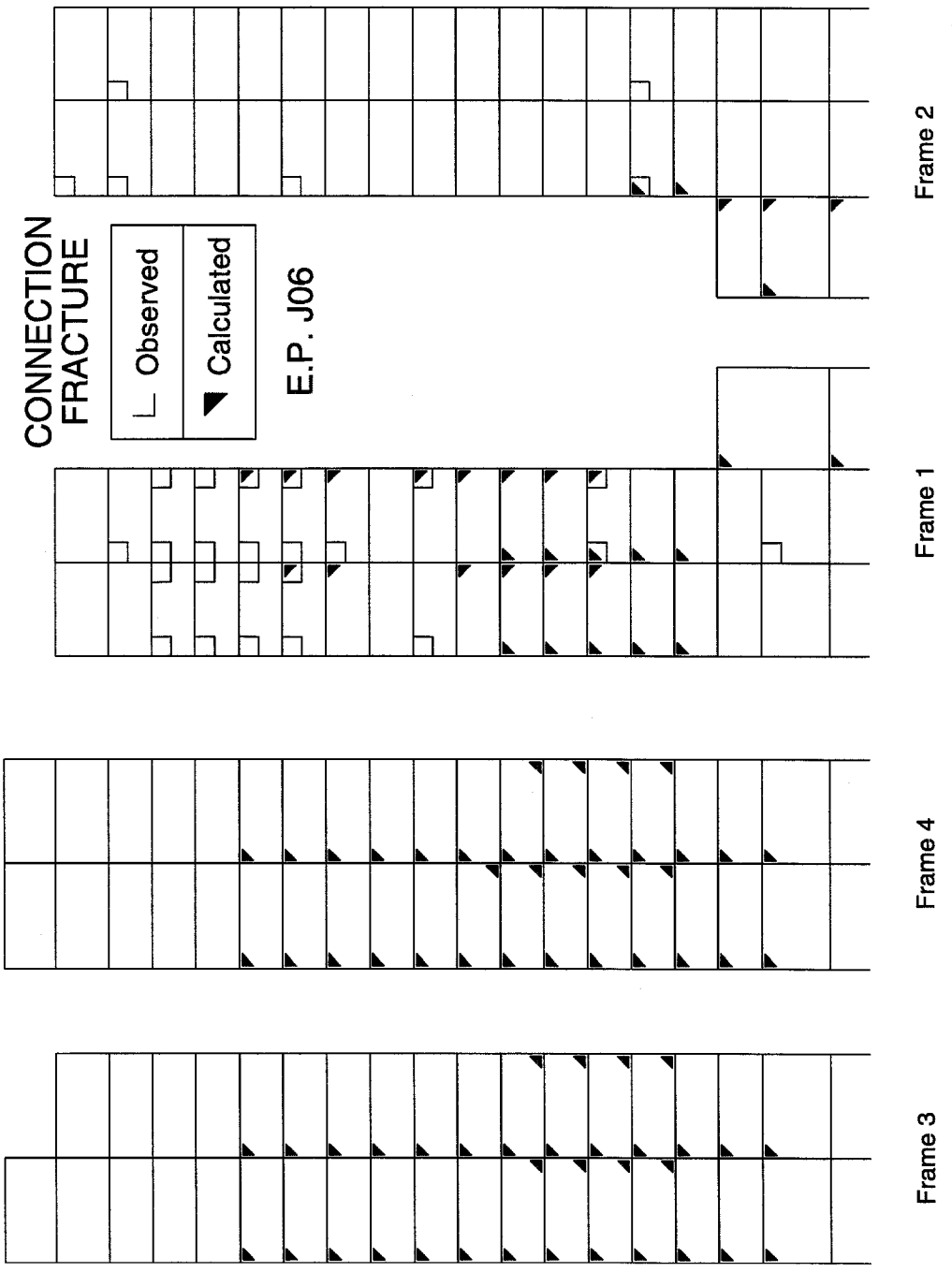

Figure 8.60 Fracture of member ends, poor performance model and E. P. J06 record.

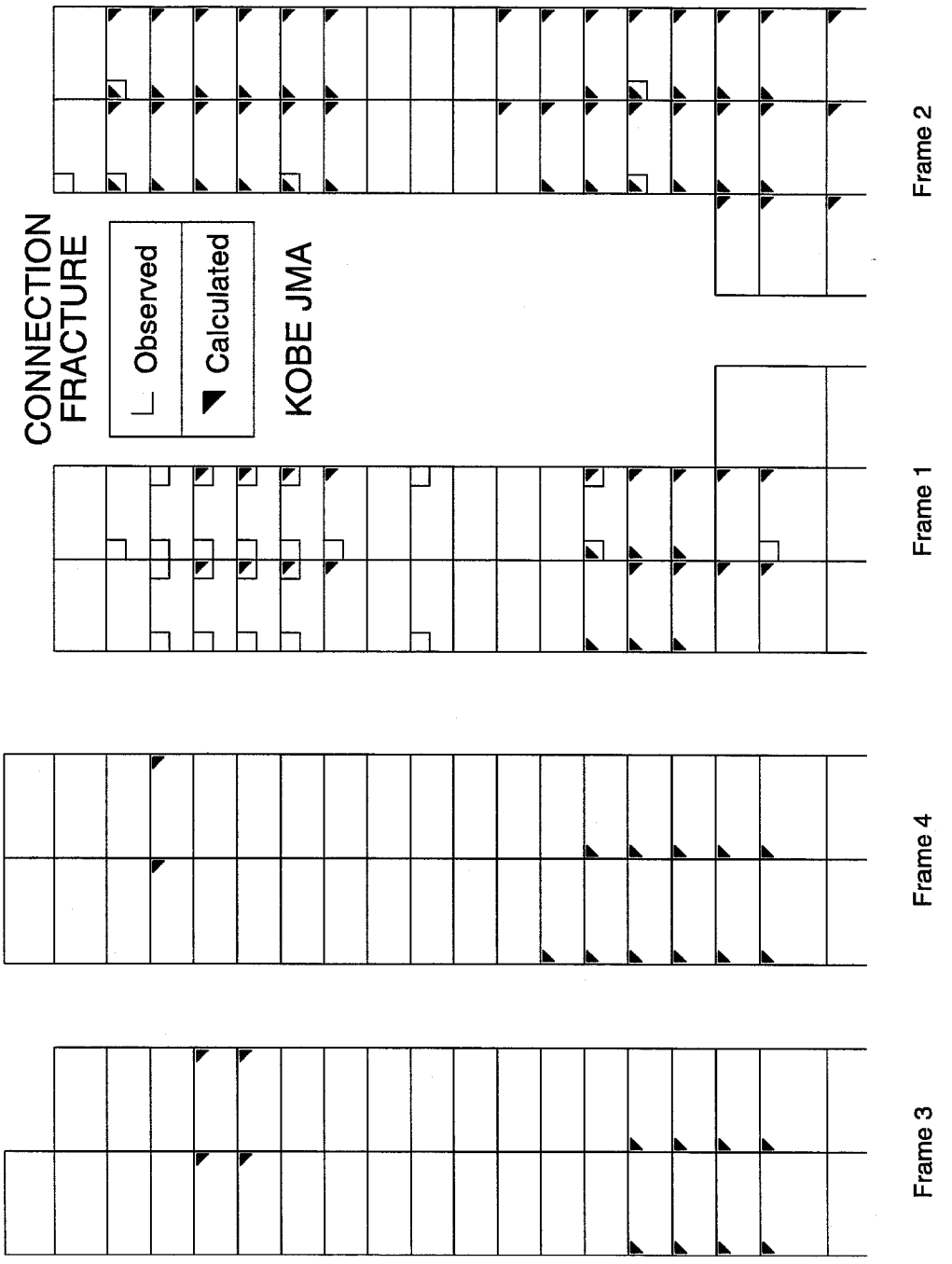

Figure 8.61 Fracture of member ends, poor performance model and Kobe JMA record.

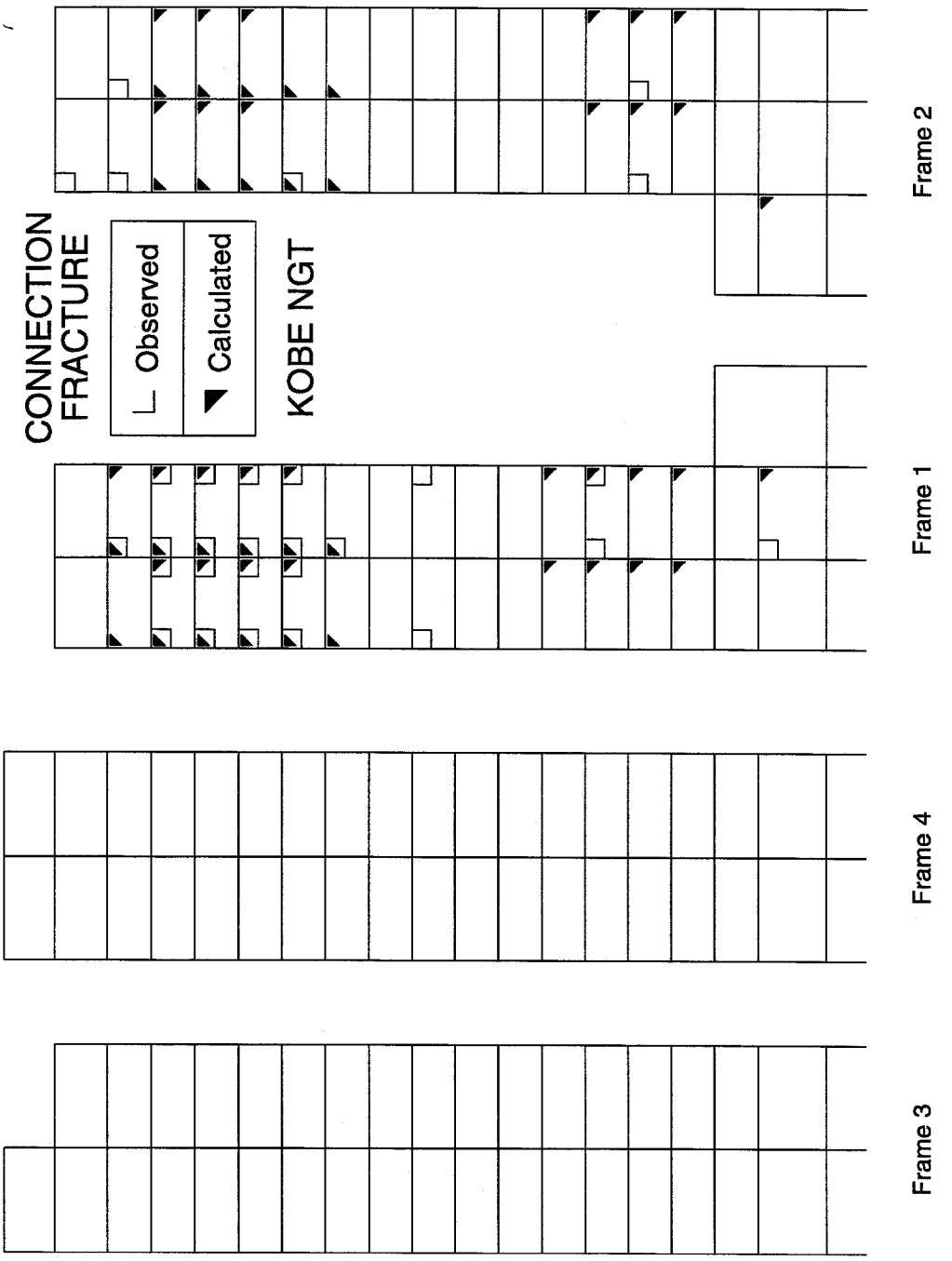

Figure 8.62 Fracture of member ends, poor performance model and Kobe NGT record.

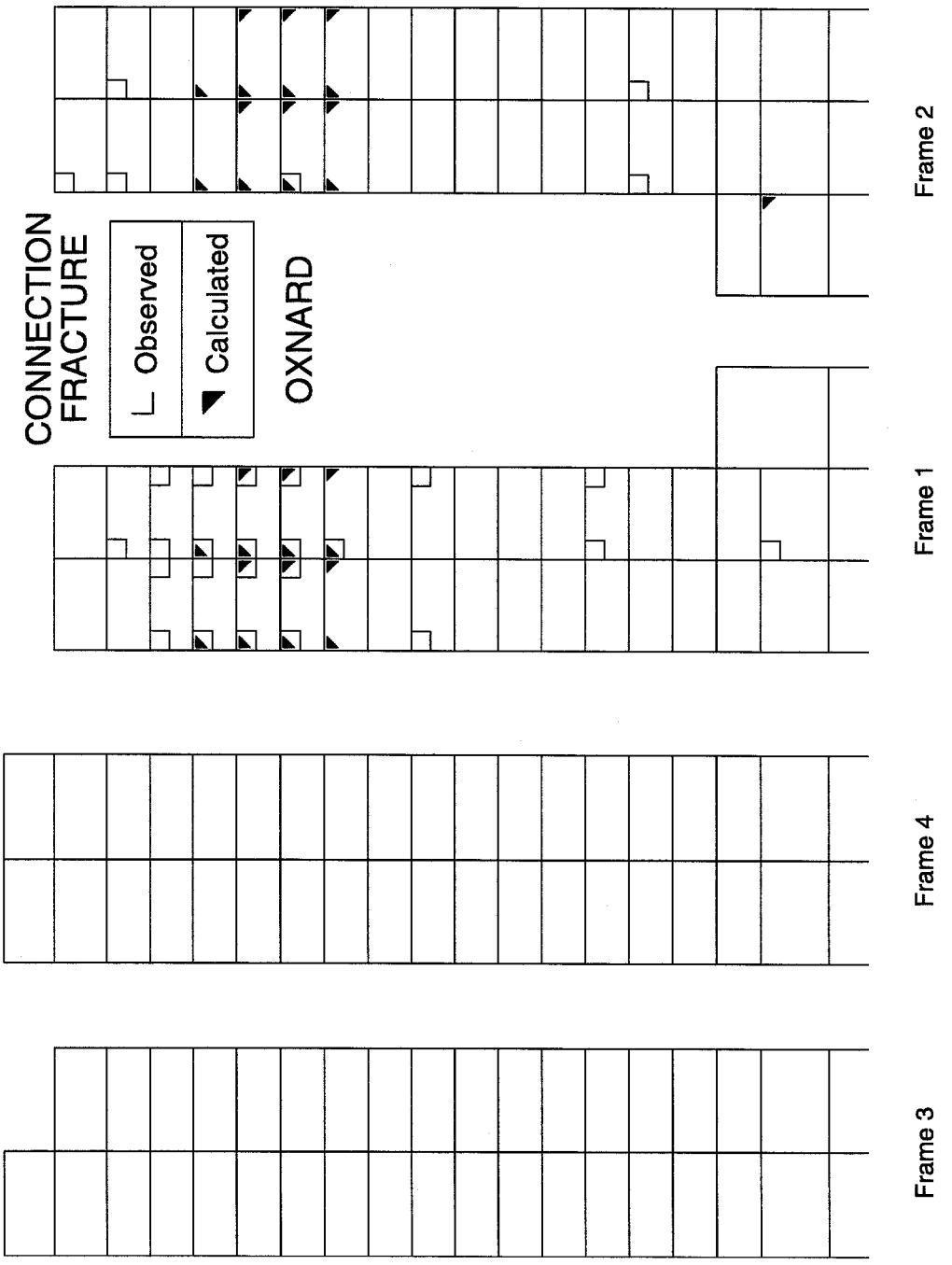

Figure 8.63 Fracture of member ends, 2D poor performance model and Oxnard record.

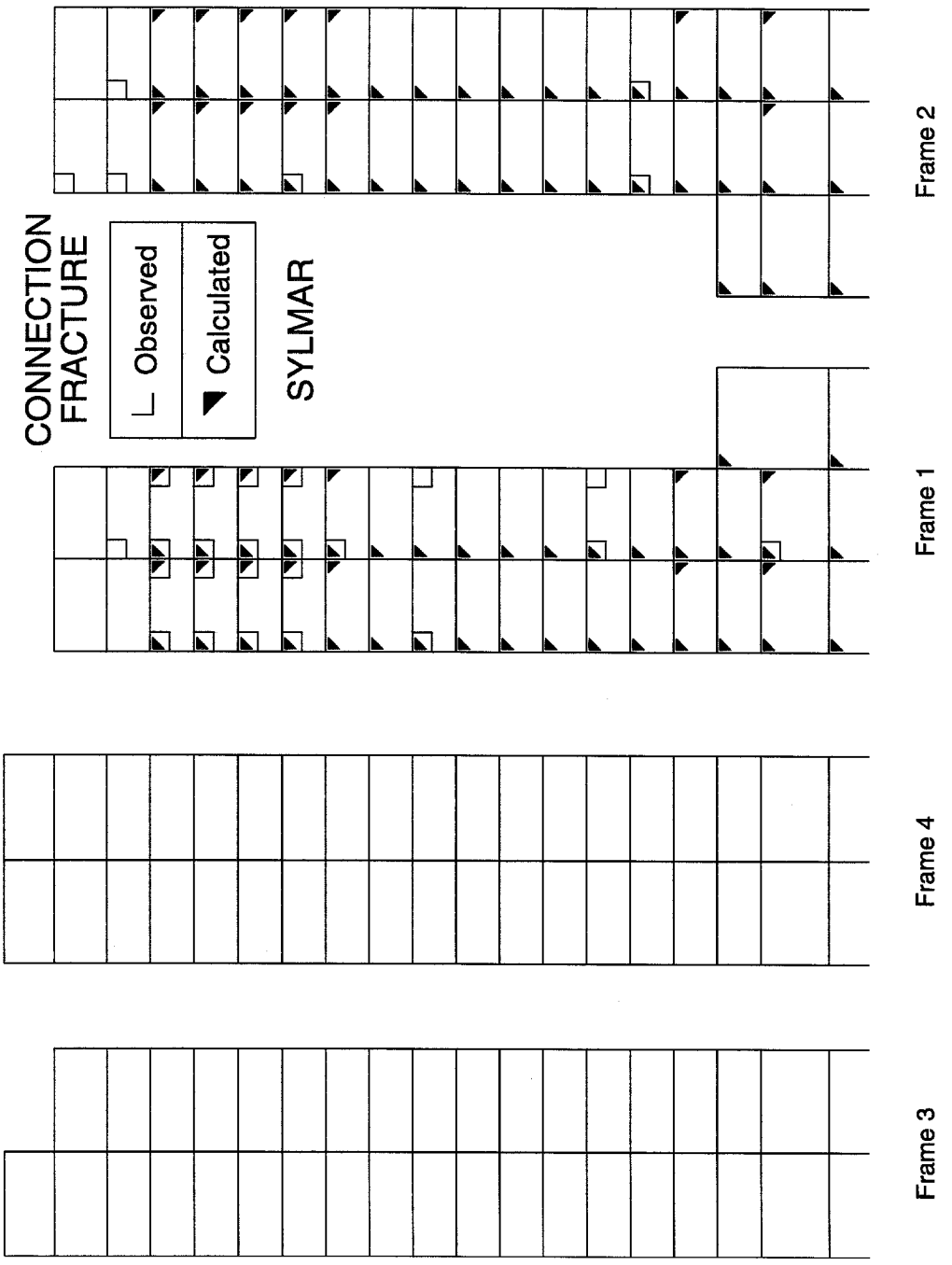

Figure 8.64 Fracture of member ends, 2D poor performance model and Sylmar record.

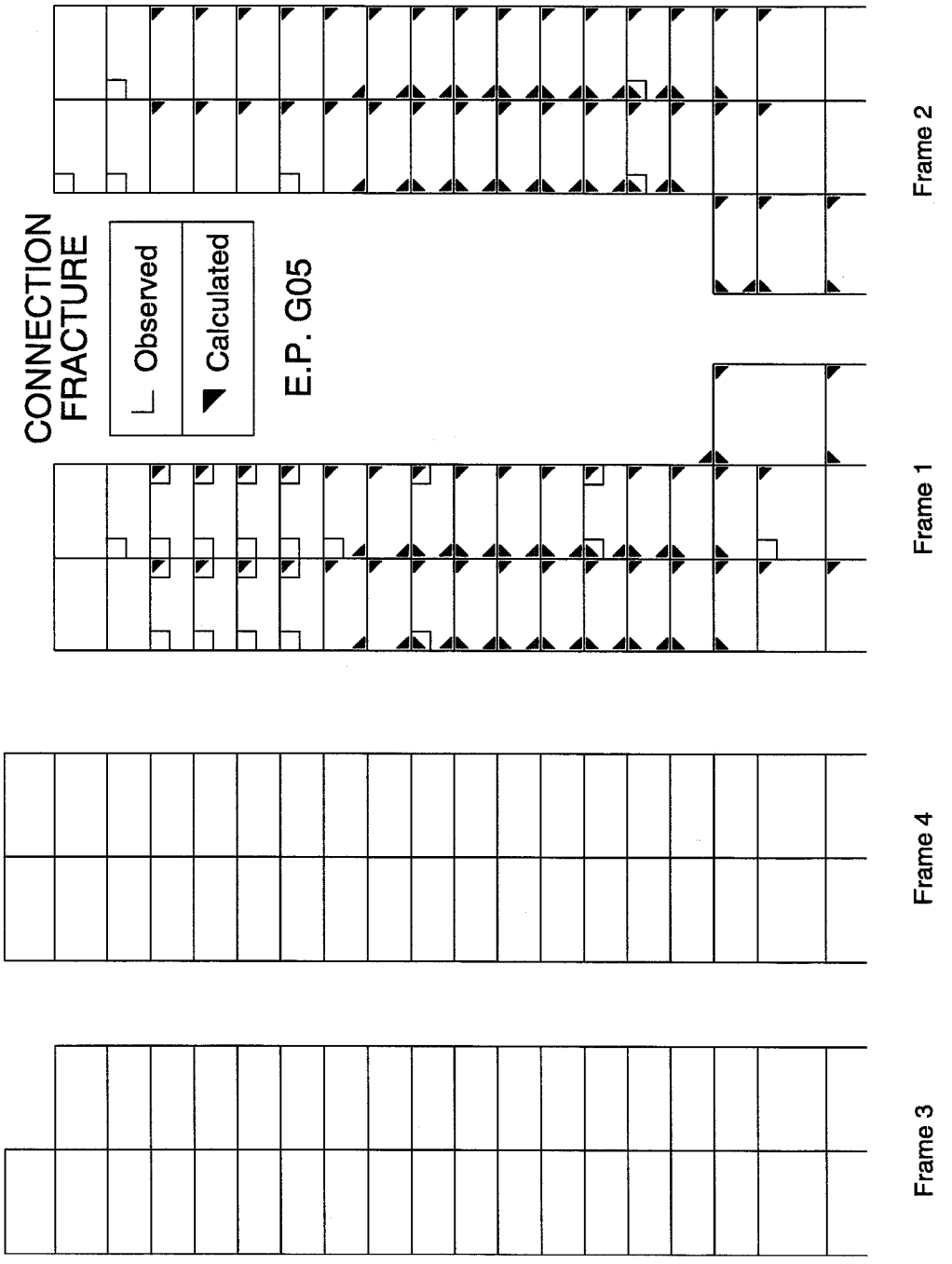

Figure 8.65 Fracture of member ends, 2D poor performance model and E. P. G05 record.

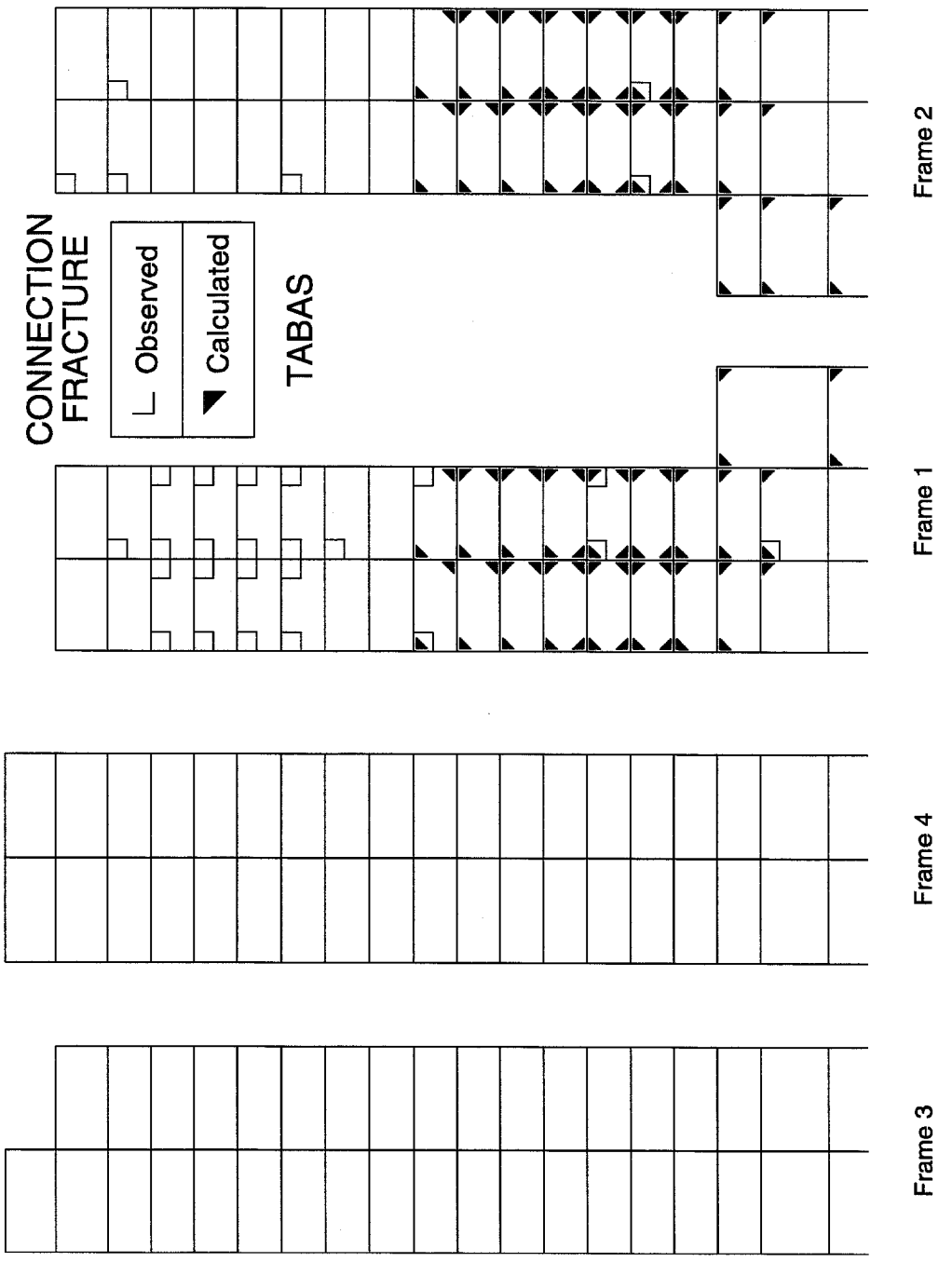

Figure 8.66 Fracture of member ends, 2D poor performance model and Tabas record.

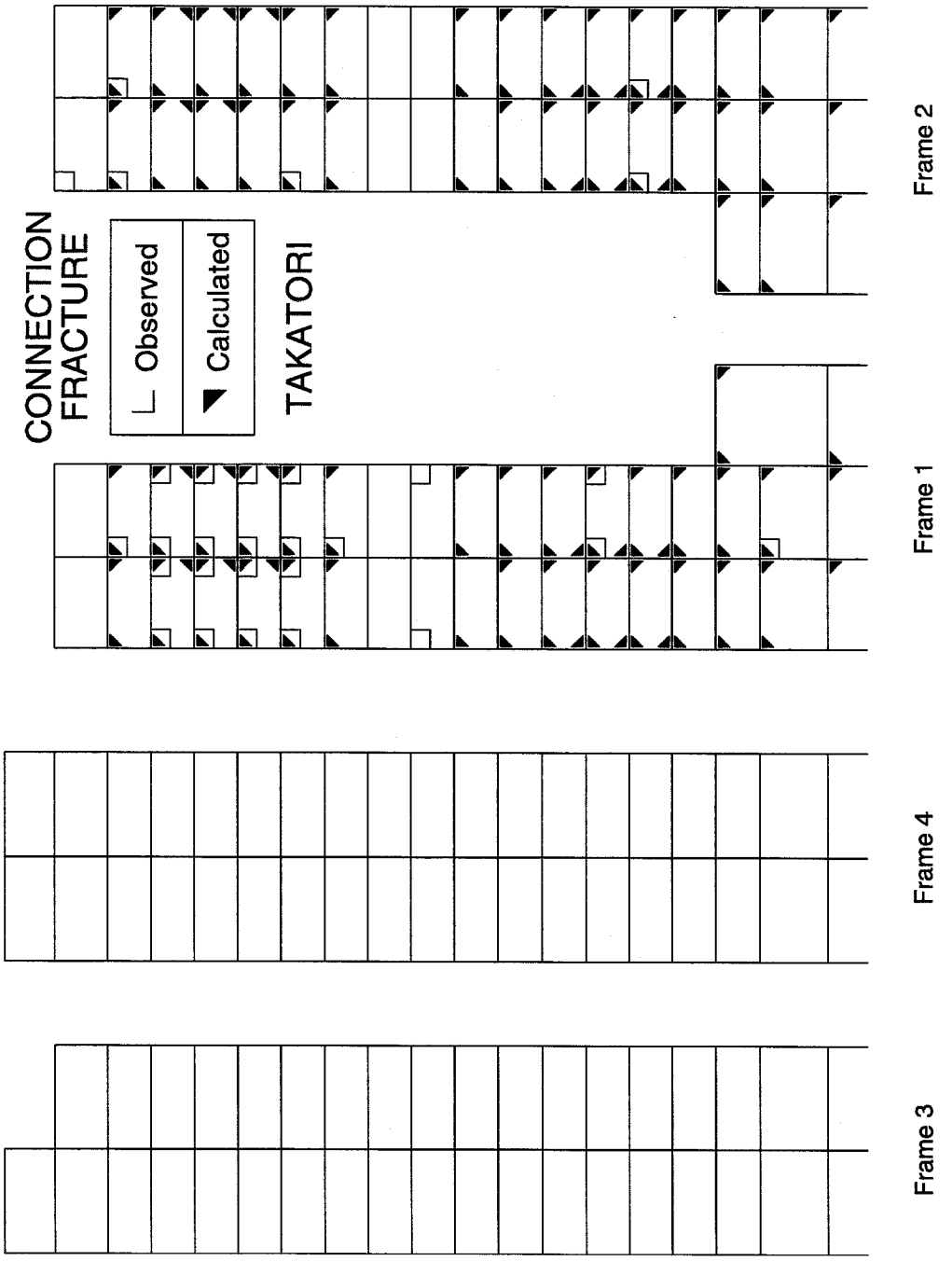

Figure 8.67 Fracture of member ends, 2D poor performance model and Takatori record.

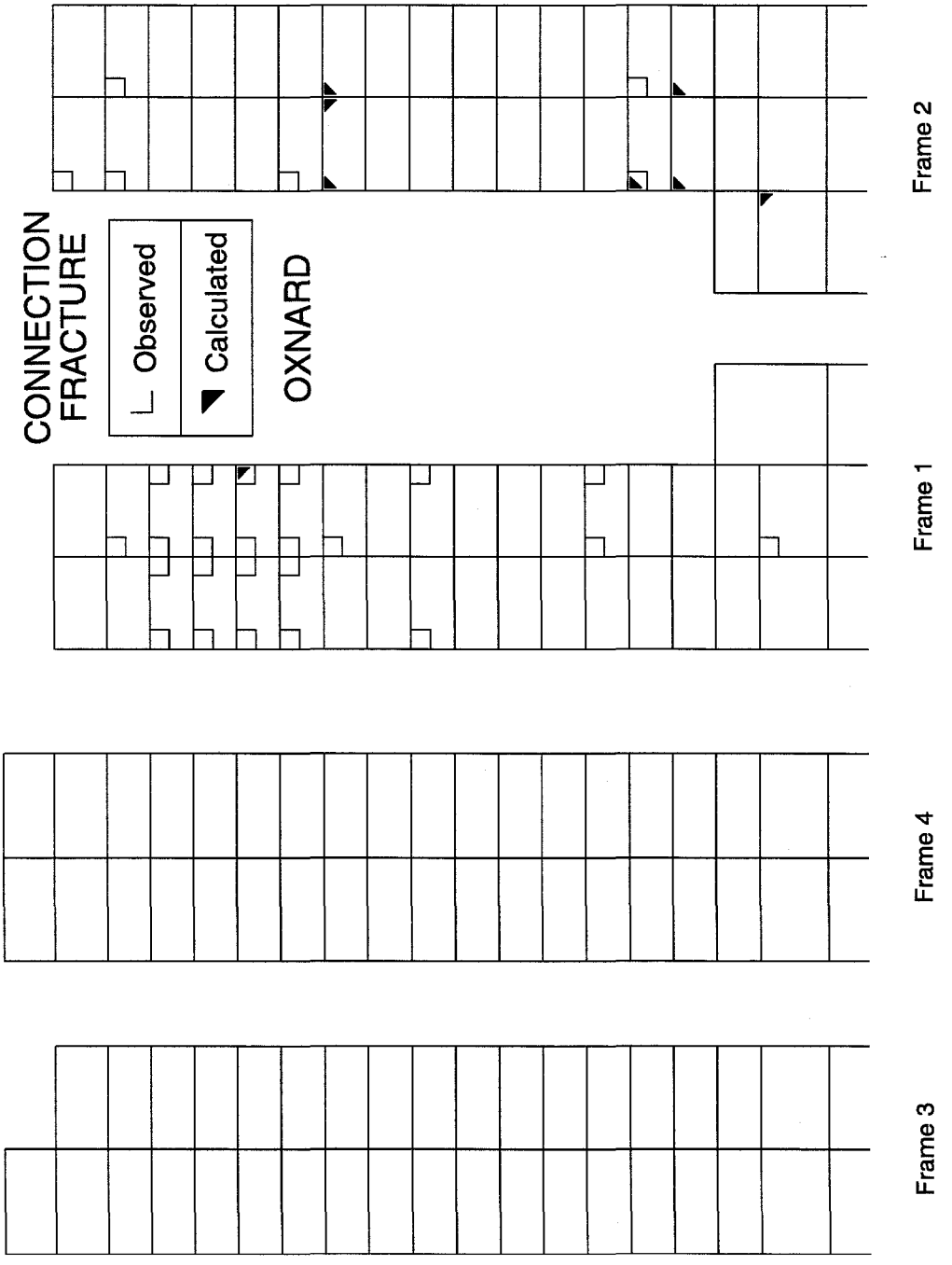

Figure 8.68 Fracture of member ends, random model and Oxnard record.

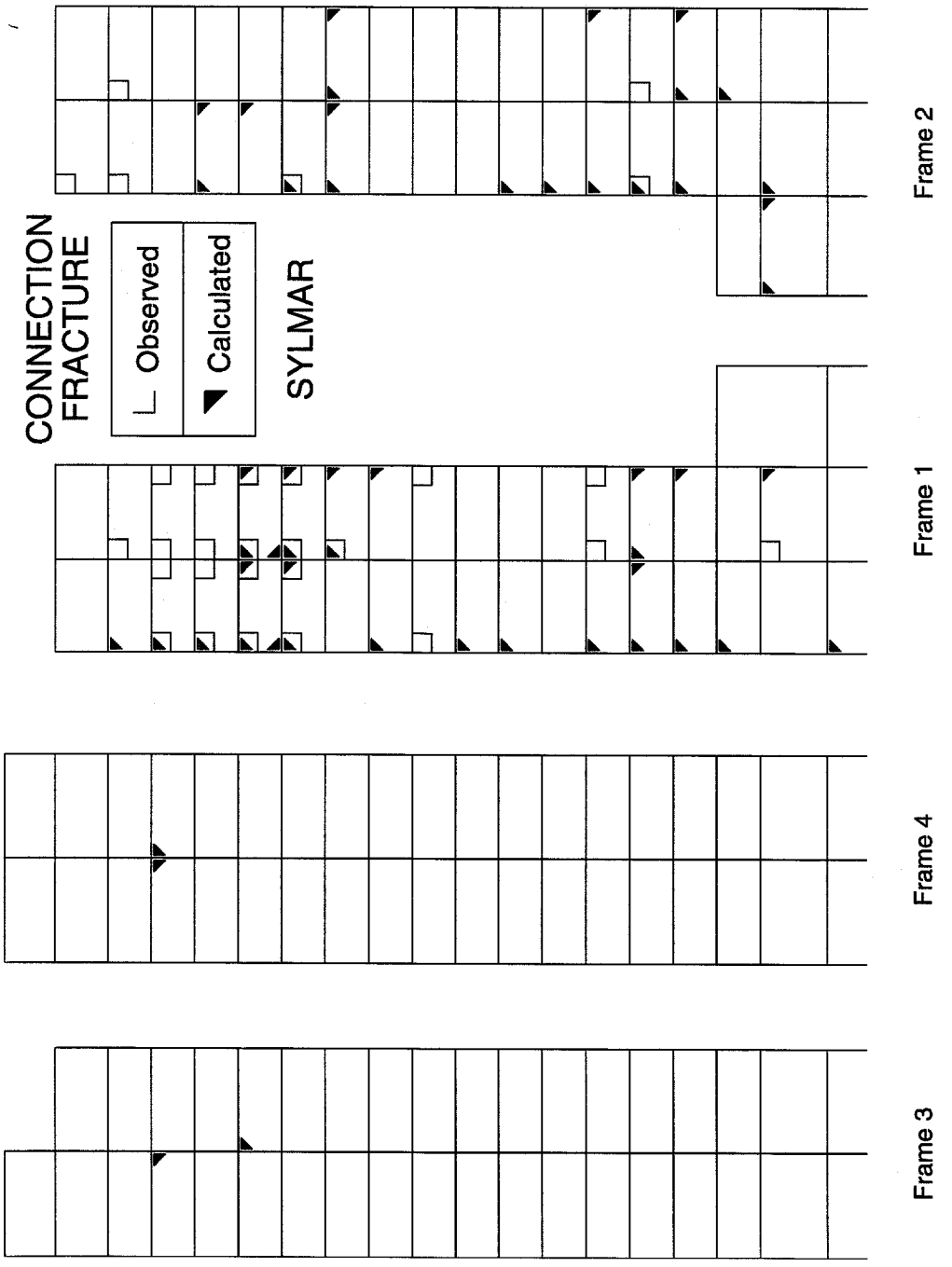

Figure 8.69 Fracture of member ends, random model and Sylmar record.

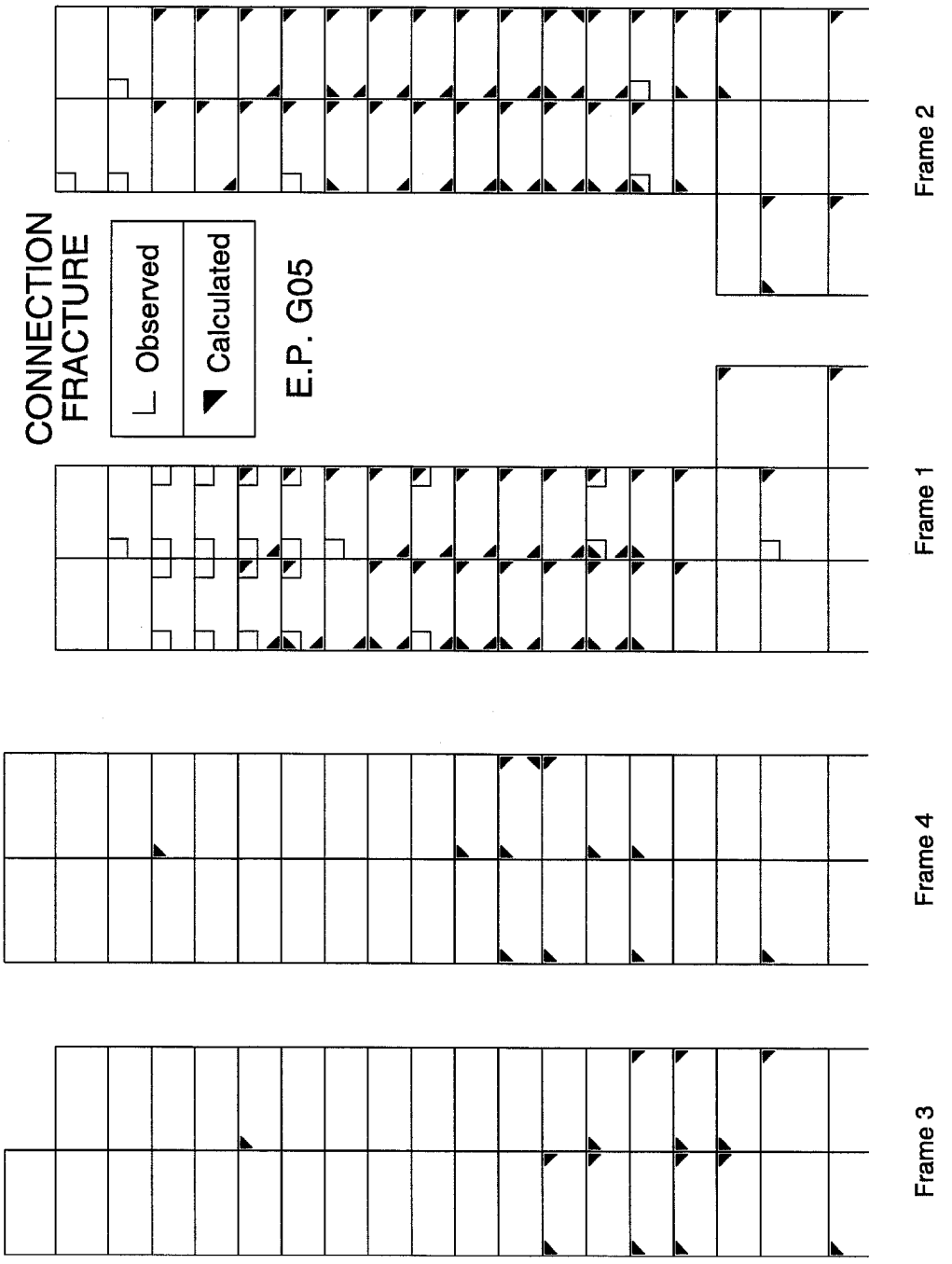

Figure 8.70 Fracture of member ends, random model and E. P. G05 record.

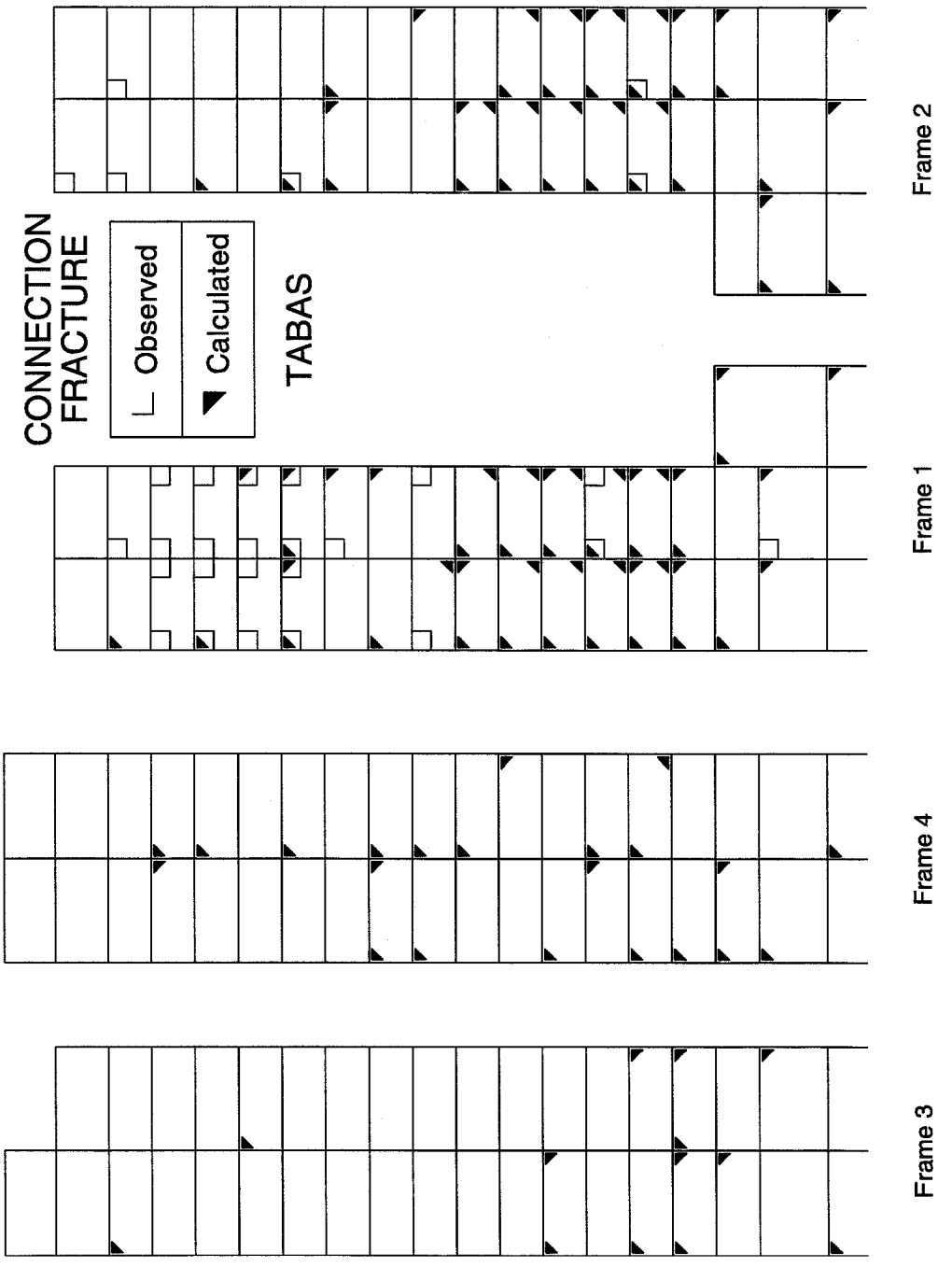

Figure 8.71 Fracture of member ends, random model and Tabas record.

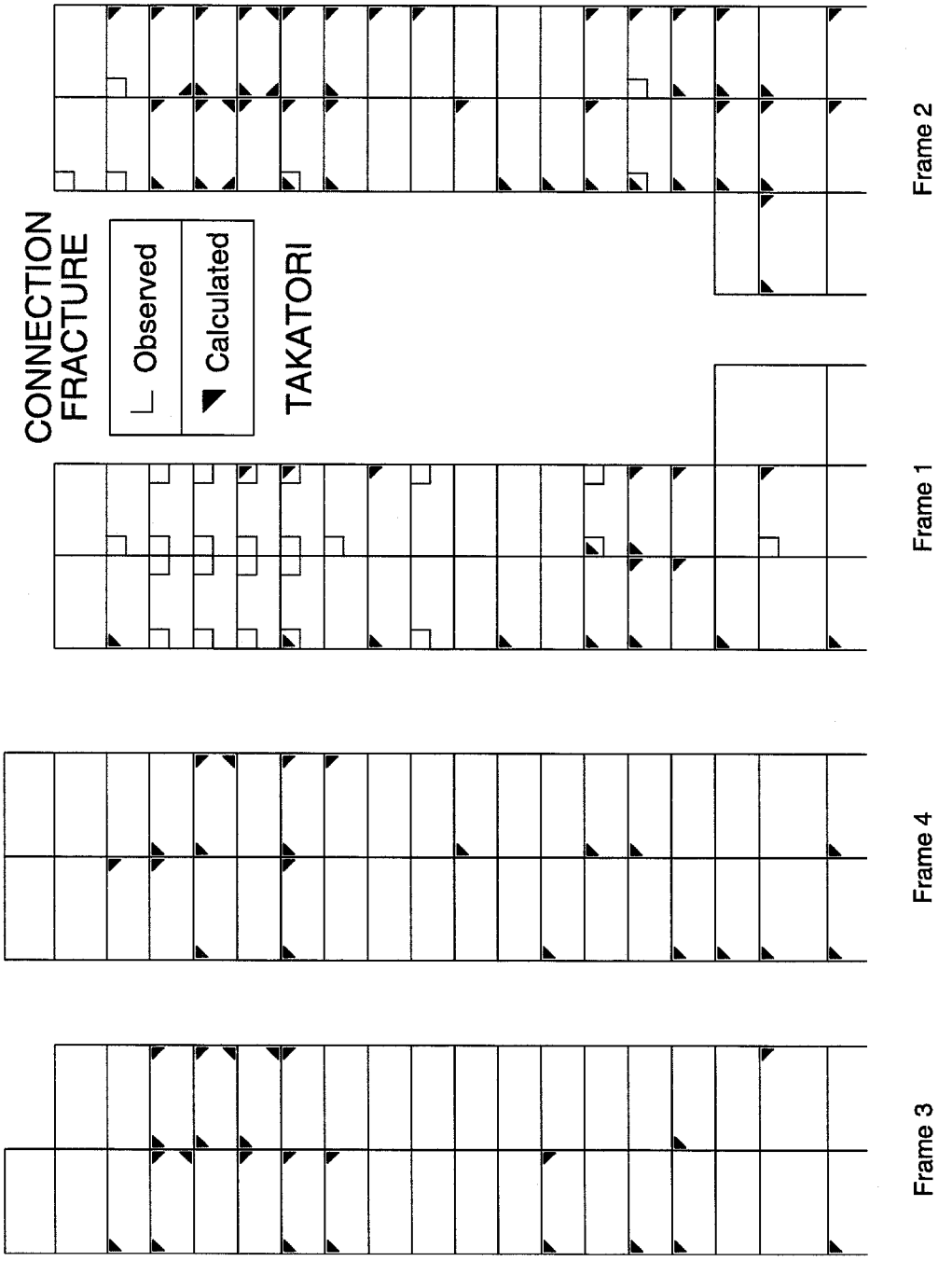

Figure 8.72 Fracture of member ends, random model and Takatori record.

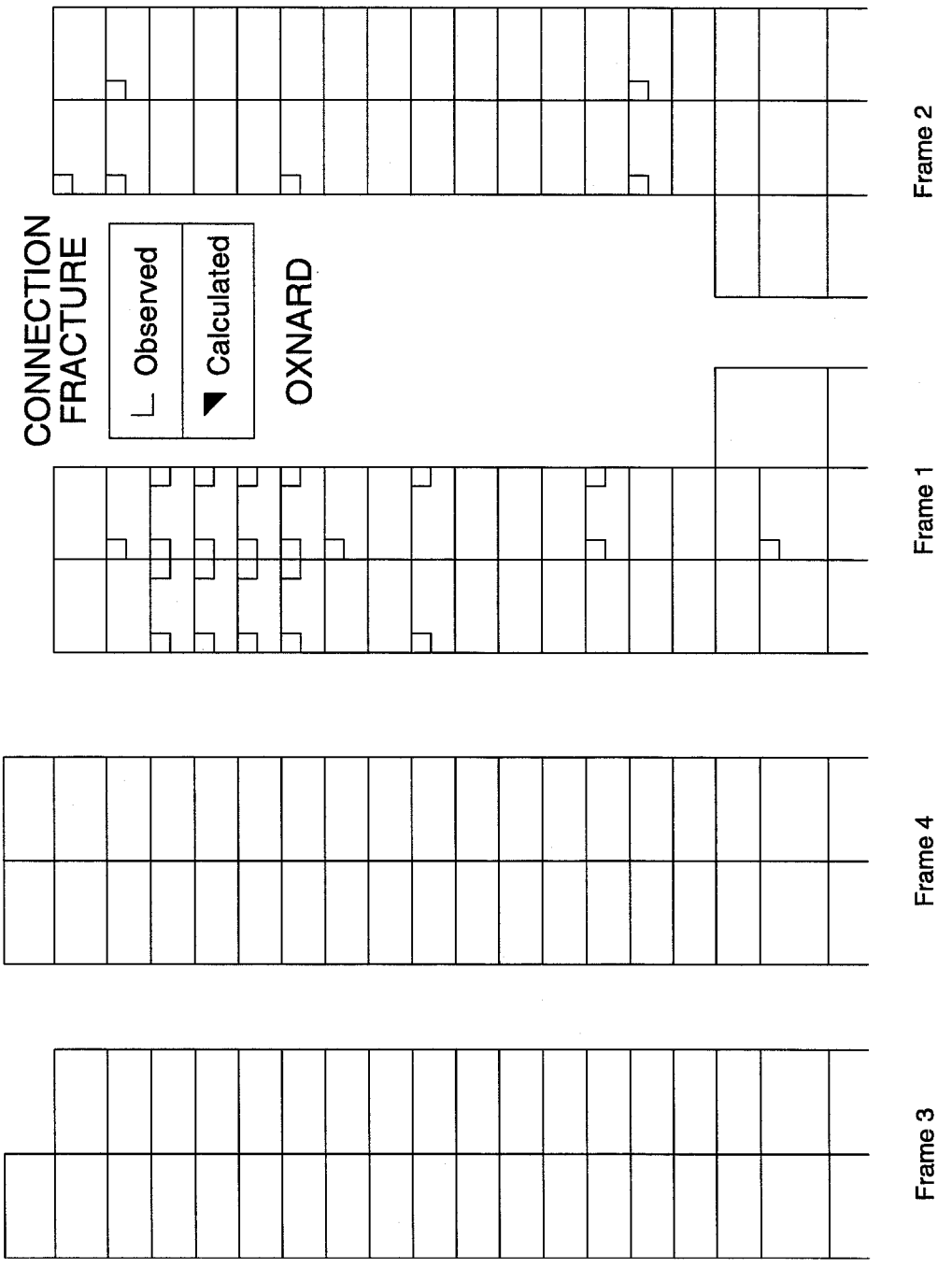

Figure 8.73 Fracture of member ends, 0.02 plastic-rotation model and Oxnard record.

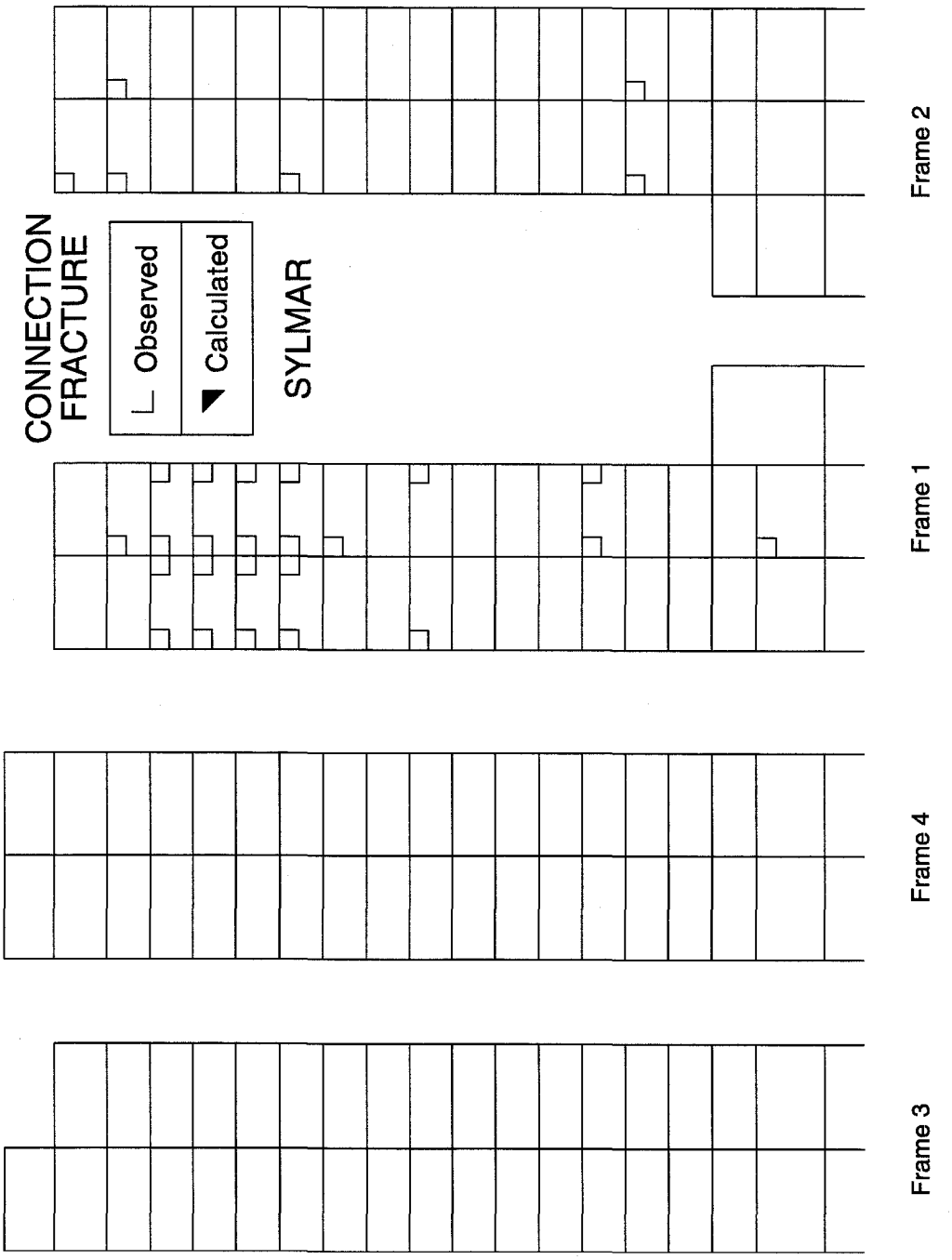

Figure 8.74 Fracture of member ends, 0.02 plastic-rotation model and Sylmar record.

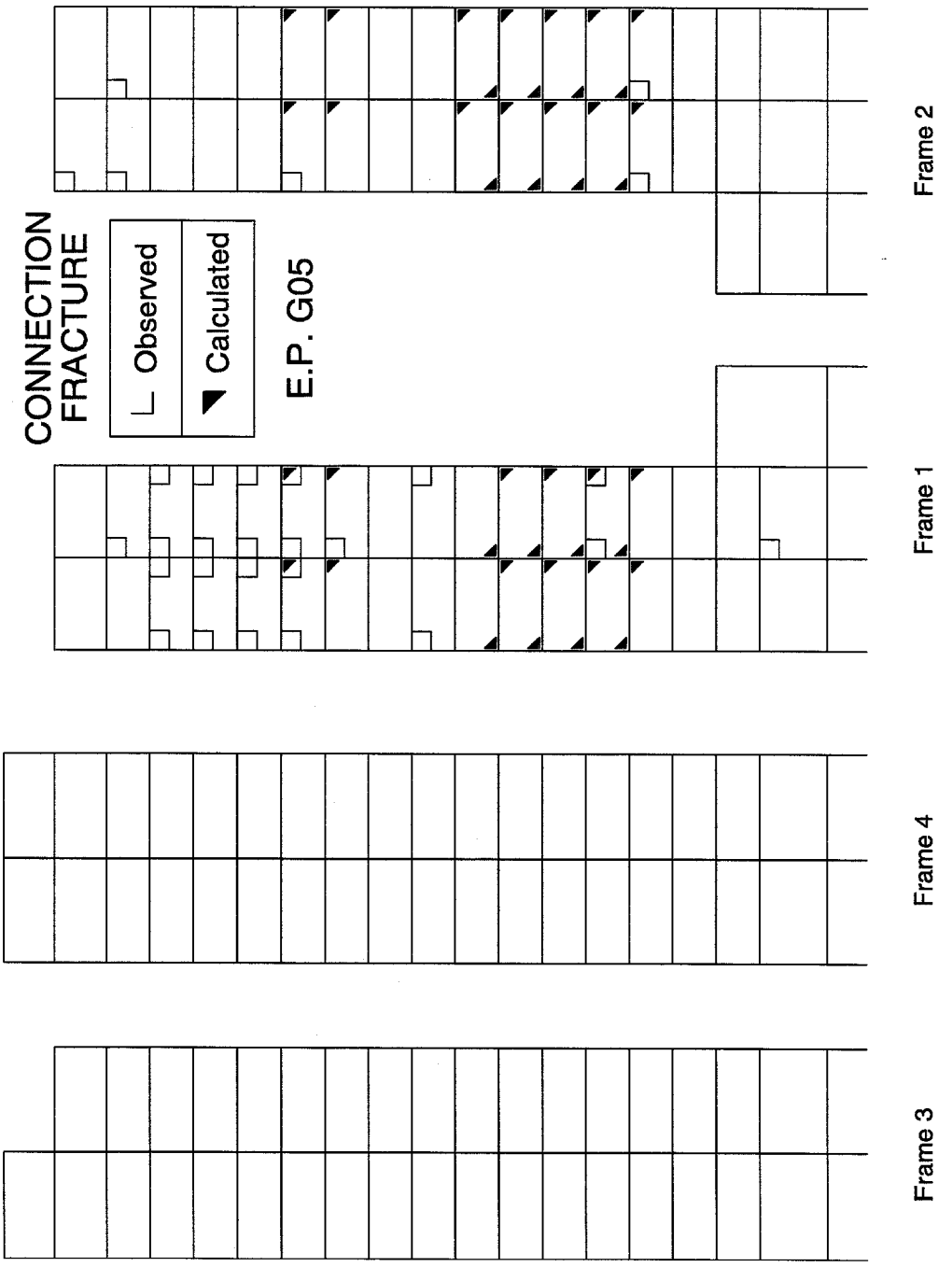

Figure 8.75 Fracture of member ends, 0.02 plastic-rotation model and E. P. G05 record.

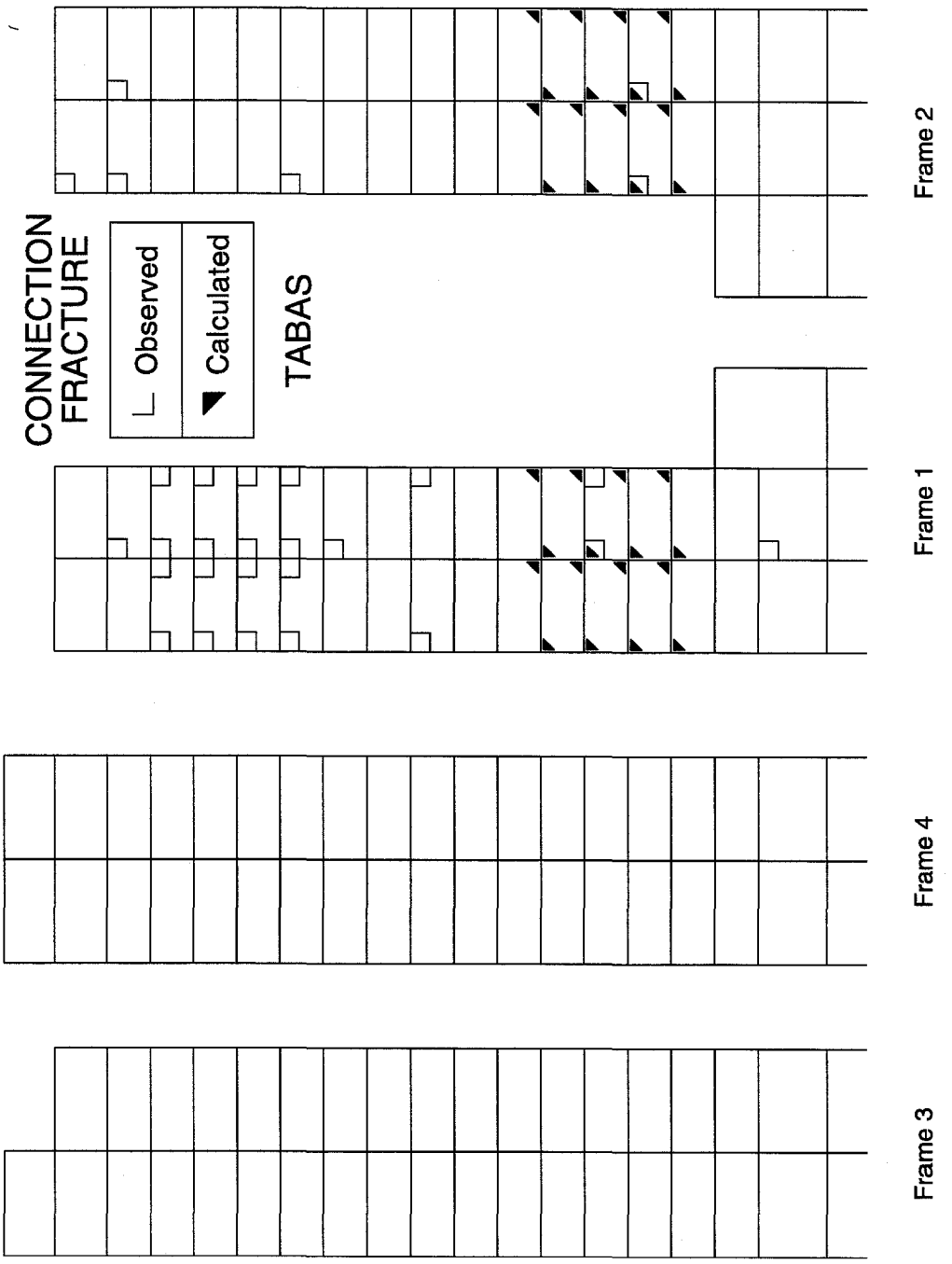

Figure 8.76 Fracture of member ends, 0.02 plastic-rotation model and Tabas record.

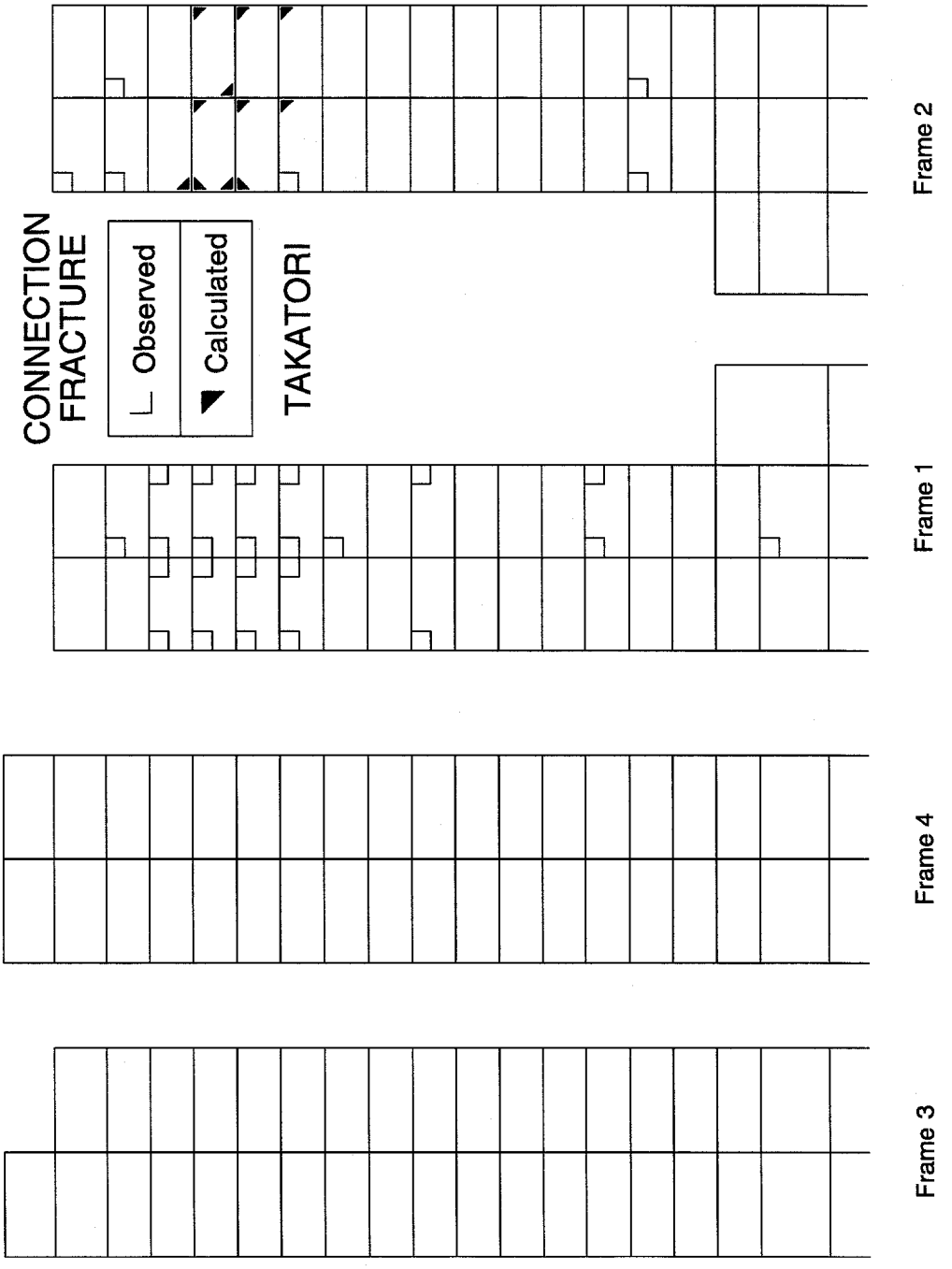

Figure 8.77 Fracture of member ends, 0.02 plastic-rotation model and Takatori record.

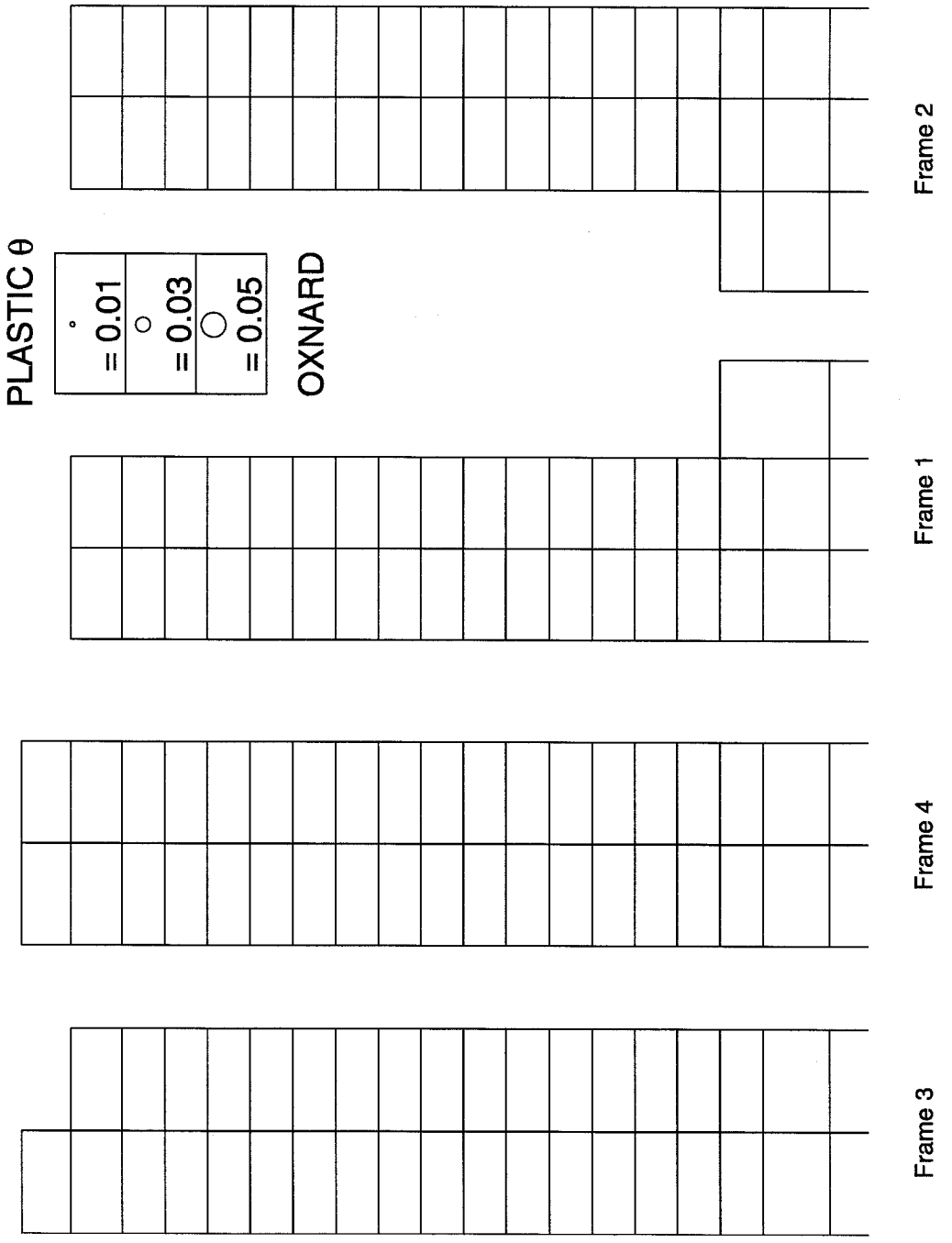

Figure 8.78 Plastic rotations at member ends, inelastic model and Oxnard record.

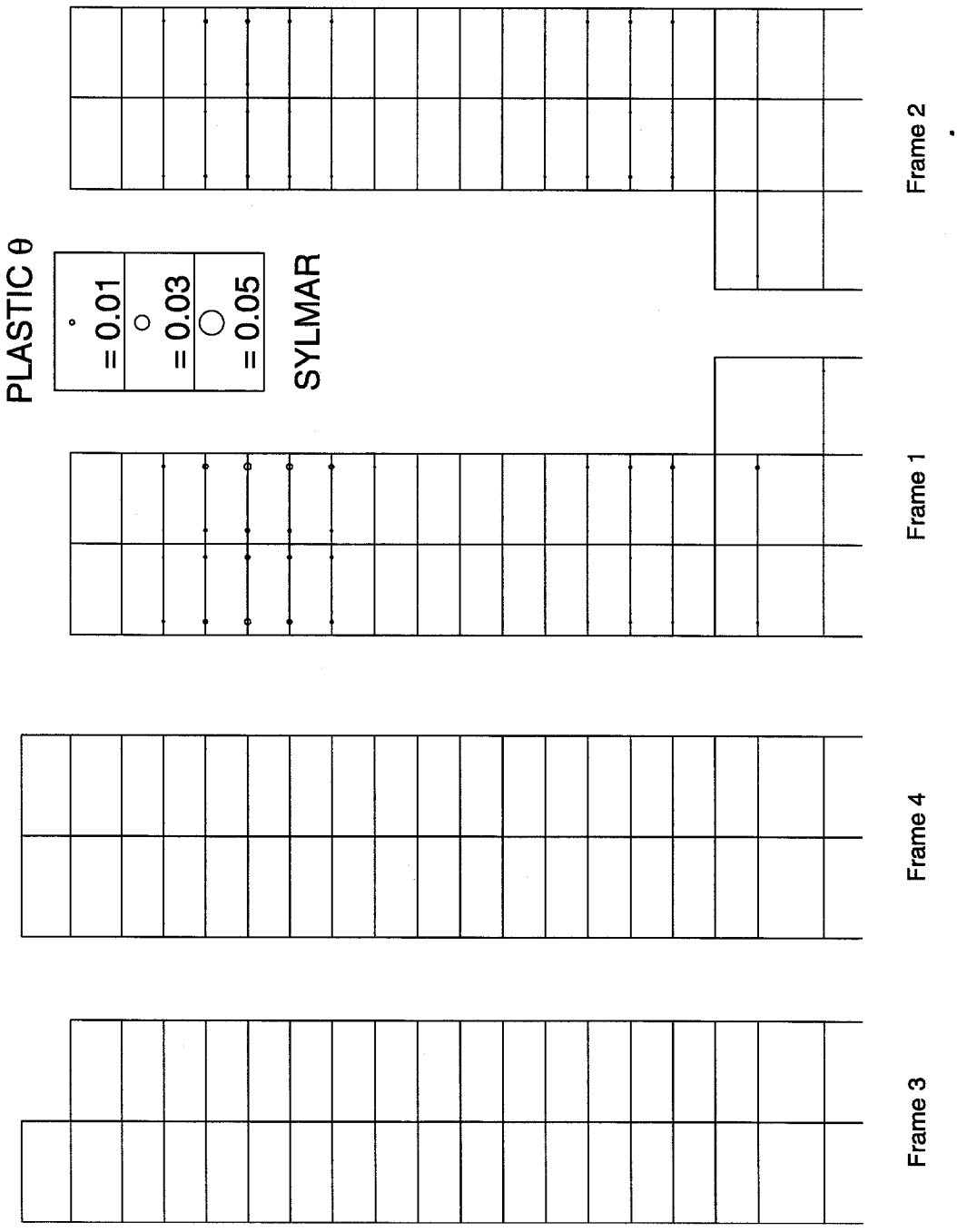

Figure 8.79 Plastic rotations at member ends, inelastic model and Sylmar record.

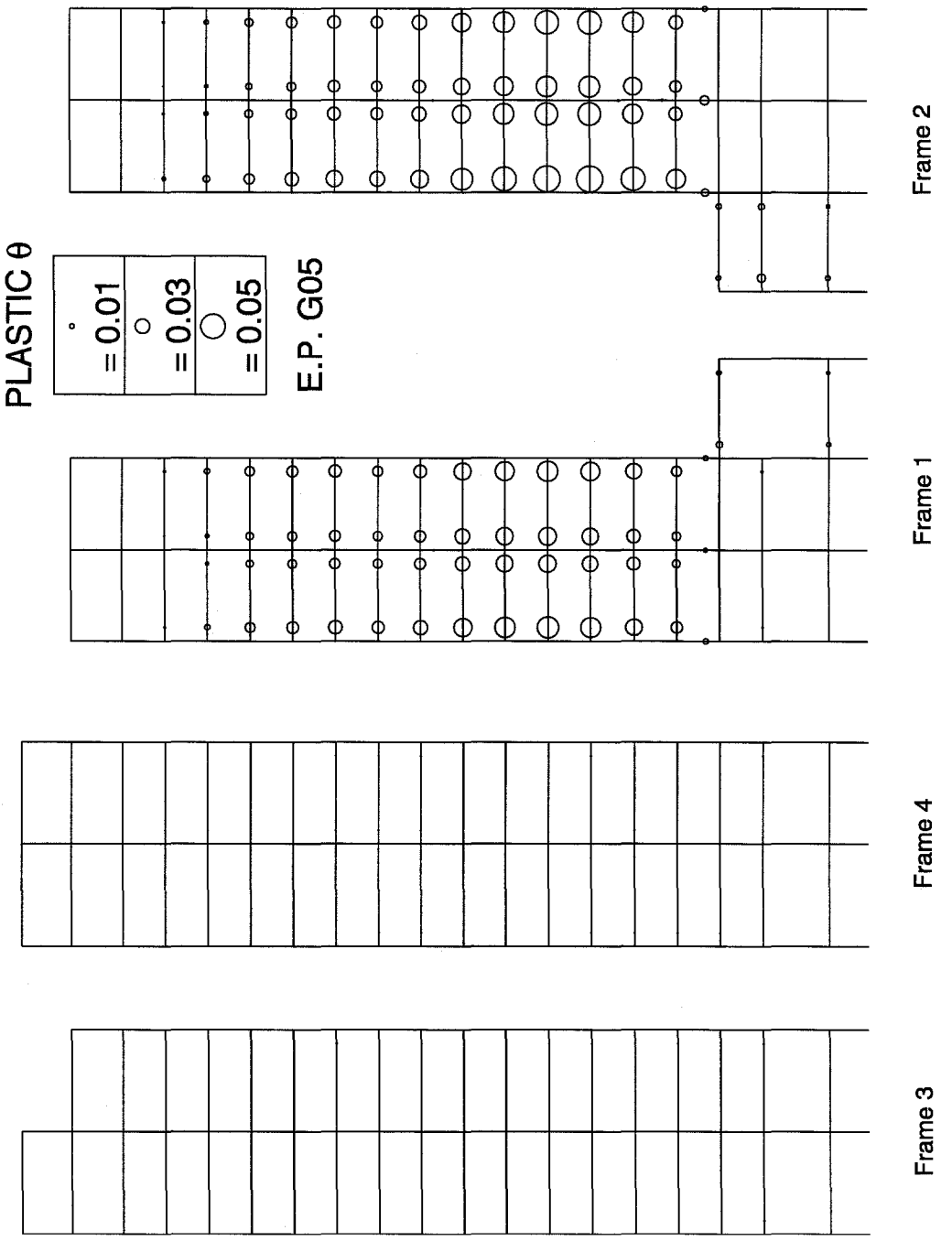

Figure 8.80 Plastic rotations at member ends, inelastic model and E. P. G05 record.

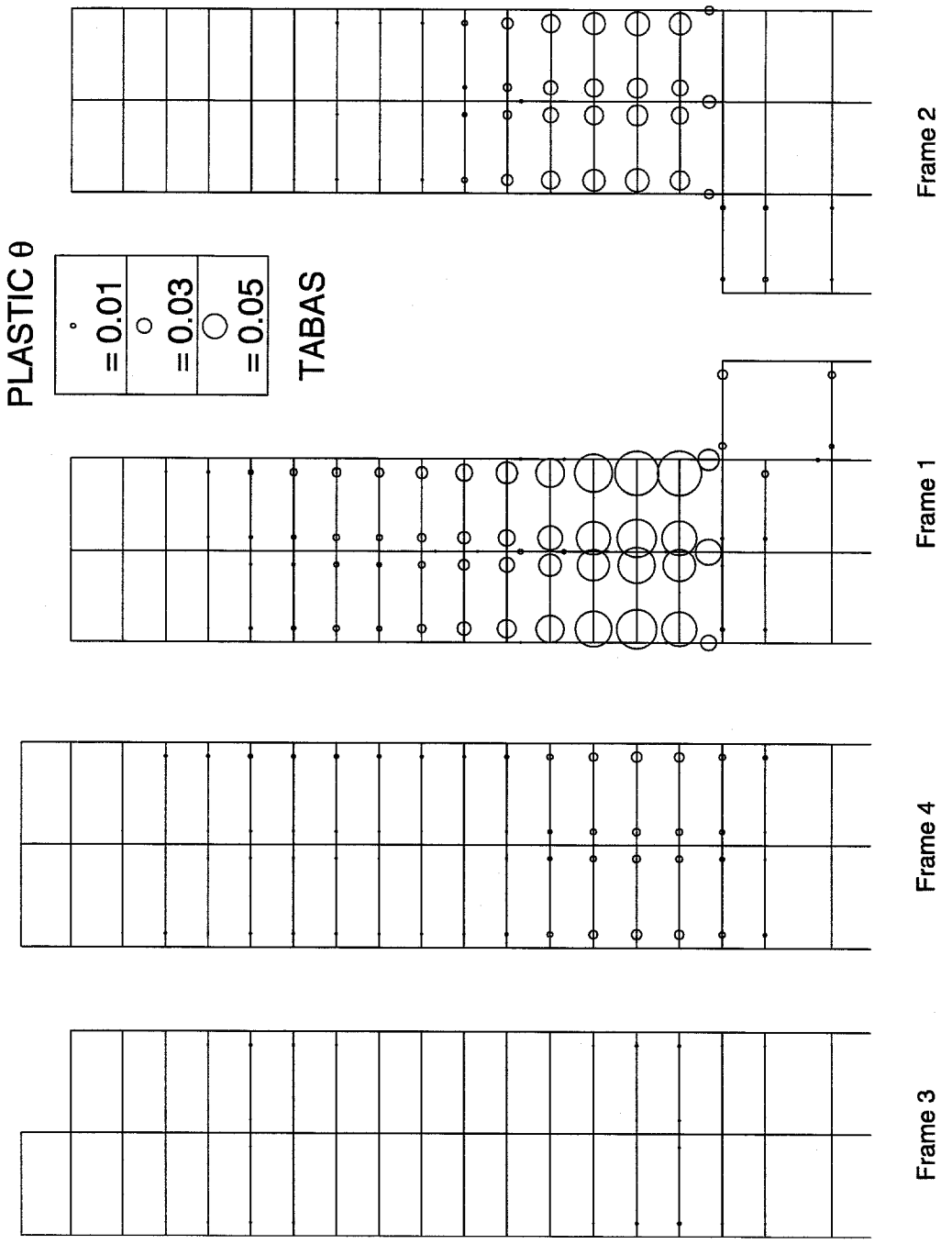

Figure 8.81 Plastic rotations at member ends, inelastic model and Tabas record.

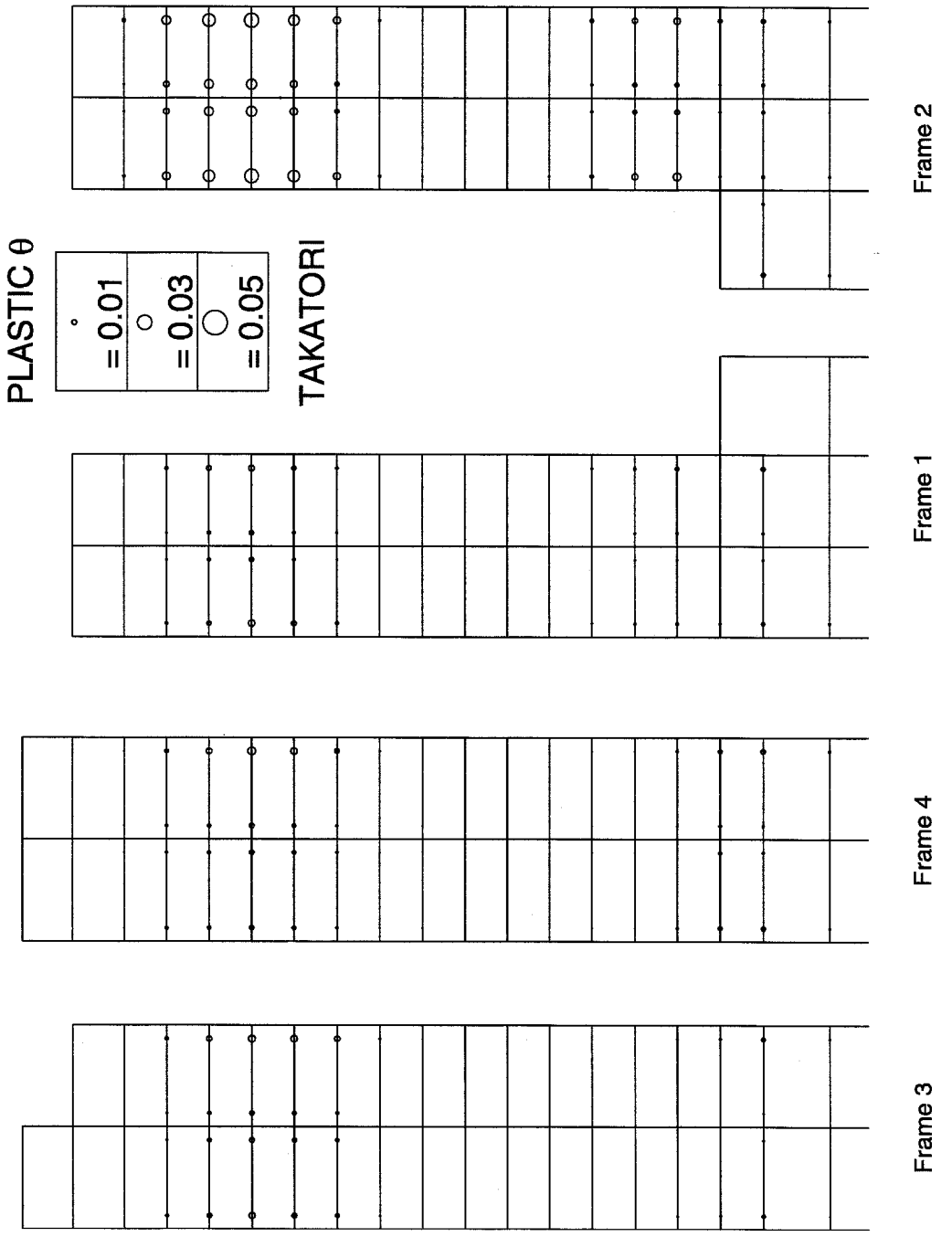

Figure 8.82 Plastic rotations at member ends, inelastic model and Takatori.

8.7 Tables

17-Story Building: Poor Performance Fracture Model				
Ground Motion	Maximum Drift	Maximum Δ_P (cm)	Maximum V/W	Number of Fractures
Oxnard	0.0113	53	0.060	22
Sylmar	0.0190	85	0.104	108
E.P. G05	collapse	—	—	—
Tabas	collapse	—	—	—
Takatori	0.0226	79	0.108	241
Canoga	0.0124	45	0.064	26
Rinaldi	0.0214	75	0.112	147
E.P. D05	collapse	—	—	—
E.P. J06	0.0119	127	0.062	101
Kobe JMA	0.0123	54	0.087	102
Kobe NGT	0.0163	52	0.071	53

Table 8.2 Damage indicators: poor performance model.

17-Story Building: 2D Poor Performance Fracture Model				
Ground Motion	Maximum Drift	Maximum Δ_P (cm)	Maximum V/W	Number of Fractures
Oxnard	0.0128	42	0.059	29
Sylmar	0.0189	77	0.103	96
E.P. G05	collapse	—	—	—
Tabas	collapse	—	—	—
Takatori	0.0273	57	0.103	145

Table 8.3 Damage indicators: 2D poor performance model.

17-Story Building: Random Fracture Model				
Ground Motion	Maximum Drift	Maximum Δ_P (cm)	Maximum V/W	Number of Fractures
Oxnard	0.0097	54	0.060	8
Sylmar	0.0207	86	0.129	53
E.P. G05	collapse	—	—	—
Tabas	collapse	—	—	—
Takatori	0.0253	97	0.113	110

Table 8.4 Damage indicators: random fracture model.

17-Story Building: $\theta_{\text{plastic}} = 0.02$ Fracture Model				
Ground Motion	Maximum Drift	Maximum Δ_P (cm)	Maximum V/W	Number of Fractures
Oxnard	0.0097	55	0.060	0
Sylmar	0.0213	88	0.141	0
E.P. G05	collapse	—	—	—
Tabas	collapse	—	—	—
Takatori	0.0311	106	0.154	11

Table 8.5 Damage indicators: $\theta_{plastic} = 0.02$ model.

17-Story Building: Inelastic Model				
Ground Motion	Maximum Drift	Maximum Δ_P (cm)	Maximum V/W	# of Plastic Rotations > 0.01 rad
Oxnard	0.0097	55	0.060	0
Sylmar	0.0213	88	0.141	4
E.P. G05	0.0613	283	0.142	103
Tabas	0.0742	246	0.132	87
Takatori	0.0278	106	0.154	38

Table 8.6 Damage indicators: inelastic model.

17-Story Building: Oxnard				
Model	Maximum Drift	Maximum Δ_P (cm)	Maximum V/W	Number of Fractures
Poor Performance	0.0113	53	0.060	22
2D Poor Performance	0.0128	42	0.059	29
Random	0.0097	54	0.060	8
$\theta_{plastic} = 0.02$	0.0097	55	0.060	0
Inelastic	0.0097	55	0.060	—
Elastic	0.0094	57	0.062	—

Table 8.7 Damage indicators: Oxnard record.

17-Story Building: Sylmar				
Model	Maximum Drift	Maximum Δ_P (cm)	Maximum V/W	Number of Fractures
Poor Performance	0.0190	85	0.104	108
2D Poor Performance	0.0189	77	0.103	96
Random	0.0207	86	0.129	53
$\theta_{plastic} = 0.02$	0.0213	88	0.141	0
Inelastic	0.0213	88	0.141	—

Table 8.8 Damage indicators: Sylmar record.

17-Story Building: Takatori				
Model	Maximum Drift	Maximum Δ_P (cm)	Maximum V/W	Number of Fractures
Poor Performance	0.0226	79	0.108	241
2D Poor Performance	0.0273	57	0.103	145
Random	0.0253	97	0.113	110
$\theta_{plastic} = 0.02$	0.0311	106	0.154	11
Inelastic	0.0278	106	0.154	—

Table 8.9 Damage indicators: Takatori record.

Chapter 9

13-Story Building

The 13-story building investigated here exhibited brittle fracture in beam-to-column connections during the Northridge earthquake. The building is square in plan and the lateral system consists of steel perimeter moment-frames with five bays on each face. The corner columns are built-up box sections with flanges (see figure 5.10). See figure 9.1 for the plan of the building, and note that because of the voluminous nature of the output in this chapter, the tables and figures are at the end of the chapter. This structure can be analyzed using the techniques and finite elements developed in this work, including the three-dimensional corner columns.

The investigated building was instrumented at its roof, sixth floor and basement levels to record three orthogonal motions at each level. The building was fully inspected, providing data on all the beam-to-column connections that exhibited fracture. The building is a great candidate for investigation because of experiencing some damage and having basement, sixth floor and roof records. The basement record is the Oxnard record used as an input ground motion for all three buildings investigated. Some investigators question the use of foundation flexibility in a model when using base motion as input, claiming that tilting and other base-motion behaviors are already incorporated into the record. Considering the size of this structure and the fact that the lateral system is located on the perimeter, it is unlikely that rocking experienced by the perimeter will be transmitted to the center of the basement floor where the recording was made. For this reason, the author

includes foundation flexibility when using this basement record.

This building has been investigated extensively with 2D and 3D elastic analysis and 2D inelastic analysis (Uang, Yu, Sadre, Bonowitz, and Youssef 1995), (Uang, Yu, Sadre, Bonowitz, Youssef, and Vinkler 1997) and (Maison and Kasai 1997). None of these investigations included three-dimensional nonlinear analysis. Maison and Kasai (1997) modeled connections with trilinear rotational springs that have a yield level determined from a statistical fit to the measured data.

The 13-story building is a good candidate for investigation because of the preceding reasons. The following issues are examined:

- Ability of bare steel frame model to predict damage location through standard code static analyses.
- Ability of 3D nonlinear model to reproduce fracture pattern observed.
- Ability of 3D nonlinear model to reproduce measured roof response.
- Comparison of different models.
- Effect of larger ground motions.

9.1 Building Description

Geometry and Materials

The building has 13 stories plus one basement level. The plan dimensions of the building are 48.77 m by 48.77 m (160 ft by 160 ft), and a typical story height is 401 cm (158 in). The first story height is 488 cm (192 in). Frame columns range in size from W14x176 to W14x500, and girders from W27x84 to W36x230 (figures 9.2–9.5). In these figures, the minor axes of corner columns are noted so that the member orientation can be determined. See table 9.2 for dimensions of the built-up box sections referenced on these elevations as 'B14x#', where # refers to the weight per length of the member in pounds per foot. The columns and girders are A36 steel. The members have a yield strength of 324 kN/mm^2 (47 ksi) and an ultimate strength of 389 kN/mm^2 (56.4 ksi). Smaller members are used for the

gravity system. The beams have metal deck and lightweight concrete on top, but due to the age of this building (1973 UBC design code), it is presumed there are not enough shear studs to act compositely.

Mass

The seismic mass and center of gravity are calculated for each floor based on the loading and assumed properties from Uang, Yu, Sadre, Bonowitz, and Youssef (1995). The weight of the building was estimated to be 140 MN (31450 k). The weight of the steel moment frames is 11.1 MN (2497 k).

Basement Stiffness

Concrete basement walls are assumed to exist in each direction, and the steel columns extend to the base of the walls. The stiffness of the walls is modeled by shear springs assuming the walls at the perimeter of the building are 30.48 cm (12 in) thick.

Story Stiffness

The gravity framing, partitions, and nonstructural walls are assumed to be capable of some lateral resistance provided by shear springs. The total lateral force capacity in each direction provided by the shear springs is set to 1% of the story shear forces produced by the seismic design loads computed for $V/W = 1$. The sum of shear spring stiffnesses in a story is set to 10% of the minimum UBC story stiffness (see section 7.1.6). This corresponds to spring yielding at a story drift of H/170.

Foundation

The foundation has an elastic stiffness of 2.626 MN/cm (1500 k/in) horizontally and vertically and a secondary stiffness of 0.394 MN/cm (225 k/in). Yield strengths are 26.9 MN (6000 k) horizontally and downward and 13.34 MN (3000 k) upward. See section 7.1.5 for formulation of these values.

Damping

Inter-story damping is capped at a force level corresponding to 0.01W, reached at an inter-story velocity of 8.13 cm/sec (3.2 in/sec). This corresponds to 4.5% of critical damping in the linear range of the fundamental modes. The total damping is 5.0%, with an additional 0.5% of critical damping provided by linear stiffness proportional damping.

Fracture Models

End segments of girders representing the welds to the columns are allowed to fracture. The post-earthquake inspection of the building found fractures at both bottom and top flange welds of the girders. Since the girders did not exhibit any local buckling or other signs of plastification, a strain level below yield is reasonable for the bottom flange. The top flange is most likely a better weld since continuous passes can be made, and so a higher fracture strain there is justified. Early investigations not included in this work using uniform poor performance fracture limits resulted in fracture patterns that did not corroborate the observed damage which is definitely random in nature. Maison and Kasai (1997) developed a random distribution of plastic rotation capacities based on the observed damage and grouped the distributions according to member size. The intent of using this distribution is to properly model the level of damage observed. The same model can then be used to predict behavior of stronger ground motions. In the distributed random fracture model (Maison), the fracture strain levels are randomly chosen from the distribution shown in table 7.3. Groups A, B and C represent the W36's, W33x152's, and lighter member sizes, respectively. These strain values are determined by displacement control analysis of beam-to-column assemblies monotonically loaded until the desired plastic rotation is achieved as described in section 7.1.3. The resulting distribution can be seen in figure 9.6. The lowest strain levels in this distribution are $0.7\epsilon_y$ for both the bottom and top fibers, depending on the member size group.

The 13-story building has measured ground (basement) input and sixth-floor and roof response. In an effort to make the best model possible, an additional fracture model is used. The pre-fractured model assigns a tensile fracture strain of

$0\epsilon_y$ to all the locations where damage was observed. The assumption here is that a few of the welded connections were bad to begin with, ready to fail under any strong motion. Note that under distributed gravity loading of a moment connected girder, the bottom flanges will be in compression, so some finite level of excitation is necessary to fail the connection.

A third model for fracture levels assumes that the individual girders can achieve 0.02 radians of plastic rotation before failure (see section 7.1.3 and table 7.3). In this model, groups B and C described above are combined into one group B corresponding to all members more shallow than W36's.

Modal properties

The model possesses natural periods of vibration of 2.90 seconds in the east-west and north-south directions, and 2.03 seconds in torsion. See figures 9.7–9.12 for depictions of the first six natural modes.

9.2 Building Design

The lateral system was designed using the 1973 Uniform Building Code (ICBO 1973). No site-specific provisions existed, so the design would be as follows. The parameters used for design are:

- Moment Space Frame
- $W = DL$
- $Z = 1$, zone 3 for California
- $T = 0.1N$, N = number of stories, must be used if lateral system is 100% moment space frame
- $K = 0.67$
- $C = \frac{0.05}{\sqrt[3]{T}} \leq 0.10$
- $V = ZKCW$, base shear

- $F_t = 0.004V(\frac{h_n}{D_S})^2 \leq 0.15V$, where D_S is the plan dimension of the vertical lateral force resisting system and h_n is the roof height.
- $F_t = 0$ if $(\frac{h_n}{D_S}) \leq 3$
- $F_x = \frac{(V-F_t)w_x h_x}{\sum w_i h_i}$, force at floor x
- No drift limit

The resulting values are:

- $T = 1.3$ sec
- $C = 0.0458$
- $V = 0.0307W$
- $F_t = 0$ since $(\frac{h_n}{D_S}) = 1.18 \leq 3$

Note that the equivalent static force, V, is near the lower limit for the 1994 UBC ($V = 0.03W$).

A model with rigid foundations and solely the lateral system steel columns and girders providing resistance is used for the design. A static analysis using the UBC forces above produces a roof displacement of 12.2 cm (4.82 in) E-W or N-S. There was no drift limit in the 1973 UBC, but this roof displacement produces an average drift lower than the limits imposed by the 1994 UBC.

The resulting demand capacity ratios (DCR's) for the structure from the static analysis can be seen in figures 9.13 and 9.14 for the E-W and N-S directions, respectively. See section 8.2 for an explanation of the DCR ratio and the method of showing them in the figures. As a comparison, the DCR ratios for the Oxnard time history are given using the actual values of member material strengths and the inelastic model without fracture (figure 9.15). See section 9.4 for an explanation of the inelastic model.

9.3 Pushover Analysis

The bare-steel frame and inelastic models were subjected to a pushover analysis using the 1973 UBC static force distribution (figure 9.16). Only the N-S direction is presented, as most of the ground motions are strongest in that direction and the building is symmetric except for small flanges on the corner column box sections. The base model includes just the bare-steel frame (BF). The inelastic model includes the foundation (FN) and inter-story stiffness (SB). Recall that composite action is assumed not to occur. The base model has an ultimate strength of 0.1325W at a roof displacement of 85 cm (33.5 in) and the inelastic model without fracture (BF+FN+SB) has an ultimate strength of 0.1426W at 89 cm (35 in).

9.4 Simulations

Several time-history analyses of various types are performed to seek answers to the issues mentioned at the beginning of the chapter. In each instance, a time step of 0.02 seconds and a total duration of 25 seconds for each record are used. Only 25 seconds are used since the measured response at the roof stopped after 22 seconds. The basement record (Oxnard) is used to represent the ground motion at the site. The Sylmar, Elysian Park G05, Tabas and Takatori records are also used to represent stronger ground motions. Table 9.1 shows the analyses performed for each ground motion. The analysis types include elastic analysis, inelastic analysis without fracture, and inelastic analysis with connection fracture.

9.4.1 Figure Descriptions

Time Histories

The relative-to-ground roof displacement response is tracked for the duration of the analyses, 25 seconds. The response at the center of mass (master node location) and at two corner locations is calculated so that torsional effects can be observed (figure 9.17). Note that the same scale is used wherever possible to compare the response levels for the different ground motions. The responses are grouped by

Ground Motion	Maison Random Fracture	$\theta_{plastic} = 0.02$ Fracture	Inelastic	Elastic	Pre-Fractured
Oxnard	•	•	•	•	•
Sylmar	•	•	•		
E.P. G05	•	•	•		
Tabas	•	•	•		
Takatori	•	•	•		

Table 9.1 Time history analyses performed for 13-story building model.

ground motion instead of by model. For each ground motion, the Maison random fracture model and the inelastic model results are presented.

- See figures 9.18 and 9.27 for the relative roof histories from the Oxnard, Sylmar, Elysian Park G05, Tabas and Takatori ground motions, in that order.

To get a better understanding of the global building behavior, relative histories of each floor are shown together for the N-S component of motion only. The N-S direction is the stronger ground motion in every case, so the N-S response alone will suffice to present this behavior. The responses are grouped by ground motion. For each ground motion, the Maison random fracture model and the inelastic model results are presented.

- See figures 9.28 and 9.37 for the building histories from the Oxnard, Sylmar, Elysian Park G05, Tabas and Takatori ground motions, in that order.

The measured roof and sixth floor responses are compared to the calculated responses for the pre-fractured model, which most closely represents the actual behavior of the building.

- See figure 9.38 for the comparison of absolute roof and sixth floor displacements resulting from the measured response and from the Oxnard motion applied to the pre-fractured model.

The Oxnard motion is used for all three buildings to investigate the differences in models used for each building. The difference in roof and sixth floor response for the Maison fracture model, the inelastic model and the elastic model are presented.

- See figure 9.39 for the comparison of relative roof displacements resulting from the Oxnard motion due to various models.

Three fracture models are also compared for the Oxnard record. The difference in roof and sixth floor response for the Maison fracture model, the $\theta_{plastic} = 0.02$ fracture model and the pre-fractured model are presented.

- See figure 9.40 for the comparison of relative roof displacements resulting from the Oxnard motion due to various fracture models.

Inter-Story Drifts

The maximum drifts in the N-S direction for each story are used as a damage indicator. Note that the same scale is used for all plots. Values that exceed these limits are plotted on the right-hand side of the figure.

- See figures 9.41–9.43 for the maximum story drifts for each record. Each figure represents the response to a different model: Maison fracture, $\theta_{plastic} = 0.02$ fracture, and inelastic.

- See figure 9.44 for the maximum story drifts for each model resulting from the Oxnard record.

Fractures

The member end fractures are plotted for each simulation that uses a fracture model. Top and bottom girder-flange to column-flange connection fractures are distinguished separately. For comparison, the actual fractures discovered after the Northridge earthquake are also plotted.

- See figures 9.45–9.49 for the fractures resulting from the Maison distributed fracture model.

- See figures 9.50–9.54 for the fractures resulting from the $\theta_{plastic} = 0.02$ fracture model.

- See figure 9.55 for the fractures resulting from the pre-fractured model. This shows perfect agreement, of course.

Plastic Rotations

The member end plastic rotations are plotted for each simulation using an inelastic model with no fracture. In these figures, the circle diameter is proportional to the plastic rotation and the circle is drawn offset from the member end to distinguish multiple members framing into a joint.

- See figures 9.56–9.60 for the plastic rotations resulting from the inelastic model.

9.4.2 Table Descriptions

Damage Indicators for Model Type

Several indicators of damage include the maximum drift, the roof displacement, the base shear and the number of fractures. These have been summarized for each model comparing across ground motions. The ratio of base shear V to building weight W is used in these tables. For the inelastic model, the number of member end plastic rotations greater than 0.01 radians is used in place of the number of fractures.

- See tables 9.3–9.5 for the damage indicators for each model: Maison random fracture, $\theta_{plastic} = 0.02$ fracture and inelastic.

Damage Indicators for Ground Motion

The same data is presented for each ground motion comparing across model type. The Elysian Park G05 record is not presented in this form since collapse occurred for both fracture models.

- See tables 9.6–9.9 for the damage indicators for each ground motion.

9.5 Discussion

Static Analysis

The bottom two levels of the building have large W36 girders to provide stiffness for the taller plaza (basement) and ground (first) levels. This gives them a lower stress demand. Based on the DCR values, one would expect the most damage in the third through sixth level girders. The demand drops off toward the top of the building. This distribution is quite different from the 17-story building distribution that was uniform throughout.

The DCR results for the Oxnard record using actual material properties show that inelastic behavior has occurred. Many beams in the N-S frames have exceeded the elastic limits due to excessive bending. No columns have exceeded the elastic limit.

Pushover Analysis

The base shear ratio V/W at ultimate levels is greater than four times the UBC design base shear ratio, even for the bare frame. Notice that combined stiffness of the shear building and foundation provide an overall stiffness close to the bare frame stiffness.

The ductility of this structure is greater than for the 17-story building. The 17-story building has a large drop off in force level after reaching ultimate load whereas the 13-story building can sustain a larger percentage of its larger ultimate load for larger building drifts. The 13-story building is shorter and its lateral system is wider, so overturning and associated P-Δ effects are smaller. There are also more bays of framing that provide more redundancy than the 17-story building lateral system does.

Relative Roof Displacements

These time history plots (figures 9.18–9.27) show the response level of the roof in lateral directions, and by plotting three locations on the roof, they indicate torsional response by differences in the histories. The five representative ground motions are

used as input on the 13-story building model with the Maison model of fracture strains and the inelastic model without fracture. The building is symmetric with centered mass. Even with a random distribution of fracture strains, little to no torsion is observed in any of the five records. Note that the five histories are drawn to the same scale for comparison.

The results are similar between the fracture and inelastic models for Oxnard, Sylmar, and Takatori, which indicates that inelastic behavior occurs from these records even with perfect connections. If the response were elastic for the inelastic model (perfect connections), and fractures only occurred below yield for the fracture model, a larger difference would be seen between the responses. In general, the later peaks in the records are larger for the inelastic runs than for the fracture runs because the opening and closing of cracks provide more damping through release of strain energy than the inelastic deformations can provide through hysteresis.

The Oxnard response has no permanent offset. Looking at the roof response alone, it cannot be determined if any inelastic behavior has occurred. Knowing that fractures occurred due to this ground motion in the fracture model allows one to conclude that the inelastic model also experiences inelastic behavior because of the similarities in roof response.

The Sylmar response shows some permanent offset to the east and south. Notice the low level of response after 10 seconds that indicates large damping levels from strain energy release (fracture model) or inelastic hysteresis (fracture and inelastic models).

The G05 fracture model response shows collapse of the building. The G05 record does not cause collapse for the inelastic model, but a large permanent offset — roughly 150 cm or 2.5% of the building height — is observed.

The Tabas record does show a dramatic difference in behavior between the two models. In the fracture model, there is roughly 50 cm offset to the south and in the inelastic model there is about 25 cm offset to the north. The N-S ground motion (see figure A.11) is essentially a double pulse. The fracture model suffered more damage, so upon the end of the pulse about 15 seconds into the record, it damped

future energy whereas the inelastic model allows the building to be whipped to the north as seen by the response at 15–17 seconds. This allows a permanent northward offset to occur rather than the southward offset of the fracture model.

The Takatori responses show evidence of more damping in the fracture model than the inelastic model.

Relative Floor Displacements

In these figures (9.28–9.37), each floor response is shown for the Maison fracture model and the inelastic model. The Oxnard response shows nearly elastic response. There is no permanent offset observed in any level, although some amount of reversing inelastic behavior could occur without these histories depicting it.

The Sylmar record shows slight offset to the south for the cracked model, and slightly larger offset to the south for the inelastic model. The predominant offset is actually in the E-W direction. The ground motion is not as intense in this direction based on maximum displacements or pseudo-acceleration values at the fundamental modes. The difference is that the energy is more directed in this direction than for the N-S direction. The E-W direction has two eastward pulses, but the N-S direction has a stronger bi-directional pulse which corrects any offset created from the first half of the pulse. See the discussion of the fracture figures for further explanation of this behavior.

The G05 record shows collapse occurring the same way it does for the 17-story building. The top of the building is still moving south while the ground is accelerating to the north. The original northward motion seen prior to 10 seconds is more representative of the ground moving south than of the roof moving north. This is like loading a slingshot, and similar to the stone being loaded, the building never comes back. The inelastic model barely recovers from the ground pulse, with most of the offset in five stories close to a collapse state.

The Tabas record shows additional offset, smoothing and damping for the fracture model relative to the inelastic model. The fracture damaged model has roughly a five second periodic response while the inelastic model still responds to the higher

frequency input of the Tabas ground motion. Notice the smoothing of the highly damped fracture model versus the travel of high frequency motion through several stories of the inelastic model.

Comparing the response at the end of the record for the Takatori ground motion, the inelastic model looks like free response in the fundamental mode whereas the fracture model has some offset and higher mode effects. The smoothed inelastic model response and higher frequency cracked model response is the opposite behavior to that observed for the Tabas record. This could be due to the localized fracturing from each ground motion. The Tabas record causes damage in the lower stories of the building, elongating the fundamental period and damping out higher mode response. The Takatori record causes two zones of damage, both high and low in the building. Energy can still travel up into the building, and even though there is more damping than the corresponding inelastic model, the damage may actually be producing shorter period internal reflections that do not exist for the more smooth inelastic response.

Time History Comparisons

The distribution of the connection fractures indicates material or construction defects rather than higher demands at these locations. An additional fracture model was analyzed in which all of the observed connection fractures are pre-fractured. The assumption is that these are the only bad connections in the building. Considering that there is some inelastic behavior observed for the Oxnard record on the model without fracture (figure 9.15), the demand on the members is high, so this assumption is warranted. Recall that the Oxnard record is the actual basement record of the 13-story building. This pre-fractured model gives the best fit to the sixth floor and roof responses of all the simulations in this work.

The response of the pre-fractured model to the Oxnard ground motion is compared to the measured sixth floor and roof response in figure 9.38. Relative displacements are used, and the measured relative displacements are determined by subtracting the basement record from the sixth floor and roof records. The simula-

tion has displacement peaks that are too high, but overall it is a close match. This match validates the model for this particular ground motion.

The pre-fractured, inelastic and elastic models are compared to the measured response for the Oxnard ground motion in figure 9.39. The small differences in model responses indicate very little inelastic behavior in the E-W direction. These three models differ from the measured response in terms of damping more than in terms of stiffness. The period of response matches well, indicating the stiffness and mass of the model accurately represent the actual building. The peaks in response are too high, especially at the end of the record, indicating too little damping. Looking at the N-S histories, it is obvious the response is inelastic. The elastic model has peaks twice the magnitude of measured response in some portions of the record. The inelastic model greatly reduces the magnitude of response, but the pre-fractured model comes the closest to matching the building response.

The three fracture models — pre-fractured, Maison model, and $\theta_P = 0.02$ — are compared to the measured response for the Oxnard ground motion in figure 9.40. The Maison fracture model has nearly equivalent response to the pre-fracture model. They both produce 52 connection fractures (coincidentally) with different distributions. By using a random fracture distribution and matching the level of roof response and number of fractures, the Maison fracture model allows confident predictions of building response to other ground motions.

The $\theta_P = 0.02$ model produces no fractures, and is thus identical to the inelastic model. As discussed in chapter 7, the $\theta_P = 0.02$ model represents an overestimate of the fracture strength of better than average pre-Northridge connections. In the case of this building, it unconservatively assumes higher strength.

Drift Ratios

Different drift ratio comparisons are shown in figures 9.41–9.44. The five representative ground motions are used, and drifts for the distributed random (Maison) fracture, $\theta_P = 0.02$ and inelastic models are given. For the Oxnard record, drifts for the various models are compared.

For the Maison fracture model, the Oxnard drift distribution is proportional to the static analysis DCR values. This could indicate predominantly fundamental mode response since the DCR values are based on an inverted triangular code-prescribed distribution. The Sylmar record drifts are uniform except for stories 2–4. The G05 record has very high drifts for stories 2–6 leading to collapse. The Tabas record also has locally high drifts in stories 2–5. The Takatori record is different in that its highest drifts are in upper stories 7–10. This is indicative of the high-frequency content seen in the peaks of the Takatori response spectrum.

Similar results can be seen for the $\theta_P = 0.02$ and inelastic models.

The comparison for various models subjected to the Oxnard motion shows significantly more drift in the elastic model than the other models. This reflects the damping provided by inelastic behavior. This differs from the 17-story building that responds elastically to this same ground motion.

Fracture Distributions

The calculated fractures for the various fracture models are depicted in figures 9.45–9.54. The Maison fracture model and the $\theta_P = 0.02$ model for the five representative ground motions are depicted. Additionally, the pre-fractured model for the Oxnard motion is given.

The Maison model assumes different fracture strains for the W33 and W36 girders in the building. The $\theta_P = 0.02$ model has different fracture strains for these different member sizes. These models differ from a uniform fracture model in which member connections will fail at the same strain level, regardless of location, depth or flange thickness. If a uniform fracture model were used as in the case of the 17-story building, many fewer fractures would occur in the second floor girders. This is contrary to the observed fractures, which were predominantly in this level. The DCR values also indicate low stresses in this level, but the member has thicker flanges, so it may be more prone to lower strain level fractures. More passes are required to deposit weld material for the thicker flanges which also are more likely to possess imperfections from the rolling process than for a thinner section. The

$\theta_P = 0.02$ model does not take these factors into account in calculating the fracture strain, and the calculated response reflects this. No fractures are recorded in this level for any of the ground motions for this model. The Maison model *does* assume lower fracture strains for larger flange thicknesses, so some fractures are observed on this level for the various ground motions.

The Oxnard record for the Maison model produces the same level of damage as the pre-fractured model, even though the distribution in the building cannot be predicted.

The Sylmar record produces connection fractures occurring for both northward and southward motions in Frame 4 and Frame 9. The E-W oriented frames, Frame B and Frame G, have most fractures associated with an eastward motion. Because of these fracture patterns, one would expect an offset to the east. The equal levels of northward and southward damage do not permit conjecture on which direction, if any, will exhibit offset for N-S motions. This corroborates the higher offset noticed for the weaker E-W ground motion as discussed in the roof response section. The E-W motion is directed even though it is not as strong as the N-S motion.

The G05 record clearly shows that all the damage occurs in one southeastward direction (south for 4 & 9 and east for G & B). The Tabas record shows damage in both directions. The Takatori record shows localized damage both low and high and damage in both directions. Localized damage for all three ground motions is consistent with the story drift plots.

Moving on to the $\theta_P = 0.02$ model responses, the Oxnard record exhibits no fractures. As mentioned, there is still some inelastic response even without any fractures. The stronger Sylmar and Takatori ground motions also produce no fractures, and the Tabas record produces a single top-flange fracture.

The G05 record has directed southward local damage.

Plastic-Rotation Distributions

The plastic rotations at member ends for the inelastic model are presented in figures 9.56–9.60.

The Oxnard response has slight inelastic response in the N-S direction, but is mostly elastic response.

The Sylmar response shows localized lower level inelastic behavior. Note that the E-W direction has higher plastic rotations, even though the response spectra for E-W and N-S motions do not predict this. From the other discussions of this model, the E-W response is directed whereas the N-S response reverses. So, the E-W girder ends experience increasing large plastic rotations in one direction during the time history while the N-S girder ends repeatedly experience large but reversing plastic rotations. Looking at these results alone could not explain this behavior.

The G05 record shows localized severe behavior. The Tabas record also exhibits localized lower inelastic behavior. The Takatori record shows local inelastic behavior in both lower and upper levels.

Damage Indicator Summary Tables

The five representative ground motion responses for the Maison, $\theta_P = 0.02$ and inelastic models are summarized in tables 9.3–9.5, respectively. Drift, roof displacement, base shear, and number of fractures are the damage indicators tabulated. The G05 ground motion causes collapse for the two different fracture models, so damage indicators for those records are unreliable for quantitative comparisons.

The discussion of damage indicators for the 17-story building concluded that several basic indicators are not good predictors of damage, and the same conclusions can be drawn for the results of the 13-story building. The base shear ratio V/W for the Sylmar and Tabas records for either of the fracture models is about equal, but the Sylmar maximum drift, maximum roof displacement and number of fractures are all much smaller. The base shear ratio alone cannot predict or measure the differing damage levels.

The maximum roof displacement for the Takatori record is about two-thirds of the Tabas roof displacement, yet the Takatori record causes more damage in the Maison model. The Sylmar and Takatori roof displacements are similar, but the Takatori record causes more damage. The maximum roof displacement alone

cannot predict or measure these inelastic responses.

The maximum drift is a slightly better indicator of damage, with better correlation to the number of fractures. The extent of the damage throughout the building is lost, though. The maximum drift could be the same for damage to one level or many.

For the inelastic model, the base shear ratio exceeds the ultimate value from the pushover analysis ($V/W = 0.1425$ at 89 cm) for all ground motions other than the Oxnard record. Some records exceed the roof displacement at ultimate pushover base shear. As mentioned in the 17-story building discussion, higher mode effects can achieve the higher levels of response.

Comparing the inelastic and Maison model responses for the Sylmar record, the inelastic response has higher base shear ratio and roof displacement, but slightly lower maximum story drift. The fractures provide more damping through strain energy release than the inelastic behavior alone can provide through hysteresis, so they act as a beneficial fuse reducing the response of further excitation. If the ground motion is strong enough or directional, the damage resulting from the fracture model will produce larger drifts and possibly collapse as in the case of the G05 record.

The same information in the tables mentioned above is tabulated for each ground motion to compare the responses of different models (tables 9.6–9.9). A couple of interesting trends are worth noting. Except for the mostly elastic response to the Oxnard record, the ground motions produce decreasing base shear ratios for increasing damage. The Maison random model has higher maximum drifts than the inelastic model. Except for the Tabas record, the Maison model has lower roof response than the inelastic model. While combined energy release and inelastic hysteresis allows the fracture model to lessen the response to a greater degree than the inelastic model, this is not necessarily beneficial due to the increased drifts and collapse of the G05 record.

9.6 Figures

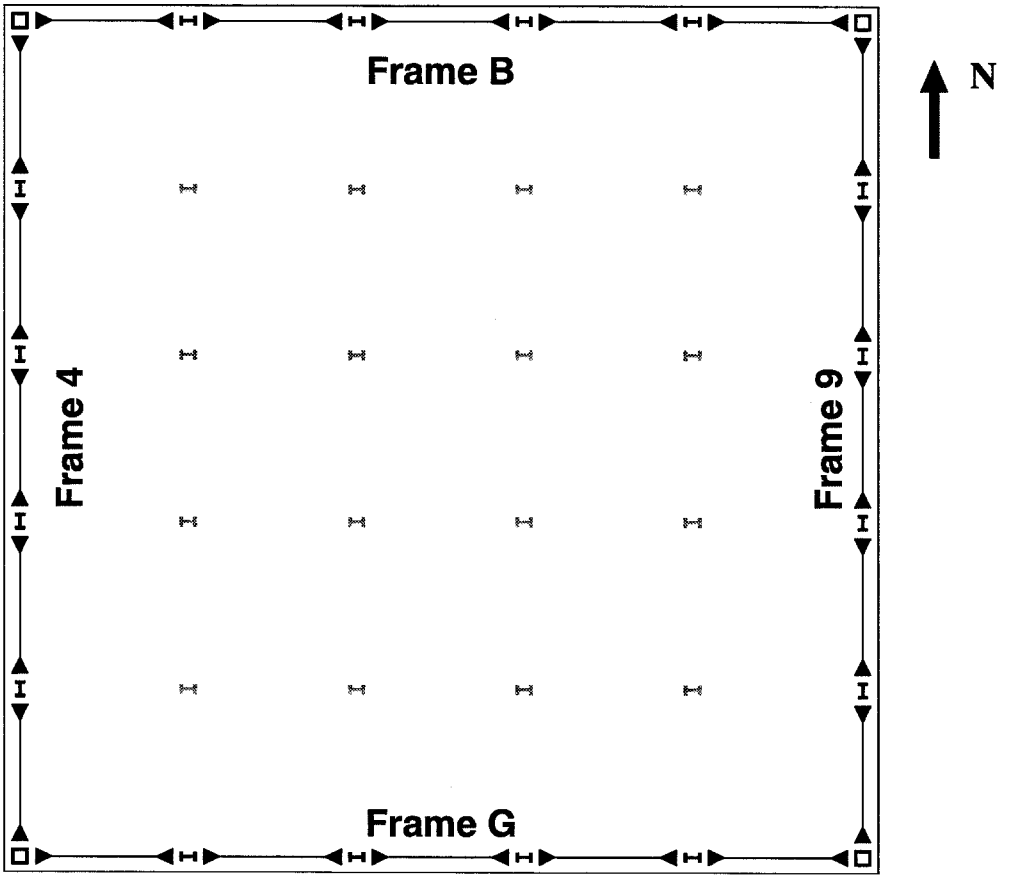

Figure 9.1 Plan of building with frame labels.

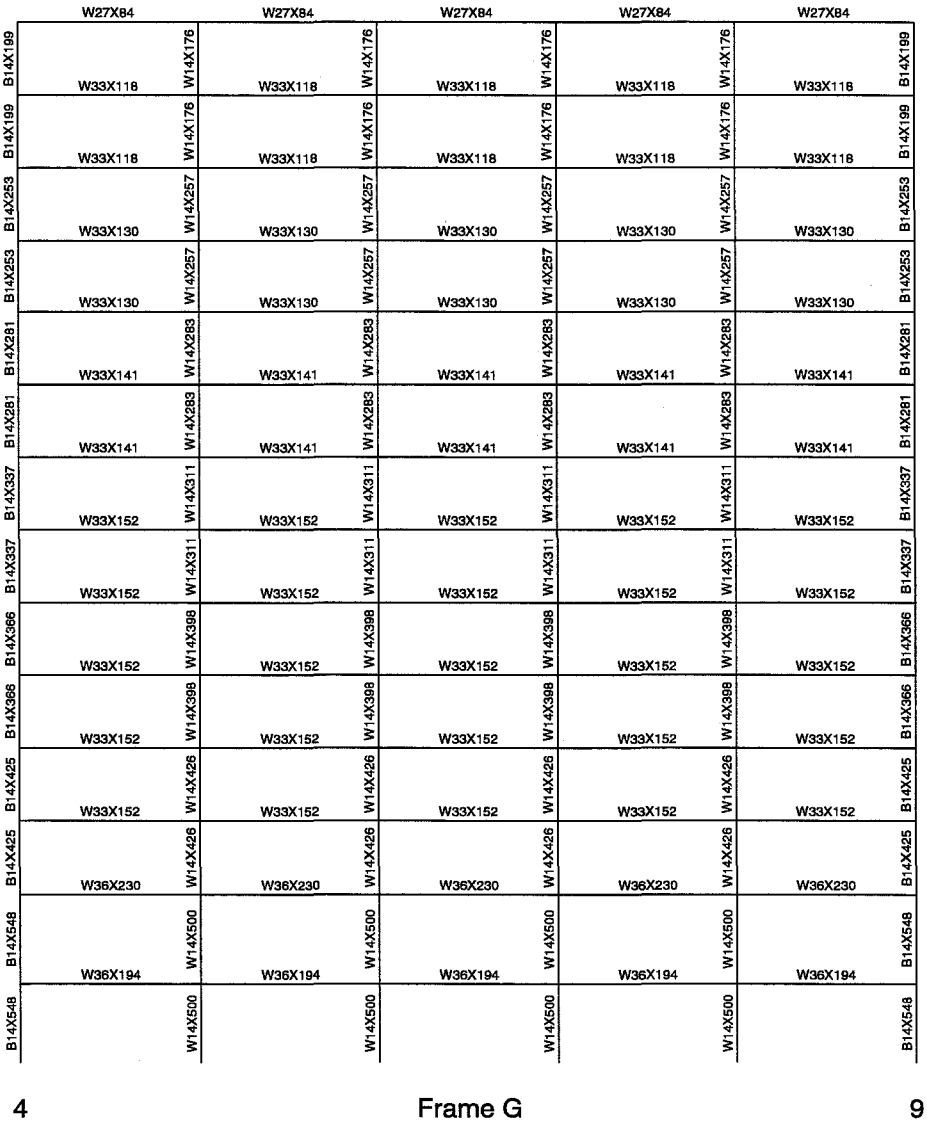

Figure 9.2 South frame section properties.

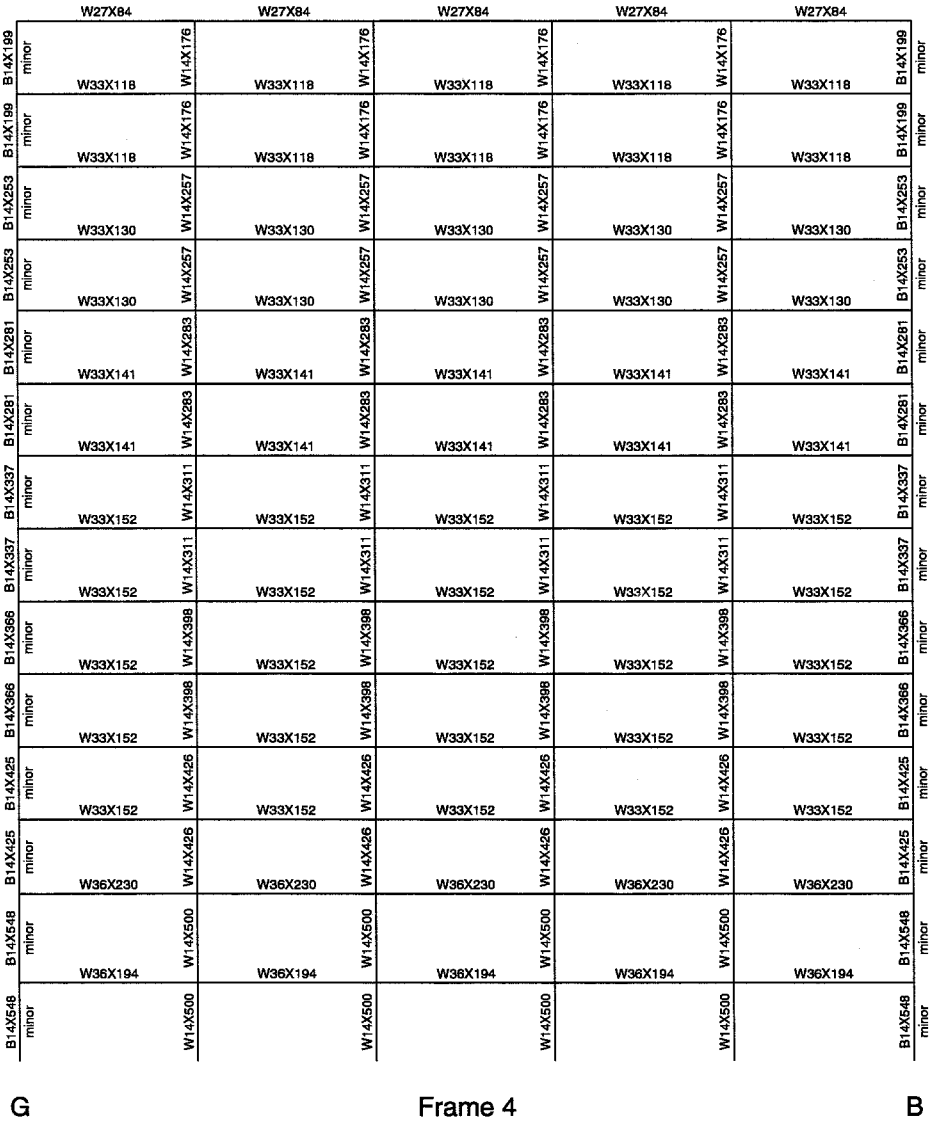

Figure 9.3 West frame section properties.

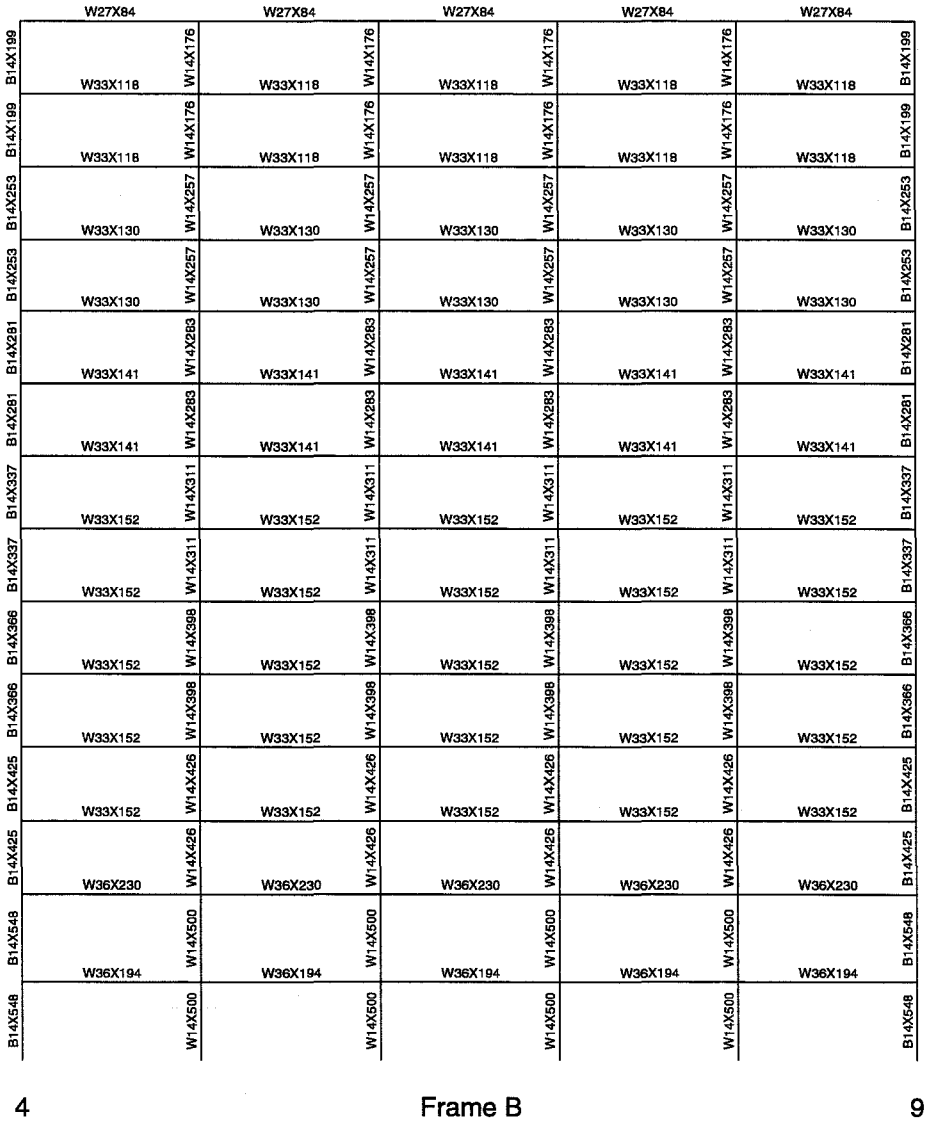

Figure 9.4 North frame section properties.

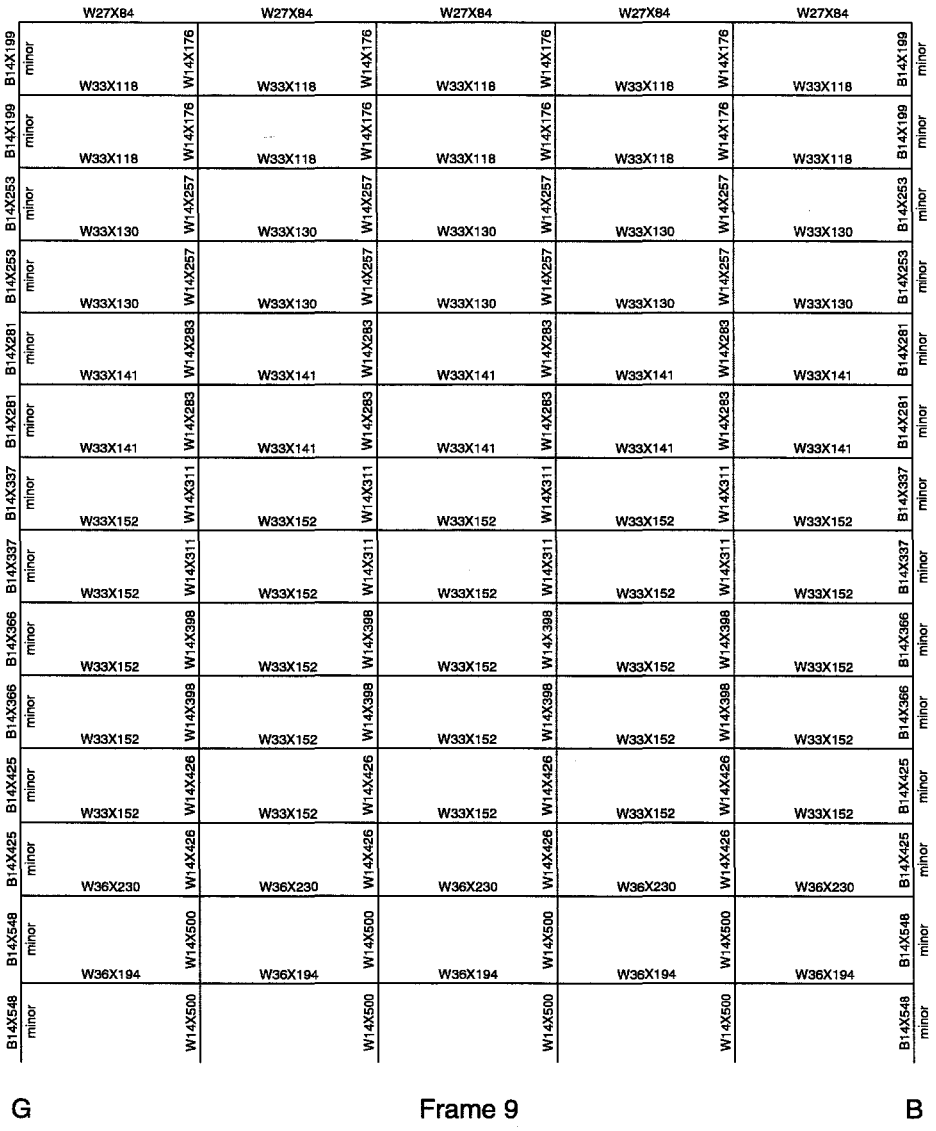

Figure 9.5 East frame section properties.

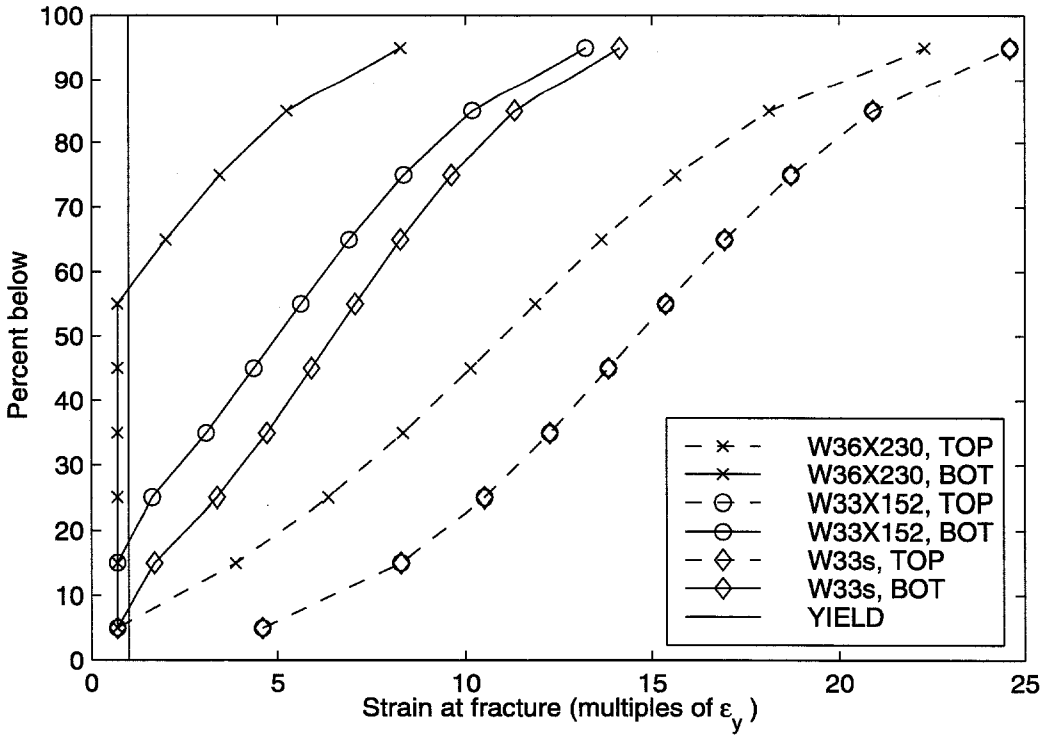

Figure 9.6 Distribution of Maison strain at failure.

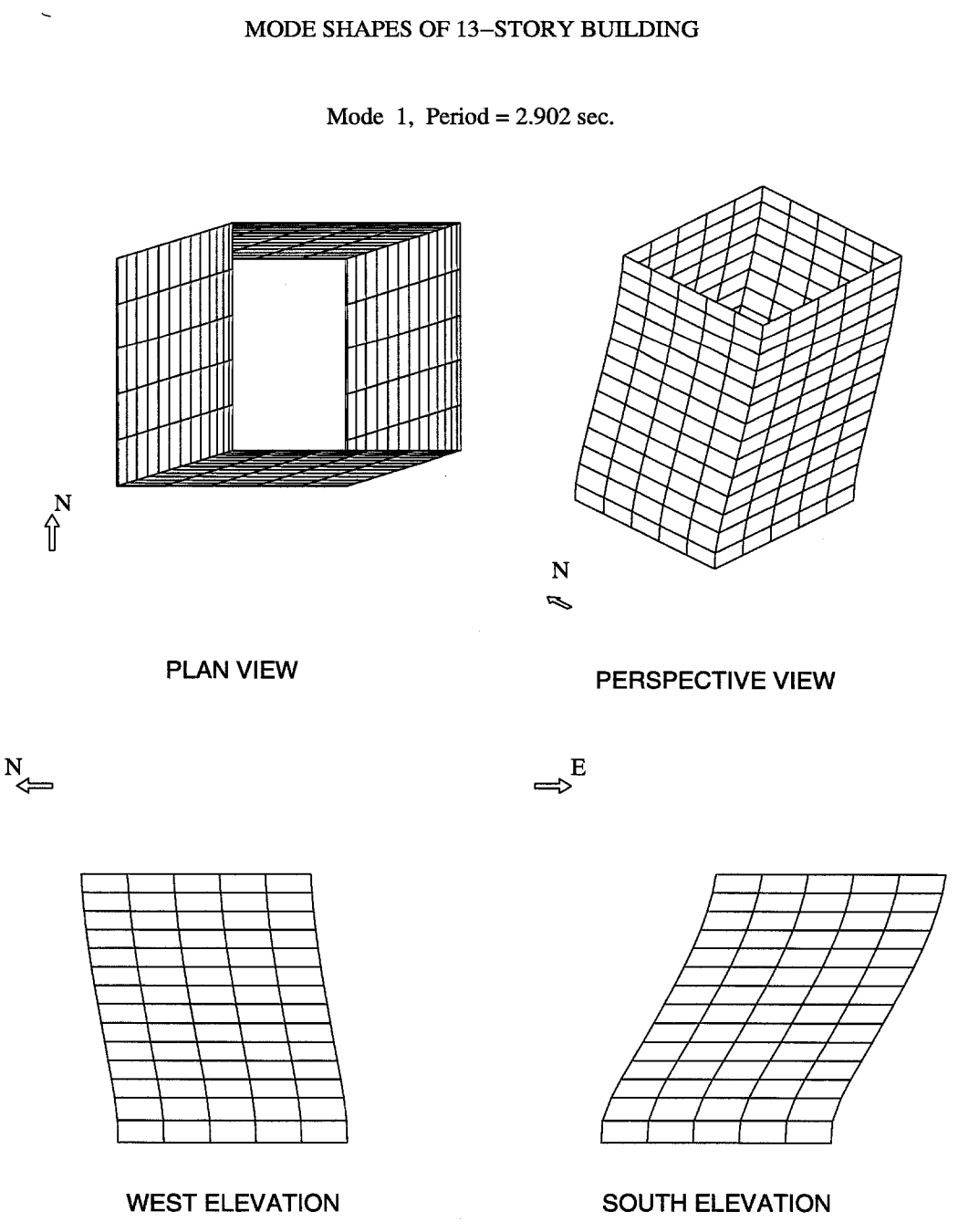

Figure 9.7 13-story building mode 1.

MODE SHAPES OF 13–STORY BUILDING

Mode 2, Period = 2.900 sec.

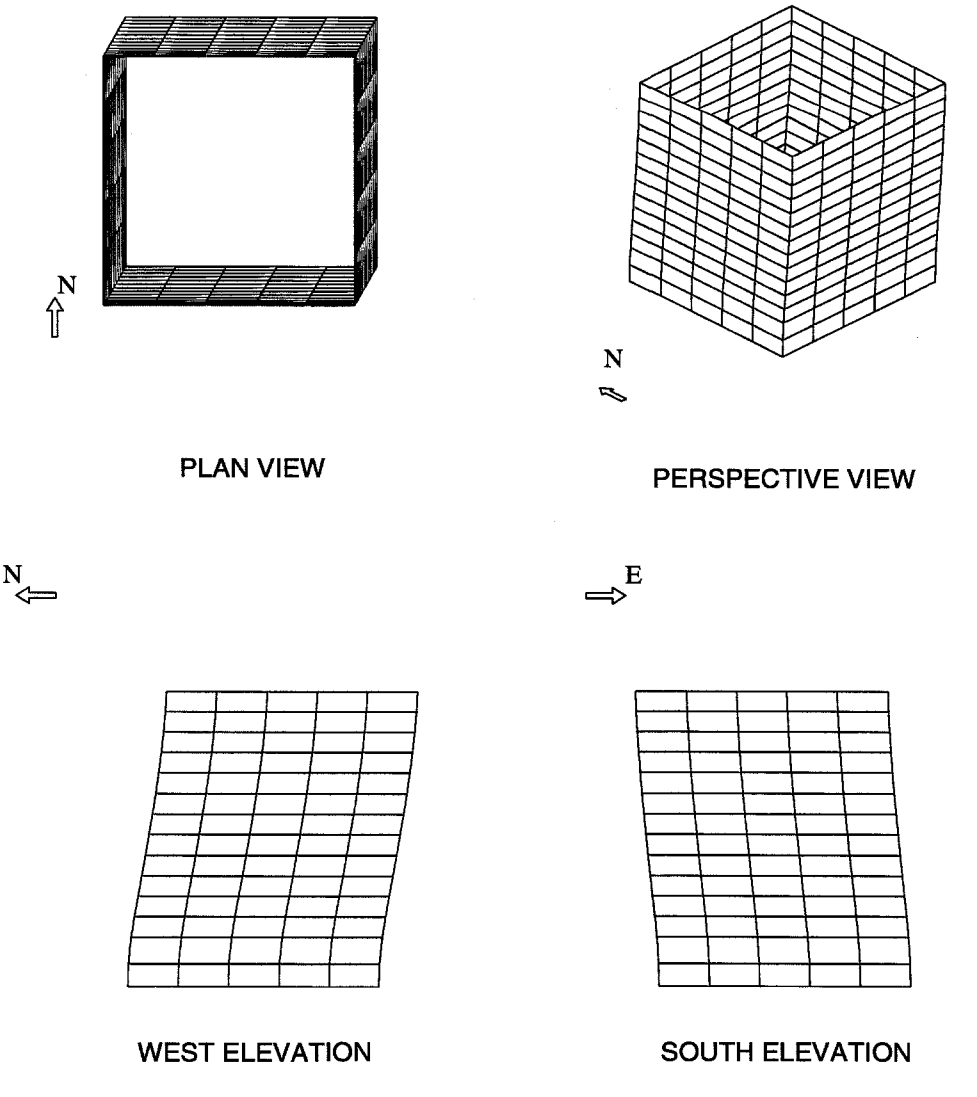

Figure 9.8 13-story building mode 2.

MODE SHAPES OF 13–STORY BUILDING

Mode 3, Period = 2.025 sec.

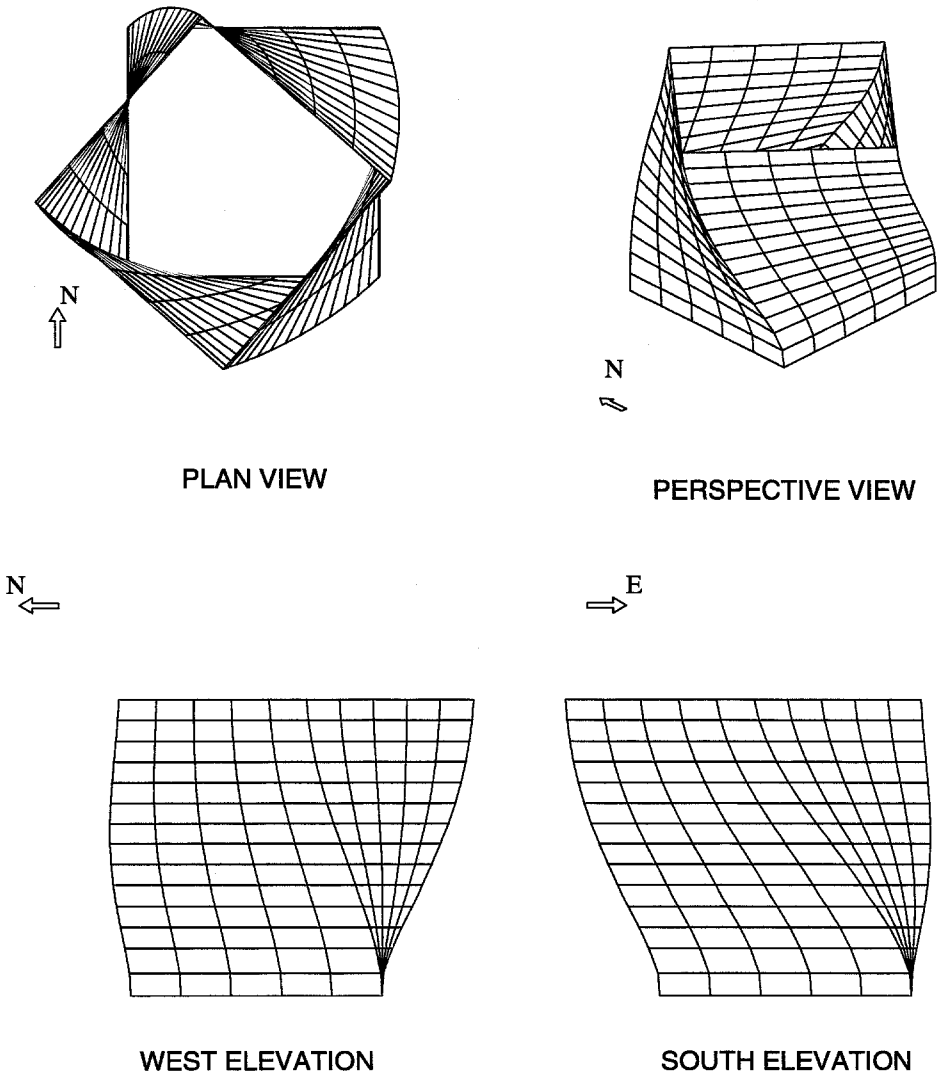

Figure 9.9 13-story building mode 3.

MODE SHAPES OF 13–STORY BUILDING

Mode 4, Period = 0.995 sec.

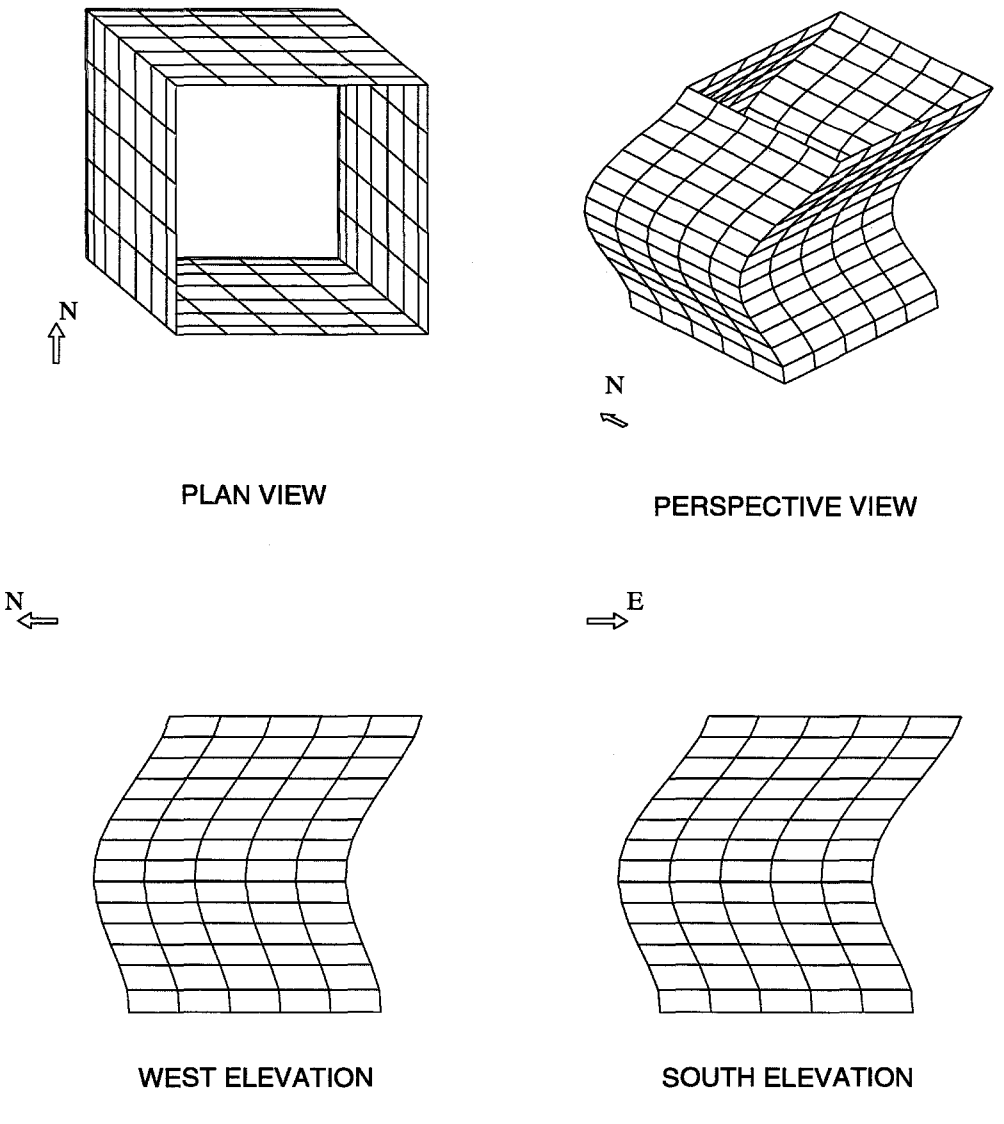

Figure 9.10 13-story building mode 4.

MODE SHAPES OF 13–STORY BUILDING

Mode 5, Period = 0.995 sec.

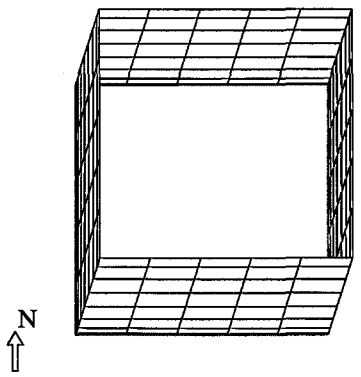

PLAN VIEW

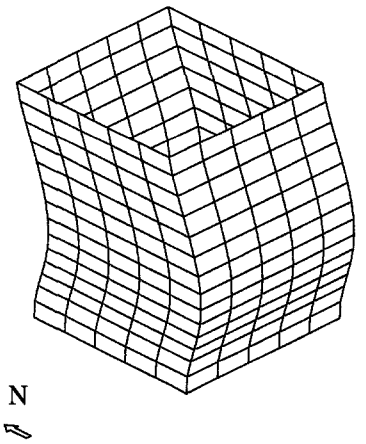

PERSPECTIVE VIEW

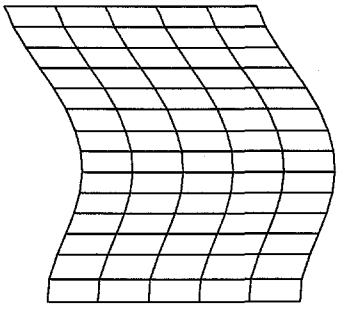

WEST ELEVATION

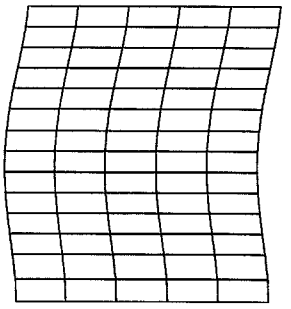

SOUTH ELEVATION

Figure 9.11 13-story building mode 5.

MODE SHAPES OF 13–STORY BUILDING

Mode 6, Period = 0.716 sec.

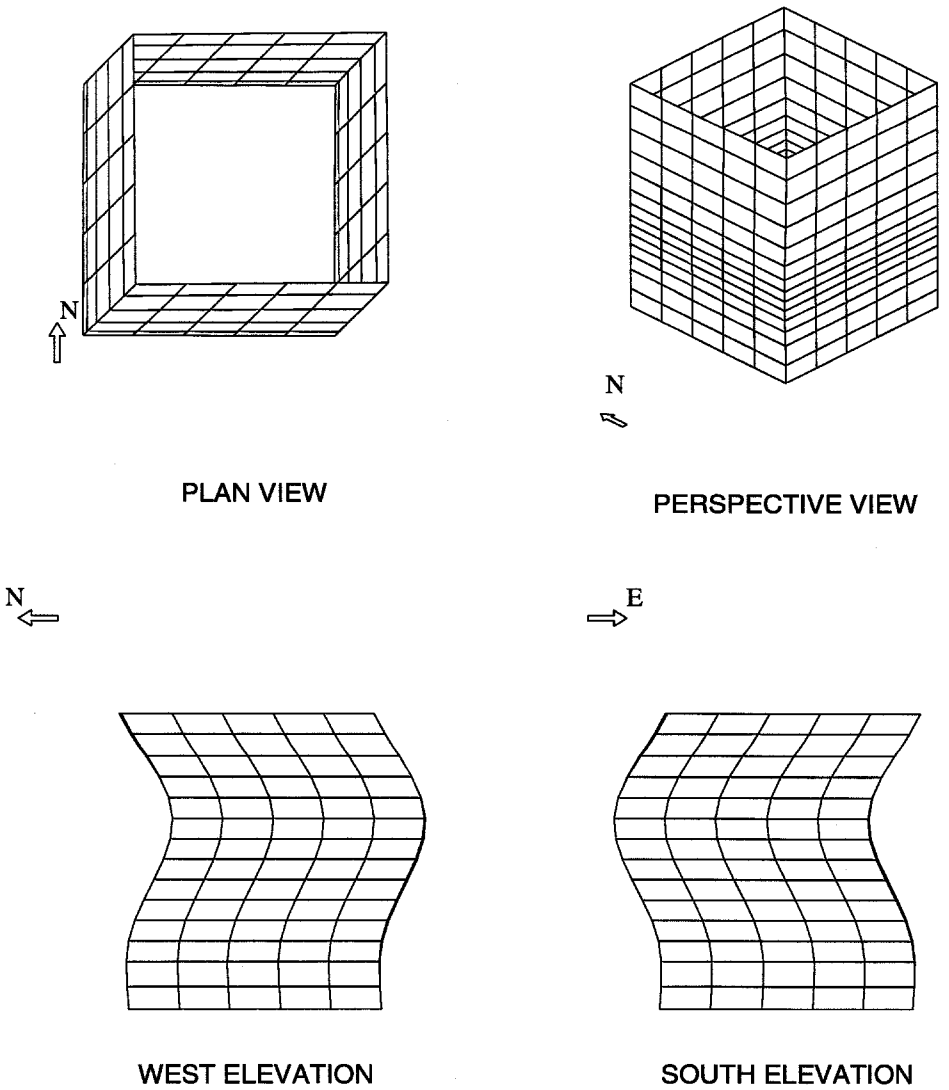

Figure 9.12 13-story building mode 6.

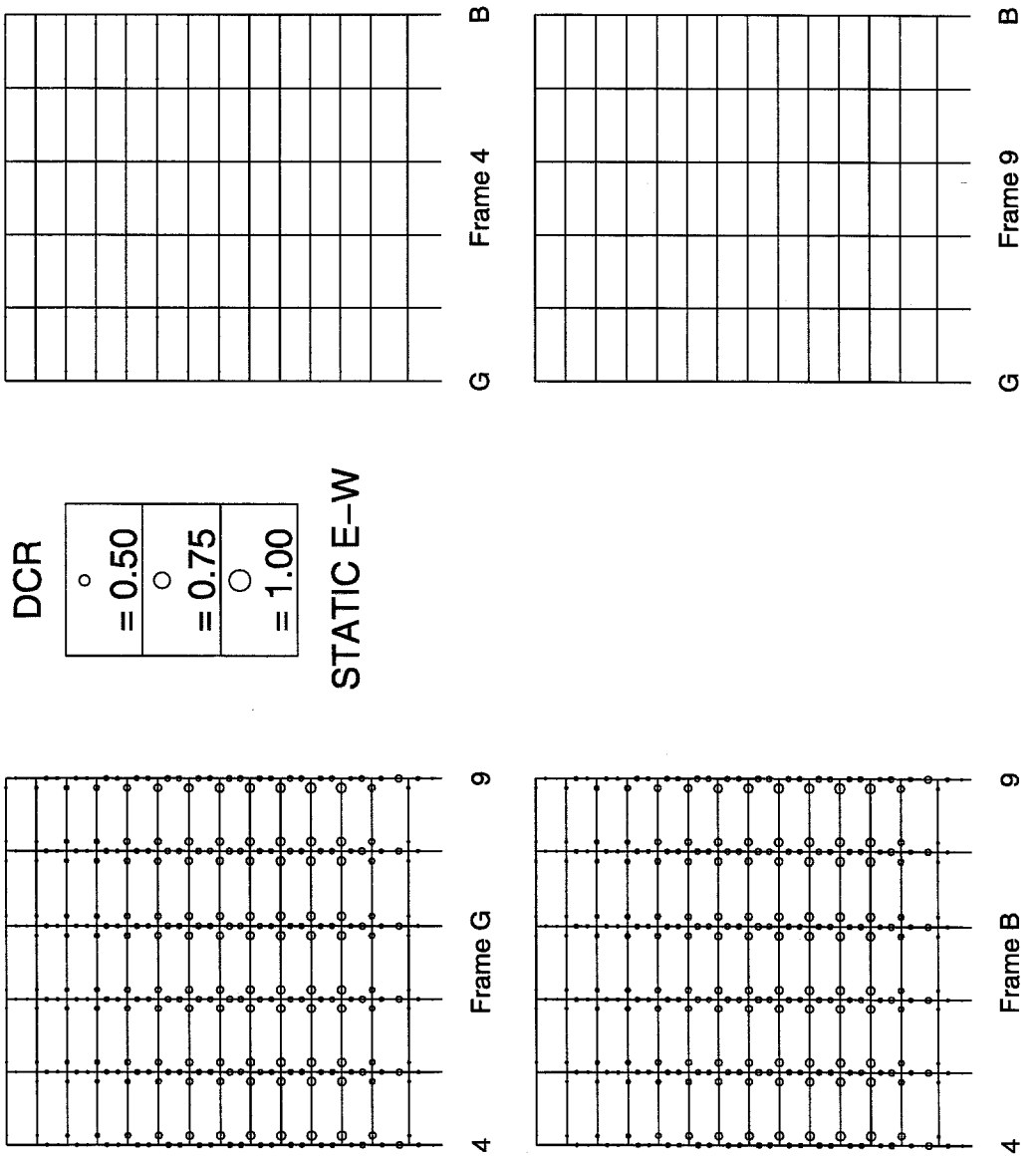

Figure 9.13 13-story building demand capacity ratios, E-W direction.

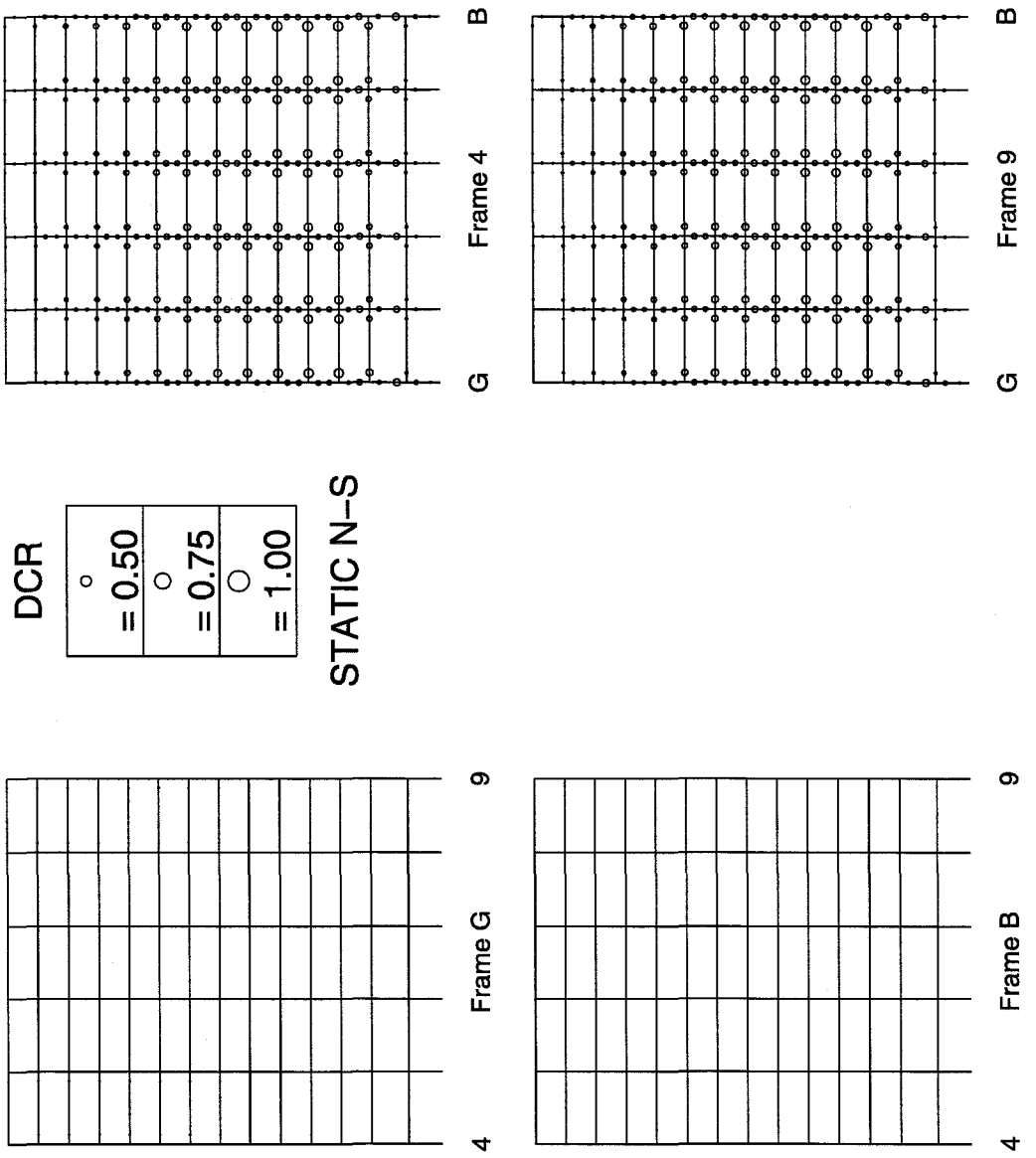

Figure 9.14 13-story building demand capacity ratios, N-S direction.

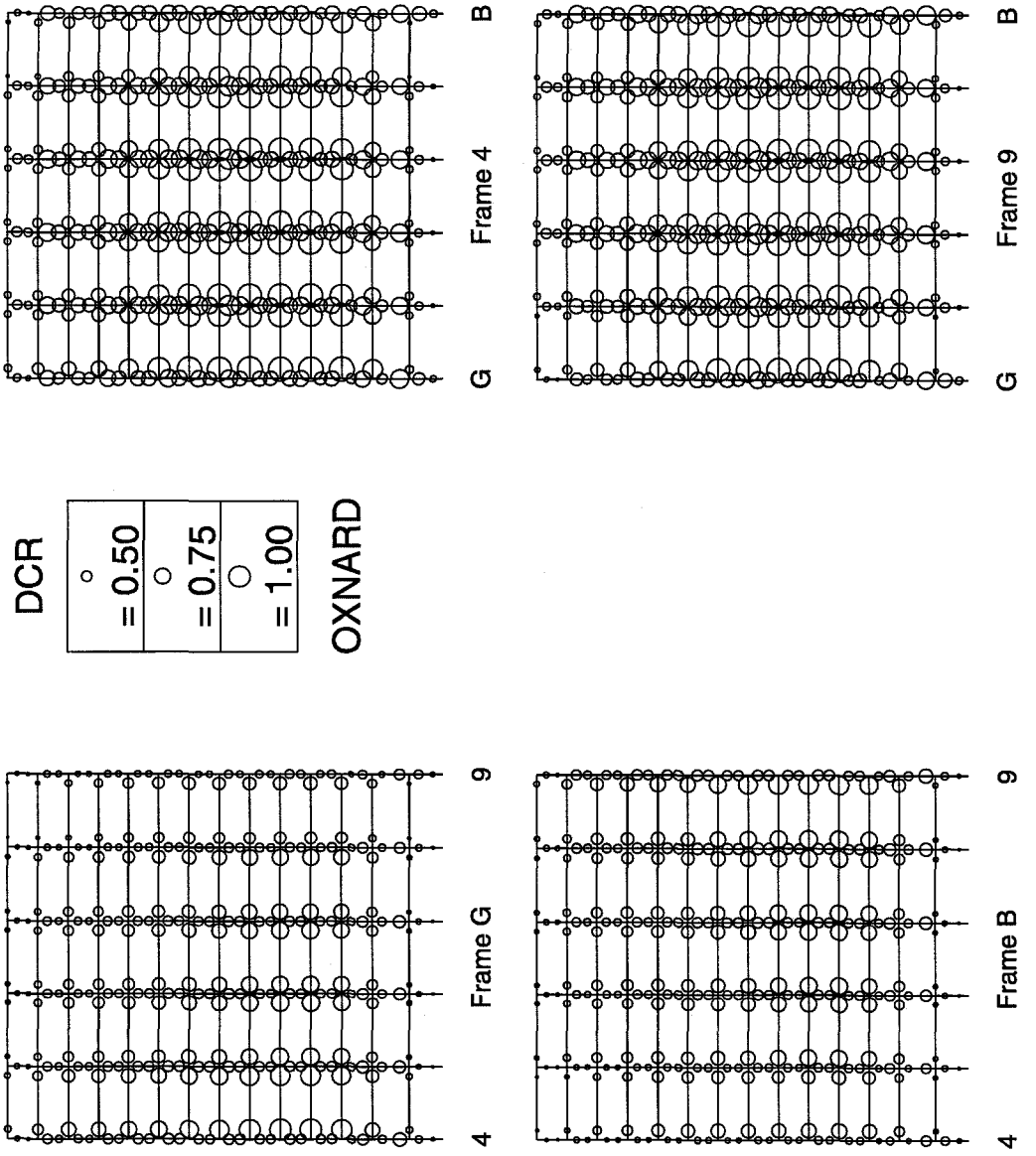

Figure 9.15 13-story building demand capacity ratios, Oxnard record.

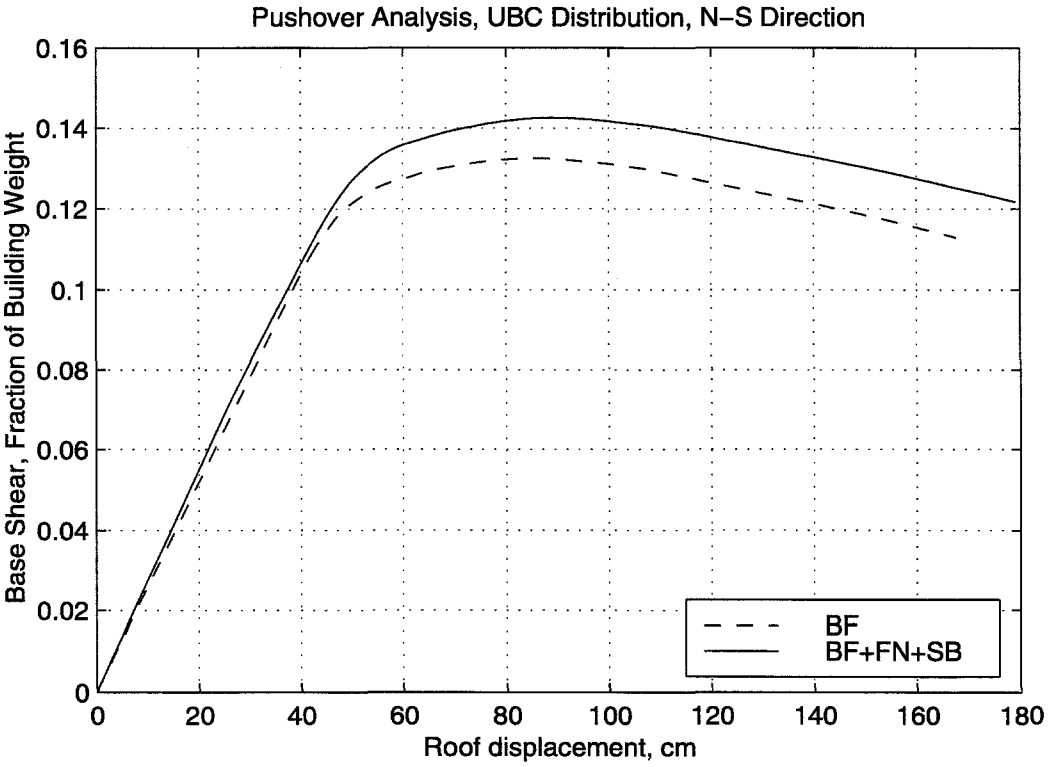

Figure 9.16 13-story pushover analysis.

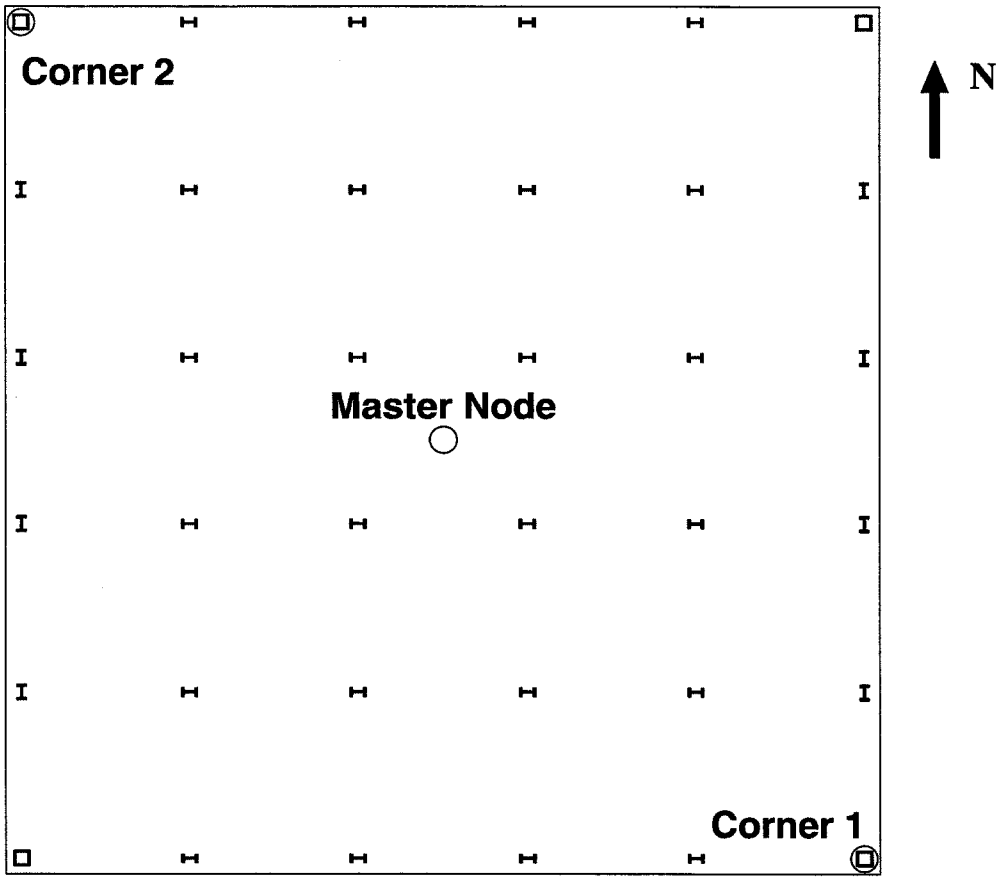

Figure 9.17 Locations at roof for time histories.

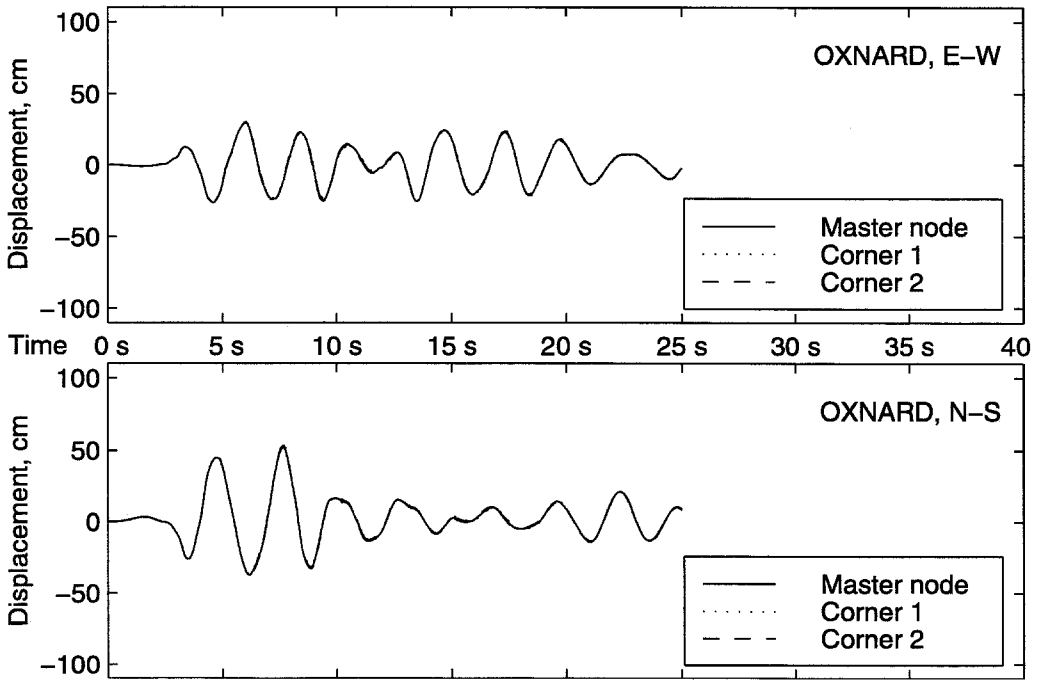

Figure 9.18 Relative roof displacements, Maison fracture model and Oxnard record.

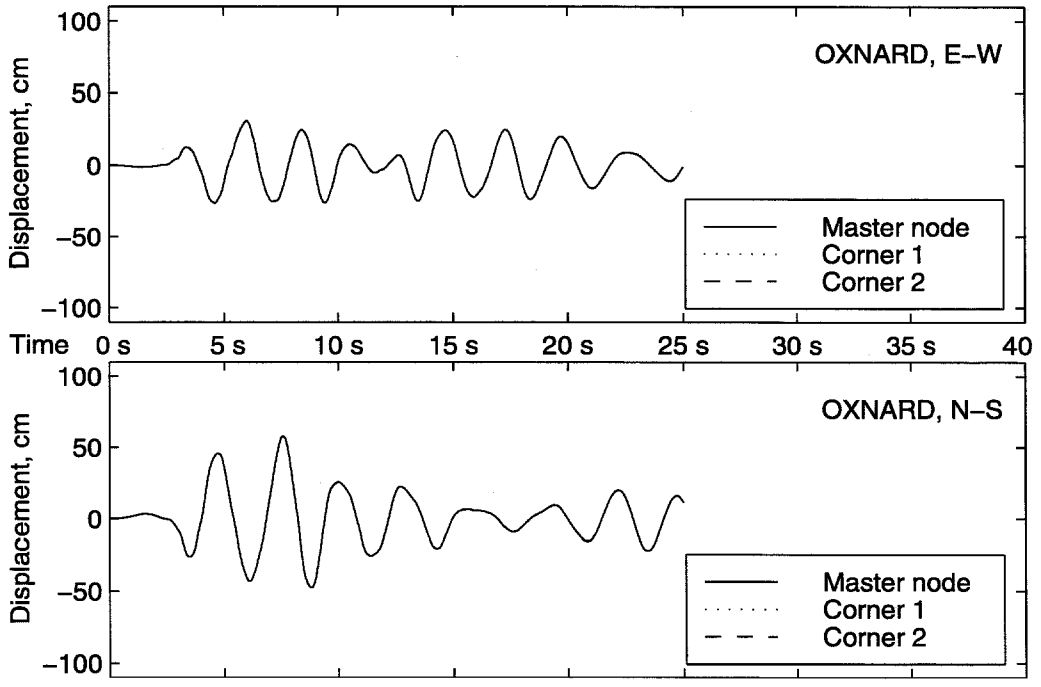

Figure 9.19 Relative roof displacements, inelastic model and Oxnard record.

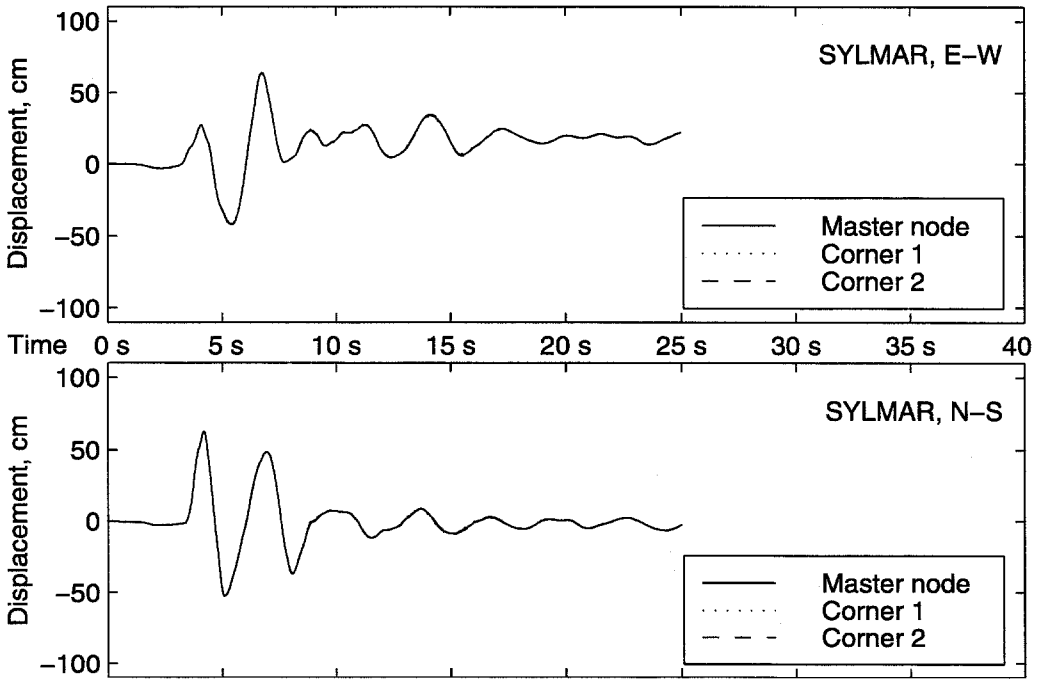

Figure 9.20 Relative roof displacements, Maison fracture model and Sylmar record.

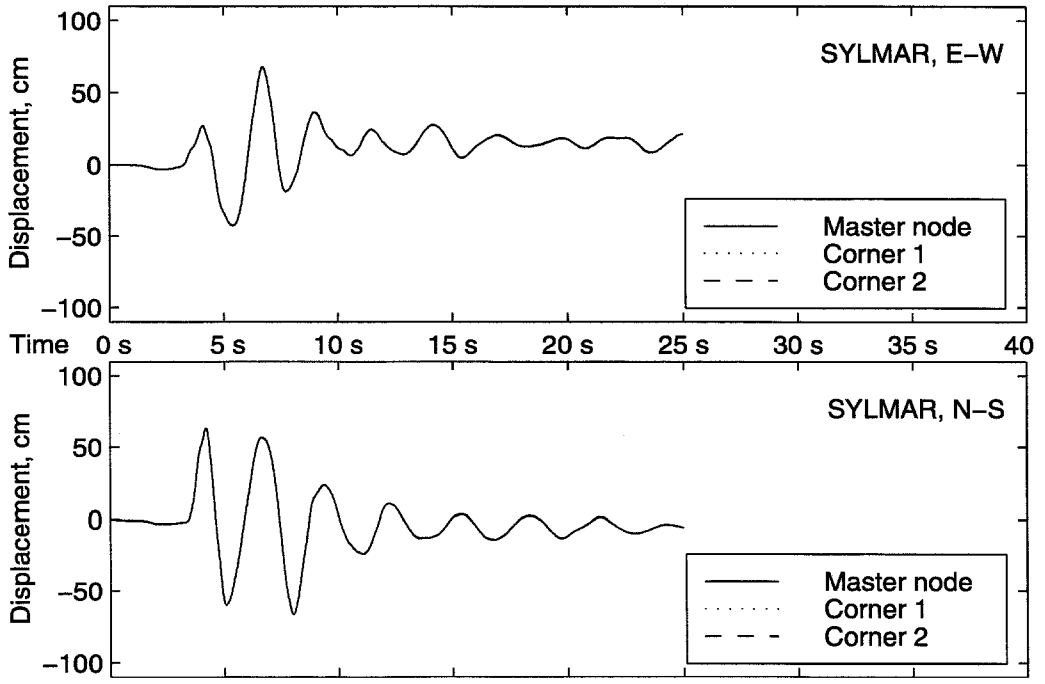

Figure 9.21 Relative roof displacements, inelastic model and Sylmar record.

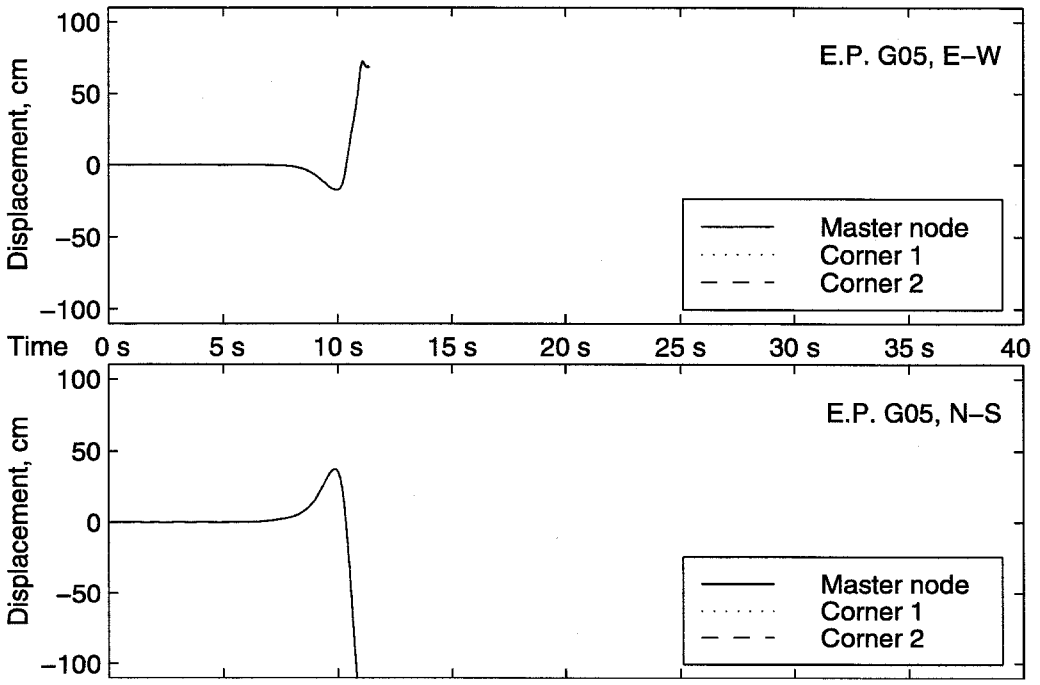

Figure 9.22 Relative roof displacements, Maison fracture model and E. P. G05 record.

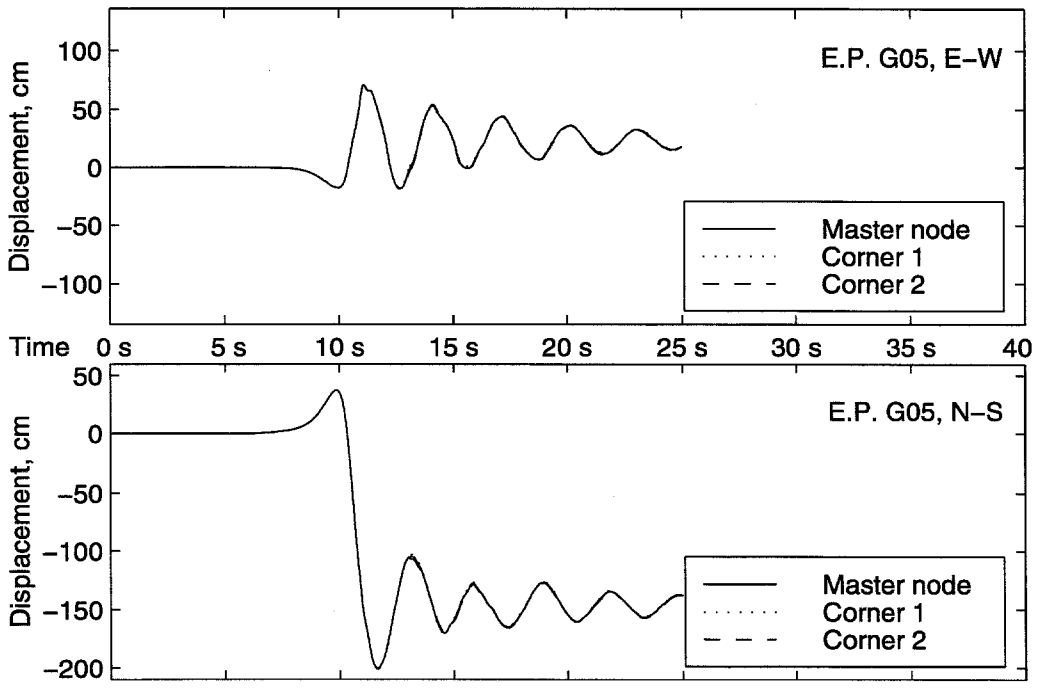

Figure 9.23 Relative roof displacements, inelastic model and E. P. G05 record.

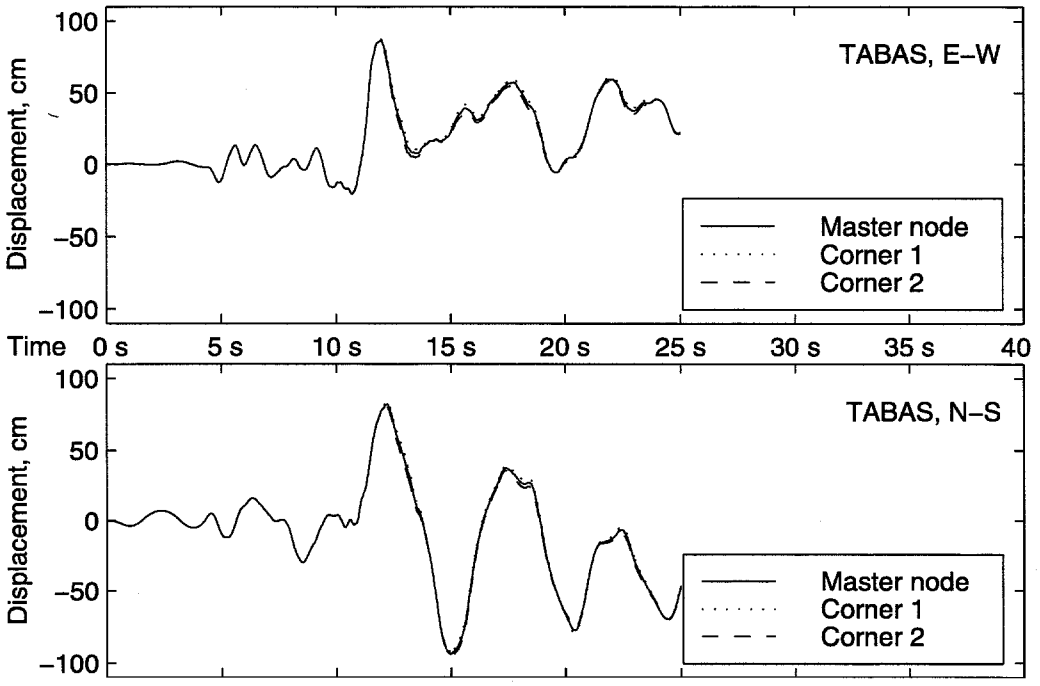

Figure 9.24 Relative roof displacements, Maison fracture model and Tabas record.

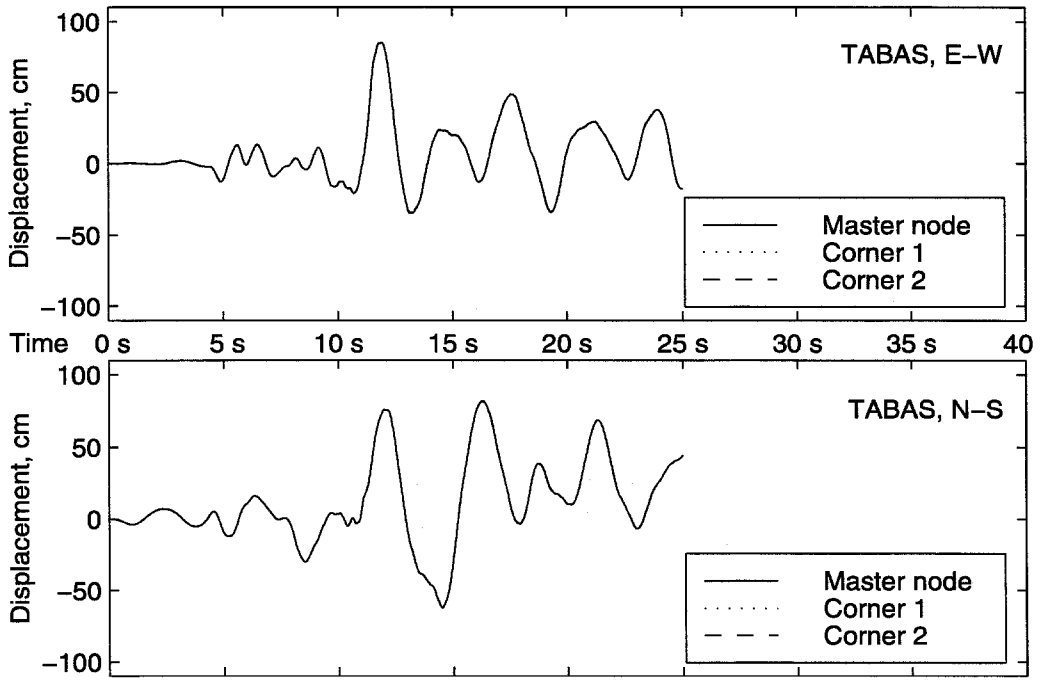

Figure 9.25 Relative roof displacements, inelastic model and Tabas record.

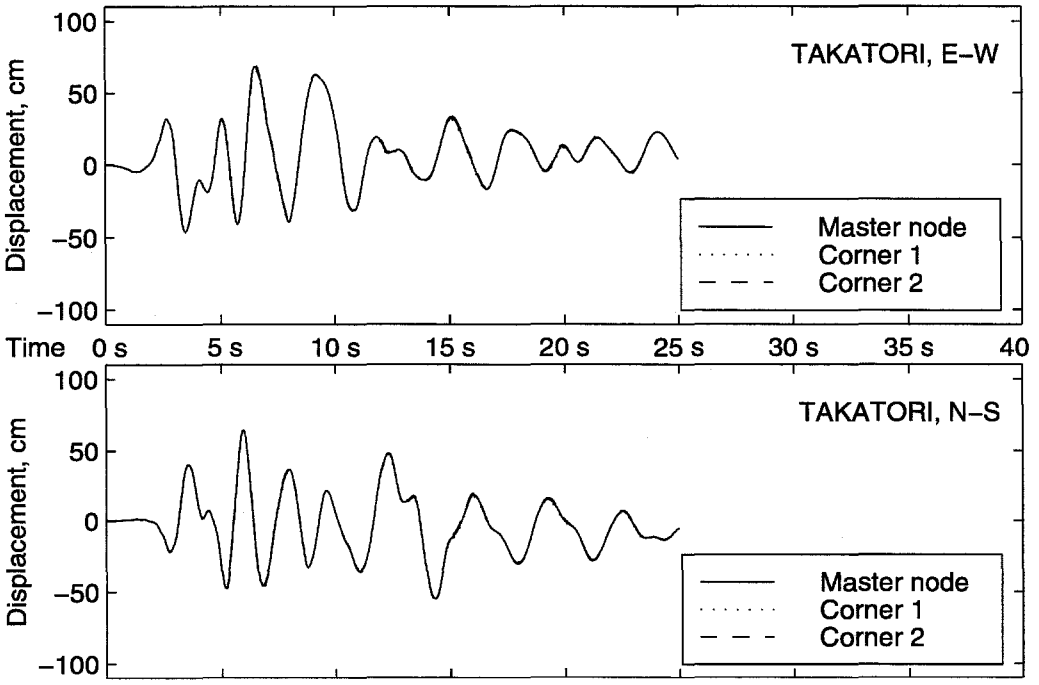

Figure 9.26 Relative roof displacements, Maison fracture model and Takatori record.

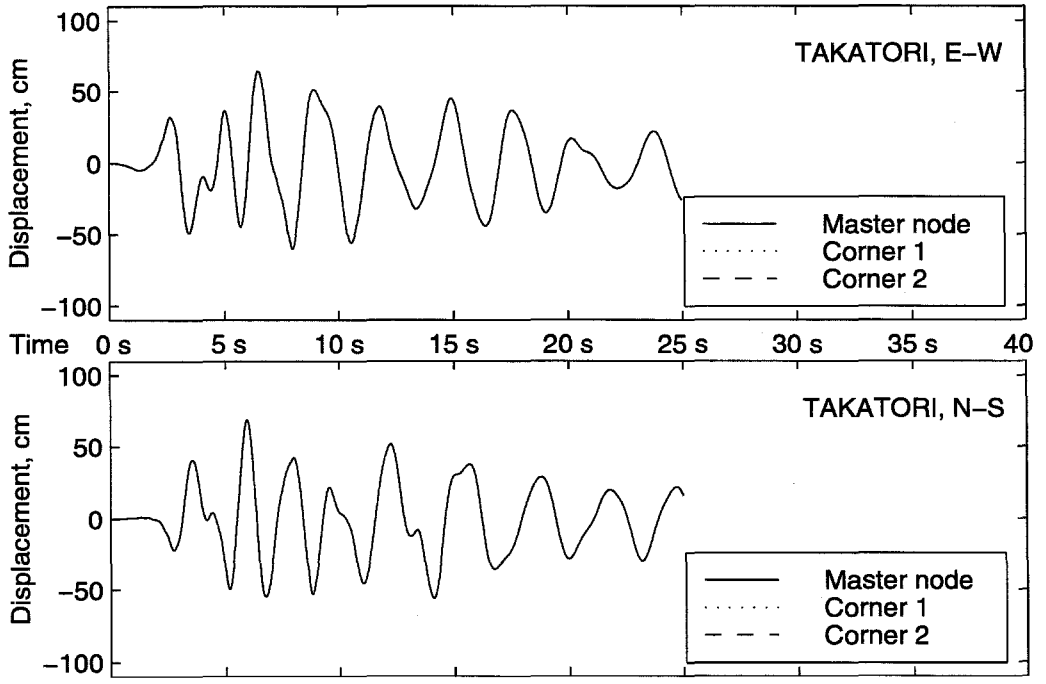

Figure 9.27 Relative roof displacements, inelastic model and Takatori record.

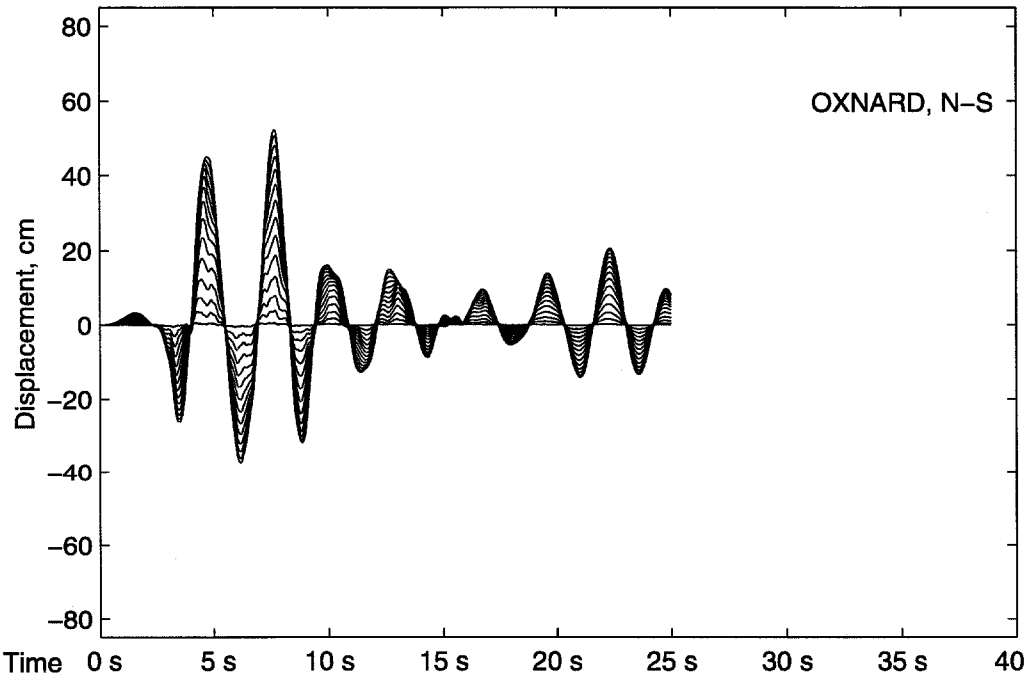

Figure 9.28 Relative floor displacements, Maison fracture model and Oxnard record.

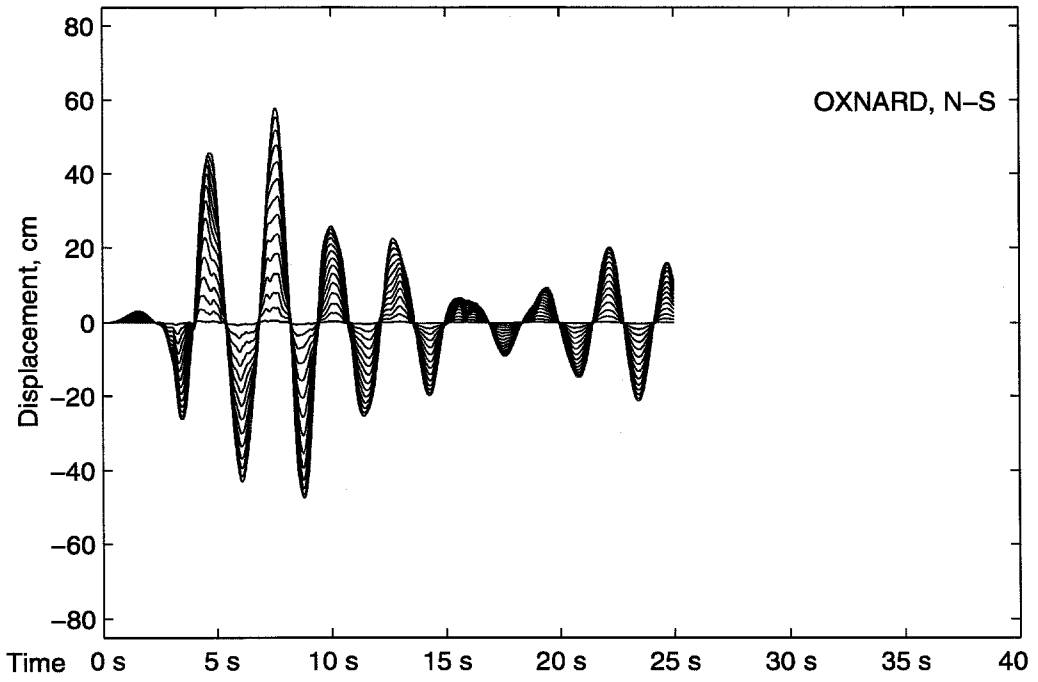

Figure 9.29 Relative floor displacements, inelastic model and Oxnard record.

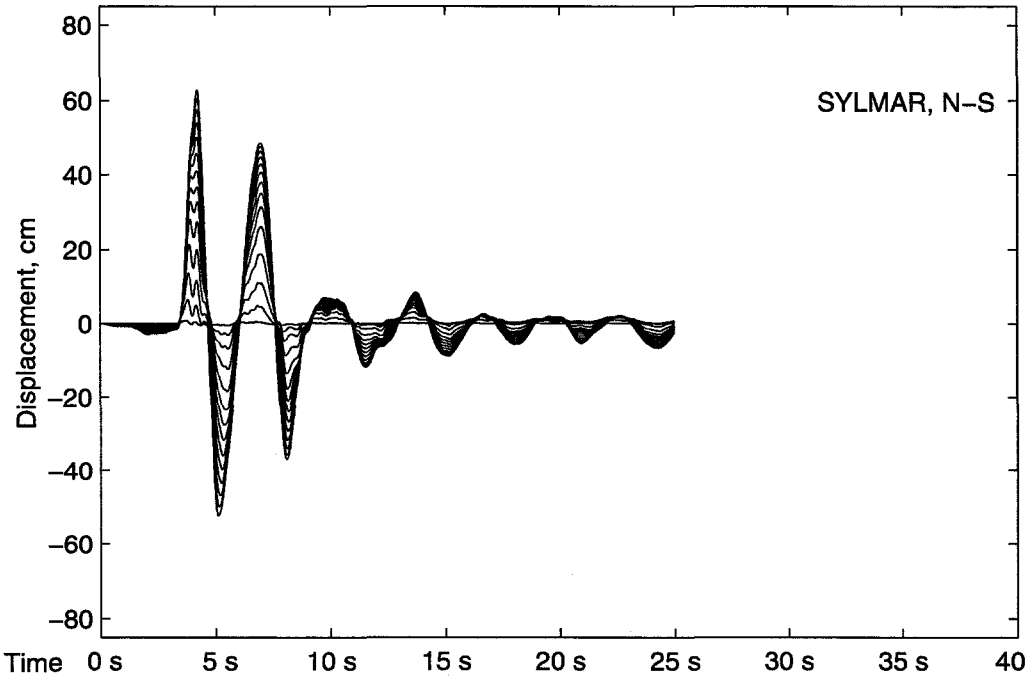

Figure 9.30 Relative floor displacements, Maison fracture model and Sylmar record.

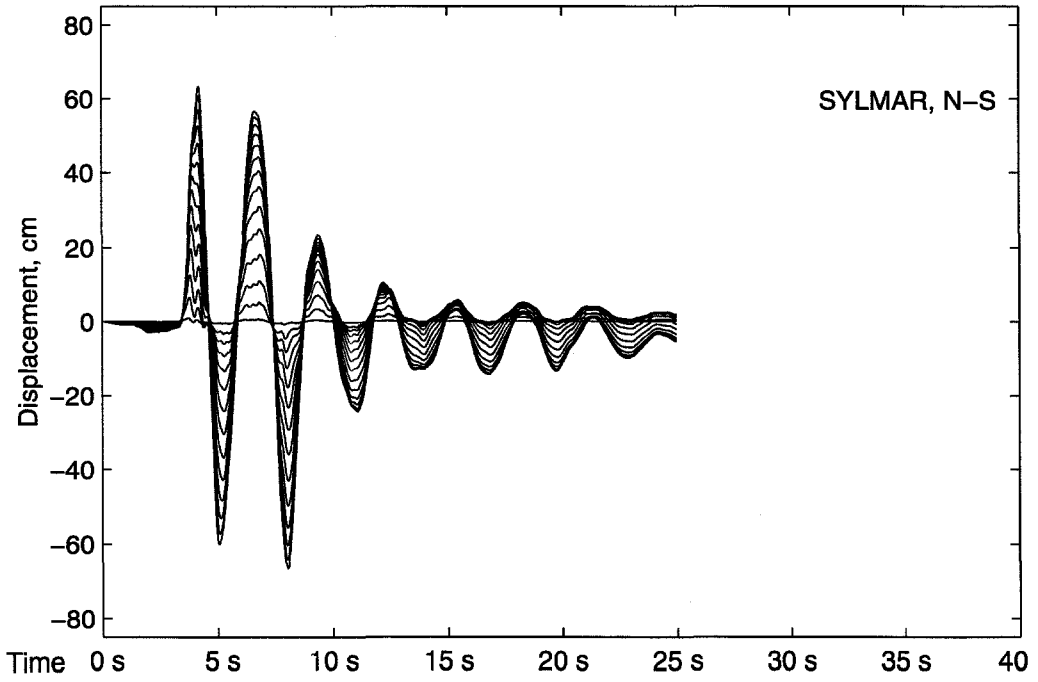

Figure 9.31 Relative floor displacements, inelastic model and Sylmar record.

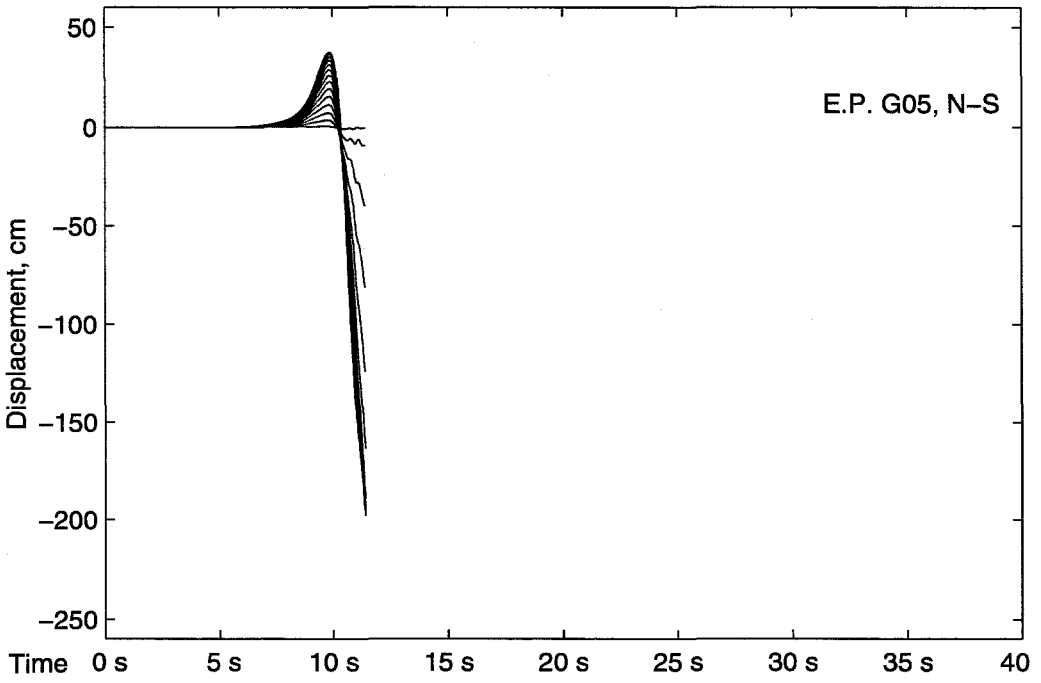

Figure 9.32 Relative floor displacements, Maison fracture model and E. P. G05 record.

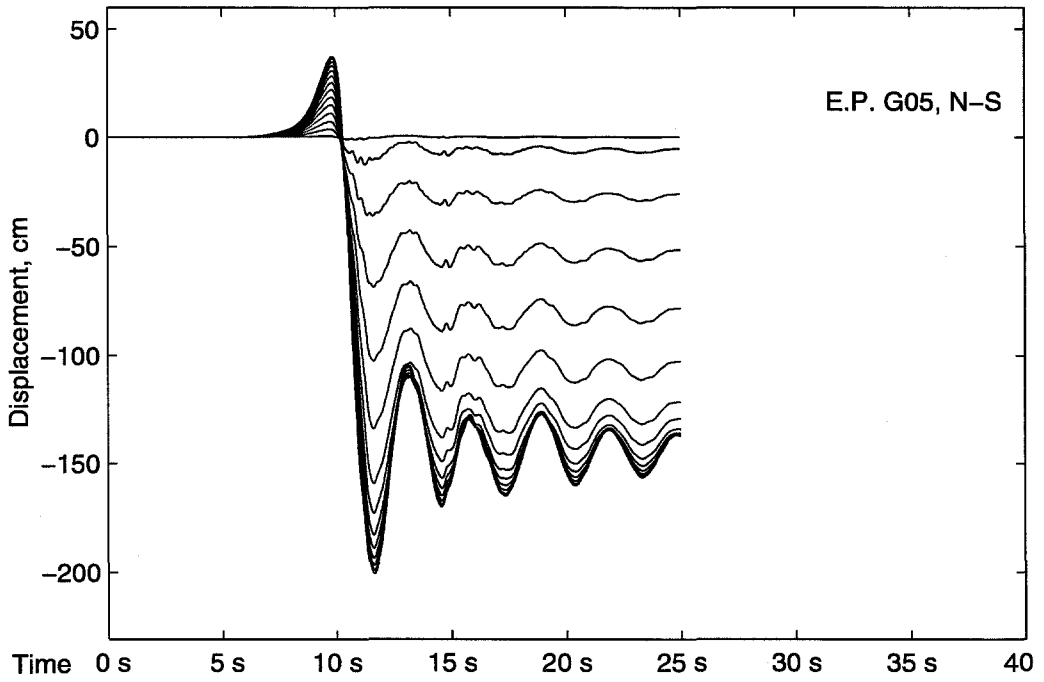

Figure 9.33 Relative floor displacements, inelastic model and E. P. G05 record.

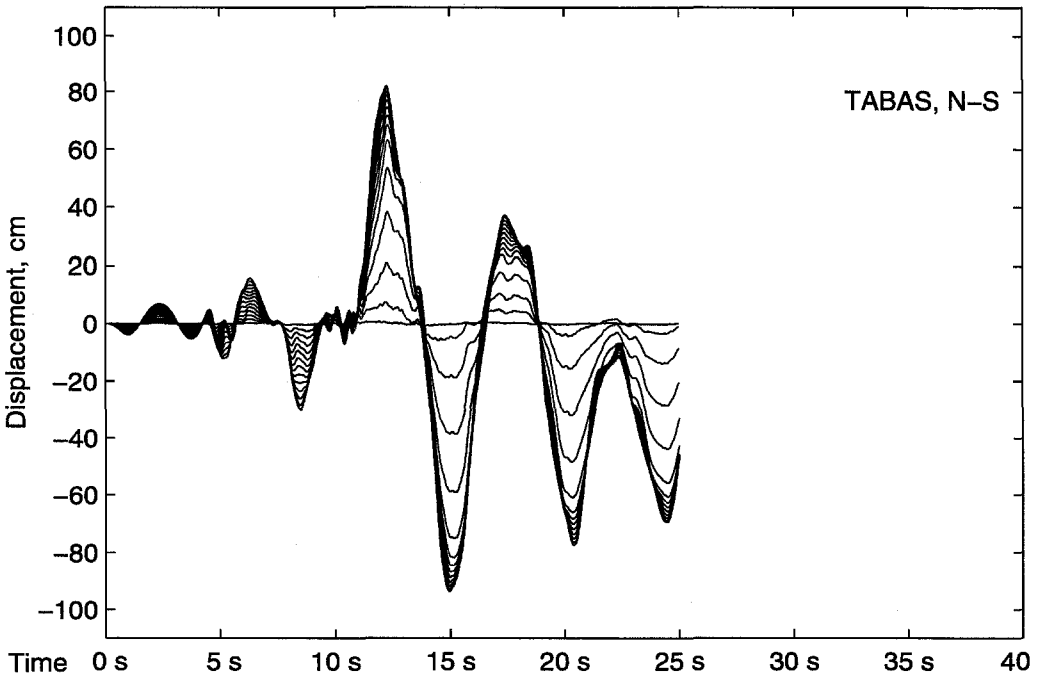

Figure 9.34 Relative floor displacements, Maison fracture model and Tabas record.

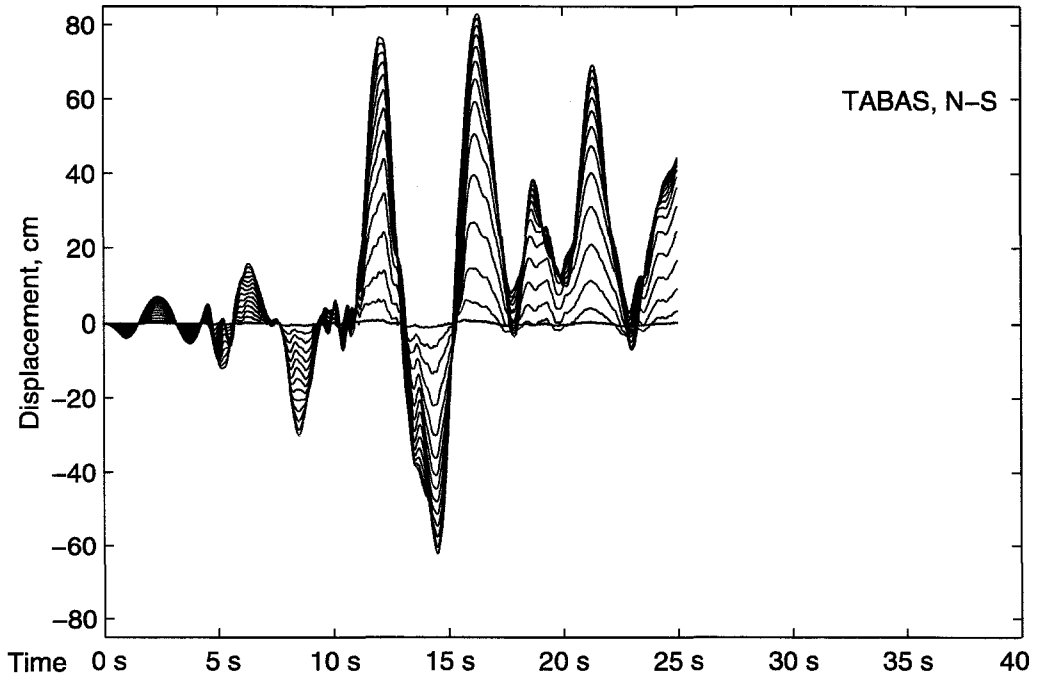

Figure 9.35 Relative floor displacements, inelastic model and Tabas record.

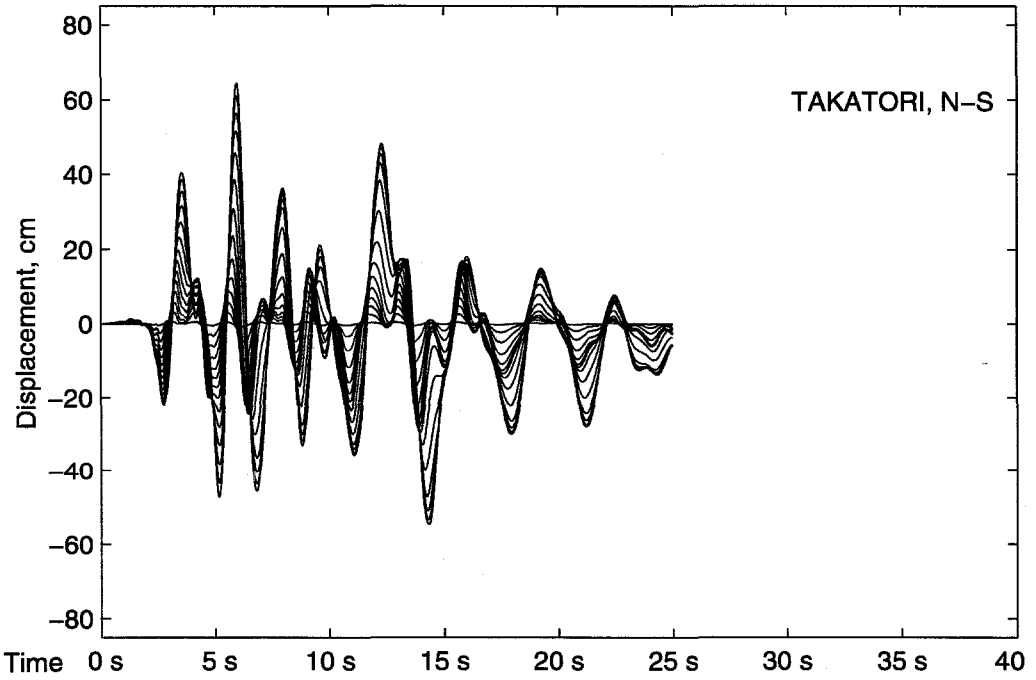

Figure 9.36 Relative floor displacements, Maison fracture model and Takatori record.

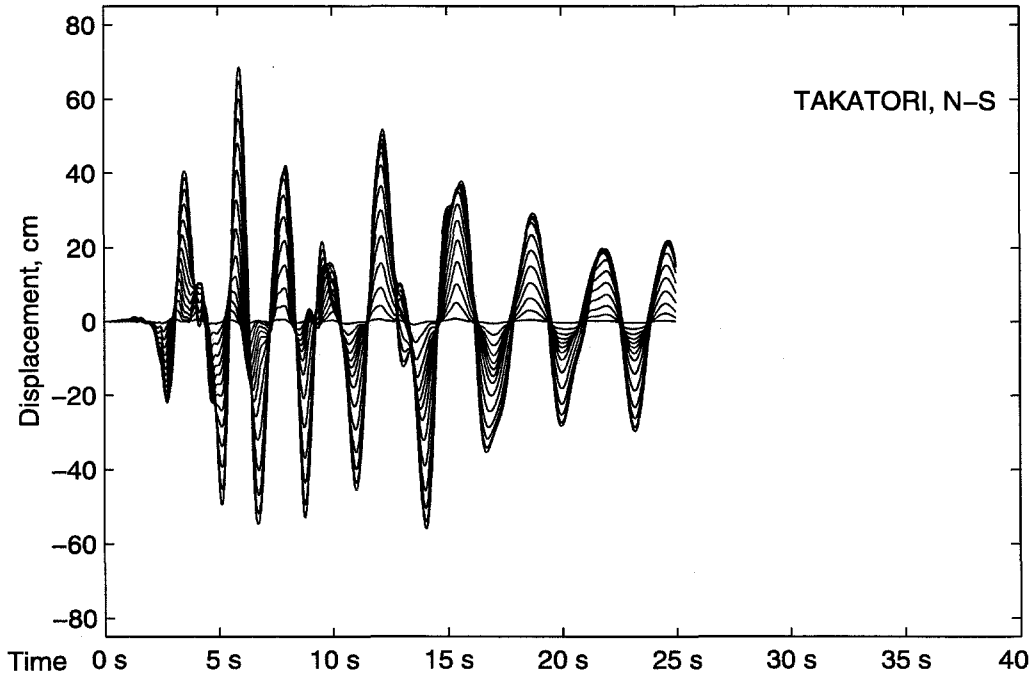

Figure 9.37 Relative floor displacements, inelastic model and Takatori record.

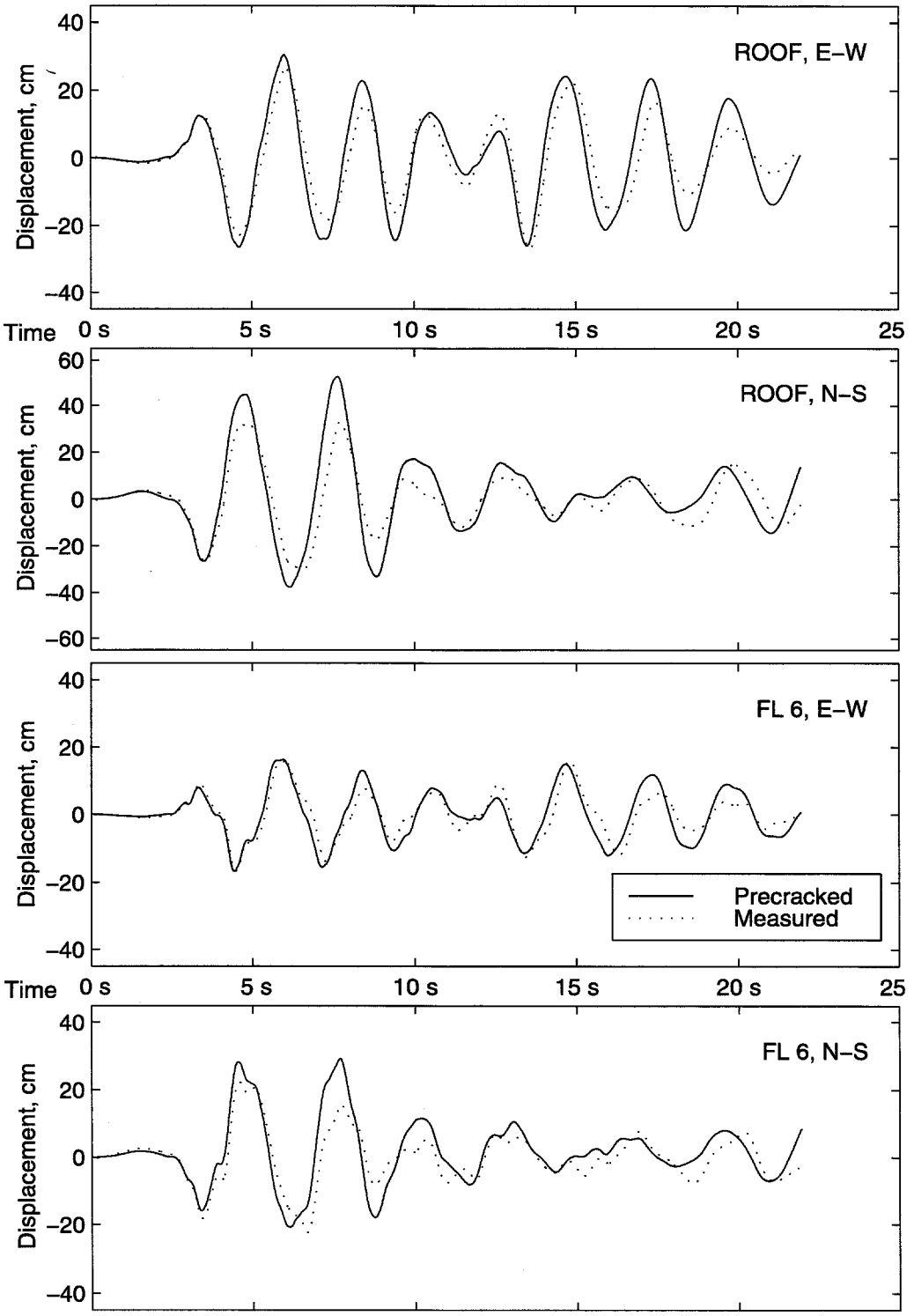

Figure 9.38 Measured vs. calculated response to Oxnard record using prefractured model.

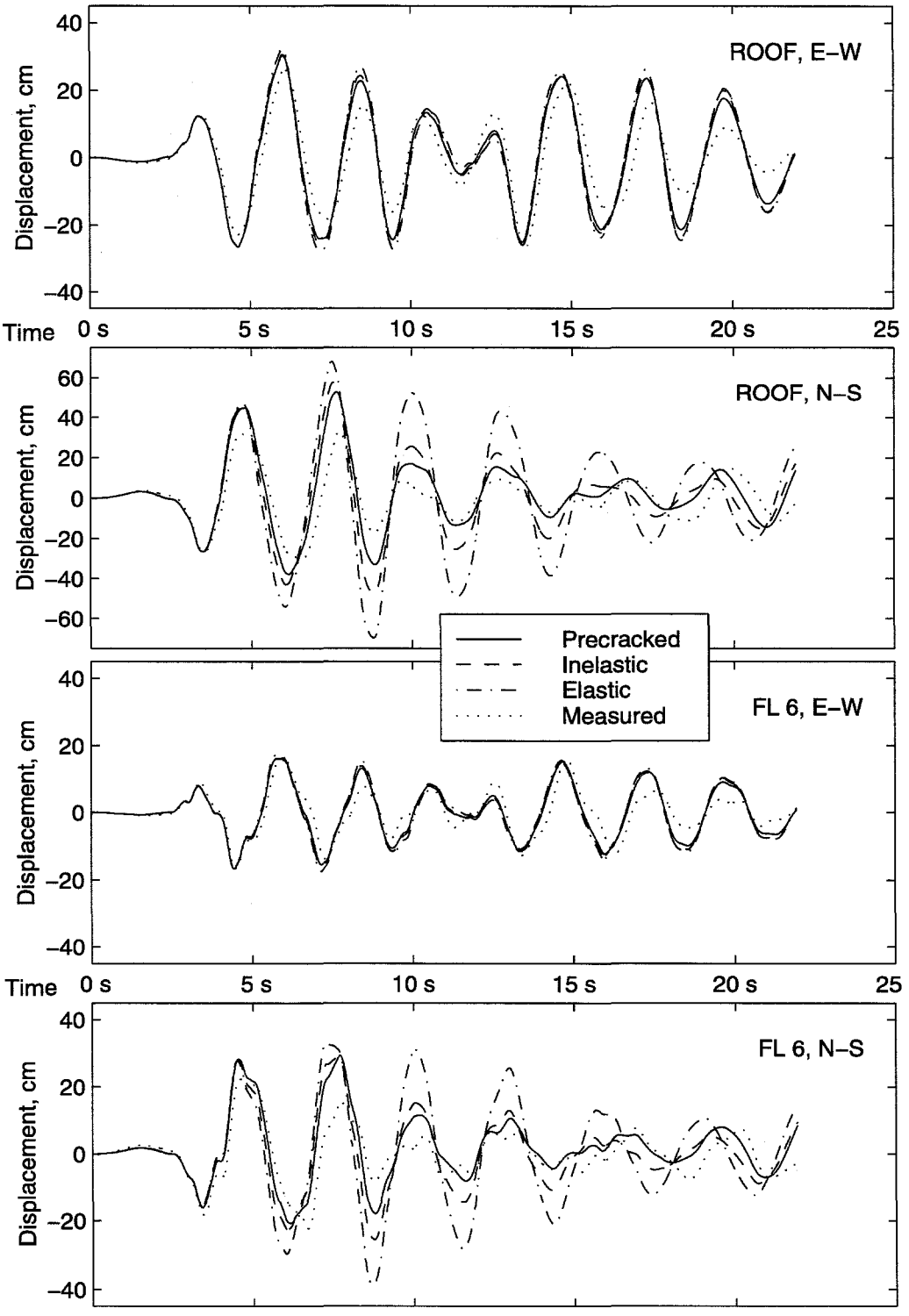

Figure 9.39 Model comparison for Oxnard record.

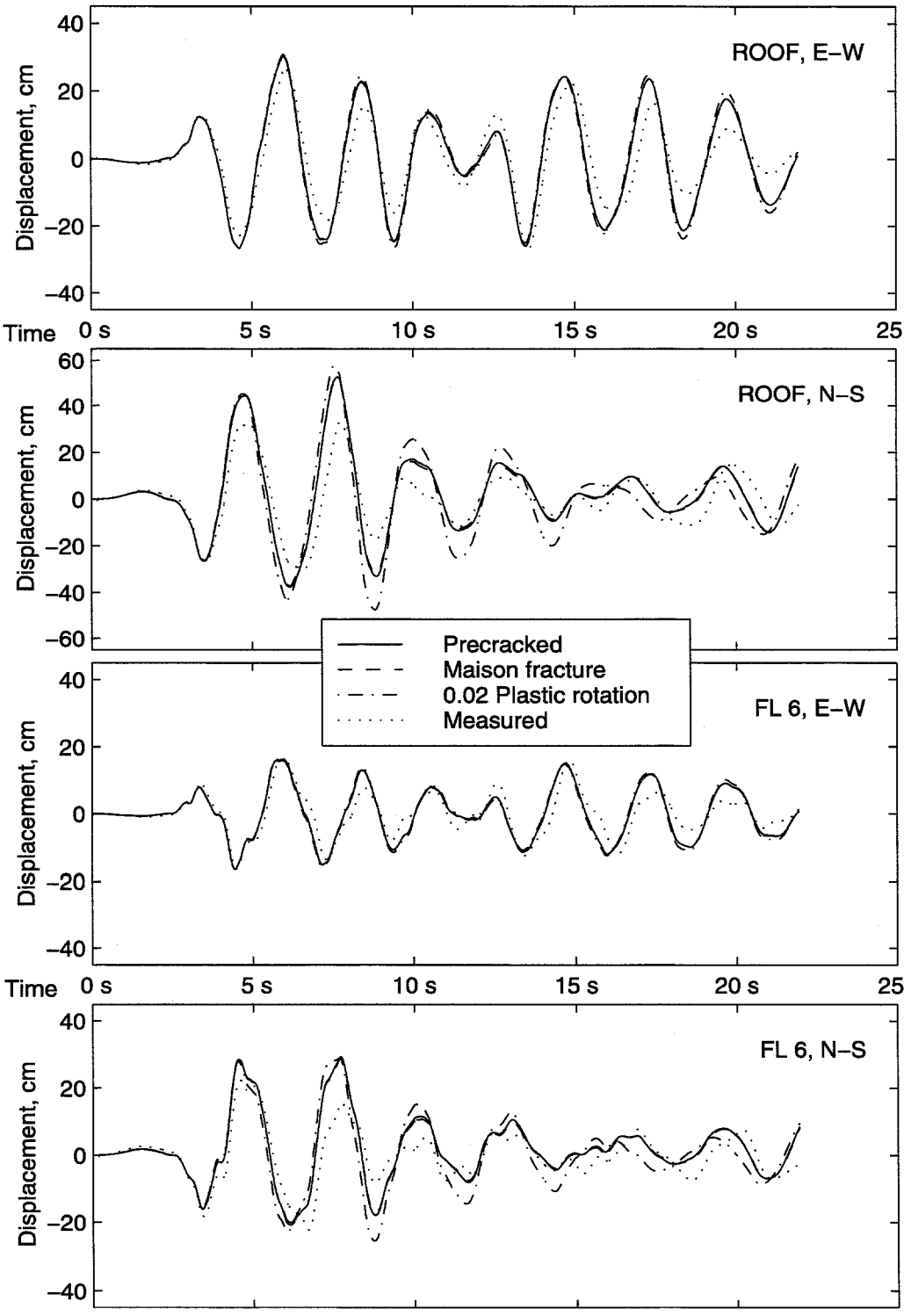

Figure 9.40 Fracture model comparison for Oxnard record.

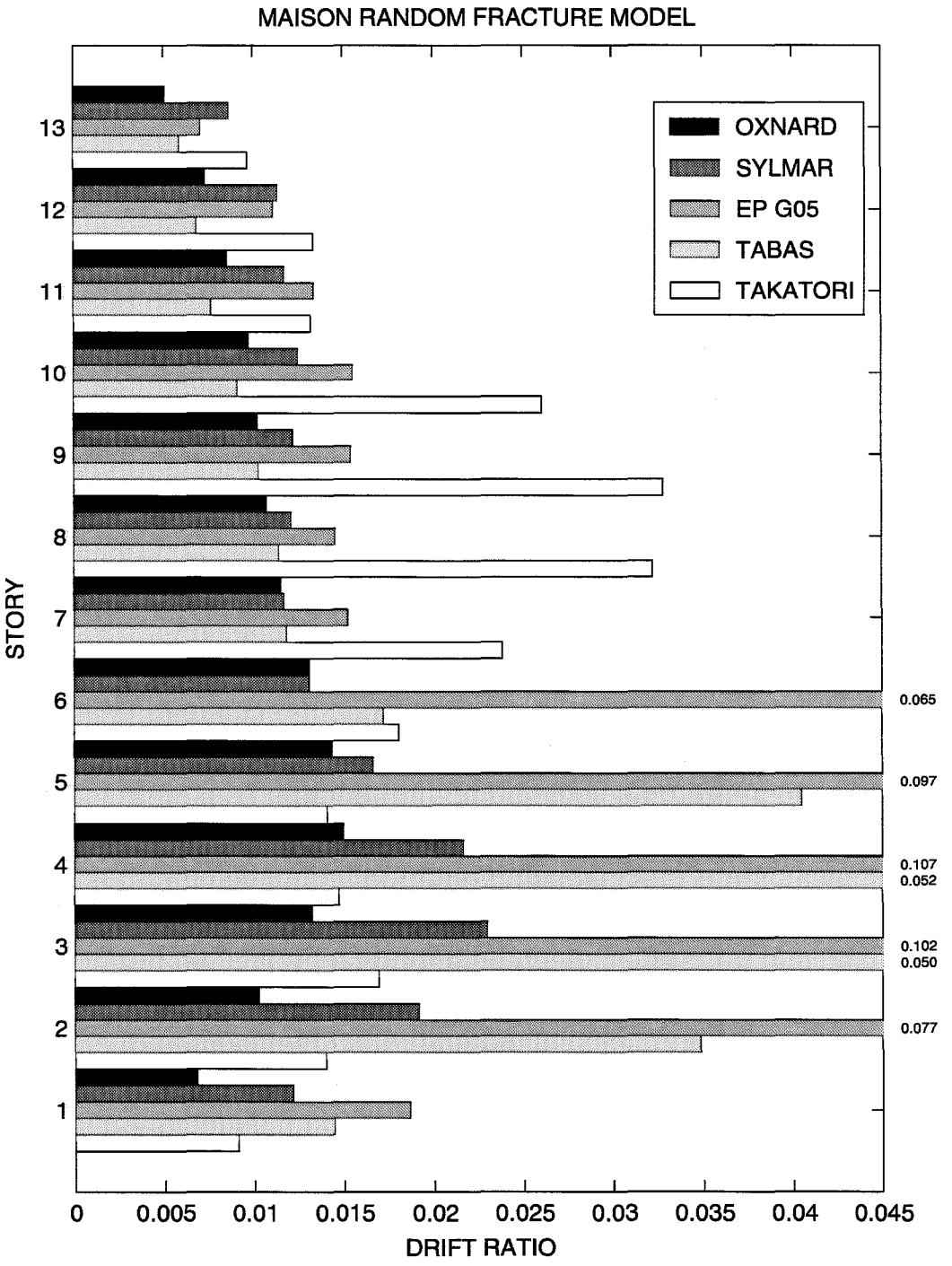

Figure 9.41 13-story building peak drift ratios for distributed random fracture model.

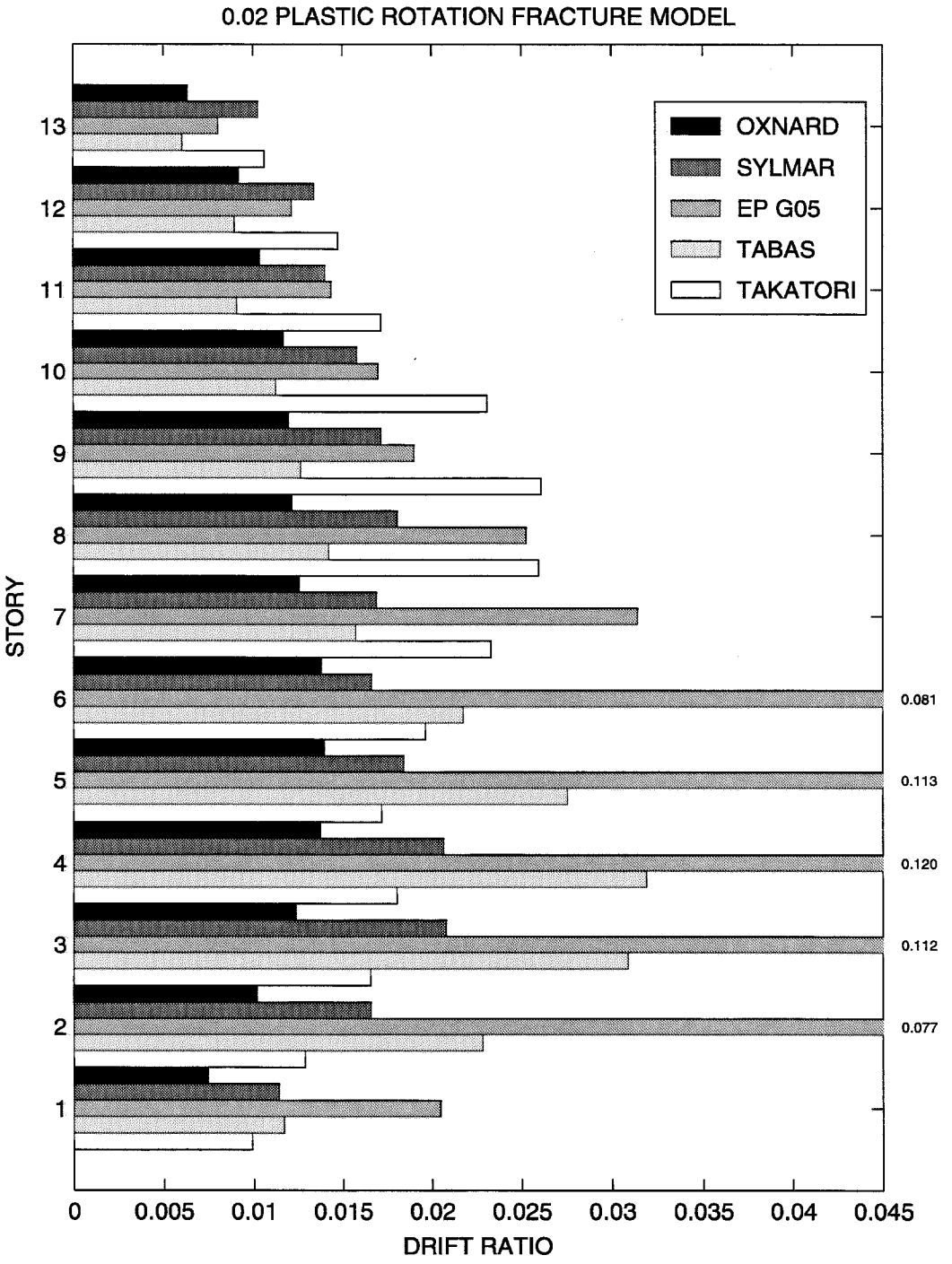

Figure 9.42 13-story building peak drift ratios for 0.02 plastic-rotation fracture model.

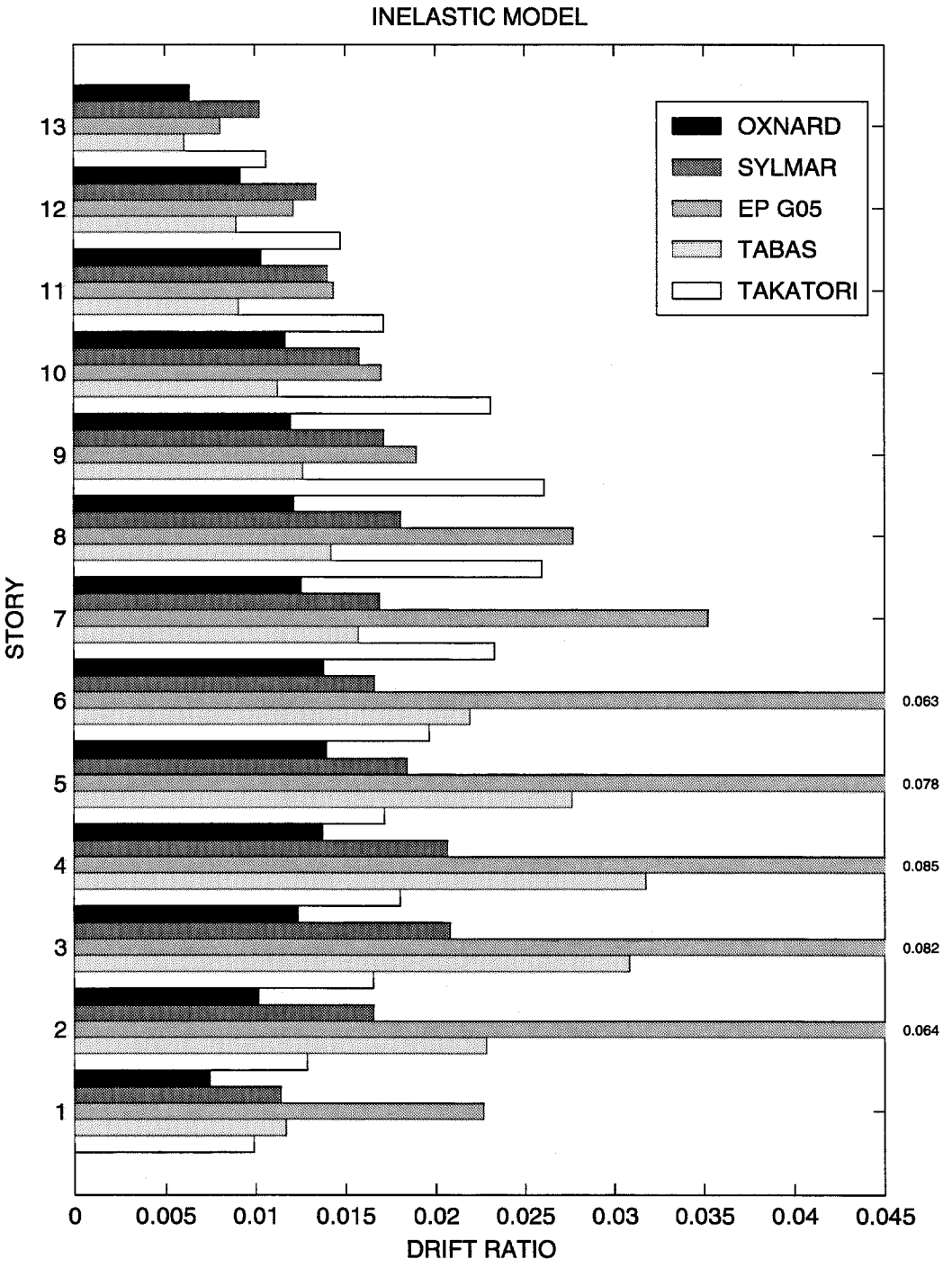

Figure 9.43 13-story building peak drift ratios for inelastic model.

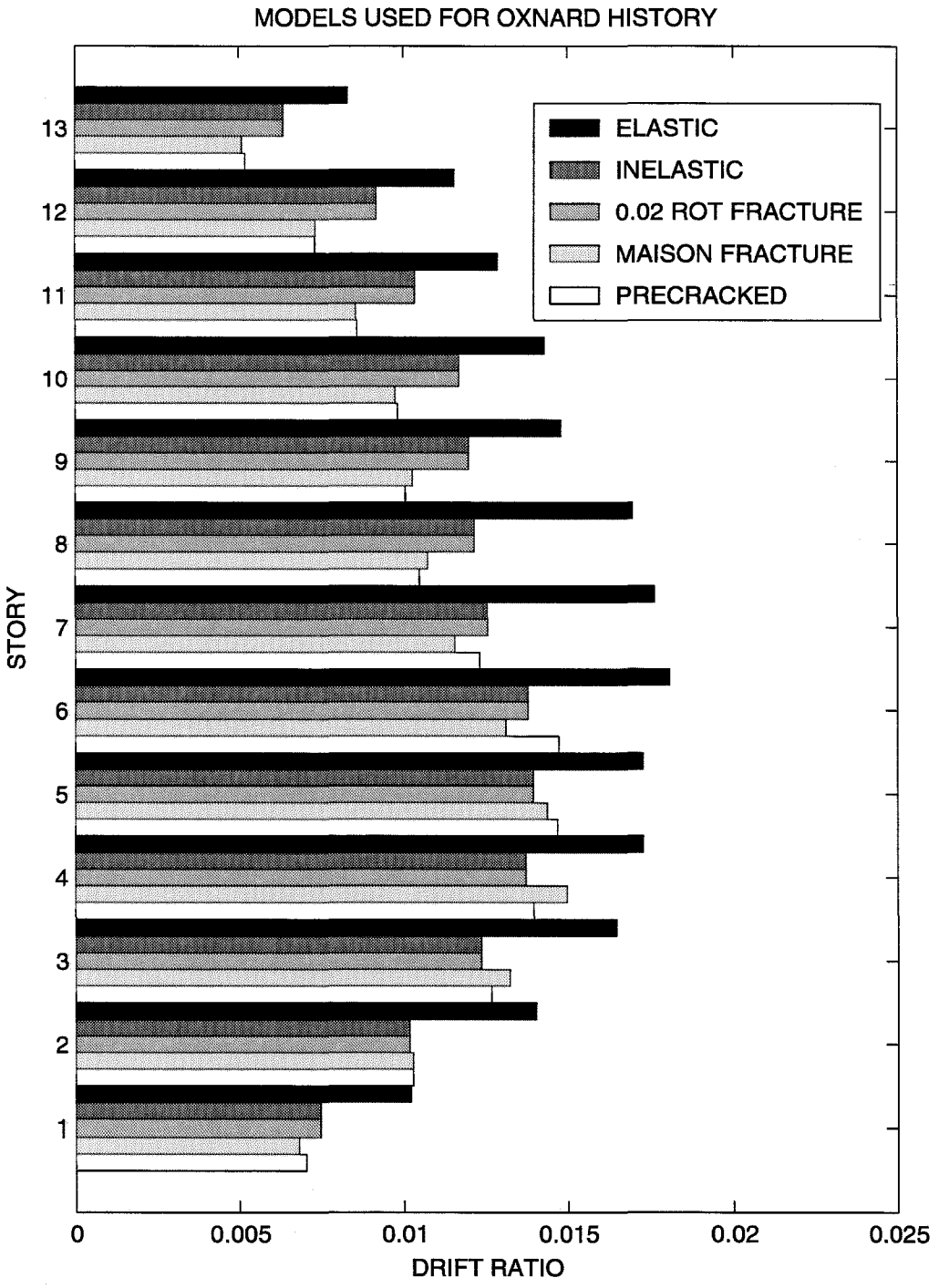

Figure 9.44 13-story building peak drift ratios for Oxnard history.

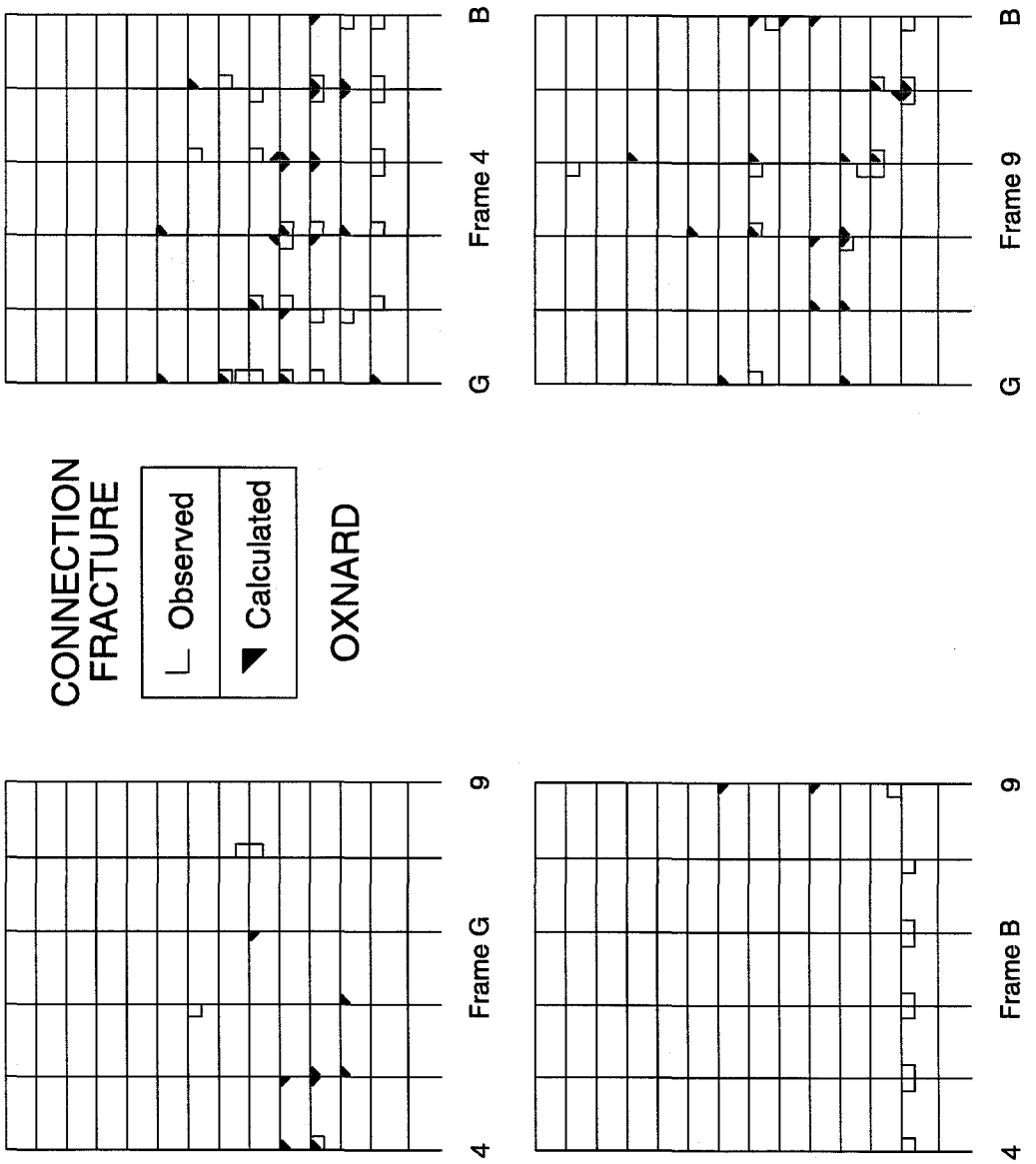

Figure 9.45 Fracture of member ends, Maison random model and Oxnard record.

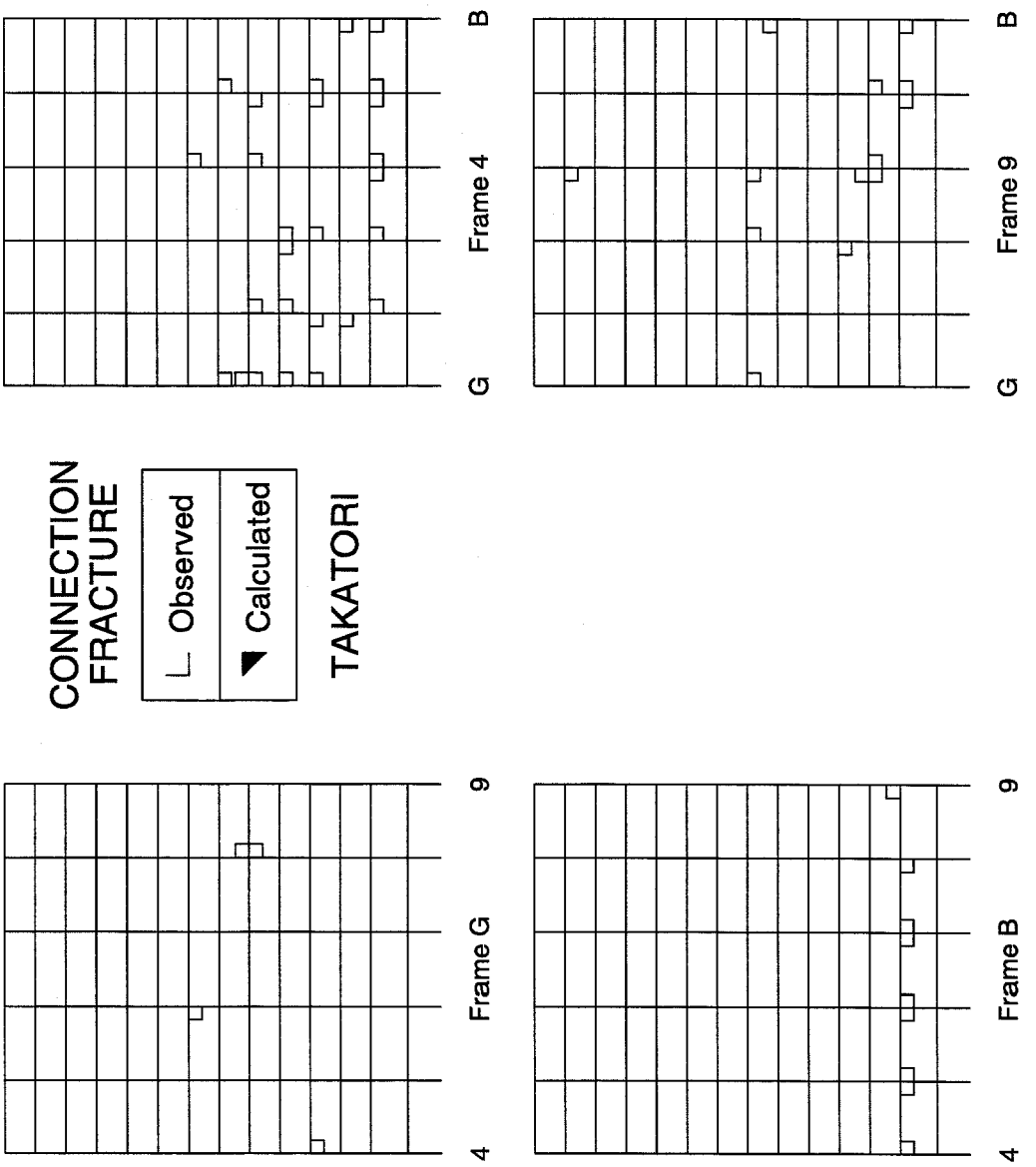

Figure 9.54 Fracture of member ends, 0.02 plastic-rotation model and Takatori record.

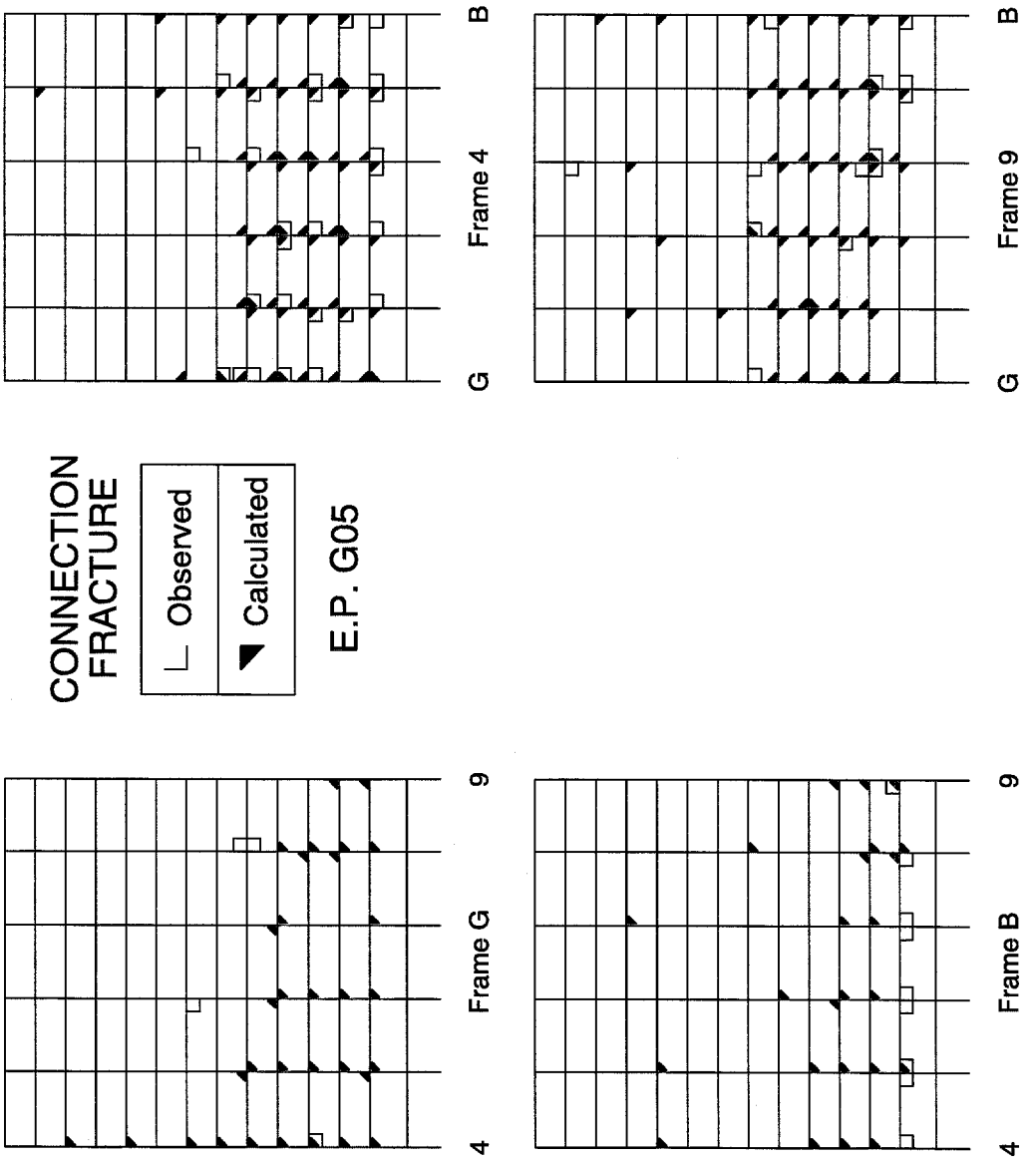

Figure 9.47 Fracture of member ends, Maison random model and E. P. G05 record.

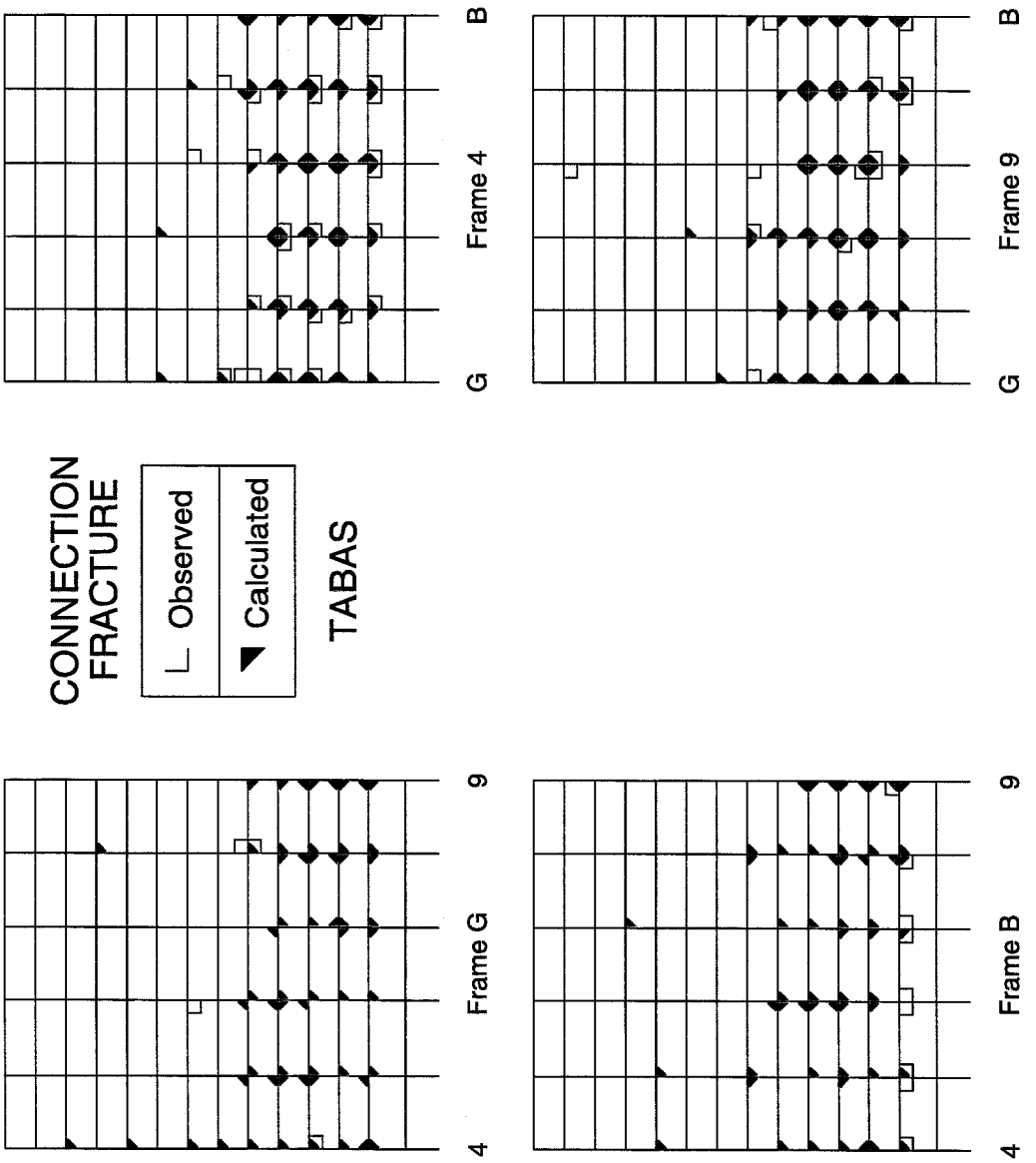

Figure 9.48 Fracture of member ends, Maison random model and Tabas record.

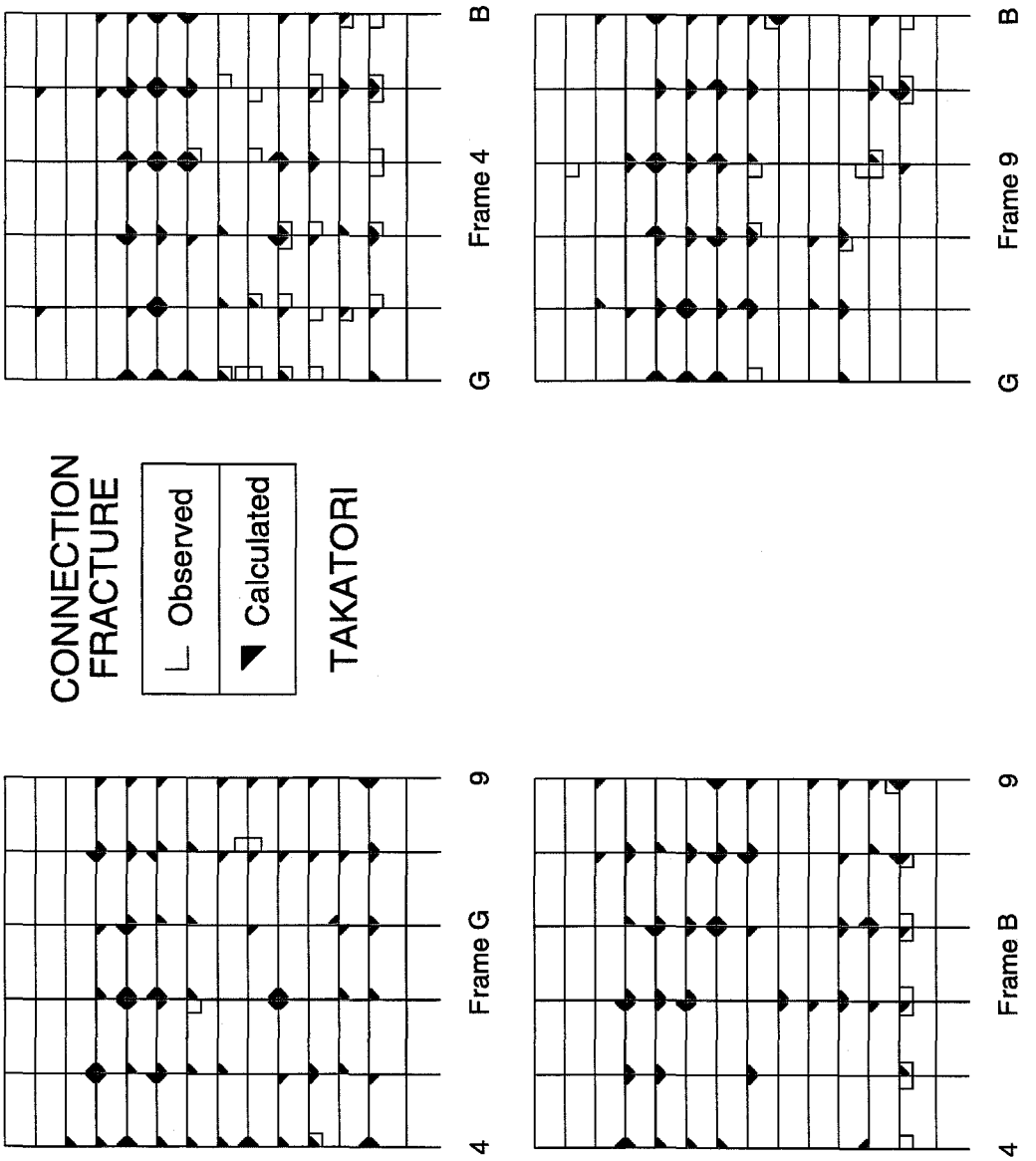

Figure 9.49 Fracture of member ends, Maison random model and Takatori record.

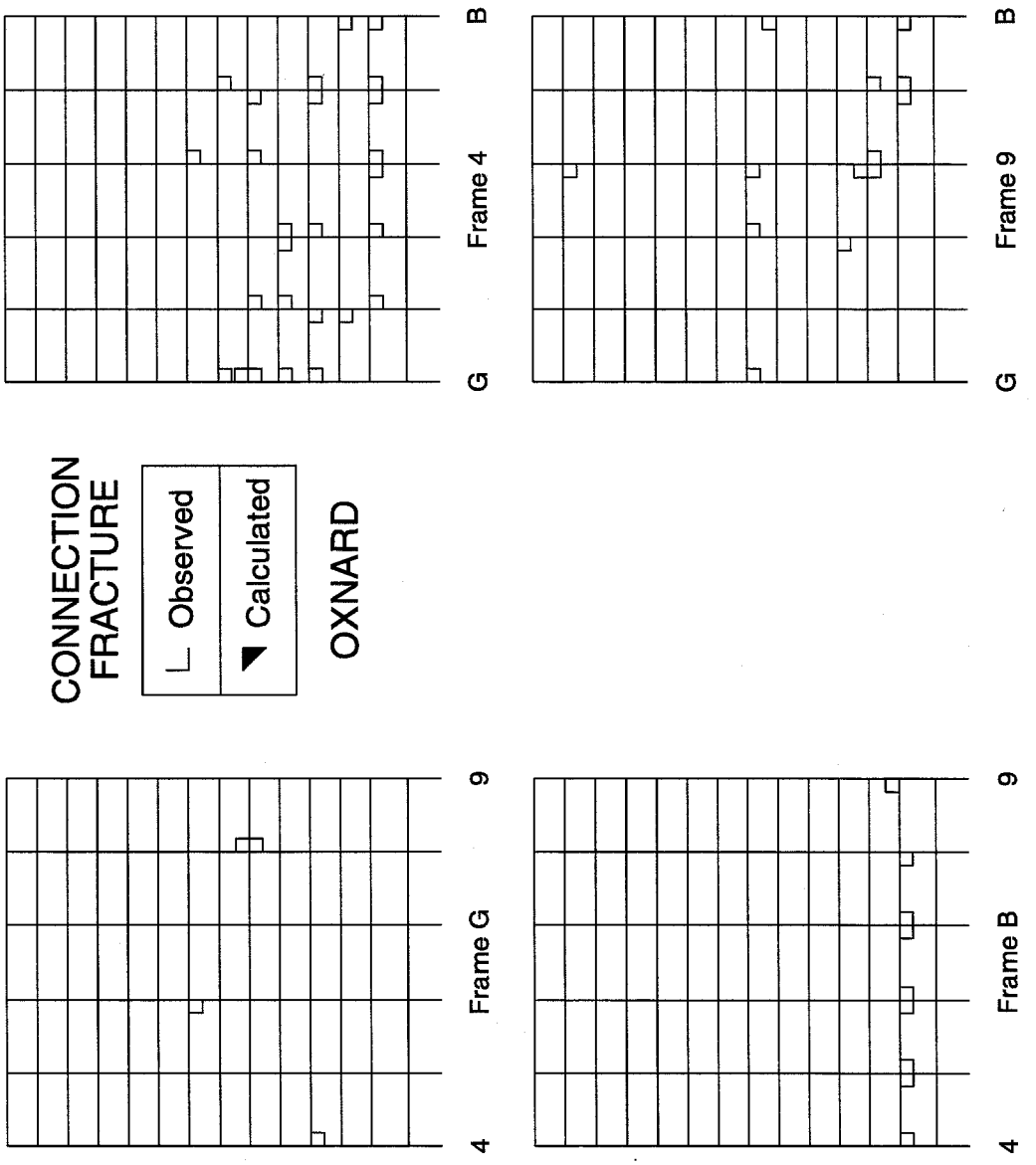

Figure 9.50 Fracture of member ends, 0.02 plastic-rotation model and Oxnard record.

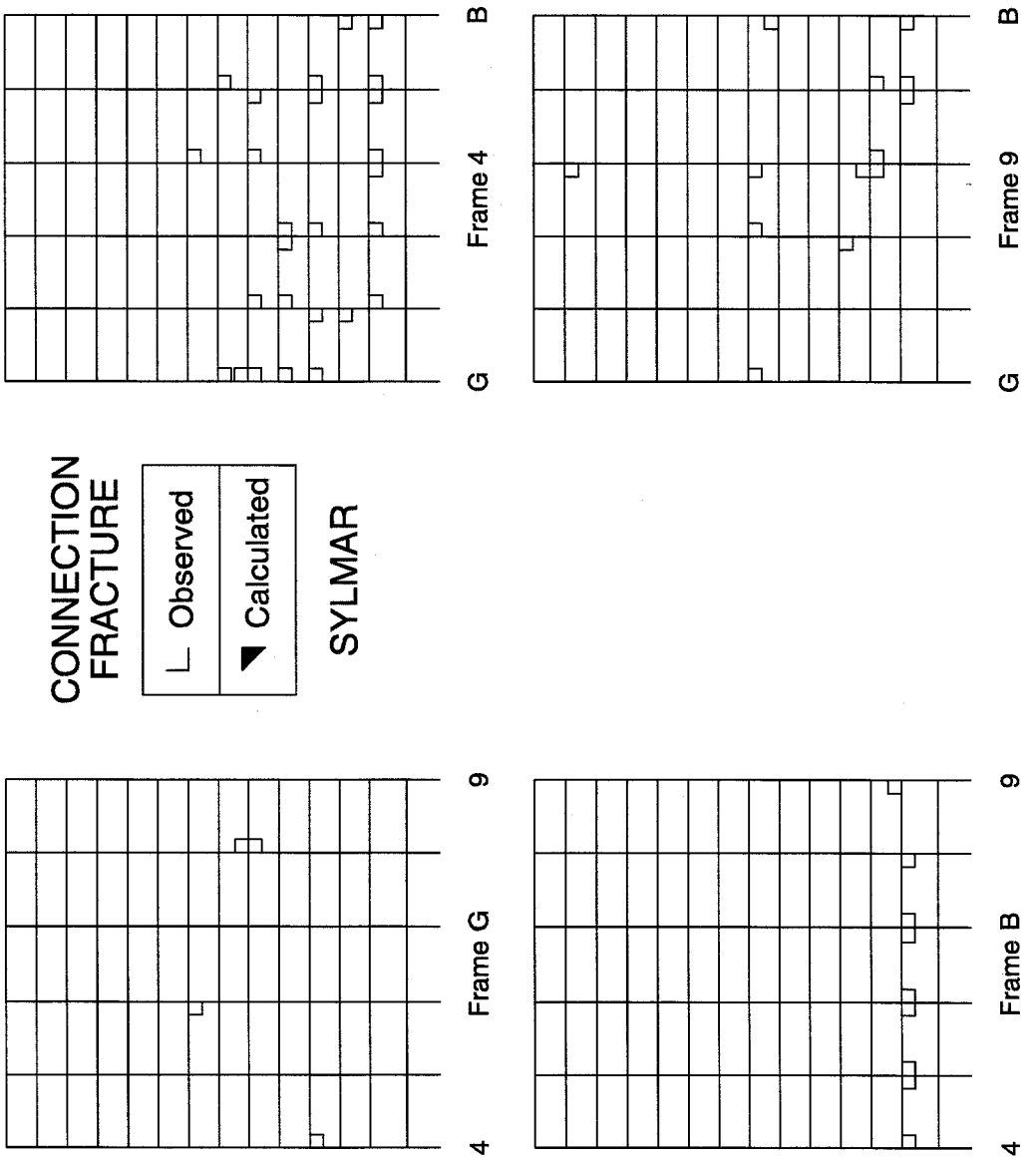

Figure 9.51 Fracture of member ends, 0.02 plastic-rotation model and Sylmar record.

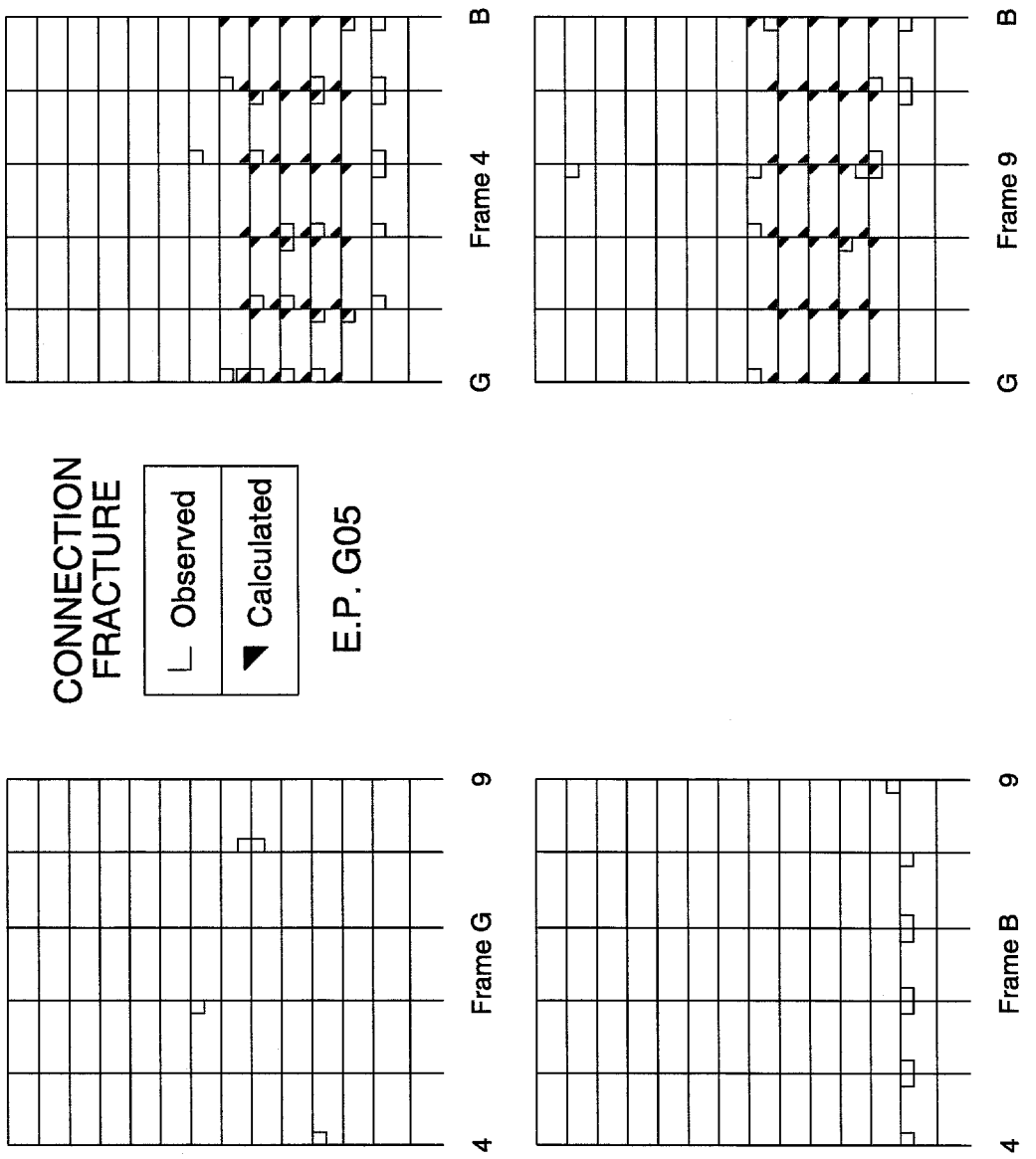

Figure 9.52 Fracture of member ends, 0.02 plastic-rotation model and E. P. G05 record.

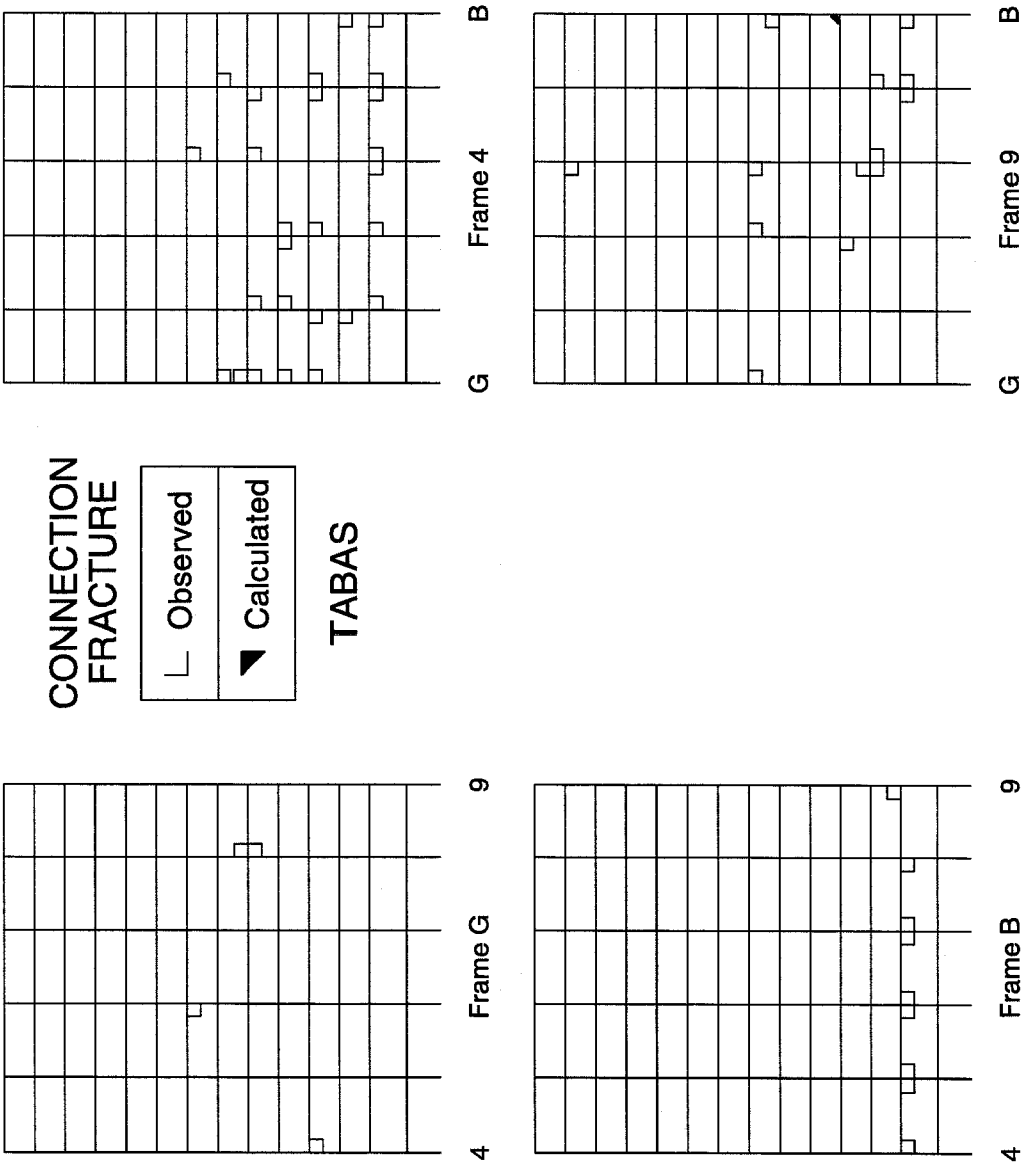

Figure 9.53 Fracture of member ends, 0.02 plastic-rotation model and Tabas record.

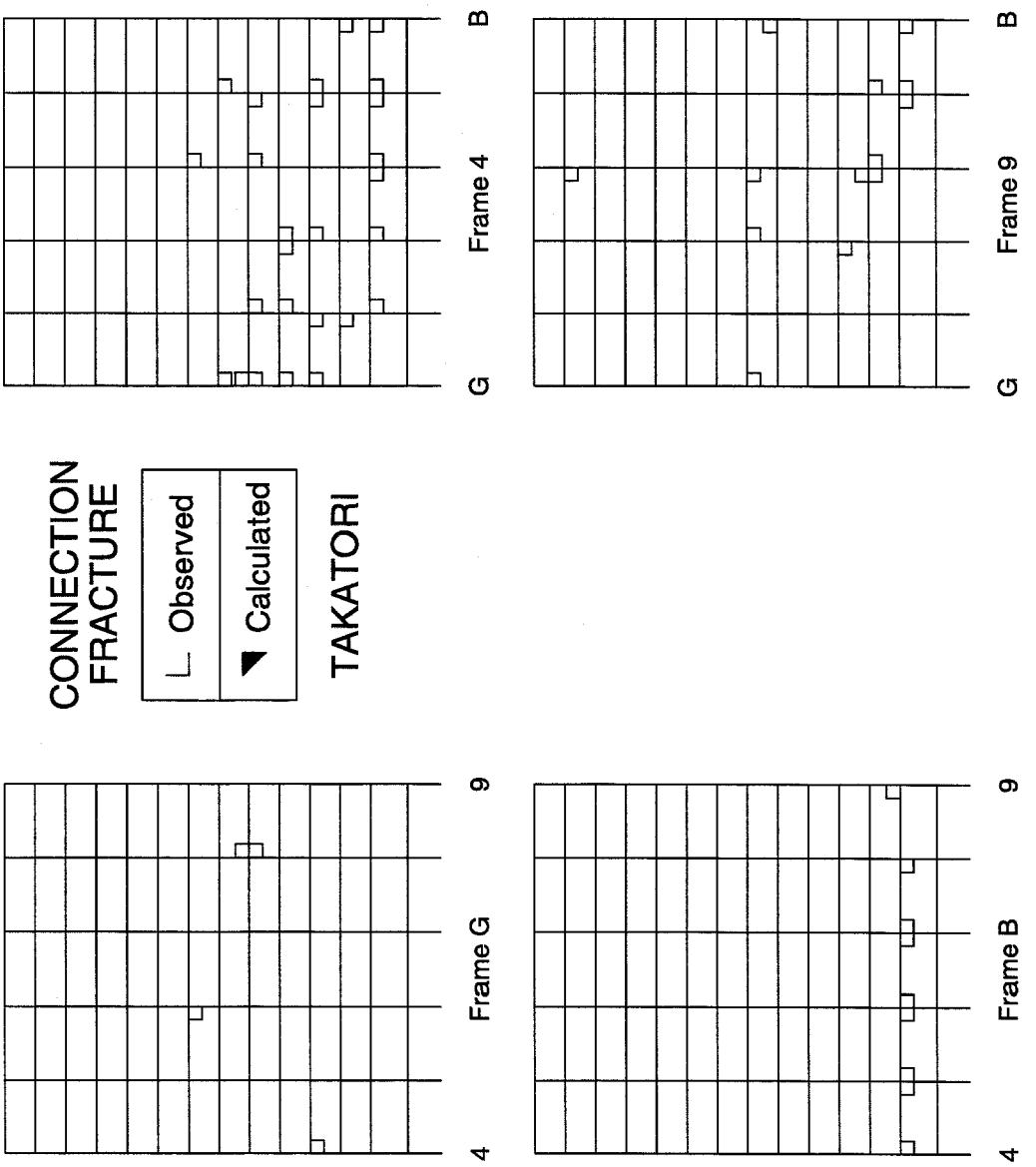

Figure 9.54 Fracture of member ends, 0.02 plastic-rotation model and Takatori record.

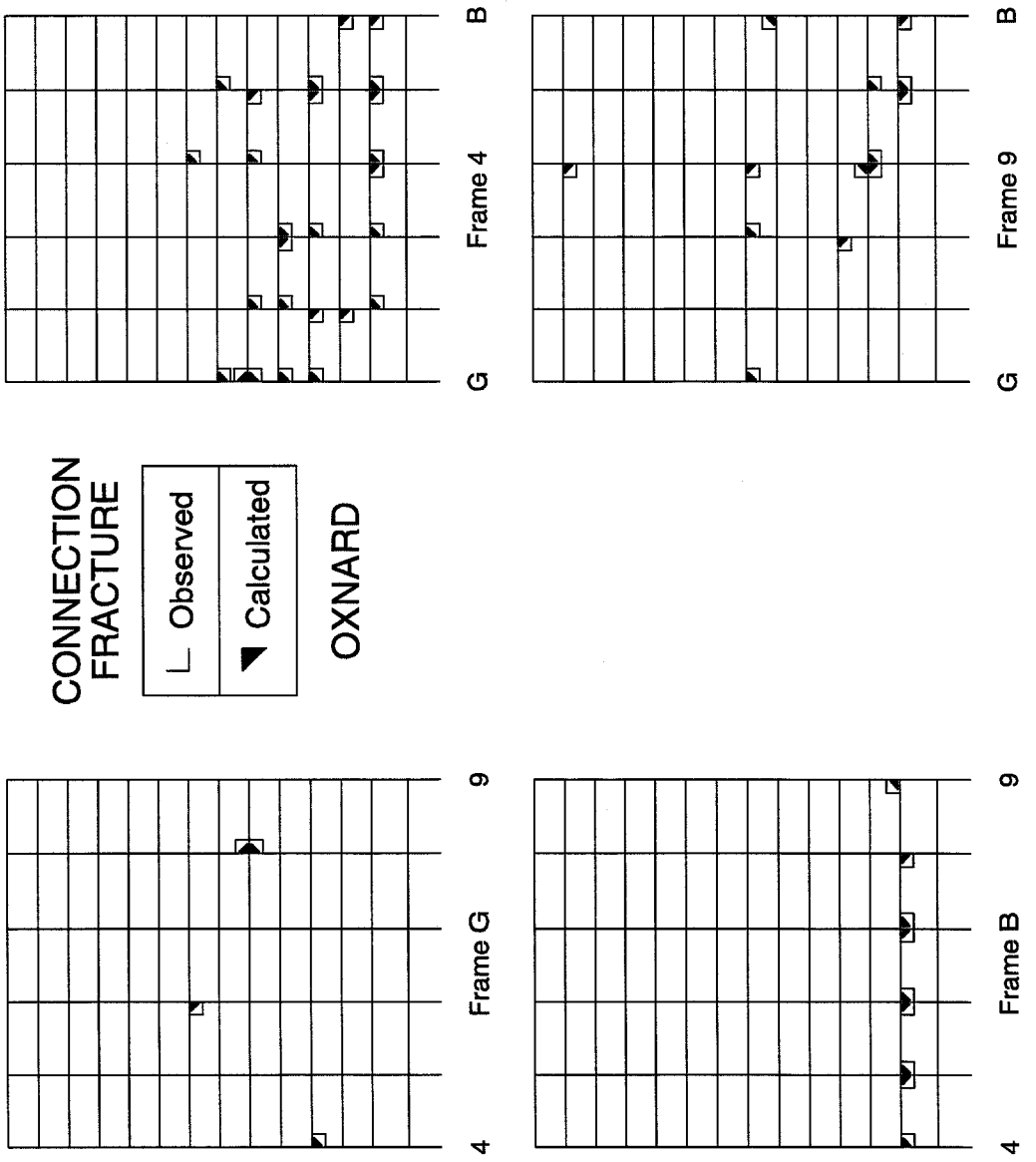

Figure 9.55 Fracture of member ends, pre-fractured model and Oxnard record.

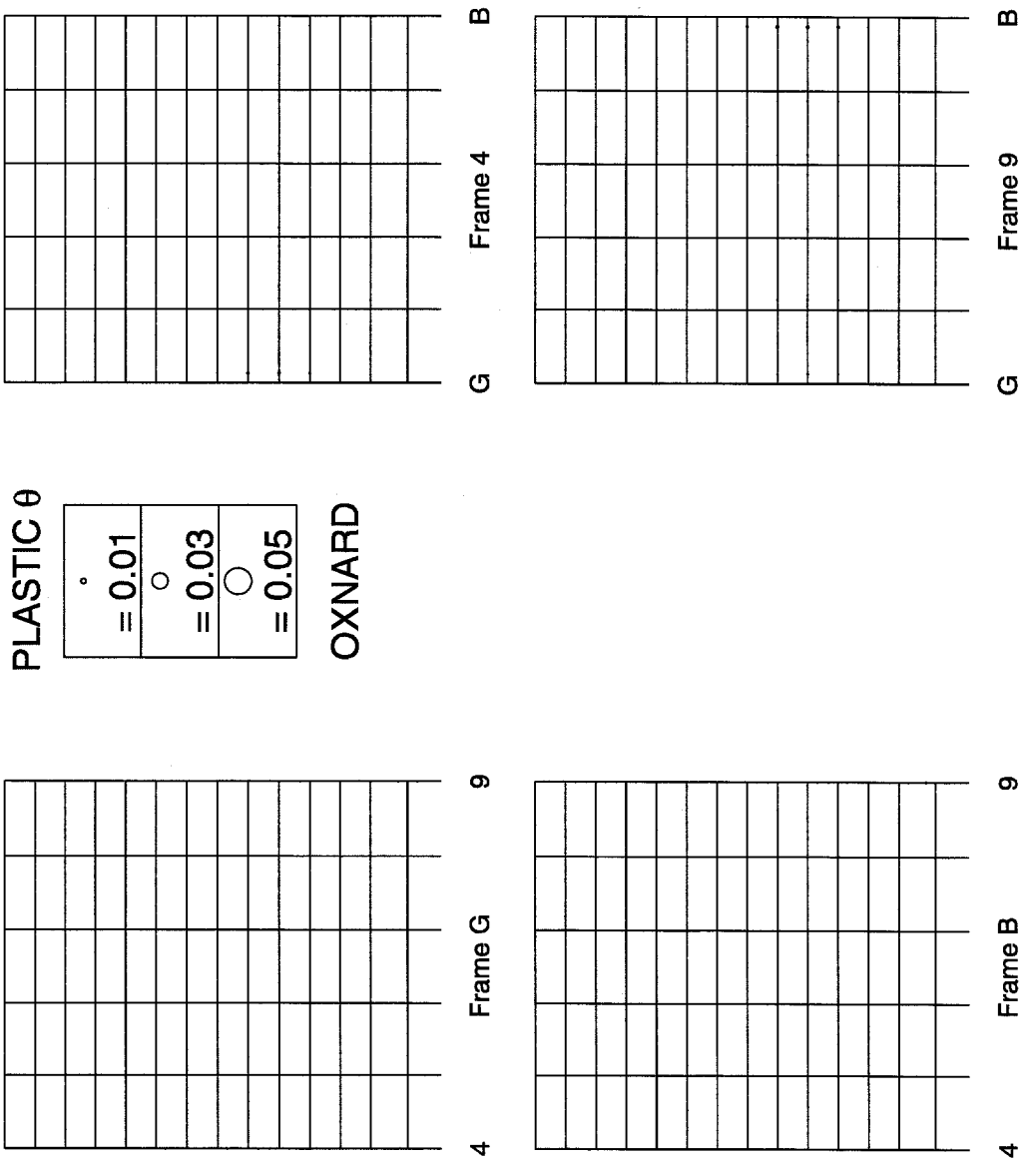

Figure 9.56 Plastic rotations at member ends, inelastic model and Oxnard record.

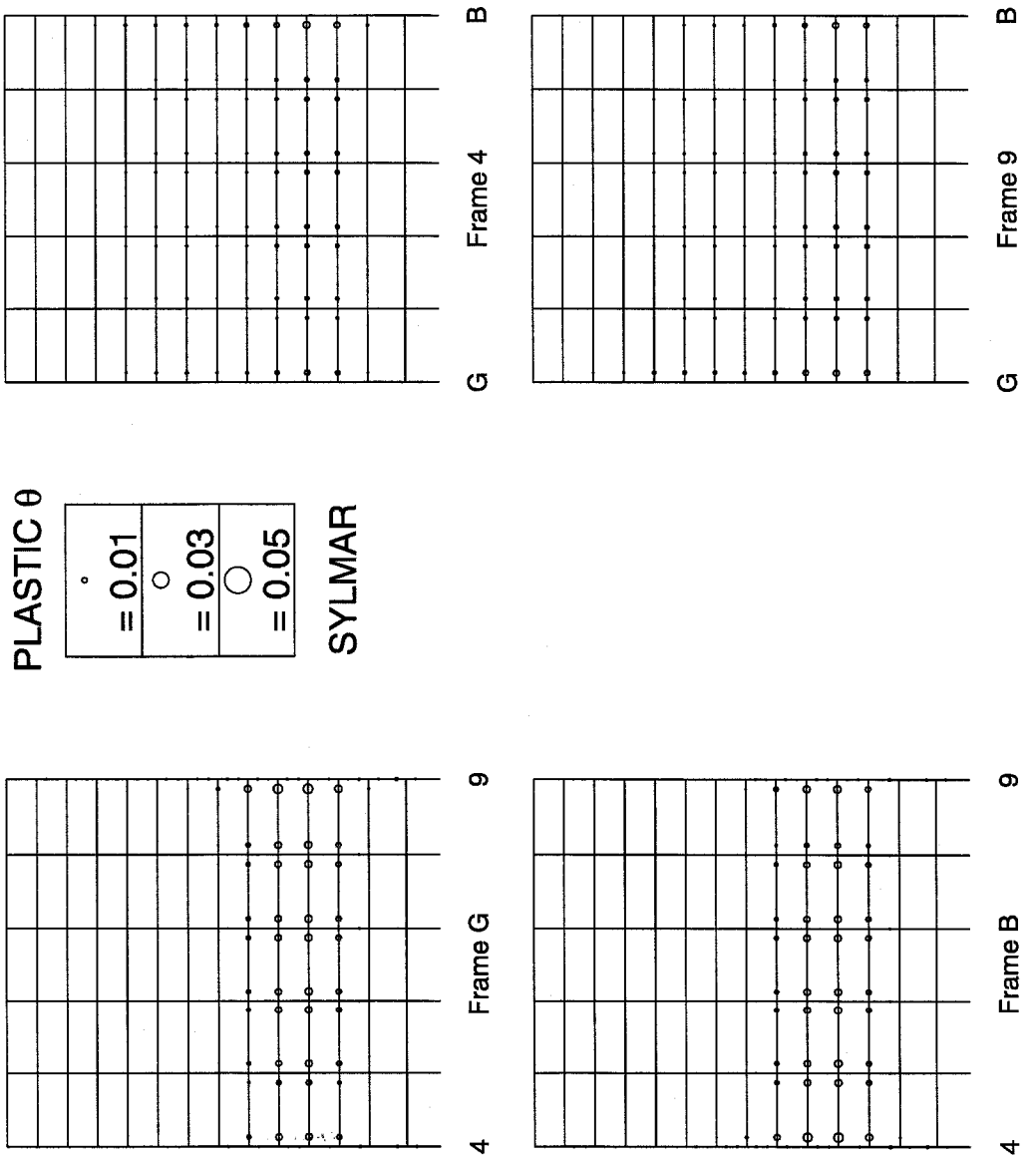

Figure 9.57 Plastic rotations at member ends, inelastic model and Sylmar record.

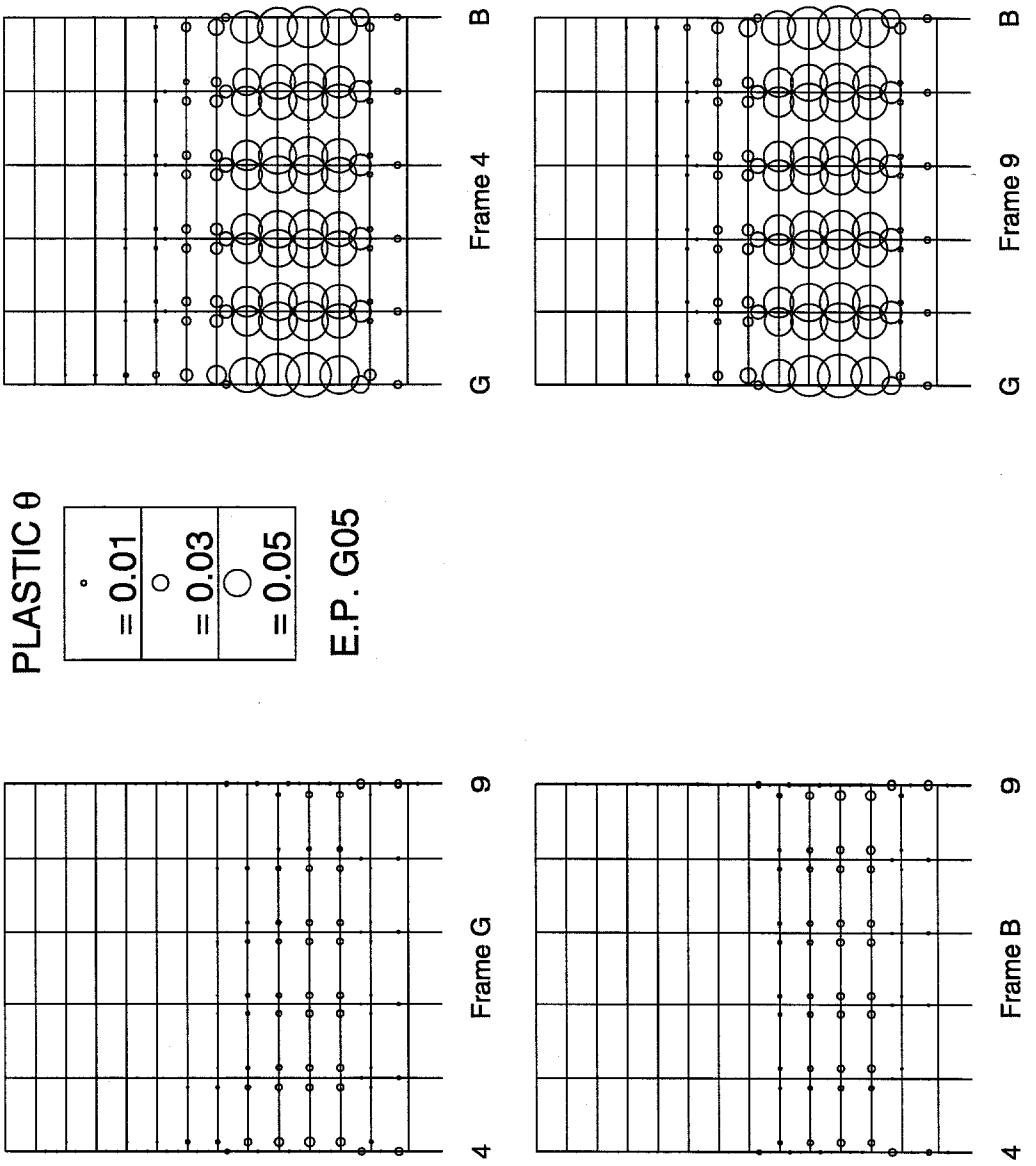

Figure 9.58 Plastic rotations at member ends, inelastic model and E. P. G05 record.

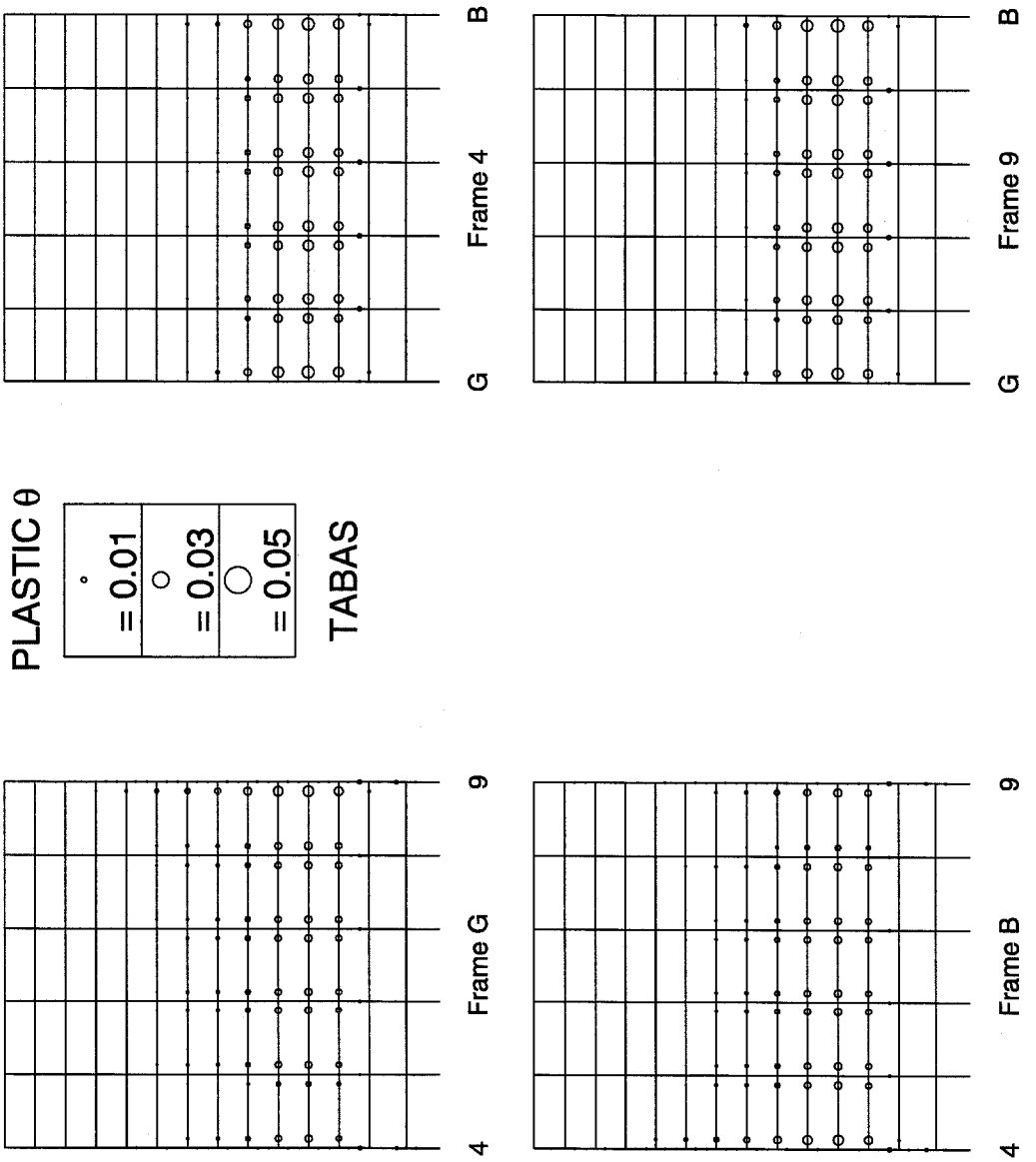

Figure 9.59 Plastic rotations at member ends, inelastic model and Tabas record.

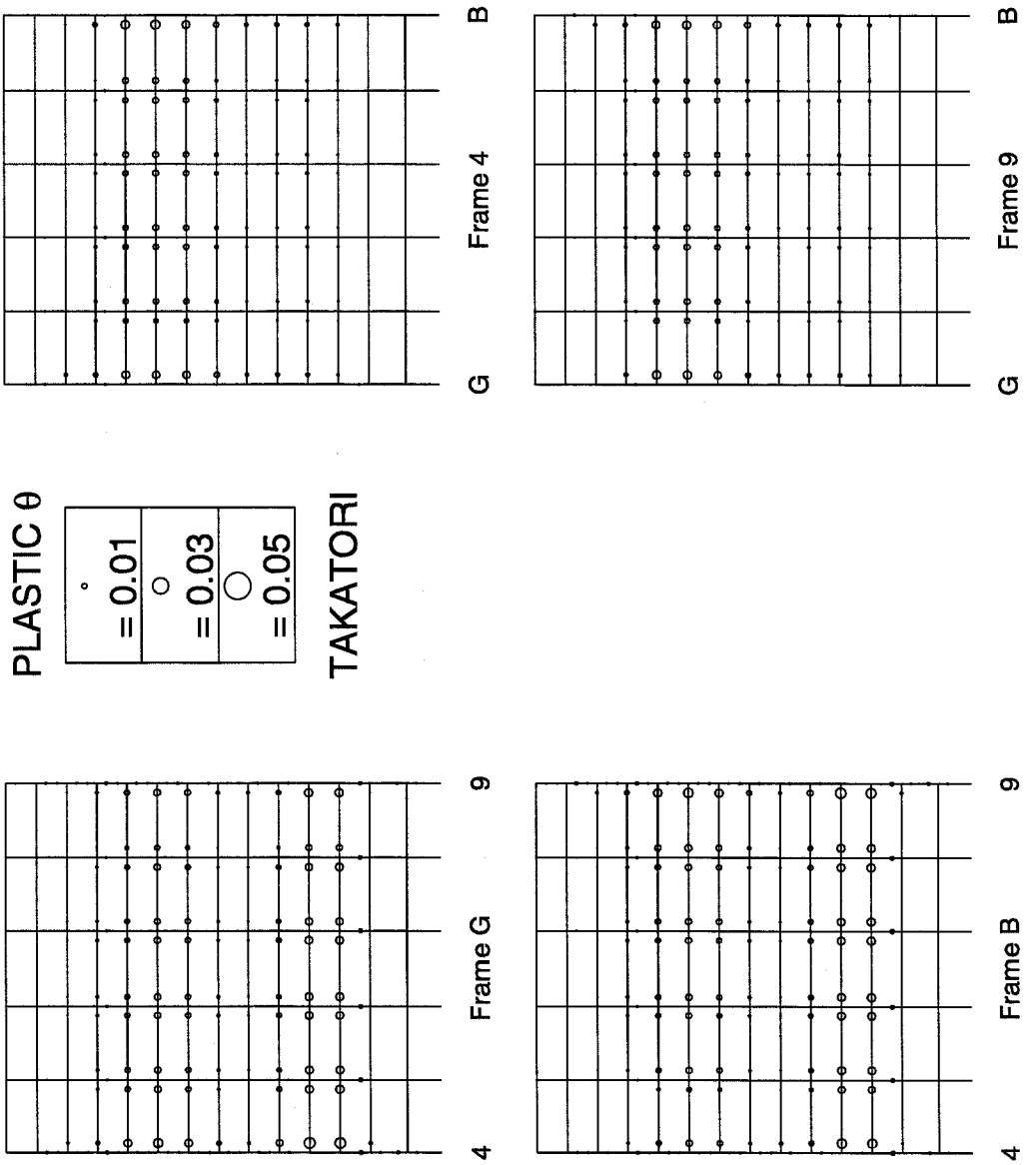

Figure 9.60 Plastic rotations at member ends, inelastic model and Takatori.

9.7 Tables

13-Story Building: Built-up Box Section Properties			
Member Designation	Plate Thickness cm (in)	Outer Dimension* cm (in)	Inner Dimension cm (in)
B14X548	6.35 ($2\frac{1}{2}$)	44.77 ($17\frac{5}{8}$)	32.07 ($12\frac{5}{8}$)
B14X425	5.08 (2)	42.23 ($16\frac{5}{8}$)	32.07 ($12\frac{5}{8}$)
B14X366	4.45 ($1\frac{3}{4}$)	40.96 ($16\frac{1}{8}$)	32.07 ($12\frac{5}{8}$)
B14X337	4.13 ($1\frac{5}{8}$)	40.32 ($15\frac{7}{8}$)	32.07 ($12\frac{5}{8}$)
B14X281	3.49 ($1\frac{3}{8}$)	39.05 ($15\frac{3}{8}$)	32.07 ($12\frac{5}{8}$)
B14X253	3.18 ($1\frac{1}{4}$)	38.42 ($15\frac{1}{8}$)	32.07 ($12\frac{5}{8}$)
B14X199	2.54 (1)	37.15 ($14\frac{5}{8}$)	32.07 ($12\frac{5}{8}$)

Table 9.2 Built-up box section dimensions. * The outer dimension does not include four 2.54 cm (1 in) flanges. See figure 5.10.

13-Story Building: Maison Random Fracture Model				
Ground Motion	Maximum Drift	Maximum Δ_R (cm)	Maximum V/W	Number of Fractures
Oxnard	0.0150	54	0.098	52
Sylmar	0.0278	78	0.147	169
E.P. G05	collapse	—	—	—
Tabas	0.0517	116	0.143	267
Takatori	0.0367	76	0.135	297

Table 9.3 Damage indicators: Maison random fracture model.

13-Story Building: $\theta_{\text{plastic}} = 0.02$ Fracture Model				
Ground Motion	Maximum Drift	Maximum Δ_R (cm)	Maximum V/W	Number of Fractures
Oxnard	0.0140	60	0.114	0
Sylmar	0.0259	88	0.171	0
E.P. G05	collapse	—	—	—
Tabas	0.0319	114	0.169	1
Takatori	0.0284	77	0.159	0

Table 9.4 Damage indicators: $\theta_{plastic} = 0.02$ model.

13-Story Building: Inelastic Model				
Ground Motion	Maximum Drift	Maximum Δ_R (cm)	Maximum V/W	# of Plastic Rotations > 0.01 rad
Oxnard	0.0140	60	0.114	0
Sylmar	0.0259	88	0.171	57
E.P. G05	0.0848	208	0.186	230
Tabas	0.0317	114	0.169	135
Takatori	0.0284	77	0.159	140

Table 9.5 Damage indicators: inelastic model.

13-Story Building: Oxnard				
Model	Maximum Drift	Maximum Δ_R (cm)	Maximum V/W	Number of Fractures
Prefractured	0.0147	55	0.094	52
Random	0.0150	54	0.098	52
$\theta_{plastic} = 0.02$	0.0140	60	0.114	0
Inelastic	0.0140	60	0.114	—
Elastic	0.0181	72	0.153	—

Table 9.6 Damage indicators: Oxnard record.

13-Story Building: Sylmar				
Model	Maximum Drift	Maximum Δ_R (cm)	Maximum V/W	Number of Fractures
Random	0.0278	78	0.147	169
$\theta_{plastic} = 0.02$	0.0259	88	0.171	0
Inelastic	0.0259	88	0.171	—

Table 9.7 Damage indicators: Sylmar record.

13-Story Building: Tabas				
Model	Maximum Drift	Maximum Δ_R (cm)	Maximum V/W	Number of Fractures
Random	0.0517	116	0.143	267
$\theta_{plastic} = 0.02$	0.0319	114	0.169	1
Inelastic	0.0317	114	0.169	—

Table 9.8 Damage indicators: Tabas record.

13-Story Building: Takatori				
Model	Maximum Drift	Maximum Δ_R (cm)	Maximum V/W	Number of Fractures
Random	0.0367	76	0.135	297
$\theta_{plastic} = 0.02$	0.0284	77	0.159	0
Inelastic	0.0284	77	0.159	—

Table 9.9 Damage indicators: Takatori record.

Chapter 10

10-Story Building

The 10-story building was designed for the 1994 UBC (ICBO 1994) to investigate three-dimensional effects of a realistic irregular building. The building is shaped like a square with a corner cut off and the lateral system is a steel moment frame that follows the perimeter with six bays on each long face. The corner columns are built-up square box sections. See figure 10.1 for the plan of the building, and note that because of the voluminous nature of the output in this chapter, the tables and figures are at the end of the chapter. This structure can be analyzed using the techniques and finite elements developed in this work.

The following issues are examined for this building:

- Ability of bare steel frame model to predict damage location through standard code static analyses.
- Ability of 3D nonlinear model to capture directional effects.
- Comparison of different models.
- Effect of larger ground motions.

10.1 Building Description

Geometry and Materials

The building has ten stories, with one basement level. The plan dimensions of the building are 54.86 m by 54.86 m (180 ft by 180 ft), and a typical story height is

427 cm (168 in). The first story height is 549 cm (216 in). Frame columns range in size from W14x193 to W14x550, and girders from W24x76 to W36x280 (figures 10.2–10.5). In these figures, the minor axes of corner columns are noted so that the member orientation can be determined. See table 10.2 for dimensions of the built-up square box sections referenced on these elevations as 'B14x#', where # refers to the weight per length of the member in pounds per foot. The columns are A572 Grade 50 and the girders are A36 steel. The columns have a yield strength of 345 kN/mm^2 (50 ksi) and an ultimate strength of 448 kN/mm^2 (65 ksi) and the beams have yield 248 kN/mm^2 (36 ksi) and ultimate 400 kN/mm^2 (58 ksi). Note that these are the design stress levels, so the strong-column/weak-beam (SCWB) assumption can be investigated. The SCWB assumption would be more likely violated if realistic strengths were used. Smaller members are used for the gravity system. The beams are all composite with metal deck and lightweight concrete on top.

Mass

The seismic mass and center of gravity are calculated for each floor based on the assumed properties discussed in section 7.1.2. The weight of the building was estimated to be 126.6 MN (28460 k). The weight of the steel moment frames is 11.1 MN (2500 k).

Basement Stiffness

Concrete basement walls are assumed to exist in each direction, and the steel columns extend to the base of the walls. The stiffness of the walls is modeled by shear springs assuming the walls at the perimeter of the building are 30.48 cm (12 in) thick.

Story Stiffness

The gravity framing, partitions, and nonstructural walls are assumed to be capable of some lateral resistance provided by shear springs. The total lateral force capacity in each direction provided by the shear springs is set to 1% of the story shear forces produced by the seismic design loads computed for $V/W = 1$. The sum of shear

spring stiffnesses in a story is set to 10% of the minimum UBC story stiffness (see section 7.1.6). This corresponds to spring yielding at a story drift of H/126.4.

Foundation

There is no foundation in this model.

Damping

Inter-story damping is capped at a force level corresponding to 0.01W, reached at an inter-story velocity of 13.34 cm/sec (5.25 in/sec). This corresponds to 2.5% of critical damping in the linear range of the fundamental mode. The total damping is 3.0%, with an additional 0.5% of critical damping provided by linear stiffness proportional damping.

Fracture Models

End segments of girders representing the welds to the columns are allowed to fracture. The Hall random fracture model is used, where the fracture strain levels are randomly chosen from the distribution shown in table 7.3. The lowest strain levels in this distribution are $0.9\epsilon_y$ and $10.0\epsilon_y$ for the bottom and top fibers, respectively. This fracture model produced results that underestimated the damage in the 17-story building, so it has an appropriate level of conservatism for predicting damage in a building assumed to have some poor connections.

The 0.02 radian plastic-rotation model is not analyzed for this building.

Modal properties

The model possesses natural periods of vibration of 2.16 and 2.06 seconds for fundamental lateral modes and 1.52 seconds for torsion. See figures 10.6–10.11 for depictions of the first six natural modes.

10.2 Building Design

The lateral system was designed using the 1994 Uniform Building Code (ICBO 1994). No site-specific data exists, so the design would be as follows. The parameters

used for design are:

- Special Moment Resisting Frame (SMRF)
- $W = DL$
- $Z = 0.4$, zone 4 for California
- $I = 1$
- $S = 1.2$, assumed soil distribution (medium-dense)
- $R_w = 12$, steel SMRF reduction/ductility factor
- $C_t = 0.035$ for steel SMRF
- $T = C_t(h)^{0.75}$, h = height of structure, method A
- $T_{max} = 1.3T$, T determined from method A
- $C = \frac{1.25S}{T^{2/3}} \leq 2.75$ and $C \geq 0.075R_w$
- $V = \frac{ZIC}{R_w}W$, base shear
- $F_t = \min(0.07TV, 0.25V)$ for $T \geq 0.7$ and $F_t = 0$ otherwise
- $F_x = \frac{(V-F_t)w_xh_x}{\sum w_ih_i}$, force at floor x
- Drift limit $= 0.03/R_w$

The resulting values are:

- $T = 1.99$ sec (Using T_{max}, knowing actual is higher)
- $C = 0.948$
- $V = 0.0316W$
- F_t =557 kN (125.3 k)
- Drift limit $= 0.0025$

Note that the equivalent static force, V, is near the lower limit for the 1994 UBC ($V = 0.03W$).

Additional stringent code provisions were met in a full design of the lateral system, including accidental torsion and seismic compactness. Stiffness, strength, and strong-column/weak-beam provisions are satisfied by the following respective results: the maximum drift is .00247, the maximum stress ratio is 0.71, and the maximum B/C ratio is 0.93.

The strong-column/weak-beam provision of the code is an attempt to ensure that the proportions of the members will provide the maximum ductility and redundancy. Yielding and plastic hinging will occur in beams rather than columns if the members are sized to have more strength in the columns than in the beams at every panel zone in the building. As moment is redistributed at a joint, the beams will yield before the columns do, allowing more load to be attracted. If the columns yield first, the stability of the structure could be greatly compromised by producing a weak story, whereas beam yielding may lead to larger deformation at higher load levels. The 1994 UBC has the following criteria that must be met at each joint in a SMRF:

$$\sum Z_c(F_{yc} - f_a)/\sum Z_b F_{yb} > 1 \tag{10.1}$$

$$\text{or} \quad \sum Z_c(F_{yc} - f_a)/1.25\sum M_{pz} > 1, \tag{10.2}$$

where $f_a > 0$, b refers to beams, c refers to columns, and M_{pz} is the sum of beam moments when the panel zone shear strength reaches the value V calculated as

$$V = 0.55F_y d_c t\left[1 + \frac{3b_c t_{cf}^2}{d_b d_c t}\right] \tag{10.3}$$

The first criterion states that the column plastic moment capacity should exceed the beam plastic moment capacity at a joint and the second criterion states that the column plastic capacity should exceed the beam moment that corresponds to the strength of the panel zone (Bruneau, Uang, and Whittaker 1998). The largest moment that can be transmitted into the panel zone by the beam is the beam plastic

moment, so the more stringent first criterion is used.

The inverse of the strong-column/weak-beam criterion is the B/C ratio. Meeting the criterion means that the B/C ratio is *less* than 1.0 at every joint.

A model with rigid foundations and solely the lateral system steel columns and girders providing resistance is used for the design. A static analysis using the UBC forces above produces a roof displacement of 7.72 cm (3.04 in) E-W or N-S.

The resulting demand capacity ratios (DCR's) for the structure from the static analysis can be seen in figures 10.12 and 10.13 for the E-W and N-S directions, respectively. See section 8.2 for an explanation of the DCR ratio and the method of showing them in the figures. As a comparison, the DCR ratios for the Oxnard time history are given using the actual values of member material strengths and the inelastic model without fracture (figure 10.14). For this building, the actual strengths are the nominal strengths. See section 10.4 for an explanation of the inelastic model.

10.3 Pushover Analysis

The bare-steel frame and inelastic models were subjected to a pushover analysis using the 1994 UBC static force distribution (figure 10.15). The base model includes just the bare-steel frame (BF). The inelastic model includes the inter-story stiffness (SB) and composite action of the girders (CM). Practicing engineers do not require steel moment frame buildings to resist drifts larger than 3%, so the analyses were stopped at a roof displacement of 152.4 cm (60 in) which corresponds to a drift of 0.0325. The base model at the final drift of 0.0325 has an "ultimate" strength of 0.200W and the inelastic model without fracture (BF+SB+CM) has an "ultimate" strength of 0.220W. These models did not reach their true ultimate loads, but were pushed to higher drift ratios than the other two buildings.

10.4 Simulations

Several time history analyses of various types are performed to seek answers to the issues mentioned at the beginning of the chapter. In each instance, a time step of 0.02 seconds and a total duration of 40 seconds for each record are used. The same five records used for the 17-story and 13-story simulations are used: Oxnard, Sylmar, Elysian Park G05, Tabas and Takatori. Two of the five records are rotated to see the effect of directivity on the building response. The Oxnard record N-S and E-W ground motions are rotated 22.5°, 45°, 67.5° and 90° and the Hall random fracture model is used. The rotations are measured positive counter-clockwise. The Sylmar N-S record is isolated for the second suite of rotated simulations. It is applied at 0°, −45°, 45°, 180° and 135°. Table 10.1 shows the analyses performed for each ground motion. The analysis types include elastic analysis, inelastic analysis without fracture, and inelastic analysis with random connection fracture (Hall random fracture model).

Ground Motion	Random Fracture	Inelastic	Rotated Random Fracture	Elastic
Oxnard	•	•	••••	•
Sylmar	•	•		
E.P. G05	•	•		
Tabas	•	•		
Takatori	•	•		
Sylmar(N-S)			•••••	

Table 10.1 Time history analyses performed for 10-story building model.

10.4.1 Figure Descriptions

Time Histories

The relative-to-ground roof displacement response is tracked for the duration of the analyses, 40 seconds. The response at the center of mass (master node location)

and at two corner locations is calculated so that torsional effects can be observed (figure 10.16). Note that the same scale is used to compare the response levels for the different ground motions. The Hall random fracture and inelastic model results are presented for each ground motion.

- See figures 10.17–10.26 for the relative roof histories from the Oxnard, Sylmar, Elysian Park G05, Tabas and Takatori ground motions, in that order.
- See figures 10.27–10.31 for the roof histories of the Oxnard rotated runs using the Hall random fracture model.
- See figures 10.32–10.36 for the roof histories of the Sylmar N-S rotated runs using the Hall random fracture model.

To get a better understanding of the global building behavior, relative histories of each floor are shown together for the N-S component of motion only. The N-S direction is the stronger ground motion in every case, so the N-S response alone will suffice to present this behavior. The Hall random fracture and inelastic model results are presented for each ground motion. Note that the same scale is used wherever possible to compare the response levels for the different ground motions.

- See figures 10.37–10.46 for the building histories from the Oxnard, Sylmar, Elysian Park G05, Tabas and Takatori ground motions, in that order.

The Oxnard motion is used for all three buildings to investigate the differences in models used for each building. The difference in roof response for the Hall random fracture model, the inelastic model and the elastic model are presented.

- See figure 10.47 for the comparison of relative roof displacements resulting from the Oxnard motion due to various models.

Inter-Story Drifts

The maximum drifts in the N-S direction for each story are used as a damage indicator. Note that the same scale is used for all plots. Values that exceed these limits are plotted on the right-hand side of the figure.

- See figures 10.48 and 10.49 for the maximum story drifts for each record for the Hall random fracture and inelastic models, respectively.
- See figure 10.50 for the maximum story drifts for each model resulting from the Oxnard record.

Fractures

The member end fractures are plotted for each simulation that uses a fracture model. Top and bottom girder-flange to column-flange connection fractures are distinguished separately.

- See figures 10.51–10.55 for the fractures resulting from the Hall random fracture model.
- See figures 10.56–10.60 for the fractures resulting from the rotated Oxnard record and the Hall random fracture model.
- See figures 10.61–10.65 for the fractures resulting from the rotated Sylmar N-S record and the Hall random fracture model.

Plastic Rotations

The member end plastic rotations are plotted for each simulation using an inelastic model with no fracture. In these figures, the circle diameter is proportional to the plastic rotation and the circle is drawn offset from the member end to distinguish multiple members framing into a joint.

- See figures 10.66–10.70 for the plastic rotations resulting from the inelastic model.

10.4.2 Table Descriptions

Damage Indicators for Model Type

Several indicators of damage include the maximum drift, the roof displacement, the base shear and the number of fractures. These have been summarized for each model comparing across ground motions. The ratio of base shear V to building weight W

is used in these tables. For the inelastic model, the number of member end plastic rotations greater than 0.01 radians is used in place of the number of fractures.

- See tables 10.3 and 10.4 for the damage indicators for the Hall random fracture and inelastic models, respectively.

Damage Indicators for Ground Motion

The same data is presented for the Oxnard ground motion comparing across model type. Other records only have two model types represented, so they are not tabulated.

- See table 10.5 for the damage indicators for the Oxnard ground motion.

Damage Indicators for Rotated Ground Motion

The damage indicators as a function of the angle of ground motion input are presented for the Oxnard and Sylmar N-S rotated records.

- See tables 10.6–10.7 for the damage indicators for the rotated ground motions.

10.5 Discussion

Static Analysis

The demand capacity ratios (DCRs) of this building are uniform and low. Drift and stiffness rather than strength governed the design of the building. There is some drop off in DCR values toward the top of the building. The lowest levels have more uniform DCRs compared to the rest of the building and relative to the other two buildings investigated. The 17-story building has extra bays at the lowest level in the N-S direction reducing demand, and the 13-story building has much larger sections at the lowest levels to provide tall-story stiffness. The 45° plane of symmetry of the building can be seen by examining the similarities in N-S and E-W load applications. Lack of torsion can be seen by examining the low demand in frames transverse to load direction. The uniform nature of the DCRs for both static lateral force applications provides no indication of concentrated yielding.

The DCR results for the Oxnard record show that inelastic behavior has occurred. A large percentage of members have exceeded the elastic limits due to excessive bending.

Pushover Analysis

The base shear ratio V/W at ultimate levels is greater than six times the UBC design base shear ratio, even for the bare frame. This building exhibits exceptional ductility and strength. This is due in large part to the inherent redundancy. There are 12 bays activated in the direction of loading. The 13-story building has ten bays activated, but they are weaker and softer than the bays of the 10-story building. The 17-story building has only four bays activated. Additionally, the 10-story building has lower DCR values from static analysis than the other buildings, so it has more reserve capacity at design levels of base shear.

Relative Roof Displacements

These time history plots (figures 10.17–10.26) show the response level of the roof in lateral directions, and by plotting three locations on the roof, they indicate torsional response by differences in the histories. The five representative ground motions are used as input on the 10-story building with the Hall random fracture strain model and the inelastic model without fracture. The building has one axis of symmetric and its center of mass is very close to its center of rigidity. For inelastic response without fracture, very little torsion is observed. Note that the five histories are drawn to the same scale for comparison.

The Oxnard response has a small amount of torsion introduced by non-uniform fracturing due to the random distribution of poor connections. The response is damped from the inelastic hysteresis of the members. In general, the later peaks in the records are larger for the inelastic runs than for the fracture runs because the fractures release more strain energy than the hysteretic damping can release. Once this energy is released, future opening and closing of cracks also release stored strain energy, reducing response with each cycle. For the inelastic model, the Oxnard response shows no torsion, but a beating phenomenon clearly occurs. Both

fundamental lateral modes are excited and the energy is transferred back and forth due to changes in the excitation frequency. The lack of torsion shows that the centers of mass and stiffness in the building are close to coinciding. Low levels of inelastic behavior do not induce torsion in the building.

The Sylmar response produces a permanent offset to the southwest. For the fracture model, the southward offset is roughly 40 cm. A small amount of permanent twist can also be seen. Note that the traces of the three positions of the roof response do not cross, indicating that they are permanently offset from each other at an angle. The response is highly damped, indicating a great deal of damage. The inelastic response has almost no torsion. The record beyond 15 seconds looks like fundamental-mode damped free response. Notice that the reduction in response is a lot lower for the inelastic model than the fracture model. The permanent offset is also smaller.

The G05 fracture model response shows severe permanent offset (about 3.6% building drift), but no collapse. This offset exceeds the pushover analysis results. Notice there is a substantial permanent twist also. This is the only building that survives this ground motion with a fracture model. The inelastic model has large permanent offset (about 1.2%) and modest torsion. The N-S motions are damped out to a greater degree than the E-W motions.

The Tabas response of the fracture model has high frequency content forcing the building. There is very little torsion, and about 25 cm of northward offset. The damage in the N-S direction increases the periodic response to roughly 3.9 seconds. The inelastic model has similar response up to 12 seconds in the record, but the response after that is periodic with a substantially different period of roughly 2.3 seconds. There is little offset in the inelastic model. The inelastic behavior lengthens the period from 2.16 to 2.3 seconds, as opposed to the fracture model inelastic response dramatically reducing the stiffness and increasing the period to 3.9 seconds. This can best be explained by the fractures observed and will be discussed in the fracture distribution section.

The Takatori response of the fracture model has northwestern offset with some

angular offset also. The inelastic response has eastern instead of northwestern offset and less torsion. The energy stays in the two lateral fundamental modes with beating as observed in the Oxnard record instead of torsional mode excitation. The fracture model has more damping than the inelastic model.

Relative Roof Displacements, Oxnard rotated record

These time history plots (figures 10.27–10.31) show the response level of the roof for the Oxnard ground motion rotated at 0°, 22.5°, 45°, 67.5° and 90° counterclockwise. The responses of all but the 90° motion are largely the same, with expected changes in E-W and N-S responses due to the rotation of the record. Only the 90° record produces unusual results. From 10–25 seconds in the record, large levels of torsion are observed, and beyond that the response is greatly reduced relative to the response for all the other angles of ground motion input.

Relative Roof Displacements, Sylmar N-S rotated record

These time history plots (figures 10.32–10.36) show the response level of the roof for the Sylmar N-S ground motion rotated at 0°, −45°, 45°, 180° and 135° counterclockwise. Only the N-S component of the Sylmar record is used to investigate the three-dimensional effects of rotating unidirectional ground motion input.

The first comparison that should be made is between response to the full Sylmar ground motion and the Sylmar N-S applied at 0° rotation. Note that most of the E - W response and the torsion are removed by not including the E-W ground motion input. Since this building has well balanced mass and stiffness, a 2D simulation might provide good results for the 0° load application. The offset frames do not lend themselves to 2D approximations, however, and earthquakes do not usually line up with a building's axes.

The −45° record is applied in the building's plane of symmetry. The random distribution of fracture strains introduces some torsion into the response that could not be there otherwise. Note the overall symmetry of the orthogonal responses.

The 45° record is applied transverse to the building's plane of symmetry. Large torsions are introduced and significant hysteretic damping occurs. Some twisting

offset is apparent.

The 180° record is applied in the opposite direction to the 0° record and the 135° record is applied in the opposite direction to the −45° record. Little difference in response is observed between these opposite direction inputs other then the expected negated histories.

Relative Floor Displacements

In these figures (10.37–10.46), each floor response is shown for the Hall random fracture model and the inelastic model.

The Oxnard fracture model response shows some permanent offset while the inelastic model appears to be nearly elastic response. There is no permanent offset observed in any level, although some amount of reversing inelastic behavior could occur without these histories depicting it. The large difference in the response between these two models can be explained by the time histories which show beating in the inelastic model response and energy release in the fracture model response.

The Sylmar record shows southward offset for both models, with significantly more damage and response reduction in the fracture model. The lower stories are responsible for most of the total drift.

The G05 record shows southward offset concentrated in three lower stories. The scale was modified for the plot of the fracture model to see the entire response. As with the Sylmar record, the inelastic model has less offset and damping relative to the fracture model.

The Tabas record has more offset for the fracture model than for the inelastic model. A significant difference in the period of the response can be seen between these two models. This was explained in the time history figure discussion.

The Takatori model shows different responses for the two different models. They both experience some permanent offset, but the fracture model has it concentrated in the lower stories and the inelastic model has it spread throughout the building.

Time History Comparisons

Three different models were analyzed for the Oxnard ground motion — Hall random fracture, inelastic and elastic (figure 10.47). There is a big difference in the amplitude of response between the elastic and inelastic response, which means the Oxnard ground motion induces inelastic behavior in this building. The 13-story and 17-story buildings had largely elastic response to this ground motion. The reason for inelastic behavior in this building relative to the other two can be explained by examining the response spectra for this ground motion (see figure A.2). Larger pseudo accelerations occur at the fundamental period of this building than for the other buildings.

Comparing all three models, beating is seen in the elastic and inelastic responses whereas damage and damping in the fracture model prevent beating.

Drift Ratios

Different drift ratio comparisons are shown in figures 10.48–10.50. The five representative ground motions are used, and drifts in the N-S direction for the Hall random fracture and inelastic models are given. For the Oxnard record, drifts for the various models are compared.

For the fracture model, all five records have the highest drifts in stories 1–4. This indicates predominant first-mode response to all the ground motions. Higher mode effects would produce some larger drifts in the upper stories.

The inelastic model also has large lower story drifts, but the Tabas and Takatori drifts indicate some higher mode response with increased drift in the eighth story.

The Oxnard record drifts differ based on model type. The elastic model has some higher mode response and the fracture model has more significant local drifts causing damage in the lower stories.

Fracture Distributions

The calculated fractures for the Hall random fracture model are depicted in figures 10.51–10.65. This includes the five representative ground motions, the rotated Oxnard motions, and the rotated Sylmar N-S motions.

All five representative ground motions have lower-level damage. This corresponds to the larger lower-story drifts observed. The G05 response shows distinct southward motion damage in the N-S frames (the even numbered frames on the right of the figure). The Tabas damage is spread throughout the E-W frames.

A large increase in the period of roof response was observed in the N-S time history of the Tabas record (figure 10.23). As can be seen from the fracture distribution, there is a lot more concentrated damage in the two lowest levels than for other records. The damage is both above and below the tall first story, so there is an amplified effect of increasing the period of the building.

The Oxnard rotated ground motions produce similar fractures independent of input angle. While the fracture strains were chosen randomly, the same set of strains is used for each run. The same low-strain connections fracture independent of the angle of input since the Oxnard motion has similar levels of orthogonal input. A similar peak input enters each plane of frames. Looking at the time history responses (figures 10.27–10.31), the peak displacement in each direction (N-S and E-W) is roughly the same, independent of input angle.

The Sylmar N-S rotated ground motions produce two levels of damage. If the input is in the plane of the frames (0° or 180°), fractures occur in coplanar frames only. If the input is diagonal to the frames, damage occurs in all the frames. The damage is not very different between input in the plane of symmetry (−45° or 135°) or transverse to it (45°). The roof response is quite different for these orthogonal directions, however.

Plastic-Rotation Distributions

The plastic rotations at member ends for the inelastic model are presented in figures 10.66–10.70.

The plastic rotations are concentrated in the lower levels for all of the ground motions. The Takatori record produces a larger spread of plastic rotations throughout the building. A disturbing trend in the response to all of the ground motions is significant column-end plastic rotations. In the G05 response, the column yield-

ing could easily occur after beam yielding. Looking at the difference in resulting rotations, the beams could yield first and further lateral movement could cause the column plastification. However, column yielding clearly occurs before beam yielding in the upper stories of the Takatori response. The building design meets the strong-column/weak-beam provisions of the 1994 UBC. The increased axial compressive force in the columns reduces the effective column strength, increasing the B/C ratio. The code provision may be satisfied for static loading, but if the axial force is greater than anticipated the columns may yield before the beams.

Another explanation for the column yielding is consideration of the ground motion as a pulse travelling up through the building. This will be discussed more in section 11.1.

Damage Indicator Summary Tables

The five representative ground motion responses for the Hall random fracture and inelastic models are summarized in tables 10.3 and 10.4, respectively. Drift, roof displacement, base shear, and number of fractures are the damage indicators tabulated.

The discussion of damage indicators for the 17-story and 13-story buildings concluded that several basic indicators are not good predictors of damage. Similar conclusions can be drawn from the 10-story building. The base shear ratio V/W is similar for all the ground motions, but the damage levels vary greatly. The maximum roof displacement, however, cannot be discarded for this building. The roof displacements correlate well with the damage levels. The maximum story drift is also correlated with the damage except for the Takatori record that spreads the damage throughout the building. This means only the roof displacement is a reliable predictor for this building. These conclusions can be drawn from the fracture or inelastic models.

An elastic model is subjected solely to the Oxnard ground motion. The damage indicators for the three model types (fracture, inelastic and elastic) are given in table 10.5. The base shear ratio is much larger for the elastic model. The Oxnard

record produces inelastic behavior in this building to a much greater extent than in the other buildings. This means the ratio of elastic to inelastic model base shear ratios will be larger for the 10-story building and it also explains why the elastic base shear ratio itself is so much larger. There is a much larger demand on this building, so it suffers more inelastic behavior.

The fracture model has a lower base shear ratio and maximum roof displacement than the inelastic model, yet it has a larger maximum drift. This behavior was explained for the 13-story building. The fractures reduce response through the release of stored energy to a greater extent than the inelastic behavior of hysteretic damping alone can. The disadvantage is that localized damage (story drift) is larger, so overall there is not necessarily a benefit.

The rotated Oxnard and Sylmar responses are also tabulated in tables 10.6 and 10.7, respectively. Comparing maximum to minimum damage indicators, the Oxnard record can produce maximum drifts 20% larger depending on the angle of excitation. The maximum roof response can vary by 35%, the base shear ratio by 6% and the number of fractures by 17%. For the Sylmar record, the maximum drift can vary by 48%, the maximum roof displacement by 24%, the base shear ratio by 21%, and the number of fractures by 70%. These ranges of damage indicators arise from merely rotating the angle of input excitation and are definitely of significance for engineering design.

10.6 Figures

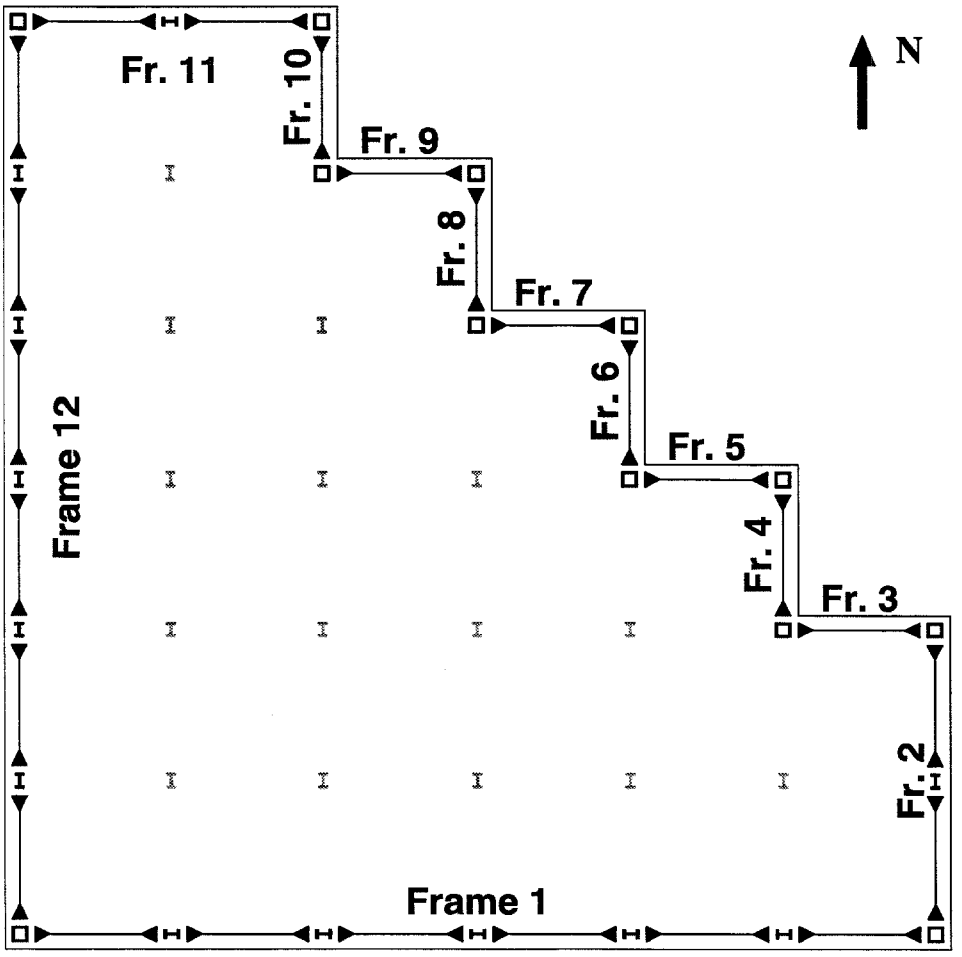

Figure 10.1 Plan of building with frame labels.

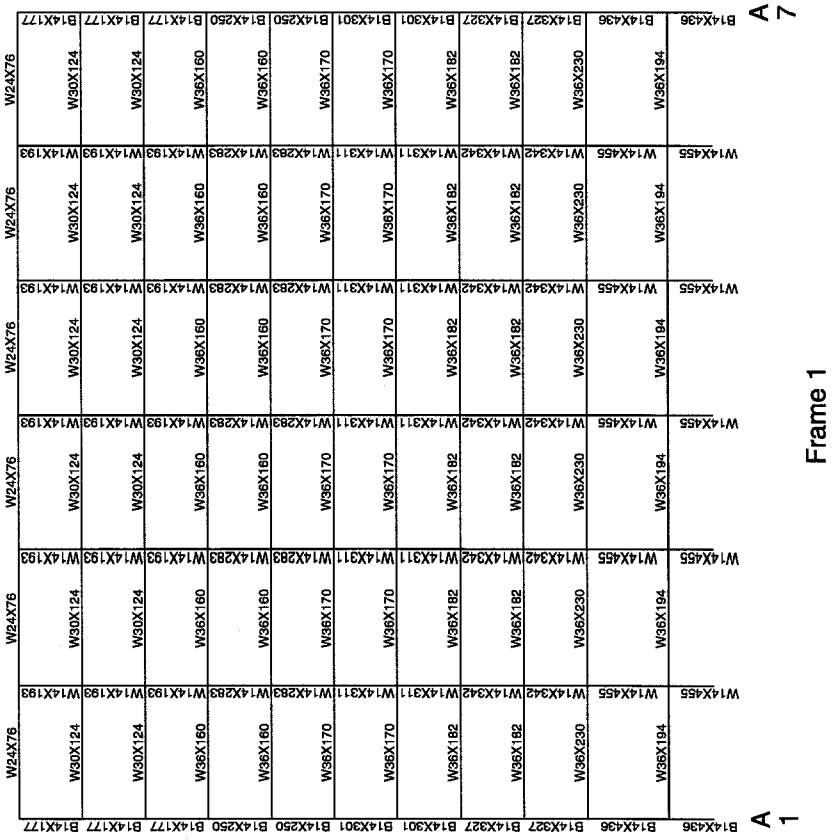

Figure 10.2 South frame section properties.

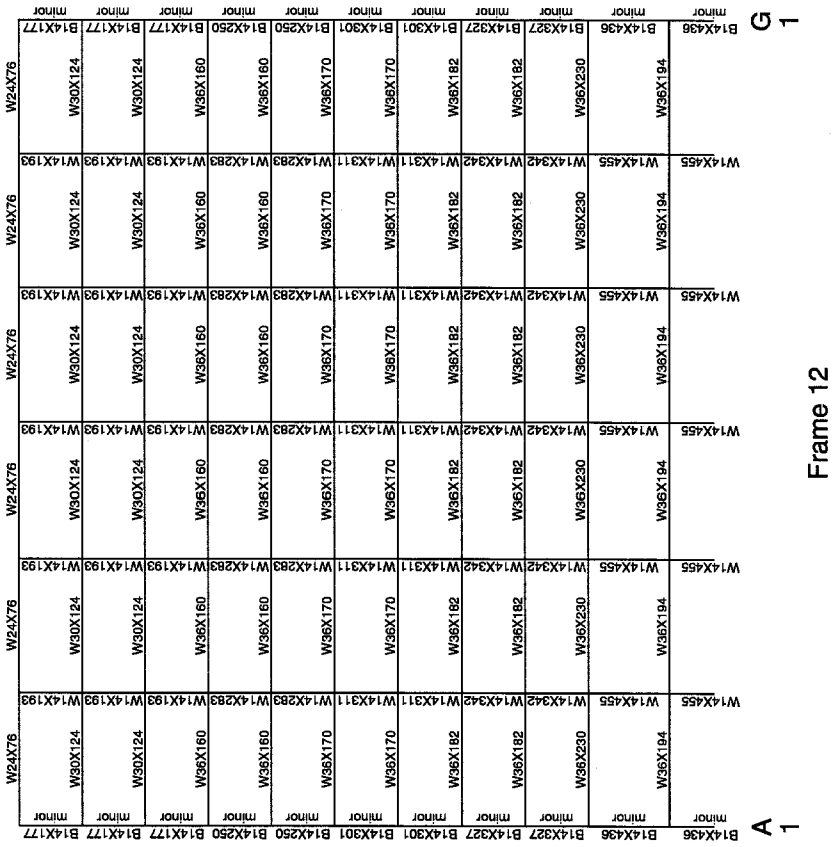

Figure 10.3 West frame section properties.

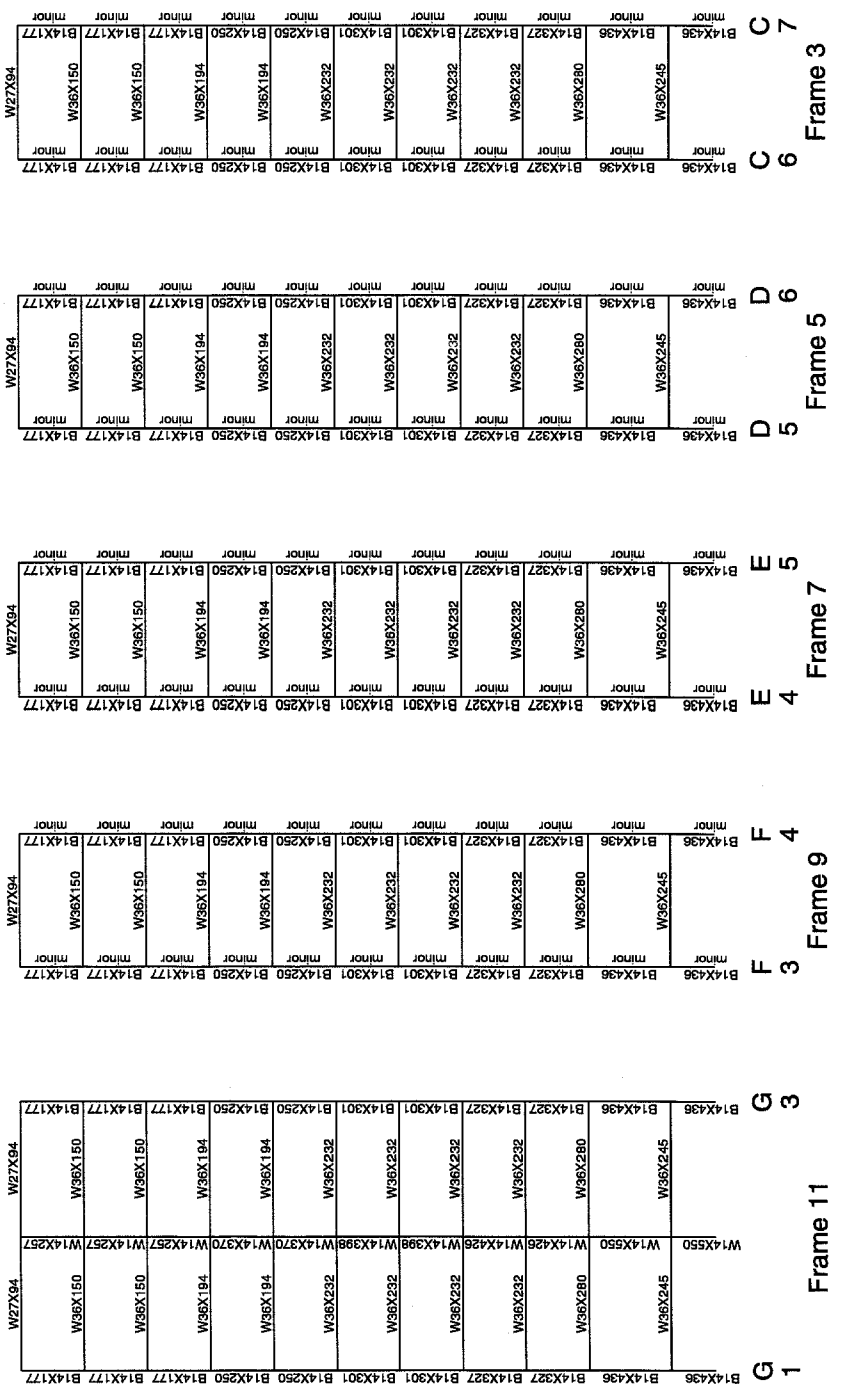

Figure 10.4 North frames section properties.

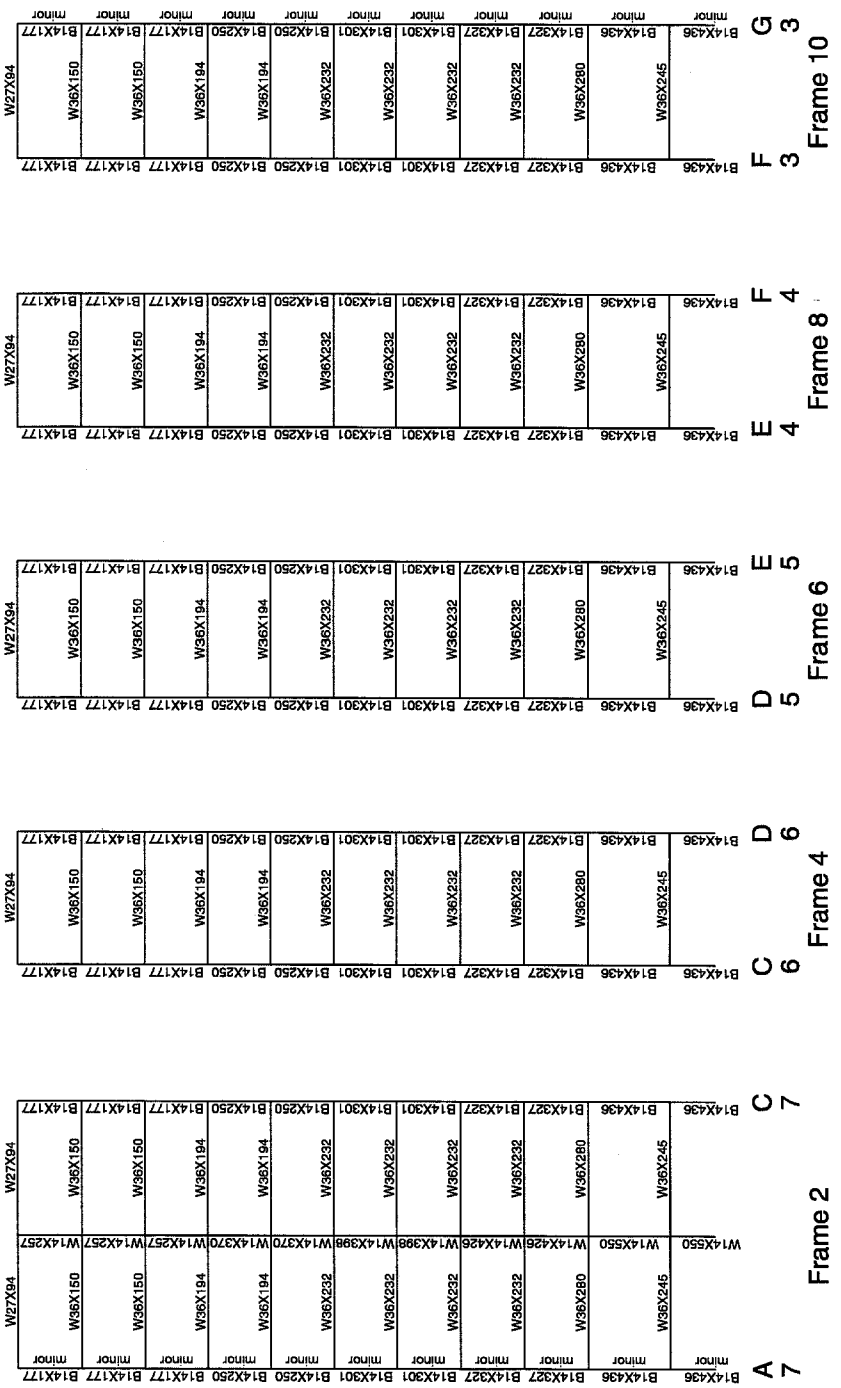

Figure 10.5 East frames section properties.

MODE SHAPES OF 10–STORY BUILDING

Mode 1, Period = 2.160 sec.

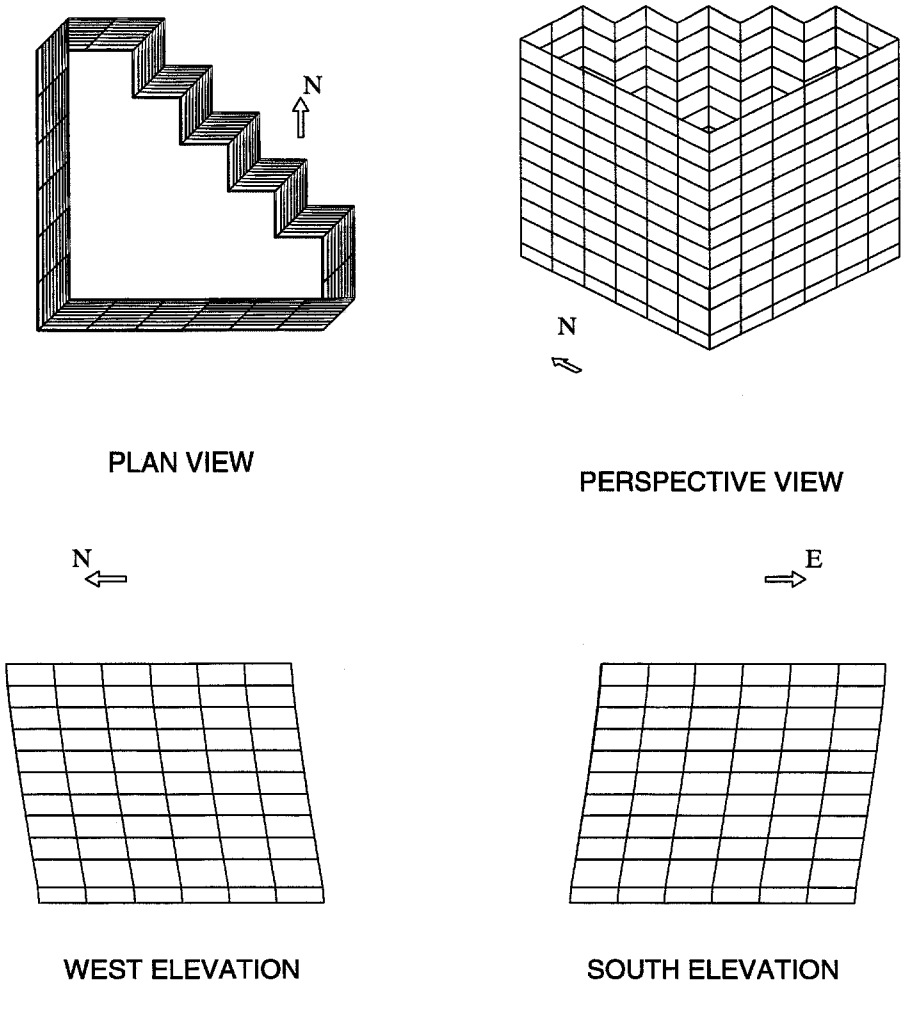

Figure 10.6 10-story building mode 1.

MODE SHAPES OF 10–STORY BUILDING

Mode 2, Period = 2.065 sec.

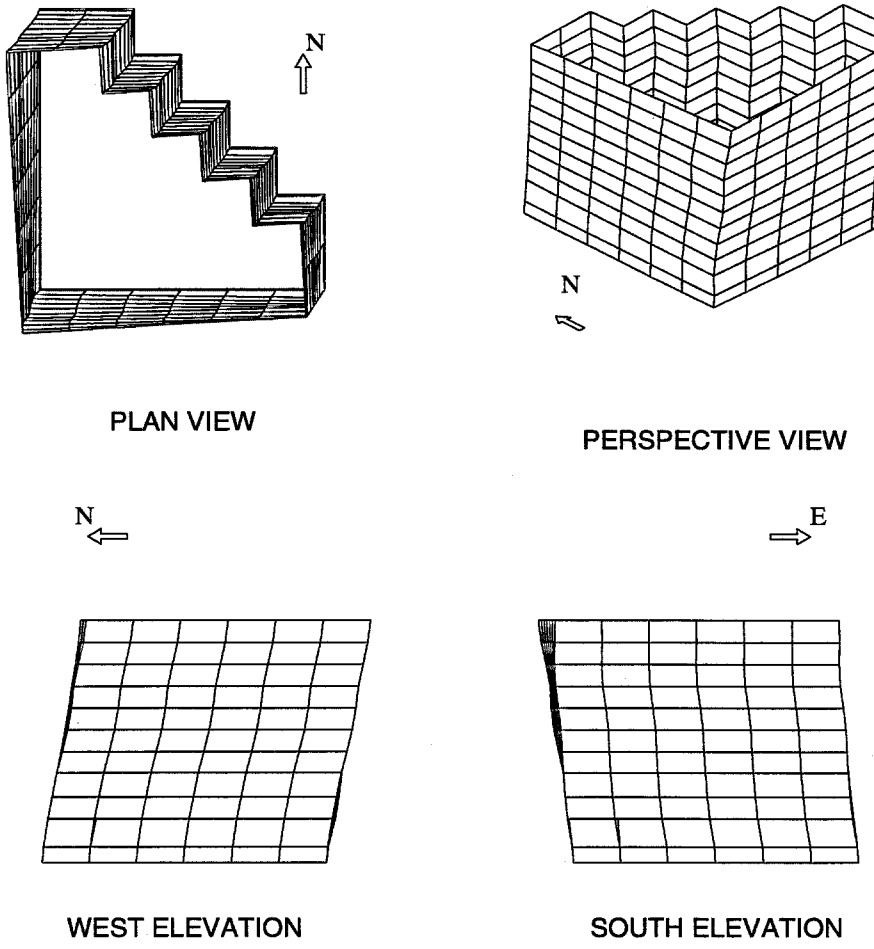

Figure 10.7 10-story building mode 2.

MODE SHAPES OF 10–STORY BUILDING

Mode 3, Period = 1.517 sec.

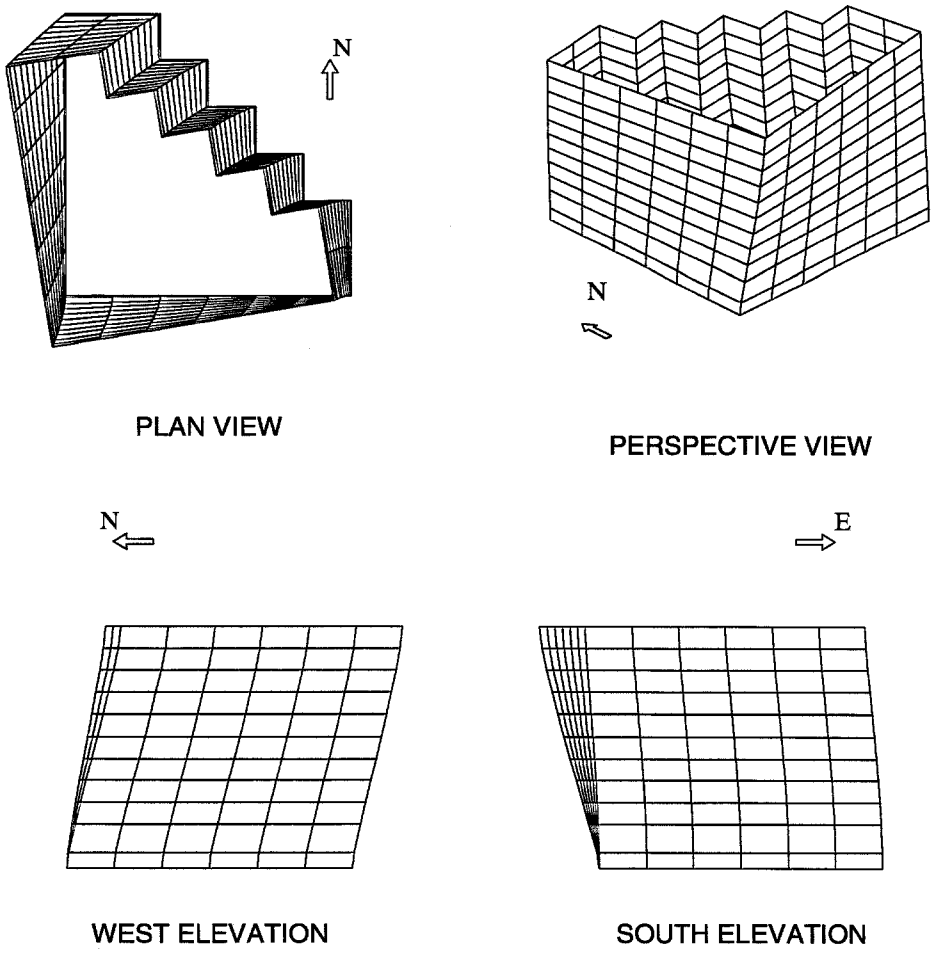

Figure 10.8 10-story building mode 3.

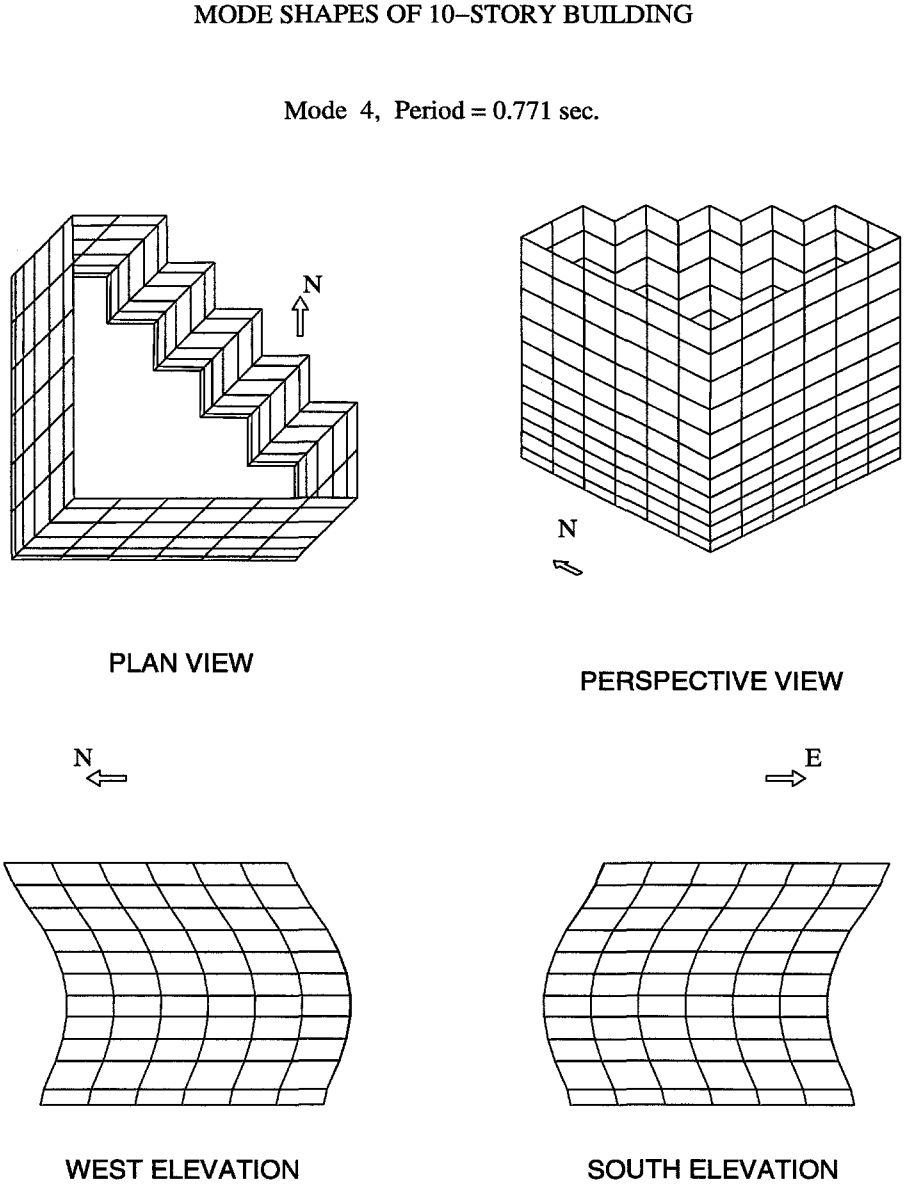

Figure 10.9 10-story building mode 4.

MODE SHAPES OF 10–STORY BUILDING

Mode 5, Period = 0.749 sec.

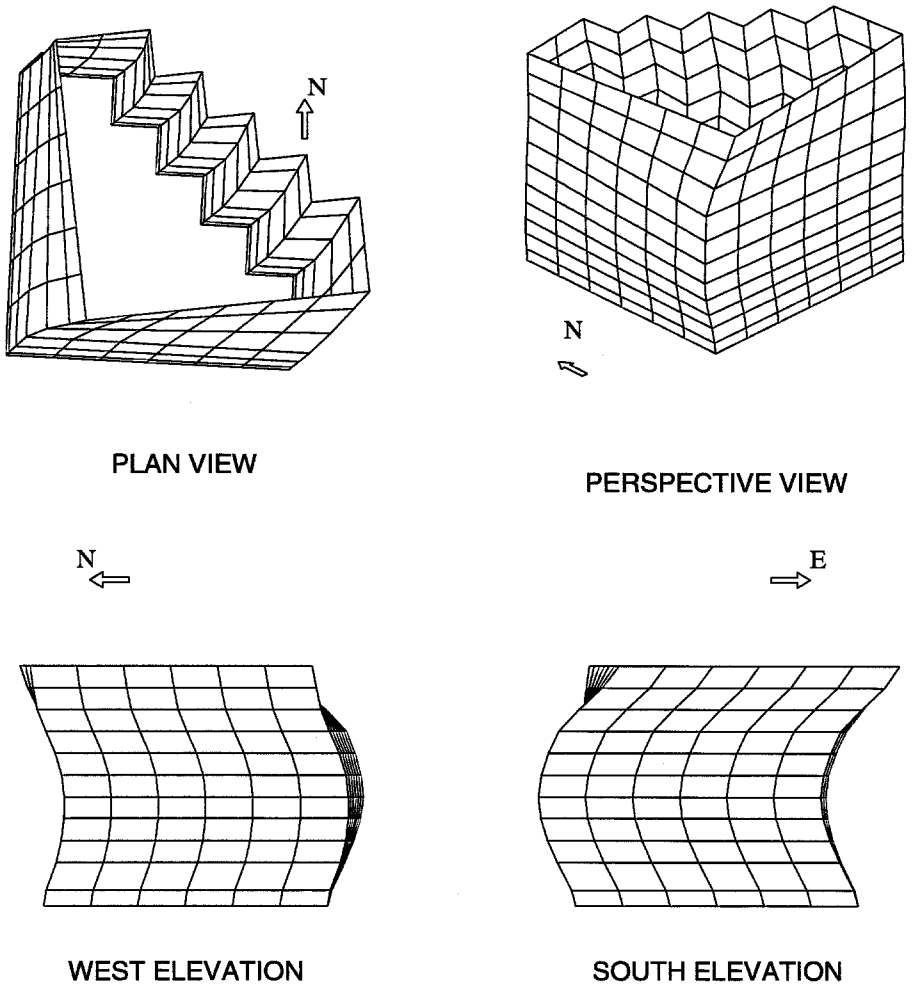

Figure 10.10 10-story building mode 5.

MODE SHAPES OF 10–STORY BUILDING

Mode 6, Period = 0.549 sec.

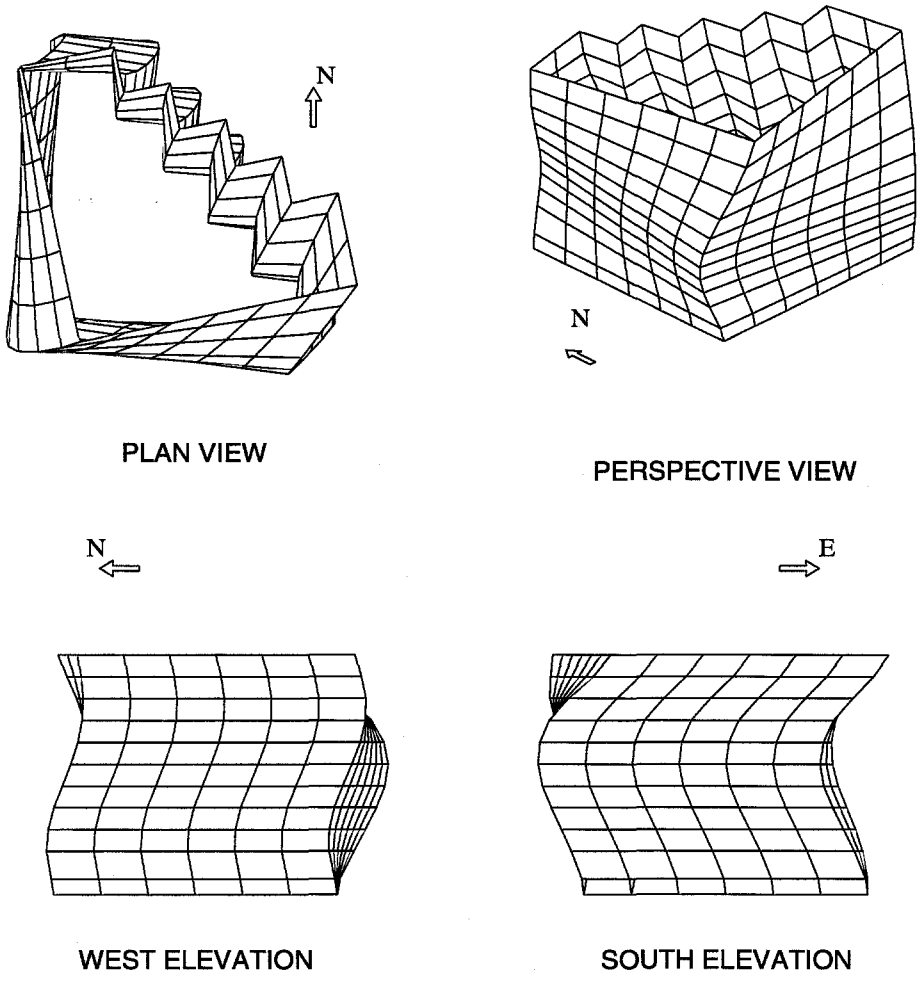

Figure 10.11 10-story building mode 6.

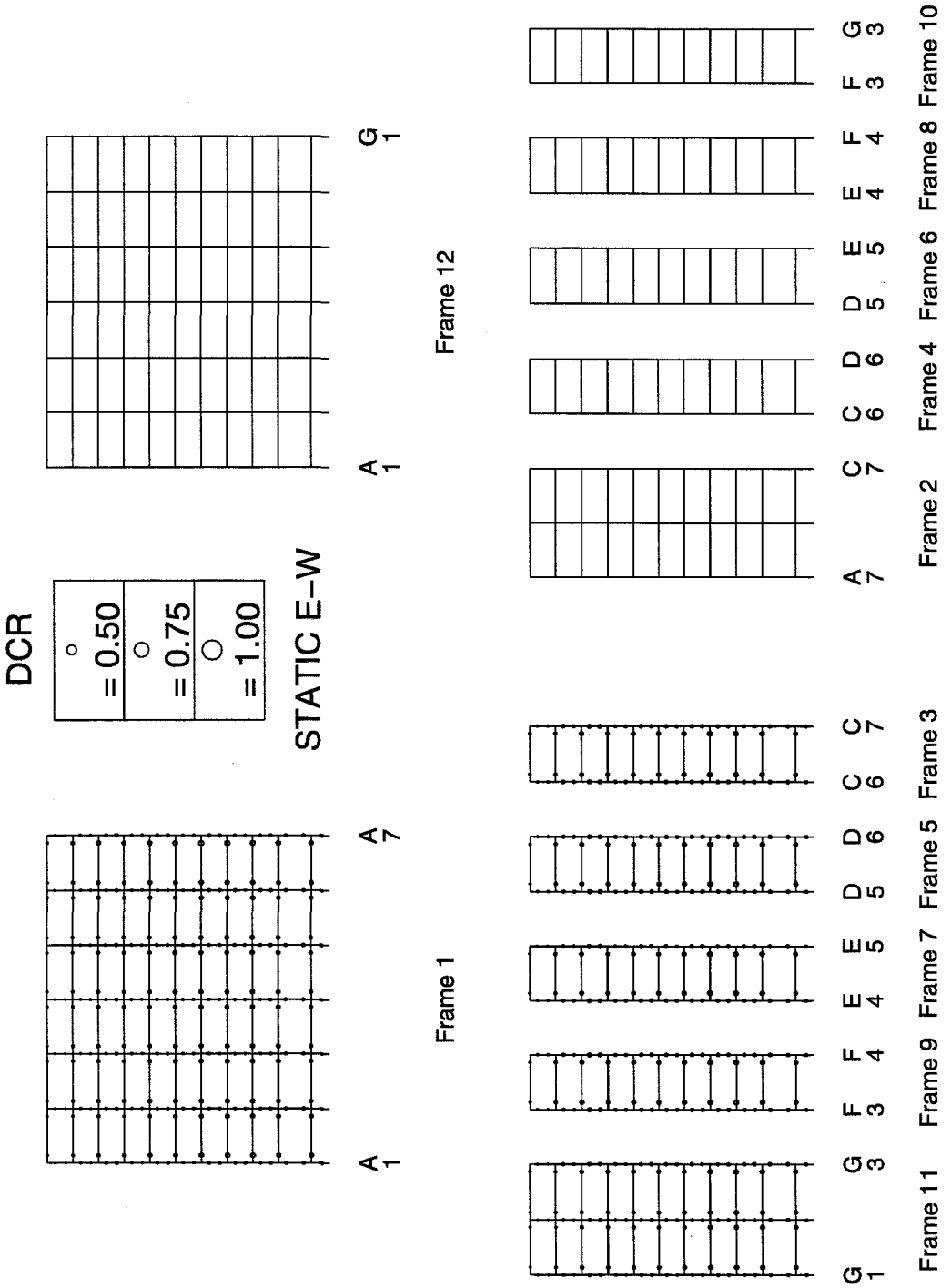

Figure 10.12 10-story building demand capacity ratios, E-W direction.

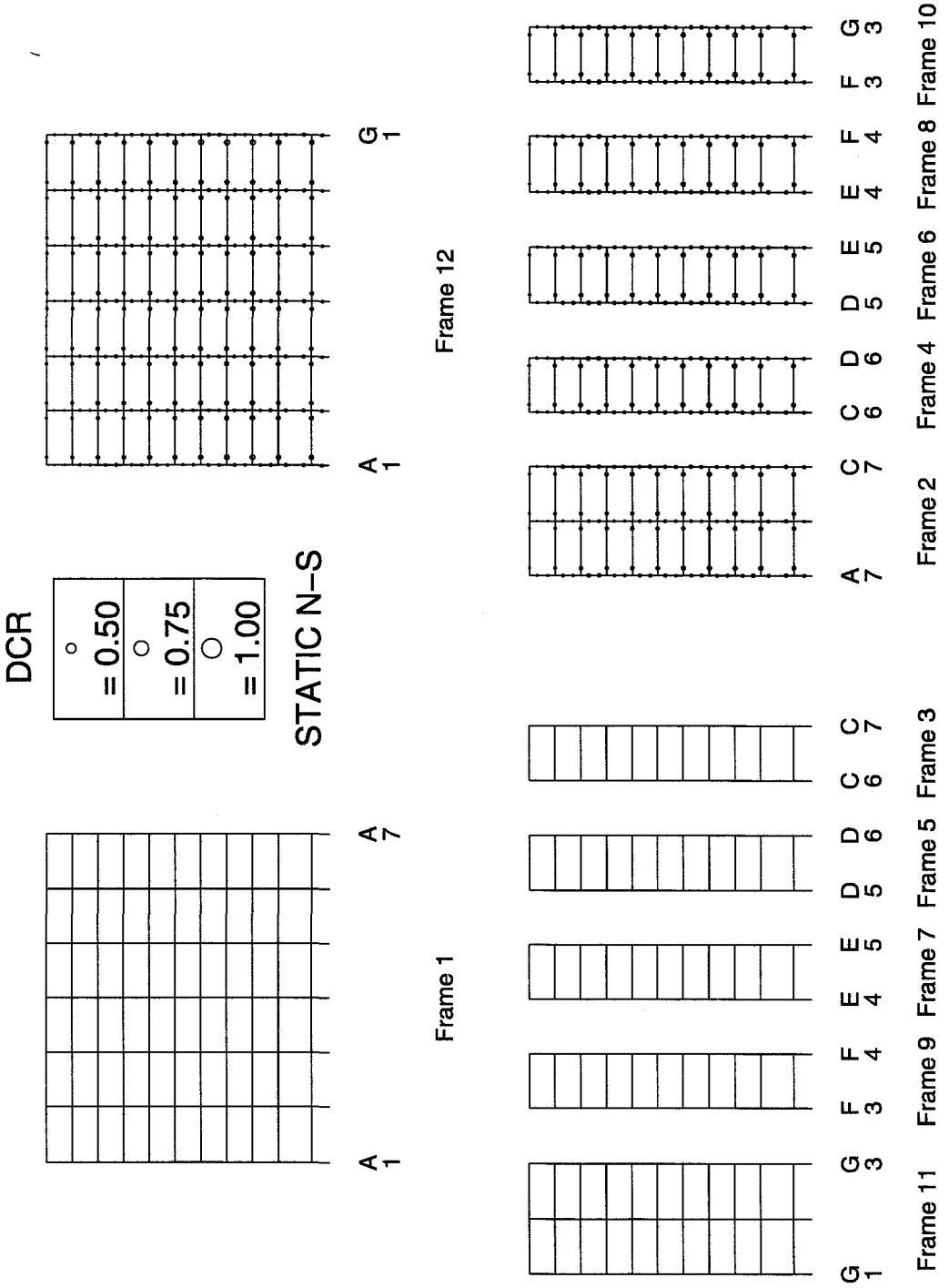

Figure 10.13 10-story building demand capacity ratios, N-S direction.

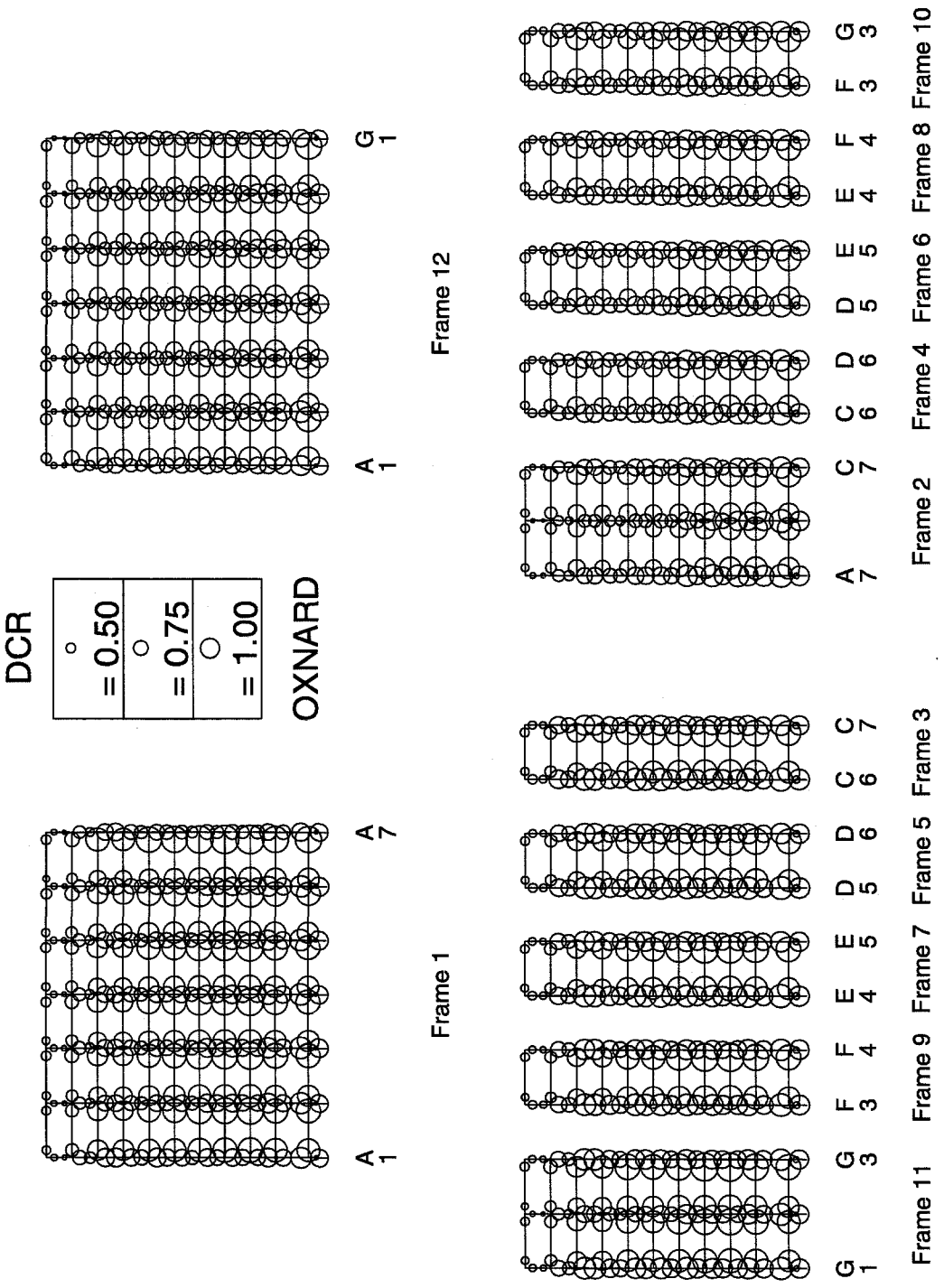

Figure 10.14 10-story building demand capacity ratios, Oxnard record.

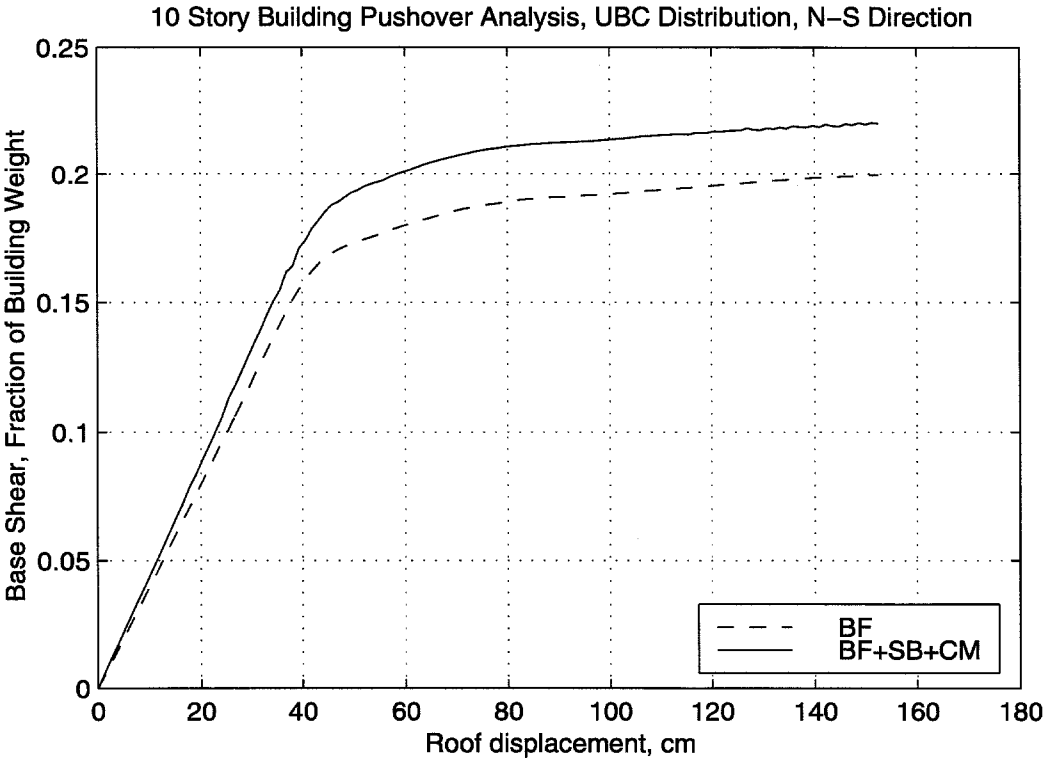

Figure 10.15 10-story pushover analysis.

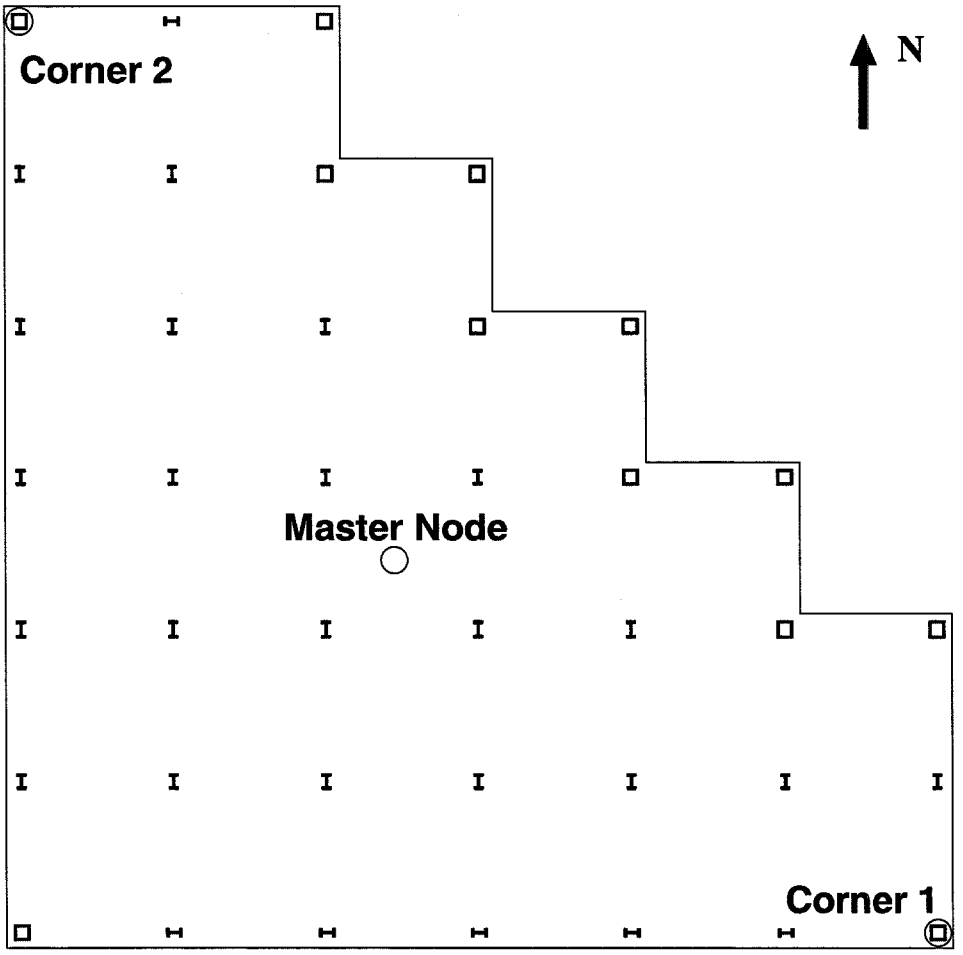

Figure 10.16 Locations at roof for time histories.

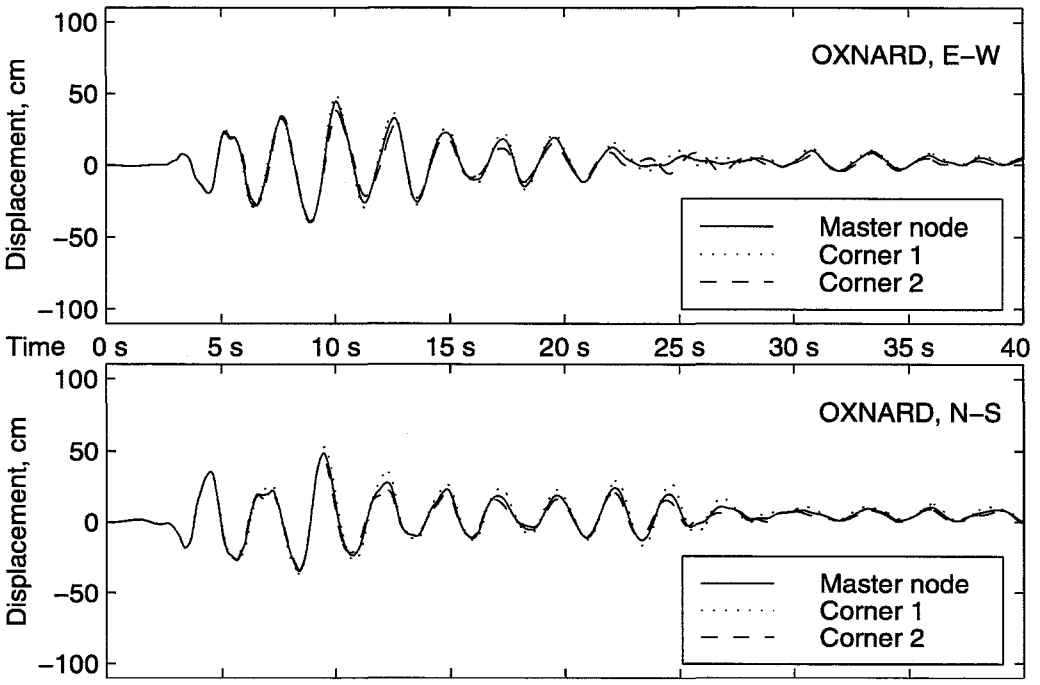

Figure 10.17 Relative roof displacements, Hall fracture model and Oxnard record.

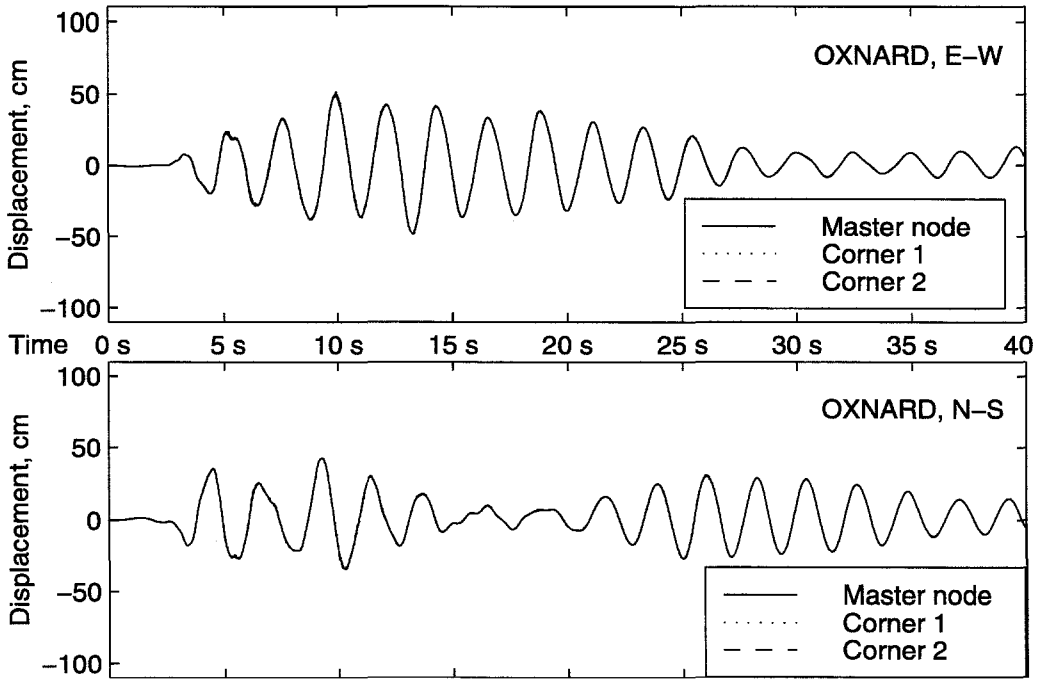

Figure 10.18 Relative roof displacements, inelastic model and Oxnard record.

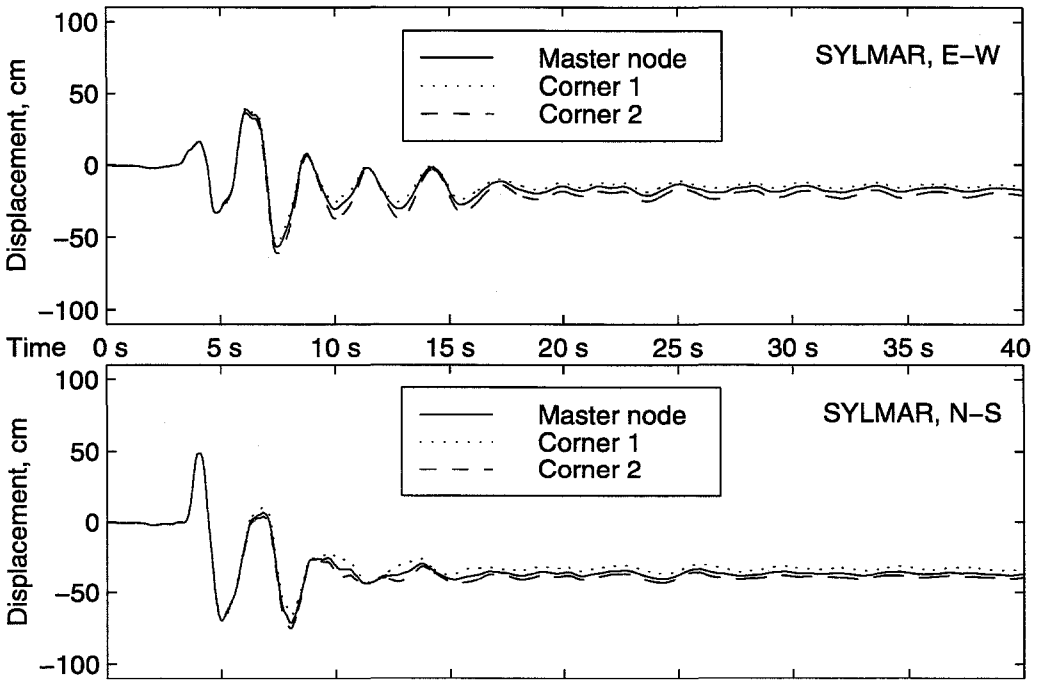

Figure 10.19 Relative roof displacements, Hall fracture model and Sylmar record.

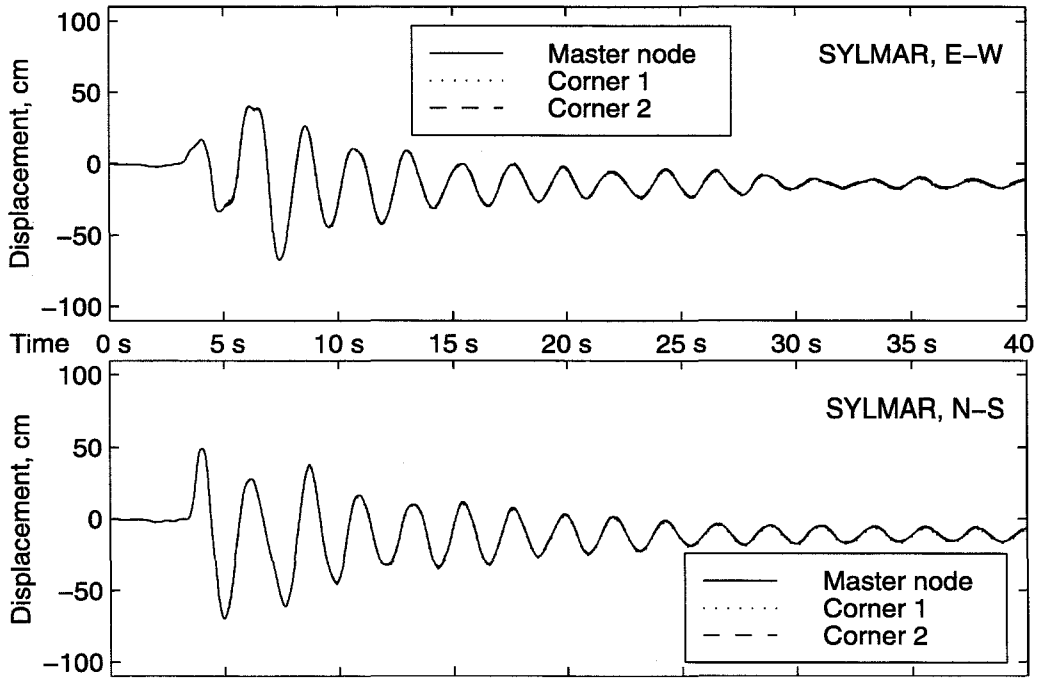

Figure 10.20 Relative roof displacements, inelastic model and Sylmar record.

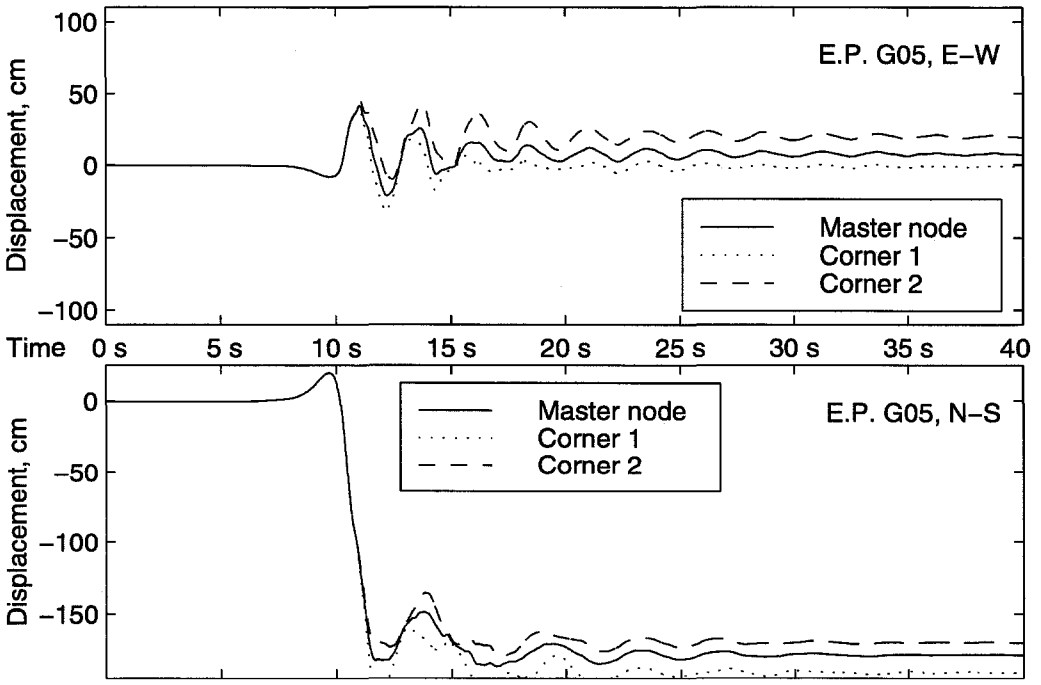

Figure 10.21 Relative roof displacements, Hall fracture model and E. P. G05 record.

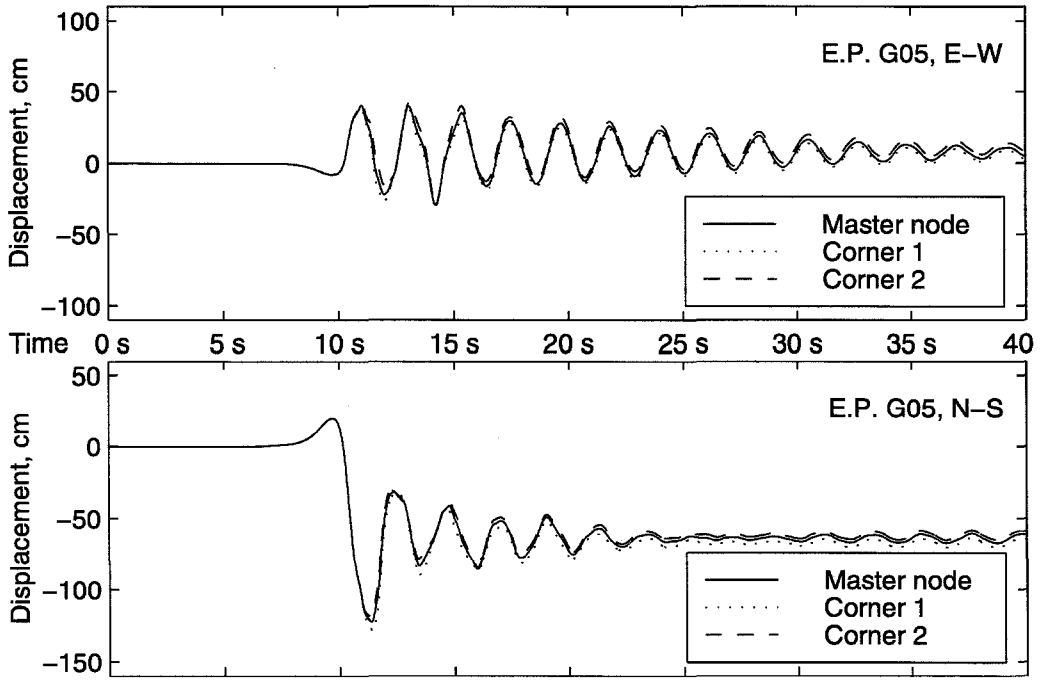

Figure 10.22 Relative roof displacements, inelastic model and E. P. G05 record.

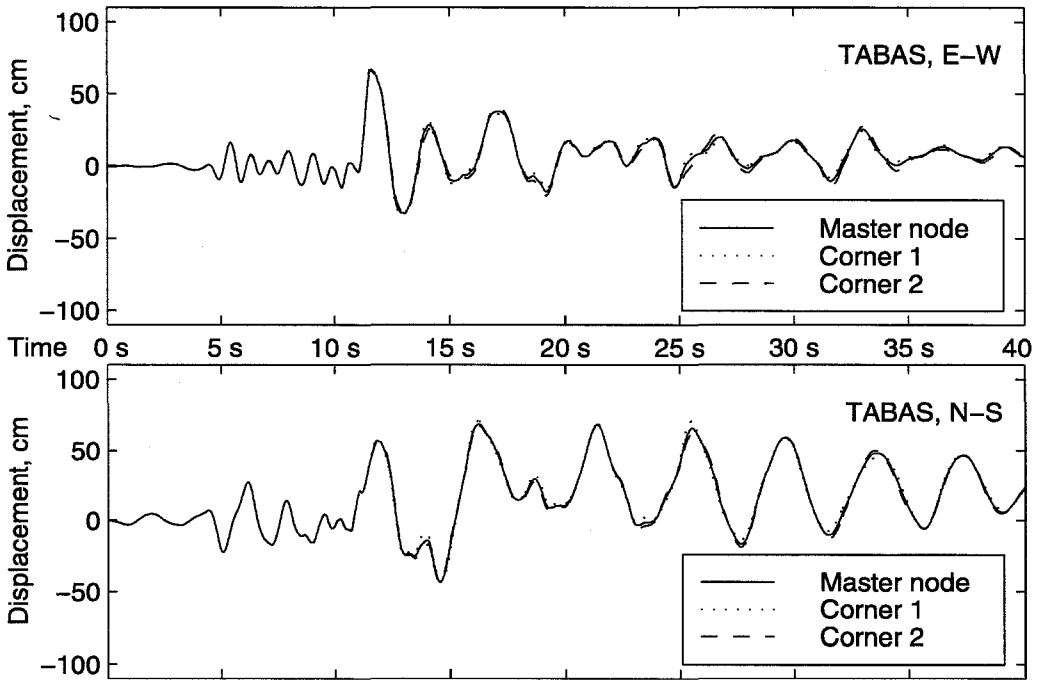

Figure 10.23 Relative roof displacements, Hall fracture model and Tabas record.

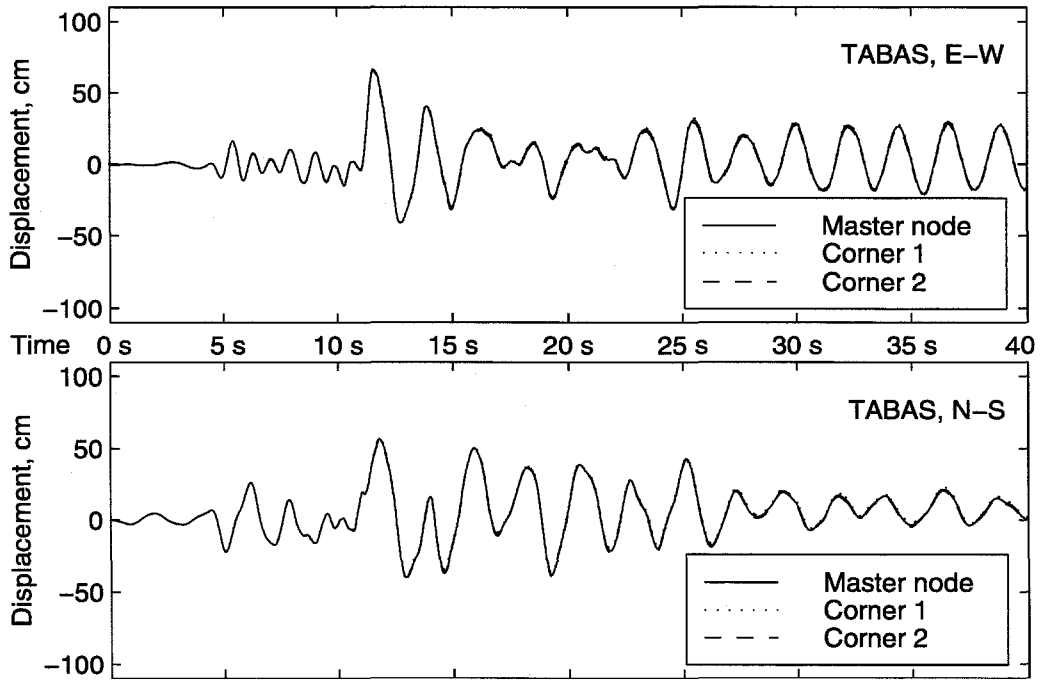

Figure 10.24 Relative roof displacements, inelastic model and Tabas record.

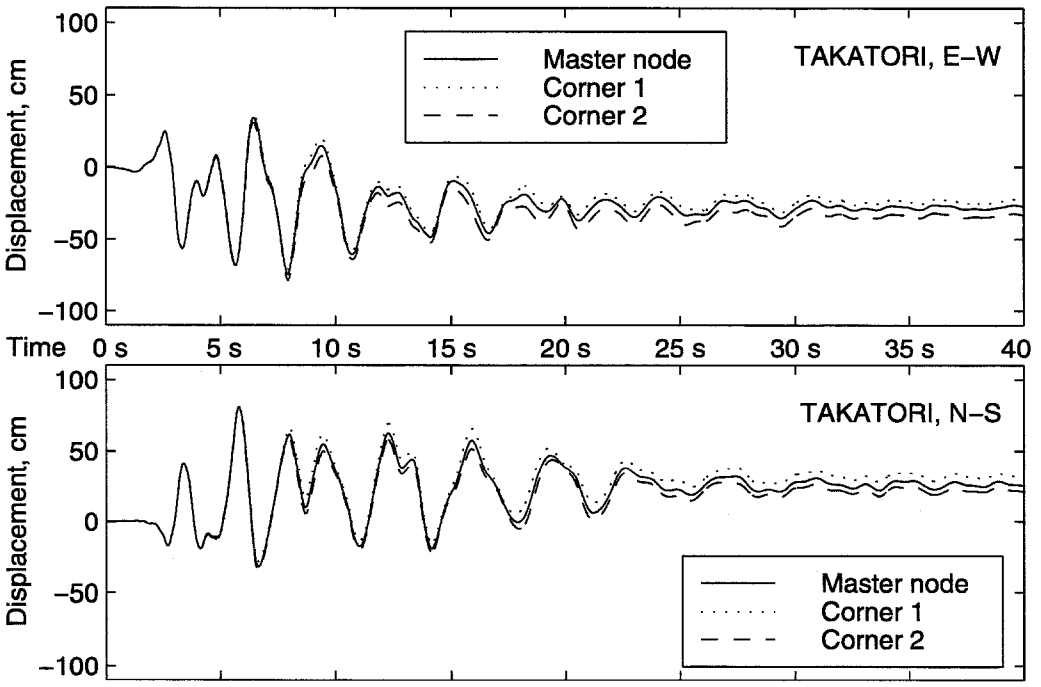

Figure 10.25 Relative roof displacements, Hall fracture model and Takatori record.

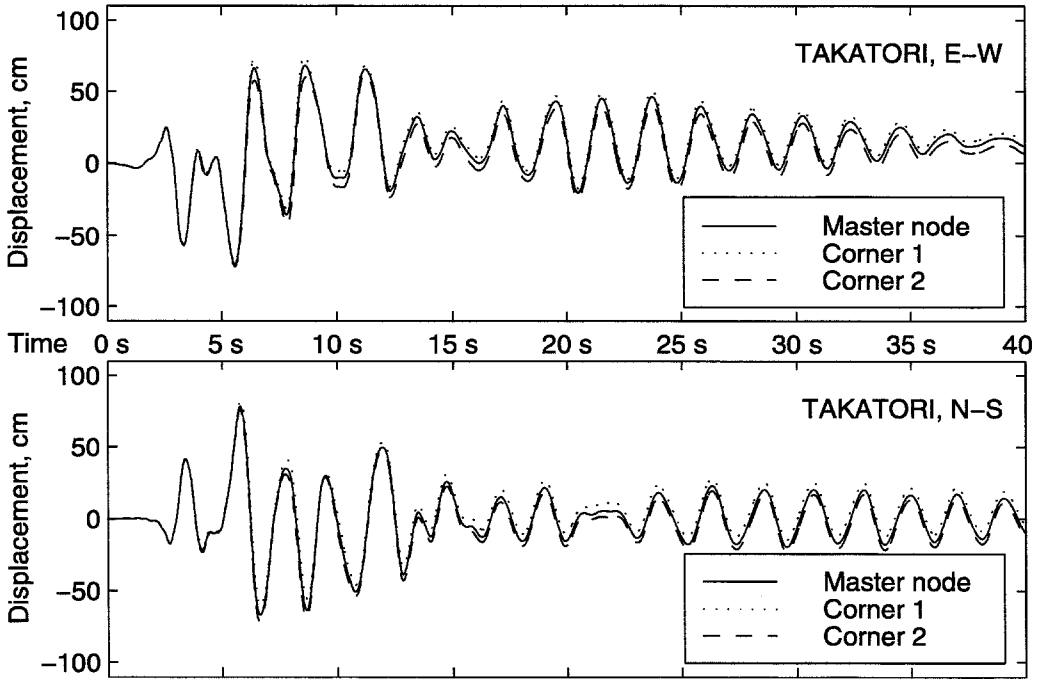

Figure 10.26 Relative roof displacements, inelastic model and Takatori record.

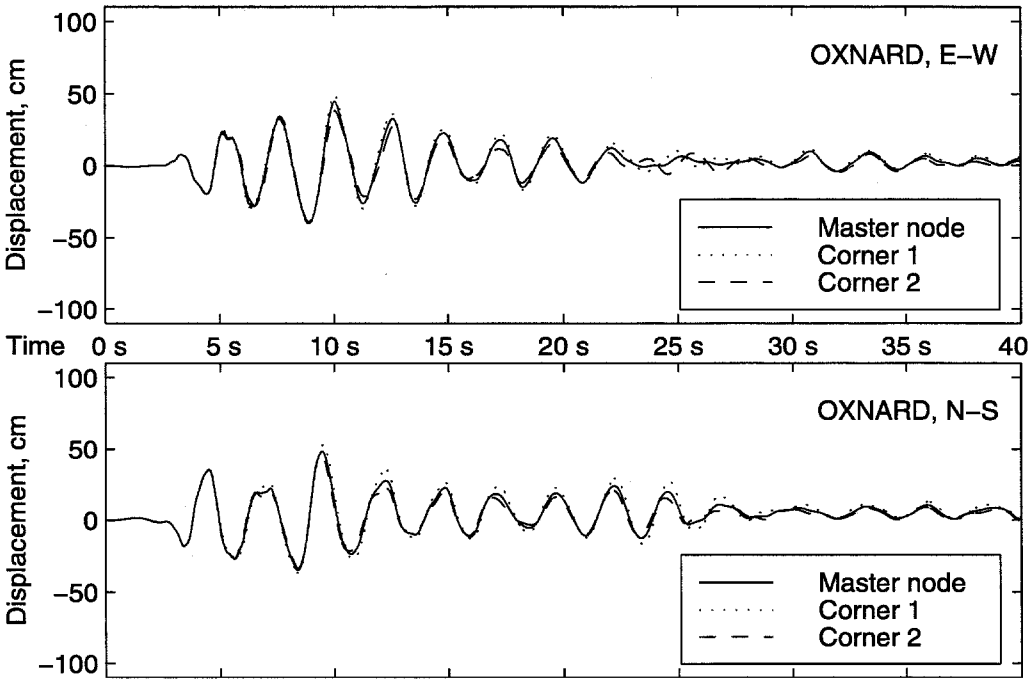

Figure 10.27 Relative roof displacements, Hall fracture model and Oxnard rotated 0°.

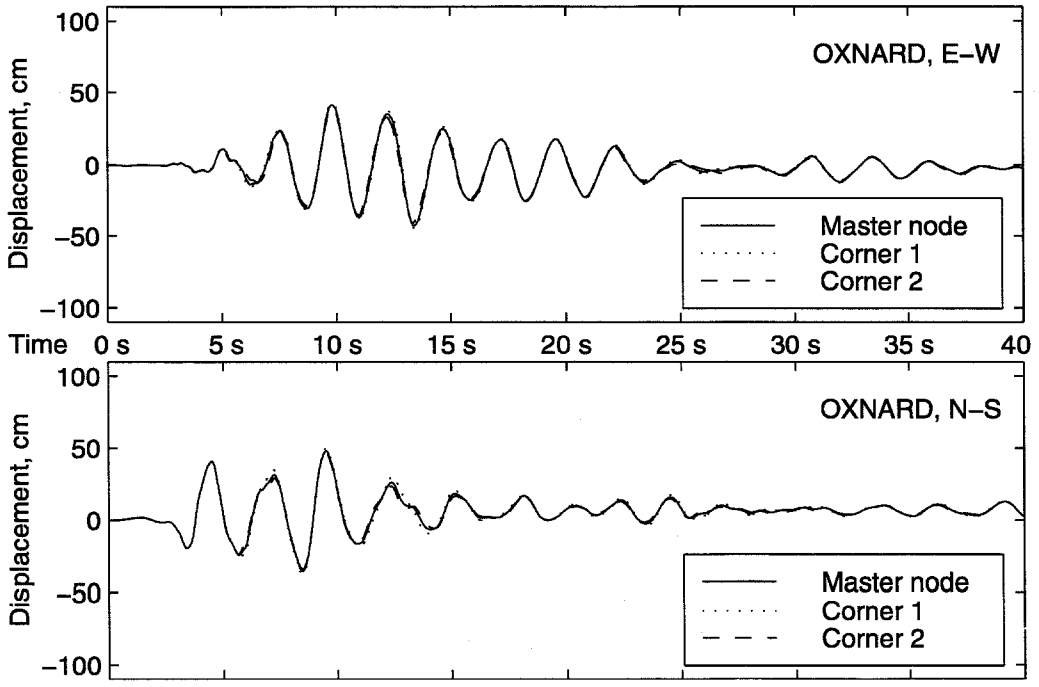

Figure 10.28 Relative roof displacements, Hall fracture model and Oxnard rotated 22.5°.

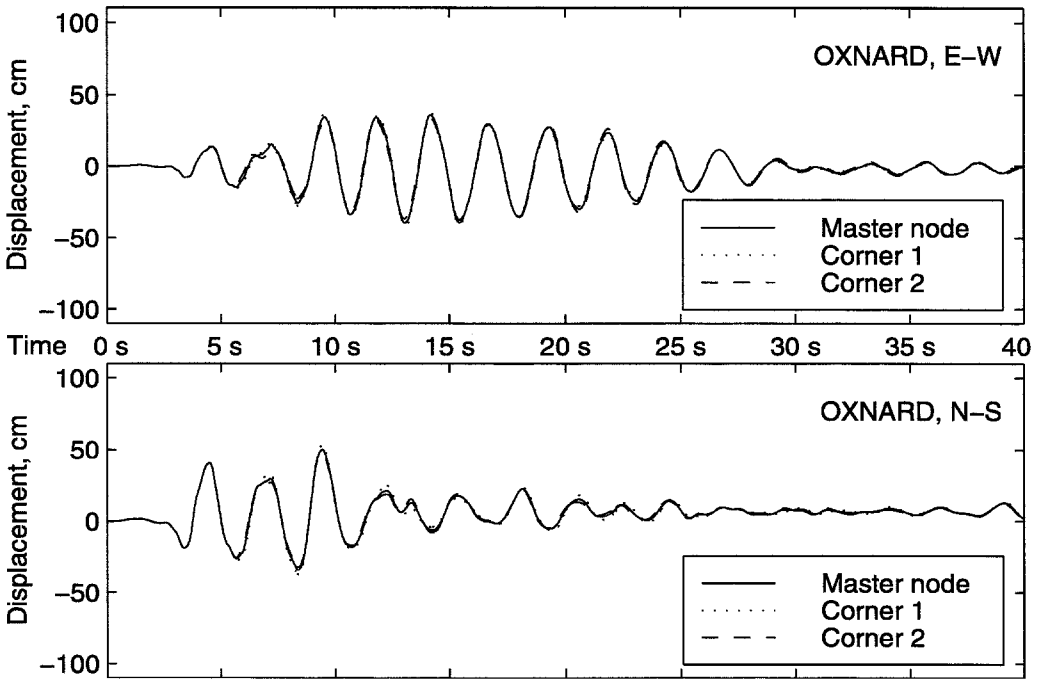

Figure 10.29 Relative roof displacements, Hall fracture model and Oxnard rotated 45°.

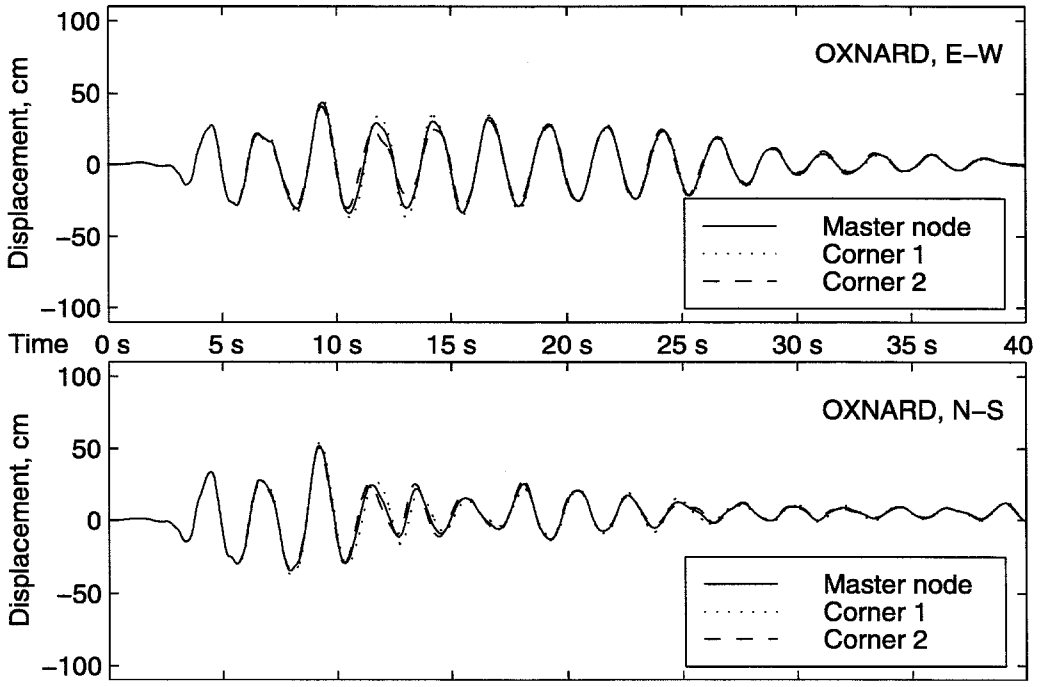

Figure 10.30 Relative roof displacements, Hall fracture model and Oxnard rotated 67.5°.

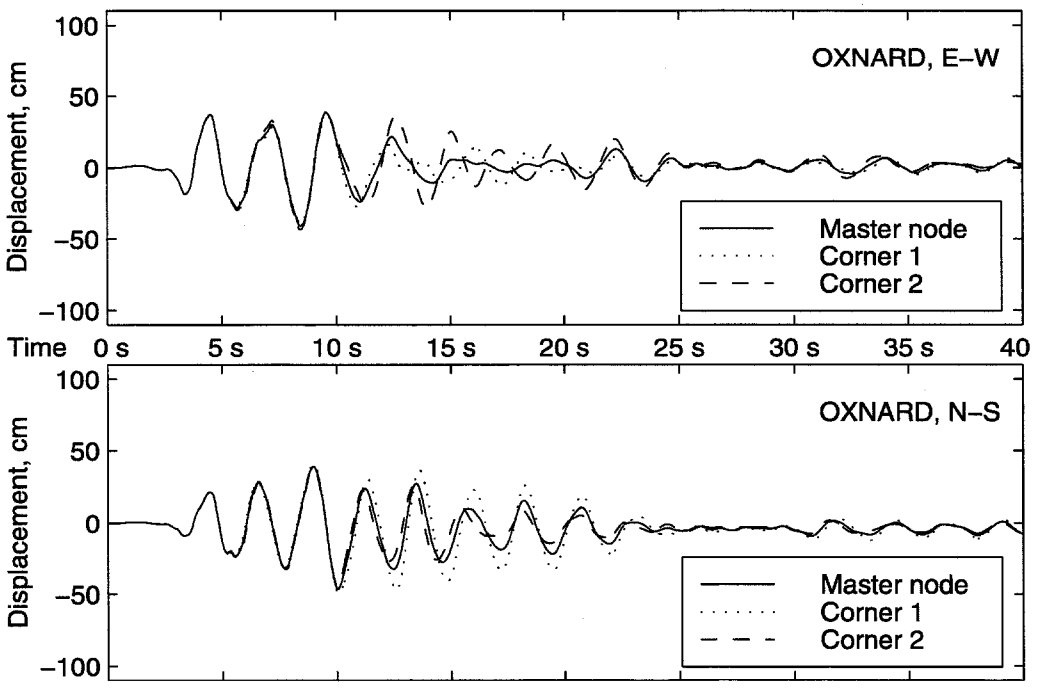

Figure 10.31 Relative roof displacements, Hall fracture model and Oxnard rotated 90°.

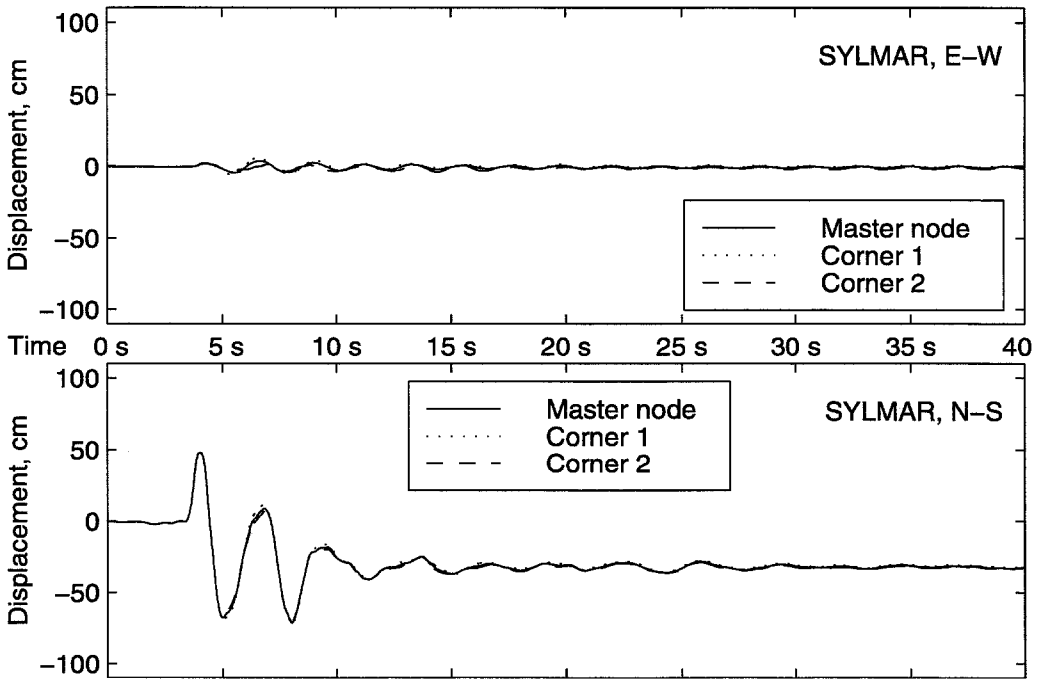

Figure 10.32 Relative roof displacements, Hall fracture model and Sylmar N-S rotated 0°.

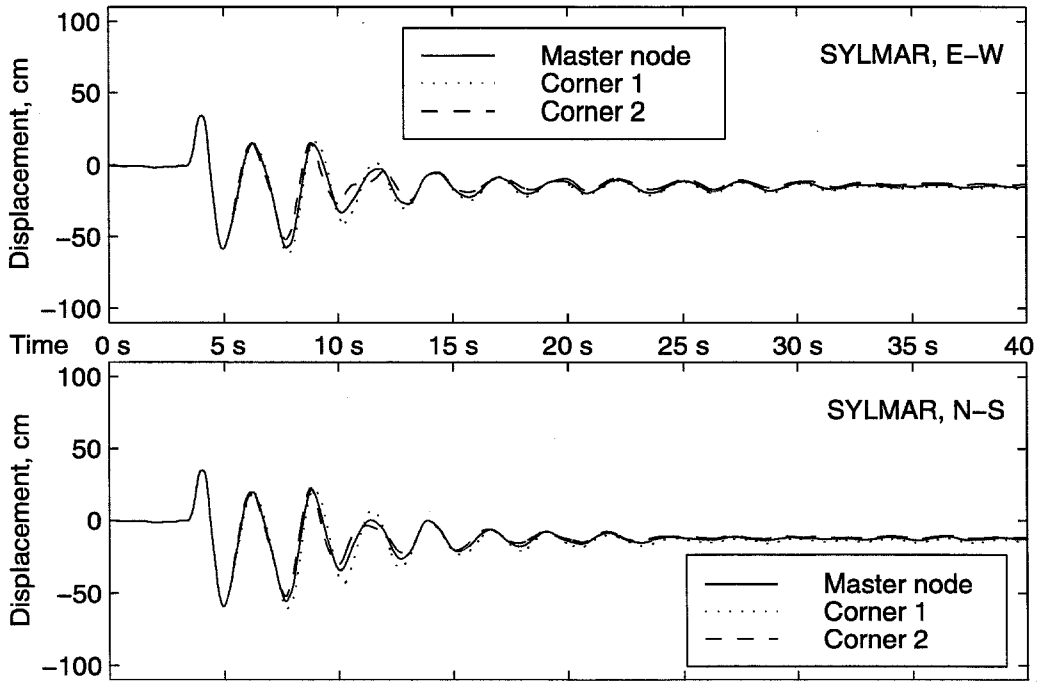

Figure 10.33 Relative roof displacements, Hall fracture model and Sylmar N-S rotated −45°.

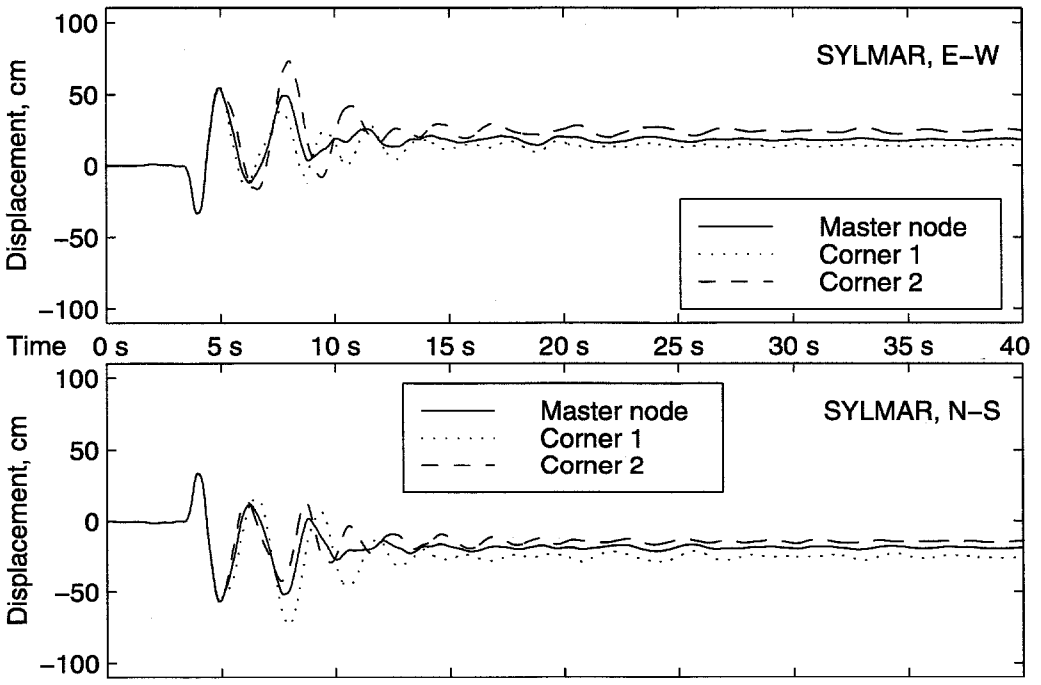

Figure 10.34 Relative roof displacements, Hall fracture model and Sylmar N-S rotated 45°.

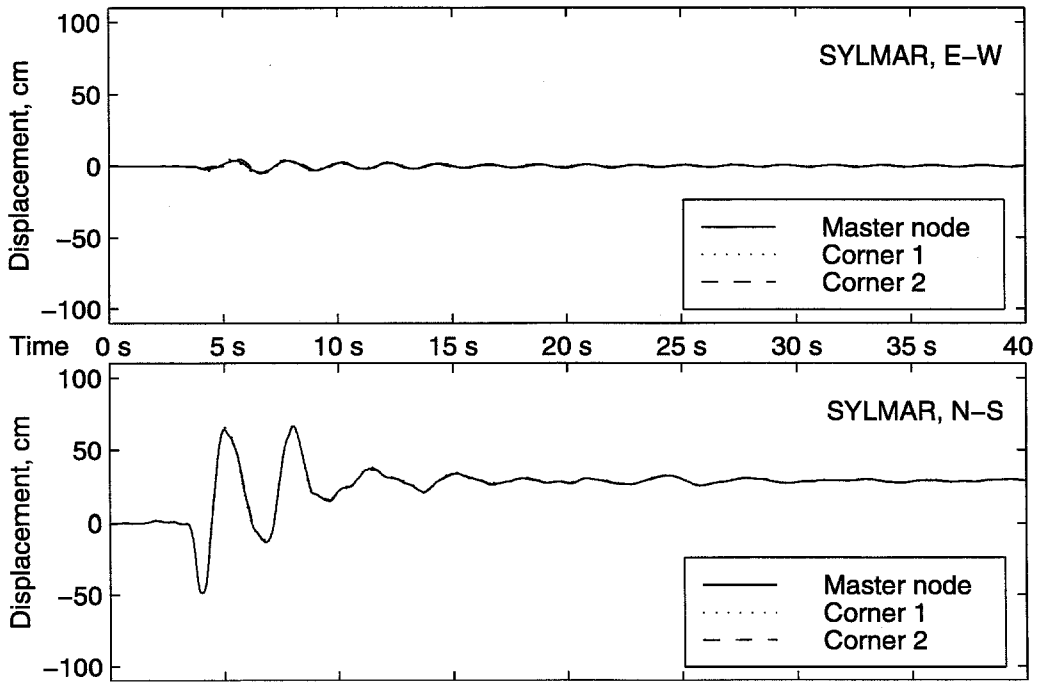

Figure 10.35 Relative roof displacements, Hall fracture model and Sylmar N-S rotated 180°.

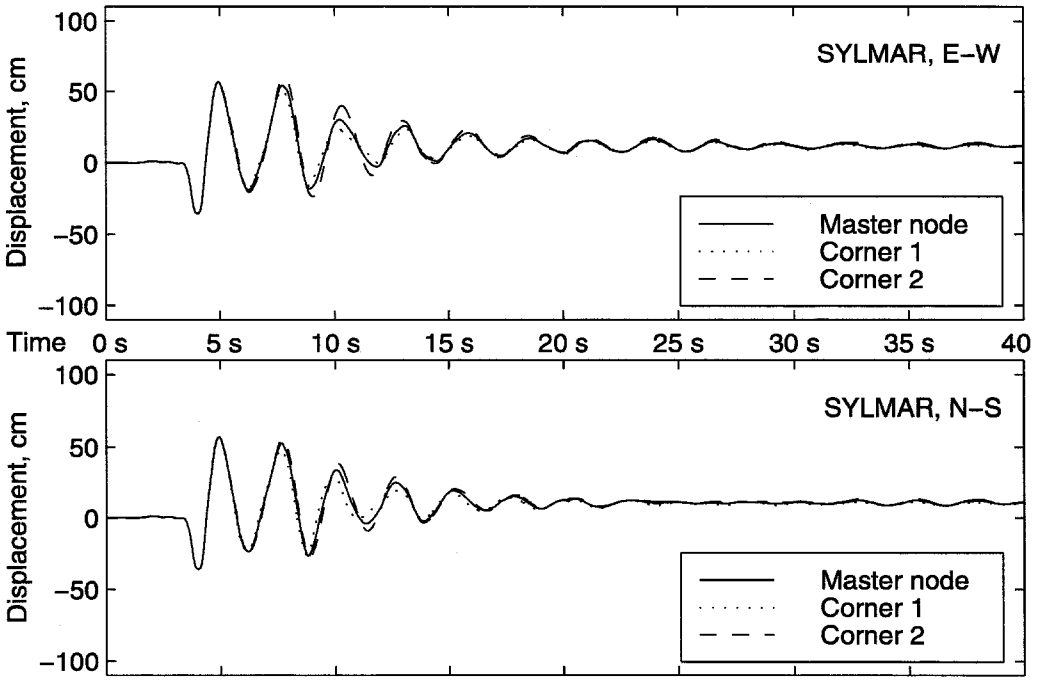

Figure 10.36 Relative roof displacements, Hall fracture model and Sylmar N-S rotated 135°.

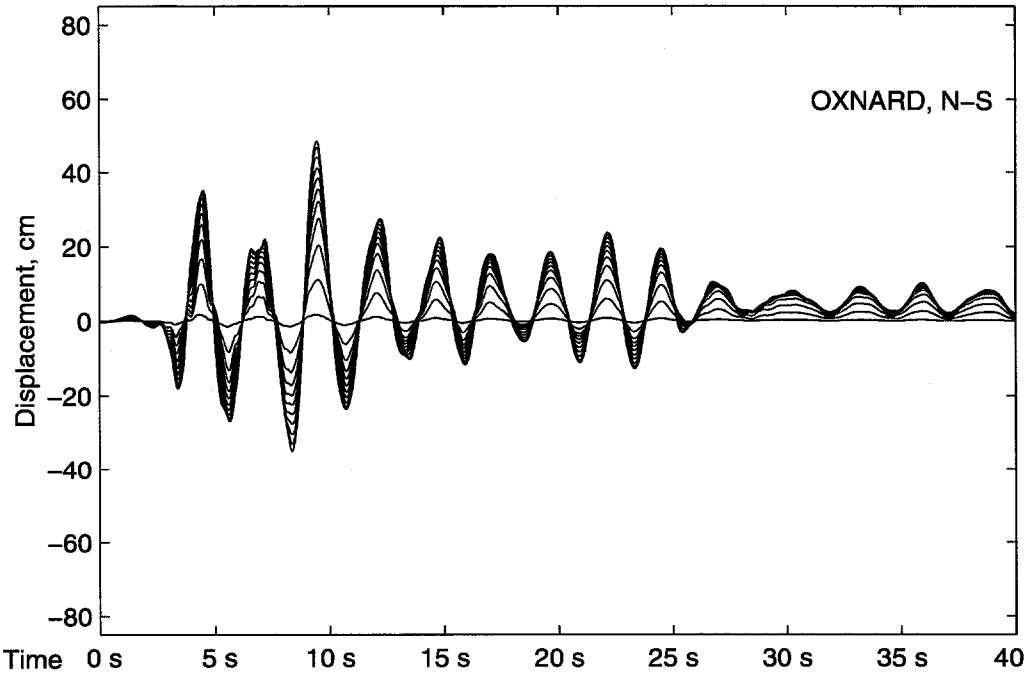

Figure 10.37 Relative floor displacements, Hall fracture model and Oxnard record.

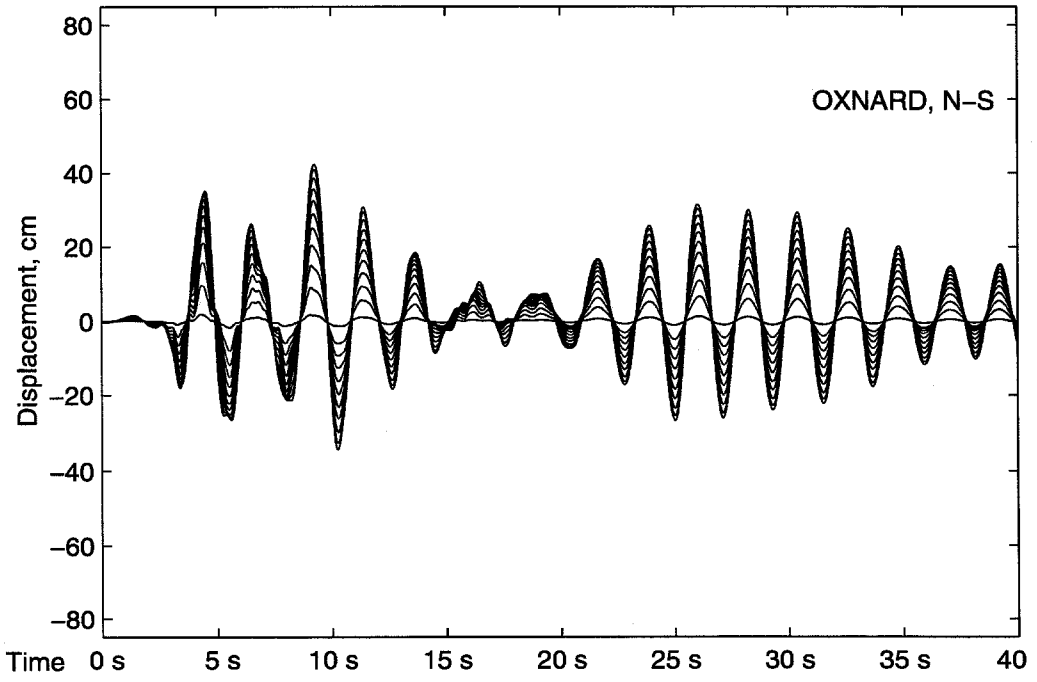

Figure 10.38 Relative floor displacements, inelastic model and Oxnard record.

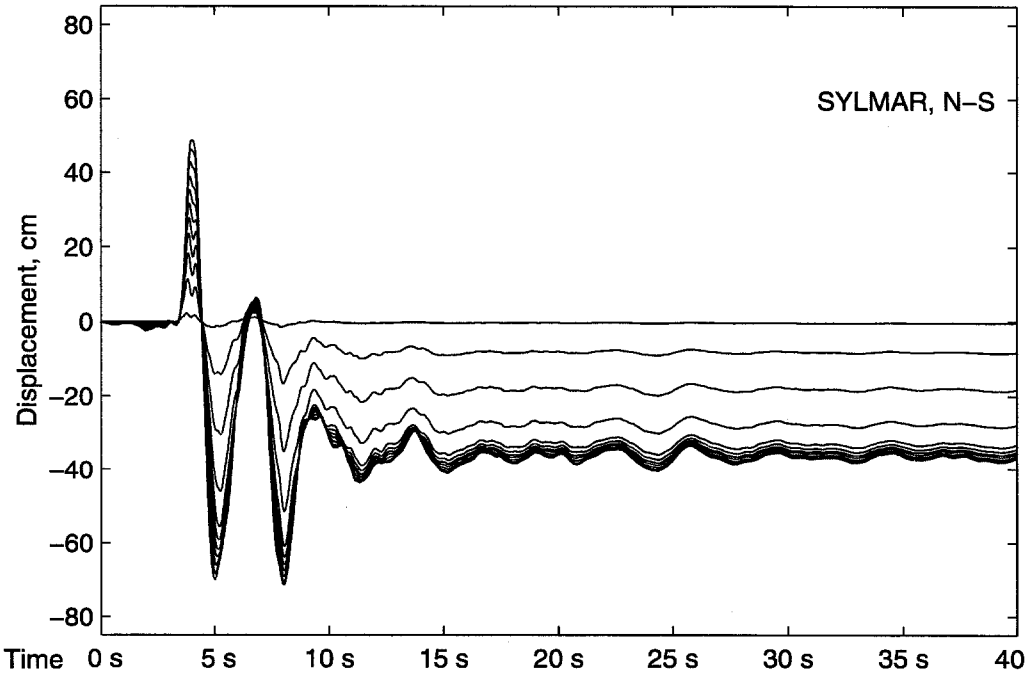

Figure 10.39 Relative floor displacements, Hall fracture model and Sylmar record.

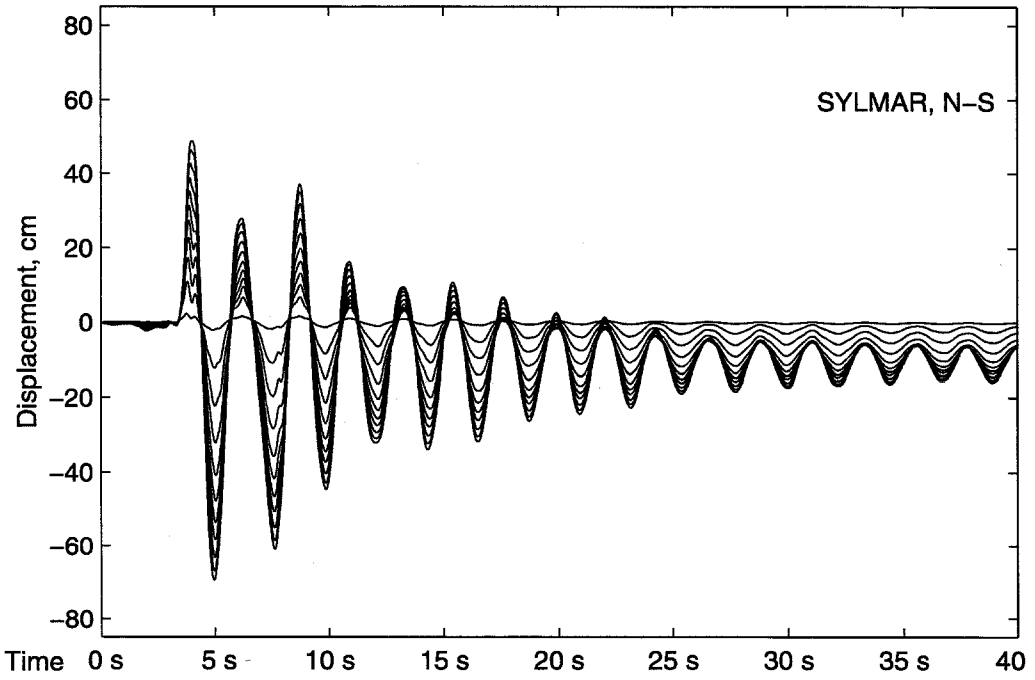

Figure 10.40 Relative floor displacements, inelastic model and Sylmar record.

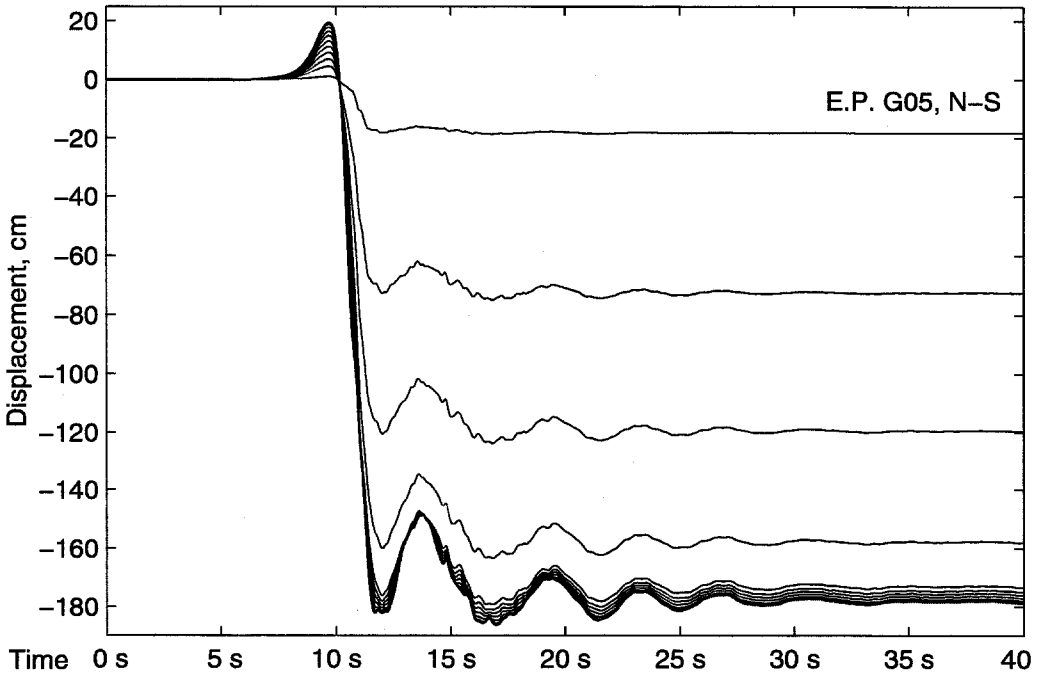

Figure 10.41 Relative floor displacements, Hall fracture model and E.P. G05 record.

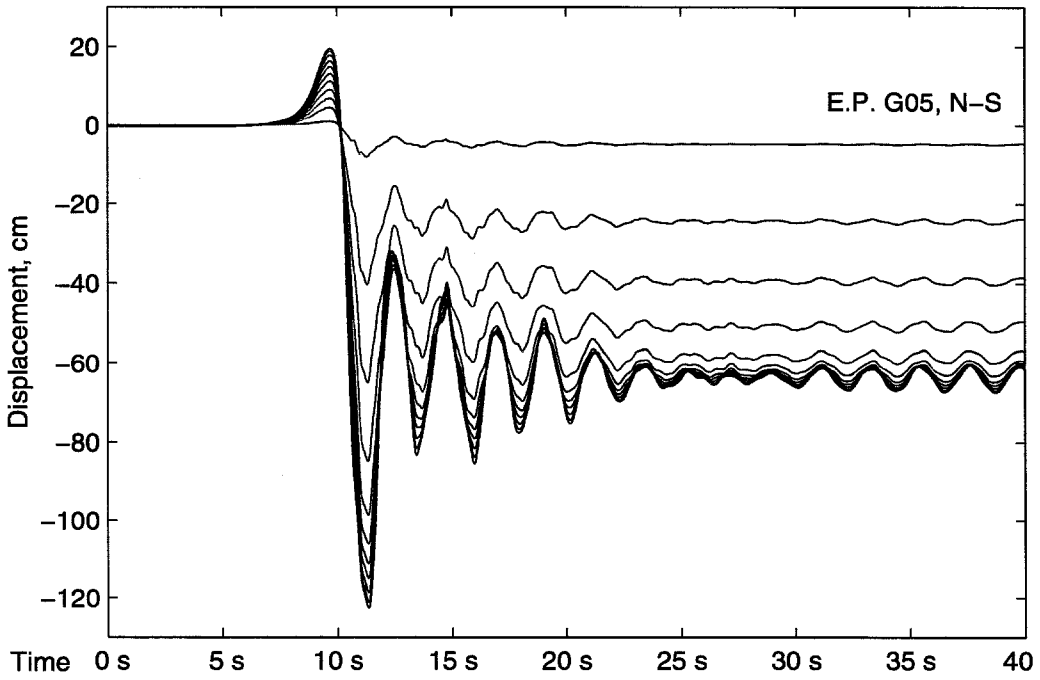

Figure 10.42 Relative floor displacements, inelastic model and E.P. G05 record.

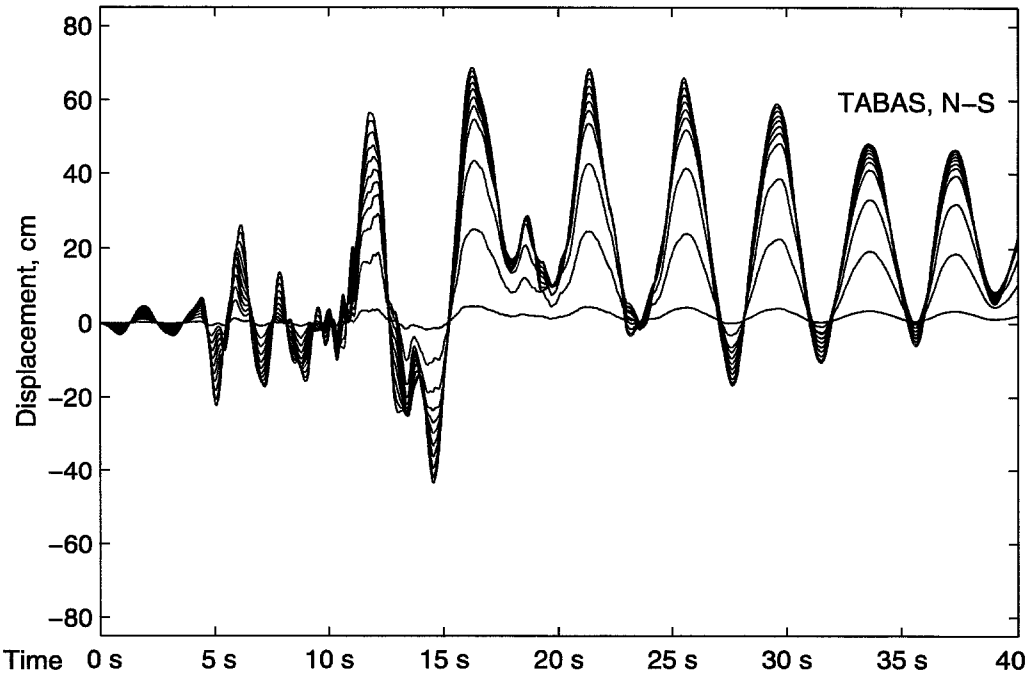

Figure 10.43 Relative floor displacements, Hall fracture model and Tabas record.

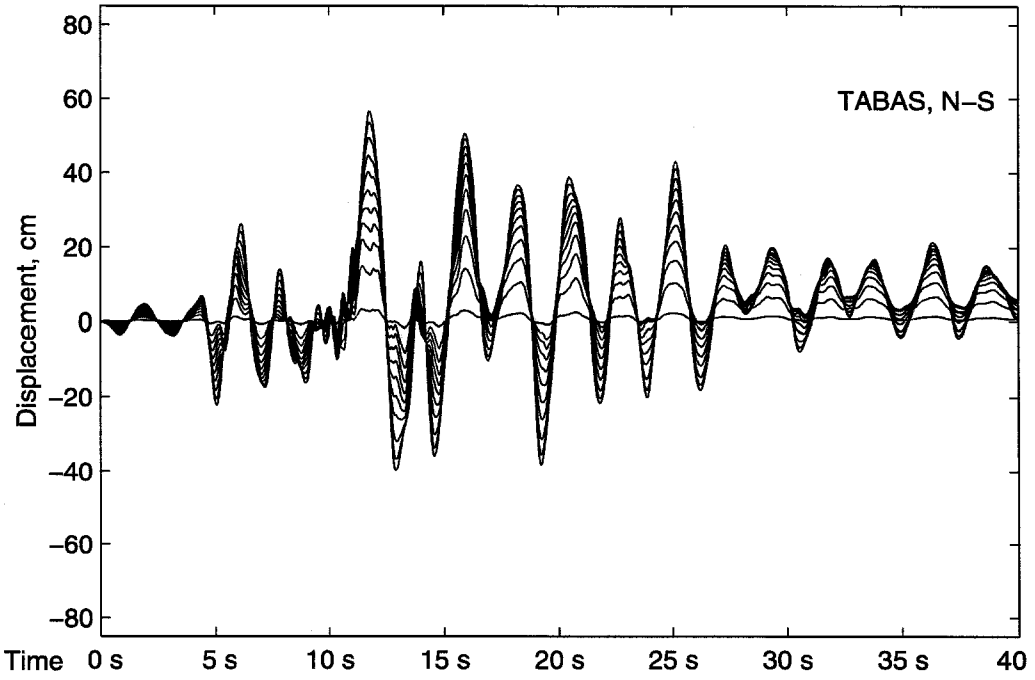

Figure 10.44 Relative floor displacements, inelastic model and Tabas record.

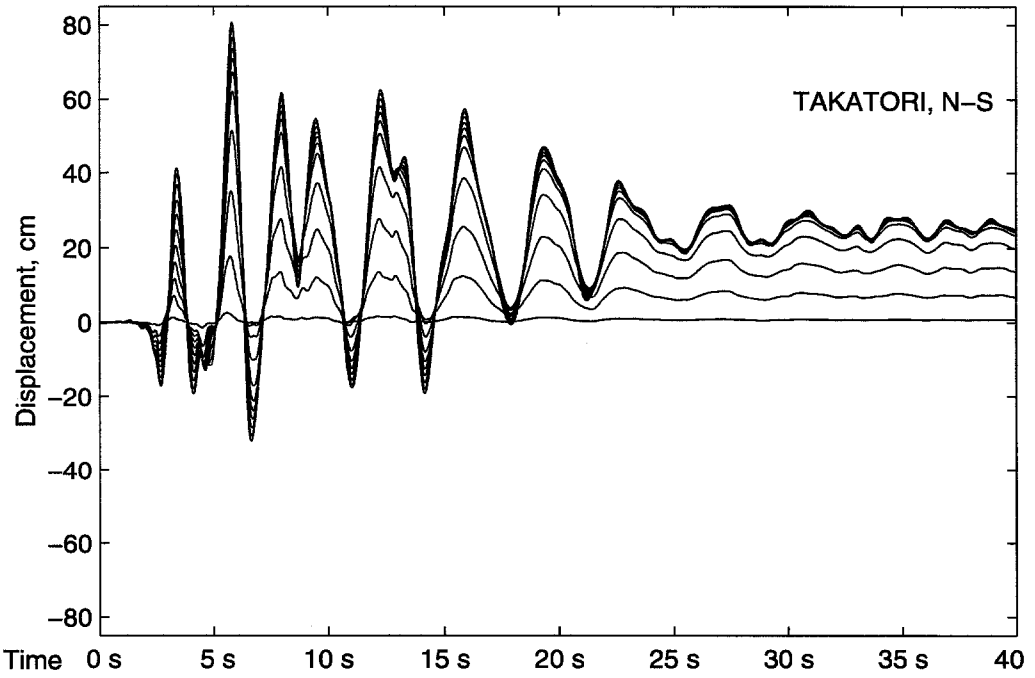

Figure 10.45 Relative floor displacements, Hall fracture model and Takatori record.

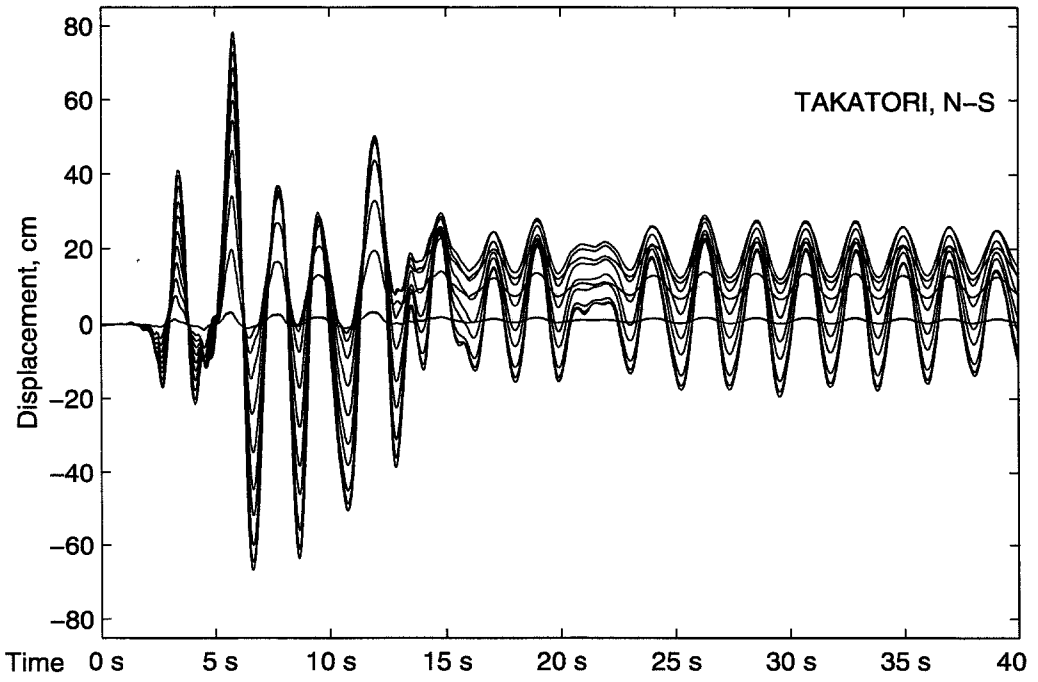

Figure 10.46 Relative floor displacements, inelastic model and Takatori record.

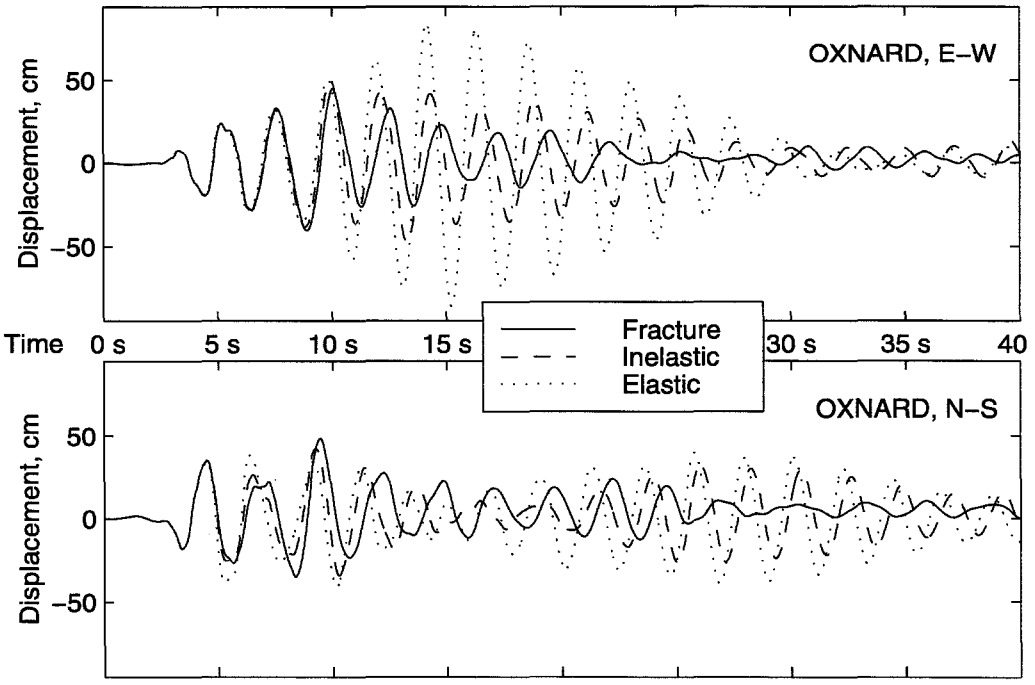

Figure 10.47 Model comparison for Oxnard record.

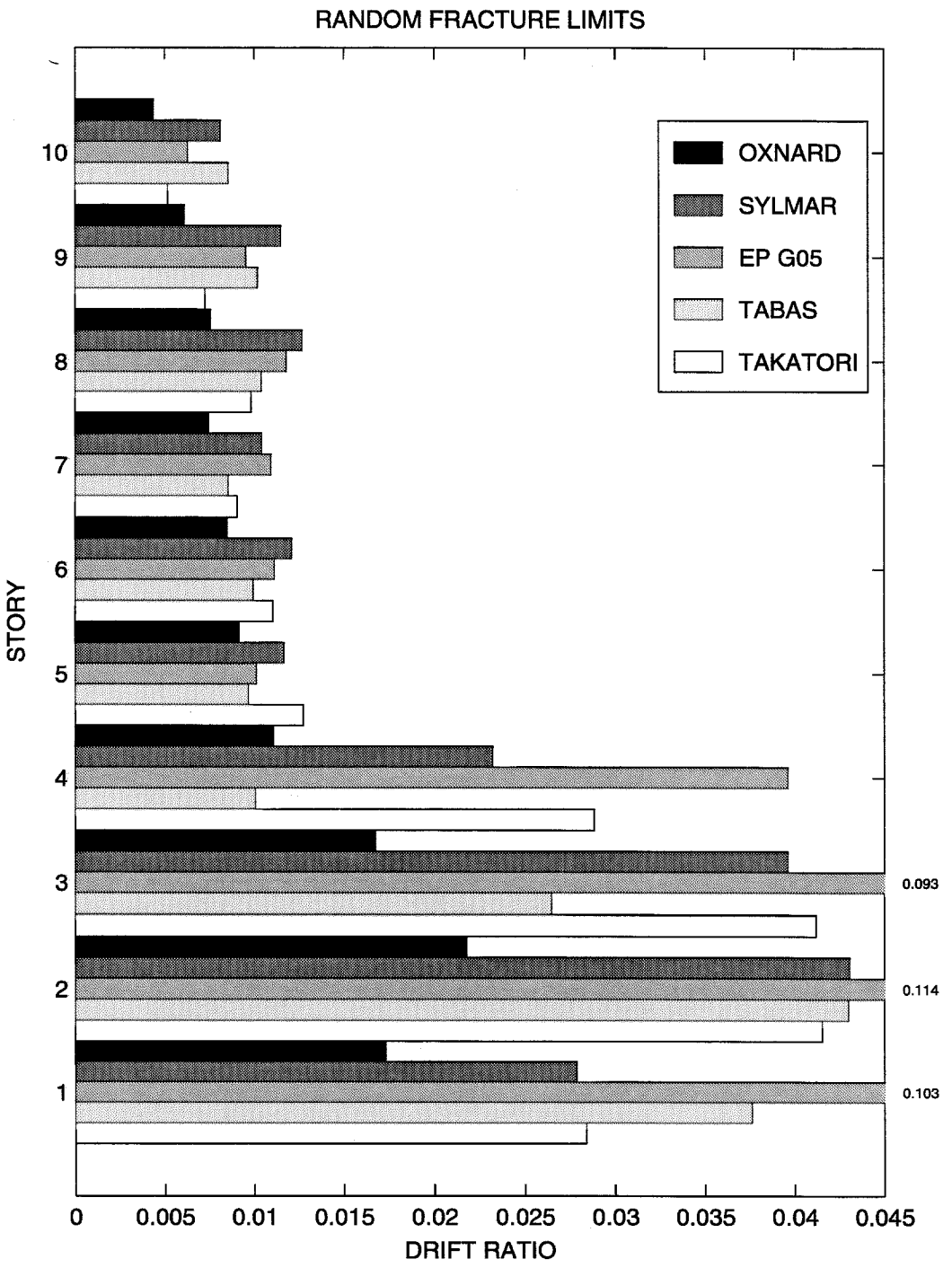

Figure 10.48 10-story building peak drift ratios for Hall random fracture model.

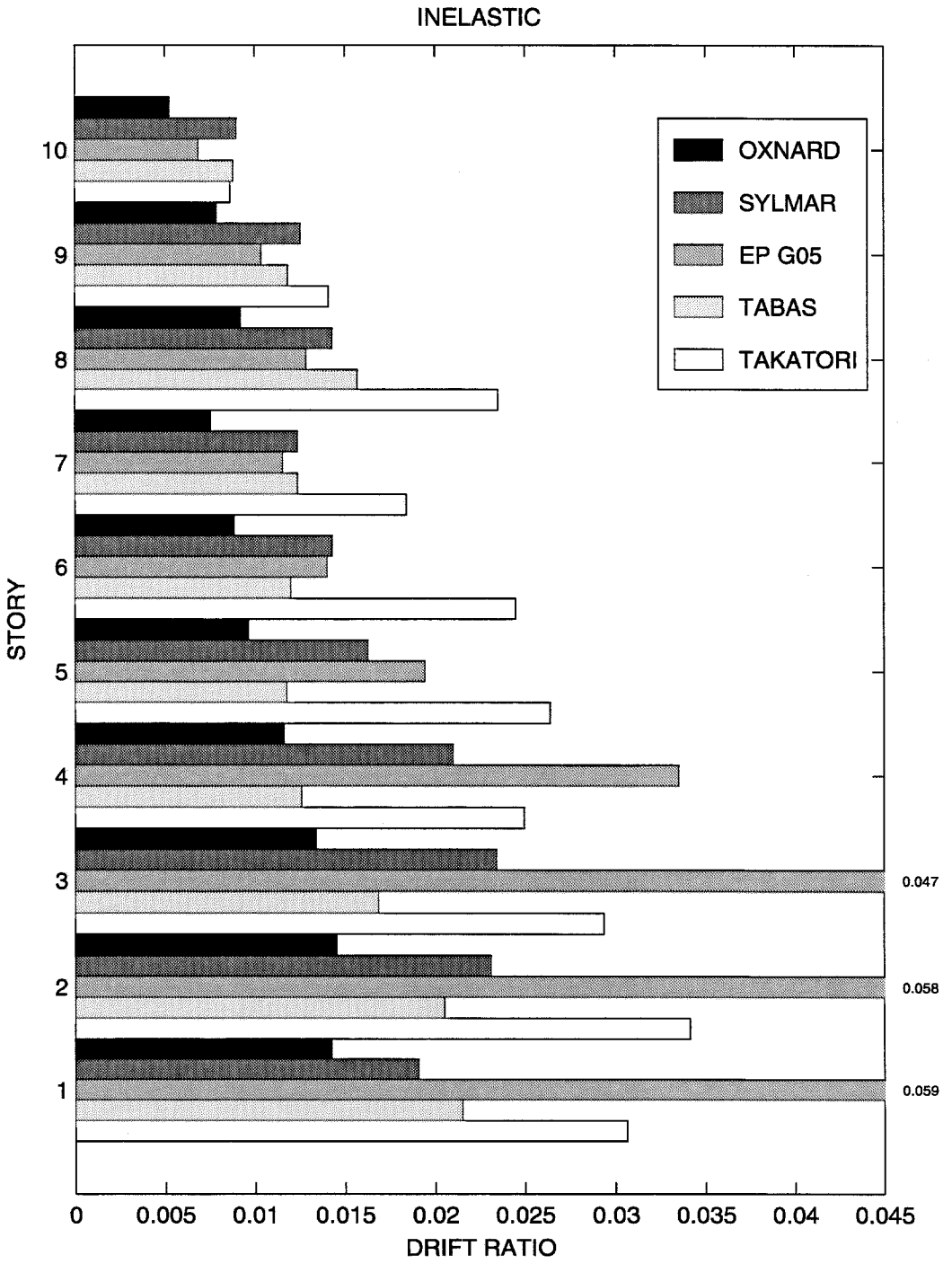

Figure 10.49 10-story building peak drift ratios for inelastic model.

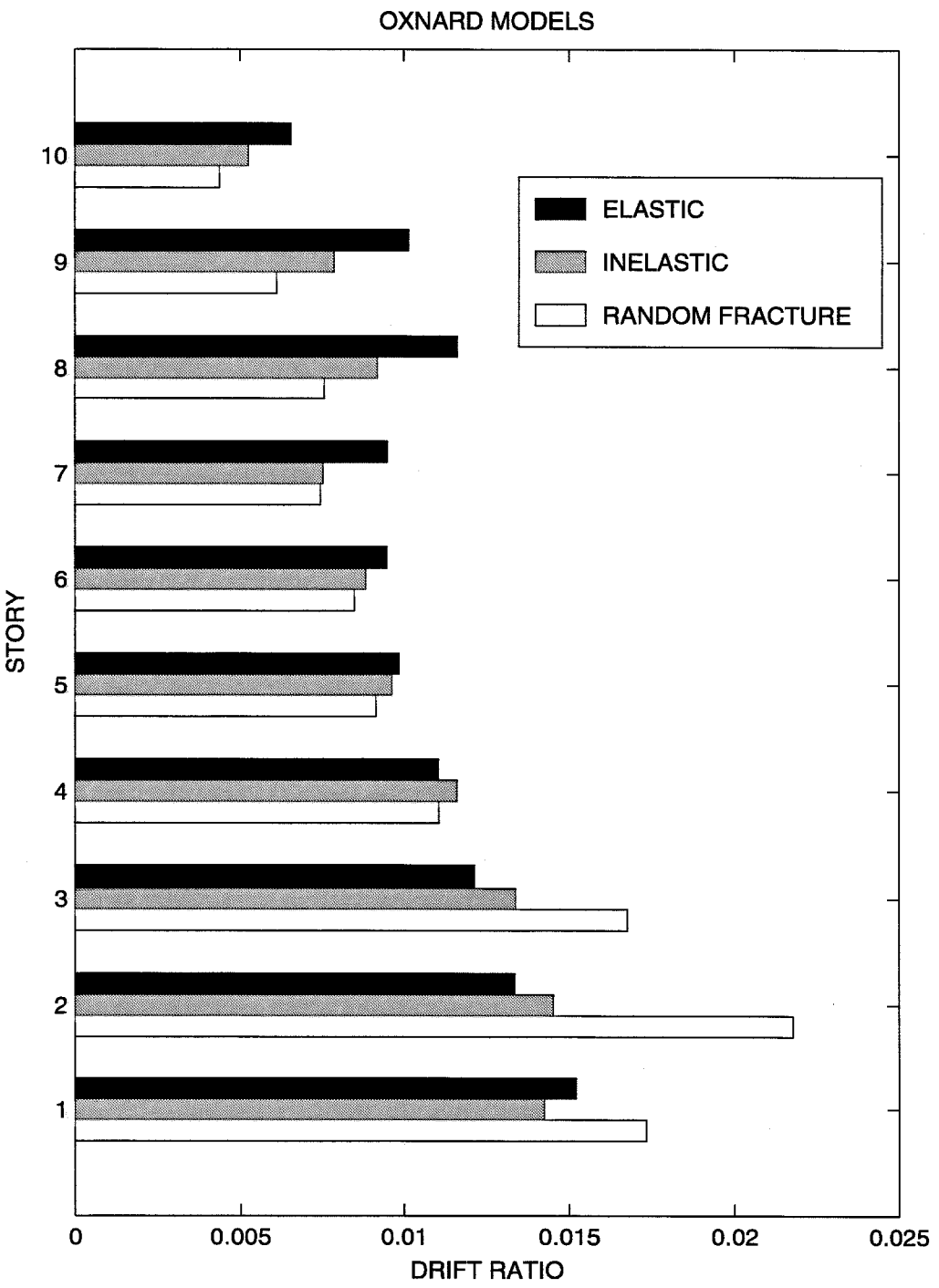

Figure 10.50 10-story building peak drift ratios for Oxnard history.

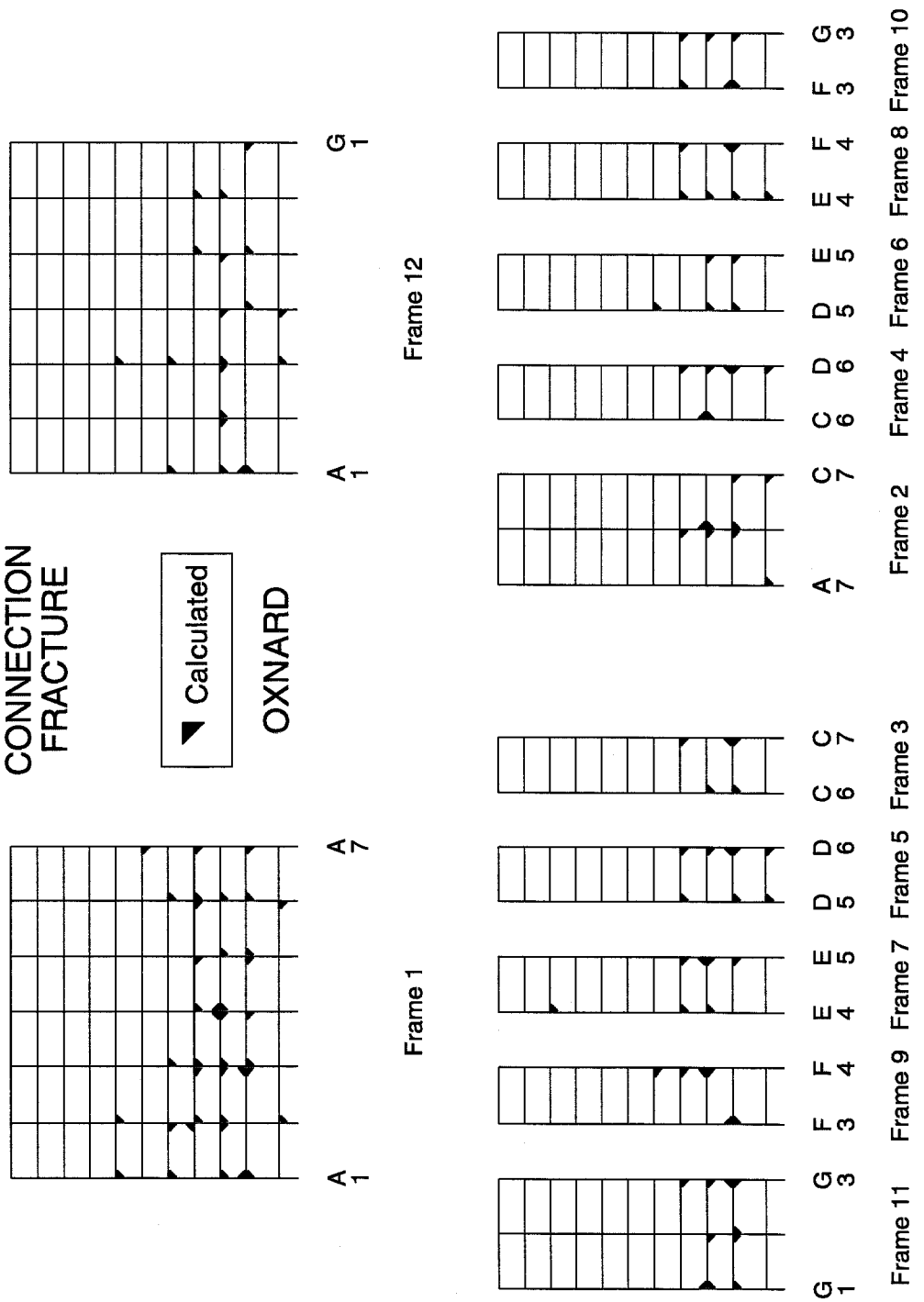

Figure 10.51 Fracture of member ends, Hall random fracture model and Oxnard record.

Bruneau, M., C.-M. Uang, and A. Whittaker (1998). *Ductile Design of Steel Structures.* McGraw-Hill, Inc.

Carlson, A. E. and J. F. Hall (1997). Three-Dimensional Analysis of a Tall Building Under Northridge Earthquake. In *Proceedings of the NEHRP Conference and Workshop on Research on the Northridge, California Earthquake of January 17, 1994*, Volume III-A, pp. 330–337. CUREe.

Challa, V. R. M. (1992, June). Nonlinear Seismic Behavior of Steel Planar Moment Resisting Frames. Technical Report No. EERL 92-01, Earthquake Engineering Research Laboratory, California Institute of Technology, Pasadena.

Challa, V. R. M. and J. F. Hall (1994). Earthquake Collapse Analysis of Steel Frames. *Earthquake Engineering & Structural Dynamics 23*(11), 1199–1218.

Chen, W. F. and T. Atsuta (1977). *Theory of Beam-Columns, Volume 2: Space behavior and design.* McGraw-Hill, Inc.

Chen, X. D. and W. D. Iwan (1994). Rinaldi Station Corrected Record.

Chi, W.-M. (1996, August). Inelastic Analyses of a High-Rise Steel Moment-Frame Building Damaged in the Northridge Earthquake. Master's thesis, Cornell University.

Chi, W.-M., S. El-Tawil, G. G. Deierlein, and J. F. Abel (1996). Inelastic Analyses of a 17 Story Steel Framed Building Damaged During Northridge. *Engineering Structures.* Accepted for publication.

Chopra, A. K. (1995). *Dynamics of Structures: theory and applications to earthquake engineering.* Prentice-Hall, Inc.

Clough, R. W. and J. Penzien (1993). *Dynamics of Structures* (Second ed.). McGraw-Hill, Inc.

Cook, R. D., D. S. Malkus, and M. E. Plesha (1989). *Concepts and Applications of Finite Element Analysis* (Third ed.). John Wiley & Sons.

Darragh, R., T. Cao, C. Cramer, M. Huang, and A. Shakal (1994, February). Processed CSMIP Strong-Motion Records from the Northridge, California Earth-

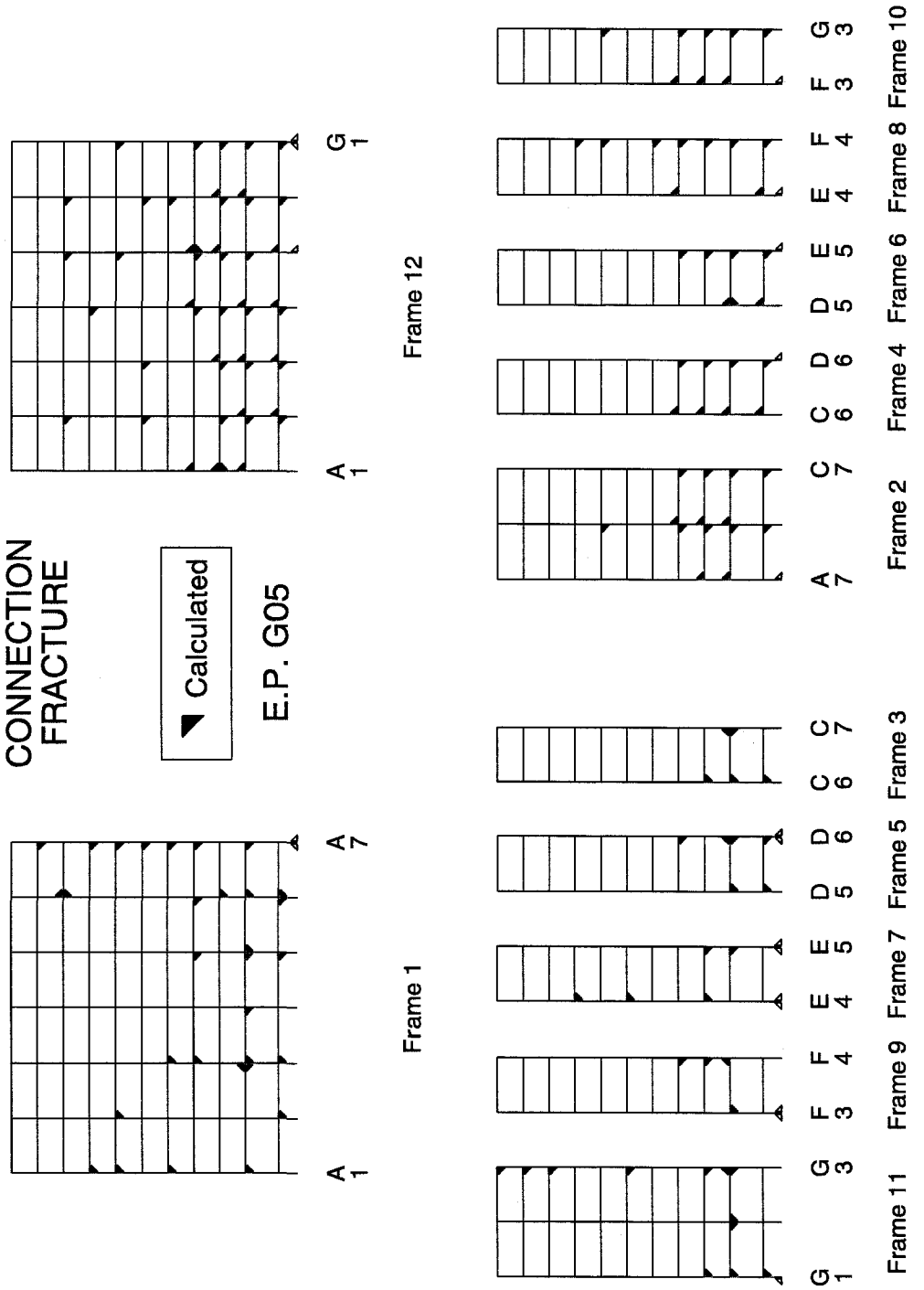

Figure 10.53 Fracture of member ends, Hall random fracture model and E. P. G05 record.

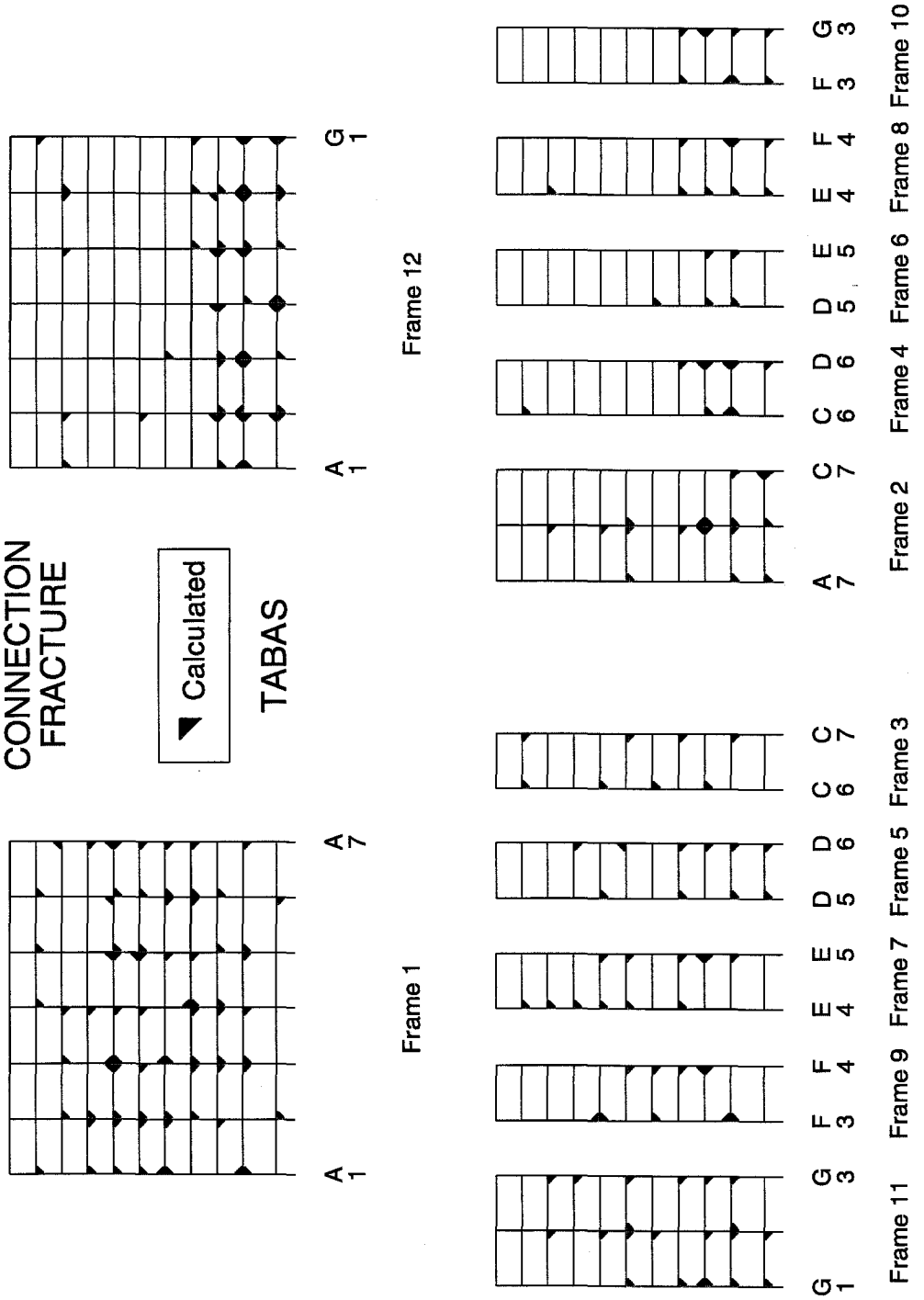

Figure 10.54 Fracture of member ends, Hall random fracture model and Tabas record.

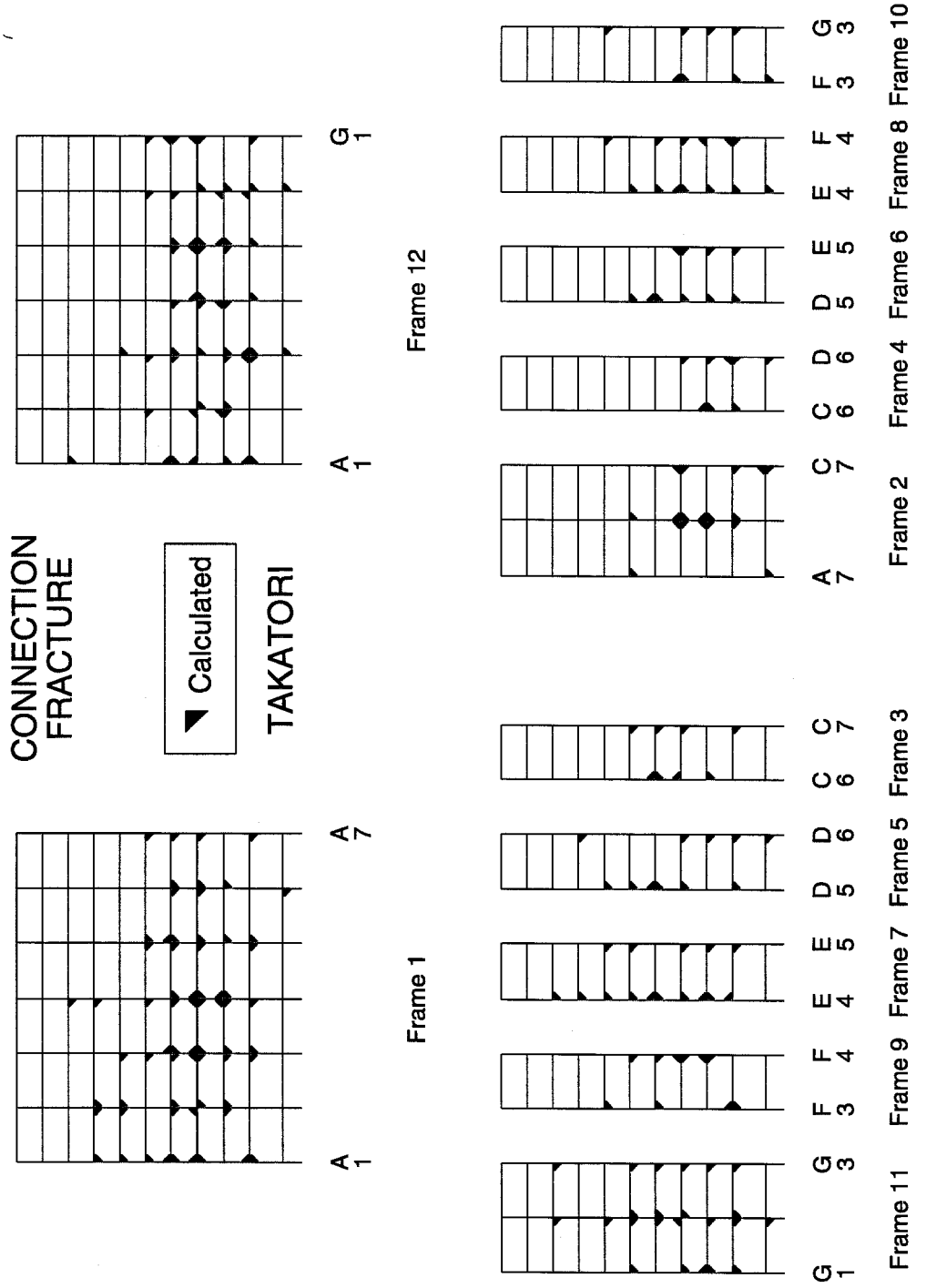

Figure 10.55 Fracture of member ends, Hall random fracture model and Takatori record.

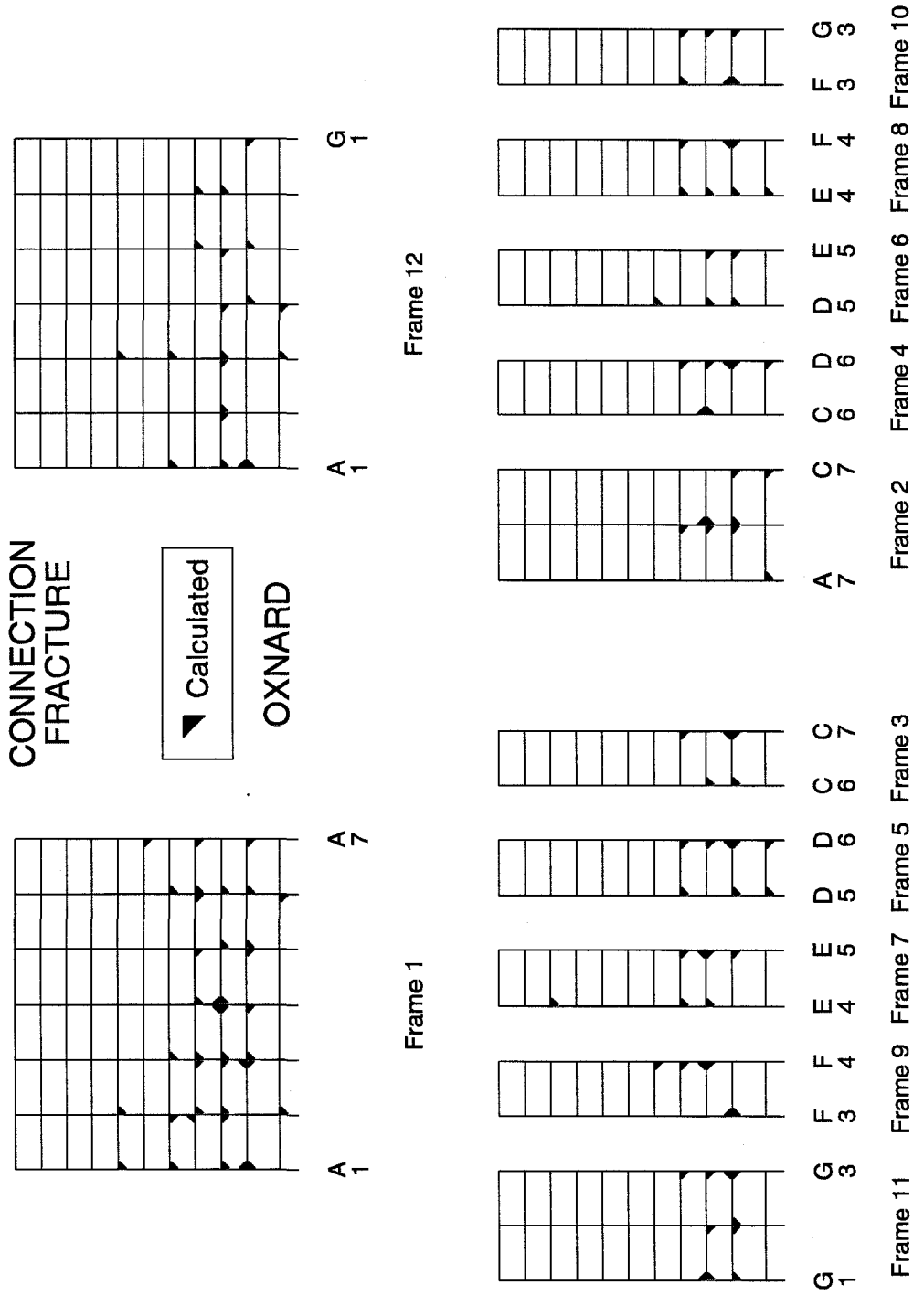

Figure 10.56 Fracture of member ends, Oxnard rotated 0°.

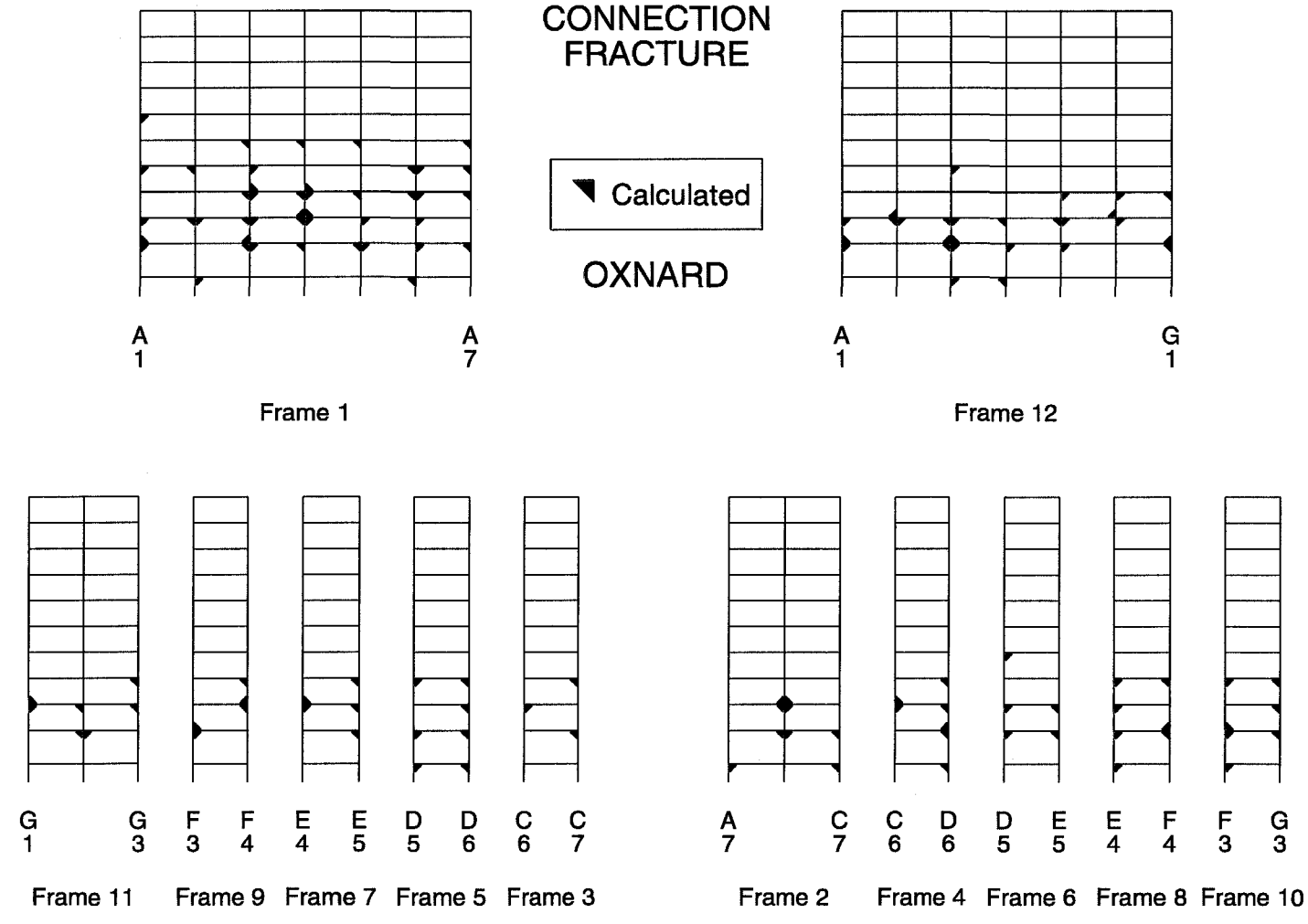

Figure 10.57 Fracture of member ends, Oxnard rotated 22.5°.

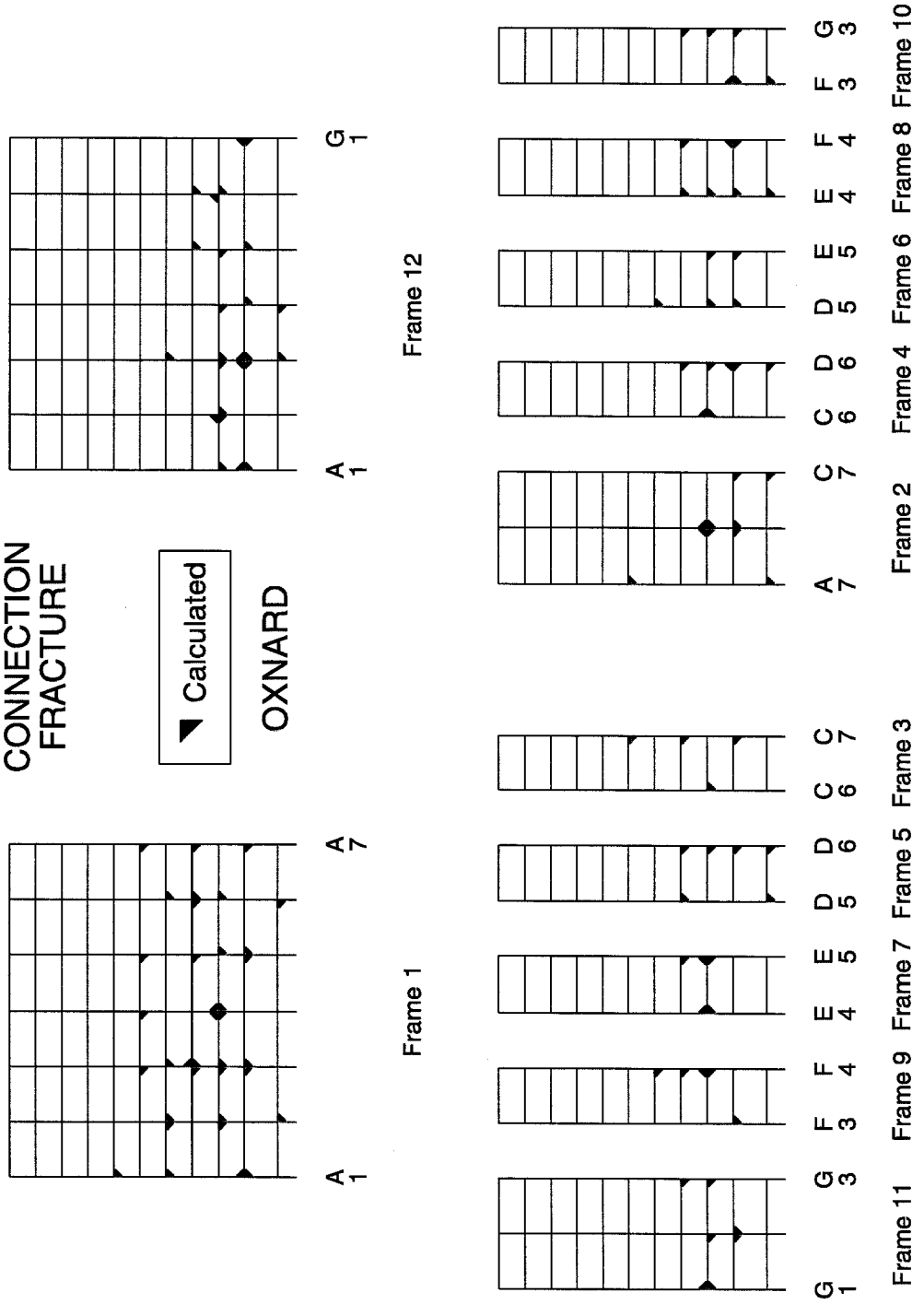

Figure 10.58 Fracture of member ends, Oxnard rotated 45°.

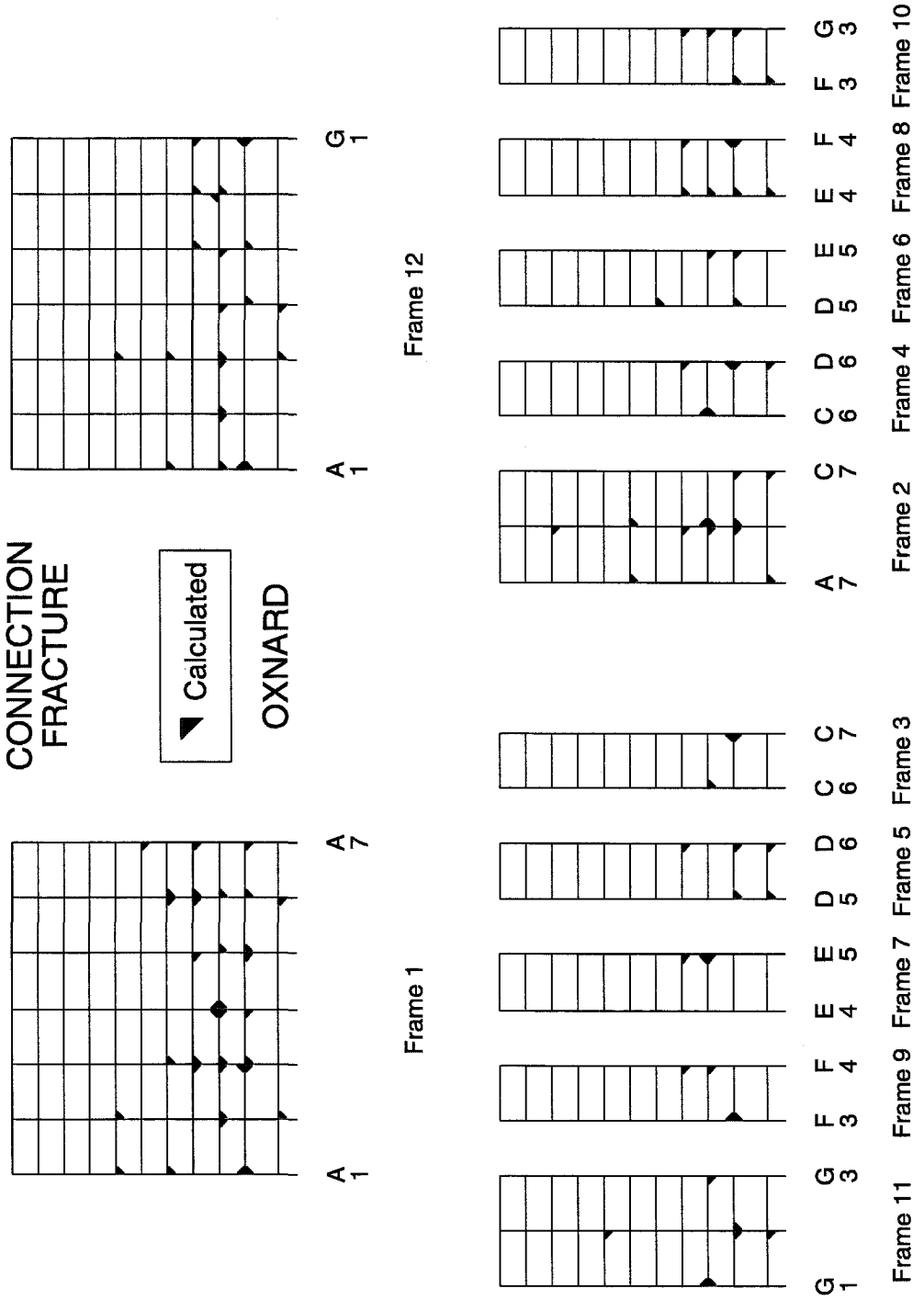

Figure 10.59 Fracture of member ends, Oxnard rotated 67.5°.

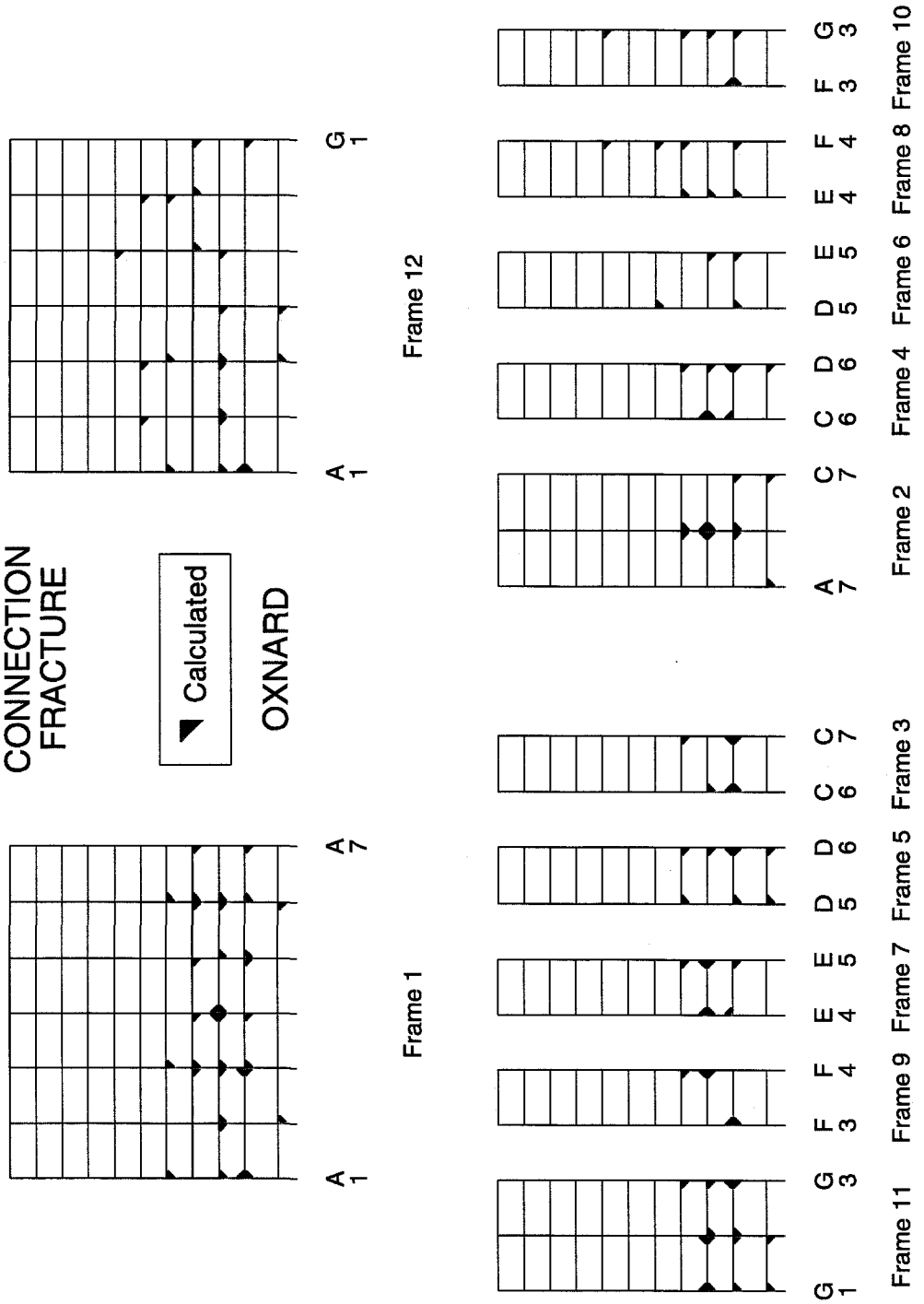

Figure 10.60 Fracture of member ends, Oxnard rotated 90°.

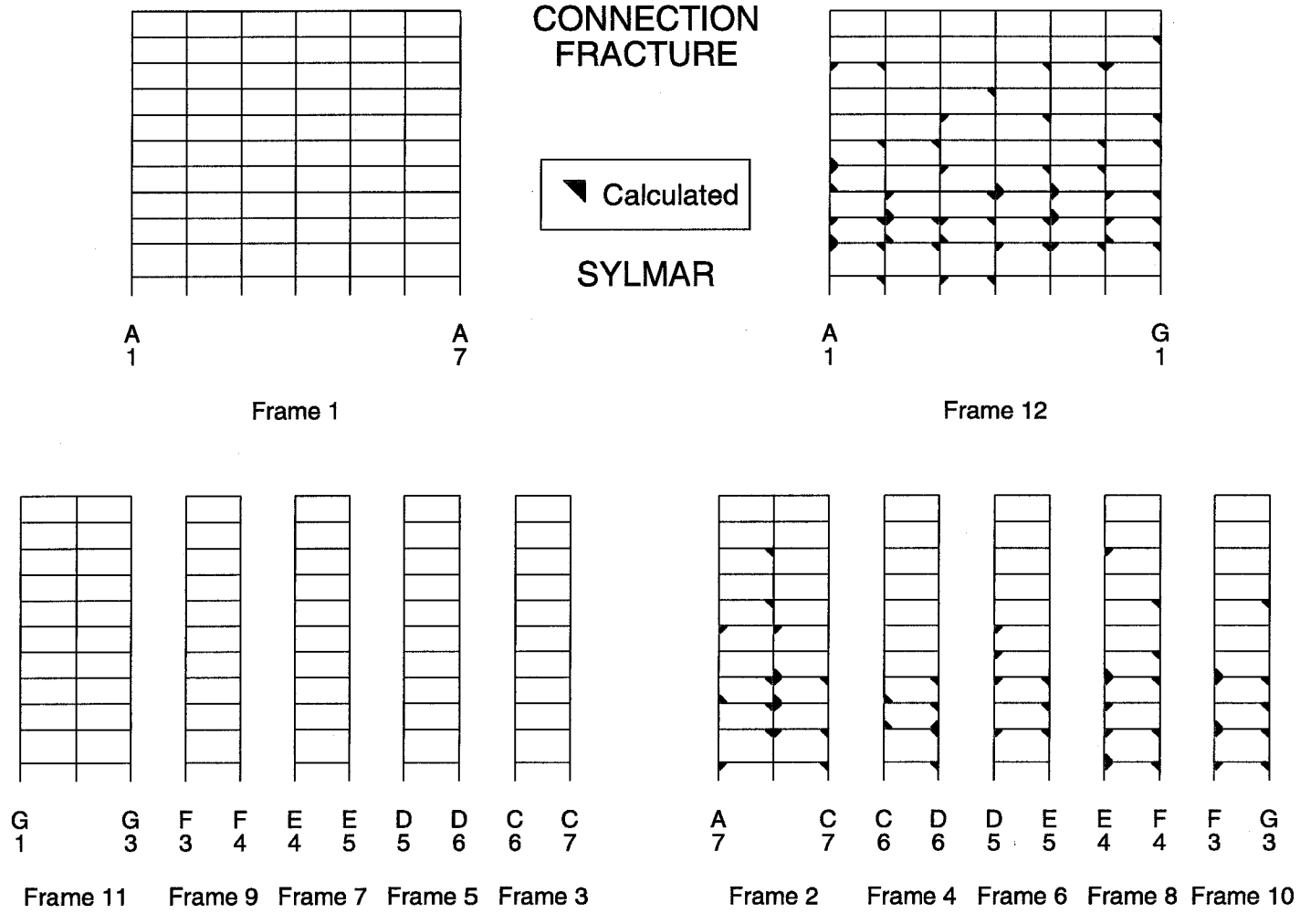

Figure 10.61 Fracture of member ends, Sylmar N-S rotated 0°.

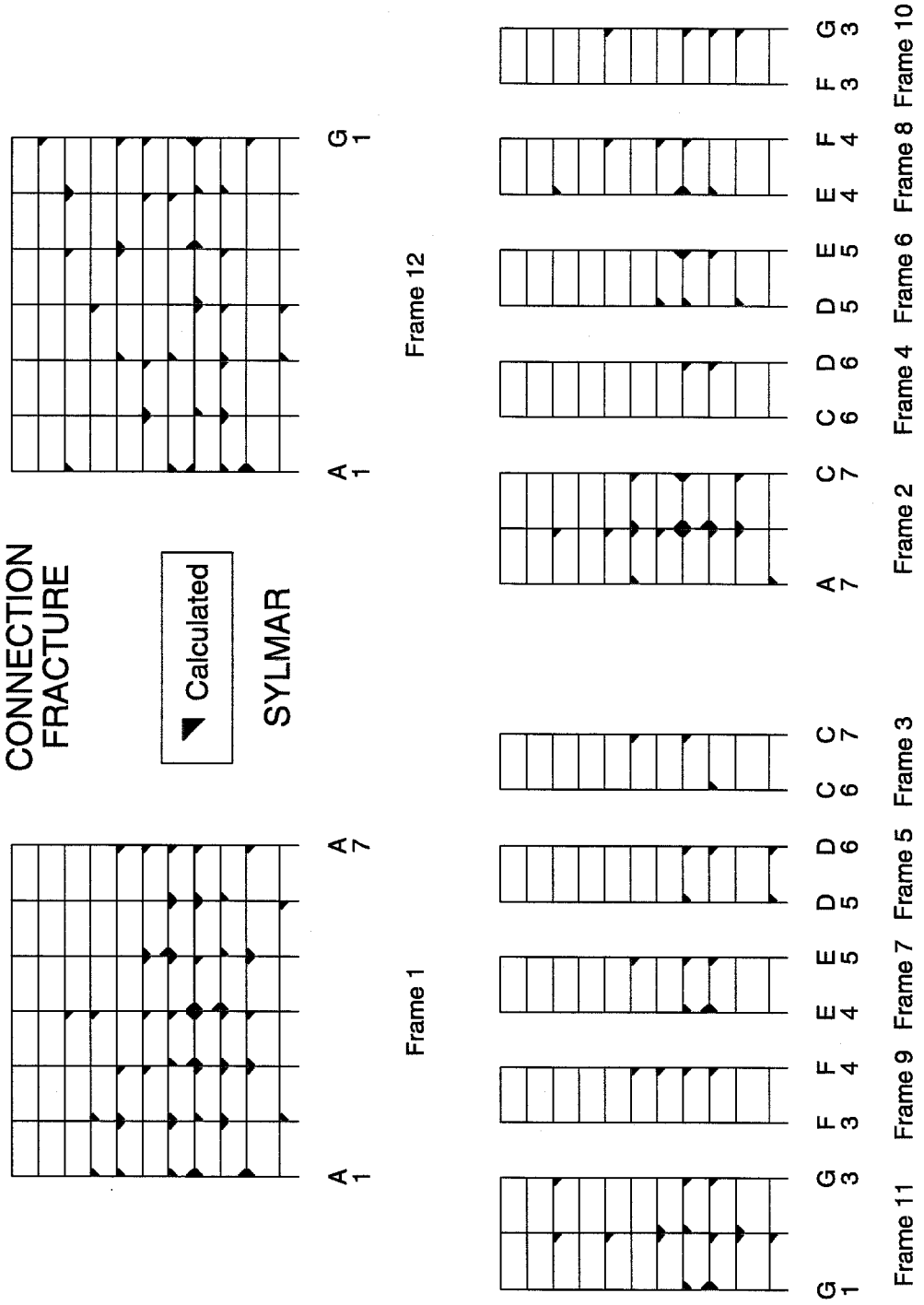

Figure 10.62 Fracture of member ends, Sylmar N-S rotated −45°.

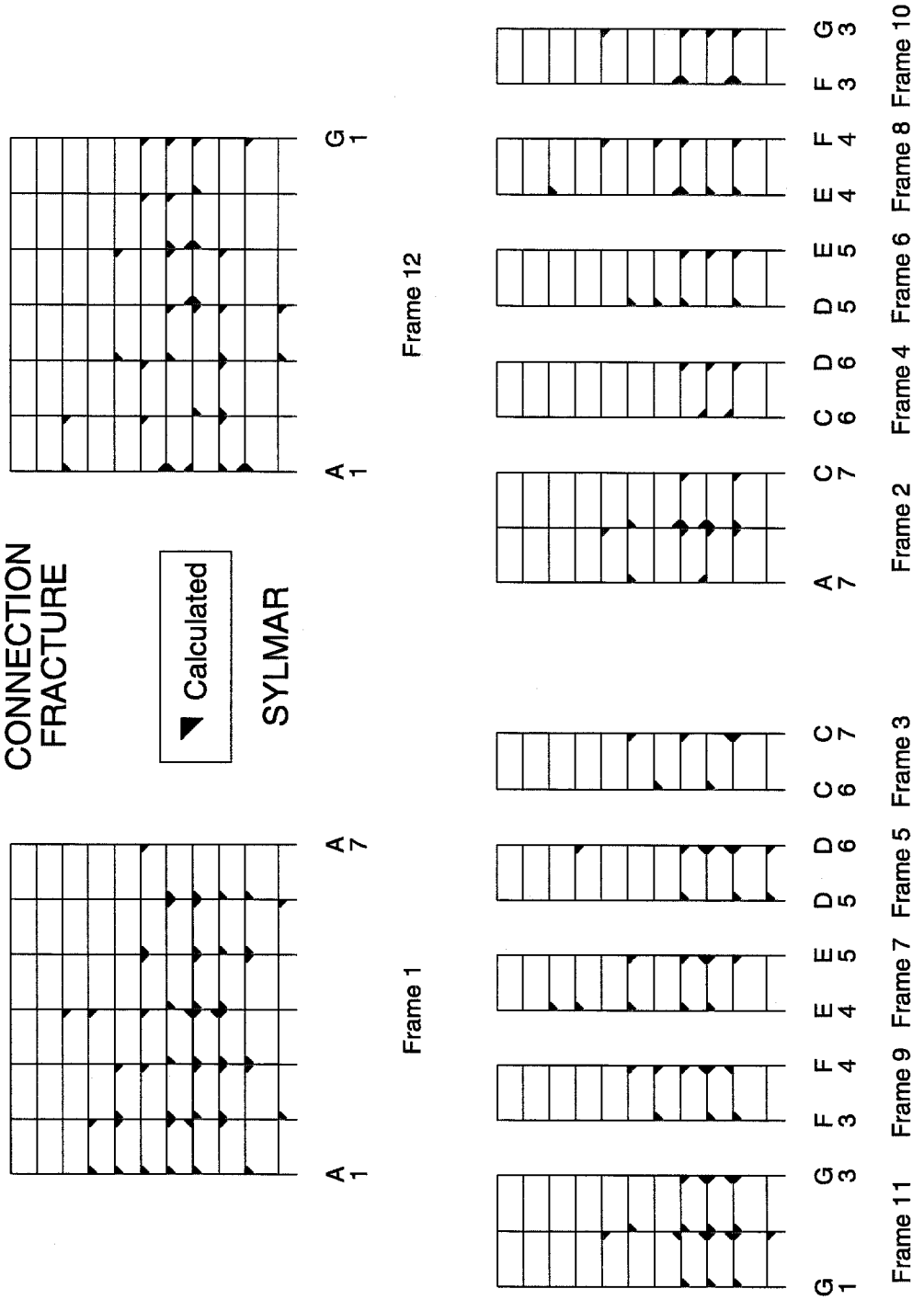

Figure 10.63 Fracture of member ends, Sylmar N-S rotated 45°.

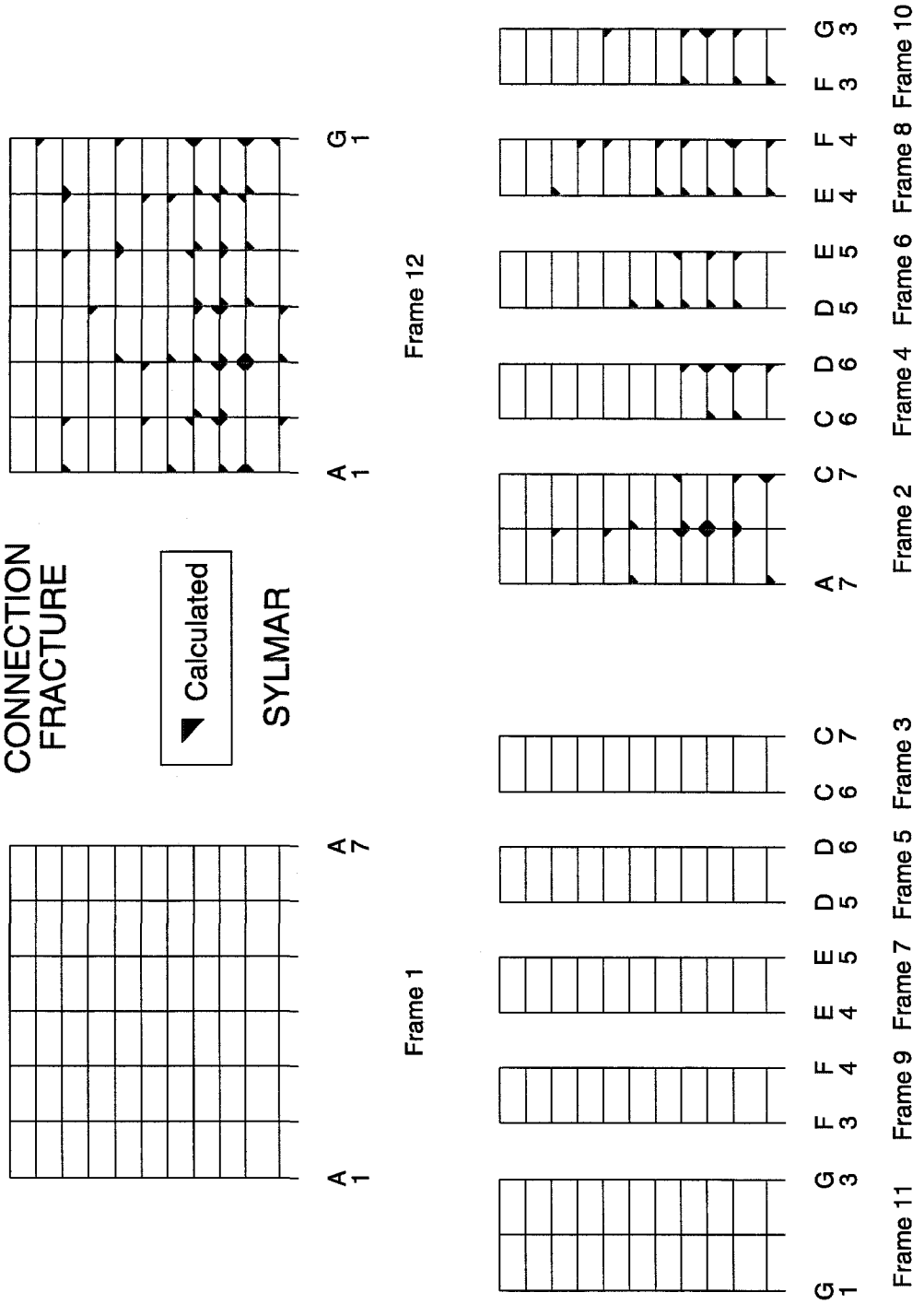

Figure 10.64 Fracture of member ends, Sylmar N-S rotated 180°.

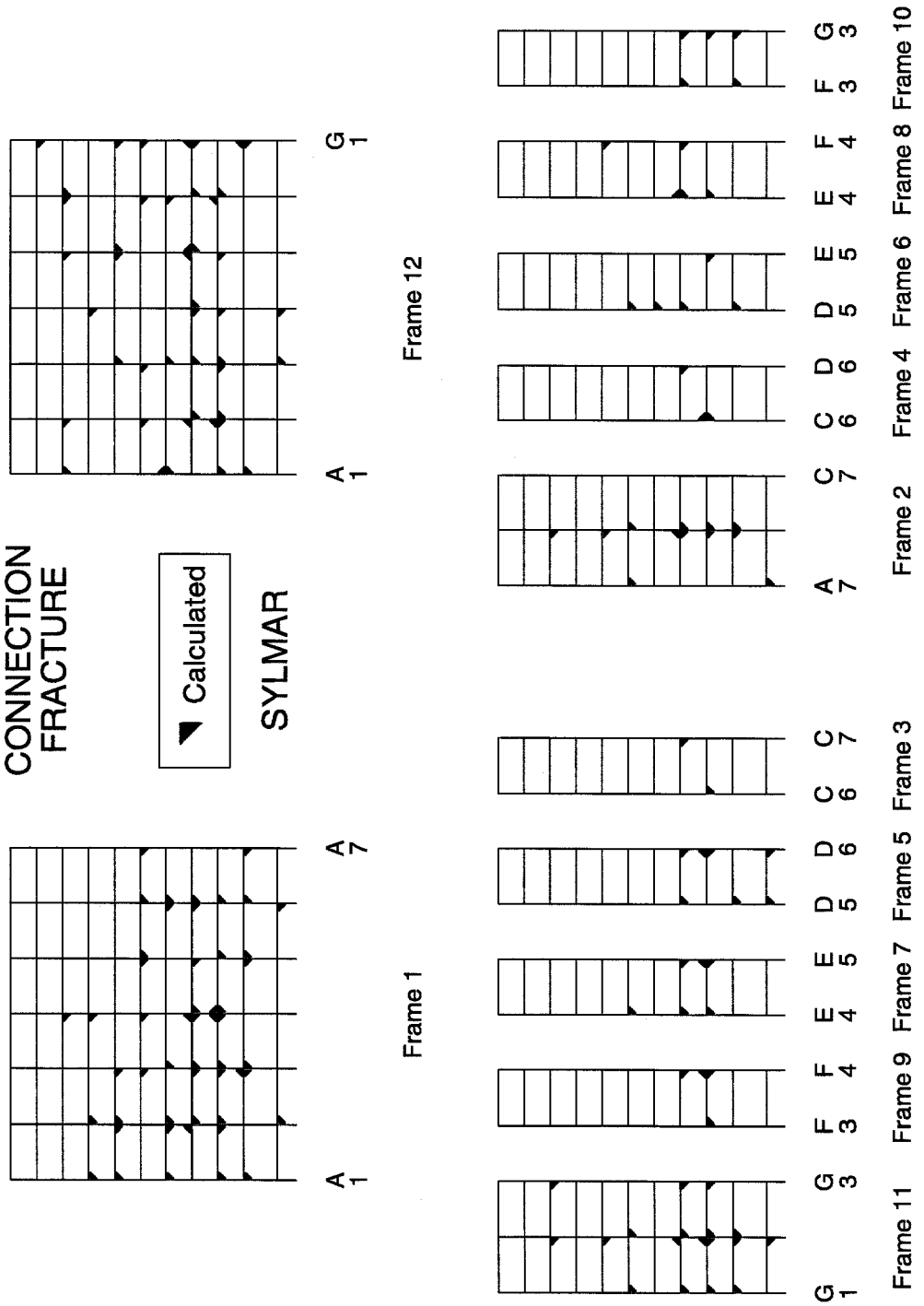

Figure 10.65 Fracture of member ends, Sylmar N-S rotated 135°.

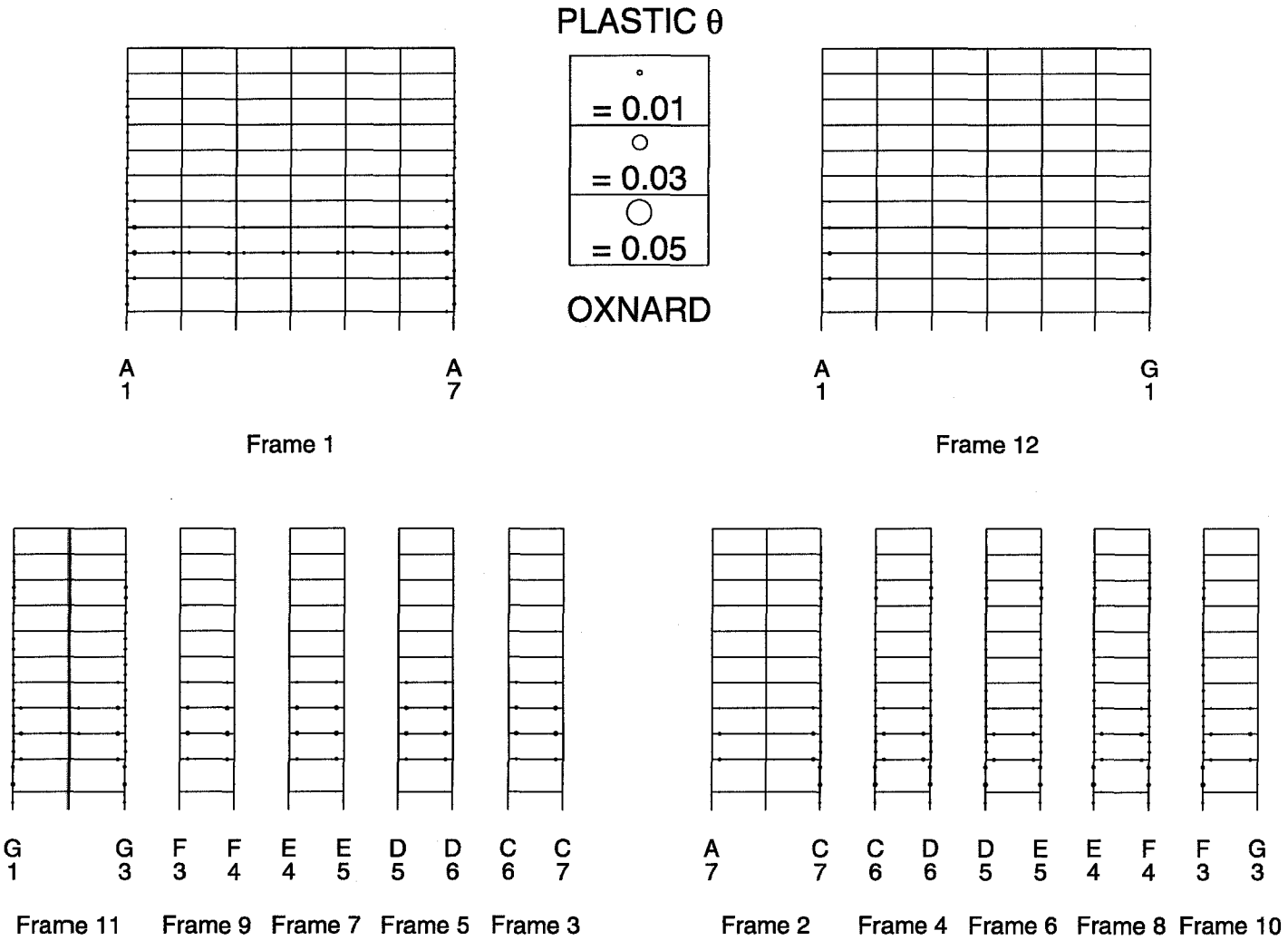

Figure 10.66 Plastic rotations at member ends, Oxnard record.

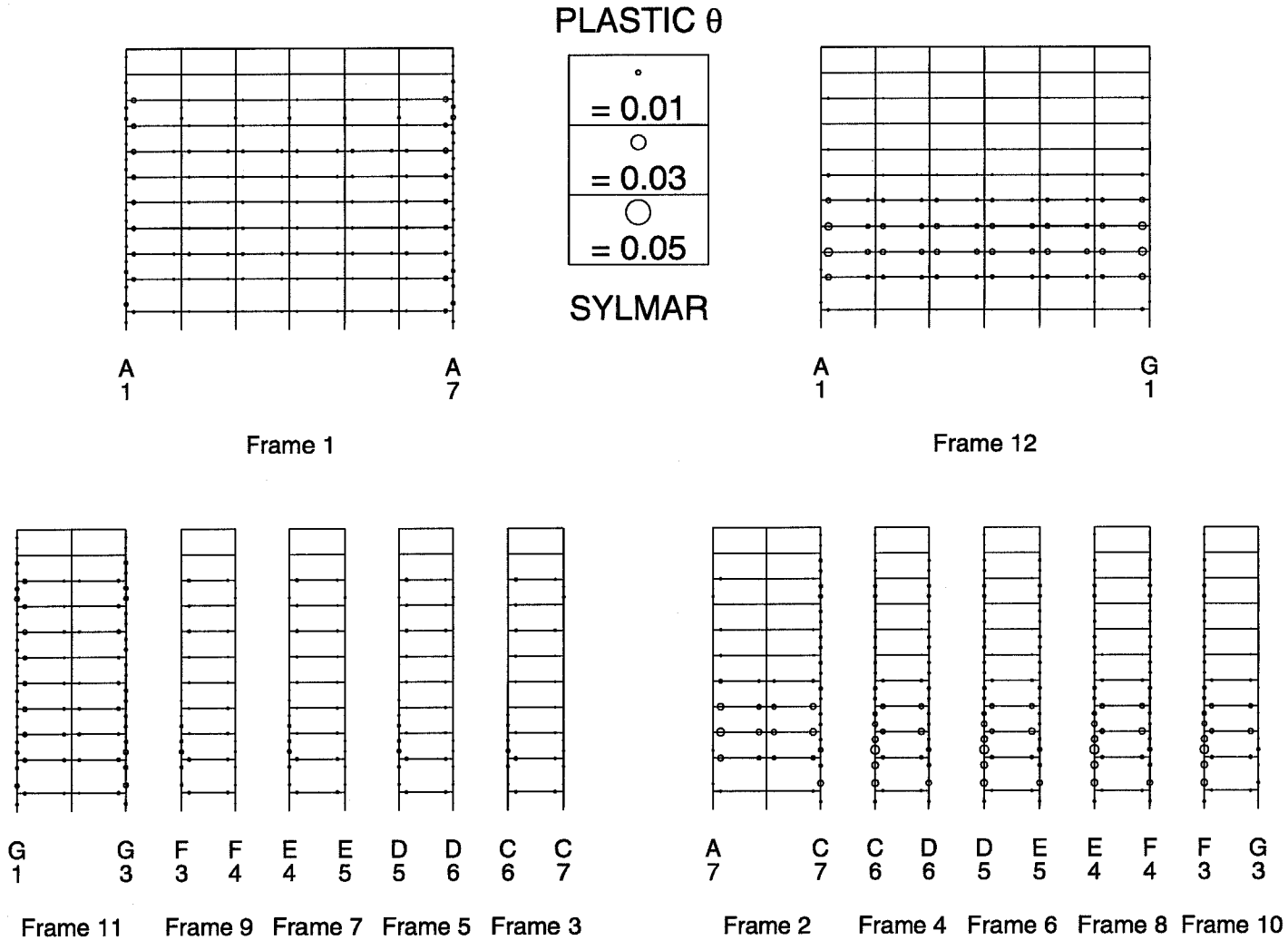

Figure 10.67 Plastic rotations at member ends, Sylmar record.

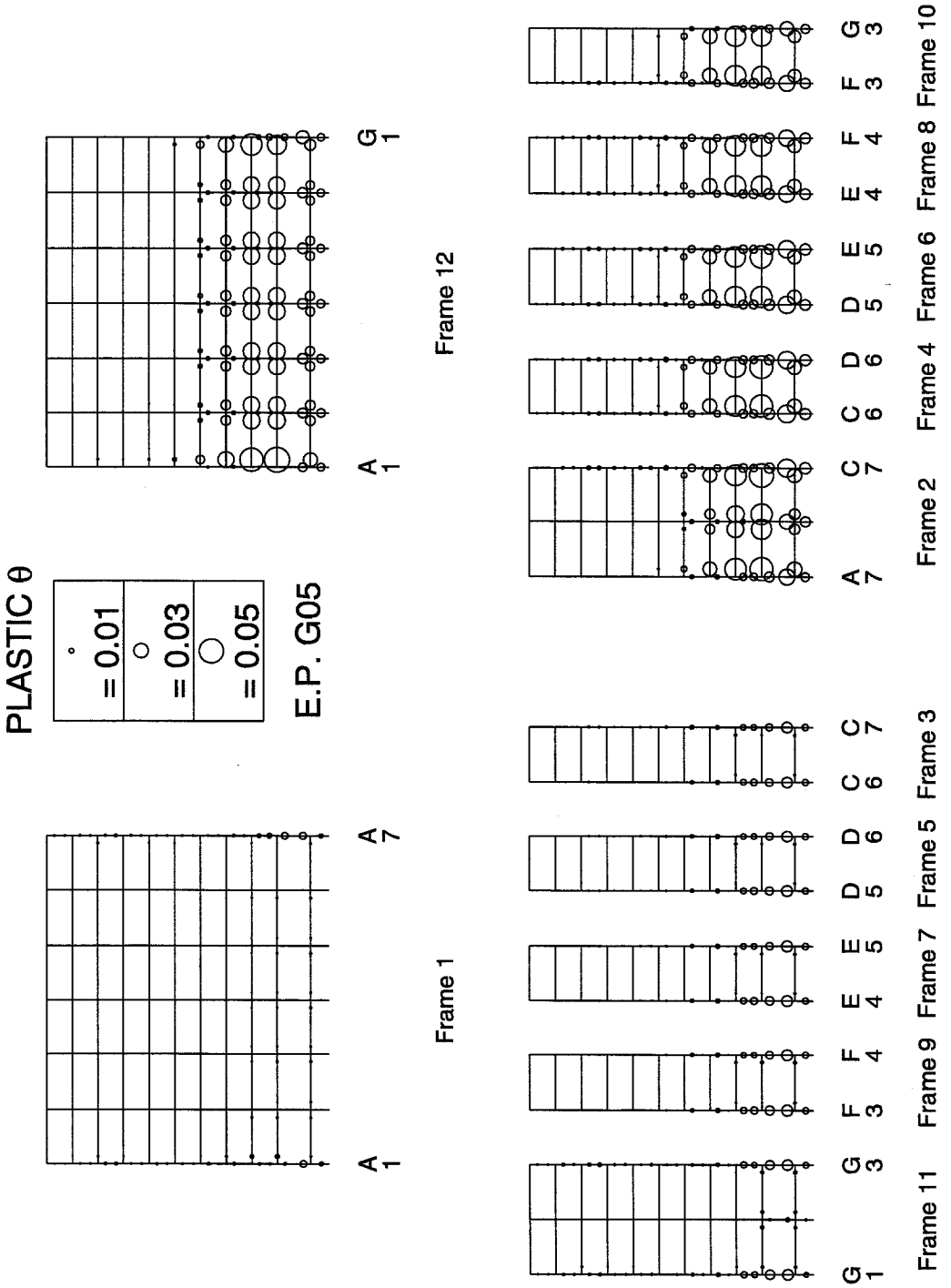

Figure 10.68 Plastic rotations at member ends, E. P. G05 record.

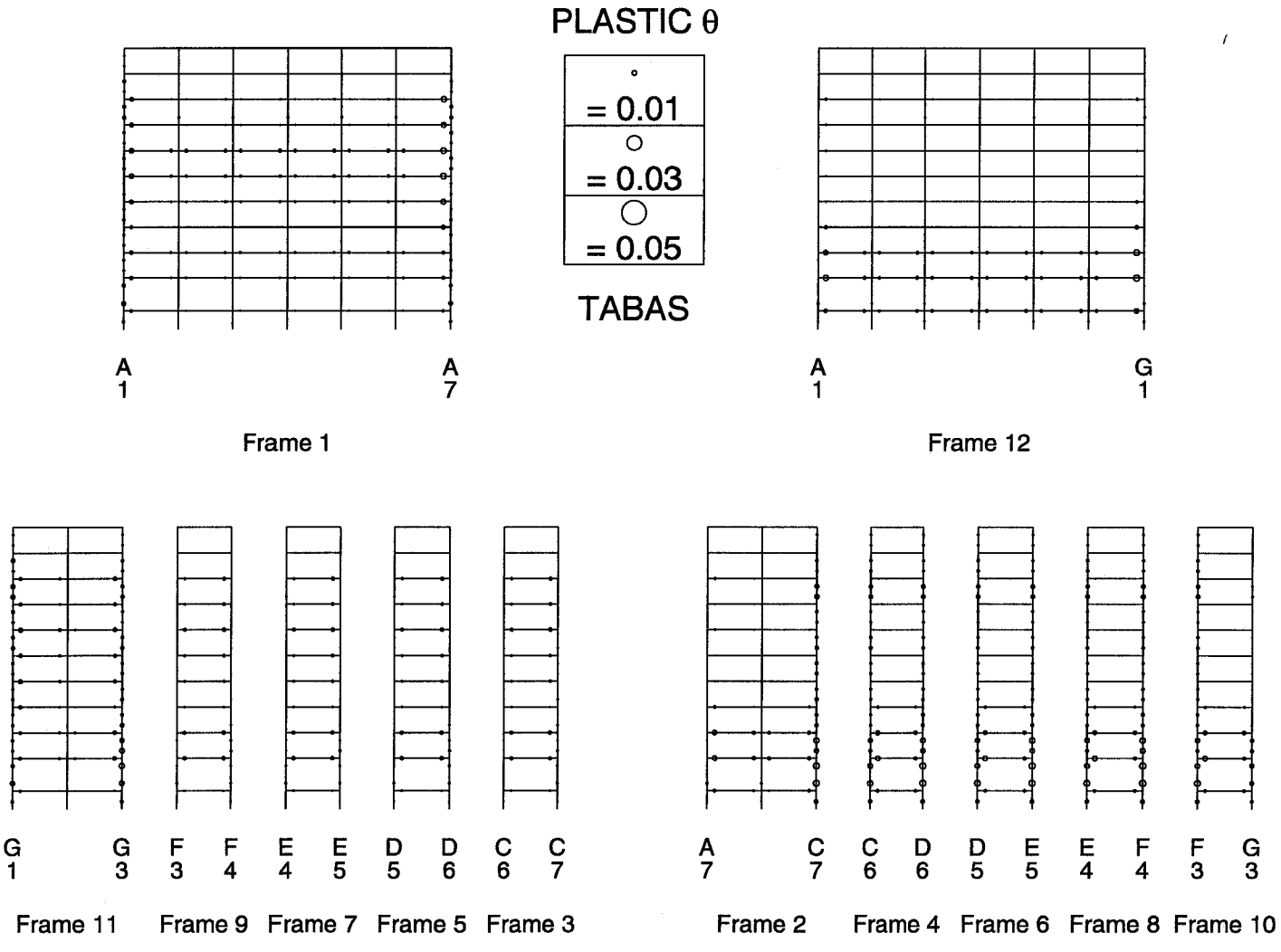

Figure 10.69 Plastic rotations at member ends, Tabas record.

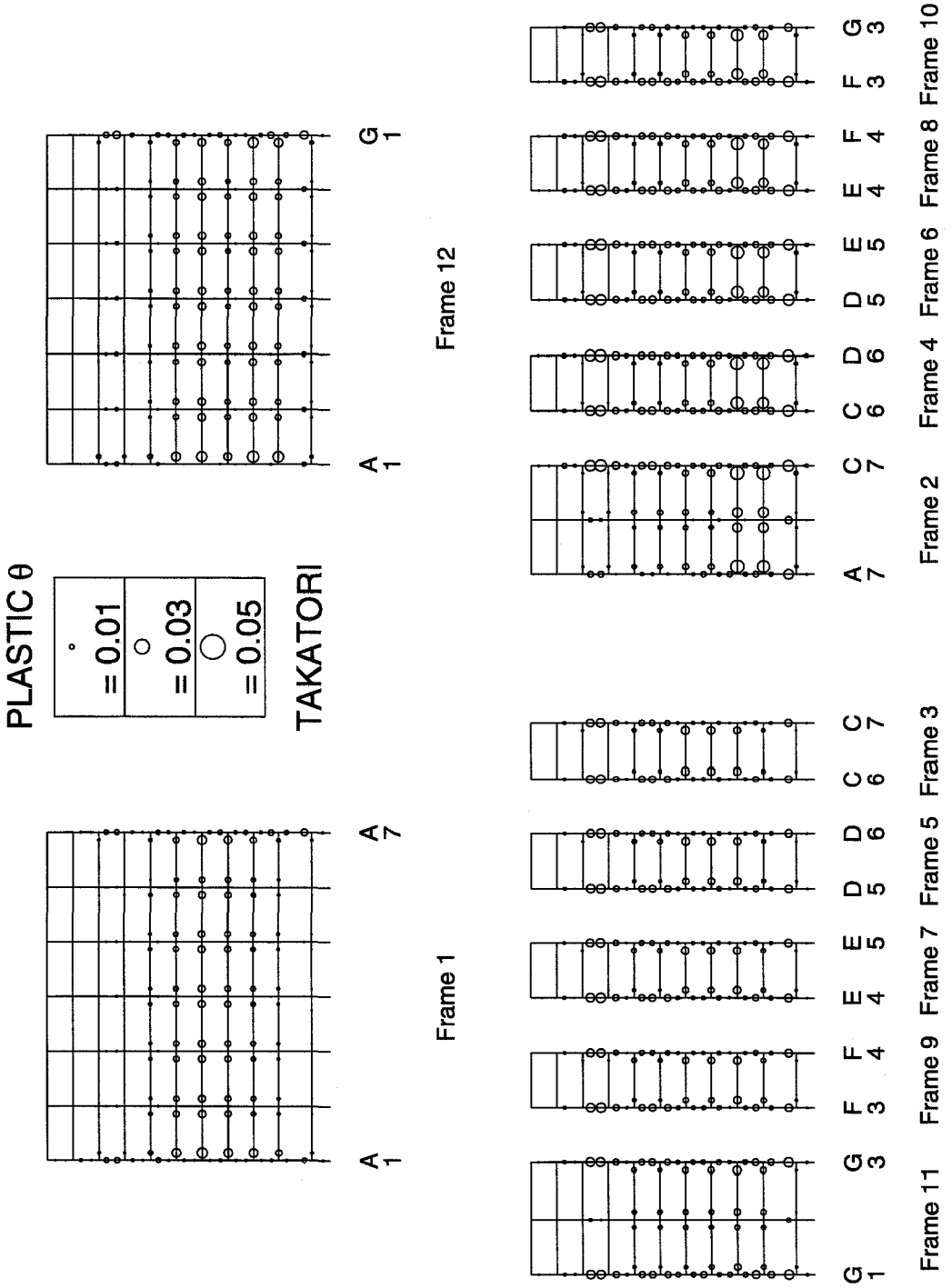

Figure 10.70 Plastic rotations at member ends, Takatori.

10.7 Tables

10-Story Building: Built-up Square Box Section Properties			
Member Designation	Plate Thickness cm (in)	Outer Dimension cm (in)	Inner Dimension cm (in)
B14X436	5.72 ($2\frac{1}{4}$)	41.91 ($16\frac{1}{2}$)	30.48 (12)
B14X327	4.45 ($1\frac{3}{4}$)	39.37 ($15\frac{1}{2}$)	30.48 (12)
B14X301	4.13 ($1\frac{5}{8}$)	38.74 ($15\frac{1}{4}$)	30.48 (12)
B14X250	3.49 ($1\frac{3}{8}$)	37.47 ($14\frac{3}{4}$)	30.48 (12)
B14X177	2.54 (1)	35.56 (14)	30.48 (12)

Table 10.2 Built-up box section dimensions.

10-Story Building: Hall Random Fracture Model				
Ground Motion	Maximum Drift	Maximum Δ_R (cm)	Maximum V/W	Number of Fractures
Oxnard	0.0218	49	0.206	129
Sylmar	0.0431	82	0.229	210
E.P. G05	0.1144	186	0.220	157
Tabas	0.0430	85	0.234	243
Takatori	0.0415	102	0.218	246

Table 10.3 Damage indicators for 10-story building model.

10-Story Building: Inelastic Model				
Ground Motion	Maximum Drift	Maximum Δ_R (cm)	Maximum V/W	# of Plastic Rotations > 0.01 rad
Oxnard	0.0159	54	0.213	0
Sylmar	0.0234	88	0.243	66
E.P. G05	0.0588	125	0.260	246
Tabas	0.0215	84	0.245	37
Takatori	0.0341	98	0.236	403

Table 10.4 Damage indicators for 10-story building model.

10-Story Building: Oxnard			
Model	Maximum Drift	Maximum Δ_R (cm)	Maximum V/W
Random	0.0218	49	0.206
Inelastic	0.0159	54	0.213
Elastic	0.0236	87	0.421

Table 10.5 Damage indicators for 10-story building model.

10-Story Building: Oxnard Rotated				
Rotation	Maximum Drift	Maximum Δ_R (cm)	Maximum V/W	Number of Fractures
0°	0.0218	49	0.206	129
22.5°	0.0250	58	0.215	133
45°	0.0256	60	0.214	123
67.5°	0.0220	66	0.202	114
90°	0.0211	51	0.203	132

Table 10.6 Damage indicators for 10-story building model.

10-Story Building: Sylmar Rotated				
Rotation	Maximum Drift	Maximum Δ_R (cm)	Maximum V/W	Number of Fractures
0°	0.0401	71	0.231	108
−45°	0.0283	83	0.194	170
45°	0.0276	79	0.197	184
180°	0.0380	67	0.228	112
135°	0.0271	81	0.191	163

Table 10.7 Damage indicators for 10-story building model.

Chapter 11

Building Comparisons

Several issues pertaining to the results of the three buildings are investigated together in this chapter. Trends and correlations are determined or refuted.

11.1 Inelastic Model

The response of the inelastic model for the three buildings to the five ground motions are tabulated for various parameters. In table 11.1, the number of member ends exceeding 0.03 radians of plastic rotation are given.

The G05 record produces significant plastic rotations in all three buildings. It is interesting to note that the 17-story building does not have the base of every column in one story yielding significantly the way the 13 and 10-story buildings do for this record (figures 8.80, 9.58, and 10.68). The G05 ground motion is a strong displacement pulse. The period of the 17-story building allows the ground pulse to spread the inelastic behavior throughout the building. The pulse duration and building period are such that the response is proportional to the first mode, and hence is spread throughout the structure. The pulse is too strong for the stiffer 13 and 10-story buildings to gradually spread resistance leading to the development of a weak story with yielded column bases.

The Tabas record causes large plastic rotations only in the 17-story building (figure 8.81). As opposed to the G05 pulse that caused more local damage to the 10 and 13-story buildings, the frequency content of the Tabas motion is closer to the

fundamental period of the 17-story building, so this building suffers more damage than the other buildings.

The amount of severe plastic hinging is limited to the G05 record for all buildings and to the Tabas record for the 17-story building. In table 11.2, the number of member ends exceeding 0.01 radians of plastic rotation are given. This level is moderate, and below the capacity that engineers expect connections to safely reach without fracture. The Oxnard ground motion is the only record that causes no yielding above 0.01 radians. As mentioned in the previous chapters, this excitation produces only modest inelastic response. The other four records clearly produce inelastic behavior in the buildings.

From the perspective of the Uniform Building Code, buildings are allowed an 0.03 inelastic drift (the elastic analysis drift limit is $0.03/R_w = 0.0025$ for SMRF buildings). This implies that ground motions larger than the code specifies have been used in this work. The Tabas record produces story drifts greater than 0.03 in the 13 and 17-story buildings, the Takatori record in the 10-story building, and the G05 record in all three buildings. All the other ground motion and building combinations produce maximum story drifts below this limit.

The columns in the 17 and 13-story buildings do not yield much, but a significant number of the columns in the 10-story building do yield. This behavior is interesting, and should be compared to the strong-column/weak-beam (SCWB) code provisions discussed in section 10.2. In table 11.3, the number of joints in each building that exceed a B/C ratio of 1.0 are given for each of the five ground motions and the static analysis. Note that actual, not nominal, yield strengths are used to calculate these values and recall that the 10-story building analyses assume that the nominal values are the actual values. The B/C ratio is a function of member size and material strength. Differences exist due to the column plastic moment strength being reduced for axial forces that result from each analysis.

Figures 11.1–11.3 show the B/C values for static analysis using actual strengths. The 17-story building has only 16 joints where the SCWB provision is not met. They are in upper levels that are not loaded as severely for a pulse ground motion

like the G05 record. The 13-story building has 80 joints that exceed the limit. Note that this code provision was recommended by SEAOC in 1990 (SEAOC 1990), so neither of these buildings were required to satisfy it. For the 13-story building, most of the joints that fail the criterion are in the upper levels. The second story interior joints, however, barely meet the provision with B/C ratios of 0.99. The column yielding seen in the G05 response occurs at this level. As mentioned earlier, the 17-story building did not exhibit this behavior for the G05 record, and the lower B/C ratios could partially explain this.

Every joint in the 10-story building satisfies the SCWB provision for static loading. The column yielding experienced in the G05 response does not correlate with the B/C ratios for this building, even when calculated for the axial forces of the G05 ground motion instead of the static case (figure 11.4). Thus, the B/C ratio cannot explain the behavior resulting from the G05 ground motion. Many simplifying assumptions are made in the SCWB provision about moment distribution at a frame joint.

This behavior is better explained by considering the ground motion as a shear wave travelling up the building. The shear strain induced in the building can be approximated as the ground velocity divided by the building wave velocity (Heaton 1995). This strain is analogous to story drift. The wave velocity in a building can be approximated by dividing the height of the building by the time difference between peak ground and roof displacements during a pulse motion. For the three buildings investigated, the wave velocity is roughly 80 m/sec. As damage occurs, this will reduce. Three of the five records exceed 120 cm/sec maximum ground velocity so the corresponding strain will thus be 0.015. The maximum story drifts for these three records (Sylmar, G05, and Takatori) all exceed this value. A strain of 0.015 is large enough to induce inelastic behavior, so the larger drifts can be attributed to yielding.

Assuming the first story is 4 meters tall, the time it takes a ground pulse to reach the second story is 0.05 sec. If the ground is moving at 120 cm/sec, it will have displaced 6 cm before the travelling shear wave begins to act on the second

story. Looking back at the plastic rotation plots for all three buildings responding to the G05 record (figures 8.80, 9.58, and 10.68), the lowest non-stiff story has plastic rotations at the column bases in the N-S direction that can be explained by this time lag in response. This dynamic consideration of pulses travelling through buildings has not been considered much by practicing engineers. Şafak (1997) considers vertical shear-wave propagation in a layered medium that includes the building stories and bedrock layers. Further development of such simplified techniques may provide more information about structural behavior than other code-accepted techniques such as pushover and response spectrum analysis.

Referring again to the SCWB results in table 11.3, it can be seen that the load level of all five ground motions exceeds the static loading. Each record produces more joints that exceed allowable B/C ratios than the static loading does. The 10-story building has the greatest difference between static and time-history results, which can partially be attributed to the fact that it has more joints with B/C close to 1.0 than the other buildings do.

The number of joints with B/C exceeding 1.0 does not correlate with the number of columns exceeding 0.01 radians plastic rotation (table 11.2). This indicates that the B/C ratio is not a good indicator of potential column yielding. The fact that so many joints do not meet the SCWB criterion for the 13-story building while so few columns exceed 0.01 radians of plastic rotation for the five ground motions also indicates that failing the SCWB criterion does not necessarily mean columns will yield before beams do.

The plastic rotations of the panel zones for the inelastic model are given for each building and ground motion in table 11.4. The panel zones in all three buildings have been sized to meet the provision discussed in section 7.1.4. Little inelastic behavior is observed in the panel zones relative to the beam or column ends. Only the 10-story building with the G05 record produces panel zone plastic rotations greater than 0.01 radians. For this same record, 138 column ends exceed 0.01 radians of plastic rotation. While investigating the SCWB provisions of the 94 UBC, it was found that the moments in beams corresponding to panel zone shear strength always

exceeded the beam plastic moment for the all three buildings. This means that the beams should yield before the panel zone does. The panel zones in all three buildings are strong and so further study of them is not warranted in this work.

The maximum story drift, the maximum base shear ratio V/W, and the percentage of member ends with plastic rotations exceeding 0.01 radians are compared for each building and ground motion in table 11.5. The information in the table is also presented in figure 11.5. No correlation can be seen between drift and base shear, drift and plastic rotations, or base shear and plastic rotations. One trend can be seen for the relationship between base shear and period. It appears to be a roughly inverse relationship. The UBC calculates V/W as a function of 1/T, so this result is well established. The stiffer the building (smaller T), the more load it attracts, even under damaged conditions as extensive as collapse.

Returning to the table, the maximum story drift has substantial variation between the three buildings. The highest drift in the 13-story building occurs for the G05 and Takatori records. The highest drift in the 13-story building occurs for the G05 record. The highest drift in the 17-story building occurs for the Tabas record. Local damage indicated by the maximum story drift cannot be predicted by simplistic code formulas that consider only the fundamental period in a tall building. A static analysis with load distributions that assume predominantly first-mode response will also be a poor indicator of local damage that can occur from ground motions with energy at higher frequencies.

Looking at the figures of response parameters, the base shear ratio is roughly constant for all three buildings if the Oxnard record is omitted. The Oxnard response is mostly elastic, whereas the response to the other ground motions results in saturated values of base shear. Once inelastic response occurs, further loading is limited by changes to the building period and hysteretic damping. This could explain why very different levels of damage could exist for each ground motion response while the base shear remains almost constant.

11.2 Fracture Models

The fracture models which best represent the measured response are used for comparison: the poor performance fracture model for the 17-story building, the Maison random fracture model for the 13-story building, and the Hall random fracture model for the 10-story building. The maximum story drift, the maximum base shear ratio V/W, and the percentage of beam connections that fracture are compared for each building and ground motion in table 11.6. The information in the table is also presented in figure 11.6, which shows little correlation between drift and damage, drift and base shear, or base shear and damage. As with the inelastic model, the V/W ratio is again inversely proportional to the building fundamental period and roughly constant when inelastic response occurs.

In terms of the maximum story drift, the strong pulse records (G05 & Tabas) affect the taller, longer period buildings. The ranking of the drift is the same as the base shear for the remaining records. The stiffer 10-story building attracts more load and suffers greater local damage. As with the inelastic model, local damage (story drift) and global damage (% fractures) do not correlate with each other or with base shear.

11.3 Fracture vs. Inelastic Models

Figure 11.7 compares the percentage of damage resulting from the fracture and inelastic models. There is no apparent correlation, which means an inelastic analysis will not predict the level of damage to occur if the building is susceptible to fractures.

An additional comparison is made between the inelastic and fracture models in figure 11.8. Comparing base shear values, the fracture model has consistently lower base shears. This implies the buildings were damaged more, reducing their stiffness and the amount of load they can attract. Looking at the drifts, the fracture model almost always has larger maximum story drifts. Note that the three collapses for the fracture model are not plotted, but they also support this behavior. The correlation between drift ratios and base shear ratios is not perfect due to the fact

that damage can be localized or spread. An example in which the fracture model has lower base shear *and* lower maximum drift is the response of the 17-story building to the Takatori ground motion. In this case, the fractures are spread over a large portion of the building, which releases a large amount of stored strain energy and limits further loading due to reduced stiffness. The inelastic model remains stiffer, which allows load to reach the weak upper stories that end up with more damage than if lower levels yield as in the case of the fracture model. See figure 11.9, which shows the building at the time of maximum story drift for both the fracture and inelastic models. The horizontal displacements are scaled by a factor of 20. For most other cases, fracture damage will be more severe than yielding, leading to higher maximum drifts and lower base shear.

11.4 Peak Ground Motion Quantities

The damage of each building for both the fracture and inelastic models is ranked in table 11.7. The ordering is based on both local damage (story drift) and global damage (percentage of fractured connections or yielded ends) and is subjective to some extent. If story drift is worse for one record than another record and the percent of damaged connections is worse for the other record, the ranking is considered equal. If collapse or significant drift occurs, this governs over the spread of damage since it represents a severe condition.

Several peak parameters are presented for the five representative ground motions in tables 11.8–11.10. The square root of the sum of the squares (SRSS) for the N-S and E-W ground motions are present in the first table. The values corresponding to N-S and E-W ground motions are presented in the following tables. For the SRSS values, each of the parameters is ranked for the ground motions.

Comparing tables 11.7 and 11.8, the 17 and 13-story buildings correlate with the peak displacement and peak displacement difference very well. The 10-story building correlates better with peak velocity quantities. This makes sense considering the response of a single degree of freedom (SDOF) oscillator. As $T \rightarrow \infty$, the response

(relative displacement) of the SDOF oscillator is proportional to the peak ground displacement. As $T \rightarrow 0$, the response (force, acceleration) is proportional to the peak ground acceleration. In between, there is a range of periods in which the response is proportional to the peak ground velocity. The 17 and 13-story buildings have longer periods, so their response and resulting damage are more proportional to peak ground displacement. The 10-story building has a shorter period, so its response and resulting damage correlate better with the peak ground velocity. The UBC design of buildings uses acceleration based force levels, which tend to be more accurate for even shorter period structures. The response of longer period structures will not necessarily be proportional to the static loading imposed by the code. The UBC does insist on further analysis for buildings taller than 73 m (240 ft), but this can be limited to response spectrum analysis in many cases.

11.5 Response Spectra & Code Provisions

Response spectrum analysis is not performed in this work. Many simplifying assumptions are made to perform such an analysis, even for elastic analysis. It is highly approximate, and the difficulties of adjusting values for inelastic response limit its use to elastic analysis. These ground motions cause inelastic nonlinear response and Wilson (1997) states, "The use of nonlinear spectra, which are commonly used, have very little theoretical background and should not be used for the analysis of complex three-dimensional structures. For such structures true nonlinear time-history response should be used."

The response spectra for the ground motions are investigated to determine if there are any correlations to be made with building damage. The pseudo-spectral accelerations (PSA) corresponding to the fundamental mode of each building are given in table 11.11. The full spectra for each ground motion can be seen in the figures of Appendix A. Comparing the tabulated PSA values to damage levels shows that they clearly do not correlate. Looking solely at the fundamental mode spectral value ignores higher mode response. A weighted average or other means could be

used to attempt to account for higher modes, as in a full response spectrum analysis. Even then, pulses and periodic ground motion may appear to have the same PSA even though a pulse can sometimes be much more damaging.

One interesting comparison to be made using the response spectra is with the code spectrum. The five representative ground motions and the unreduced 1994 UBC spectrum are shown together in figure 11.10. To get a better look at the range of periods of concern for the buildings investigated, the five ground motion spectra are plotted as multiples of the UBC spectrum in figure 11.11. The values corresponding to the fundamental period of the three buildings are marked for each ground motion on these plots. For the 10-story building, all five ground motions produce accelerations that exceed the code value. For the 13-story building, all five N-S ground motion components and four E-W ground motion components exceed the code value. The 17-story building has only two E-W and N-S components exceed the code value.

The UBC has changed the spectrum in light of the Northridge earthquake and other recent strong ground motion recordings. In the 1997 UBC (ICBO 1997), they include near-source and soil-specific modifications to the spectrum to account for the previously unknown and unrecorded strong motions. A typical site in Los Angeles will have the following parameters:

- Source B
- Soil S_C
- Distance $\leq$ 2 km

This represents a site situated over any one of a number of large faults in Los Angeles County with very dense soil or soft rock. Figure 11.12 shows the resulting 1994 and 1997 spectra plotted together. While the 1997 spectrum is roughly 35% larger than the 1994 spectrum for a broad range of periods, the five ground motions will still exceed the response spectra code values to a great extent.

The code allows the base shear obtained from a response spectrum analysis to be scaled to the base shear of the static lateral force procedure. These static forces

are higher under the new code, with special lower limits imposed that increase the force on buildings with higher periods (figure 11.13). In this figure, strength design is assumed and the base shears are scaled appropriately for the code-specific load factors. The 1997 UBC has a 34% increase in design load for structures with periods larger than 2.1 seconds.

For tall buildings with long periods, the drift limits govern the design rather than the stresses. The base shear used to calculate drift limits divided by the drift limit itself will give a minimum story stiffness. This unitless stiffness requirement is shown in figure 11.14 for each code. Both codes have different drift limits for periods above and below 0.70 seconds, which explains the discontinuities in the figure. The 1997 code requires 40% more stiffness than the 1994 code for a period of 2.0 seconds, and 160% more for a period of 5.0 seconds.

A comparison of relative force levels for strength design and stiffness design are given in table 11.12. The equivalent stiffness takes into account differences in both drift limits (Δ) and the forces (V) used to calculate story drifts. If strength governed the design, the 10, 13, and 17-story buildings would all have to be 1.34 times stronger to satisfy the 1997 code as compared to the 1994 code. Assuming drift limits govern the design of tall moment frames, the 10, 13, and 17-story buildings would have to be 1.50, 1.83, and 2.59 times stiffer, respectively, for the 1997 code compared to the 1994 code.

It is unclear as to whether making steel moment frames stiffer is going to be advantageous. Engineers may use even larger members than before that are more susceptible to flaws in materials and construction. Fortunately, the 1997 UBC has also introduced a factor (ρ) that requires a certain level of redundancy in the system. By this provision alone, the lateral system of the 17-story building would not be permitted, regardless of member sizes and corresponding strength and stiffness.

11.6 Figures

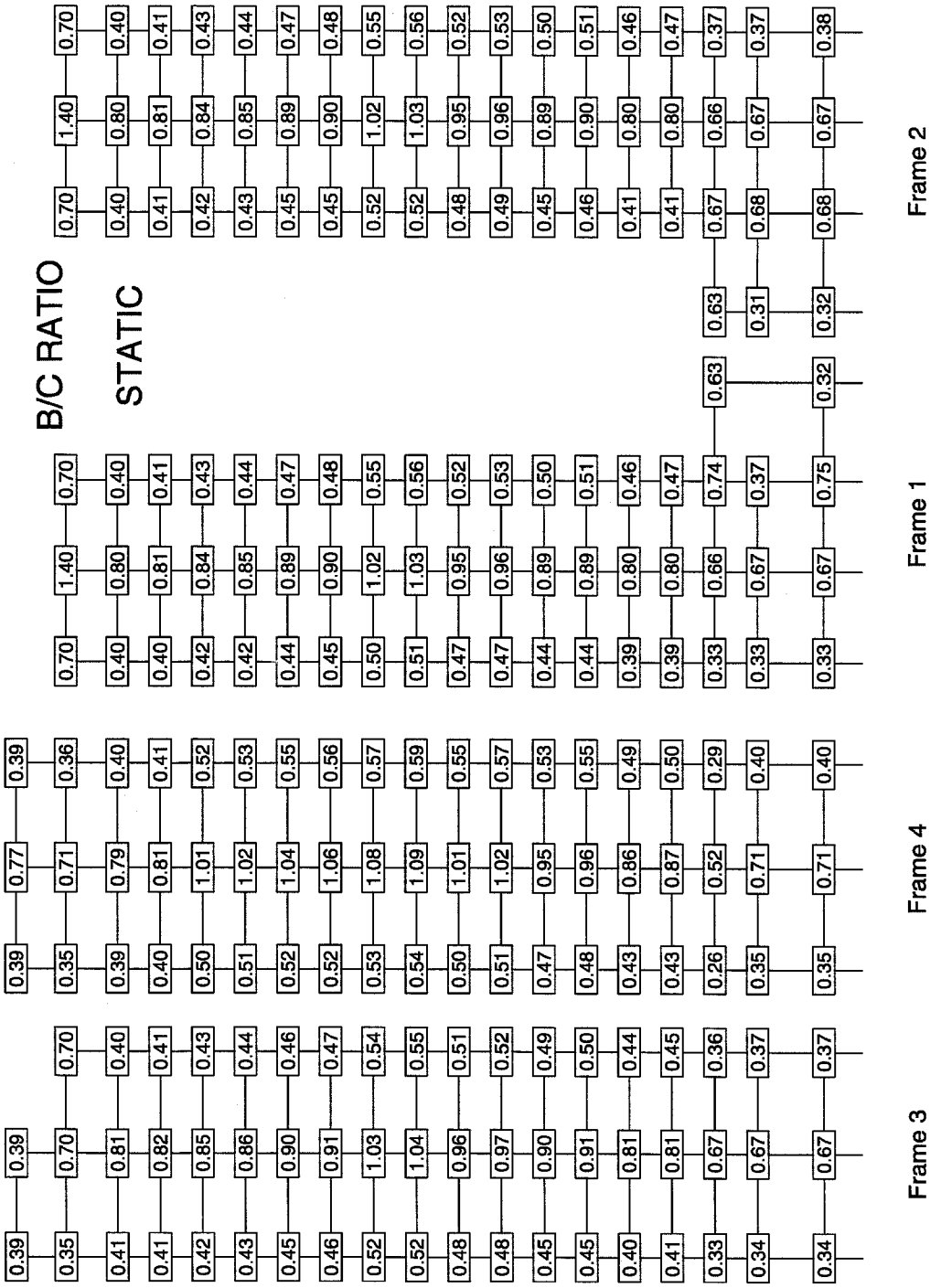

Figure 11.1 B/C ratios for the 17-story building and static analysis.

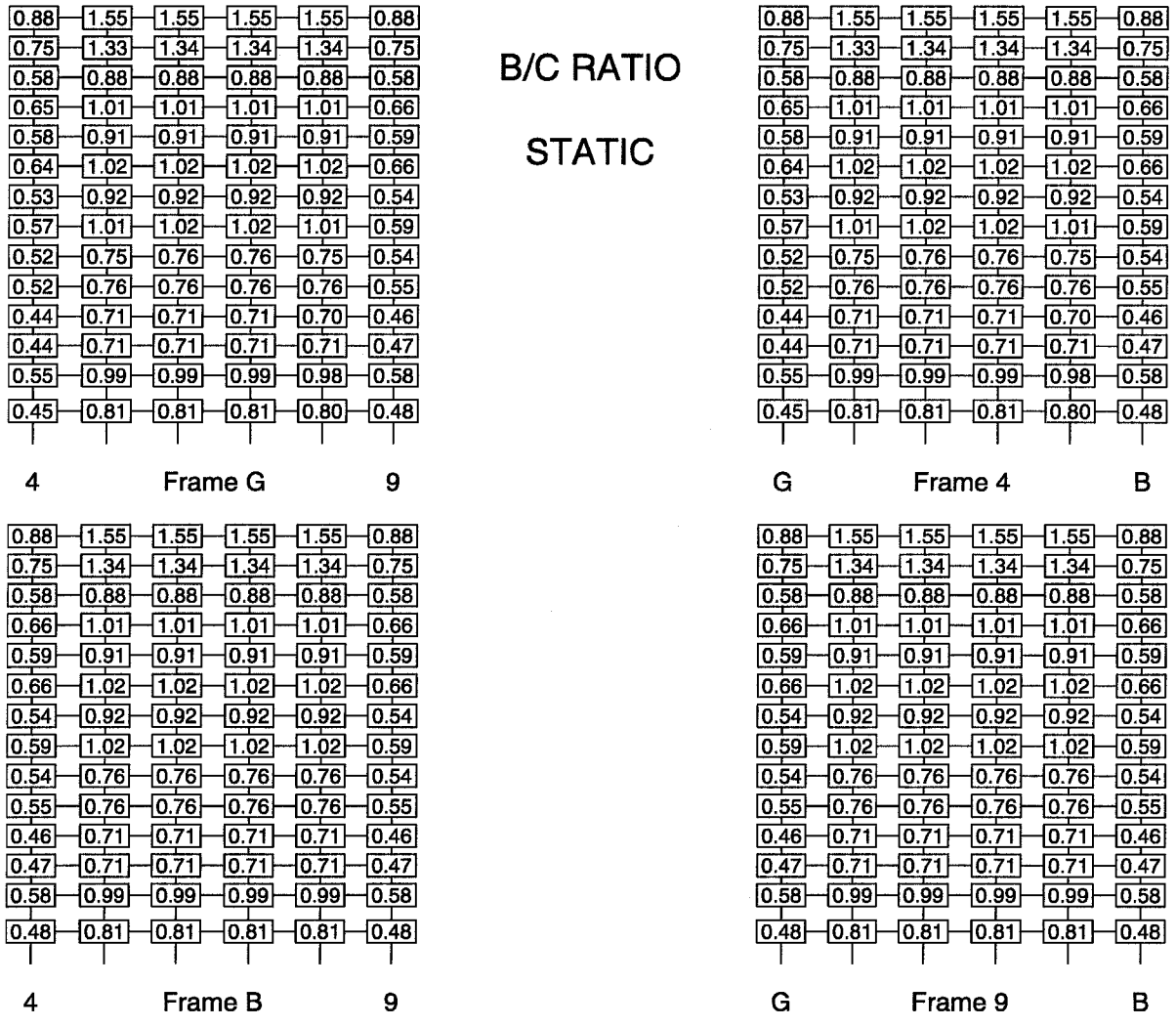

Figure 11.2 B/C ratios for the 13-story building and static analysis.

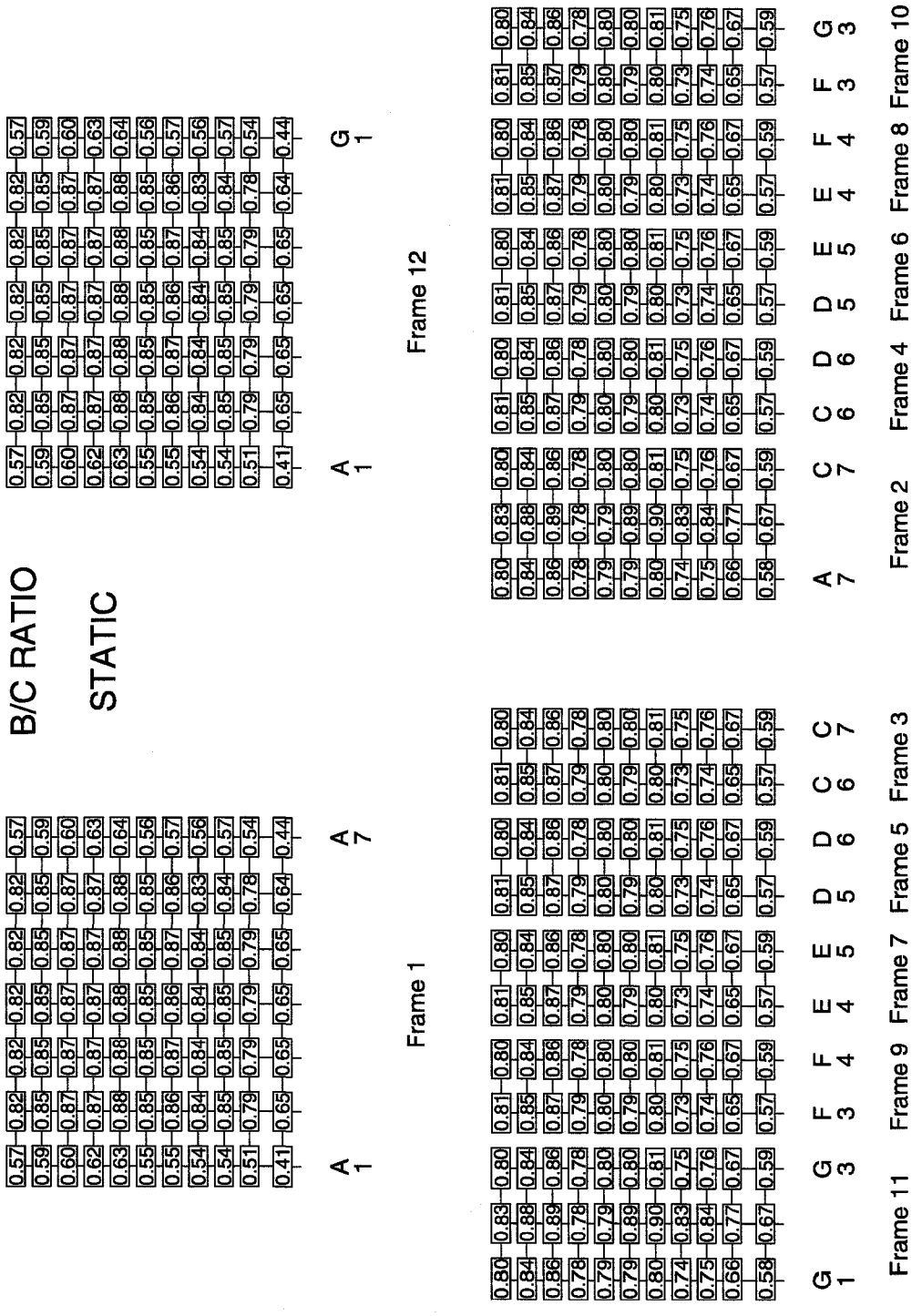

Figure 11.3 B/C ratios for the 10-story building and static analysis.

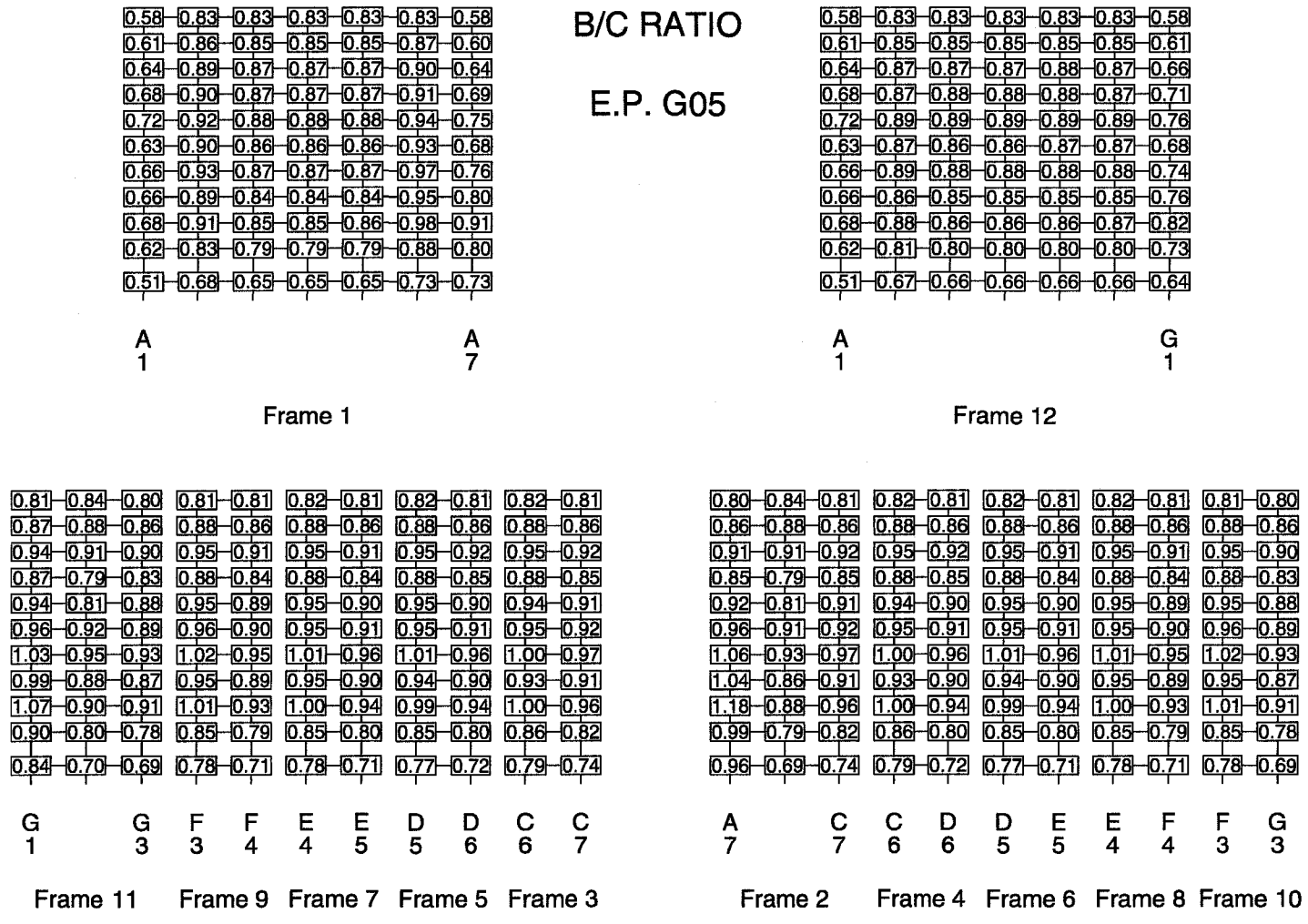

Figure 11.4 B/C ratios for the 10-story building and the E. P. G05 ground motion.

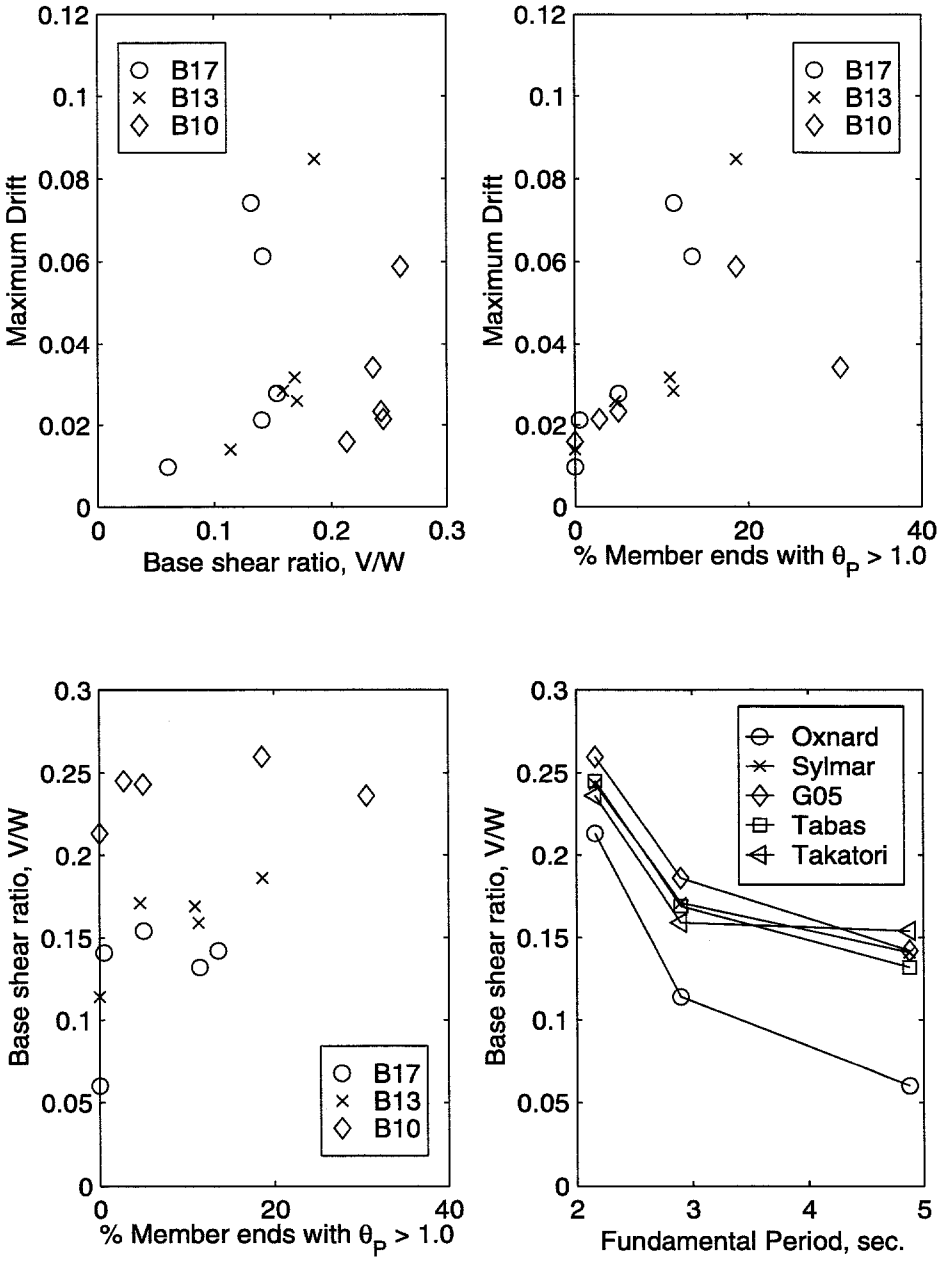

Figure 11.5 Response parameters for the inelastic model.

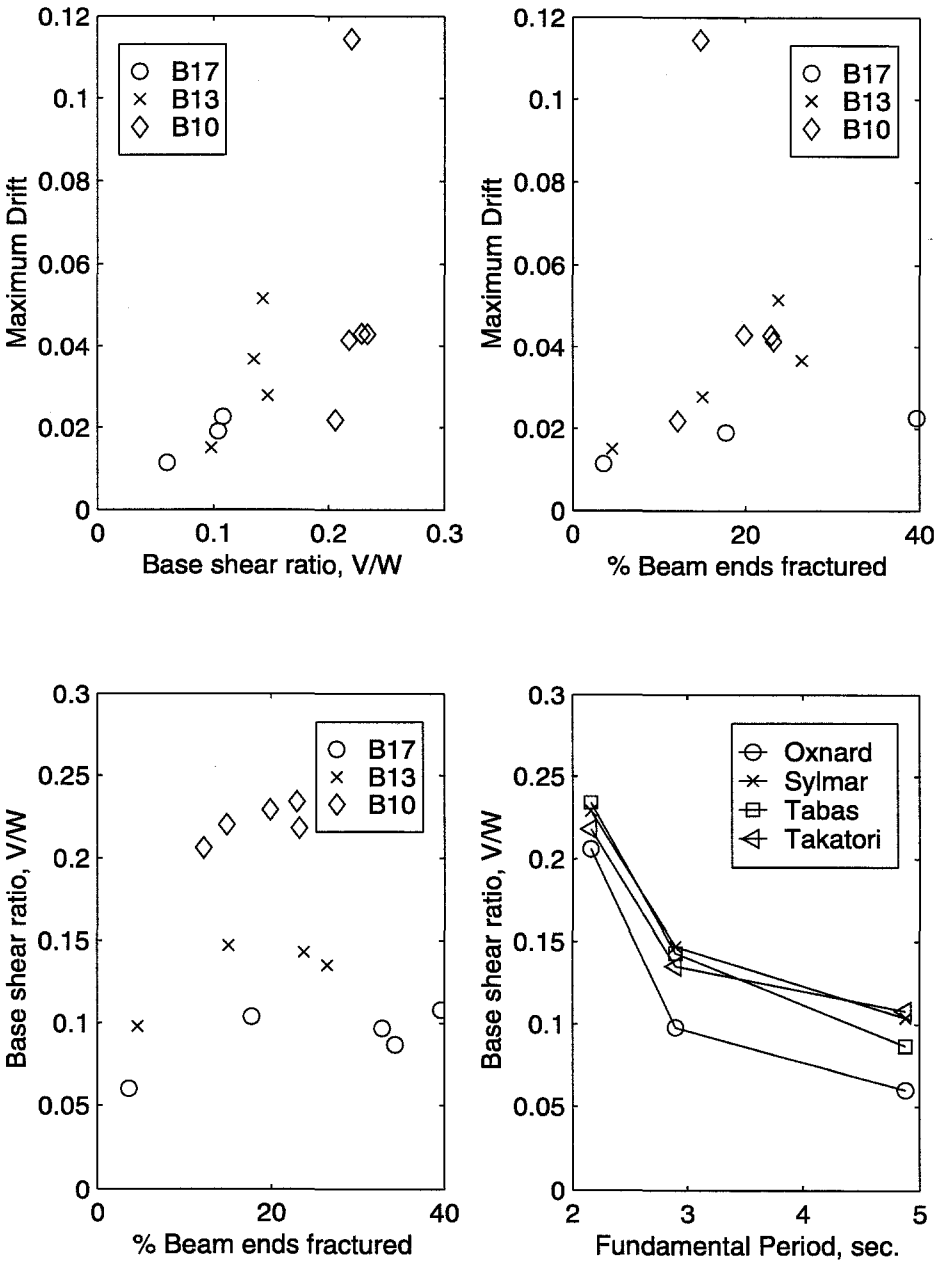

Figure 11.6 Response parameters for the fracture models.

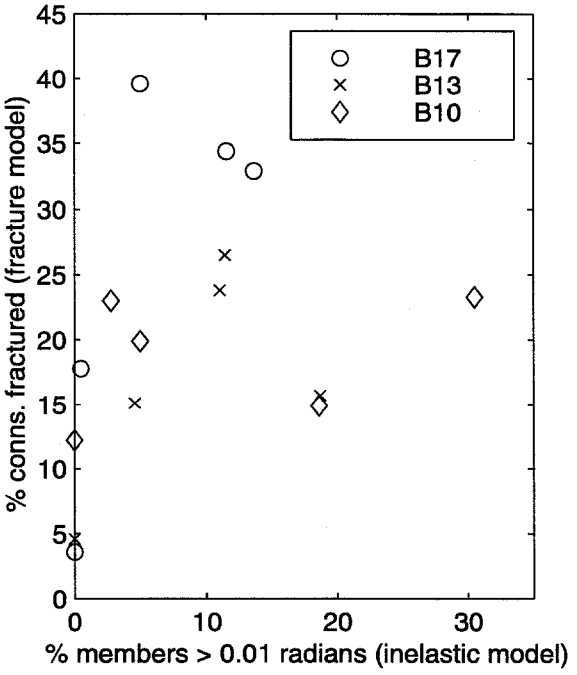

Figure 11.7 Damage indicators compared for the inelastic and fracture models.

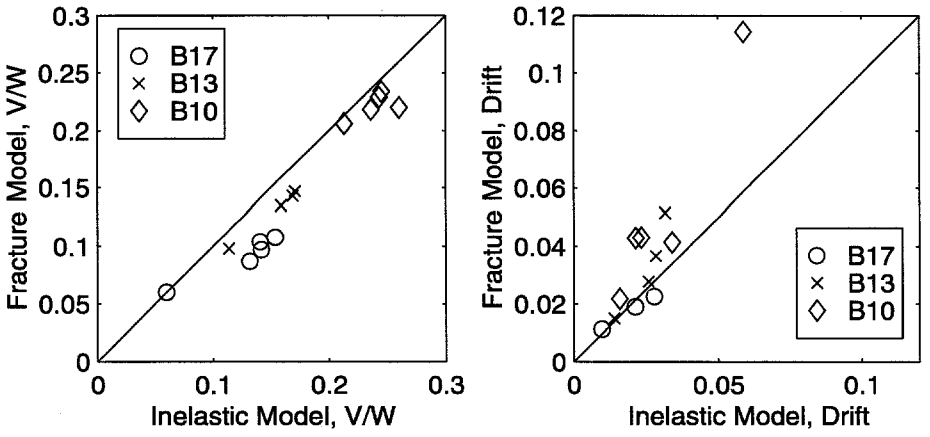

Figure 11.8 Base shear and drift compared for the inelastic and fracture models.

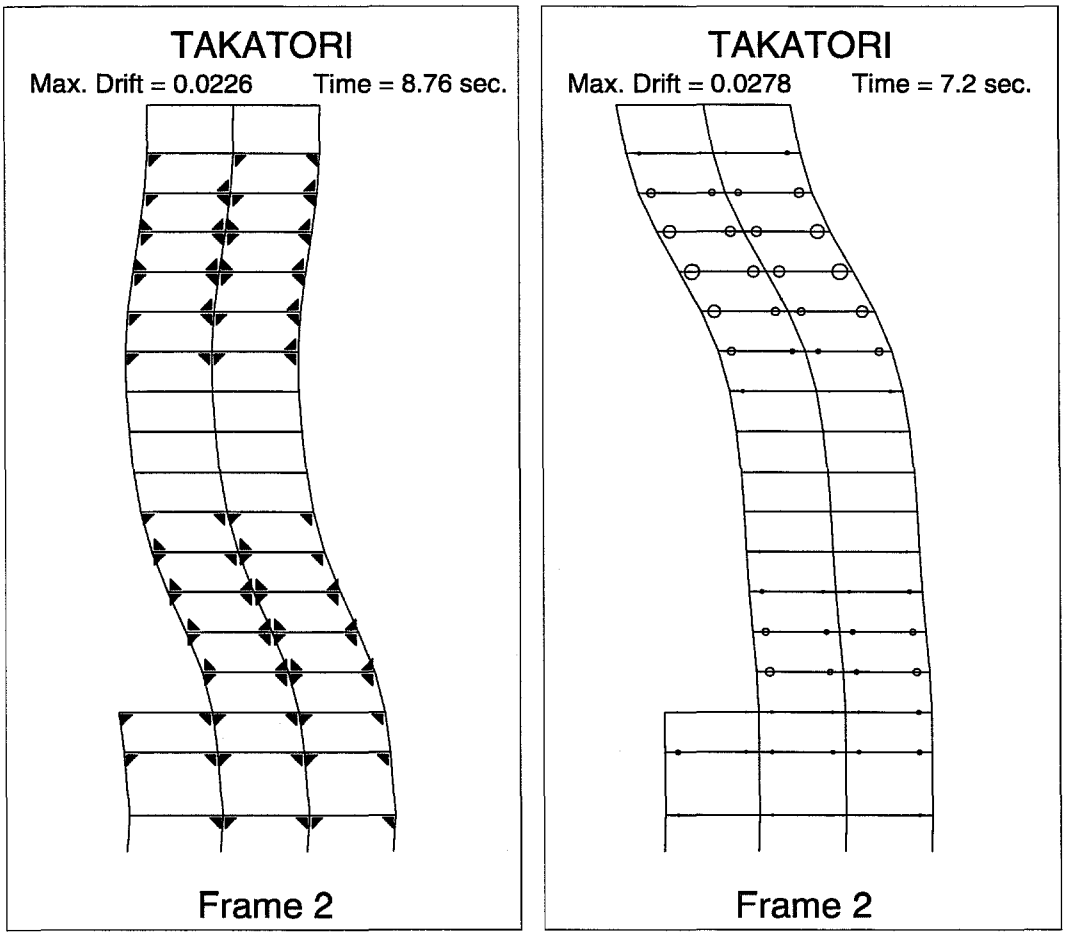

(a) Fracture model

(b) Inelastic model

Figure 11.9 Maximum story drift in the 17-story building.

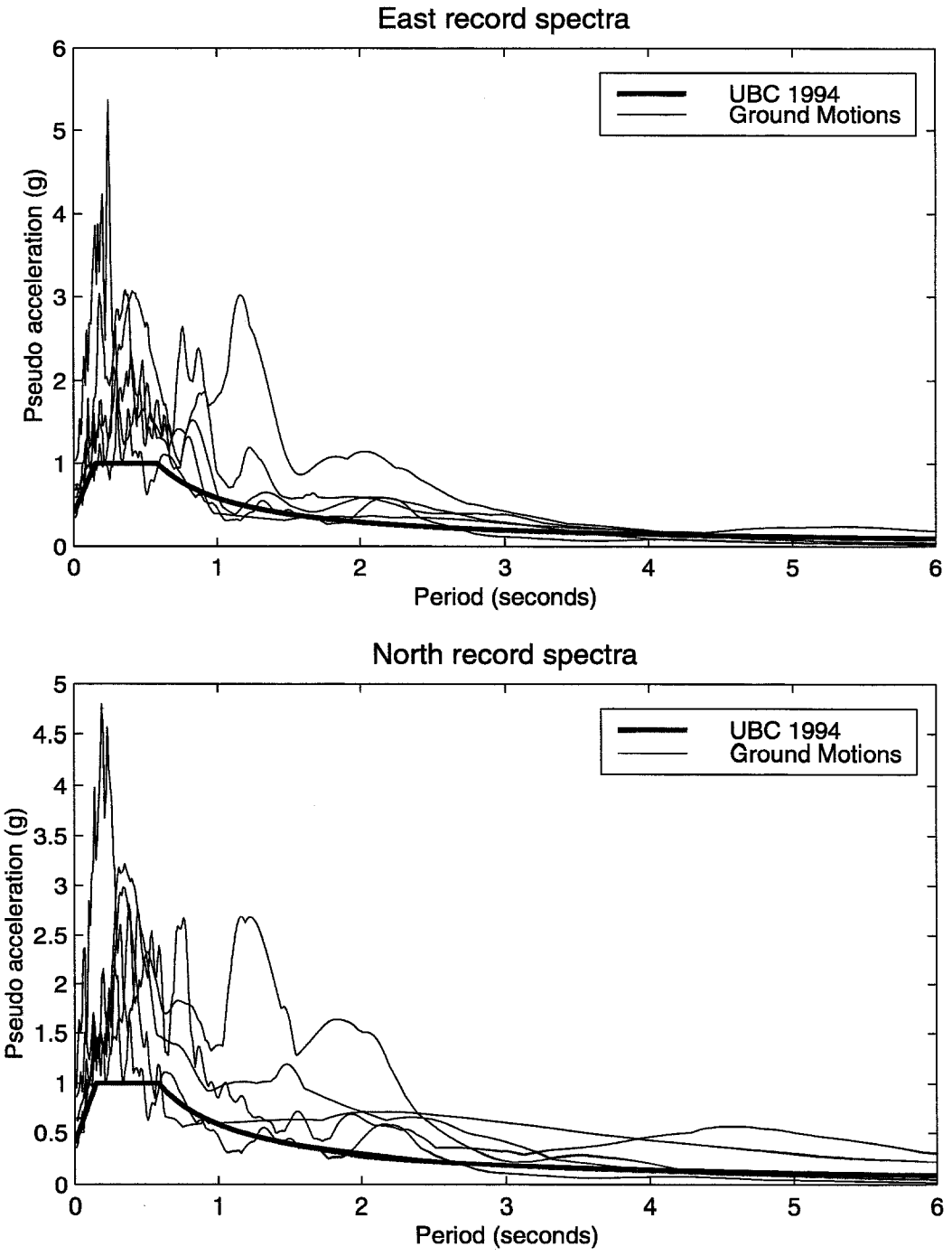

Figure 11.10 Response spectra of time histories.

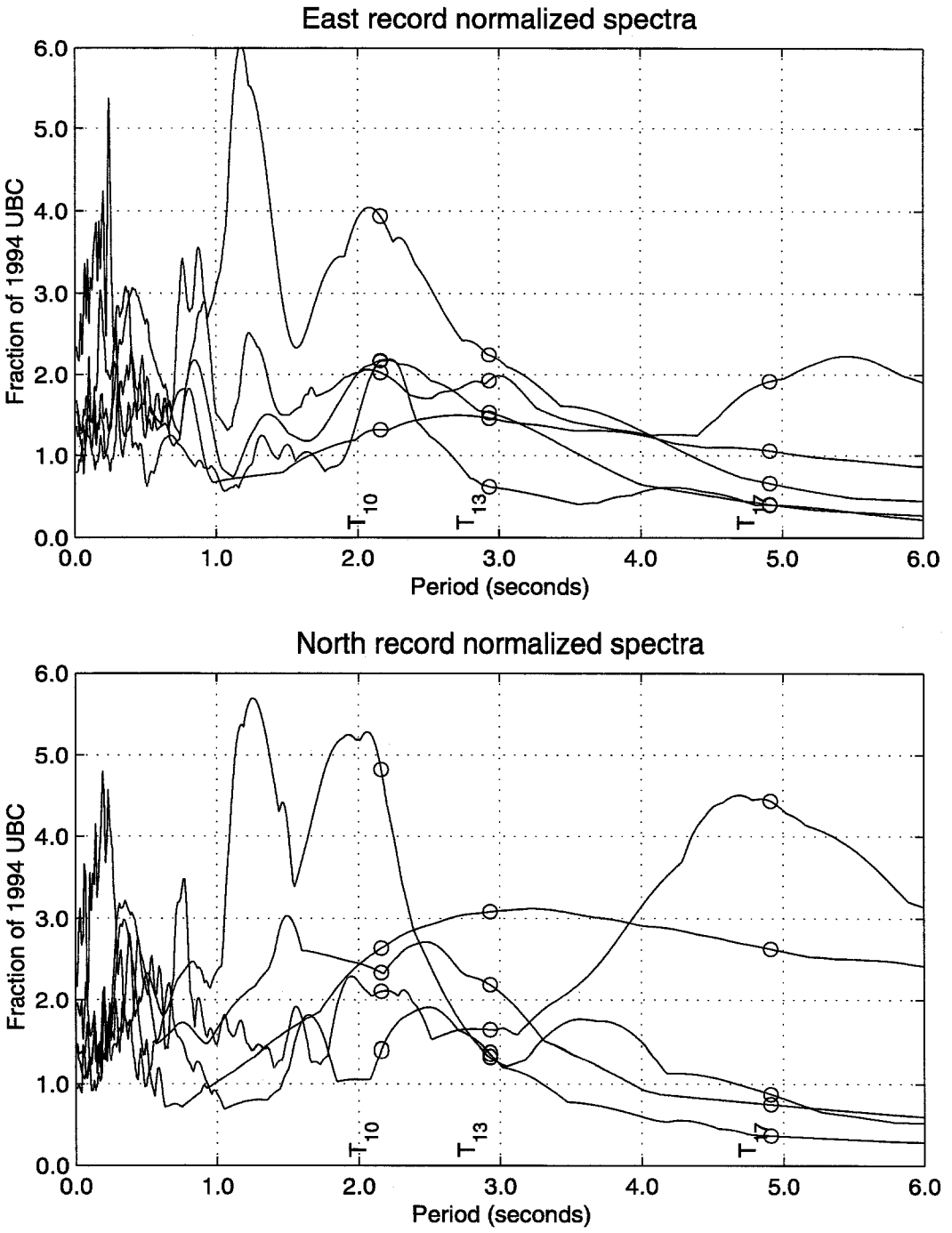

Figure 11.11 Response spectra normalized to 1994 UBC spectrum.

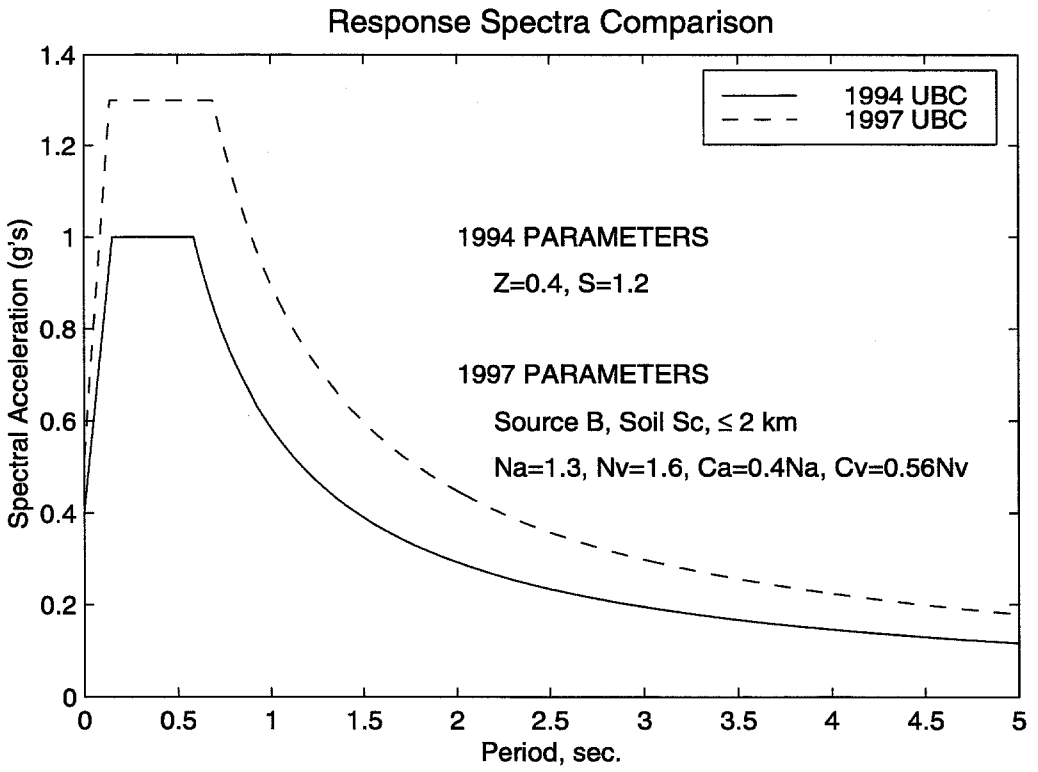

Figure 11.12 Comparison of 1994 and 1997 UBC response spectra.

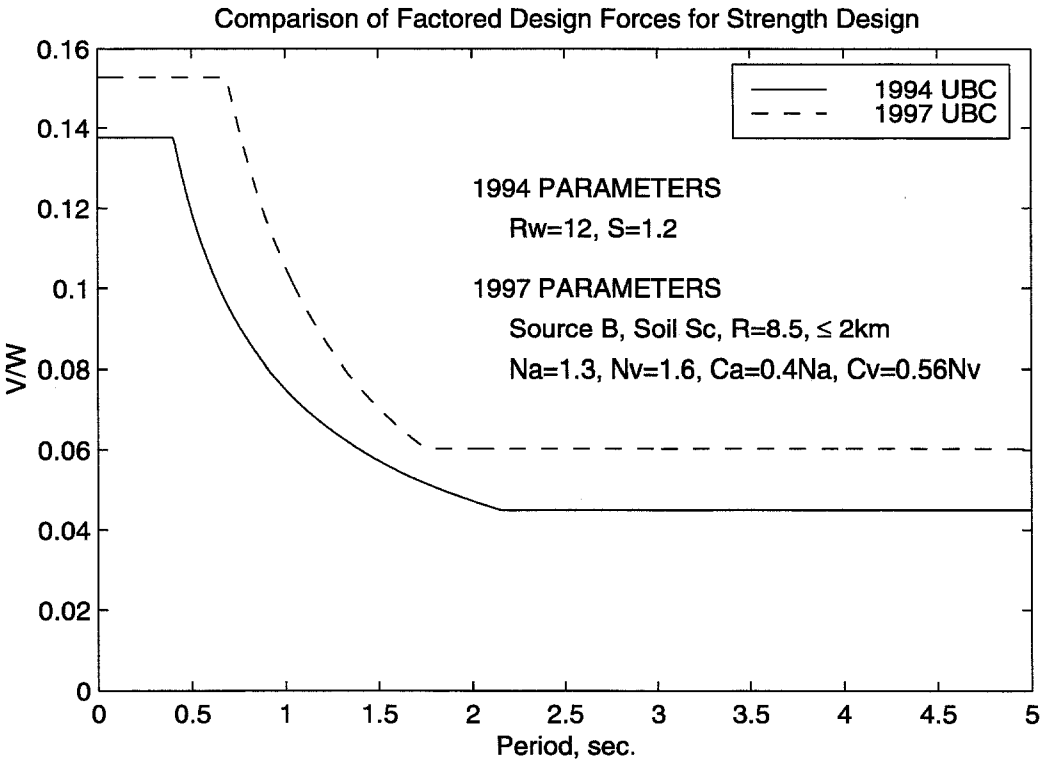

Figure 11.13 1994 and 1997 UBC force levels, allowable stress design.

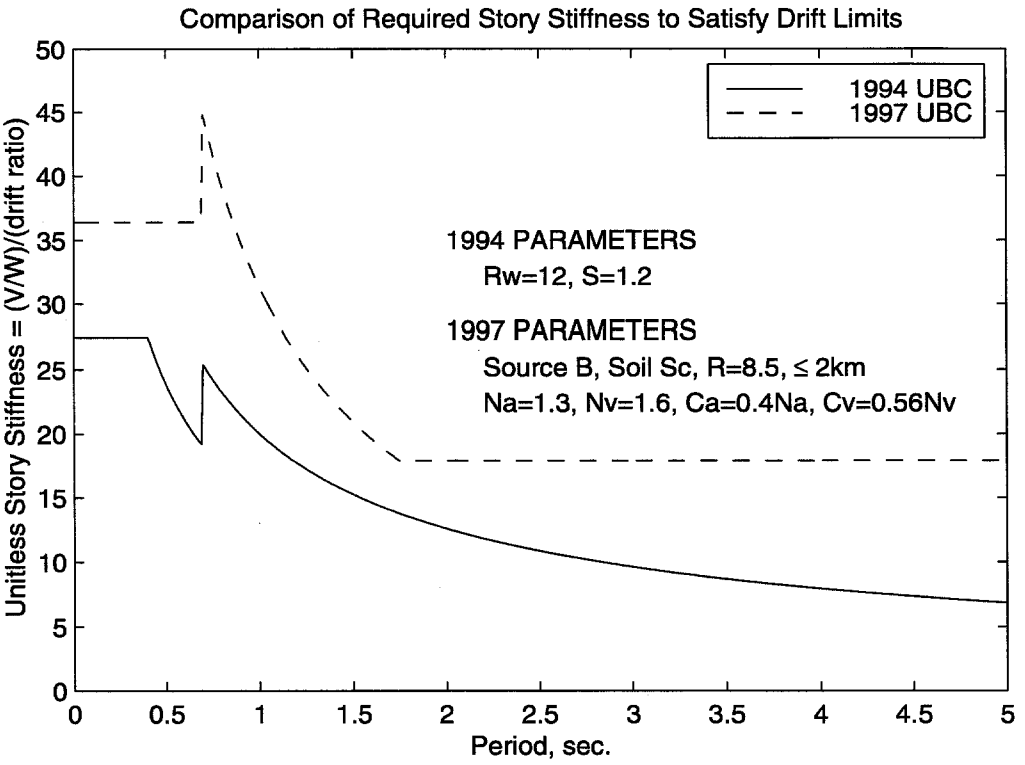

Figure 11.14 1994 and 1997 UBC force levels, displacement calculations.

Plastic Rotations Greater than 0.03 Radians for Inelastic Models						
Building		Oxnard	Sylmar	E.P. G05	Tabas	Takatori
17-Story	Girders	0	0	41	36	0
	Columns	0	0	0	3	0
13-Story	Girders	0	0	82	0	0
	Columns	0	0	12	0	0
10-Story	Girders	0	0	54	0	0
	Columns	0	0	10	0	0

Table 11.1 Member-end plastic rotations for inelastic models.

Plastic Rotations Greater than 0.01 Radians for Inelastic Models						
Building		Oxnard	Sylmar	E.P. G05	Tabas	Takatori
17-Story	Girders	0	4	98	80	38
	Columns	0	0	5	7	0
13-Story	Girders	0	57	186	135	140
	Columns	0	0	44	0	0
10-Story	Girders	0	40	108	13	191
	Columns	0	26	138	24	212

Table 11.2 Member-end plastic rotations for inelastic models.

11.7 Tables

Strong-Column/Weak-Beam Criterion						
	Number of joints with B/C $\geq$ 1.0					
Building	Static	Oxnard	Sylmar	E.P. G05	Tabas	Takatori
17-Story	16	18	18	17	24	17
13-Story	80	96	97	90	107	96
10-Story	0	20	109	15	149	57

Table 11.3 Joints not meeting the strong-column/weak-beam criterion.

Panel Zone Plastic Rotations in Radians for Inelastic Models						
Building		Oxnard	Sylmar	E.P. G05	Tabas	Takatori
17-Story	$\theta_P \geq 0.005$	0	0	18	10	5
	$\theta_P \geq 0.010$	0	0	0	0	0
13-Story	$\theta_P \geq 0.005$	0	0	40	0	0
	$\theta_P \geq 0.010$	0	0	0	0	0
10-Story	$\theta_P \geq 0.005$	0	9	31	29	46
	$\theta_P \geq 0.010$	0	0	17	0	0

Table 11.4 Panel zone plastic rotations for inelastic models.

Comparison of Building Response for Inelastic Models				
		Maximum Story Drift	Maximum V/W	% of Member Ends with $\theta_p > 0.01$
Oxnard	17-Story	0.0097	0.060	0
	13-Story	0.0140	0.114	0
	10-Story	0.0159	0.213	0
Sylmar	17-Story	0.0213	0.141	0.5
	13-Story	0.0259	0.171	4.6
	10-Story	0.0234	0.243	5.0
E.P. G05	17-Story	0.0613	0.142	13.6
	13-Story	0.0848	0.186	18.7
	10-Story	0.0588	0.260	18.6
Tabas	17-Story	0.0742	0.132	11.5
	13-Story	0.0317	0.169	11.0
	10-Story	0.0215	0.245	2.8
Takatori	17-Story	0.0278	0.154	5.0
	13-Story	0.0284	0.159	11.4
	10-Story	0.0341	0.236	30.5

Table 11.5 Comparison of damage parameter for five records.

Comparison of Building Response for Fracture Models				
		Maximum Story Drift	Maximum V/W	% of Beam Ends with Fractures
Oxnard	17-Story	0.0113	0.060	3.6
	13-Story	0.0150	0.098	4.6
	10-Story	0.0218	0.206	12.2
Sylmar	17-Story	0.0190	0.104	17.8
	13-Story	0.0278	0.147	15.1
	10-Story	0.0431	0.229	19.9
E.P. G05	17-Story	collapse	0.097*	32.9*
	13-Story	collapse	—**	15.7*
	10-Story	0.1144	0.220	14.9
Tabas	17-Story	collapse	0.087*	34.4*
	13-Story	0.0517	0.143	23.8
	10-Story	0.0430	0.234	23.0
Takatori	17-Story	0.0226	0.108	39.6
	13-Story	0.0367	0.135	26.5
	10-Story	0.0415	0.218	23.3

Table 11.6 Comparison of damage parameter for five records. * Indicates values prior to collapse. ** Indicates program crashed and data lost.

Ranking of Damage						
	17-Story inelastic model	17-Story fracture model	13-Story inelastic model	13-Story fracture model	10-Story inelastic model	10-Story fracture model
Oxnard	5	5	5	5	5	5
Sylmar	4	4	4	4	3	2
E.P. G05	1	1	1	1	1	1
Tabas	1	2	2	2	4	2
Takatori	3	3	2	3	1	2

Table 11.7 Ranking of damage for each building and five ground motions.

Peak SRSS Ground Motion Quantities and Ranking						
	A_{max} cm/sec^2	V_{max} cm/sec	D_{max} cm	A_{max}-A_{min} cm/sec^2	V_{max}-V_{min} cm/sec	D_{max}-D_{min} cm
Oxnard	510 (5)	71 (5)	14 (5)	960 (5)	135 (5)	28 (5)
Sylmar	1018 (2)	150 (3)	37 (4)	1675 (4)	225 (4)	63 (4)
E.P. G05	960 (3)	171 (2)	179 (1)	1831 (2)	312 (2)	179 (1)
Tabas	1261 (1)	150 (3)	95 (2)	2298 (1)	285 (3)	177 (2)
Takatori	894 (4)	173 (1)	49 (3)	1701 (3)	315 (1)	86 (3)

Table 11.8 Peak SRSS ground motion quantities with ranking.

Peak N-S Ground Motion Quantities						
	A_{max} cm/sec^2	V_{max} cm/sec	D_{max} cm	A_{max}-A_{min} cm/sec^2	V_{max}-V_{min} cm/sec	D_{max}-D_{min} cm
Oxnard	403	57	12	759	111	23
Sylmar	827	129	31	1405	186	55
E.P. G05	632*	134	164	1236*	263	164
Tabas	919	114	88	1649	222	163
Takatori	606*	123	39	1131*	238	64

Table 11.9 Peak N-S ground motion quantities. * Indicates E-W is larger.

Peak E-W Ground Motion Quantities						
	A_{max} cm/sec^2	V_{max} cm/sec	D_{max} cm	A_{max}-A_{min} cm/sec^2	V_{max}-V_{min} cm/sec	D_{max}-D_{min} cm
Oxnard	313	42	8	587	76	16
Sylmar	593	77	20	912	127	30
E.P. G05	723*	106	72	1351*	168	72
Tabas	863	98	36	1601	179	70
Takatori	657*	122	30	1270*	207	57

Table 11.10 Peak E-W ground motion quantities. * Indicates N-S is smaller.

Pseudo-Spectral Accelerations (in g's) for 5% Damping						
Building		Oxnard	Sylmar	E.P. G05	Tabas	Takatori
17-Story	E-W	.05	.05	.13	.23	.08
	N-S	.04	.09	.31	.53	.10
13-Story	E-W	.12	.31	.29	.38	.45
	N-S	.27	.44	.62	.33	.26
10-Story	E-W	.59	.59	.36	.55	1.07
	N-S	.38	.63	.71	.57	1.31

Table 11.11 PSA values at the fundamental period of each building.

Building	Period (seconds)	Strength V_{97}/V_{94}	Equivalent Stiffness $(V/\Delta)_{97}/(V/\Delta)_{94}$
10-Story	2.16	1.34	1.50
13-Story	2.93	1.34	1.83
17-Story	4.91	1.34	2.59

Table 11.12 Code comparison of design base shears.

Chapter 12

Conclusions

A sophisticated three-dimensional nonlinear inelastic program has been developed that can accurately model many nonlinear properties commonly ignored or approximated in other programs. The program can assess and predict severely inelastic response of steel buildings due to strong ground motions.

Two buildings damaged in the Northridge earthquake have been investigated to verify the ability of the program to predict the level of response and the extent and location of damage measured. A third building has been studied to assess three-dimensional effects on a realistic irregular building.

The effect of larger near-source ground motions has been explored. Various response parameters are used to determine what correlations can be made for inelastic response.

12.1 Conclusions

Several conclusions can be made based on the analyses performed with the program. These are grouped into modeling issues, ground motions, and building response.

12.1.1 Modeling Issues

Validation

The three-dimensional constraints and column elements developed in this work have been validated by successful use of the program to match measured data of two buildings damaged in the Northridge earthquake. The damage and the penthouse response matched reasonably well for the 17-story building for two representative ground motions recorded close to the building site. No basement motion recordings were made, so a closer match to the data is not expected. The calculated response and damage of the 13-story building match the actual levels well. These matching responses give confidence in using the program to predict damage levels for other excitation levels or to assess retrofit schemes.

Three-Dimensional Analysis

More damage is observed in one of two parallel frames in the 17-story building, indicating the importance of three-dimensional analysis. Reversing the transverse component of the ground motions causes the damage to switch sides. Ground motion direction must be considered carefully.

The 10-story building has one vertical plane of symmetry, and the center of mass coincident with this plane. Random fractures can introduce torsion to a balanced symmetric structure loaded in the plane of symmetry.

A two-dimensional record applied at arbitrary angles to the 10-story building produces torsional response of significantly different levels. The 10-story building is irregular in plan, but the center of mass and center of rigidity match well, reducing torsional response. In addition to torsional response, damage levels are significantly affected by rotation of ground motion input.

Nonlinear Time-History Analysis

Engineers expect buildings to suffer some inelastic response to strong ground motions, but current practice does not predict the localized, higher-mode and other

responses seen in this work. Nonlinear time-history analysis should be a requirement for buildings with longer periods. Care must be taken in drawing conclusions from highly variable nonlinear response.

Model Comparisons

Unfortunately, the inelastic model will not predict the level of damage to occur if the building is susceptible to fractures. Dramatic changes in building response can occur depending on which model is being used. Inelastic models can provide insight into how a building will respond to severe ground motions. If an existing building that has potentially bad welds or connections is being investigated, it would be prudent to use a separate model with fractures represented if life safety is a concern.

12.1.2 Ground Motions

Strong Ground Motions

The Elysian Park G05 simulated ground motion causes damage greater than the code expects from current design levels. Even with perfect connections, many plastic rotations greater than 0.03 radians are recorded for all three buildings. This is a practical limit of ductile response, since engineers do not expect steel moment frames to sustain larger inelastic deformations. The 17-story building also suffers more damage from the Tabas ground motion than one would expect from the code. While these ground motions produce building drifts exceeding code-anticipated levels, four of the five selected ground motions cause moderate to severe inelastic behavior even with perfect connections.

Pulses

A moderate ground pulse can cause greater observable damage (story offset) relative to strong random-like ground motion that can cause hidden fractures throughout a building with little observed offset or damage. Damage is not proportional to any ground motion parameters that were examined.

Maximum story drifts may be equal for very different ground motions. A pulse causing localized damage in lower stories may produce the same maximum story drift as a sustained random or quasi-periodic ground motion that causes damage throughout the height of a building.

Strong ground motion pulses can cause lower level columns to yield before the energy can reach the next level. Code prescribed formulas for ensuring that columns are stronger than beams do not prevent pulses from initiating column yielding prior to beam yielding.

Dynamics

Internal reflections at higher frequencies can occur in buildings with zones of local damage producing reflecting surfaces. This type of amplified response at higher frequencies cannot be approximated with response spectra or elastic analyses.

The energy imparted to a building can transfer from lateral to torsional modes as damage occurs during the excitation. These changing energy levels point out the importance of nonlinear time history analysis over response spectrum or elastic time history analysis.

Pulses and other dynamic effects are not considered in building codes. New provisions attempt to account for stronger ground motions through the use of near-source factors. Buildings designed with these codes will be stronger and stiffer, but the dynamic nature of the ground motion can produce results that the larger static forces and spectral quantities cannot predict.

Directivity

The importance of ground motion directivity is clear. Rotation of ground motion input can significantly affect damage observed.

12.1.3 Building Response

Higher-Mode Response

The 17-story building has uniform strength as determined from static analysis, but local upper level damage occurs due to some ground motions, showing the importance of higher mode response on tall buildings. Static analysis will not account for such effects.

For the same ground motion, differences in building period can cause buildings to react in the first mode only or in higher modes.

Buildings are designed to specified base shear levels in the Uniform Building Code. Higher mode effects are not associated with the largest base shear in general. The base shear will be higher when all masses in the building are accelerating in the same direction (first mode) rather than when masses move in opposite directions (higher modes). A code design for specified base shear and drift limits is based on first mode response. Higher-mode loading reversals can cause a great deal of damage while limiting both the base shear and the maximum roof drift.

Damage

The number of fractures in a building does not necessarily correlate with the extent of damage or cost of retrofit. Spread damage can be good in some instances when it releases stored strain energy and changes the natural frequencies, preventing concentrated damage that could cause extreme story drifts. Repairing fractured connections throughout a building that has its beams and columns remain essentially elastic is cheaper than demolishing a building that has localized plastification in a lower story and no fractures.

The damage levels resulting from strong motions can be dramatically different based on the model. A good example of this is the difference in response between the inelastic and fracture models of the 13-story building responding to the Tabas ground motion.

Fractures

The fractured connections of the 13-story building could easily have existed before the Northridge earthquake. The best match of measured data occurs when all the failed connections are pre-fractured.

For the 13-story building, it is not possible to match the data without considering size effects on the quality of welded connections. The building suffered many fractured connections in the lower story W36 girders, yet static analysis and inelastic time-history analysis do not predict such behavior. Even the strong pulse motions do not fracture these lower stories when using the $\theta_P = 0.02$ radians model.

Fractures can reduce the building response by releasing more energy than inelastic yielding of members can through hysteretic damping. For certain levels of excitation, fractures can result in lower permanent offsets. However, stronger ground motions can cause fracturing that produces drift levels far in excess of inelastic yielding behavior.

Fracture models have lower maximum base shears than the inelastic models, but not necessarily higher maximum drifts. The inelastic-model displacement response will not always be a lower bound to fracture-model response.

Panel Zones

Panel zones of the three buildings investigated have strengths exceeding the beam plastic moments, so plastic rotations are small and not a large contribution to the overall inelastic behavior.

Strong-Column/Weak-Beam Provisions

The 13-story building responses show that failing to meet the strong-column/weak-beam (SCWB) criterion does not mean column hinging will necessarily occur during inelastic response. The 10-story building responses show that meeting this code provision for static loading may not prevent column yielding. The SCWB criterion should be reassessed.

The yielding of column bases in all three buildings in response to strong ground pulses cannot be predicted with current code provisions. This behavior is better explained by considering the ground motion as a pulse travelling up the building.

Base Shear

For elastic and minimal inelastic response, increased damage *increases* drift with *rising* load levels. However, higher levels of damage increase damping and *lower* load levels while *reducing* displacement response levels.

The 10-story building did not collapse under any of the ground motions considered. Newer designs can survive ground motions while attracting more load.

Correlations

No correlation was observed between story drift and base shear, story drift and damage, or damage and base shear for either the inelastic or fracture models.

Even under damaged conditions as severe as collapse, the base shear correlates reasonably well with the inverse of the fundamental period. Beyond a certain level of inelastic behavior, the base shear is saturated. A wide range of damage levels can exist for relatively constant maximum base shear, so it is a poor indicator of building response.

Larger period buildings correlate best with peak displacement parameters of ground motions. Medium period buildings correlate best with peak velocity parameters. The code is based on accelerations, which are the best match for shorter period buildings.

Code Issues

Pulses and random or quasi-periodic ground motion may appear to have the same pseudo-spectral accelerations used in response spectrum design even though the pulse can sometimes be much more damaging.

The maximum story drift occurs in each of the three buildings for different records. Since drift does not correlate well with base shear or other ground motion

parameters, one cannot predict which record will be the most damaging for each building.

Local damage does not correlate with code provisions that are based on first mode response, indicating a need to include higher-mode response in future revisions to the code.

The 1997 UBC will not necessarily produce safer tall buildings. The buildings will definitely be stiffer and possibly stronger, but designers may end up using larger section sizes more susceptible to fracture. Stiffer buildings will attract more load, which may be more problematic if the building does not have a corresponding increase in strength.

12.2 Final Remarks

It is the author's strong belief that nonlinear time history analysis is the only tool available that can properly assess three-dimensional response of buildings to extreme ground motions. Little correlation between design response parameters and damage indicators was observed in this work. The author would like to see code provisions adopted that require such analyses for tall buildings located in the near-field of fault zones.

12.3 Future Work

Areas that require further study are listed below.

- Look at buildings in which panel zones are weaker than beams to assess the inelastic response of such existing buildings.
- Explore eccentrically braced frames and other systems that depend on fuse mechanisms to dissipate energy. Determine their behavior for extreme ground motions that may invalidate the design philosophy.
- Further development of simplified techniques to examine ground motions as waves travelling through buildings. These techniques can be corroborated

with use of this program and may provide more information about structural behavior than other code-accepted techniques such as pushover and response spectrum analysis.

- Perform a parametric study of realistic irregular buildings with varying distances between the center of mass and center of rigidity. Most existing studies are on regular buildings with eccentric mass. Studies of realistic buildings will be beneficial to future design.

- Perform a parametric study of near-source pulse ground motions. Much of the damage observed in the building investigations occurred during the first five seconds of ground motions. Code-specified pulses in conjunction with other existing provisions may limit the need for multiple nonlinear time history analyses to adequately predict near-source behavior.

- Add additional elements to the program that can model base isolators, friction pendula, unbonded braces, and other dissipative devices that are gaining use in seismic applications.

- Improve modeling of soil-structure interaction. Currently, a bilinear spring with kinematic hardening and different yield levels for compression and tension is being used.

Appendix A

Recorded Motions

Ground motions used in this report were recorded during the 1994 Northridge earthquake, the 1995 Great Hanshin earthquake and the 1978 Tabas, Iran earthquake. Additionally, ground motions from an Elysian Park simulation are used. In all cases, corrected accelerations were used with constant time steps. Ground motions with time steps other than 0.02 seconds were decimated using MATLAB. The table below provides pertinent information of each ground motion used and includes the two roof records used.

Each ground motion is presented graphically in the following figures. The corrected recorded ground acceleration for east-west (E-W) and north-south (N-S) motions are plotted. Velocity and displacement histories are integrated assuming constant acceleration time steps. Some de-trending is performed in these integrations. The maximum and minimum of acceleration, velocity and displacement are given on their respective plots. The ground acceleration records are used to calculate response spectra for 5% damping. The pseudo accelerations are plotted, including the maximum value and the values which coincide with the three building fundamental periods, denoted T_{17}, T_{13} and T_{10}. Each plot type — acceleration, velocity, displacement, response spectrum — uses the same total scale for each ground motion to facilitate comparisons between the various records. Some axes are shifted, but the scale is the same.

Recorded Motion	Reference	Time Step (sec)	Notes
Oxnard #4	Darragh et al. 1994	0.02	13-Story basement and roof
Canoga #2	Darragh et al. 1994	0.02	17-Story roof only
Canoga	USC 1994	0.02	Free field near above buildings
Sylmar	Darragh et al. 1994	0.02	Parking lot free field
Rinaldi	Chen and Iwan 1994	0.005	Largest Northridge ground motion
E.P. D05	Wald 1994	0.02	Velocity converted to acceleration
E.P. G05	Wald 1994	0.02	Velocity converted to acceleration
E.P. J06	Wald 1994	0.02	Velocity converted to acceleration
Tabas	Tabas 1978	0.02	Used in SAC studies
Takatori	Kobe 1995	0.01	Strong periodic motion from Kobe
Kobe JMA	Kobe 1995	0.02	
Kobe NGT	Kobe 1995	0.01	

Table A.1 Summary of recorded motions used in this work.

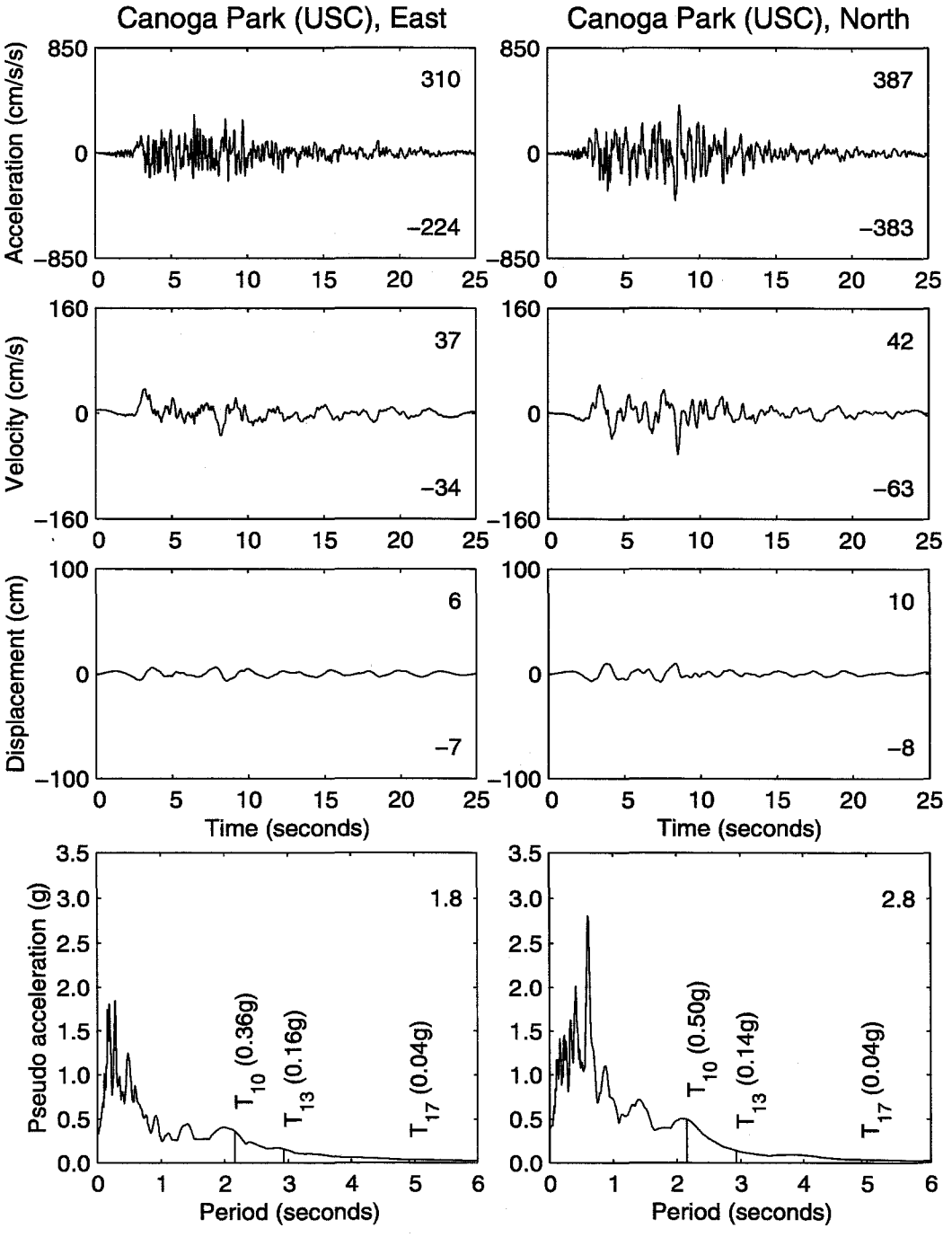

Figure A.1 Canoga Park record parameters.

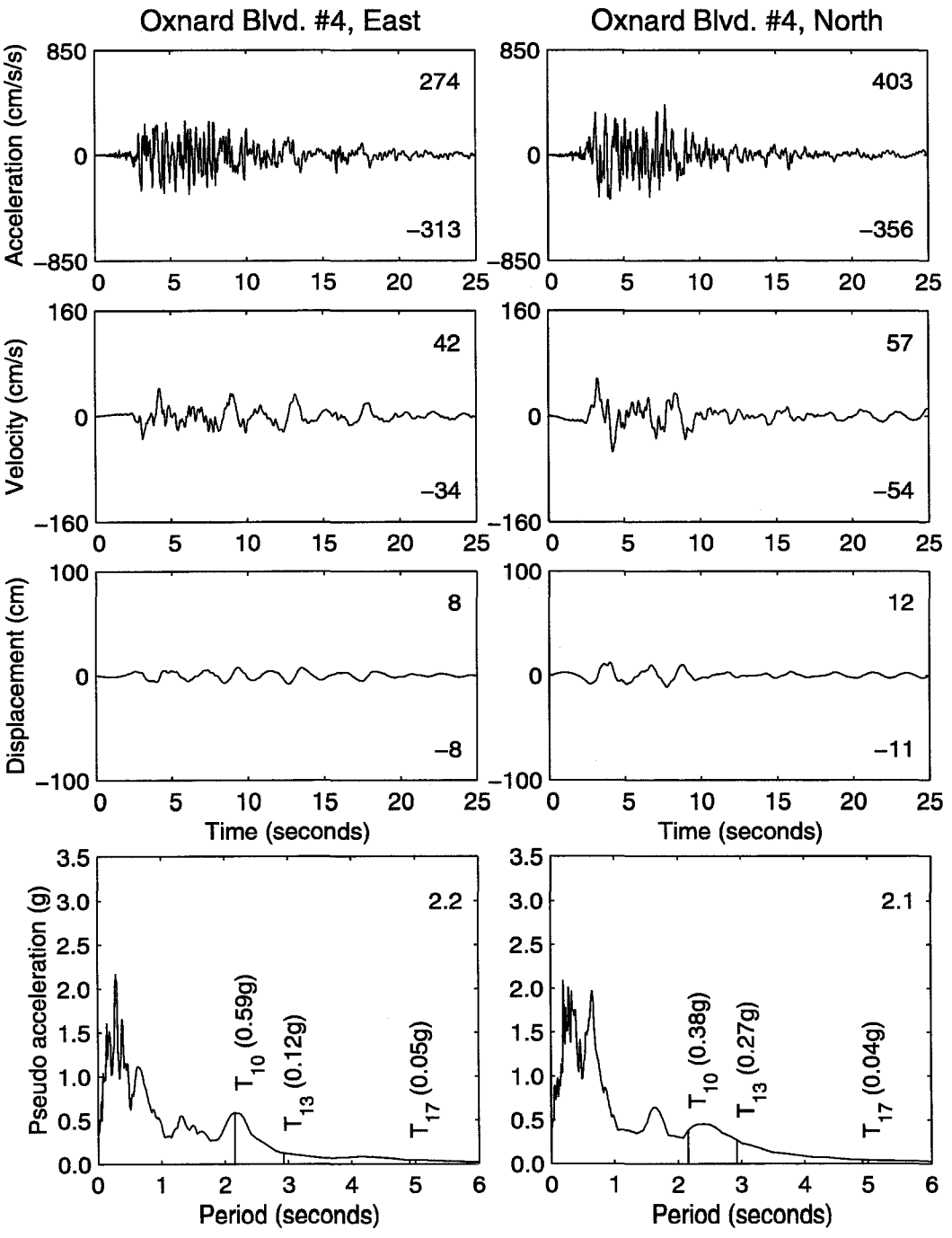

Figure A.2 Oxnard Blvd. #4 record parameters.

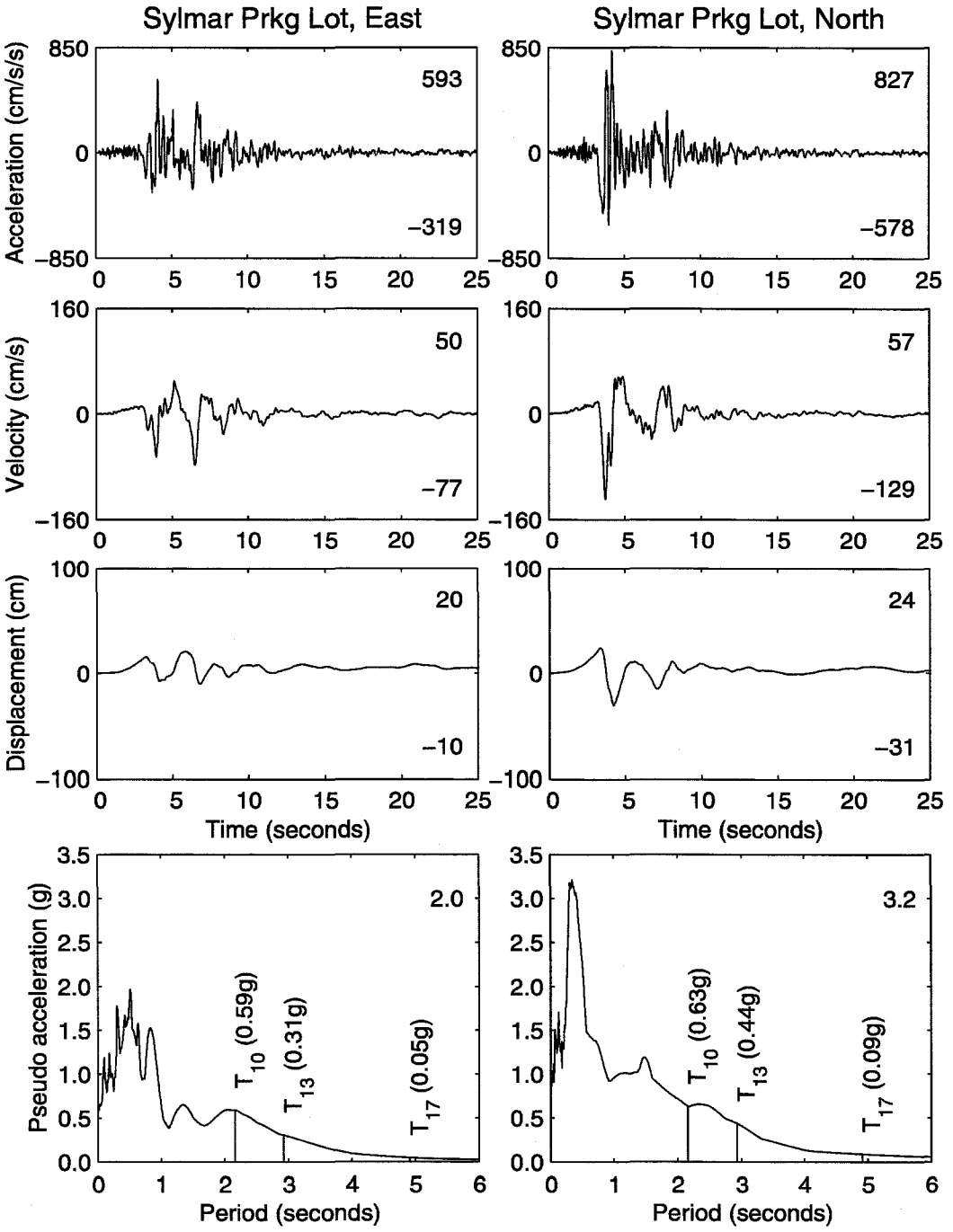

Figure A.3 Sylmar parking lot record parameters.

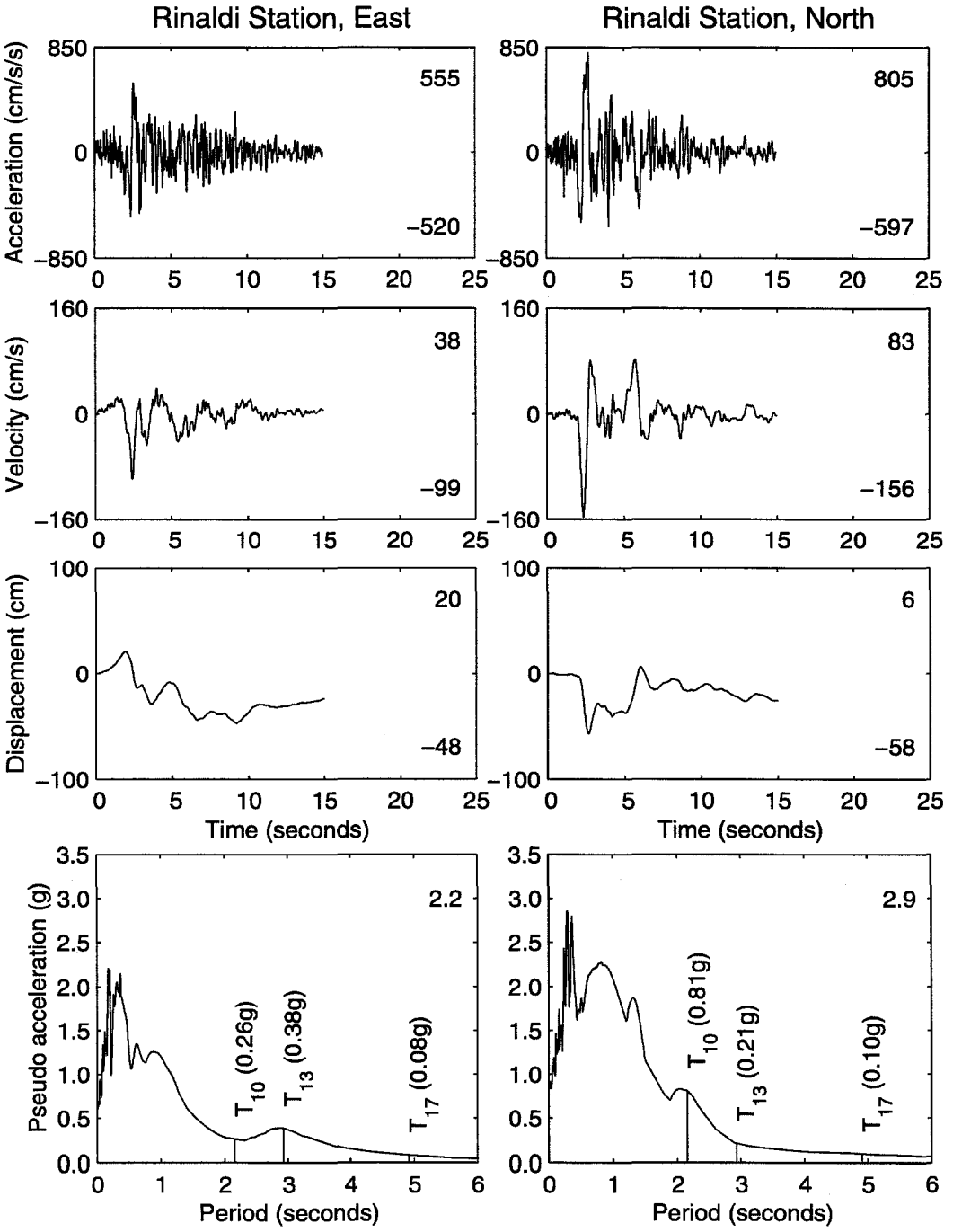

Figure A.4 Rinaldi Station record parameters.

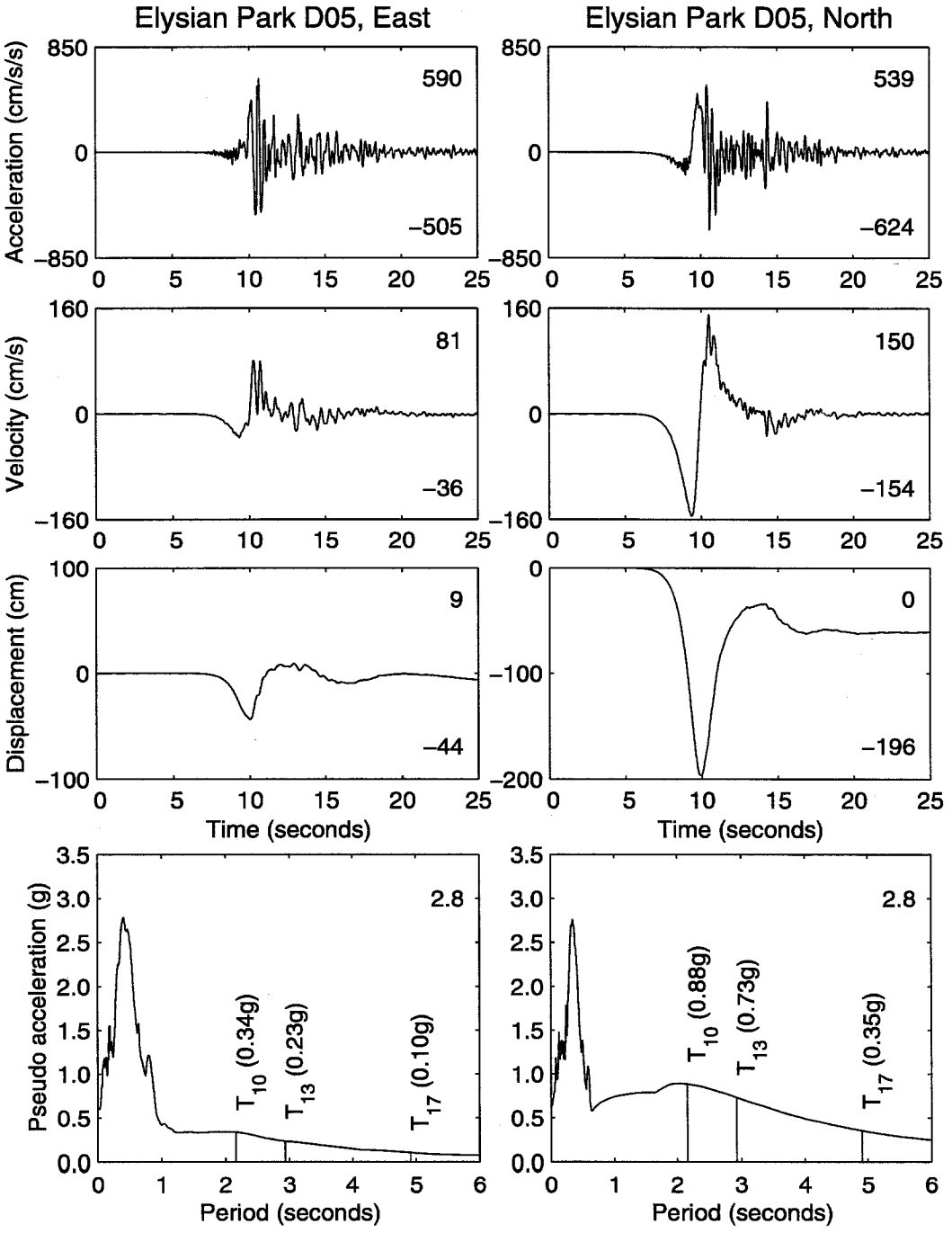

Figure A.5 Elysian Park, D05 simulated record parameters.

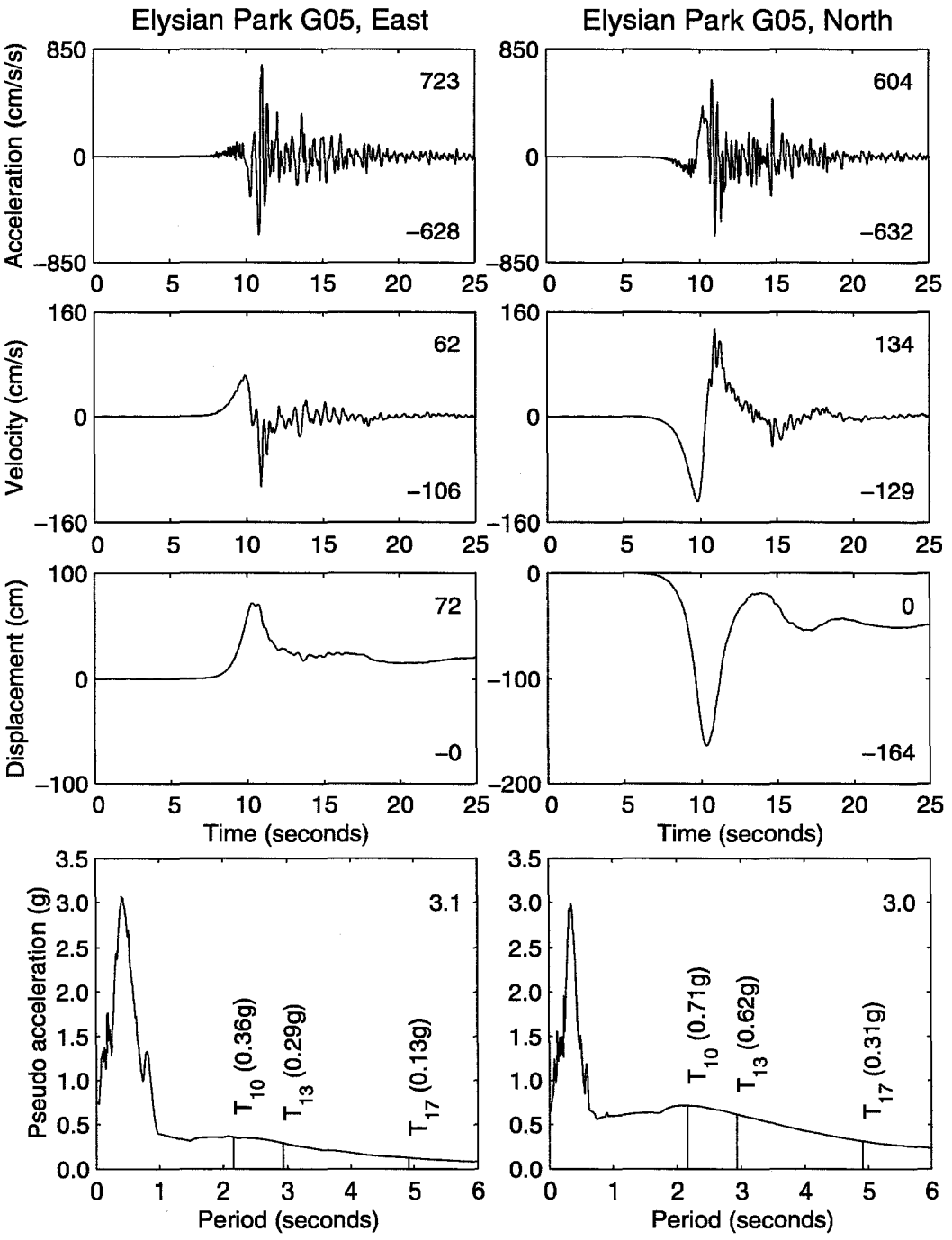

Figure A.6 Elysian Park, G05 simulated record parameters.

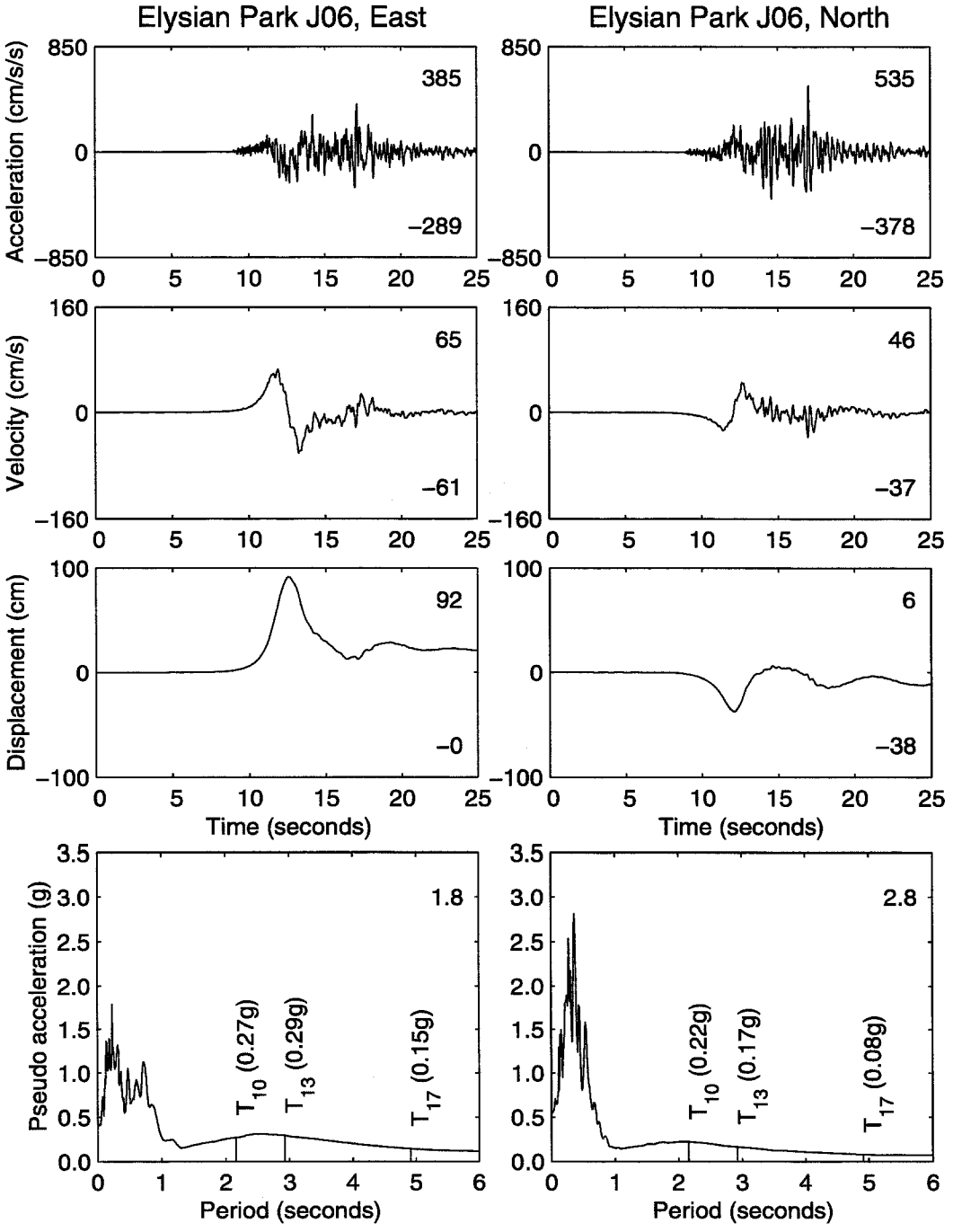

Figure A.7 Elysian Park, J06 simulated record parameters.

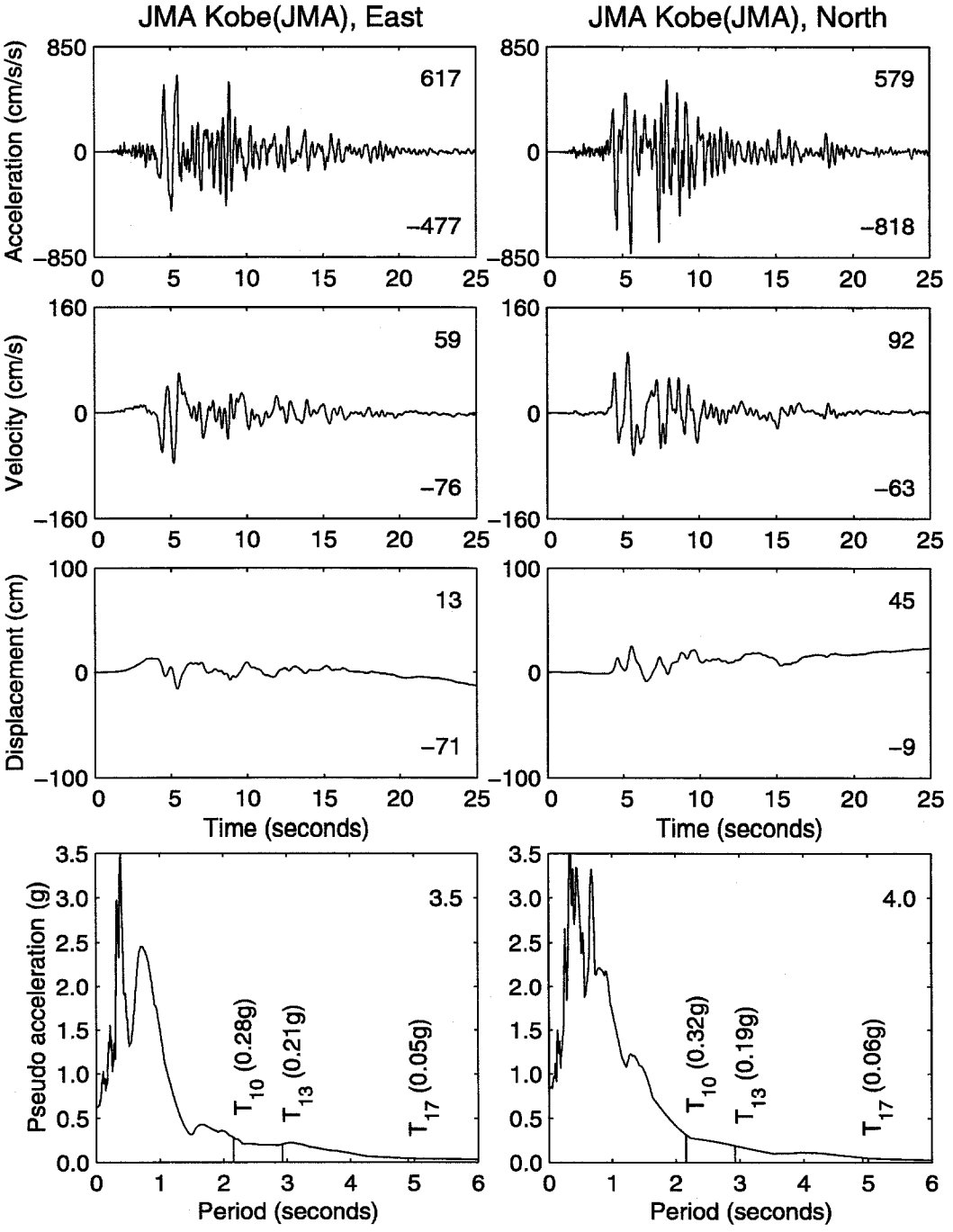

Figure A.8 Kobe JMA record parameters.

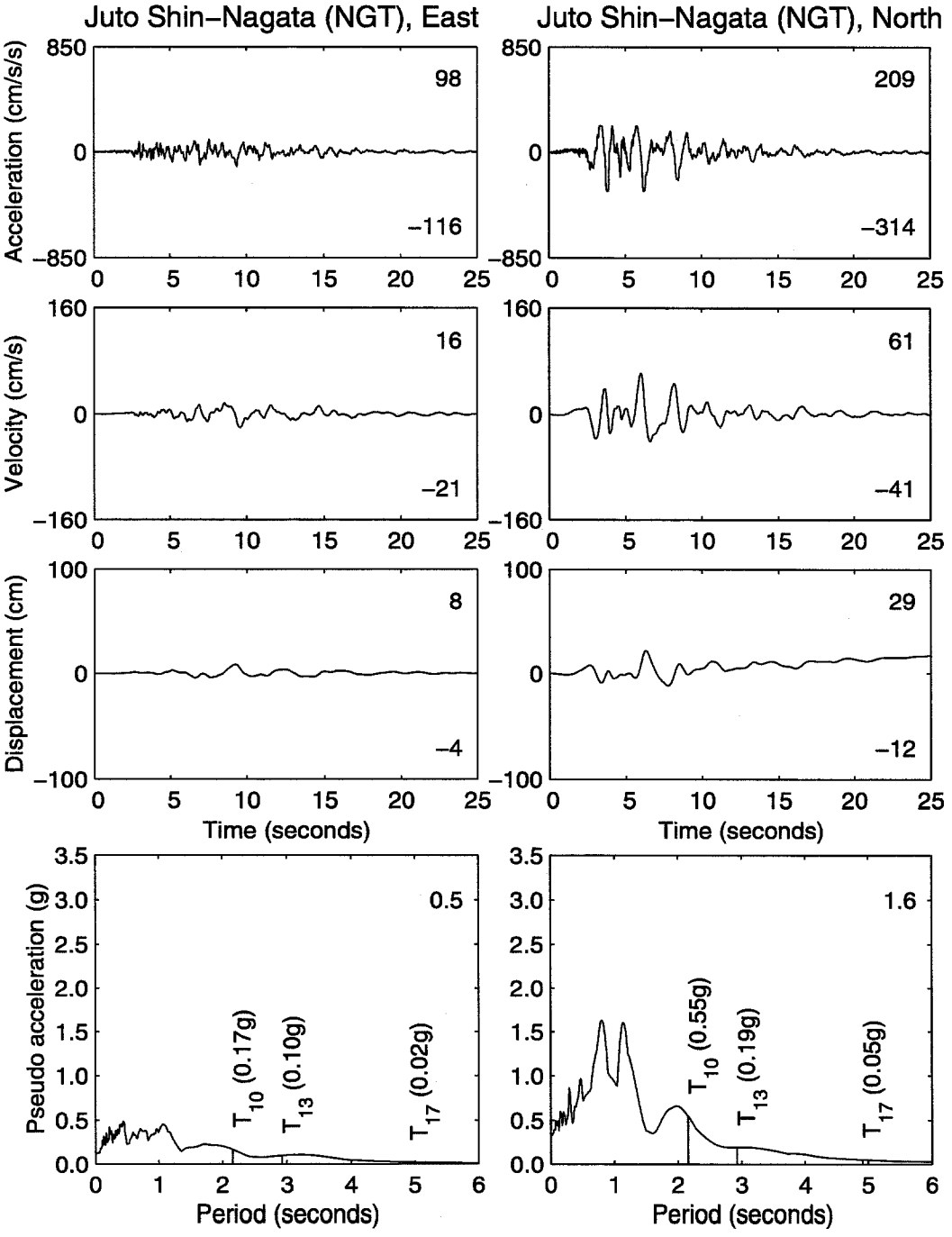

Figure A.9 Kobe NGT record parameters.

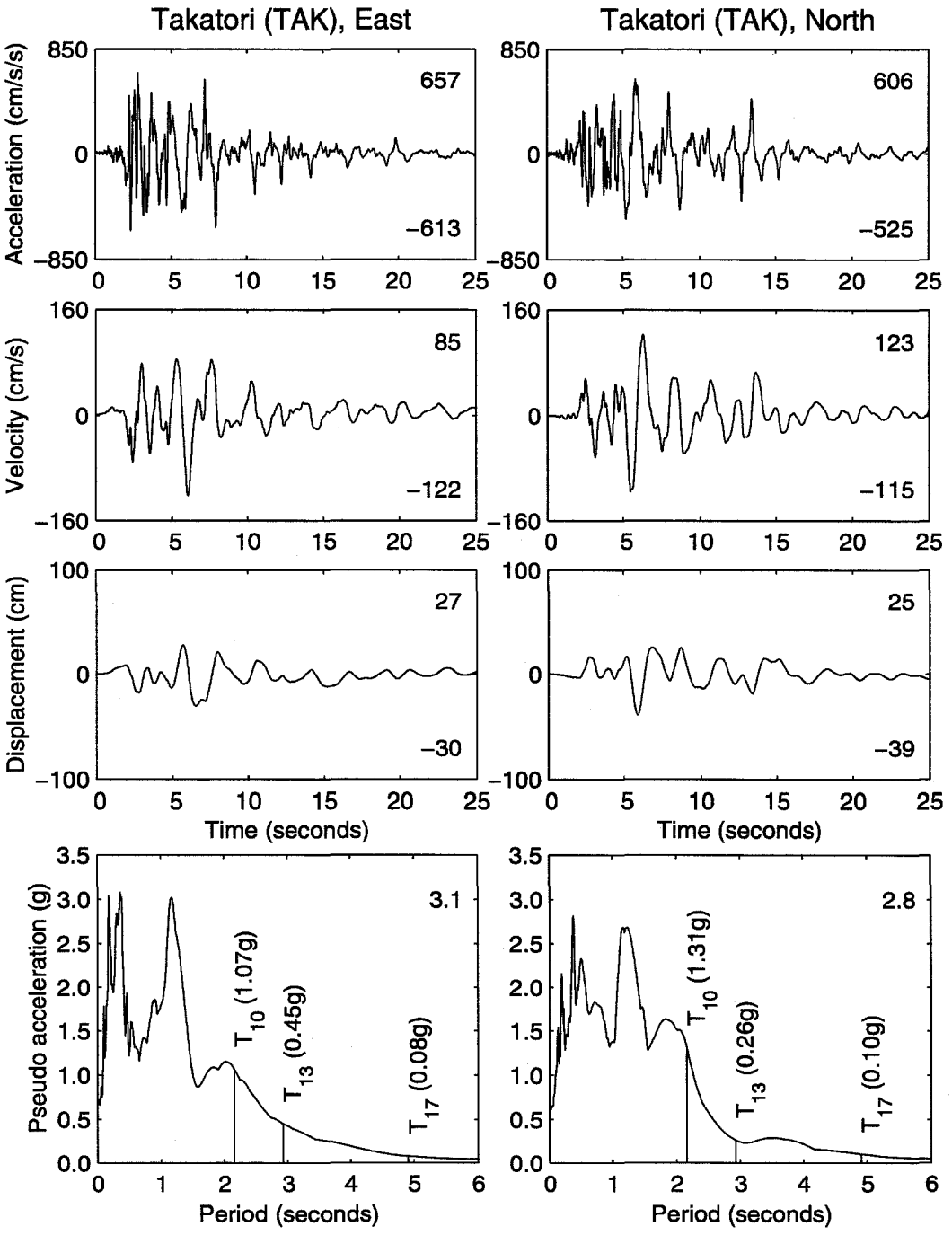

Figure A.10 Kobe TAK record parameters.

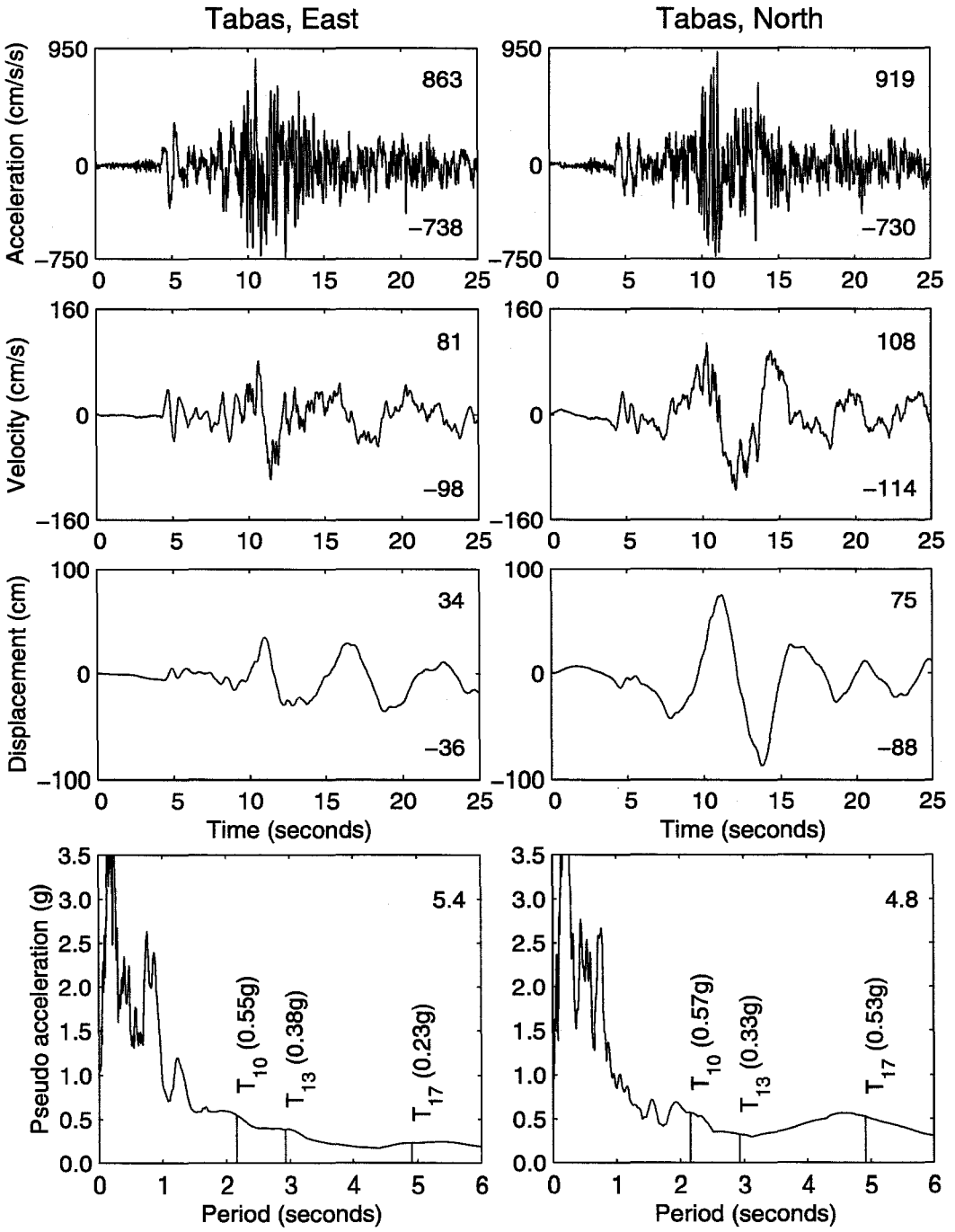

Figure A.11 Tabas record parameters.

Bibliography

AISC (1989). *Manual of Steel Construction, Allowable Stress Design* (Ninth ed.). American Institute of Steel Construction, Inc.

Allahabadi, R. and G. H. Powell (1988, March). DRAIN-2DX User Guide. Technical Report No. UCB/EERC 88-06, Earthquake Engineering Research Center, University of California, Berkeley.

Anderson, J. C. and V. V. Bertero (1987). Uncertainties in Establishing Design Earthquakes. *Journal of Structural Engineering 113*(8), 1709–1724.

Anderson, J. C. and F. C. Filippou (1995). Dynamic Response Analyses of a 17-Story Building. Technical Report SAC 95-04, Part 2, Chapter 12, SAC Joint Venture.

Attalla, M. R., G. G. Deierlein, and W. McGuire (1994). Spread of Plasticity: Quasi-Plastic-Hinge Approach. *Journal of Structural Engineering 120*(8), 2451–2473.

Bathe, K. J. (1996). *Finite Element Procedures.* Prentice-Hall, Inc.

Bertero, V. V., J. C. Anderson, and H. Krawinkler (1994). Performance of Steel Building Structures During the Northridge Earthquake. Technical Report No. UCB/EERC 94-09, Earthquake Engineering Research Center, University of California, Berkeley.

Bertero, V. V., S. A. Mahin, and R. A. Herrara (1978). Aseismic Design Implications of Near-Fault San Fernando Earthquake Records. *Earthquake Engineering & Structural Dynamics 6*, 31–42.

Bruneau, M., C.-M. Uang, and A. Whittaker (1998). *Ductile Design of Steel Structures.* McGraw-Hill, Inc.

Carlson, A. E. and J. F. Hall (1997). Three-Dimensional Analysis of a Tall Building Under Northridge Earthquake. In *Proceedings of the NEHRP Conference and Workshop on Research on the Northridge, California Earthquake of January 17, 1994*, Volume III-A, pp. 330–337. CUREe.

Challa, V. R. M. (1992, June). Nonlinear Seismic Behavior of Steel Planar Moment Resisting Frames. Technical Report No. EERL 92-01, Earthquake Engineering Research Laboratory, California Institute of Technology, Pasadena.

Challa, V. R. M. and J. F. Hall (1994). Earthquake Collapse Analysis of Steel Frames. *Earthquake Engineering & Structural Dynamics 23*(11), 1199–1218.

Chen, W. F. and T. Atsuta (1977). *Theory of Beam-Columns, Volume 2: Space behavior and design.* McGraw-Hill, Inc.

Chen, X. D. and W. D. Iwan (1994). Rinaldi Station Corrected Record.

Chi, W.-M. (1996, August). Inelastic Analyses of a High-Rise Steel Moment-Frame Building Damaged in the Northridge Earthquake. Master's thesis, Cornell University.

Chi, W.-M., S. El-Tawil, G. G. Deierlein, and J. F. Abel (1996). Inelastic Analyses of a 17 Story Steel Framed Building Damaged During Northridge. *Engineering Structures.* Accepted for publication.

Chopra, A. K. (1995). *Dynamics of Structures: theory and applications to earthquake engineering.* Prentice-Hall, Inc.

Clough, R. W. and J. Penzien (1993). *Dynamics of Structures* (Second ed.). McGraw-Hill, Inc.

Cook, R. D., D. S. Malkus, and M. E. Plesha (1989). *Concepts and Applications of Finite Element Analysis* (Third ed.). John Wiley & Sons.

Darragh, R., T. Cao, C. Cramer, M. Huang, and A. Shakal (1994, February). Processed CSMIP Strong-Motion Records from the Northridge, California Earth-

quake of January 17, 1994: Release No. 1. Technical Report No. OSMS 94-06B, California Strong Motion Instrumentation Program, Sacramento.

Darragh, R., T. Cao, V. Graizer, A. Shakal, and M. Huang (1994, December). Los Angeles Code-Instrumented Building Records from the Northridge, California Earthquake of January 17, 1994: Processed Release No. 1. Technical Report No. OSMS 94-17, California Strong Motion Instrumentation Program, Sacramento.

El-Tawil, S. and G. G. Deierlein (1996). Inelastic Dynamic Analysis of Mixed Steel-Concrete Space Frames. Technical Report Structural Engineering No. 96-05, Cornell University, Ithaca, NY.

Engelhardt, M. D. and A. S. Husain (1993, December). Cyclic-Loading Performance of Welded Flange-Bolted Web Connections. *Journal of Structural Engineering 119*(12), 3537–3550.

Englekirk, R. (1994). *Steel Structures: Controlling Behavior Through Design.* John Wiley & Sons, Inc.

Filippou, F. C. (1995). Nonlinear Static and Dynamic Analysis of a 17-Story Building with FEAP-STRUC. Technical Report SAC 95-04, Part 2, Chapter 11, SAC Joint Venture.

Goel, R. K. and A. K. Chopra (1997, December). Vibration Properties of Buildings Determined from Recorded Earthquake Motions. Technical Report No. UCB/EERC 97-14, Earthquake Engineering Research Center, University of California, Berkeley.

Hall, J. F. (1995). Parameter Study of the Response of Moment-Resisting Steel Frame Buildings to Near-Source Ground Motions. Technical Report No. EERL 95-08, Earthquake Engineering Research Laboratory, California Institute of Technology, Pasadena.

Hall, J. F. (1997). Seismic Response of Steel Frame Buildings to Near-Source Ground Motions. Technical Report No. EERL 97-05, Earthquake Engineering Research Laboratory, California Institute of Technology, Pasadena.

Hall, J. F. (1998). Seismic Response of Steel Moment Frame Buildings to Near-source Ground Motions. *Earthquake Spectra*. Accepted for publication.

Hall, J. F. and A. E. Carlson (1998). Collapse Analysis for Buildings Subjected to Extreme Ground Motions. In *Proceedings of the 1998 Structural Engineers World Congress*. ASCE.

Hall, J. F. and V. R. M. Challa (1995). Beam-Column Modeling. *Journal of Engineering Mechanics ASCE 121*(12), 1284–1291.

Hall, J. F., T. H. Heaton, M. W. Halling, and D. J. Wald (1995). Near-Source Ground Motion and Its Effects on Flexible Buildings. *Earthquake Spectra 11*(4), 569–605.

Hallquist, J. O. (1988). DYNA3D User's Manual (Nonlinear Dynamic Analysis of Solids in Three Dimensions). Technical Report No. UCID-19156, Rev. 4, University of California, Lawrence Livermore National Laboratory.

Heaton, T. H. (1995, January). Class Notes, CE180, Caltech.

Heaton, T. H. (1997). Urban Earthquakes. *Seismological Research Letters 66*(5), 37–40.

Heaton, T. H., J. F. Hall, D. J. Wald, and M. W. Halling (1995). Response of Highrise and Base-isolated Buildings to a Hypothetical M(W)7.0 Blind Thrust Earthquake. *Science 267*(5195), 206–211.

ICBO (1973). *Uniform Building Code* (1973 ed.). Whittier, CA: International Conference of Building Officials.

ICBO (1982). *Uniform Building Code* (1982 ed.). Whittier, CA: International Conference of Building Officials.

ICBO (1994). *1994 Uniform Building Code*, Volume 2. Whittier, CA: International Conference of Building Officials.

ICBO (1997). *1997 Uniform Building Code*, Volume 2. Whittier, CA: International Conference of Building Officials.

Kato, B. (1982). Beam-to-Column Connection Research in Japan. *Journal of the Structural Division ASCE 108*(12), 343–360.

Kobe (1995). Kobe corrected records from various stations. Received via e-mail from John Hall.

Krawinkler, H., A. Alali, C. C. Thiel, and J. M. Dunlea (1995). Analysis of a Damaged 4-Story Building and an Undamaged 2-Story Building. Technical Report SAC 95-04, Part 1, Chapter 3, SAC Joint Venture.

Lobo, R. F. (1994). Inelastic Dynamic Analysis of Reinforced Concrete Structures in Three Dimensions IDARC-3D. Technical report, State University of New York at Buffalo, Buffalo, NY.

Lobo, R. F., M. J. Skokan, S. C. Huang, and G. C. Hart (1998). don't know. In *1998 Annual Meeting of the Los Angeles Tall Buildings Structural Design Council*, pp. 69–82. LATBSDC.

Maison, B. F. and K. Kasai (1997). Analysis of Northridge Damaged Thirteen-Story WSMF Building. *Earthquake Spectra 13*(3), 451–473.

McGuire, W. (1968). *Steel Structures.* Prentice-Hall, Inc.

McGuire, W. and R. H. Gallagher (1979). *Matrix Structural Analysis.* John Wiley & Sons, Inc.

Naeim, F. (1997). Research Overview: Seismic Response of Structures. In *Proceedings of the NEHRP Conference and Workshop on Research on the Northridge, California Earthquake of January 17, 1994*, Volume III-A, pp. 1–23. CUREe.

Paret, T. F. and K. K. Sasaki (1995). Analysis of a 17-Story Steel Moment Frame Building Damaged by the Northridge Earthquake. Technical Report SAC 95-04, Part 2, Chapter 10, SAC Joint Venture.

Popov, V. V., N. R. Amin, J. J. C. Louie, and R. M. Stephen (1985). Cyclic Behavior of Large Beam-Column Assemblies. *Earthquake Spectra 1*(2), 203–238.

Popov, V. V. and R. M. Stephen (1970, July). Cyclic Loading of Full-Size Steel

Connectons. Technical Report No. UCB/EERC 70-3, Earthquake Engineering Research Center, University of California, Berkeley.

Prakash, V., G. H. Powell, and S. Campbell (1994). DRAIN-3DX: Base Program Description and User Guide, Version 1.10. Technical Report No. UCB/SEMM 94/07, Department of Civil Engineering, University of California, Berkeley.

Prakash, V., G. H. Powell, and F. C. Filippou (1992). DRAIN-2DX: Base Program User Guide. Technical Report No. UCB/SEMM 92/09, Department of Civil Engineering, University of California, Berkeley.

Roeder, C. W. (1997). Overview of Post Northridge Research on Steel Buildings. In *Proceedings of the NEHRP Conference and Workshop on Research on the Northridge, California Earthquake of January 17, 1994*, Volume III-A, pp. 30–43. CUREe.

SAC (1994, November). Invitational Workshop on Steel Seismic Issues, Proceedings. Technical Report No. 94-01, SAC Joint Venture.

SAC (1995). Analytical and Field Investigations of Buildings Affected by the Northridge Earthquake of January 17, 1994. Technical Report SAC 95-04, SAC Joint Venture.

SAC (1997a, June). Connection Test Summaries. Technical Report FEMA 289, Federal Emergency Management Agency.

SAC (1997b, March). Interim Guidelines—Advisory No. 1. Technical Report FEMA 267a, Federal Emergency Management Agency.

SAC (1998). Update on the Seismic Safety of Steel Buildings. Technical report, FEMA and SAC Joint Venture.

Şafak, E. (1997). Propagation of Seismic Waves in Tall Buildings. In *Fourth Conference on Tall Buildings in Seismic Regions*, pp. 69–82. LATBSDC.

SEAOC (1990). *Recommended Lateral Force Requirements and Commentary.* Seismological Committee, Structural Engineers Association of California.

Tabas (1978). Tabas Station Corrected Record. Received via e-mail, record used in SAC 95-04 studies.

Taucer, F., E. Spacone, and F. C. Filippou (1991). A Fiber Beam-Column Element for Seismic Response Analysis of Reinforced Concrete Structures. Technical Report No. UCB/EERC 91/17, Earthquake Engineering Research Center, University of California, Berkeley.

Tsai, K. C. and E. P. Popov (1988, November). Steel Beam-Column Joints in Seismic Moment Resisting Frames. Technical Report No. UCB/EERC 88-19, Earthquake Engineering Research Center, University of California, Berkeley.

Uang, C.-M., Q.-S. Yu, A. Sadre, D. Bonowitz, and N. Youssef (1995). Performance of a 13-Story Steel Moment-Resisting Frame Damaged in the 1994 Northridge Earthquake. Technical Report SAC 95-04, Part 2, Chapter 7, SAC Joint Venture.

Uang, C.-M., Q.-S. Yu, A. Sadre, D. Bonowitz, N. Youssef, and J. Vinkler (1997). Seismic Response of an Instrumented 13-Story Steel Frame Building Damaged in the 1994 Northridge Earthquake. *Earthquake Spectra 13*(1), 131–149.

USC (1994). Canoga Park Corrected Record. Received via e-mail from Nancy Smith.

Wakabayashi, M. (1986). *Design of Earthquake-Resistant Buildings.* Prentice-Hall, Inc.

Wald, D. J. (1994). Elysian Park Simulation. Received via e-mail from David Wald.

Weaver, W. and M. F. Nelson (1966). Three-Dimensonal Analysis of Tier Buildings. *Journal of the Structural Division ASCE 92*(ST6), 385–404.

Wilson, E. L. (1997). *Three Dimensional Analysis of Structures with Emphasis on Earthquake Engineering.* Computers and Structures, Inc.

Wilson, E. L. and R. Allahabadi (1975, March). (Extended) TABS. Technical Report No. UCB/EERC 75-13, Earthquake Engineering Research Center, Uni-

versity of California, Berkeley.

Wilson, E. L. and A. Habibullah (1987). Static and Dynamic Analysis of Multi-Story Buildings, Including P-Delta Effects. *Earthquake Spectra 3*(2), 289–298.

Xue, M., E. J. Kaufmann, L.-W. Lu, and J. W. Fisher (1997). Fracture and Ductility of Welded Moment Connections Under Dynamic Loading. In *Proceedings of Structures Congress XV*, Volume 1, pp. 607–613. ASCE.

Yang, Y.-B. and S.-R. Kuo (1994). *Theory & Analysis of Nonlinear Framed Structures*. Prentice-Hall, Inc.